

An Experimental Study of Effects of Egg Shell and Snail Shell Powder on Rheological and Filtration Properties of Potassium Chloride Polymer Drilling Fluids

Olugbenga Olamigoke¹, Toritseju T. Aghante¹, Felix Iyalla²

¹ *Department of Chemical and Petroleum Engineering, University of Lagos, Nigeria*

² *Department of Petroleum Engineering, Covenant University, Ota, Ogun State, Nigeria*

Received April 23, 2019; Accepted July 22, 2020

Abstract

In this paper, the effect of two potential drilling fluid bio-additives, egg shell, and snail shell powders, on the rheological and filtration properties of 11ppg potassium chloride (KCl) polymer drilling fluid samples as determined experimentally is analyzed. The control mud sample was formulated with bentonite, caustic soda, xanthan gum, potato starch, potassium chloride, and barite in water. Rheology and filtration experiments were conducted at room temperature for the control mud sample and ten samples in which potato starch was replaced with either egg shell or snail shell powder at different concentrations - 2g, 5g, 10g, 15g, and 20g. Five additional 11ppg KCl-polymer mud samples, one with the control mud formulation and samples with 2g eggshell, 5g eggshell, 2g snail shell, and 5g snail shell powder respectively, were aged for 16 hours in a roller oven at 250°F prior to the rheology and filtration experiments.

The results obtained at 120°F show that 2g and 5g concentration of the bio-additives further decreased the 15cp control sample plastic viscosity by an average of 34%, which was within expected limits, while the yield point, which was 62% above typical values, was decreased with 2g and 5g concentration of egg shell powder by 8% and 15% respectively. A 10% decrease in yield point was observed with 5% snail shell powder concentration. The 10 min. gel strength was decreased to expected typical values for 2g egg shell powder, 5g egg shell powder, and 5g snail shell powder by 7%, 7%, and 11%, respectively. The filtrate loss was minimized by 2g egg shell powder and 5g snail shell powder to 23mL and 24mL from 25mL for the control sample. The addition of 2g egg shell powder resulted in a cake thickness less than 0.1mm. The results show that on aging and at room temperature, eggshell and snail shell powder at 2g and 5g, respectively, can serve as a good substitute for conventional additives in improving the rheological and filtration properties of KCl-polymer drilling fluid. However, only 2g egg shell powder concentration can serve as a substitute in improving the filtration properties of the KCl-polymer mud as it had the best cake quality and least filtrate volume loss.

Keywords: *KCl-polymer drilling fluid; Egg shell powder; Snail shell powder; Rheological and filtration properties.*

1. Introduction

The need for drilling fluid systems, which are both environmentally friendly and effective for drilling through troublesome formations like sloughing shales, has led to several investigations into suitable plant extracts and agricultural wastes that can improve the rheological and filtration properties of water based drilling fluids. Oak seed extract [1] and black myrobalan [2] used at laboratory scale in water based mud as deflocculants, preserved the stability of bentonite in the presence of salts, reducing rheological parameters and fluid loss value. Some of the additives that have been evaluated and reported to be effective for minimizing fluid loss and mud cake thickness include rice husk ash [3], periwinkle shell ash [4], and corn cob cellulose [5].

The potential for using egg shell and snail shell powder as mud weight and pH enhancers for water based drilling mud has been investigated [6] with egg shell powder found more effective in enhancing water based drilling mud weight while snail shell powder more effective in pH enhancement. Both materials were compared because of their high calcium carbonate (CaCO₃) content with predominant minerals being aragonite and calcite in eggshell and snail

shells respectively. The rheological properties of water-based mud with pure calcium carbonate as a weighting agent were compared to samples prepared with calcium carbonate extracted from egg shells. Though higher amounts of CaCO₃ from egg shells were needed to achieve a mud weight of 10.5ppg as compared to mud formulated from pure CaCO₃, the rheological properties obtained for both formulations were similar [7].

The effect of calcium carbonate, a commonly used bridging agent on the rheological and filtration properties on water-based drilling fluids on drilling fluid compositions prepared for geothermal reservoirs, was evaluated by the addition of 10ppb calcium carbonate to different polymer suspensions. The formation of impermeable filter cake led to a decrease in filtration fluid loss; however, the calcium carbonate did not improve the rheological properties of the drilling fluid [8]. In a study to investigate the effect of different particle size distributions of calcium carbonate used as the bridging agent on the rheological properties of drill-in fluids made up of water, xanthan, starch, potassium hydroxide, and potassium chloride, it was found that the particle size distribution of the calcium carbonate did not change the rheological properties of the evaluated drill-in fluids. However, the filtration properties of the drill-in fluids depend on the permeability obtained from the permeability plugging tester discs [9].

Rheological and filtration experiments were performed to design a drilling fluid system for a stratum with carbonaceous slate. The requirement was to minimize fluid loss and enhance mud salinity. The results showed that for a potassium-based polymer, treatment with 1.5% calcium carbonate is an inexpensive but effective option for achieving good plugging effect and improved mud cake quality [10]. The aim of this paper is to experimentally investigate the effect of egg shell and snail shells on the rheological and filtration properties of 11.0 ppg KCl-polymer water-based mud.

2. Experimental section

2.1. Materials and instruments

The effect of egg shell powder and snail shell powder on the rheological and filtration properties of KCl-polymer water-based drilling mud was independently investigated. The control mud sample composition is shown in Table 1, while compositions for the samples treated with egg shell powder and snail shell powder are shown in Table 2 and Table 3, respectively. All drilling fluid samples were prepared on the basis of a pilot test volume of 350 mL, which is equivalent to one barrel of the actual system volume. The instruments used for the experiments include mud balance, pH meter, roller oven, aging cells, direct-indicating viscometer (Fann Model 35 6-Speed Viscometer), and standard filter press (low-temperature/low-pressure filtration apparatus).

Table 1. Control mud sample composition (11ppg)

Constituents	Concentration	Function
De-ionized water	304 mL	Base fluid
API bentonite	7 grams	Viscosifier
Caustic potash	0.25 grams	Alkalinity Control
Xanthan gum	1 gram	Viscosifier
Potato starch	4 grams	Filtration Control
Potassium chloride (KCl)	20 grams	Inhibition Source of K ⁺ ion
Barite	126 grams	Weighting agent

Table 2. Composition of Egg Shell Powder treated Mud Samples (11ppg)

Constituents	A	B	C	D	E
Water (mL)	305	303	299	295	291
API bentonite (g)	7	7	7	7	7
Caustic potash (g)	0.25	0.25	0.25	0.25	0.25
KCl (g)	20	20	20	20	20
Egg shell (g)	2	5	10	15	20
Barite (g)	128	127	126	125	124

Table 3. Composition of Snail Shell Powder treated Mud Samples (11ppg)

Constituents	F	G	H	I	J
Water (mL)	304	301	294	288	282
API bentonite (g)	7	7	7	7	7
Caustic potash (g)	0.25	0.25	0.25	0.25	0.25
KCl (g)	20	20	20	20	20
Egg shell (g)	2	5	10	15	20
Barite (g)	129	130	131	132	133

2.2. Methods

2.2.1. Preparation of egg shell (ES) and snail shell (SS) powders

Egg shells and snail shells were first extracted from boiled eggs and de-shelled snails, respectively. The extracted shells were crushed into smaller sizes; this ensured a large surface area for effective drying and ease of grinding. The broken shells were sun-dried for 3-5 days to remove water content. The dried samples were ground, using a manual grinder, and then stored in a clean petri-dish.

The ground samples were sieved using a sieve shaker, and particles retained on the 75 μ m mesh size (i.e., particle sizes between 150 μ m and 75 μ m) were stored for experimental use (for both ground samples). The specific gravity of the egg shell powder and snail shell powder for this particle size distribution was 1.17 and 0.84, respectively.

2.3. Procedure

The control mud sample was formulated with xanthan gum as a viscosifier to supplement the pre-hydrated bentonite and potato starch to provide filtration control in KCl-polymer drilling fluid. The recipes for all samples tested (the control samples and those with the bio-additives) were formulated to obtain a mud weight of 11ppg. The viscosity at varying shear rates (600rpm, 300rpm, 200rpm, 100rpm, and 6rpm) was measured using a six-speed direct-indicating viscometer. Gel strength readings were taken at the 3-rpm speed after allowing the sample to stand undisturbed for 10 seconds and then after 10 minutes. Filtration properties were obtained using a Standard filter press. The filtrate volume collected was measured using a measuring cylinder in milliliters over 30 minutes, while the thickness of the mud cake was measured to the nearest millimeter. The rheological and filtration experiments were conducted for ten samples (A-J) according to API specifications [11]. Five samples of 11ppg KCl-polymer drilling fluid had egg shell powder in weight proportions ranging from 2g to 20g (samples A-E) while five additional samples (samples F-J) had snail shell powder in similar weight proportions of 11ppg KCl-polymer drilling fluid (2g, 5g, 10g, 15g, and 20g). These bio-additives were used in place of the potato starch. Five samples, the control mud, a sample with 2g egg shell powder, 2g snail shell powder, 5g egg shell powder, and a sample containing 5g snail shell powder, were aged for 16 hours and at a temperature of 250°F in a roller oven. Rheology and filtration experiments were then conducted on the aged samples. Plastic viscosity (PV) was obtained from the difference in the viscometer dial readings at 600 and 300 rpm while the yield point (YP) was obtained by subtracting the PV value from the 300-rpm reading. The pH range for the samples was 8.8–10.5, with the pH increasing with increasing bio-additive concentration.

The performance of the mud samples was benchmarked against typical rheological and filtration properties for KCl-polymer mud with mud weight of 10 to 11 ppg at 120°F, which includes a plastic viscosity range of 15 to 25 cp, yield point between 7 and 15 lb/100 ft², 10 sec. The gel strength of 2 to 8 cp, 10 min. The gel strength of 8 to 15 cp, and API filtrate of 5 to 8 mL/30 min.

3. Results and discussion

3.1. The effect of varying additive concentration on mud rheology

The measured PV and YP values for the control sample at ambient conditions are 19 cp and 39 lb/100 ft², respectively. While the PV value was within the expected range, the YP value

obtained was much higher than typical values. The general trend observed with the addition of either egg shell powder or snail shell powder, as shown in Figure 1, is the decrease in both PV and YP for 2g and 5g concentration. For the samples with 10g of the bio-additives, PV and YP values are close to control sample measured values. A decrease in PV values with a corresponding increase in YP was observed for samples with 15g and 20g concentration of the bio-additives. At 20g concentration, the PV values are below the expected minimum values (53% and 68% below the control PV value for egg shell powder and snail shell powder, respectively) while the YP values exceeded the control sample values by 46% and 51% for egg shell powder and snail shell powder respectively. This is indicative of high concentrations of colloidal solids. The PV values for 10g concentration were within the expected range, but the YP values were not. The optimal concentrations of bio-additives in terms of PV and YP are 2g of egg shell powder and 5g of snail shell powder.

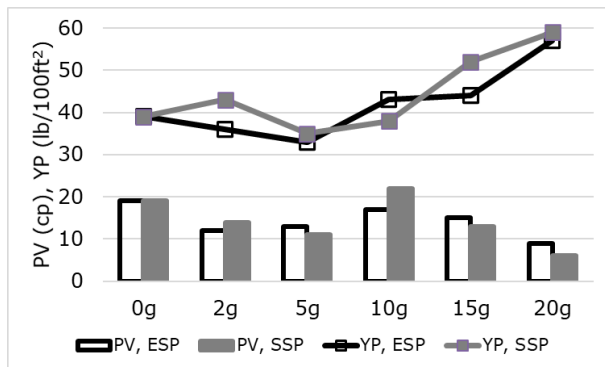


Figure 1. Effect of egg shell and snail shell powder on plastic viscosity and yield point at ambient conditions

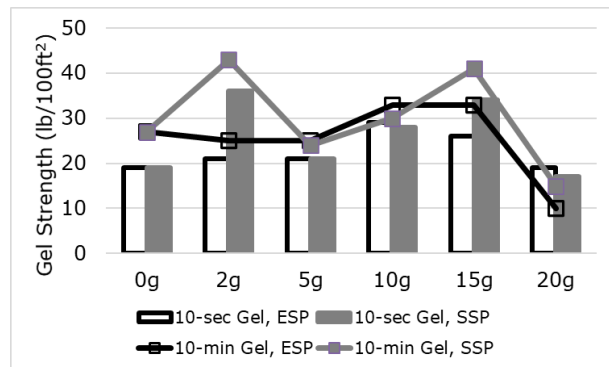


Figure 2. Effect of egg shell and snail shell powder on gel strength (10sec and 10min) at ambient conditions

The gel strength measured at 10 seconds and 10 minutes for the control fluid both exceeded the typical, expected values (19 and 27 lb/100 ft² as compared to 8 and 15 lb/100 ft²). Increasing concentrations of egg shell powder by 2g, 5g, 10g, and 15g in the KCl-polymer mud resulted in an increase in the 10 sec. gel strength by 11%, 11%, 53%, and 37%, respectively, compared to the control sample value. A similar trend was observed for snail shell powder except for an 89% in the 10 sec. gel strength for the sample with 2g concentration, as shown in Figure 2. The bio-additives dropped the 10 min. gel strength values for 2g and 5g egg shell powder and 5g snail shell powder by 7%, 7%, and 11%, respectively. As observed for the 10 sec. gel strength, at concentrations of 10g and 15g the 10 min. gel strength is increased further. It can be inferred that at 2g and 5g concentration, the bio-additives have a deflocculating effect on the KCl-polymer drilling fluid, while above 10g, the high colloidal content increases the gel strength. At 20g concentration of the bio-additives, the gel strength values were observed to unexpectedly decline below the measured values for the control samples at ambient conditions.

3.2. The effect of bio-additive concentration on filtration properties

For a mud formulated at 11ppg, a filtrate volume range of 5–8 mL/30min is typical. All samples tested, the control sample inclusive, had filtrate volume loss in excess of the typical values, as shown in Figure 3. The filtration properties of the KCl-polymer drilling fluid were improved by 2g of egg shell powder and 5g of snail shell powder with 8% and 4% reduction in filtrate loss, respectively. As expected, the general trend observed for bio-additive concentration of 10g and above is increasing filtrate loss with filtrate loss volume in excess of 160mL observed for 20g concentration.

A linear relationship between the bio-additive concentration (2-15 g) and mud cake thickness for 2g to 15g exists for both egg shell powder and snail shell powder. The mud cake

thickness increased by about 1000% over the control mud value of 0.1mm for the 20g concentration of the bio-additives. The sample with 2g egg shell powder concentration produced the best cake quality.

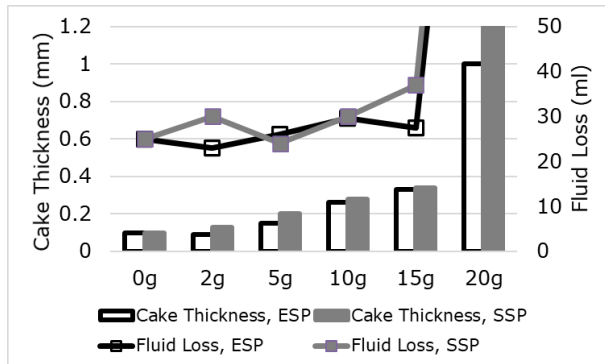


Figure 3. Effect of egg shell and snail shell powder on fluid loss and filter cake thickness at ambient conditions

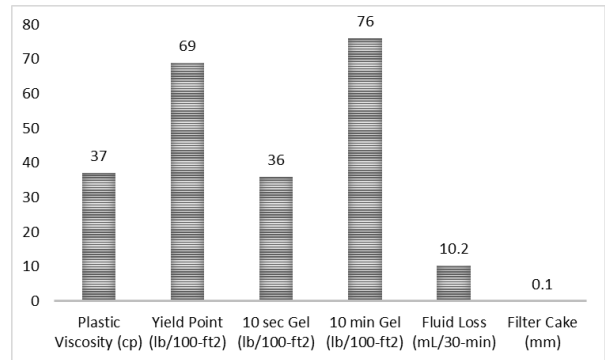


Figure 4. Rheological and Filtration properties for the aged control sample

3.3. The effect of bio-additives on aged samples

Following the rheological and filtration experiments carried out at ambient conditions, two concentrations (2g and 5g) were investigated further. The rheological and filtration properties for aged samples based on the control mud recipe, 2g bio-additive concentration, and 5g bio-additive concentration are presented in Figure 4, Figure 5, and Figure 6, respectively.

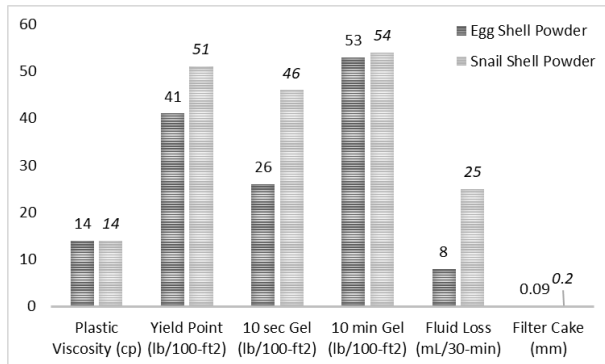


Figure 5. Rheological and Filtration properties for 2g bio-additive concentration (aged samples)

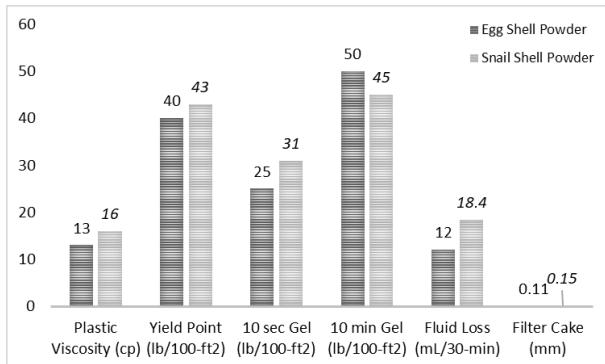


Figure 6. Rheological and Filtration properties for 5g bio-additive concentration (aged samples)

The plastic viscosity and yield point of the 11ppg KCl-polymer mud were improved by the bio-additives at 2g and 5g concentration for both egg shell powder and snail shell powder with similar PV and YP values. An average reduction of 61% and 37% in PV and YP was observed for the aged samples.

The 10-sec. gel strength was reduced by 28% and 31% for 2g and 5g egg shell powder concentration compared to the control sample value. It is worth noting that a 100% increase in gel strength was observed in the aged samples over the samples evaluated at ambient conditions. For the samples with snail shell powder, the 10-sec. gel strength increased by 28% for 2g concentration but reduced 14% for 5g concentration. The 10-min. the gel strength of the 11ppg KCl-polymer mud was improved by the bio-additives at 2g and 5g concentration for both egg shell powder and snail shell powder with an average reduction of 34% observed for the aged samples.

The filtration properties of the KCl-polymer mud aged were not improved by 5g egg shell powder, 2g snail shell powder, or 5g snail shell powder concentration. Higher filtrate loss and filter cake poorer in quality were observed for these bio-additive concentrations. The exception is the 2g egg shell powder concentration with 8 mL/30 min. filtrate loss and < 1 mm cake

thickness. Treatment of the 11ppg KCl-polymer mud with 2g egg shell powder concentration resulted in 22% and 10% reduction in filtrate loss and filter cake thickness, respectively.

4. Conclusions

Egg shell powder at low concentrations, 2g in this study, is effective in improving both the rheological and filtration properties of KCl-polymer water-based drilling mud. Snail shell powder at 5g concentration has a higher potential of enhancing drilling fluid rheology as compared to its filtration properties. Egg shell powder and snail shell powder at low concentrations have a deflocculating effect on KCl-Polymer mud. At concentrations above 10g, the bio-additives have a reverse flocculating effect on the drilling fluid. Egg shell powder at low concentrations, 2g in this study, has the potential to both supplement pre-hydrated bentonite and provide filtration control for KCl-polymer water-based drilling mud.

Recommendation

Based on these results and conclusions of the experimental research study, the following recommendations are suggested for future work:

- The effect of egg shell powder on the rheology and filtration properties of different water-based mud formulations below 2g concentration should be investigated at HTHP conditions.
- The effect of egg shell powder on KCl-polymer mud in the presence of starch should be investigated.

Acknowledgments

The authors would like to thank Prof. O.D. Orodu, the Head of the Department of Petroleum Engineering, Covenant University, Ota, Ogun State, Nigeria.

References

- [1] Hafshejani KS, Moslemizadeh A, Balhasan S, Shahbazi K. A novel bio-based deflocculant for bentonite drilling mud. *Appl. Clay Sci.* 2016; 127: 23-34.
- [2] Neshat J, Shadzadeh SR. Evaluation of a Naturally-derived Deflocculant (*Terminalia Chebula*) in Bentonite Dispersions. *Iranian Journal of Oil & Gas Science and Technology.* 2016; 5(2): 21-44.
- [3] Biltayib BM, Rashidi M, Balhasan S, Alothman R, Kabuli MS. Experimental analysis on rheological and fluid loss control of water-based mud using new additives. *J. Petroleum Gas Eng.* 2018; 9(3): 23-31.
- [4] Igwe I, Kinate BB. The Use of Periwinkle Shell Ash as Filtration Loss Control Agent in Water-Based Drilling Mud. *International Journal of Engineering Research and General Science.* 2015; 3(6): 375-381.
- [5] Nmegbu CGJ, Bekee B. Evaluation of Corn Cob Cellulose and its Suitability for Drilling Mud Formulation. *Int. Journal of Engineering Research and Applications.* 2014; 4(5): 112-117.
- [6] Onolemhemhen RU, Olamigoke O, Kaka AQO. The Suitability of Egg Shell and Snail Waste for pH and Mud Weight Enhancement of Water Based Drilling Mud. *Pet Coal.* 2019; 61(2): 371-376.
- [7] Iqbal R, Zubair M, Pirzada F. An Experimental Study on the Performance of Calcium Carbonate Extracted from Eggshells as Weighting Agent in Drilling Fluid. *Engineering, Technology & Applied Science Research.* 2019; 9(1): 3859-3862.
- [8] Toka B, Toka N. Preparing Drilling Fluid Compositions for Geothermal Reservoirs. *Pet. Sci. Proceedings World Geothermal Congress 2015. Melbourne, Australia, 19-25 April 2015, 1-8.*
- [9] Gaurina-Medimurec N. Laboratory Evaluation of Calcium Carbonate Particle Size Selection For Drill-In Fluids. *Rud.-geol.-naft. zb.,* 2002; 14: 47-53.
- [10] Yang H, Lu Y. Research & Application of the Drilling Fluid for Water Sensitive Stratum. *Procedia Engineering.* 2014; 73; 299-304.
- [11] API RP 13B-1, Recommended Practice for Field Testing Water-Based Drilling Fluids.

To whom correspondence should be addressed: Dr. Oluğbenga Olamigoke, Department of Chemical and Petroleum Engineering, University of Lagos, Nigeria, E-mail: oolamigoke@unilag.edu.ng

Anti-collision Planning Optimization in Directional Wells

Abdulrahman Mohamed

Department of Petroleum Engineering and Gas Technology, Faculty of Energy and Environmental Engineering, The British University in Egypt, Cairo, Egypt

Received April 21, 2019; Accepted July 22 2020

Abstract

One of the most application of the directional drilling is drilling multiple wells from one location or platform. In drilling multiple wells from one location the major problem that faced is avoiding the collision with the offset wells that drilled near the proposed well in the same region. Therefore, the potential of collision between the wells can cause severe catastrophic accidents such as an explosion or oil spill. Several measurements of proximity calculation or methods have been adopted to control the distance between the wells, avoid the collision, increasing the clearance along with smoothing the trajectory, Reducing the drilling time based on the anti-collision rules. A real case study of an offshore directional horizontal well drilled from the platform is studied through the paper. The proposed well is drilled in the neighboring of three offset wells that should be planned completely to avoid the collision with them. The well is planned through an advanced anti-collision method that results in preventing the collision of well with optimized drilling performance through Oriented separation factor (OSF). This factor yields appropriate separation with OSF greater than 5. This yield efficient separation with offset well 1, offset well 2 and offset well 3 greater than 5, In addition to optimized drilling performance of 84% drilling versus 16% sliding that results in the completion of the well in 50 days with positive income that result in 8.55 Return on Investment (ROI).

Keywords: *Anti-Collision Planning; Proximity Methods; Oriented Separation Factor; Anti-Collision Rules; Separation Factor; Alert Zones.*

1. Introduction

Directional drilling is one of the most challenging and attractive techniques that help to solve many problems that vertical drilling cannot solve as drilling multiple wells from the same location in offshore drilling instead of having a platform for each well [1]. However, the drilling of multiple wells in the same location causes a high risk of Collision between the wells that can cause severe catastrophic accidents and loss of production. Therefore, the distance between the center of the offset and subject well must be calculated in order to avoid the collision by an offset well [2]. This can be achieved by accurate well planning taken into consideration separation from the offset wells. Another challenging problem is arising in determining the distance between the wells by the surveying because the surveying instrument does not give an accurate distance between the wells [3]. Poedjono [4] indicated that the center to center distance can be considered as the distance between the planned or subject well to the offset well which scanned by the minimum perpendicular method. Moreover, Spidle [5] stated that there is a more accurate method than the perpendicular method to estimate the accurate distance through horizontal distance measurement. Moreover, there is some uncertainty should be defined well and calculated to ensure the accurate positioning of the wellbore [6]. Therefore, gathering accurate information about the offset wells in the same working area is significant for avoiding the collision and for the future well planning [7]. In conclusion, another method than the calculation of the distance between the wells is to graph the subject well along with offset wells to control the collision in real-time [8].

2. Methods

The anti-collision planning methods were used for the field data of the subject well through determining the distance between the proposed well and offset wells. Then evaluating the distance between the wells through including the uncertainty of the surveying position through radii of uncertainty. After quantifying the separation between the wells, the well is classified and monitored through anti-collision rules to prevent the collision and redesign the high-risk segment of the wells. The more details of the used method are shown below.

2.1. Proximity method used

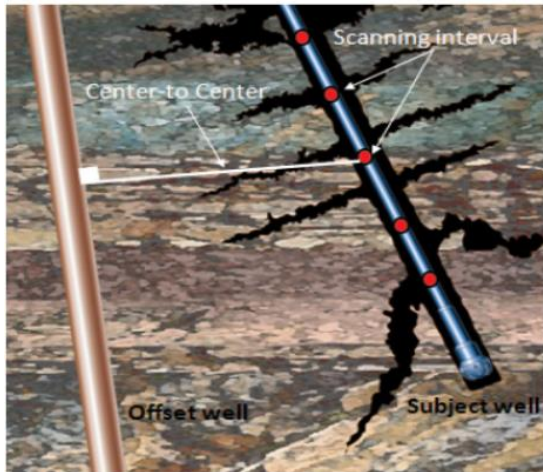


Fig. 1. 3D Least Distance Proximity Method

The first step in proximity is gathering information from the database of the working area to identify the offset wells that have high collision risk. These data showed three offset wells that show the high significant risk of collision. These wells were evaluated through the calculation of the distance between them and the proposed well through 3D least Distance Proximity method. This method is the most accurate method as it measures the shortest distance between the wells with high accuracy as it divided the well into small intervals and measure the shortest distance as shown in Fig.1 shows the distance measurement method.

2.2. Proximity calculations used

The proximity calculations were made after determining the distance between the offset well and subject well through proximity method. These method results in the center to center distance between wells but is not of high accuracy due to uncertainty of positioning of wells during the surveying method. Therefore, more proximity calculate is carried out to correct the separation between the wells as following.

2.2.1. Separation factor (SF)

SF, corrects the separation between the wells by considering the uncertainty of position between the subject well and the offset well.

Mathematically, it represents the ratio between the center to center distance between the offset and subject well to the sum of the radii of the ellipsoid of uncertainty (EOU).

$$SF = S / (er + eo) \quad (1)$$

where S is the distance between the center to center of the reference and offset well; er semi-major radius of the ellipsoid of the uncertainty of reference well; eo semi-major radius of the ellipsoid of the uncertainty of offset well.

2.2.2. Oriented separation factor (OSF)

OSF provides a more accurate method for quantifying the separation between the wells and the EOR separation by taking into consideration the fixed probability of collision as described by SF equal to one. Furthermore, OSF considers the shape and geometry of the EOU resulting that all scenarios with the same SF have the same probability or chance of collision. Mathematically, describes as in the equation (2);

$$OSF = Clearance / (Relative Positional Uncertainty) \quad (2)$$

2.2.3. Allowable deviation from the plan (ADP)

The allowable deviation from plane provides the drilling channel that created due to the avoidance of any proximity approach violation detected by oriented separation factor. It represented by distance radially from the plan at any point to the distance which the drilled can be allowed to deviate or depart from plan through drilling process in order to increase the drilling efficiency along without violating the anti-collision rules.

2.2.3. Minimum allowable separation (MAS)

The minimum allowable separation (MAS) measure the minimum distance between the center to center of the subject and offset well that is allowable with emphasizing on anti-collision rules. Therefore, the actual distance between the center to center between subject and offset wells during the normal drilling process can be obtained by summing the minimum allowable separation with allowable deviation from the plan.

2.3. Anti-collision rules used based on proximity calculations

Anti-collision planning between the offset wells and subject well is controlled through anti-collision rules that characterize and classify the risk degree of the collisions. These classifications are divided as alert zones, a minor risk well and major risk well as shown in the Fig.2.

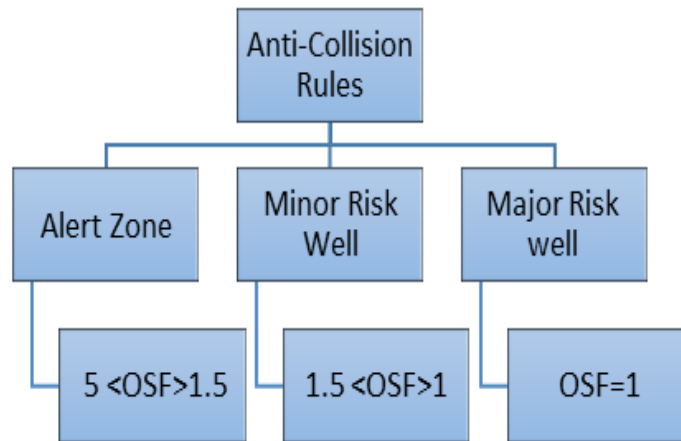


Fig. 2. Anti-Collision rules

3. Results

Real Case study of offshore horizontal well for Company X is used for anti-collision planning optimization through a novel method of OSF. The results below show the optimization and controlling of the directional well to control the collision through calculations and graphical methods.

3.1. Results of the anti-collision proximity calculations of the offset wells 1

Table 1 shows the clearance calculations between the subject well and the offset well 1 with respect of MD, TVD, North and East coordinates of both wells. In addition to the closest distance between the two wells. From the calculations, it shows that distance between the subject and offset well 1 were 1.29 ft at 278.87 ft MD and increase gradually till reaching the target at 3796.24 ft at 9071.29 MD. This indicated that the separation between the two wells was to low and increase as deepening of the well according to the OSF method that must keep OSF greater than 5.

Table 1. Clearance calculations (Offset Well1)

Refer-ence	Refer-ence	Reference	Reference	Offset	Offset	Offset	Offset	Angle From	Closest Ap- proach Distance
MD [ft]	TVD [ft]	North[ft]	East[ft]	MD [ft]	TVD [ft]	North[ft]	East[ft]	High side [deg]	[ft]
82.02	82.02	0.00N	0.00E	82.02	82.02	0.00N	0.00E	0	0
278.87	278.87	0.00N	0.00E	278.86	278.86	0.95N	0.87E	42.3	1.29
393.7	393.7	0.00N	0.00E	393.65	393.63	2.42N	2.19E	42.3	3.26
1312.34	1310.05	56.05S	0.00E	1303.9	1302.55	36.70N	33.35E	-159.9	98.85
1430.45	1427.28	70.44S	0.00E	1419.13	1417.36	43.95N	39.93E	-160.4	121.56
2119.42	2114.55	112.47S	0.00E	2091.08	2085.12	99.05N	90.00E	23.1	231.75
2736.22	2731.34	112.47S	0.00E	2690.09	2677.07	166.71N	151.48E	28.5	322.24
4265.09	4260.22	112.47S	0.00E	4138.37	4089.54	401.72N	365.03E	35.4	653.28
4429.13	4424.26	112.47S	0.00E	4287.53	4233.1	431.67N	392.24E	35.8	697.48
4986.88	4975.88	72.39S	58.96W	4786.73	4710.61	539.33N	490.07E	92.7	863.71
7208.01	6502.9	758.72N	1281.44W	6042.34	5888.05	861.31N	782.63E	84.6	2156.15
7381.89	6545.82	853.43N	1420.75W	6072.78	5916.12	870.03N	790.56E	79.3	2299.28
7665.62	6586.53	1011.18N	1652.79W	6095.1	5936.7	876.43N	796.37E	69.1	2537.49
7988.68	6611.93	1192.26N	1919.13W	6101.06	5942.19	878.14N	797.92E	69.4	2815.96
8087.66	6617.48	1247.58N	2001.02W	6100.7	5941.86	878.03N	797.83E	64.8	2902.85
9071.29	6650.26	1795.60N	2817.18W	6075.45	5918.58	870.80N	791.26E	63.7	3796.24

3.2. Results of the anti-collision proximity calculations of the offset wells 2

Table 2 also, shows the clearance calculations between the subject well and the offset well 2 with respect of MD, TVD, North and East coordinates of both wells. In addition to the closest distance between the two wells. Accordingly, it shows that distance between the subject and offset well 2 were 4.27 ft at 278.87 ft MD and increase gradually till reaching the target at 5736.22 ft at 9071.29 MD. This indicated that the separation between the two wells was to low and increase as deepening of the well according to the OSF method that must keep OSF greater than 5.

Table 2. Clearance calculations (Offset Well 2)

Refer-ence	Refer-ence	Reference	Reference	Offset	Offset	Offset	Offset	Angle From	Closest Ap- proach Distance
MD [ft]	TVD [ft]	North[ft]	East[ft]	MD [ft]	TVD [ft]	North[ft]	East[ft]	High side [deg]	[ft]
82.02	82.02	0.00N	0.00E	82.02	82.02	0.00N	0.00E	0	0
278.87	278.87	0.00N	0.00E	278.77	278.71	3.79N	1.97E	27.4	4.27
393.7	393.7	0.00N	0.00E	393.19	392.94	9.51N	4.93E	27.4	10.74
1312.34	1310.05	56.05S	0.00E	1269.51	1251.88	76.44N	146.50E	-130.3	205.92
1430.45	1427.28	70.44S	0.00E	1373.94	1350.33	84.35N	180.37E	-128.7	249.83
2119.42	2114.55	112.47S	0.00E	1926.83	1847.11	124.75N	417.71E	60.4	549.8
2736.22	2731.34	112.47S	0.00E	2373.97	2214.07	154.73N	671.09E	68.3	888.45
4265.09	4260.22	112.47S	0.00E	3491.75	3076.43	207.91N	1379.74E	76.9	1845.98
4429.13	4424.26	112.47S	0.00E	3628.43	3180.79	210.90N	1467.95E	77.6	1950.81
4986.88	4975.88	72.39S	58.96W	3988.14	3455.64	214.97N	1699.96E	125.2	2342.55
7208.01	6502.9	758.72N	1281.44W	4331.99	3714.32	216.86N	1926.49E	36.6	4284.93
7381.89	6545.82	853.43N	1420.75W	4252.58	3654.5	216.45N	1874.26E	31.2	4429.74
7665.62	6586.53	1011.18N	1652.79W	4120.73	3555.73	215.81N	1786.93E	24.8	4652.96
7988.68	6611.93	1192.26N	1919.13W	4020.33	3480.01	215.19N	1720.99E	23.6	4900.42
8087.66	6617.48	1247.58N	2001.02W	3971.42	3442.98	214.86N	1689.04E	21.5	4975.99
9071.29	6650.26	1795.60N	2817.18W	3545.91	3117.77	209.16N	1414.71E	17.1	5736.22

3.3. Results of the anti-collision proximity calculations of the offset wells 3

In addition, Table 3 shows the clearance calculations between the subject well and the offset well 3 with respect of MD, TVD, North and East coordinates of both wells. In addition to the closest distance between the two wells. Accordingly, it shows that distance between the subject and offset well 3 were 2.63 ft at 278.87 ft MD and increase gradually till reaching the target at 1813 ft at 9071.29 MD. This separation is lower than in offset well 1 and offset well

2 which yield that well 3 had a high potential of the collision but it keeps away from the subject well by considering the OSF greater than 5.

Table 3. Clearance report (Offset Well 3)

Reference	Reference	Reference	Reference	Offset	Offset	Offset	Offset	Angle From High side [deg]	Closest Approach Distance [ft]
MD [ft]	TVD [ft]	North[ft]	East[ft]	MD [ft]	TVD [ft]	North[ft]	East[ft]		
82.02	82.02	0.00N	0.00E	82.02	82.02	0.00N	0.00E	0	0
278.87	278.87	0.00N	0.00E	278.83	278.81	1.35N	2.26E	59.2	2.63
393.7	393.7	0.00N	0.00E	393.52	393.43	3.38N	5.67E	59.2	6.61
1312.34	1310.05	56.05S	0.00E	1287.93	1279.93	50.46N	101.55E	-135.1	150.21
1430.45	1427.28	70.44S	0.00E	1396.67	1385.83	60.69N	123.96E	-135.3	185.15
2119.42	2114.55	112.47S	0.00E	2034.88	2003.05	150.11N	257.67E	44.5	384.41
2736.22	2731.34	112.47S	0.00E	2627.91	2567.68	300.38N	356.03E	40.8	569.2
4265.09	4260.22	112.47S	0.00E	4205.45	4062.25	742.51N	186.78E	12.3	897.26
4429.13	4424.26	112.47S	0.00E	4370.83	4216.88	786.20N	147.66E	9.3	934.04
4986.88	4975.88	72.39S	58.96W	4898.09	4713.85	918.90N	32.13E	58.5	1029.37
82.02	82.02	0.00N	0.00E	82.02	82.02	0.00N	0.00E	0	0
278.87	278.87	0.00N	0.00E	278.83	278.81	1.35N	2.26E	59.2	2.63
393.7	393.7	0.00N	0.00E	393.52	393.43	3.38N	5.67E	59.2	6.61
1312.34	1310.05	56.05S	0.00E	1287.93	1279.93	50.46N	101.55E	-135.1	150.21
1430.45	1427.28	70.44S	0.00E	1396.67	1385.83	60.69N	123.96E	-135.3	185.15
2119.42	2114.55	112.47S	0.00E	2034.88	2003.05	150.11N	257.67E	44.5	384.41

3.4. Clearance between the subject well and offset wells

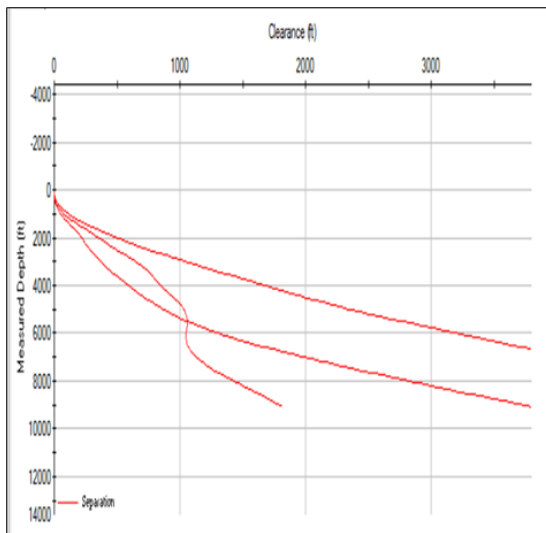


Fig. 3. Clearance vs. measured depth

Fig.3 shows the clearance results between the subject well and offset well 1, offset well 2 and offset well 3. It shows from the graph that MD of these offset wells and their distance from the subject or planned wells. This graph summarizes the results obtained in table 1 to table 3 as shows that the three wells keep away from the planned well with adequate separation that maintains the separation control rule.

3.5. Anti-collision separation results

Table 4 shows the anti-collision summary of the proximity calculation of the subject well and three offset wells. The proximity calculations were Separation centre to centre distance, allowable deviation separation factor and minimum allowable separation. These calculations are carried between the subject well and three offset wells 1,2 and 3 in terms of Measured depth (MD) and True Vertical Depth (TVD). The separation factor for offset well (1) ranges from 11 to 377.9 at the target depth. While the separation factor for offset well (2) ranges from 3 to 290.61 at the target depth. In addition to these wells, offset well (3) have a separation factor range from 6.21 to 215.99 at the target depth. From these data, the most risk well is offset well (2) as it is the closest well to the subject well. Furthermore, this is confirmed through minimum allowable separation as it ranges from 3.75-390.6 ft, 3.75- 436.65, 3.75-487.74 ft for offset wells 1,2 and 3 respectively.

Table 4. Anti-collision proximity calculations summary

Offset trajectory	Separation Ct-Ct (ft)	Allowable deviation (ft)	Separation factor	MAS	Subject trajectory	
					MD ft	TVD ft
Offset well 1	30	26.25	11	3.75	0	0
	30	26.25	11	3.75	100	100
	29.96	26.14	598	3.82	200	200
	30.25	25.09	29..57	5.16	400	400
	46.73	39.1	17.08	7.63	700	699.63
	75.39	64.8	15.99	10.59	1300	1292.6
	9500	9109.14	377.8	390.86	11082.91	2500
Offset well 2	10	6.25	3	3.75	0	0
	10	6.25	3	3.75	0	0
	7.81	1.78	3.5	6.03	500	499.98
	7.01	0.66	2.6	6.35	600	599.88
	11	3.99	3.91	7.01	700	699.63
	40.75	30.51	8.84	10.24	1200	1196.07
	9500	9063.35	290.61	436.65	11082.91	2500
Offset well3	18.03	14.28	6.21	3.75	0	0
	18.03	14.28	6.21	3.75	100	100
	16.14	10.54	11.04	5.6	400	400
	24.57	17.36	9.56	7.21	700	699.63
	47.75	39.06	13.73	8.69	1200	1196.07
	49.62	39.8	11.64	9.82	1300	1292.6
	9500	9012.26	215.99	487.74	11082.91	2500

Table 5 shows the detailed anti-collision report for the subject well and the three offset wells. This report shows the centre to centre distance, separation factor (OSF), classification of the OSF according to the alerts and the status. From the results, the OSF for offset well 1 and offset well is greater than 5 that drilled safely with an appropriate separation. While for offset well 2, the separation factor (OSF) is 5 along with MD depth from 500 ft to 7000 ft. In addition, according to the rules for OSF, this well enters the alert zone at 500 and exit at 7000 ft. Moreover, the subject well is saved from the collision with offset well 2 through consideration of the novel OSF method.

Table 5. Anti-collision proximity calculations summary

Offset trajectory	Separation Ct-Ct (ft)	Separation factor			Alert	Status
		Alert	Minor	Major		
Offset well 1	30				Surface	Pass
	30				MintPt-O-SF	
	29.96				MintPt-CTCT	
	30.25				MinPt-O-ADP	
	46.73				MintPt-O-SF	
	75.39				MintPt	
	9500				TD	
Offset well 2	10	5			Enter Alert	
	10	5			Exist alert	
	7.81	5			Enter Alert	
	7.01				MinPts	
	11	5			Exist alert	
	40.75				MinPts	
	9500				TD	
Offset well 3	18.03				surface	Pass
	18.03				MintPt-O-SF	
	16.14				MinPts	
	24.57				MintPt-O-SF	
	47.75				MinPts	
	49.62				MintPt-O-SF	
	9500				TD	

3.6. Graphical result of anti-collision planning

3.6.1. Travelling cylinder plots

Fig.4 Shows the travelling cylinder plot for the subject well and the three offset wells. The plot shows the MD of these wells and their azimuth in comparison with the subject well. This plot yield that subjects well is drilled safely with appropriate separation from the offset wells from 120 degrees to 320-degree azimuth at the target depth.

Moreover, Fig.5 shows the travelling cylinder plot of these offset wells with respect to subject well as shown in Fig.4 but have drilling tunnel that comparing the position of the projection versus the NO-GO zones. The circles of NO-GO are plotted around the trajectories of the offset wells and subject well for a depth through using the circle radius equal to minimum allowable separation MAS as calculated in proximity calculations.

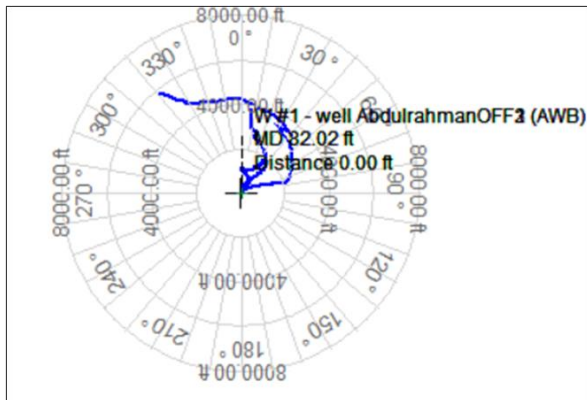


Fig. 4. Travelling cylinder plot of anti-collision well planning

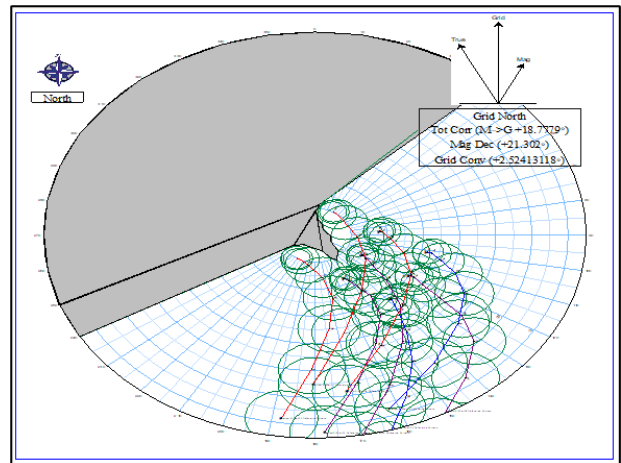


Fig. 5. Traveling cylinder plot with drilling tunnel

3.6.2. Spider plot

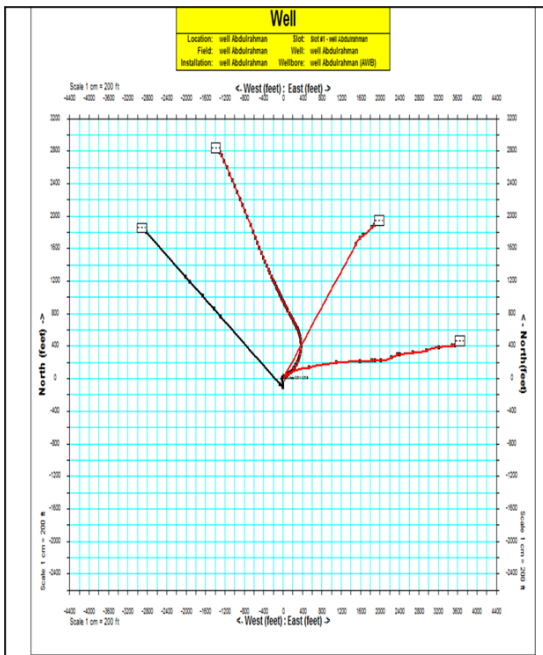


Fig.6 shows spider plot result that shows the offset wells in red line and the subject well in black colour that shows the direction of the offset wells and planned wells with respect to the north and west or east coordinates. From this plot, the subject well has clear distance from the offset wells at 0 degrees at the surface to 3200-degree West at target and 0 at 0 degrees at the surface to 1800-degree North at target.

Fig. 6. Spider plot

3.7. Optimization of the drilling performance results

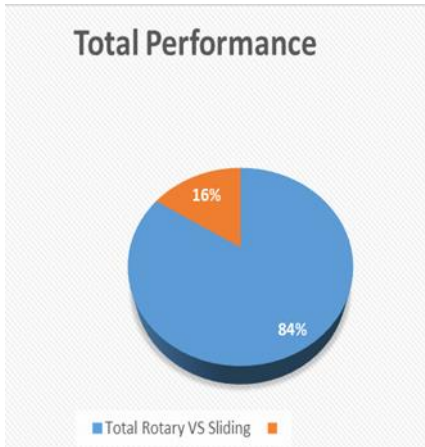


Fig. 7 Total Performance of drilling

Fig.7 shows the comparison between the total rotation versus the sliding of the drill string due to the adequate planning of the anti-collision well, as shown the rotation represents 84 % while the sliding is 16 %. This result indicates good drilling performance as the rotation is greater than sliding due to the sliding cause more friction force on the drill string, cause limitation of the weight on the bit which results in lower ROP. While the Rotation results in better hole cleaning, lower friction, higher ROP and higher WOB. Accordingly, the drilling time is faster with greater rotation than sliding.

3.8. Economic results

3.8.1. Progress and cost chart

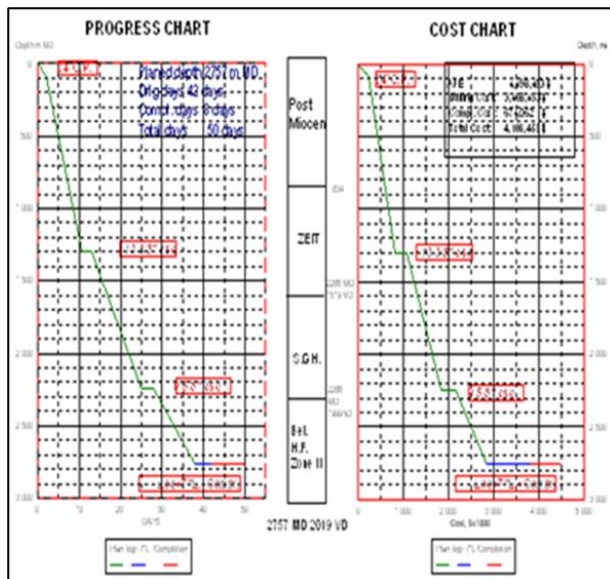


Fig. 8. Progress and cost chart

Fig.8 shows the progress and cost chart. The progress chart shows in the x-axis days and the Y-axis depth which shows the progress of drilling operation about 50 days with the total cost of 4,498,453 K \$.

3.8.2. Economic analysis

The NPV of 305.7 million \$ and the lifetime of the project will be 34 years with the internal rate of return of 105 %, rate of return of 8.55 and the discounted rate of return of 4.57.

It can be shown from the Fig.9 pay-out time is obtained at 0.7 years which is the point of intersection where the NPV becomes zero. Fig.10 shows the discount factor percentage in the X-axis the net present value (NPV) in the Y-axis. The intersection of the line with the Discount factor percentage that results in the NPV to be zero. This IRR gives an indication of the profitability of the project where appear in this plot at 105%.

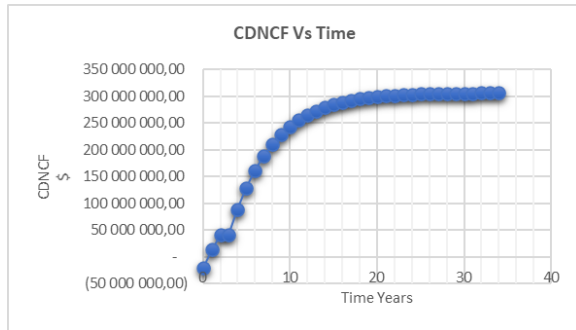


Fig. 9. CDNCF vs time

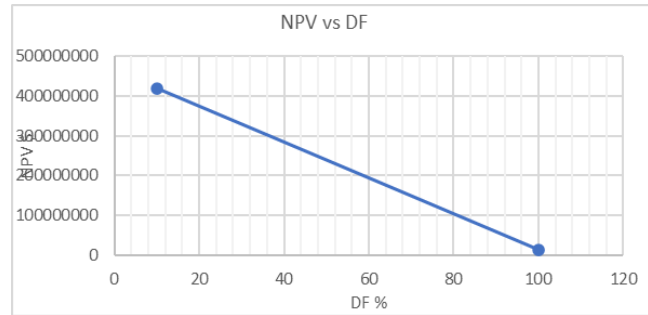


Fig. 10. NPV vs DF

4. Conclusion

The proposed well is drilled in the neighbouring of Offset well 1, Offset well 2 and Offset well 3 safely according to the separation rules. The anti-collision summary shows that the well is entered only the alert zone and redesign the plan to exit from the alert zone to drill safely and avoid the collision of the offset wells. The travelling cylinder plot that shows the clearance of the planned well and the offset wells through the measured depth and the azimuth of the wells which helps in avoid the collision with offset wells. Similarly, the spider plot shows the projection of the horizontal plane that appear the wells that exist in a given area as if not isolation on it as the earth was transparent which is used to avoid the collision between the wells an ensure the separation between the wells is maintained similarly to the travelling cylinder. The drilling is optimized as the rotation represent 84 % while the sliding is 16 %. This result indicates good drilling performance as the rotation is greater than sliding due to the sliding cause more friction force on the drill string. The drilling and completion time of the well is 50 days and along with the cumulative cost of 4,498,453 K \$. Finally, economic analysis shows positive income as NPV of 305.7 Million \$ and the lifetime of the project will be 34 years with the internal rate of return of 105 %, rate of return of 8.55 and the discounted rate of return of 4.57.

References

- [1] Aadnoy B, Cooper I, Miska S, Mitchell RF, and Payne ML. Advanced Drilling and Well Technology. Society of Petroleum Engineers 2009, ISBN10 1555631452.
- [2] Bourgoyne AT, Milheim KK, Chenevert ME, Young Jr FS. Applied Drilling Engineering. Society of Petroleum Engineers 1986, .
- [3] Poedjono B,Chinh PV, Isevcan E, Walker JR, Gonzalez LF, McCulloch S, Juarez F, Moreno VH. Case Studies in the Application of an Effective Anti-collision Risk Management Standard. SPE International Conference on Health, Safety and Environment in Oil and Gas Exploration and Production, 12-14 April, Rio de Janeiro, Brazil, SPE-126722-MS. <https://doi.org/10.2118/121040-MS>.
- [4] Chen DC-K. Integrated BHA Modeling Delivers Optimal BHA Design. SPE/IADC Middle East Drilling and Technology Conference (p. 11). Cairo 2007, SPE-106935-MS. <https://doi.org/10.2118/106935-MS>.
- [5] Spidle K. Drilling Office X (DOX) Technical Manual/Anti-Collision. Schlumberger 2012, 41.
- [6] Adly E. Rotary Steerable System Technology Case Studies in the Canadian Foothills. American Association of Drilling Engineers 2007, 9.
- [7] Montecinos J. Directional Control & Surveying Procedures. ENI 2012, 67.
- [8] Wilson G. Radius of Curvature Method for Computing Directional Surveys. SPWLA 9th Annual Logging Symposium, Louisiana 1968: SPWLA-1968-D.

To whom correspondence should be addressed: Abdulrahman Mohamed, Department of Petroleum Engineering and Gas Technology, Faculty of Energy and Environmental Engineering, The British University in Egypt, Cairo, Egypt, E-mail: abdulrahman.mohammed@hotmail.com

Physicochemical Fuel Properties and Carbonization Kinetics of Duduguru Coal

Bemgba B. Nyakuma^{1,2*}, Aliyu Jauro³, Segun A. Akinyemi⁴, Mohammed B. Nasirudeen⁵, Olagoke Oladokun², Aliyu A. Bello², Tertsegha J-P. Ivase⁶, Tuan Amran T. Abdullah^{1,2}

¹ Hydrogen and Fuel Cell Laboratory, Institute of Future Energy, Universiti Teknologi Malaysia, Malaysia

² School of Chemical and Energy Engineering, Faculty of Engineering, Universiti Teknologi Malaysia, Johor, Malaysia

³ National Centre for Petroleum Research and Development (NCPRD), Abubakar Tafawa Balewa University, P. M. B 0248, Bauchi State, Nigeria

⁴ Environmental Remediation and Geopollution Group, Department of Geology, Ekiti State University, P. M. B. 5363, Ado Ekiti, Ekiti State, Nigeria

⁵ Department of Chemistry, Faculty of Science, Federal University of Lafia, P.M.B 146, Lafia, Nasarawa State, Nigeria

⁶ Bio-Resource Development Centre (BIODEC), National Biotechnology Development Agency, Makurdi, Benue State, Nigeria

Received May 6, 2019; Accepted September 21, 2020

Abstract

The growing demand for cheap electricity and the significant discovery of new coal deposits in developing nations like Nigeria has increased interest in coal-fired power generation. Conversely, comprehensive data on the fuel properties, emissions profiles, and environmental impacts of coal exploration and energy exploitation remain scarce. Therefore, this study examines the physico-chemical, microstructure, mineralogical, and thermo-kinetic properties of Duduguru (DDG) coal from a newly discovered deposit in Obi Local Government Area of Nasarawa State, Nigeria. The results showed that DDG contains high carbon and hydrogen but low oxygen contents, which accounts for its higher heating value (HHV) of 28.39 MJ/kg. Based on its volatile matter content and HHV, DDG is ranked as a high volatile bituminous C coal, which typically exhibits HHV in the range 26.70 MJ/kg - 30.20 MJ/kg. The microstructure and chemical analyses indicated that DDG consists of heterogeneous sized particles with a distinct white lustre. This could be ascribed to the presence of mineral and metal components such as quartz, kaolinite, and the metal elements (such as Ti and Fe) typically found in coal structure. Thermal analysis revealed that the change in heating rates and temperature significantly affected the thermal degradation behaviour and temperature profile characteristics of DDG. As a result, DDG experienced significant mass loss ($M_L = 39.32\%$ to 41.28%) and residual mass ($RM = 58.72\%$ to 60.68%). Furthermore, the results showed that the increase in heating rates from lower to higher values enhances the formation of a higher mass of residuals. In general, DDG is a high-rank coal, which may be suitable for steam generation for electricity or metallurgical coke for steel production.

Keywords: Carbonization; Kinetics; Fuel Characterisation; Duduguru; Coal; Nigeria.

1. Introduction

Coal remains an integral part of the global energy mix [1-2]. It is also the most abundant and widespread fossil-based fuel on the planet. Current estimates indicate that coal accounts for over 60% or 1 trillion tonnes of all fossil fuels that can be economically recovered on planet earth. Currently, coal accounts for 40% or ~ 8200 TWh (terawatt hours) of coal-fired electricity generation around the world [3]. With the increasing demand for cheap electricity around the world, it is estimated that coal-fired electricity generation could increase in the near future [4-5]. According to the International Energy Agency (IEA), the global demand for coal increased by 1% to ~7600 Mt in the year 2017 driven by robust power generation due to industrial output

and high electricity demand in India, China, and other developing nations such as Vietnam. Likewise, coal power generation worldwide expanded by 3% or 250 TWh, which represents 40% and 38% of additional power generation and global energy mix, respectively [6].

In the same vein, the discovery of large deposits in traditionally energy deficient nations in the developing world is projected to increase the utilization of coal in the future [7]. Due to the significant deficit in electric power generation, developing countries will require over 900 TWh to meet their energy demands. According to the World Bank, over 1 billion people lack access to stable electricity supply [8], resulting in a severe energy crisis that affects over 33% of economies including Nigeria [9]. In spite of Nigeria's position as the largest economy in Africa, the nation routinely experiences epileptic power supply in the form of perennial power cuts, black-outs, and load shedding resulting in epileptic power supply yearly [10-11]. These setbacks are ascribed to the nation's low power generation, inefficient distribution, poor infrastructure, among other problems [12]. Furthermore, the poor state of the electricity sector has significantly impacted the socio-economic growth and sustainable development of the nation [13-14].

Given these issues, the nation's energy policy seeks to diversify power generation from biomass, petroleum (including oil and gas) and hydropower which account for 83%, 16% and 1% of Nigeria's energy mix, respectively [15]. Likewise, Nigeria is rich in both renewable energy resources and other fossil fuels [16] such as coal. According to analysts, Nigeria's coal supplies are estimated at 2.75 billion tonnes of which a known reserve of 690 million (comprising 12% lignite, 49% sub-bituminous, and 39% bituminous), and 39% bituminous are located across the nation's sedimentary basins [17-19]. The strategic location of Nigeria's coal deposits in various geopolitical regions presents significant opportunities for the nation to locate and generate on-site coal-fired electricity. Furthermore, the integration of coal will create a structured energy mix that could potentially address energy shortage, stimulate socio-economic growth and catalyse infrastructural development, particularly in developing countries like Nigeria.

The recent discovery of vast new deposits in Duduguru, Shankodi-Jangwa, Atito-Akpuneje, and Lafia-Obi have raised awareness on the potentials of exploiting Nigeria's coal for energy, chemicals and various other applications [20-23]. However, there is limited data on the fuel properties of the many newly discovered Nigerian coal deposits, particularly Duduguru located in Duglu village in Obi Local Government Area of Nasarawa State, Nigeria. Therefore, this study seeks to examine the fuel, carbonization, and kinetic characteristics of Duduguru coal from Nigeria. Typically, fuel properties are required to classify coal into various ranks and evaluate its suitability for various applications. It is envisaged that the findings of this study will present novel insights into the energy recovery potential of Duduguru coal from Nasarawa state located in the Middle Benue Trough in Nigeria.

2. Materials and methods

2.1. Physicochemical analyses

The physicochemical fuel properties of Duduguru (DDG) coal was examined based on ultimate (elemental), proximate, and calorific value analyses. DDG coal is a newly discovered coal sample from Duduguru village in Obi Local Government Area of Nasarawa State, Nigeria. The elemental analysis of DDG was determined by CHNS analysis (Model: vario MACRO Cube Analyser, Germany) to determine the carbon, hydrogen, nitrogen, and sulphur composition. The proximate analysis was carried out using a muffle furnace (Model: Ney Vulcan D-130, USA) based on the ASTM standards D3173-75 for moisture, ash, and volatile matter composition. Lastly, the calorific value was carried out through bomb calorimetry (Model: LECO AC350, UK) to determine the higher heating value (HHV) of the sample. All measurements were performed in duplicate to confirm the reliability of the results.

2.2. Microstructure and mineralogical analyses

The morphological and chemical composition of Duduguru coal was conducted by scanning electron microscopy (SEM) and energy dispersive x-ray (EDX) methods, respectively. Before the SEM/EDX analyses, the DDG sample was sputter-coated with gold (Au) using the Quorum

Q150R S equipment. Next, the sputter-coated sample was placed in the sample chamber of the SEM/EDX analyser and degassed to remove residual foreign matter and any oxidative gases. Next, the SEM/EDX microscope was initiated to scan for the microstructure and chemical composition of the sample. The operational settings of the SEM/EDX analyser were set at voltage 20 kV, working distance 5 mm, and a magnification of $\times 1000$. In the end, the SEM image was examined using the proprietary AZTEC EDX software from Oxford Instruments (UK). Next, the point ID and mapping program of the software was initiated to determine the elemental composition of DDG coal in weight per cent (wt. %).

2.3. Carbonization analysis

The carbonization characteristics of Duduguru (DDG) coal were examined through non-isothermal thermogravimetric analysis (TGA). The process was examined based on the multiple heating rate programmes. For each run, about 16 mg of the powdered DDG coal sample was heated from 30°C to 900°C based on different heating rates from 10°C/min to 30°C/min ($\Delta 10^\circ\text{C}/\text{min}$) using the thermogravimetric analyser (TGA Model: Shimadzu TG-50 Japan). During the tests, the TG system was flushed with ultra-pure (99.99%) nitrogen (N₂) gas to remove evolved gases from DDG and maintain an inert environment for carbonization. The flow rate of N₂ gas during the tests was 50 mL/min. On completion, the mass loss (%) and derivative mass loss data (%/min) were plotted as the TG and DTG graphs. Subsequently, the temperature profile characteristics (TPCs) of the DDG coal carbonization process were determined from the TG/DTG plots. The TPCs including; the ignition (T_i), midpoint (T_m), peak decomposition (T_p), and burnoff (T_f) temperatures along with the mass loss (M_L , %) and residual mass (R_M , %) were determined based on the procedural features of the Shimadzu Thermal analysis software (Version: Workstation TA-60WS). Based on the TPCs deduced, the carbonisation degradation kinetics of DDG was determined from the peak decomposition (T_p) values substituted into the Kissinger Kinetic Model (KKM). The fundamental theory and model equations of KKM are presented in section 2.4.

2.4. Carbonisation kinetic analysis

The Kissinger Kinetic Model (KKM) was adopted to examine the carbonisation kinetic properties of DDG coal in this study. The fundamental theory and model equations of KKM are derived from the general Arrhenius equation for thermally degrading carbon materials described as follows;

$$k(T) = A \exp\left(-\frac{E_a}{RT}\right) \quad (1)$$

where the terms; $k(T)$, A (min^{-1}), E_a (kJ mol^{-1}), and R ($\text{J mol}^{-1} \text{K}^{-1}$) denote the temperature-dependent rate constant, frequency factor, activation energy, and molar gas constant, respectively.

Therefore, the thermal degradation of DDG coal under non-isothermal, multiple heating rates, and oxidative combustion conditions can be described by the equation;

$$\frac{d\alpha}{dT} = \frac{A}{\beta} \exp\left(-\frac{E_a}{RT}\right) f(\alpha) \quad (2)$$

where the terms β denotes the heating rate ($\beta = 10^\circ\text{C}/\text{min}$, $20^\circ\text{C}/\text{min}$, $30^\circ\text{C}/\text{min}$) and $f(\alpha)$ denotes the function of reaction model for the combustion kinetics of DDG coal. Next, the separation and integration of variables were performed to deduce the governing model equations for the Kissinger kinetic model (KKM). Consequently, the peak decomposition (T_p) of the DTG plots was substituted into Eq 3 to determine the kinetic parameters for the thermal degradation of DDG. The KKM equation is given by as follows;

$$\ln\left(\frac{\beta}{T_p^2}\right) = \ln\left(\frac{AR}{E_a}\right) - \ln\left(\frac{E_a}{RT_p}\right) \quad (3)$$

Subsequently, Eq. 3 was adopted to compute the activation energy, E_a and frequency factor (A) from the straight plot of $\ln(\beta/T_p^2)$ against $1/T_p$ - where p is the peak temperatures for drying (T_{DRY}), and devolatilization (T_{DEV}) deduced from the DTG peaks for drying and devolatilization respectively.

3. Results and discussion

3.1. Physicochemical properties

Table 1 presents the physicochemical properties of DDG coal based on ultimate (elemental), proximate, and calorific value analyses. The results are all reported in dry basis (*db*) except for the moisture content, which is reported in as-received basis (*ar*).

Table 1. Physicochemical fuel properties of Duduguru (DDG) coal

Analyses	Element	Symbol (Unit)	Composition
Ultimate	Carbon	C (wt.%)	63.77
	Hydrogen	H (wt.%)	5.87
	Nitrogen	N (wt.%)	1.39
	Sulphur	S (wt.%)	0.66
	Oxygen	O (wt.%)	28.31
Proximate	Moisture content	M* (wt.%)	6.48
	Volatile matter	VM (wt.%)	81.71
	Ash content	A (wt.%)	0.54
	Fixed carbon	FC (wt.%)	17.75
Calorific	High Heating Value	HHV (MJ/kg)	28.39

As observed, DDG has high contents of carbon and hydrogen but low oxygen. Likewise, it contains high volatile matter along but low ash, nitrogen, and sulphur content. The results of the calorific analysis revealed that DDG has a higher heating value (HHV) of 28.39 MJ/kg. The high heating value of coals is typically ascribed to the high carbon, hydrogen, and low oxygen contents [24]. In comparison, the HHV of DDG is significantly higher than other Nigerian coals; Owukpa (26.51 MJ/kg), Amansiodo (27.48 MJ/kg) [18], Shankodi-Jangwa (27.22 - 27.37 MJ/kg) [20, 22]. The results indicate the high energy potential of DDG for future energy recovery applications. Furthermore, the HHV of DDG was adopted to predict the rank of the sample using the ASTM standard D388 [25]. Based on the HHV, DDG could be classified as high volatile bituminous C coal, which typically exhibits HHV in the range 26.70 MJ/kg - 30.20 MJ/kg. Based on the results of this study, DDG could be effectively utilised thermally for steam generation or metallurgical coke production for power generation or the manufacture of cement, iron, and steel. However, further tests are required to ascertain the rank, classification, and future applications of DDG.

3.2. Microstructure and chemical properties

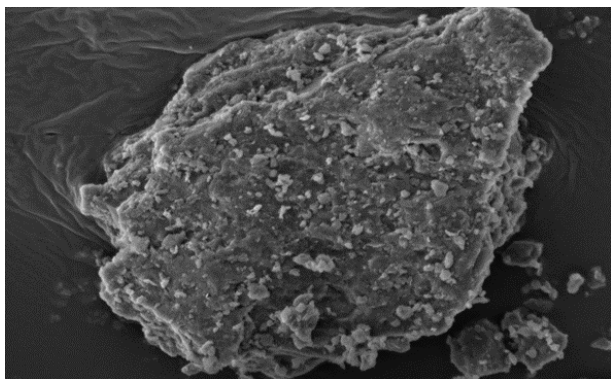


Figure 1. SEM Micrograph of Duduguru (DDG) coal

The SEM micrograph (magnification $\times 1000$) showing the microstructural and chemical properties of DDG are shown in Figure 1.

The results show that the morphology and microstructure of DDG revealed a solid but rough surface comprising various sized particles ranging from fine to coarse grains. As observed, the coarse particles are characterised by a distinct white sheen, whereas the small and finer particles showed a darker hue. According to previous studies [26-27], the white lustre is ascribed to the existence of quartz, kaolinite, and other metal-

based elements such as Ti and Fe typically found in the structure of coal. Therefore, the chemical composition of DDG was further examined by EDX analysis, as presented in Table 2.

As observed in Table 2, the EDX analysis revealed the presence of C, O, Mg, Al, Si, S, Ca, Ti, and Fe in the structure of DDG. The major elements detected were C and O with

atomic/weight compositions above 80% and 13%, respectively. The high carbonaceous nature of DDG is due to its rank classification as a high volatile bituminous class C coal. However, the O may be due to the presence of bonded oxygen groups in various forms as oxides of the metals Mg, Al, and Si typically present in coal samples.

Table 2. EDX chemical composition of DDG coal

Elements in coal	Symbol of element	Weight composition (Wt.%)	Atomic composition (wt. %)
Carbon	C	80.35	85.20
Oxygen	O	17.53	13.96
Magnesium	Mg	0.05	0.03
Aluminium	Al	0.46	0.22
Silicon	Si	0.52	0.23
Sulphur	S	0.59	0.23
Calcium	Ca	0.11	0.04
Titanium	Ti	0.21	0.06
Iron	Fe	0.17	0.04

The minor elements detected were; Mg, Al, Si, S, Ca, Ti, and Fe based on their low compositions detected below 1%. The elements Mg, Al, and Si, exist as oxides MgO, Al₂O₃, and SiO₂, whereas S and Ca exist as FeS₂ and Wollastonite. Lastly, Ti and Fe were detected in elemental form and could be responsible for the lustre of DDG as observed during SEM analysis.

3.3. Carbonization (pyrolysis) characteristics

The TG and DTG plots obtained based on the mass loss from the carbonisation studies are shown in Figures 2 and 3. Typically, TG analysis is performed to examine the thermal degradation behaviour and temperature profile characteristics (TPCs) of materials under various oxidative/non-oxidative along with isothermal/non-isothermal conditions. In this study, the effect of temperature and multi-heating rates was examined for DDG coal under non-oxidative (using nitrogen (N₂) gas flow) and dynamic conditions. The objective is to also simulate its thermal degradation behaviour and determine its characteristic temperature profiles during pyrolysis otherwise termed carbonisation.

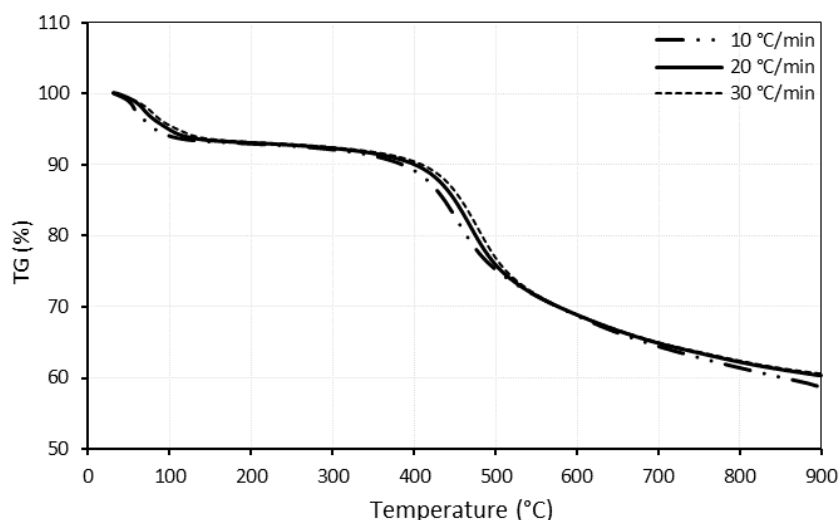


Figure 2. TG (%) Mass loss plots for carbonisation of DDG coal

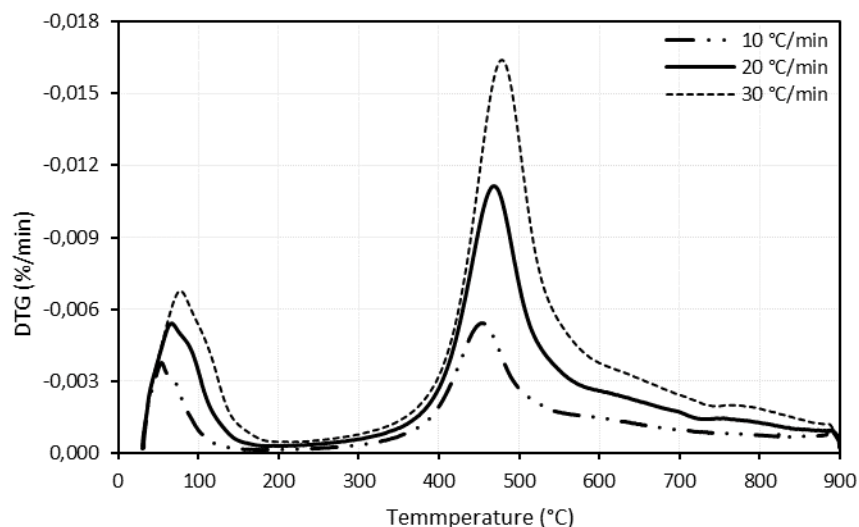


Figure 3. DTG (%) Mass loss plots for carbonisation of DDG coal

As observed, the effect of dynamic heating from RT to 900 °C resulted in the loss of mass of the sample during TGA. Furthermore, the results show that the increase in temperature and heating rates significantly influenced the thermal degradation behaviour of DDG coal, thereby resulting in mass loss from the initial condition of 100% to approximately 40%, on average for the heating rates. Typically, the higher heating rates tend to increase in the mass loss of coal during pyrolysis as reported by Shi et al., [28]. This observation is ascribed to an increase in the evolution of volatile matter, which occurs at higher heating rates during coal thermal analysis. Furthermore, the results showed that the increase in heating rates resulted in a shift of the TG plots to the right-hand side indicating distinct changes in the TPCs, as presented in Table 3. The shift in TG plots is reportedly ascribed to thermal lag that alters the time required for thermally degrading samples to attain equilibrium during TGA [29-30].

Table 3. TPCs for DDG coal based on TG plots

Heating rate (°C/min)	Onset temp. (°C, T_{ons})	Midpoint temp. (°C, T_{mid})	Endset temp. (°C, T_{end})	Mass loss (M_L , %)	Residual mass (R_M , %)
10	374.24	460.20	561.40	41.28	58.72
20	381.18	470.39	562.89	39.64	60.36
30	388.67	478.42	570.61	39.32	60.68

Table 3 shows that the onset (T_{ons}), midpoint (T_{mid}), and endset (T_{end}) temperature profiles for DDG all increased as the heating rates increased from 10 °C/min to 30 °C/min. As stated earlier, the shift in the TG plots to the right-hand side is as a result of the thermal lag, which results in distinct changes in the TPCs of the samples. In this study, the onset (T_{ons}) temperatures occurred in the range 374.24°C to 388.67°C or 381.36°C on average; whereas the midpoint (T_{mid}) temperatures were from 460.20 °C to 478.42°C or 469.67°C on average and lastly the endset (T_{end}) temperatures were from 561.40°C to 570.61°C or 564.97°C on the average. Furthermore, the change in heating rates also affected the mass loss (M_L) and the mass of residuals (R_M) after the TG analysis. As observed, the mass loss (M_L) decreased from 41.28% to 39.32%, which resulted in the mass of residuals (R_M) in the range from 58.72% to 60.68%. The results showed that the increase in heating rates from lower to higher values enhances the formation of a higher mass of residuals (R_M). Due to the non-oxidative nature of the thermal environment during TGA, the mass of residuals (R_M) could be reasonably used as an indication of the coke formed whereas the mass loss (M_L) denotes the volatiles (gas or liquid products) produced by the sample during carbonisation. Hence, the results indicate that the thermal degradation of DDG coal under non-oxidative or carbonisation conditions could

result in an average mass of volatiles of 40.08% and 59.92% coke. However, the coke potential of DDG needs to be determined by ASTM techniques.

Next, the degradation mechanism for the non-oxidative thermal analysis of DDG was examined by derivative thermogravimetric analysis (DTG). Figure 3 presents the DTG plots for DDG coal at various heating rates (10, 20, and 30°C/min) during TGA from RT to 900 °C.

As observed, the DTG plots for each heating rate was characterised by two sets of endothermic peaks with the temperature ranges from RT to 200°C and from 200°C to 600°C. As observed, the size of the peaks increased with increasing heating rate with smallest and largest peaks observed at 10°C/min and 30°C/min, respectively. Furthermore, the DTG plots indicate that the thermal degradation of DDG occurred in three (3) stages, namely; Stage I: from RT to 200 °C; Stage II from 200°C to 600°C, and finally stage III from 600°C to 900°C.

The degradation of DDG during Stage I could be ascribed to the drying or the loss of surface-bound moisture in the coal structure. In this study, the average mass loss in this stage was 5.69 %, which is in good agreement with the observed moisture content of 6.48% (Table 1). Stage II resulted in a significantly higher mass loss for the sample or an average of 25.46%, which is typically ascribed to the loss of volatile matter during thermal degradation of carbonaceous materials such as coal. As observed, the mass loss during this stage of TGA was significantly lower than the reported content of volatiles. This observation could be ascribed to the low reactivity of the DDG coal sample, resulting in only a partial loss of volatile matter. Finally, stage III resulted in an average mass loss of 8.93% thereby forming coke, fixed carbon, and some ash after thermal degradation of the DDG sample.

The effects of temperature and change in heating rates on the DTG plots was also examined through the temperature profile characteristics (TPCs), as presented in Table 4. The TPCs examined were the peak temperatures for drying (T_{DRY}) and devolatilization (T_{DEV}) along with the average rates of thermal degradation of the sample during the TGA carbonisation process.

Table 4. Temperature profile characteristics for DTG plots

Heating rate (°C/min)	Drying peak temp. (T_{DRY})	Rate (%/min)	Devolatilization peak temp. (T_{DEV})	Rate (%/min)
10	53.88	1.25	455.07	1.57
20	67.03	1.90	468.59	3.57
30	76.83	2.43	478.25	5.20

As observed, the peak temperatures for drying (T_{DRY}) and devolatilization (T_{DEV}) both increased with increase in the heating rates from 10 °C/min to 30 °C/min during the TGA carbonisation process. The findings reveal that the TPCs for DDG were significantly influenced by the change in TGA parameters. Furthermore, it can be reasonably inferred that heating the DDG sample between 53.88°C and 76.83°C or an average of 65.91°C could altogether remove surface-bound moisture from the sample. Similarly, the findings indicate that heating the samples between 374.24°C and 570.61°C can effectively devolatilize the sample based on the devolatilization (T_{DEV}) values from 455.07 °C to 478.25°C. Overall, the findings indicate that DDG is not highly reactive and will require higher temperatures to undergo complete devolatilization or thermal degradation into gas or liquid fuels during thermal conversion. In addition, the findings indicate that DDG is not low-rank coal since such coals are characterised by high reactivity during thermal conversion. Lastly, the DDG characteristics indicate it is also suited for coke production or solid products from carbonisation.

3.4. Kinetic degradation characteristics (Kissinger)

Kissinger Kinetic Model plots for the non-isothermal and multi-heating rate TGA carbonization of DDG are shown in Figures 4 and 5. The Kissinger kinetic plots for the drying and devolatilization stages were calculated from the maximum drying and devolatilization peaks deduced from Table 4.

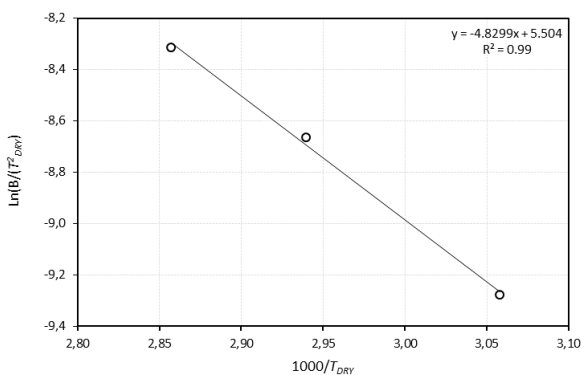


Figure 4. Kissinger kinetic plots for Drying DDG Coal

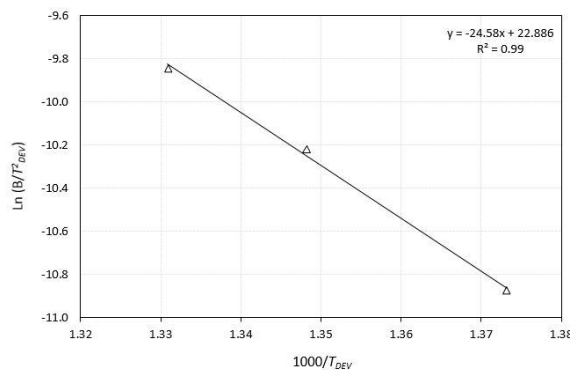


Figure 5. Kissinger kinetic plots for Devolatilization of DDG Coal

Based on the plot in Figure 4, the activation energy, E_a for drying DDG coal is 40.16 kJ/mol, whereas the frequency factor, A is $1.19 \times 10^{03} \text{ min}^{-1}$. Likewise, the kinetic parameters for devolatilization were computed based on Figure 5. Therefore, the activation energy, E_a for the devolatilization of DDG is 204.36 kJ/mol, whereas the frequency factor (A) is $1.54 \times 10^{11} \text{ min}^{-1}$. The values for the kinetic parameters for drying and devolatilization of DDG were computed at high $R^2 = 0.99$, respectively. In comparison, the kinetic parameters; activation energy, $E_a = 40.16 \text{ kJ/mol}$ and frequency factor, $A = 1.19 \times 10^{03} \text{ min}^{-1}$ for drying DDG coal is higher than the $E_a = 28.86 \text{ kJ/mol}$ and $A = 5.97 \times 10^{00} \text{ min}^{-1}$ deduced for Owukpa coal. Furthermore, the values of $E_a = 204.36 \text{ kJ/mol}$ and $A = 1.54 \times 10^{11} \text{ min}^{-1}$ for the devolatilization of DDG is higher than the $E_a = 57.29 \text{ kJ/mol}$ and $A = 9.86 \times 10^{00} \text{ min}^{-1}$ deduced for Owukpa coal in the literature.

Overall, the results indicate that DDG is not a highly reactive coal, as earlier deduced, under the thermal conditions examined in this study. Based on the physicochemical and thermal properties of DDG described in this study, it can be reasonably inferred that DDG is a high-rank coal. Hence, DDG could be potentially utilized for steam generation in power generation or metallurgical coke production for the manufacture of cement, iron, and steel in the industry.

4. Conclusions

The physicochemical, calorific value, microstructure, thermal, and kinetic fuel properties of the newly discovered Duduguru (DDG) coal from Nigeria were characterised and presented in this study. The results showed that DDG has a high calorific value of 28.39 MJ/kg, which can be ascribed to its high carbon, hydrogen, and low oxygen contents. Based on its volatile matter content, DDG could be ranked as a high volatile bituminous C coal. The microstructure and chemical analyses of DDG indicated it is characterised by fine to coarse grain-sized particles with a distinct white sheen, which could be due to the presence of quartz, kaolinite, and other metal-based elements. The thermal analysis results indicated that the variation of temperature and heating rates during the TGA carbonisation significantly influenced the thermal degradation behaviour and temperature profile characteristics. Hence, DDG experienced significant mass loss (ML = 39.32% to 41.28%) and residual mass (RM = 58.72% to 60.68%). Overall, the results indicate that DDG is a high-rank coal with potentials for use in steam generation or metallurgical coke production for power generation and the manufacture of cement, iron, and steel.

Acknowledgements

The authors gratefully acknowledge Universiti Teknologi Malaysia (UTM) Malaysia, National Centre for Petroleum Research and Development (NCPRD) and Abubakar Tafawa Balewa University (ATBU) Nigeria for the material and technical support.

References

- [1] Suárez-Ruiz, I, Diez, MA, and Rubiera, F, Coal, in *New Trends in Coal Conversion*. 2019; Elsevier. p. 1-30.
- [2] Hafner, M and Wochner, A, How Tectonic Shifts in Global Energy Are Affecting Global Governance, in *Global Governance in Transformation*. 2020; Springer. p. 147-162.
- [3] OECD Working Paper, *The Global Value of Coal 2012*.
- [4] Wang, Y, Byers, E, Parkinson, S, Wanders, N, Wada, Y, Mao, J, and Bielicki, JM. Vulnerability of existing and planned coal-fired power plants in Developing Asia to changes in climate and water resources. *Energy & Environmental Science*, 2019; 12(10): 3164-3181.
- [5] Patel, V, Saha, B, and Chatterjee, K. Fuel saving in coal-fired power plant with augmentation of solar energy. in *2014 International Conference on Power, Control and Embedded Systems (ICPCES)*. 2014. IEEE.
- [6] IEA, *Market Report Series: Coal 2018*. 2018; International Energy Agency: Paris, France.
- [7] Ahmad, S. Is coal the only way to deal with energy poverty in developing economies? 2016 [cited 2019 11 November]; Available from: <https://bit.ly/2Nyl5S4>.
- [8] World Bank Group. *Ending Energy Poverty*. 2019 [cited 11 November 2019; Available from: <https://bit.ly/34S0CxI>.
- [9] Indrawati, SM. What you need to know about energy and poverty. 2015 [cited 11 November 2019]; Available from <https://bit.ly/2X225hU>.
- [10] Nyakuma, BB, Ojoko, EO, Oladokun, O, Bello, AA, Aboje, AB, Ivase, TJ-P, Al-Shatri, AH, and Alkali, H. Fuel Characterization and Thermal Degradation Behaviour of Owukpa Coal. *Petroleum & Coal*, 2018; 60(6): 1142-1148.
- [11] Nyakuma, B, Oladokun, O, Akinyemi, S, Ojoko, E, Jacob, G, Abdullah, T, Alkali, H, and Al-Shatri, A. Comprehensive Evaluation of the Combustion Kinetic Characteristics of Owukpa Coal. *Coke & Chemistry*, 2019; 62(8): 371-378.
- [12] Ohimain, EI. Can Nigeria generate 30% of her electricity from coal? *International Journal of Energy and Power Engineering*, 2014; 3(1): 28-37.
- [13] Oyedepo, SO. On energy for Sustainable Development in Nigeria. *Renewable and Sustainable Energy Reviews*, 2012; 16(5): 2583-2598.
- [14] Oyedepo, SO. Towards achieving energy for sustainable development in Nigeria. *Renewable and Sustainable Energy Reviews*, 2014; 34: 255-272.
- [15] Shaaban, M and Petinrin, J. Renewable energy potentials in Nigeria: Meeting rural energy needs. *Renewable and Sustainable Energy Reviews*, 2014; 29: 72-84.
- [16] Salman, B, Nomanbhay, S, and Foo, DCY. Carbon emissions pinch analysis (CEPA) for energy sector planning in Nigeria. *Clean Technologies and Environmental Policy*, 2019; 21(1): 93-108.
- [17] Nyakuma, B. Physicochemical Characterization and Thermal Analysis of newly discovered Nigerian coals. *Bulgarian Chemical Communications*, 2016; 48(4): 746 - 752.
- [18] Chukwu, M, Folayan, C, Pam, G, and Obada, D. Characterization of some Nigerian coals for power generation. *Journal of Combustion*, 2016; 2016.
- [19] Nyakuma, BB and Jauro, A. Chemical and Pyrolytic Thermogravimetric Characterization of Nigerian Bituminous Coals. *GeoScience Engineering*, 2016; 62(3): 1-5.
- [20] Ryemshak, SA and Jauro, A. Proximate analysis, rheological properties and technological applications of some Nigerian coals. *Int. Journal of Industrial Chemistry*, 2013; 4(1): 7.
- [21] Ocheri, C and Okafor, WCS. Metallurgical Research, Development and Raw Materials Sourcing for the Development of Steel Industries in Nigeria. *African Journal of Education, Science and Technology*, 2013; 1(2): 146-152.
- [22] Nyakuma, B, Jauro, A, Oladokun, O, Uthman, H, and Abdullah, T. Combustion Kinetics of Shankodi-Jangwa Coal. *Journal of Physical Science*, 2016; 27(3): 1-12.
- [23] Ocheri, C. Revitalization of Coal Development in Nigeria for Industrial Advancement. *SFJ Metallurgical Science*, 2017; 1(2): 1-9.
- [24] Speight, JG. *The Chemistry and Technology of Coal*. Chemical Industries, 2012: 8.
- [25] ASTM D388-12. *ASTM Standard D388-12, 2012. Standard classification of coals by rank*.
- [26] Sengupta, P, Saikia, PC, and Borthakur, PC. SEM-EDX characterization of iron-rich kaolinite clay. *Journal of Scientific and Research*, 2008; 67(1): 812-818.
- [27] Garzanti, E, Andò, S, and Vezzoli, G. Settling equivalence of detrital minerals and grain-size dependence of sediment composition. *Earth and Planetary Science Letters*, 2008; 273(1-2): 138-151.
- [28] Shi, L, Liu, Q, Guo, X, Wu, W, and Liu, Z. Pyrolysis behaviour and bonding information of coal—A TGA study. *Fuel Processing Technology*, 2013; 108: 125-132.

- [29] Damartzis, T, Vamvuka, D, Sfakiotakis, S, and Zabaniotou, A. Thermal degradation studies and kinetic modelling of cardoon (*Cynara cardunculus*) pyrolysis using thermogravimetric analysis (TGA). *Bioresource Technology*, 2011; 102(10): 6230-6238.
- [30] Słopiecka, K, Bartocci, P, and Fantozzi, F. Thermogravimetric analysis and kinetic study of poplar wood pyrolysis. *Applied Energy*, 2012; 97: 491-497.

To whom correspondence should be addressed: Dr. Bemgba B. Nyakuma, Hydrogen and Fuel Cell Laboratory, Institute of Future Energy, Universiti Teknologi Malaysia, 81310 Skudai, Johor, Malaysia, E-mail: bbnayax1@gmail.com

Depth Estimation, Structural Features and Mineralization from High Resolution Aeromagnetic and Satellite Data over Yola Arm of the Upper Benue and Adjoining Basement Regions, Northeastern Nigeria

Bello Rasaq¹, Hayatudeen Musa^{1*}, Nsikak Edet Bassey², Kaigama Usman³

¹ Physics Department, Federal University Kashere, Gombe State Nigeria

² Geology Department, Akwa Ibom state University, Mkpato Enin, Nigeria

³ Geology Department, Modibbo Adama University of Technology Yola, Nigeria

Received April 13, 2019; Accepted July 22, 2020

Abstract

High-resolution aeromagnetic and satellite data investigation was carried out over Yola arm (upper Benue) and adjoining basement regions of northeastern Nigeria, in order to carry out depth estimations structural features and mineralization potentials of the area. Total intensity magnetic map was processed using the *Oasis Montaj*™ programming software to get the residual map, analytic signal and tilt depth methods. Results show that the depth estimates are in the range of 1.2 to 4.4 km. These outcomes are similar to what has been obtained by previous researches in the study area. Satellite data processing was done using the arcGis software, in order to understand the structural frame work and mineralization potentials of the area. The structural features of the area are NE-SW and NW-SE which are pan African and pre pan African events.

Keywords: *Magnetic data; Mineralization; Satellite data; Structural features; Tilt depth.*

1. Introduction

The use of high resolution aeromagnetic and satellite data over the Yola Trough and adjoining sectors of the basement blocks was done (Fig.1) for depths estimation, structural features and mineralization potentials. The study area is located between longitude 12^o 00'-13^o30'E and Latitude 8^o 00'-10^o 00'N, which is the Yola arm of the Upper Benue Trough, and it trends in the E-W direction. The Upper Benue Trough, is an important arm of the Benue Trough, it is formed by several sub basins of which evolution and distribution were closely controlled by a fracture system where the N55^oE Benue trend is dominant in the entire Trough and the surrounding basement. A compressive phase of late Maestrichtian age is responsible for the fracturing and folding of the cretaceous cover. The style and direction of folds are greatly influence by the basement structures. Evidence of tensional movement are also known in the Yola arm, this is why the major river in the area exhibit a "V" shape channel due to control by the NE-SW and NW-SE fracture system [1].

The Benue Trough was subjected to several depositional cycle characterized by the deposition of sedimentary rocks of varied composition and closely related to the structural evolution of Gulf of Guinea [2-3].

The drainage feature of this region is the Benue River which takes its source eastward from the Cameroons and for the other part by its main affluent the Gongola River which rises from the north central high lands composed of crystalline rocks. The Yola arm of the upper Benue trough is bounded by the Hawal Massif to the north and the Adamawa Massif to the south. Both Massifs extend into Cameroon Republic. Major towns in the area are Yola, Sugu, Song, Ganje and Toungo.

1.1. Geology of the area

The study area is part of the Yola Arm of the Upper Benue Trough and some sectors of the adjoining basement terrain which are contiguous to the Yola trough. The Trough is a Cretaceous sedimentary Basin that forms a narrow band of terranes which stretches eastward and splits into small isolated basins in Cameroon. The sedimentary rocks are mainly shales, sandstones, limestones, siltstone and clay, extrusive rocks are found within the sedimentary basin and in the basement. The basement rocks are Precambrian in age and consist of granitoids, basic intrusions and metamorphic rocks.

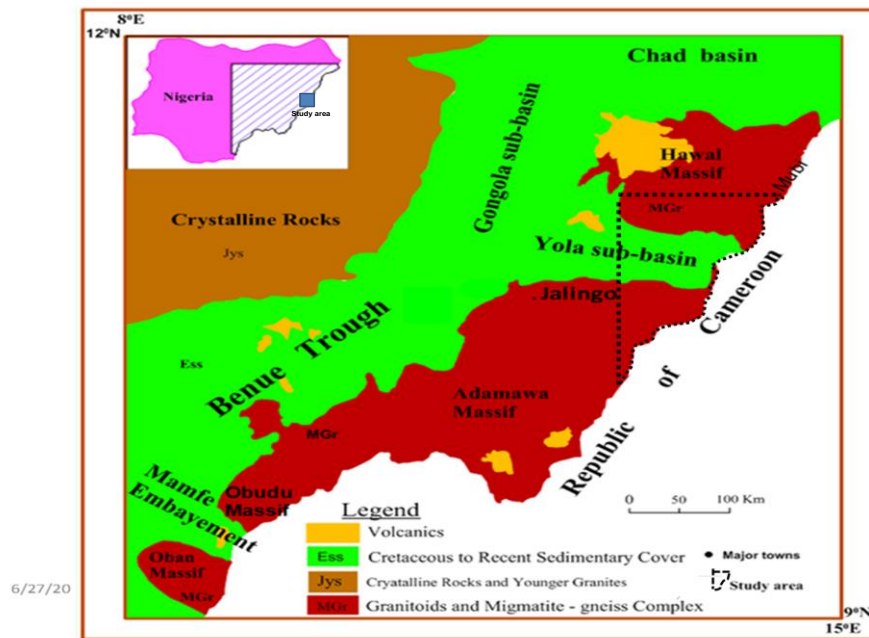


Fig.1. Regional geological map of Nigeria's eastern sector showing location of study area. Adapted from [4]

1.2. Previous studies

In 2006, Bassey [5] carried out structural study of satellite imagery over basement rocks of N.E Nigeria and Northern Cameroon, and the study revealed that lineaments in the area are attribute to the presence of joints, faults, shearing, deformation, dykes and veins which are product of pan African deformational episode.

In 1982, Benkheilil [6] studied the structure of the Upper Benue valley and concluded that folds and faults characterized the area which varies in size, style and more slightly in direction. Similar research was carried out by Benkheilil [7] where he analyzed the structure and geodynamic evolution of the intra continental Benue trough and concluded that the cretaceous Benue trough is a set of pull apart sub basin generate by sinistral displacement along pre-existing NE-SW transcurrent faults.

In 2014, Kwache *et al.* [8] studied the Geology of Dumne Area in Southeastern Hawal Massif, Northeastern Nigeria. Their result shows that the area is underlain by gneisses, migmatites, Older Granites and Tertiary basalts with granite gneiss dominating.

In their work, Opara *et al.* [9] studied the lineament and tectonic interpretation over Abakiliki area, evidences from airborne magnetic and landsat (ETM) data, the study revealed that lineaments identified in the area have principal trend directions in the NE-SW, NW-SE, N-S and E-W directions with the NE-SW trend direction been the dominant.

2. Materials and method

The high resolution aeromagnetic data used in this study were acquired for Nigeria Geological Survey Agency (NGSA) in 2010 as part of a country wide geological survey. The high reso-

lution aeromagnetic data has the following specifications, terrain clearance of 80 m, flight line spacing of 500 m and a tie line spacing 5000 m. The sheets with the following index numbers were used for this study: 175, 176, 177, 196, 197, 217 and 218. The high resolution aeromagnetic data was processed using the *Oasis Montaj*™ software in order to get the total magnetic intensity map and the residual maps. Other filtering employed are analytic signal and tilt depth methods. Tilt depth method is a simple method of estimating the depth to magnetic source bodies (assuming a vertical model) from contours of the magnetic tilt angle map [10]. The magnetic tilt method is a normalized derivative based on the ratio of the vertical and horizontal derivatives of the reduced to the pole field. The method assumes that the source structures have vertical contacts and there is no remanent magnetization and the magnetization is vertical. The tilt method was first described by [11], and further refined by [12] and is defined as

$$\theta = \tan^{-1} \left[\frac{\partial M / \partial z}{\partial M / \partial h} \right] \quad (1)$$

$$\text{where } \frac{\partial M}{\partial H} = \sqrt{\left(\frac{\partial M}{\partial x}\right)^2 + \left(\frac{\partial M}{\partial y}\right)^2} \quad (2)$$

and $\frac{\partial M}{\partial x}, \frac{\partial M}{\partial y}, \frac{\partial M}{\partial z}$ are the first order derivatives of the magnetic field M in the x, y, and z directions.

Among the interesting properties of the tilt angle is the nature of the arctan trigonometric function, which restrict all tilt angles to values between -90° and $+90^\circ$ regardless of the amplitude of the vertical or the absolute value of the total horizontal gradient.

From equations 1 and 2, it is derived that

$$\theta = \tan^{-1} \left[\frac{h}{z_c} \right] \quad (3)$$

where z_c is the depth to the top of contact on the basement.

Equation (3) indicates the tilt angle above the edges of the contact is 0° when $h=0$ and equal to 45° when $h = z_c$ and -45° when $h = -z_c$. Thus, the zero contour delineates the spatial location of the edges of the magnetic source "whilst the depth to the source is the physical distance between this zero contour and either the -45° or the $+45^\circ$ contour or their average. Therefore, half the width of the -45° to $+45^\circ$ contours provides an immediate estimate of the depth to basement". The two principal advantages of this method are its simplicity both in its theoretical derivation and its practical application. It also provides both a qualitative and a quantitative approach to interpretation by allowing the interpreter to visually inspect (spatially analyze) the tilt depth map to identify locations where depth estimates may be compromised by interfering magnetic anomalies and location where more reliable depth estimates can be made. By virtue of using first order derivatives, the method is potentially less sensitive to noise in the data than methods using second order derivatives.

While the airborne satellite data was obtained from the National Centre for Remote Sensing (NCRS) Jos, the data obtained is SPOT 5, which is polar, circular, sun-synchronous and phased. SPOT 5 was launched on May 4, 2002. The interpretation of satellite imagery map of the study area was carried out in order to understand the structural frame work and geometry of the area which can be an aid to further exploratory work. Structural studies involve extracting lineament/structures from high resolution satellite imagery map. The accuracy of extracted lineament depends strongly on the spatial resolution of the satellite imagery, higher resolution imagery results in a high quality lineament map. The spot 5 sensor provides imagery with a higher resolution of (5m) than the Nigeria satX sensor which has a resolution of (25 m), the ArcGIS software was used for this exercise.

Several digital image enhancement techniques such as general contrast stretching and edge enhancement were applied to the SPOT 5 imagery using the ArcGIS software. The first stage of structural mapping involved mapping and identifying lineaments that could be due to the contacts between two rock types of contrasting magnetic susceptibility or edges of structures that could be faults or intrusive within the sediments.

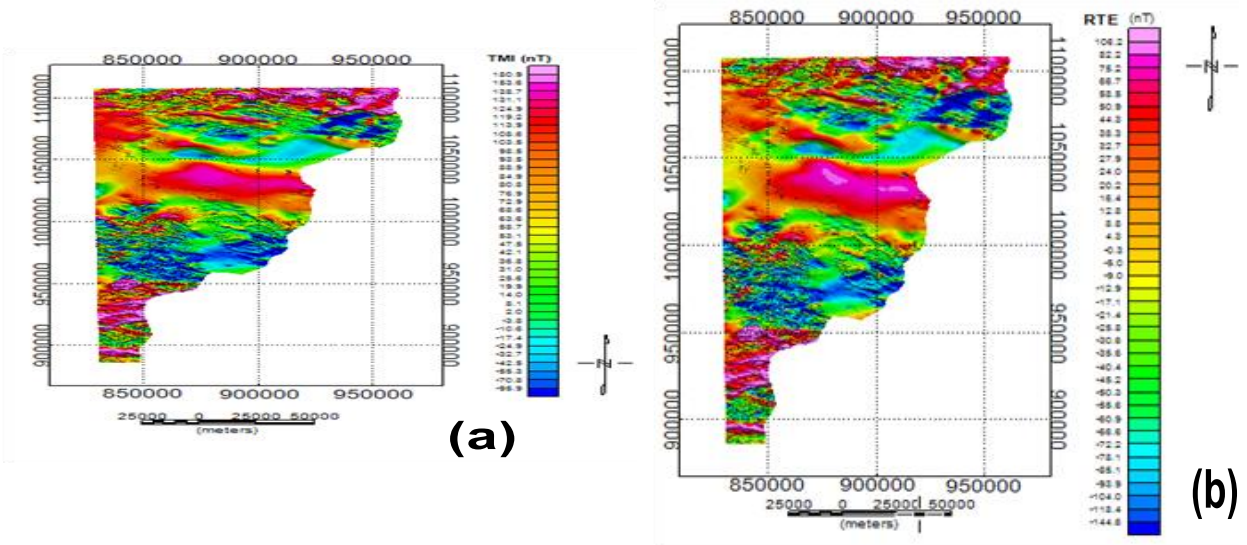
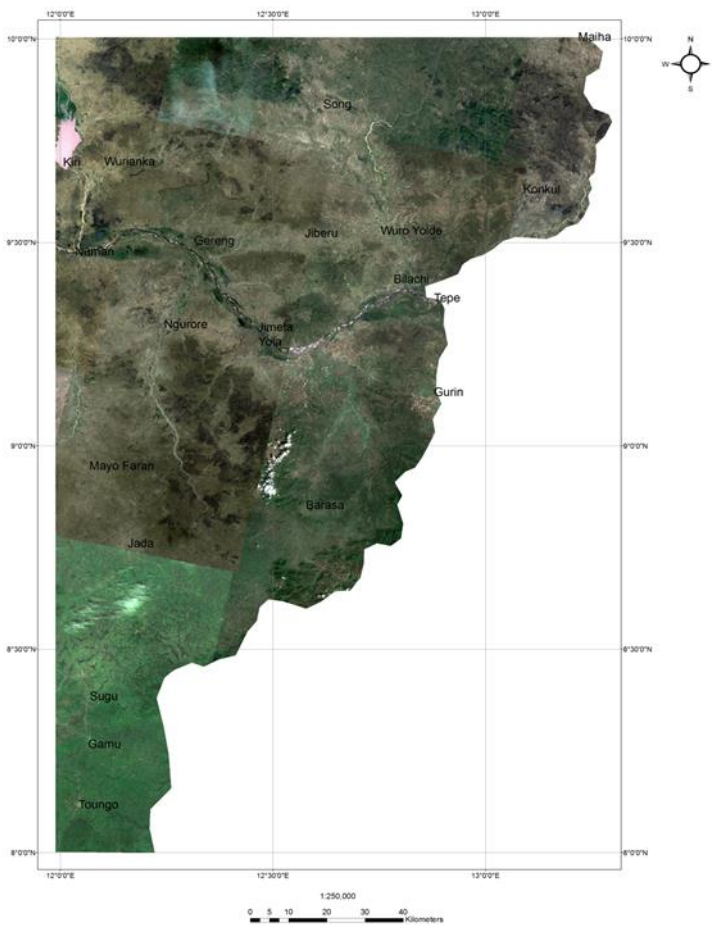


Fig. 2a and b. Total magnetic intensity and residual maps of the study area respectively



The second stage of the mapping involved identifying lineaments from the image and digitizing them on-screen and saving them as a feature class in a geodatabase. To achieve this, all the various data sets were displayed in ArcMap and by studying one layer at a time and comparing with other layers in the GIS environment. To start digitizing the lineaments, a shapefile was created in ArcCatalog and it was set to the same coordinate and spatial reference as the other data sets. The digitizing tool was then used to map out the lineaments observed from the various data sets on-screen. A rose diagram of the lineaments within the study area was created in Georient software.

Fig. 3. The spot 5 satellite imagery map of the study area [13]

3. Result and discussion

Figures 4 and 5 showed the tilt angle map with aeromagnetic data and also extrapolated, at zero with + 45 and -45, contours, and depth to basement contours map respectively. Depth

estimates range from 1.2 to 4.4 km. Maximum depth are found in the central part of the study area where the magnetic basement attain a depth of 4.4 km as shown in figure 6, these are places around the Benue river.

The northern part of the study area has a basement surface that is generally shallow, while the southern part of the study area has intermediate to shallow depth sources. This basement topography is consistent with what is obtained from the power spectrum of the study area [14].

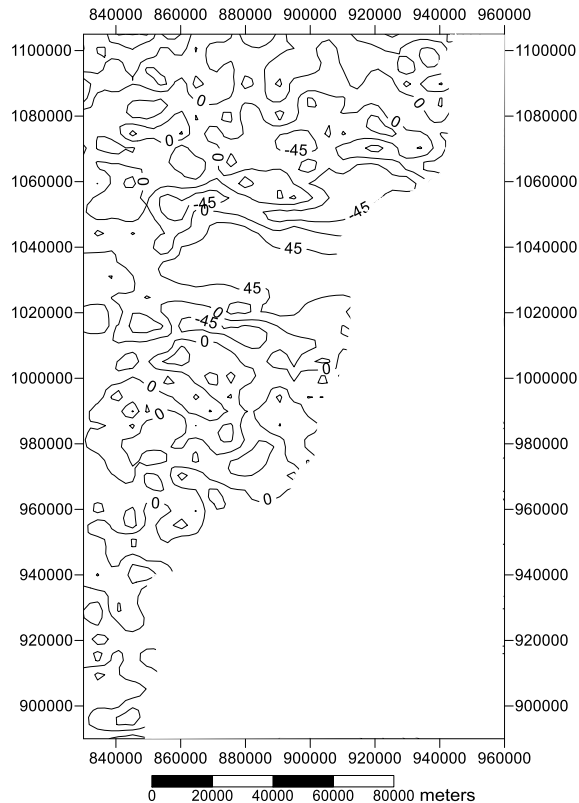


Fig. 4. Tilt Angle (in degrees) for only the area with aeromagnetic data

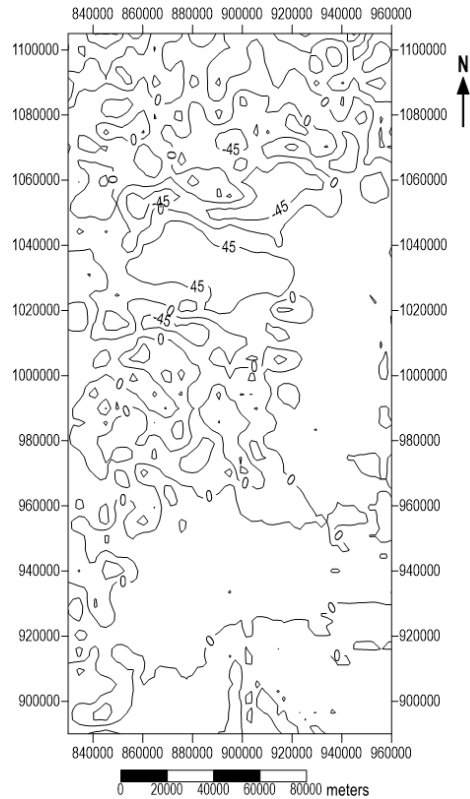
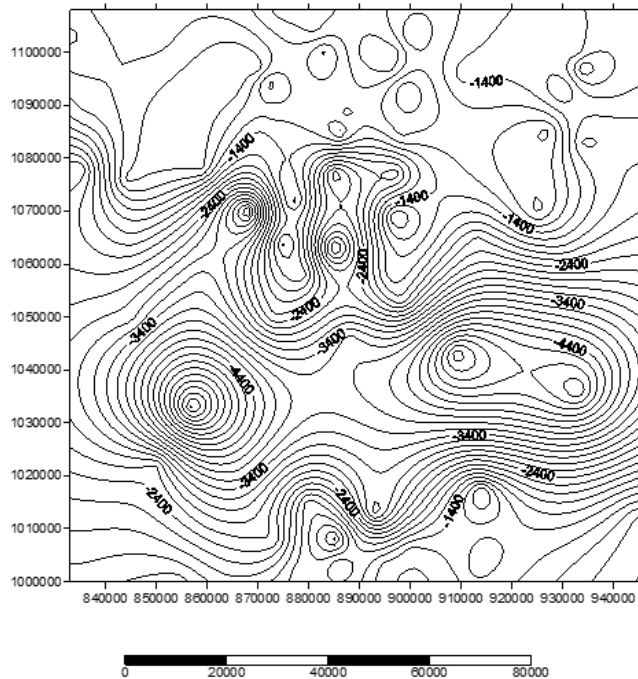


Fig. 5. Tilt Angle (in degrees) extrapolated over the entire area

The lineaments extracted from the image Spot 5, (Fig.3) range in length from 300 m to 3 km, Figure 7 is the structural map of the study area, with the rose diagram. Several faults were also mapped out within the study area such as a sinistral fault observed between Zumo and Maiha and a dextral fault close to Ganye.

The main fracture trends are gathered around the general direction of 45° and 315° . Apart from these main trends the principal sub-direction are 60° and 300° , followed by 65° and 325° . On a regional scale the general main trend of 45° and 315° parallel the main axis of the Benue trough and that of its lateral troughs. Field measurements showed that there are faults, joints and order structures in the area. The faults were identified based on striation and slicken sides with the NE-SW and NW-SE dominant trends as shown from the rose diagram. According to [1] these set of faults constitute part of conjugate set of lineaments that controls the flow direction of the Benue river. [7, 15] observed the occurrence of strike slip faults conjugate around compressive direction of 60° and 50° reverse to thrust faults in the upper Benue trough, in view of the fact that the basement dykes usually follow direction of the main fracture trend, it must be assumed that the earliest formation of the actual fracture pattern goes back to late post crystalline time. There is no evidence to suggest that certain trends were developed in later times.



This is particularly true for the trends parallel to the axis and to the margins of the Benue trough. The authors are of the believe that these trends actually apparently predated the formation of the trough, and consequently they may have had a certain influence on its orientation. Low fracture density has been notice in the central part of the area, this may also be indicative of considerable thickness. On the other hand, a considerable intensification of the fracturing in the border zones seems to have derived directly from the formation of the trough. A remarkable increase of fractures parallel to the trough margins is in fact to be noted namely in the Hawal basement and the Adamawa Massif i.e northern and southern part of the study area.

Fig. 6. Depth to basement contour map computed using tilt depth method

The result of the lineament density map of the study area is shown in (Fig.8), has two major zones of high density of lineaments and they all fall within the adjoining basement complex areas respectively. The map also gives good evidence of the general characteristics of the fracture pattern, showing in particular its great homogeneity over the area independent of the various geologic formations therefore these areas should be targeted for mineral exploration

This means that, except for local structural features, the main fractures are derived from the basement even in the sedimentary realms. With regard to fracture density it is to be noted that the basements show a greater high to the Cretaceous sediments, even though the latter are exposed to a much longer period of fracturing. A clear decrease of fracturing is to be noted in the Cretaceous sediments as shown in Figure 7, because major part of the joints and faults are older than the Cretaceous, part of the fracturing may therefore have been absorbed and rendered invisible in the upper part of the formations. The lower fracture density may also be indicative of considerable thickness in some places.

In 2011, Halilu [16] studied the stream sediment for barite mineralization around Tola, area in Mayo Belwa L. G. A. part of the Adamawa Massif, and found out that barite concentration is very low in the area, while manganese, molybdenum, chromium, lead, tellurium, lanthanum and iron, have high concentration as a result of weathering of different rock types which release these elements to the surrounding streams and major rivers. Geological and geochemical results reveal that the porphyritic granites of the area are their major source. Fault, fracture, and veins in filled with quartz are probably acting as a structural control on the concentration of these elements and their distribution pattern is mostly in the NW – SE direction. In 2014, Kwache [17] studied the composition and industrial quality of Dumne barite occurrence N.E Nigeria and found out that the barites in the area are of industrial quality. Geological and geochemical results reveal that the granites and gneisses of the area are their major source. Fault, fracture, and joints are probably acting as a structural control of the barites and their distribution pattern is mostly in the E-W direction. Faults fractures and shear zones of N40°E-N45°E are the dominant deformational features found in Dumne area of the Hawal basement complex, according to [14]. They trend in the NE-SW and E-W. Rock crystal mineralization occurs as detrital deposit in the NE-SW trending faults/joints in the granites.

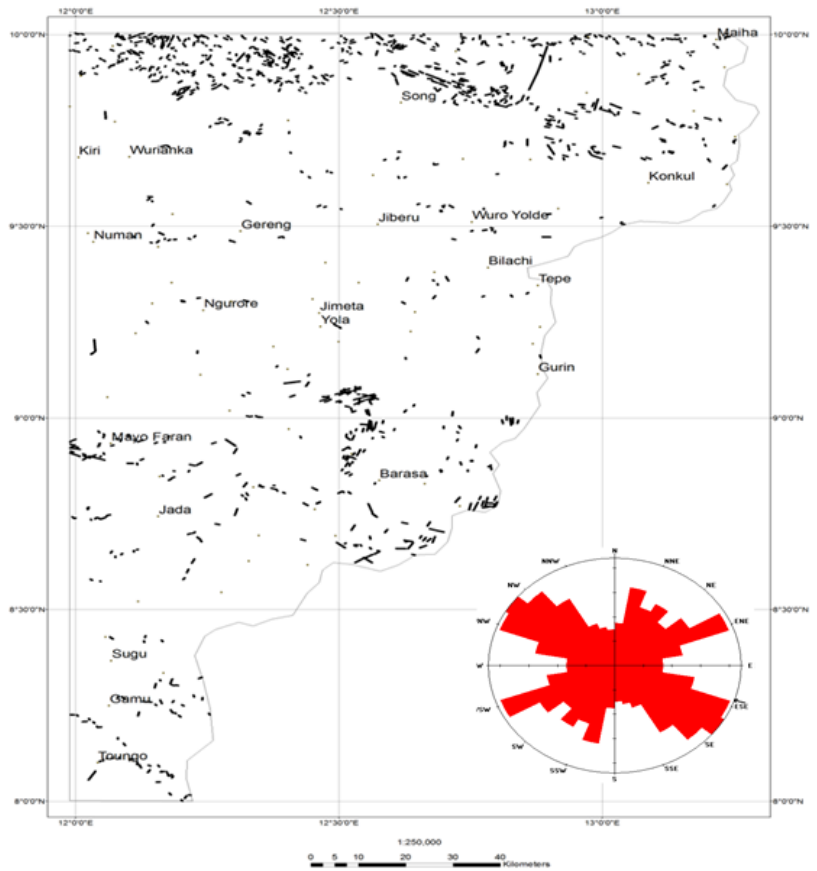


Fig. 7. Lineament map of the study area, with the rose diagram from satellite imagery (n= 207)

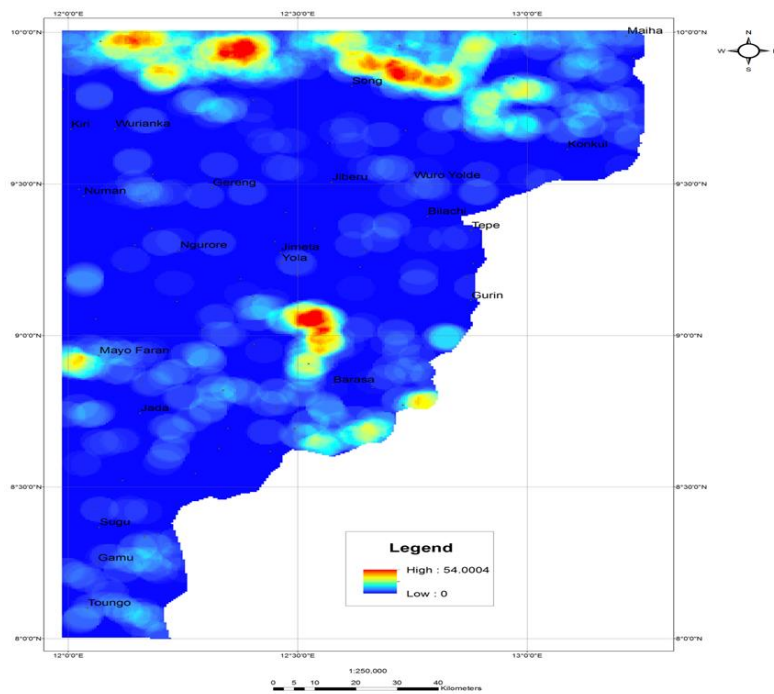


Fig. 8. Lineament density map of the study area

4. Conclusion

High resolution aeromagnetic and satellite data were used for this study in order to determine depths estimation, structural features and mineralization potentials of the area. The tilt depth method is a simple method of estimating the depth to magnetic source bodies. The magnetic tilt method is a normalized derivative based on the ratio of the vertical and horizontal derivatives of the reduced to the pole field. The method assumes that the source structures have vertical contacts and there is no remanent magnetization and the magnetization is vertical. Depth estimations are in the range of 1.2 to 4.4 km. These results are similar to what has been obtained by the same authors in their previous paper. The structural features range in length from 300 m to 3 km. Field measurements showed that there are faults, joints and order structures in the area, the faults were identified based on striation and slicken sides, several faults were also mapped out within the study area such as sinistral and dextral faults. The lineament density map and areas where lineaments intersect are particularly advantageous in modern exploration geosciences in that they offer a quick glance at the spatial distribution of the density of lineaments and thus provide a useful data base in mineral exploration, these should be targeted for mineral exploration in the area. The significance of lineament studies lies in its applicability to mineral exploration, since the same or similar condition exist for ore bearing fluids in basement areas of the world [18]. The trend of the lineament extracted from this study area are similar to those that occur in the Nigerian basement complex, and it has been suggested that they may be related to deep seated structures within the underlying basement. Some known areas of mineral occurrences have been observed to correlate with zones of high lineament density. Major lineaments observed have been accounted for in terms of faults, joints and dykes. Most of these important minerals mentioned above are mined illegally, the government should as a matter of urgency stop the illegal miners and mandate its relevant agencies both at the state and federal level to carry out detail survey of both regional and local structures most especially regionally deep seated faults and local fault intersections that are deeply inclined, these can conduct ore bearing fluids from deep to shallow sites. Many regional and local fault structures can be traced from the basement rocks onto the adjacent sedimentary rocks. Detailed structural and geologic studies of these areas should be carried out for possible bigger occurrences that are currently not known.

References

- [1] Bassej NE, Abubakar SA, and Ishiaku JM. Hill slope housing development in Vinikilang, Yola, Nigeria. A geo-disaster risk. *Jour. of Earth Sci. and Geotechnical Engineering*, 2012; 2(1): 113-129.
- [2] Kogbe CA. Correlation of the stratigraphic sequence of the Middle Benue Basin with those of the Anambra and Upper Benue Basin. *Earth Evolutionary Science*, 1985; 2: 139-143.
- [3] Ofoegbu CO. A review of the geology of the Upper Benue Trough, Nigeria. *Journal of African, Earth Science*, 1985; 3: 283-291.
- [4] Haruna IV, Orazulike DM, and Ofulume AB. Preliminary geological and radiometric studies of granitoids of Zing-Monkin area, Adamawa Massif. NE Nigeria Global. *Journal of Geological Science*, 2011; 9(2): 123-134.
- [5] Bassej NE. Brittle deformational structure of Michika area, Hawal basement complex N.E Nigeria. *Global Journal of Geological Sciences*, 2006; 6(1 & 2): 51-54.
- [6] Benkheilil J. Structural map of upper Benue valley. *Journal of Mining and Geology*, 1982; 18: 40-151.
- [7] Benkheilil J. Structural and geodynamic evolution of the intracontinental Benue Trough (Nigeria) Elf Nigeria Ltd. 1986, SNEA(P). 97-169.
- [8] Kwache JB, and Ntekim EE. The Geology of Dumne Area in Southeastern Hawal Massif, North-eastern Nigeria. *International Journal of Science and Research*, 2014; 4(11): 2477-2488.
- [9] Opara AI, Onyekuru SO, Essien AG, Onyewuchi RA, Okonkwo AC, Emberga TT, and Nosiri OP. Lineament and tectonic interpretation over Abakiliki area: evidences from airborne magnetic and landsat ETM data. *International Journal of Research and Innovations in Earth Science*, 2015; 2(4): 111-121.

- [10] Salem A, Simon W, Derek F, Dhananjay R, Richard S. Tilt depth method: A simple depth estimation method using first order-order magnetic's derivative: *The Leading Edge*, 2007; 26: 12.
- [11] Miller HG, and Singh V. Potential field Tilt – a new concept for location of potential field source. *Journal of Applied Geophysics*, 1994; 32: 213-217.
- [12] Verduco B, Fairhead JD, Green CMM. New insights into magnetic derivatives for structural mapping: *The Leading Edge*, 2004; 23: 116-119.
- [13] NCRS (2020), National Centre for Remote Sensing, Jos, Nigeria. www.ncrsjos.orj.
- [14] Bassey NE, and Valdon YB. Structural features of rock crystal mineralization in Dumne area Hawal basement complex NE. Nigeria. *Int. J. Environmental Science*, 2011; 7(3): 1-8.
- [15] Guiraud M. Geological map of part of upper Benue valley. Explanatory notes. ELF Nigeria Ltd., 1989, p16.
- [16] Halilu M. Stream sediment survey for Barite mineralization around Tola, Mayo Belwa area, Upper Benue Trough. Unpublished M.Sc Thesis, Federal University of Technology 2011. Yola.
- [17] Kwache JB. Composition and industrial quality of Dunne barites N.E. Nigeria. Unpublished M.Sc Thesis, Federal University of Technology 2014, Yola.
- [18] Odeyemi IB, Anifowose I, and Asiwaju Bello A. Multi-technique graphical analysis of fractures from remote sensing images of basement regions of Nigeria. *Journal of Mining and Geology*, 1999; 3(1): 11-21.

To whom correspondence should be addressed: Dr. Hayatudeen Musa, Physics Department, Federal University Kashere, Gombe State Nigeria, E-mail: b_hayatudeenmusa@fukashere.edu.ng

INVESTIGATING THE INFLUENCE OF SOME WELL AND FLUID PARAMETERS ON THE ACCUMULATION OF LIQUIDS IN GAS WELLS

Amieibibama Joseph*, Ngowari O. Ikiriko

Department of Petroleum Engineering, University of Port Harcourt, Port Harcourt, Nigeria

Received February 12, 2019; Revised September 8, 2020, Accepted September 10, 2020

Abstract

During gas well production, it is easier to produce accumulated liquids (water or condensate) from wells with high gas flow rates than low rate wells to the surface. As pressure depletes, the carrying capacity of gas of entrained liquids reduces, inhibiting efficient production of gas and accumulated liquids to the surface. Whereas pressure depletion is naturally synonymous with depletion of finite resource in the reservoir, inadequate design and deterioration of well and fluid properties could influence and accelerate fast depletion of bottomhole flowing pressure; which is primarily responsible for the transport of accumulated fluids in the wellbore to the surface. In this paper, some well and fluid properties (tubing size, wellhead pressure, condensate-gas ratio and water-gas ratios) are investigated to determine how they influence and exacerbate accumulation of liquids in the wellbore. It was observed that irrespective of the tubing size used, at wellhead pressures up to 2000psi, the well quits flowing and larger tubing sizes increases gas rate, however may quit flowing at early times due to slugging resulting from higher liquid rates. Also, increase in condensate-gas ratio and water-gas ratio in the wellbore promotes increase in liquid accumulation in the wellbore.

Keywords: Liquid loading; Condensate-gas ratio; Water-gas ratio; Wellhead pressure; Tubing ID.

1. Introduction

Like oil wells, gas wells experience tenacious production decline during their lifetime due to depletion and associated well problems [1]. Liquid loading is one of the imminent problems gas wells undergo and has made gas wells susceptible to early shut downs. Liquid loading is the inability of gas wells to lift and continuously lift liquids that are co-produced with the gas from the wellbore. The inability of the gas to lift produced liquids out of the well results to the accumulation of these liquids (water or condensate or both) at the wellbore and thus increase in the bottomhole flowing pressure [2-3]. The increase in the bottomhole flowing pressure imposes a back pressure on the adjacent reservoir which drastically causes outright reduction of gas production or killing of the gas well [4-5].

Liquid loading is not easy to detect [6] and upon occurrence can lead to the cessation of production if no timely identification, prevention or remediation is carried out. It is a multi-phase flow phenomenon and its occurrence has always been connected to the existential flow regimes in the wellbore [7-9]. In this paper, some well and fluid properties are investigated to determine their influence on the accumulation of liquids in the wellbore

Liquid loading does not just happen but follows a mechanism of occurrence and depending on the system, the following can constitute the source of liquids in gas wells [10].

- i. Heavier fractions condensation: mass transfer occurs between phases during condensation. Leading to liquid droplets falling out of gas and accumulating at the bottom of the wellbore or impinge on the wall of the pipe. The droplets on the wall of the pipe increase the liquid film thickness which then trickles down and accumulates at the bottom of the wellbore when it exceeds its carrying capacity.

- ii. Entrained liquid droplet deposition: this being similar to that of condensation of heavier fractions except it does not involve mass transfer between the phases but an actual phase change.
- iii. Direct incursion of liquids into the wellbore: this is a major source of liquids. Liquids are directly produced into the wellbore. This mechanism has the highest effect in liquid loading problems especially when the liquid is water from an adjacent aquifer. This hinders gas well productivity because gas is soluble in water.

Fig.1 shows the sequence of liquid loading occurrence in a typical gas well. In Fig. 1(a) the gas well flows as a mist with very high flow rate capable of lifting all produced liquids to the surface. However, due to depletion and associated well/reservoir problems, pressure declines and the liquid carrying capacity of the gas drops, leading to the emergence of annular flow where deposition and entrainment of impinged liquids on the wall of the pipe causes the build-up of liquid films. At the onset of annular flow, part of these liquids will trickle down and accumulate at the bottom of the wellbore as shown in Fig. 1(b). As flow conditions deteriorate, there ensues massive accumulation of liquids at the wellbore arising from flow reversals from liquid films from the wall and falling of liquid droplets from the core of tubing as shown in Fig.1(c). If timely measures are not taken, the conditions will deteriorate further with massive accumulation of liquids that exerts a back pressure on the adjacent formation that may eventually kill the well as shown in Fig. 1(d).

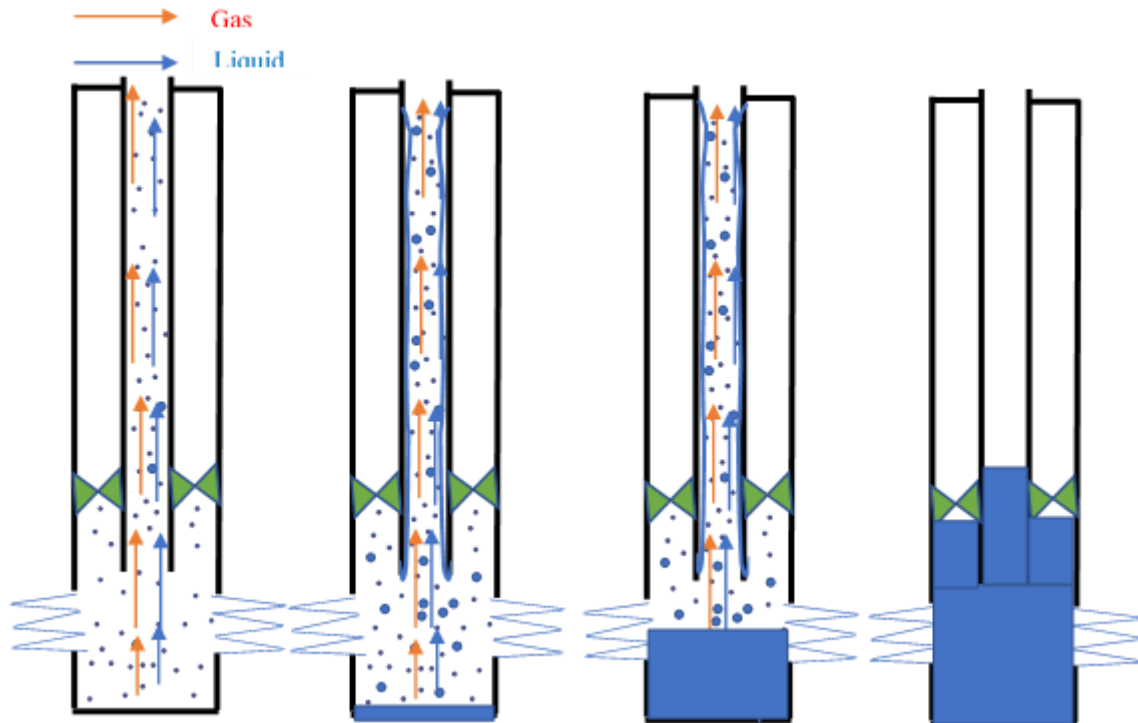
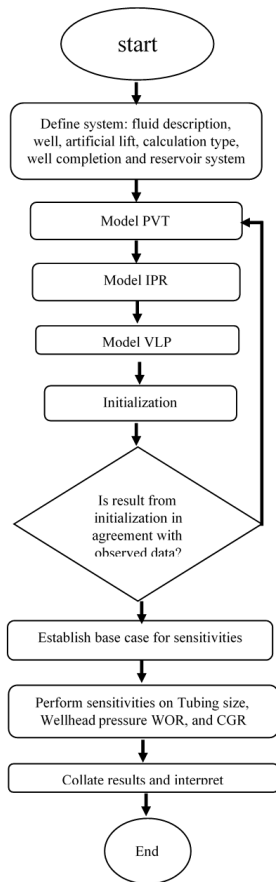


Fig. 1: Sequence of Liquid loading process in a gas well (a) Onset of gas well production with high gas rate flowing as mist flow where ever liquid produced is carried along with the gas as mist (b) Moderately high pressure gas production with entrainment and deposition liquids on the wall to build liquid film allowing some to trickle to the bottom of the well (annular flow) (c) Flow condition deteriorates with obvious liquid film reversal and deposition of liquid droplets at the wellbore liquid content (churn flow) (d) Massive liquid build-up at the wellbore and the liquid exerting a back pressure on the adjacent formation and thereby, killing the well

Liquid loading can present itself as a problem for high rate/high pressure wells as well as low rate/low pressure wells. The difference depends on tubing string size, surface pressure, amount and density of liquids produced along with the gas [12]. In this paper, the effects of

some well and fluid properties are investigated to determine their influence on liquid accumulation in gas wells.

2. Method



The principle of Nodal Analysis was used to investigate four parameters: tubing size, well head pressure, condensate-gas ratio and water-oil ratio to determine their impacts on liquid accumulation in gas wells using PROSPER. This was achieved using data from Niger Delta.

The work flow is as shown in Figure 2. Using the acquired data, the well and fluid properties were inputted to appropriately describe the system. Thereafter, pressure-volume-temperature (PVT) data was matched. The IPR which describes the flow of formation fluid into the wellbore and the VLP which describes flow of fluid from the well to the surface was simulated using the appropriate data. Using the wellbore as the solution node, initialization was done to ensure that the current flowing conditions of the well is closely/correctly predicted. Where the predicted conditions are at variance with the actual, some of the data with high degree of uncertainty were tuned until a match was obtained.

Fig. 2. Flow chart used for designing PROSPER

3. Results and discussions

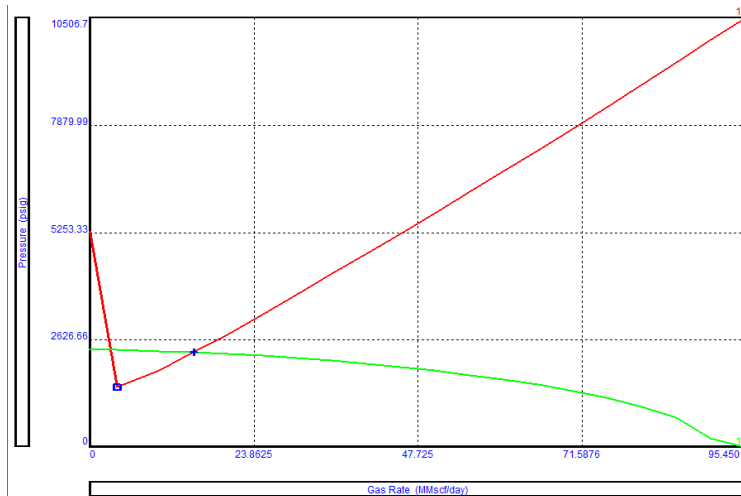


Fig. 3. System plot showing the base case scenario

After the initialization, the base case was obtained as shown in Figure 3. Figure 3 shows a gas well in metastable state with double intersections on the IPR curve. The true solution node is the point of intersection to the right rather than to the left as asterix blue at 1968.35psig and 12.498 MMscf/day whereas, the minimum point at 1520.7 psig and 4.375 MMscf/day is the onset of liquid loading in this well.

3.1. Effect of tubing sizes

Choosing optimum tubing sizes is paramount for effective and efficient production of gas wells. Various tubing sizes such as: 2.441, 3, 3.5, 4, 4.5 and 5 inches were investigated to determine their impact on liquid accumulation as shown in Figure 4. As can be seen in Figure 4 and Table 1, the larger the tubing size, the higher the gas and liquid production rates and vice versa. However, as can be seen in Table 1, the increase in the tubing sizes and the subsequent increase in the liquid production results to decrease in the bottom hole flowing pressure (BHFP). Hence, larger tubing sizes cause additional pressure loss which results to slugging and promotes liquid accumulation while smaller tubing sizes acts as velocity strings but enhances excessive frictional and erosional losses [13].

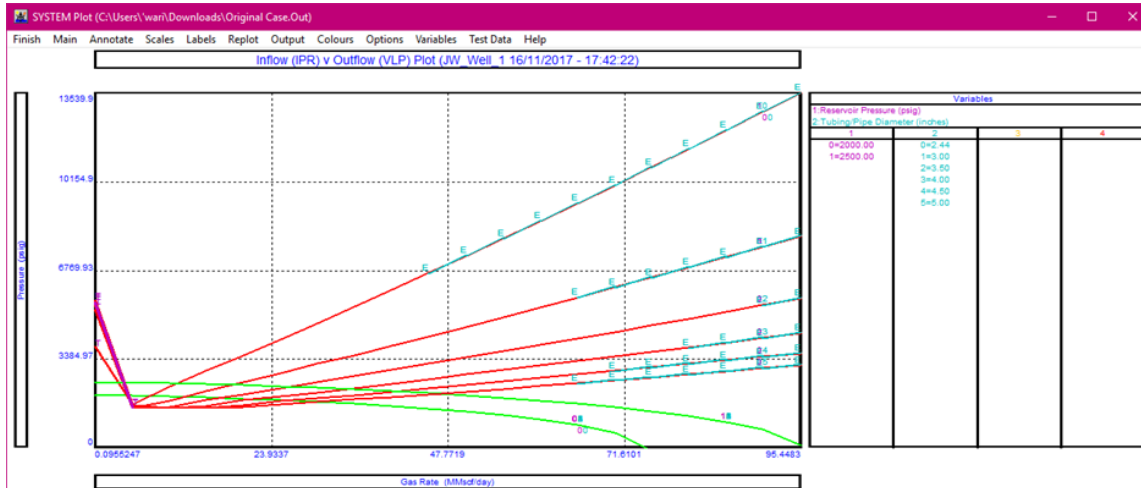


Fig. 4. VLP/IPR matching showing various tubing sizes

Table 1. Effect of variation of tubing sizes on fluid flow rates

@Wellhead pressure = 500 psig; @CGR = 40STB/MMscf
 @WGR = 2.03 STB/MMscf

Tubing size	Gas Rate (MMscf/day)	Oil Rate (STB/day)	Water Rate (STB/day)	BHFP (psig)
2.441	12.011	480.5	24.4	2447.70
3	20.237	809.5	41.1	2390.74
3.5	28.875	1155.0	48.6	2308.55
4	37.711	1508.4	76.6	2201.15
4.5	45.782	1831.3	92.9	2081.02
5	52.440	2097.6	106.5	1962.29

3.2. Effect wellhead pressure

Another parameter investigated to determine its influence on liquid loading is the wellhead pressure. Excessive increase in the wellhead pressure significantly inhibits efficient flow of hydrocarbons during production [14]. An increasing wellhead pressure will reduce the flow of gas and affect the vertical lift performance particularly when its value approaches the wellbore flowing pressure. Different values of wellhead flowing pressures of 500, 875, 1250, 1625 and 2000 psig were arbitrarily chosen and sensitized as shown in Fig. 5 with a 4inch tubing size.

From Fig. 5, out of the five wellhead pressures arbitrarily selected for a 4 in. tubing size, it was observed that the well produce at all the pressures except for the wellhead pressure 2000 psig. Moreover, as the wellhead pressure increases, the gas, oil and water rates decrease while a slight variation in the bottom hole flowing pressure was observed as shown in Table 2.

Table 2. Effect of wellhead pressures on fluid flow rates on a 4in. tubing

@Tubing size = 4 in.; @CRG = 40 STB/MMscf
 @WGR = 2.03 STB/MMscf

Wellhead Pressure	Gas Rate (MMscf/day)	Oil Rate (STB/day)	Water Rate (STB/day)	BHFP (psig)
500	37.711	1508.4	76.6	2201.15
875	34.047	1361.9	69.1	2248.93
1250	27.644	1105.8	56.1	2321.31
1650	20.887	835.5	42.4	2384.97
2000	-	-	-	-

This is as a result of the fact that the increase of the wellhead pressure imposes a restriction on the vertical lift following a slight change in the bottomhole flowing pressure (p_{wf}). For an efficient vertical lift, the difference between the bottom hole flowing pressure and wellhead pressure should be reasonably high. Similar trends were also observed with a tubing size of 2.441 in. when the wellhead pressure was gradually increased from 500 to 2000 psig at the same water-gas-ratio and condensate-gas ratio as shown in Table 3.

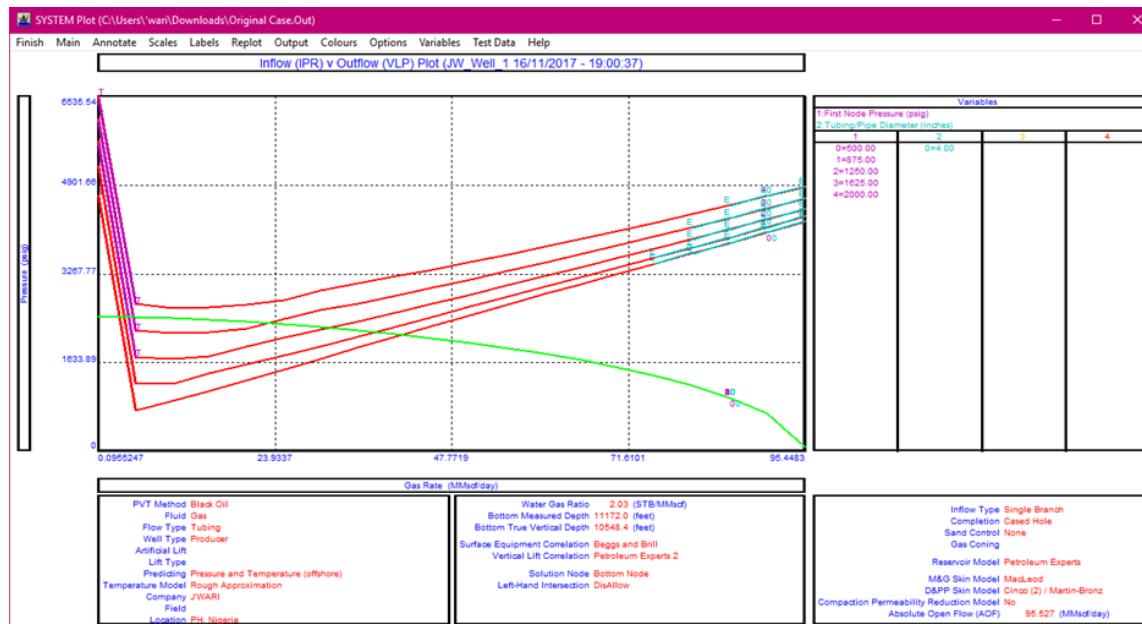


Fig. 5. System plot showing various wellhead pressures for a 4 in. tubing

Table 3. Effect of wellhead pressures on fluid flow rates on a 2.441 in. tubing

@Tubing size = 2.441 in.; @CRG = 40 STB/MMscf
 @WGR = 2.03 STB/MMscf

Wellhead Pressure	Gas Rate (MMscf/day)	Oil Rate (STB/day)	Water Rate (STB/day)	BHFP (psig)
500	12.011	480.5	24.4	2447.70
875	10.785	431.4	21.9	2455.13
1250	9.086	363.4	18.4	2464.00
1650	6.382	255.3	13.0	2476.73
2000	-	-	-	-

3.3. Water-gas ratio (WGR)

Fig.6 shows effect of varying water-gas ratio on liquid accumulation in gas wells. Again, five different values of WGR's: 2,6, 10, 25 and 50 STB/MMscf were sensitized to investigate the impact on liquid accumulation. Although the impact as shown in Fig. 6 seemingly looks

small, it is obvious that as the WGR increases, the gas and oil rates decrease while the water rate increases as shown in Table 4 respectively. The increase of the WGR could be due to direct incursion from an adjacent aquifer, channeling or leaks. Since gas is soluble in water, a sudden and significant increase in the WGR would result not only in loading but outright killing of the gas well due the back pressure it will impose on the adjacent formation [15-16].



Fig. 6. System plot showing impact of WGR on liquid loading

Table 4. Effect of variation of Water Gas Ratio on fluid flow rates on a 2.441in. tubing

@Tubing size = 2.441 in.; @CRG = 40 STB/MMscf
 @Wellhead pressure = 500 psig

Water Gas Ratio	Gas Rate (MMscf/day)	Oil Rate (STB/day)	Water Rate (STB/day)	BHFP (psig)
2.03	12.011	480.5	24.4	2447.70
6	11.792	471.7	70.7	2448.95
10	11.810	472.4	118.1	2448.75
25	11.508	460.3	287.7	2450.29
50	10.598	423.9	529.9	2455.46

3.4. Effect of condensate-gas ratio

Another parameter investigated is the condensate-gas ratio (CGR) as shown in Figure 7. Four values of CGR: 0, 40, 60 and 80 STB/MMscf were investigated. A Zero CGR value implies dry gas production; which can occur at early stages of production. As can be seen in Tables 6 and 7 at 2.441 and 4 in tubing sizes, the gas, oil and water rates decrease while the BHFP increases as the CGR increases. An increase in CGR leads to build-up of liquids [17] in the wellbore like that of WGR previously discussed. And build-up of liquids generally increases the BHFP which inhibits the flow of reservoir fluid into the wellbore by exerting back pressure on the adjacent formation.

Table .6. Effect of variation of Condensate Gas Ratio on fluid flow rates on 2.441in tubing

@Tubing size = 2.441 in.; @Wellhead pressure = 500 psig
 @WGR = 2.03 STB/MMscf

Condensate Gas Ratio	Gas Rate (MMscf/day)	Oil Rate (STB/day)	Water Rate (STB/day)	BHFP (psig)
0	13.551	0	27.5	2439.40
40	12.011	480.5	24.4	2447.70
60	11.367	682.0	23.1	2451.31
80	10.786	862.9	21.9	2454.61

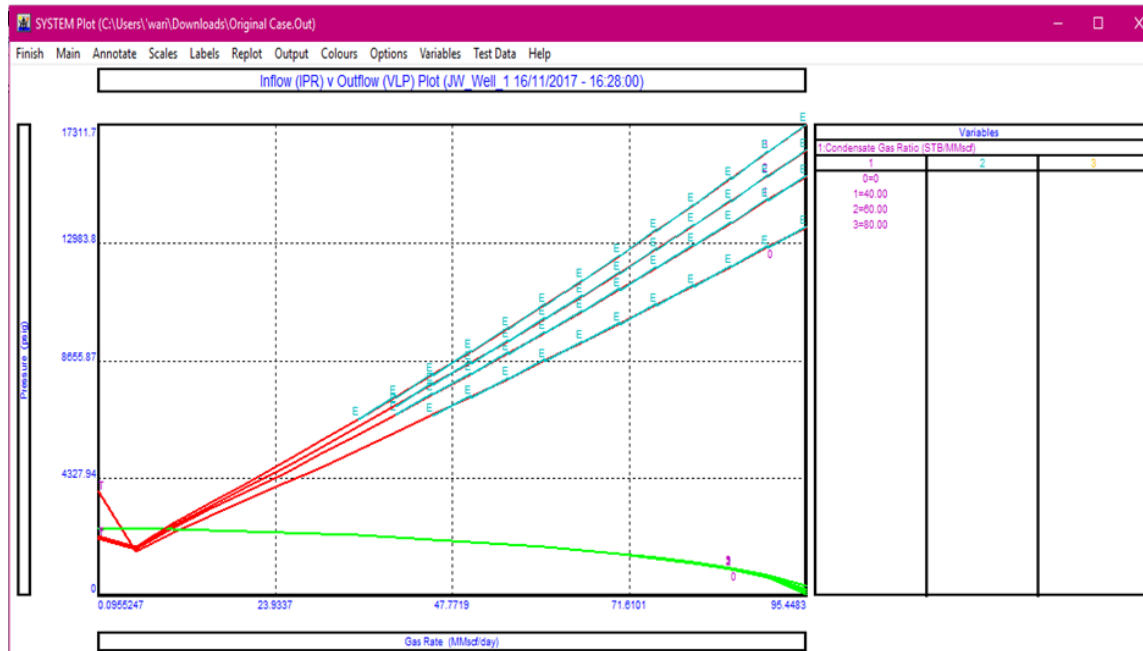


Fig. 7. VLP/IPR matching showing various CGR

Table 7. Effect of variation of Condensate Gas Ratio on fluid flow rates on 4in. tubing

@Tubing size = 4 in.; @Wellhead pressure = 500 psig
 @WGR = 2.03 STB/MMscf

Condensate Gas Ratio	Gas Rate (MMscf/day)	Oil Rate (STB/day)	Water Rate (STB/day)	BHFP (psig)
0	41.241	0	83.7	2152.60
40	37.71	1508.4	76.6	2201.15
60	36.181	2170.9	73.4	2223.00
80	34.768	2781.5	70.6	2243.05

4. Conclusion

The gas well loading phenomenon is one of the most serious problems that reduces and eventually cuts production in gas well. The phenomenon occurs as a result of liquid accumulation (water or/and condensate) in the wellbore. Over time, these liquids cause additional backpressure on the reservoir which results in a continual reduction of transport energy. Moreover, when a well starts slugging during production can give an even larger chance of liquid accumulation that completely overcomes the reservoir pressure and causes the well to die. From this investigation, it is obvious that tubing size, wellhead pressure, water-gas ratio and condensate-gas ratio can significantly impact on production from gas wells. Improperly sized tubing in gas wells can be detrimental and the wellhead pressure must be monitored to prevent excessive increase that can limit the tubing performance. In all, adequate well specific analysis is paramount to monitor and determine minimum gas rates to unload wells and investigate options for optimizations in order to efficiently and effectively produce gas wells.

References

- [1] Oudeman P. Improved prediction of wet-gas-well performance. SPE Prod. Eng., 1990; 5(03): 212-216.
- [2] Turner RG, Hubbard MG, Duckler AE. Analysis and prediction of minimum flow rate for the continuous removal of liquid from gas wells. Journal of Petroleum Technology, 1969; 21(11):1475-1482.
- [3] Joseph A, Hicks PD. Modelling mist flow for investigating liquid loading in gas wells, Journal of Petroleum Science and Engineering, Elsevier, 2018; 170: 476-484.

- [4] Guo B, Ghalambor A, Xu C. A systematic approach to predicting liquid loading in gas wells. SPE Production Operations, 2006; 21(01):81–88.
- [5] Veeken K, Hu B, Schiferli W. Gas-well liquid-loading-field-data analysis and multiphase-flow modeling. SPE Production Operations, 2010; 25(03):275–284.
- [6] Lea FJ, Nickens HV. Solving gas-well liquid-loading problems. Journal of Petroleum Technology, 2004; 56(04):30–36.
- [7] Kaichiro M, Ishii M. Flow regime transition criteria for upward two-phase flow in vertical tubes. International Journal of Heat and Mass Transfer, 1984; 27(5):723–737.
- [8] McQuillan KW, Whalley PB. Flow patterns in vertical two-phase flow. International Journal of Multiphase Flow, 1985; 11(2):161–175.
- [9] Julia JE, Hibiki T. Flow regime transition criteria for two-phase flow in a vertical annulus. International Journal of Heat and Fluid Flow, 2011; 32(5):993–1004.
- [10] Joseph A, Sands CM. Managing liquid Loading in gas wells, LAP Lambert Academic Publishing, Deutschland, Germany, Chapter1, pg. 12, 2017.
- [11] Gaol AHL. Modeling two-phase pipe flow in liquid loading gas wells using the concept of characteristic velocity, 2016, PhD Dissertation, Texas A&M, Texas, USA.
- [12] Binli O. Overview of Solutions to Prevent Liquid Loading Problems in Gas Wells. Master Thesis: The Graduate School of Natural and Applied Sciences of Middle East Technical University. 2009
- [13] Renpu W. Advanced Well Completion Engineering. Gulf Professional Publishing, Elsevier Oxford UK, 2011, Third edition, Chapter 3, pg. 117-170,
- [14] Lieberman NP. Troubleshooting Natural Gas Processing: Wellhead to Transmission. PennWell Publishing Company, Tulsa, Oklahoma, USA, First edition, 1987, Chapter 2
- [15] Luo S, Kelkar M, Pereyra E, Sarica C. A new comprehensive model for predicting liquid loading in gas wells. SPE Production. Operations, 2014; 29(04):337–349.
- [16] Hu B, Veeken CAM, Yusuf R, Holmas H. Use of wellbore-reservoir coupled dynamic simulation to evaluate the cycling capability of liquid loaded gas wells. SPE 134948, presented at the SPE Annual Technical Conference and Exhibition, 2010; 19-22 September, Florence, Italy.
- [17] Solomon FA, Falcone G, and Teodoriu C. Critical review of exiting solutions to predict and model liquid loading in gas wells. SPE 115933, presented at the SPE Annual Technical Conference and Exhibition, 2008; 21-24 September, Denver, Colorado, USA, 2008.

To whom correspondence should be addressed: Dr. Amieibibama Joseph, Department of Petroleum Engineering, University of Port Harcourt, Port Harcourt,, E-mail: Amieibibama.joseph@uniport.edu.ng

Global Overview of Fractured Basement Plays

Jenny Caddick¹, Theodhora Piperi², Cristina Martinez Tomé², Cyril Ruchonnet², Norishah Hashim³, Matthew Turner¹, William Plampton¹, Antonio Jr. Dimabuyu³, Betty Xu Wei³, Anthony Jaep¹, Tristan Reilly¹, Marie McKechnie¹, Philippe Renevey² and Michael C. Pöppelreiter⁴

¹ IHS Markit, Tetbury, UK

² IHS Markit, Geneva, Switzerland

³ IHS Markit, Singapore

⁴ South East Asia Carbonate Research Laboratory (SEACaRL), Universiti Teknologi Petronas, 31750 Tronoh, Perak, Malaysia

Received March 27, 2020; Accepted June 17, 2020

Abstract

The 'fractured basement play' remains to be one of the most 'extensive underexplored' targets for hydrocarbon exploration. Naturally fractured basement reservoirs are a global phenomenon and are often serendipitous discoveries. Despite this, these plays have proven their significance to the global geoscience community with the discovery of major hydrocarbon basement accumulations in Vietnam, China, the U.K. and Yemen. Commercial production of hydrocarbons from fractured basement is proven in 25 countries but little is known about the global variability of producing fractured basement fields. This paper synthesizes attributes of this play type semi-quantitatively based on the systematic analysis of relevant data in the IHS Markit (IHSM) International E&P Database and the IHSM US Enerdeq Browser. The analysis shows that hydrocarbon in basement reservoir discoveries exist in just 29 countries. Globally over 640 fields have been discovered, most (260 fields) are in the Far East with China hosting the majority (>160 fields). Current volumetric estimates suggest that 0.001% or 15,000 million (MM) barrels of oil equivalent (boe) of the total global estimated ultimate recovery (EUR) (approx. 1,177,500 billion boe) are stored in fractured basement. The bulk of hydrocarbon recoverable resources are currently located in Southeast Asia (approx. 4,500 MMboe), the majority of which are situated in Vietnam.

Components of the basement petroleum system resemble conventional plays. Source and top seal are typically the same lithology, mostly organic rich shale, claystone, or marl, onlapping and draping the reservoir. Because there is no source underneath the reservoir, lateral or downward charge is invoked. Structures are commonly fault blocks or buried hills. The reservoir is mostly provided by brittle magmatic intrusive rocks and the most commonly encountered lithology is granite, with porosity and permeability associated with fractures. These can be solution enlarged. Other common reservoir types include effusive magmatic (basalt, tuff) or metamorphic rocks such as gneiss, quartzite or marble; less common are pelitic metamorphic rocks. More than three thousand wells have targeted the basement so far. Most are drilled in Russia and China. Reported well rates vary between 10 bo/d to 30,000 bo/d and this range most likely reflects fracture intensity and connectivity. The synthesis presented here suggests that the play has significant potential and therefore warrants dedicated exploration and revisiting producing assets to unlock its full capacity.

Keywords: Fractured basement; Global review; Review per country.

1. Introduction

Fractured basement plays are defined here as elevated structures composed of rocks with little or no matrix porosity inspired by the definition of North [1] for buried hills. Porosity and permeability is provided by fractures only. These might be enlarged by surface or basin fluids [2]. Charge and migration are a differentiating factor of fractured basement plays compared to

conventional hydrocarbon accumulations [3]. There is usually no source rock below the reservoir (Figure 1) as organic matter in basement sequences is over mature. The source rock is developed adjacent to or above the reservoir, often onlapping and/or draping the basement above an unconformity. Charge thus occurs due to lateral (juxtaposition) migration or downward migration. Source and top seal are usually the same formation and consists predominantly of shale or marl. Intercalated in these shales or marls might be streaks of evaporite, siltstone and sandstone.

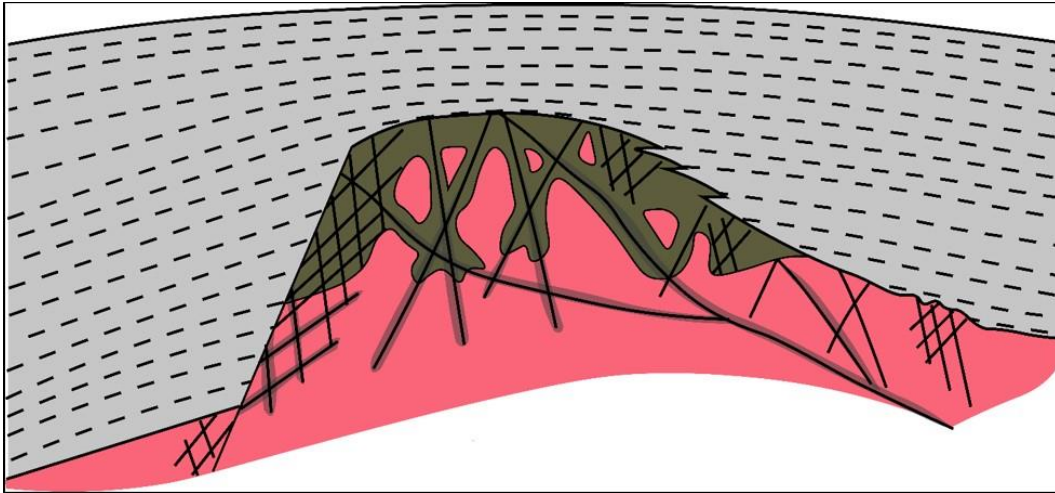


Figure 1 Schematic cross section of a faulted and fractured (black lines) granite horst (red) draped by organic rich shale (grey). Elements of the petroleum system of fractured basement plays (modified from [3])

The reservoir is a tight, brittle, magmatic or metamorphic rock penetrated by a fracture network. Fractures might be enhanced by leaching that increase porosity by up to 10%. In carbonates, solution-enlarged fractures, vugs, and cavities might further elevate reservoir quality.

The oil and gas industry typically concludes exploration activities at the 'economic basement', meaning fractured basement plays are under-explored and often discovered by chance from drilling too deep [5]. However, since the mid-'90s, the broader geoscience community took notice of the major basement discoveries in Vietnam and Yemen following successful commercial production [6]. So, what are the critical factors for this sub-set of naturally fractured reservoirs? This review provides a semi-quantitative summary of some common elements of fractured basement plays based on data from IHSM's International E&P Database and US Enerdeq Browser.

The authors would like to caution that despite our best efforts all numbers have associated uncertainties. Estimated Ultimate Recoverable figures (EUR, 2P/2C) are heavily estimated and well numbers/flow rates are approximated. The list of the biggest/significant fields is subjective due to difficulties to separate dynamically connected sub-unit(s) and/or associated EUR reserves/resources. Our best estimate suggests that of the total global EUR – roughly 1,177,500 billion boe (figure estimated from global remaining reserves (BP, 2016) and total global production to date [7]), approximately 0.001% of this is stored in basement plays (roughly 15,000 MMboe [7]).

Following is a global review of exploration and development of existing basement plays by region and where possible at country level. Due to the varied nature of oil and gas reporting by location, information is limited in places and maybe resolved at field level as opposed to basement reservoir level.

Southeast Asia is one of the regions where significant discoveries of this play type have been made, i.e. China, and Vietnam [5]. These discoveries (as well as the recent advancements in the U.K.) highlight the potential of the play and thus calls for a systematic compilation of the current knowledge to focus on future opportunities.

(Information extracted at time of writing, for exact figures and current data, please refer to IHSM's International E&P Database and US Enerdeq Browser [8].)

2. Previous studies of fractured basement play

The fractured basement play refers to paleotopographic highs that are covered by younger sediments [9]. Oil and gas fields associated with fractured basement are termed fractured basement fields. The Healdton oil field in Oklahoma, discovered in 1916, was the earliest recognized buried-hill field which belongs to fractured basement plays. With subsequent discoveries of such fields in the mid-continent United States in the 1920s [10], fractured basement fields have been discovered in other parts of the world. Landes *et al.* [11] made a review of petroleum resources in basement rocks, which consist of crystalline metamorphic and igneous rocks, in Venezuela, California, Kansas, and Morocco. Later, P'an [12] expanded the topic of petroleum in basement rocks in two aspects. First, he broadened basement rocks to include not only metamorphic and igneous rocks but also unmetamorphosed but tight lower Palaeozoic sedimentary rocks (Figure 2). Second, he added more examples of basement reservoirs in areas such as Brazil, Libya, Algeria, Egypt, and Russia, which were not covered by Landes *et al.* [11]. Fractured basement reservoirs were further documented in Petford and McCaffery [13]. Using the definition of basement rocks of Landes *et al.* [11], GeoScience Limited [14] compiled an updated database of fractured basement reservoirs throughout the world. The Cuu Long Basin in Vietnam is the best-known basin with production primarily from fractured basement granite [15-16]. It appears that the term basement reservoir became more widely used since the work of Landes *et al.* [11]. However, it should be noted that the basement reservoirs exclude the sedimentary rocks in these publications except P'an [12]. As a result, some important fractured basement fields were not included because the reservoirs contain sedimentary rocks.



Figure 2 Intensely fractured tight Carboniferous limestone in NW Malaysia. Similar fractured basement rocks produce hydrocarbons in SE Asia.

3. Database

The IHSM International E&P Database is a detailed database (Figure 3) capturing past and present worldwide E&P activities [7]. With over 13,000 E&P data attributes, International Exploration and Production Database (IRIS21) is the most comprehensive and reliable dataset available to oil and gas industry professionals today. IHSM Enerdeq Browser provides a single point of access to critical IHSM North American content [8]. Using a set of mapping, reporting, and analysis tools, Enerdeq Browser allows users to download, query and process over 5 million Well completions and over 2 million Production entities, Interpreted Formation Tops, Rig Activity and Permits, 2D/3D Seismic, Land and Lease, Pipeline and Facilities, and Spatial information.

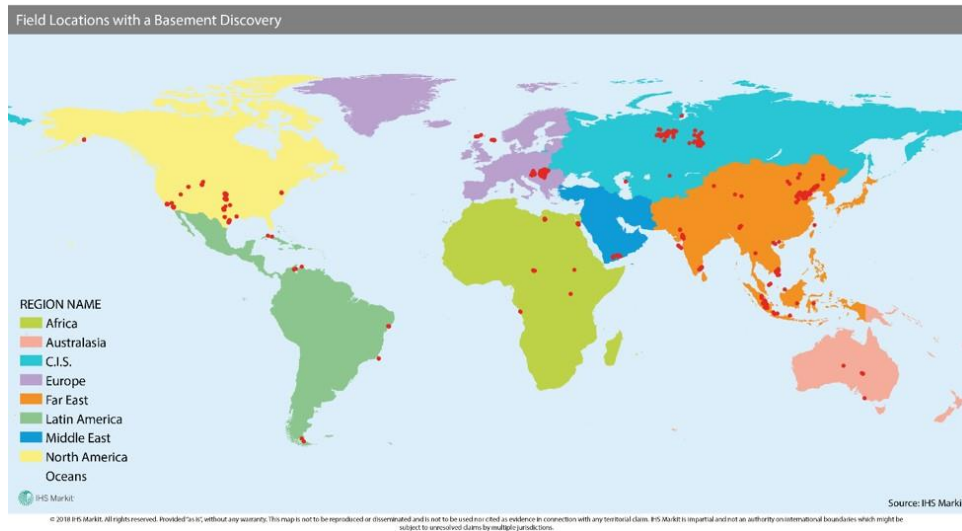


Figure 3. Image showing the global distribution of fractured basement discoveries (extracted from the IHS Markit databases)

3. AFRICA

The fractured basement plays in Africa are developed locally and have never been considered as exploration targets. They were mostly discovered “accidentally” when drilling below the main objectives, especially in rift basins, which rest unconformably above basement or above a very thin pre-rift section. Some basement reservoirs are contiguous with overlying sedimentary-rock reservoirs; in a few cases they share a common oil-water contact.

Basement reservoirs consist of fractured and weathered granitic rocks. They are sealed and sourced from the overlying pre-rift and syn-rift sequences. The fractured basement plays have been identified in 27 discoveries (Figure 4) in Egypt (13), Chad (5), Libya (4), Uganda (2), Angola (2) and South Sudan (1); with the bulk of resources (73%) located in Libya. Production from basement reservoirs is established in Egypt, Libya and Chad.

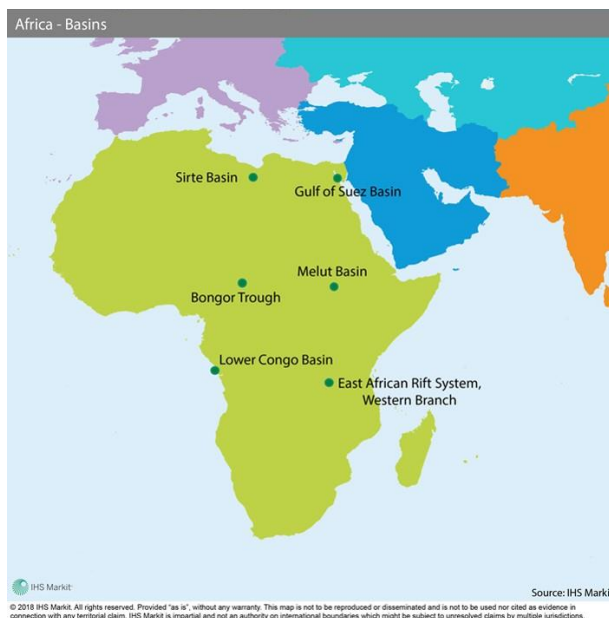


Figure 4 Image showing geological basins in Africa that host fractured basement discoveries (circles locate at basin centroid)

However, production figures are not differentiated by reservoir but at field level. Flow rates between less than 500 and 20,000 b/d of oil per well have been recorded in Libya and Egypt.

Despite small reserves, basement reservoirs have been recently considered as important targets in countries such as Chad and Sudan. Therefore, in the future more exploration activity could be expected in the Cretaceous rift basins of Chad and Sudan, and Tertiary rift basins of Uganda and Kenya that are part of the East African Rift System (EARS).

Egypt

In Egypt, the basement play is present in 13 fields/discoveries, which are located onshore and offshore in the southern Gulf of Suez Basin, where they form an important reservoir. Sidki was the first discovery in this play in early 1976, while the last one, Rabeh East, was discovered in 1997.

Recoverable reserves discovered to date in this play are currently estimated at 167 MMbbl of oil and 145 Bcf of gas. Zeit Bay is the largest field, accounting for 45% of the basement total reserves in Egypt. The field was discovered in 1981 and since then, the Precambrian basement has been considered as a secondary reservoir target in the southern Gulf of Suez Basin.

The basement is granitic, highly weathered and intensively fractured in response to tectonic activity in the area. Reservoir net-pay thicknesses vary between 10 and 300 m, and porosities are usually low (2-15%), but the fracture system is often highly permeable and productive. Some block crests were exposed to erosion during the first phases of rifting, facilitating weathering and fracturing of the basement. In almost all cases, the basement reservoir is adjoining the Pre-Miocene or Miocene reservoirs and shares a common oil-water contact with the overlying units. The best reservoir potential is in the uppermost section, corresponding to the enlargement of the fractures and vertical communications, and the intensive effect of diagenetic processes. The main directions of fractures are NW-SE, NE-SW, and ENE-WSW [17].

Basement reservoirs are producing in ten fields: Ashrafi, Ashrafi Southwest, Esh El Mellaha, Esh Melala East Marine, Geisum, Hilal (GH 404), Rabeh Est, Shoab Ali, Sidki and Zeit Bay. First production goes back to late 1970s when the Sidki and the Shoab Ali fields were brought onstream together with overlying reservoirs. Zeit Bay started producing in 1983, and the flow rates/well for the rest of the decade were in the range of 700-9,000 bo/d. Until 1988, about 60% of development wells in the field were drilled down to basement [18]. During the plateau phase in 1986, the Zeit Bay field produced around 30,000 b/d of oil from the basement as part of a total field production of 80,000 b/d. In the 1990s, the Zeit Bay and Ashrafi fields were producing up to 25,000 bo/d from basement reservoirs [19]. Production figures at reservoir level are not available.

Libya

The fractured basement rocks constitute a major play in Libya, where they form one of the main reservoirs in two giant fields, Amal (12-B/E/N/R) and Augila-Nafoora (102-D/51-A/G) discovered in 1959 and 1965 respectively. Fields Rakb (12-D) in 1962 and Rakb (12-JJ) in 1965 added some modest reserves to the play. The four fields are in the Rakb High of the eastern Sirte Basin.

Total recoverable reserves are currently estimated to be in the region of 715 MMbbl of oil and 355 Bcf of gas, of which about 95% correspond to the two giant discoveries.

The reservoirs are fractured and weathered granites, which are in direct contact with the overlying Paleozoic-Mesozoic and Lower Tertiary reservoirs. They are sealed and sourced by shales and evaporites of the Upper Cretaceous Rakb Group.

Basement reservoirs were developed and produced jointly with the other reservoirs of the fields. Oil production started in 1966 from the Amal (12-B/E/N/R) and Augila-Nafoora (102-D/51-A/G) fields, which followed the construction of the pipeline connecting them with the terminal and refinery at Ras Lanuf on the coast. The Rakb group of fields were brought onstream in 1968. There are no production figures at reservoir level.

Chad

The fractured basement play in Chad was first discovered in 2013 in the Northern Slope of the Bongor Trough. This play is developed directly below the Lower Cretaceous syn-rift play, where the lacustrine shales of the latter form the seal and source rocks for the basement reservoirs. More than 80 wells have reached the basement in the Bongor Trough, of which only five flowed commercial rates. They include the Baobab, Mimosa, Raphia South, Kubla-Phoenix and Lanea [20].

The fractured basement in the Bongor Trough is composed of granites and granodiorites arranged on rotated horst blocks and a series of faulted hills. The extensive fracturing of the basement was formed by deformation, weathering and hydrothermal alteration. Three types of basement lithology have been distinguished, depending on the intensity of the fracturing: unweathered (no fractured), leached (fault breccias and altered fractures), and fractured un-leached (regularly and intensely fractured). Fractures are arranged in two sets of ENE-WSW and WNW-ESE direction, respectively [20-21].

Effective porosity values are in the range of 4-12%, rarely reaching 30%. Reservoir properties are better in the Raphia South field than in Lanea East, and the latter shows more extensive fracturing. Raphia South shows better weathering and leaching conditions and therefore, the lithologies are more suitable for hydrocarbon accumulations [21].

Given the early stage of exploration, small amounts of resources have been discovered, totalling approximately 90 MMbbl of oil and 14 Bcf of gas. There are no production figures for the basement reservoirs. Flow well-rates of 1,500 b/d of light oil have however, been recorded. Please refer to Figure 5 for basin locations.

South Sudan

Interest in exploration of the basement play in South Sudan has been growing since the late 2000s. This play was first tested in 2008 by the Gandool Southeast 1 well, located in the northeastern part of the Melut Basin, but recovered only water. In the same year, Gandool North-Northwest 1 encountered tight basement rocks, apparently not fractured.

The Ruman North discovery in 2009 is the only example of a proven basement play in the country. The field is located in the central part of the Melut Basin. The Ruman North 2 wildcat well tested about 400 bo/d from the fractured basement at a depth of roughly 860-915 m. The well appears to have only two major contributing open-fracture zones [37]. The source rock is juxtaposed to the basement structure which means a direct charging of the hydrocarbon through the fractures and faults. In the same year, Ruman 1A, Ruman Northeast 1 and Ruman North-Northeast 1 encountered oil shows in the basement.

In 2010, the Ruman North 3A well targeted the basement reservoir, which was the primary objective. The well was located 1.5 km to the southeast of Ruman North 2 and recovered in the region of 25 bbl of heavy oil. In the same year, Ruman Central 1 encountered tight basement rocks. In 2011, the Ruman B 1 exploratory well targeted the basement as its primary objective. The well was designed to penetrate 724 m of basement to evaluate the fracture continuity and hydrocarbon distribution in the center of the Ruman basement structure. The well drilled approximately 2,500 m but the results were not released.

The Ruman North discovery found minor amounts of oil and as such, its contribution to field production is insignificant.

Uganda

In Uganda, this play is associated with few wells drilled in the basement, immediately below the rift section in the Albertine Graben of the EARS, Western Branch.

The presence of hydrocarbons in fractured granitic basement was deduced from well-logs and limited tests in the Mputa 1 and Nzizi 2 wells. Mputa 1, drilled in 2006, recovered only minor amounts of oil during a Drill Stem Test (DST) in the granitic basement, likely due to a restricted and tight fracture system. In 2007, a simple test was performed in the Nzizi 2 well at 950 m, but it did not flow oil to the surface.

Figure 5 Image showing the location of fractured basement discoveries in Africa, Middle and Australasia (red circles). The turquoise circles indicate significant basement finds.

Only very small quantities of oil have been discovered in the basement play, and no production has been established yet in the whole EARS, Western Branch in Uganda.

Angola

The fractured basement play in Angola is of minor importance. It is present in two discoveries, 37-1 and 61-1, in the Lower Congo Basin, onshore Cabinda, where they form a single-well oil pool. The 61-1 well produced 600,000 bbl of oil on an extended test from fractured basement in the early 1970s. The well was surrounded by dry holes. The 37-1 well was located on the Zila Ridge and tested 60 b/d and 24 b/d of oil [22].

4. MIDDLE EAST

Yemen

Yemen is one of the better-known countries with respect to basement exploration and development; it hosts 24 discoveries, eight of which were placed on production. Here the basement is predominantly a complex series of metasediments and metavolcanics, with granitic intrusions [5] occurring at depths below 2,400 m. Only one of the eight producing basement finds is located in the Marib-Al Jawf-Hajar Basin, the remainder of the productive fields are located in the Sayun-Masila Basin. Please refer to Figure 6 for basin locations.

Basement reservoirs provide 50% of Yemen's production [23], with an average oil density of 35° API.

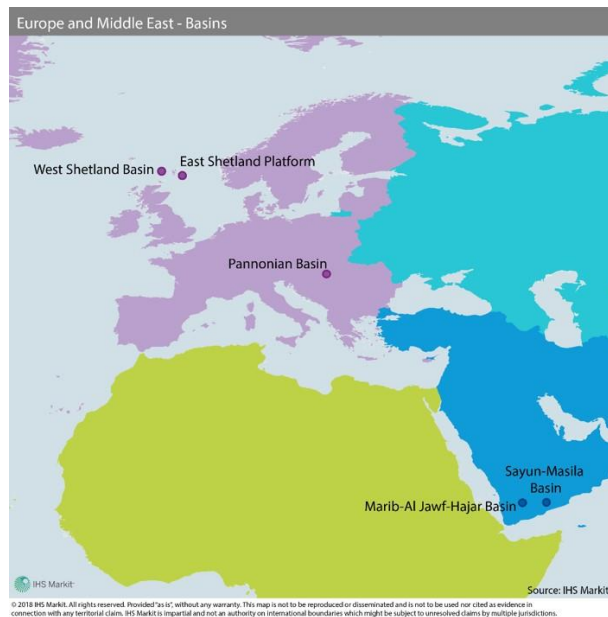


Figure 6. Image highlighting basins where fractured basement discoveries exist in the Middle East and Europe

Marib-Al Jawf-Hajar Basin

Yemen's first basement discovery was in 1988 and is situated in the Marib-Al Jawf-Hajar Basin. The Cambrian granites are trapped on structural highs and were discovered by well, Ayad East 4, drilled by Soviet Petroleum Exploration & Expedition (SPEE). This small structure is un-developed at basement level however there was a further discovery at the neighbouring structure, Ayad West (1988) which flowed approximately 20 bo/d from a 90 m basement interval. Ayad Central 2, discovered in 1989 was also reported as a non-commercial basement oil find by SPEE.

Perhaps the most well documented basement field in Yemen is Habban, situated in the Shabwa Sub-basin of the Marib-Al Jawf-Hajar and discovered in 2005 by OMV. The Habban fractured basement reservoir is extremely heterogeneous and comprised of fractured metamorphic and granitic rocks. The fractures in the basement have been characterised into two distinct groups: pervasive background fractures with a very low effective permeability, up to 0.001 mD and fracture corridors associated with faults with effective permeability from 0.01 mD up to 10 mD [24]. In Yemen, the basement reservoir is often in communication with overlying pre-rift clastics of the Kuhlan Formation. The Kuhlan has been shown to be laterally limited and displays regional variations in reservoir quality.

In 2005, OMV suspended the Habban 1 wildcat well as a fractured basement oil discovery after drilling approximately 750 m into the basement. The well was reported to have flowed in the region of 2,500 bo/d with 1.0 MMcfg/d from at least two basement tests. OMV re-entered an associated Habban well in the same year, deepening it into the fractured basement where a 430 m oil column was encountered. Subsequent tests resulted in a sustained flow of 1,800 b/d of 38° API oil from the basement and 200 bo/d from the Kuhlan Formation. Production commenced in 2006, with basement production levels reaching approximately 10,000 bo/d in 2009. The field was active in terms of basement development until end-2014. The estimated resource for the Habban basement is approximately 75 MMbo, including the contribution from the overlying Kuhlan sub-unit.

Further finds in the Marib-Al Jawf-Hajar Basin include: Al Meashar 1 discovered in 2009 by Oil Search and partners; and Tubb'a 1, a gas and condensate discovery by Total and partners also in 2009.

Sayun-Masila Basin

The majority (17) of the fractured basement finds in Yemen are located in the Sayun-Masila Basin. A significant basement exploration programme was carried out during the early 1990's in Hadhramaut province (Sayun-Masila Basin). Well Sunah 4, drilled in 1992 by Canadian Oxy Group, was the first oil discovery made in the basement complex in the Masila Sub-basin and in 2005, it was reported that the Sunah 4 well had produced over 30 MMbo.

Kharir was discovered by Total and partners in 1992. Production commenced in late-1997 at an initial rate of approximately 17,000 bo/d from four wells, and by end-2002, flow rates averaged 22,000 bo/d. Basement estimated ultimate recovery at the Kharir field amounts to 200 MMbo (including the contribution from the Kuhlan Formation), making it the largest basement find in Yemen with respect to recovery size. Further productive discoveries in this area include: Wadi Taribah (1995) and Jathma (2006).

In 2004, DNO discovered Nabrajah. This field is made up of two Cretaceous clastic reservoirs with a deeper oil pool in the basement and overlying Jurassic and Lower Cretaceous carbonate formations, the Shuqra and Nayfa. The Nabrajah deep pool contributes to production through only one well. The Nabrajah 2 well discovered hydrocarbons in the fractured basement and overlying carbonates in late 2004 however, the well was never put on production. As of mid-2014, the Nabrajah field had only one well producing from the basement.

Bashir Al Kharir K was discovered in 2006. The structure was drilled as part of a comprehensive block-wide exploration and appraisal programme by Canadian Nexen. Production from the field is assumed to have commenced in the discovery year.

Dove Energy Group and partners discovered oil in the basement with well Bayoot Southwest 2 in 2006. Production from the discovery well commenced in late 2006 and in 2013, Dove reported that the Bayoot field was producing primarily from this basement reservoir at rates in excess of 1,000 bo/d. The estimated ultimate recovery in the basement section of the Bayoot field amounts to some 11 MMbo.

Sayun Sub-basin and South Hadhramaut Uplift (Sayun-Masila Basin)

The Qarn Qaymah 1 gas, condensate and light oil discovery was made by British Gas in 1994. However, the well was considered to be uncommercial at the time. After taking over as

operator, Calvalley drilled two further appraisal wells between 2007 and 2011 which successfully tested gas, condensate and light oil from the Kuhlan and underlying basement. Unfortunately, wellbore production problems and lack of equipment restricted further appraisal work.

Henin 1, drilled in 2008 by Sinopec and partners was suspended as a granitic basement long term test after recovering 150 bbl of light oil. Following this, Judayaah 1 was confirmed as a basement oil discovery after having been logged and tested in 2010.

DNO and partners drilled Yaalen 1 in 2008 and tested gas and condensate from an open hole interval in the basement which was a secondary target. Additionally, some liquid hydrocarbons were recovered from the Kuhlan Formation by wireline testing. There has been no further appraisal of the basement at this field.

Due to the security situation in the country, further development has been suspended. The majority of Yemen's producing fields were shut-in during mid-March 2015.

5. COMMONWEALTH OF INDEPENDENT STATES (CIS)

Russia

The majority of the fractured basement reservoirs discovered in Russia are situated in the West Siberian Basin. According to the IHSM definition, this basin accounts for six sub-basins or provinces (Figure 7), which correspond from north to south, to the South Kara-Yamal, Nadym Taz, Ural-Frolov, Middle Ob, Kaymys-Vasyugan and Southern West Siberia provinces. The first basement play proven in the basin was discovered in the Ural-Frolov Province in 1961, at the Mortymya-Teterevskoye field. The well Mortyminskaya 0028, operated by Khanty-Mansiysk Neftegazgeologia, encountered oil in the weathered Paleozoic basement at approximately 1,600 m measured depth (MD).



Figure 7. Image indicating basins (and sub-basins) that host fractured basement plays in the C.I.S.

By 2016, 108 oil prone basement reservoirs had been discovered in the West Siberian Basin; the majority being in the Ural-Frolov (57) and in the Kaymys-Vasyugan (49) provinces. The Paleozoic play has also been proven in the Middle Ob, Nadym-Taz and South Kara-Yamal provinces, but in only one reservoir. Please refer to Figure 8.



Figure 8. Image depicting fractured basement discoveries (red circles) and significant finds (turquoise circles) in the C.I.S. Ural-Frolov Province

In the Ural-Frolov Province, basement reservoirs are constituted of weathered granites, brecciated metamorphic rocks, or locally by Paleozoic sediments preserved from the Upper Paleozoic-Lower Jurassic erosion phase. The average areal extent of these reservoirs is 10 km² on average and top depths range from approximately 1,490 to 3,150 m (MD). Reservoir properties are heterogeneous mainly due to differences in alteration, erosion and cementation processes. Net reservoir thickness ranges from 2 to 110 m. Effective porosity of the net pay from 10 to 25%. The top seal is provided by the lowermost shale of the Tyumen Formation or its stratigraphic equivalents of Lower to Middle Jurassic age., These unconformably onlap the oil bearing intervals. Traps usually correspond to buried-hill type structures inherited from the basement paleo-topography associated with the Paleozoic/Jurassic unconformity and faults. The majority of the basement reservoirs in the province have been sourced by the Togur Beds of Early Toarcian age.

Recoverable resources of most fields in the Ural-Frolov region are estimated to be lower than 50 MMbbl. Only four of them have volumes greater than 75 MMbbl and are found at the Krasnoleninskoye, Srednenazymyskoye, Danilovskoye (Khanty-Mansiysk) and Danilovskoye Severnoye fields. By 2016, 20 of the 57 reservoirs discovered in the province were producing. Sixteen reservoirs were awaiting development approval, 16 were considered as discoveries and three were being appraised. The latest reported activity targeting these basement reservoirs in the province was conducted by Rosneftgaz. In 2016, the operator spudded two new field wildcats in the Yamal-Nenets Autonomous Okrug, (Kharvutinskaya and Tyyaktarskaya licenses) in order to explore for basement reservoirs. To date, results have not been disclosed publicly.

Kaymys-Vasyugan Province

In the Kaymys-Vasyugan Province, the first basement reservoir was discovered in 1971 at the Festivalnoye field. The well Aykagalskaya 252 tested oil from the Paleozoic section between approximately 3,050 and 3,070 m depth (MD), flowing at roughly 155 b/d. By 2016, 49 basement reservoirs had been discovered in the western half of Kaymys-Vasyugan province. The majority of them corresponds to oil prone intervals in the Unit M, the uppermost

section of the Paleozoic basement. This unit consists of weathered granite showing a vertical extent of a few tens of meters and practically extending across the entire the province. Locally, basement reservoirs are also present in the overlying Kalinovaya Formation. This formation is comprised of elements from Unit M eroded during the Upper Paleozoic-Lower Jurassic erosion phase and preserved at the feet of Paleozoic highs.

In the Kaymys-Vasyugan Province, reservoirs have an areal extent averaging 7 km². Net thickness varies between 1 and 55 m and porosity between 3 and 30%. Net pay intervals are found in the region of 2,350 to 3,600 m depth (MD) and are sealed by the overlying Lower-Middle Jurassic formations. Traps correspond to buried-hill type structures associated with the Paleozoic/Jurassic unconformity and faulting. Most of the basement reservoirs in the province are interpreted to have been sourced by the Togur Beds (Lower Toarcian).

Recoverable reserves/resources estimated in the Kaymys-Vasyugan reservoirs average 22 MMbbl. The three largest reservoirs are found at Kalinovoye (124 MMbbl), Archinskoye (134 MMbbl) and Urmanskoye fields (180 MMbbl). In 2016, ten of the 49 reservoirs discovered in the Ural-Frolov Province were producing, 15 were being appraised, 13 were considered as a discovery, nine were awaiting development approval, and two were being developed.

Middle OB Province

By 2016, the basement plays had been proven by a single discovery made in 1963 at the Sovetskoye field (Khanty-Mansiysk Autonomous Okrug). Tomskneft discovered oil in the basement reservoir at 2,680 m depth (MD) and commenced commercial production in 1983. This reservoir is small with estimated reserves of around 2.5 MMbbl. In 2015, Lukoil spudded the well Ust-Kotukhtinskaya 105 in the Ust-Kotukhtinskaya license (Khanty-Mansiysk Autonomous Okrug), with the purpose of exploring the basement play. In early-2016, the operator tested the well without disclosing results.

Nadym-Taz Province

In the Nadym-Taz Province, the basement play was proven for the first time in 1986, at Varyeganskoye Severnoye field (Khanty-Mansiysk Autonomous Okrug). The reservoir, which was discovered at an approximate depth of 3,300 m flowed non-associated gas and condensate. It has estimated resources of some 1 Bcf gas and 130 MMbbl condensate.

South Kara-Yamal Province

In the South Kara-Yamal Province, the only basement reservoir found to-date belongs to Novoportovskoye field, in the southern Yamal peninsula. In this area, weathering processes during the Upper Paleozoic-Lower Jurassic erosional phase have created karstic intervals along NE-SW trending basement faults. The reservoir, which was discovered in 1982 contains non-associated gas and condensate (resources of 1.5 Bcf gas and 18 MMbbl condensate, respectively). In 2016, Gazprom Neft Yamal was awaiting Government approval to develop the reservoir.

Kazakhstan

Chu-Sarysu Basin

In the Chu-Sarysu Basin, a basement play is known in one field only, Ortalyk, discovered in 1976 by Aktyubneftegazgeologiya. Weathered fractured schists are sealed by Lower Carboniferous argillaceous siltstones. No development has been reported.

Mangyshlak-Central Caspian Basin

There is one basement reservoir discovery (1981) in the Mangyshlak-Central Caspian Basin. The Oymasha field's Paleozoic reservoir is associated with a weathered and fractured granite batholith overlain by Triassic shales. The field is located in the Peschanomys-Rakushech High in the west of the basin's onshore part. The trap is a buried hill-type structure. On testing, the

well flowed 20 b/d of oil from this Upper Paleozoic reservoir, and is currently producing. Productive zones of these granites extend 300 m below the basement surface. Oil flow rates in discovery well 12 achieved rates in the region of 1,500 b/d.

6. FAR EAST

India

India is host to a total of 24 basement discoveries within the Assam, Barmer, Bombay, Cambay and Cauvery Basins (see Figure 9). It is assumed from available information, that nine of the fields were put on production (one of which has since been shut-in). Basement plays remain fairly under-developed with operators concentrating on overlying sedimentary formations. Again, it is important to note, reserves/resources are estimated and the production status of basement reservoirs is often unclear.

In March 1970, Oil and Natural Gas Corporation Ltd. (ONGC) made the first basement discovery in India with the Borollah 04 well at the onshore Borholla-Changpang field in the Assam Shelf. The well was drilled to explore the Pre-Cambrian metamorphic/igneous basement after three previous wells were dry. It flowed at 730 bo/d during testing and the pool was declared commercial, changing schools of thought about basement prospectivity. Approximately 20 MMbo was estimated to be recoverable from the basement with production beginning in 1981. Fracture analysis from core samples and detailed seismic surveying has helped build a complex geological model of the field, revealing intricate fault block geometries. The most intensely fractured reservoir sections were found on the flanks of the domal structure and wells drilled here had the highest production rates with low initial GORs. Peak production from the basement occurred between 1988-89 at an average rate of roughly 1,170 bo/d; following which, a rapid increase in water cut was observed. Production has continued to present but is in decline.



Figure 9. Image showing geological basins in the Far East with fractured basement fields

In the late-1980s, the Pre-Cambrian metamorphic basement and the directly overlying Cretaceous Deccan Traps basalts at the offshore Mumbai High field in the Bombay Basin, were explored by ONGC. BH-36 was drilled in 1987 and it tested 460 bo/d (stabilized flow) from the basement. Further drilling with the wells BH-19, SY-5 and 11-7 all confirmed oil and each initially produced over 1,000 bo/d. The basement fractures were associated with major NNW-SSE trending fault zones cut by minor E-W trending faults. Approximately 160 MMbo is estimated to be recoverable from the basement and although there was initial success with wells drilled to basement, development concentrated on the prolific overlying L-III and L-II carbonate reservoirs. However, in 2011, a pilot study was initiated in which 30 wells were to be drilled into the basement with the aim of augmenting production by roughly 20,000 bo/d. If successful, the operation could see expansion under the current Phase-III re-development of the Mumbai High with a potential upside of 50,000 bo/d from the basement.

More recently, ONGC discovered oil from basement rocks in the onshore Cauvery Basin with the Madanam 3 and Pandanallur 8 exploratory wells were drilled in 2012 and 2013 respectively. The two fields lie in close proximity to one another on a NE-SW striking basement high associated with a horst and graben structure formed during rifting in the Late Jurassic/Early Cretaceous. Drilling in the Madanam area discovered the first hydrocarbons in the basin in 1969, but it wasn't until the Madanam 3 wildcat, that the first significant oil volume was encountered from the basement. The well tested more than 725 bo/d and less than 1 MMcfg/d. In 2015, ONGC approved a Field Development Plan for the Madanam field, which included drilling of 15 development wells in addition to three existing wells, envisaging cumulative production of approximately 8 MMbo and 95 Bcf. The Pandanallur 8 well tested around 190 bo/d and 0.6 MMcfg/d with the discovery currently undergoing further appraisal work. Initial estimates indicated that as much as 45 MMbo and 34 Bcf gas are present within its basement reservoir.

China

Oil and gas reserves accumulated in fractured basement plays in China are mainly distributed in its eastern rifting basins, with the majority of the largest fields discovered in the Bohai Gulf Basin. Basement fractured basement plays have been discovered in other onshore/offshore basins in China however, there are no large-scale discoveries such as Renqiu (please refer to Figure 10).

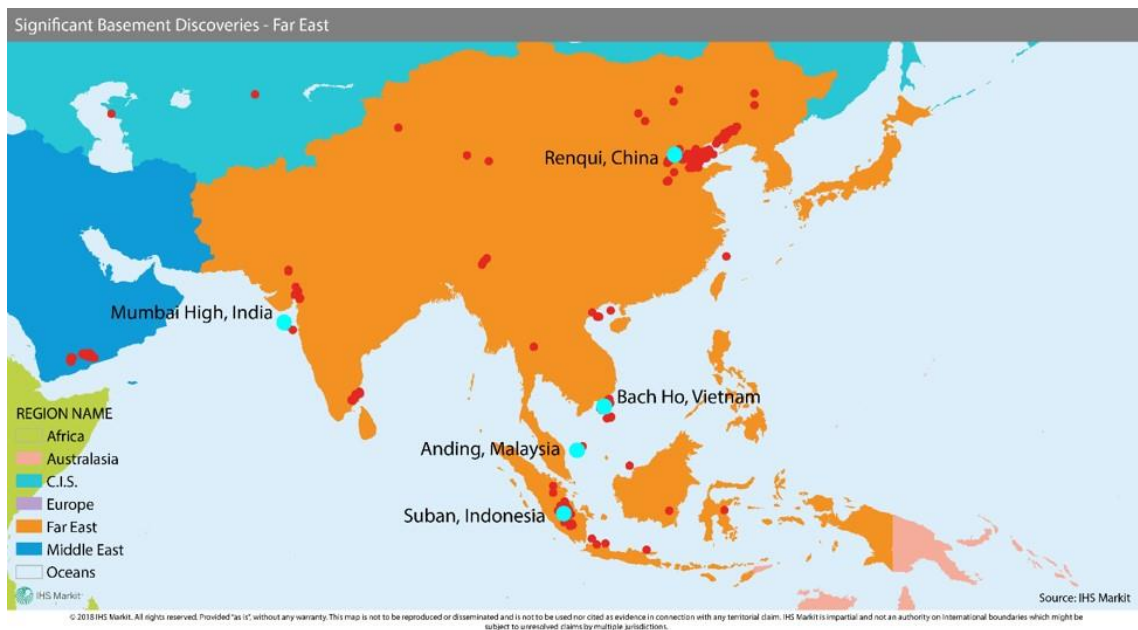


Figure 10. Fractured basement discoveries in the Far East (red dots) and significant finds (turquoise dots)

The first buried hill play was discovered in 1959 at the Yaerxia oil field located in the Jiuquan Basin, in northwestern China. Production rates were in the order of 1,000 bo/d from fractured metamorphic reservoirs of the Upper Silurian Quannaogou Formation [25].

Bohai Gulf Basin

Between 1975 and 1978, significant volumes were discovered in the basement at the Renqiu oil field in the Bohai Gulf Basin (the field was discovered in 1975). The basement is estimated to contain over 70 MMbo of recoverable reserves (2P). The Renqiu field (including non-basement reservoirs) reached its peak production at approximately 95 MMbbl of oil in 1979, amounting to roughly 10% of China's total production of that year [26].

Following this success, more than 50 basement fields were discovered in the Bohai Gulf Basin from 1975 to 1985; from 1986 to 1995, only small-scale discoveries with fractured basement reservoirs were made [27].

Since 2006 with improved seismic acquisition and processing technology, fracture identification and prediction technology, and new well completion and drilling techniques - some deep and small scale fractured basement reservoirs were discovered in the Bohai Gulf Basin, e.g., the Xinglongtai, Damintun and Niudong 1 discoveries.

Fractured basement reservoirs in the Bohai Gulf Basin are below the Cenozoic units and represent paleo-highs formed by Proterozoic and Paleozoic carbonates, Paleozoic and Mesozoic clastics, and Archean metamorphic rocks. These are mainly distributed in the Jizhong, Lower Liaohu, Jiyang, Huanghua and Bozhong depressions [28].

To date (August 2018), there are more than 120 fractured basement discoveries in the Bohai Gulf Basin, with reservoirs in Archean metamorphic to Paleozoic carbonates.

Southeast Asia

Basement plays represent key targets in some of the mature and transitional basins in Southeast Asia. Success in this play dates to 1913 when the Kluang 1 wildcat in the onshore South Sumatra Basin was drilled along an anticline in the western half of the Corridor block, originally targeting the Air Benakat Formation. The well encountered oil and gas by chance in the Cretaceous granite reservoir, 460 m below the crest of the structure with estimated recoverable reserves of less than 1.5 MMboe.

Aside from the South Sumatra Basin, the fractured granites in the offshore Cuu Long Basin produced some of the big fields in the region. More than 4.5 billion bbl of recoverable oil equivalent have been discovered in the basement plays, with the Cuu Long and South Sumatra basins accounting for 94% of these resources. Around 73 discoveries have been generated from the basement plays and these are in South Sumatra (28), Cuu Long (26), Song Hong (4), Nam Con Son (3), West Java (3), Malay (2), Central Sumatra (2), Phitsanulok (1), Tatau (1), East Java (1), Banggai (1) and Barito (1). Most of these basins are in a back-arc setting.

Almost 4 Bboe, dominated by oil, have been produced from the basement reservoirs in the region.

Around 80% of the basement plays are either in a 'structural-unconformity' and 'stratigraphic-structural-unconformity' trap setting. These combination traps contributed to around 95% of the total basement recoverable resources.

Vietnam

Cuu Long Basin

The largest basement field in the region, Bach Ho, was discovered by chance in 1988 while exploring the Oligocene section of the Cuu Long Basin. The fractured granite reservoir is estimated to contain more than 4,000 MMbbl oil in place. The recoverable reserves are estimated 1.7 billion bo). Continuous appraisal and exploration drilling is being conducted in the Bach Ho as well as adjacent fields such as Tho Trang, to evaluate near-field potential within the basin. As of November 2016, at least 25 wells successfully appraised the discovery.

Following the Bach Ho success, a series of large discoveries replicated this success namely the Rang Dong (1994), Ca Ngu Vang (2002) and Nam Rong (2004) basement reservoirs. The single production test of the Pre-Cenozoic Basement in Rang Dong 1X had one of the highest flow rates in South East Asia.

The longest well in Vietnam with an along hole length of > 6,100 m was drilled in Ca Ngu Vang field with over 2,000 m in granitic basement. The appraisal well had "tested water-free" at a maximum combined rate of approximately 13,000 boe/d.

Song Hong Basin

High H₂S readings were recorded in the Yen Tu 1X basement discovery of 2004, leading to severe operational difficulties. No further information has been reported regarding its development.

In 2008, the northwest-southeast trending carbonate fractured basement in the Ham Rong field was discovered. The well flowed approximately 5,000 bo/d from fractured and karstified carbonate basement section. The discovery well was sidetracked several times due to mechanical problems in the main borehole and the development plan was on as of mid-2016 due to the low oil price at that time.

Nam Con Son Basin

To date, only a few discoveries represent the play in this basin and there is no reported basement production. The development of the 2007 Gau Chua 1X discovery was on hold pending further exploration activity. The best quality reservoirs are found to be the weathered and fractured granitoid rocks in the upper part of the basement rocks.

Indonesia

South Sumatra Basin

In South Sumatra, large discoveries were encountered in Dayung and Sumpal basement reservoirs (following the initial Kluang 1 success of 1913). The 1994, Sumpal 1 discovery well primarily targeted sandstones of the Talang Akar and Lemat formations. Operations were ongoing in 1994 before the operator decided to terminate the well at around 2,000 m in basement. The appraisal well Sumpal 2 proved hydrocarbons deeper than previously tested on the structure and indicated a gas column of at least 750 m. The Sumpal and Dayung gas discoveries later became the focus of the Corridor Block Gas Gathering Project, the gas being earmarked for supply to Caltex's Duri Steam-flood Project in the Rokan PSC, Central Sumatra.

The giant gas reservoir in the basement of Suban field was discovered in 1998 from an outpost well, which flowed at 43.5 MMcfg/d and 365 bc/d. Hydrocarbons are in fractures sub-unconformably and paleotopography trapped. The Upper Cretaceous metamorphic/granite basement reservoirs are generally associated with Plio-Pleistocene rejuvenated faulting, which enhanced the fracture porosity and permeability. ConocoPhillips is currently planning Phase 3 development to boost production at Suban.

Barito Basin

Basement is considered a secondary target in this basin. The Tanjung field encountered oil in the basement in 1938. Resources in this play account for 14% of the total field volume.

Central Sumatra Basin

The Beruk Northeast (Beruk High) and Pulau Utara (northern end of Lirik Trend) fields have produced oil from fractured basement. Beruk produces from fractured Early Permian metaquartzite, Early Cretaceous weathered argillites and altered granite (Late Triassic-Early Jurassic). Fracture porosity generally averages 20% but the altered granite is a poor reservoir [29]. The structure is a fractured basement composed of basement and overlapped and sealed by shales of the Telisa Formation. The Pulau Utara structure is assumed to be similar but with a seal of the Tualang Formation.

Beruk Northeast (discovered in 1976) came on stream in 1981 at an initial average rate of 2,200 bo/d from one well. The field reached its optimum daily production rate in 1997 from four wells. The subsequent development wells have been less productive due to rapid water influx, separating fluid contacts and poorly developed fracture systems in the granite.

Banggai Basin

An ophiolite basement play was reported in the Dongkala 1 discovery of 1986. The well was drilled to test a presumed Miocene reef below a Pleistocene unconformity but encountered ophiolites which yielded gas at a rate of approximately 1 MMcfg/d. Its estimated recoverable resources amount to 50 Bcf gas, representing 18% of the total volumes discovered in the basin.

West Java Basin

The main reservoir is the Mesozoic basement which is made up of predominantly metamorphosed rocks. Trapping style is typically an unconformity associated with a faulted anticline controlled by igneous intrusive deposit facies. Minor oil was discovered in 1983 in the Bima Zu basement high at Asri Sub-basin. All three basement discoveries in this basin have not been developed due to non-commercial reserves.

East Java Basin

A low rate of dry gas flowed from the KE 29 1 basement reservoir, discovered in 2013. The well originally targeted the younger Eocene Ngimbang Group which is one of the major reservoirs in the basin.

Malaysia

Malay Basin

The basement in the Malay Basin exists in two fields and is composed of metasediments of Permian-Cretaceous age and crystalline granitic plutons of Permo-Triassic age. In the eastern flank of the Tenggol Arch the basement highs are draped over and abutted by Lower Tertiary sediments most likely the Group L, which provides both the source and seal for the uppermost fractured and weathered basement reservoirs.

Basement rock in the Malay Basin can be divided into a southwestern and a northwestern province [30]. In the northwest, the basement consists of Mesozoic to Carboniferous carbonates and Mesozoic granites [31].

The first basement discovery was encountered in well Anding Utara 1 in 2004, in the southwestern part of the basin. This discovery was followed by Ledang Tengah Deep 1 in 2010 wherein minor basement gas was encountered.

Tatau Province

The first and only oil discovery in the fractured basement reservoir in East Malaysia (Sarawak) was encountered in well Nuang 1 in 2015. Oil shows were observed in over 100 m of metasediments with quartzite and phyllite. Oil was proven from wireline sampling.

Thailand

Phitsanulok Basin

The only basement find in Thailand was discovered in 1991 at the Sirikit field. The basement play here comprises fractured and weathered pre-Cenozoic meta-sediments and indurated sediment reservoirs, drape sealed and sourced by the Cenozoic lacustrine shales. Further appraisal by deepening existing wells was not successful and existing seismic data was not sufficient to resolve at depths below 3,000 m

7. AUSTRALASIA

Australia

There are five proven basement discoveries in Australia (Figure 8), only one of which has produced commercially (Sturt). The first discovery, Kalangadoo 1, was in 1965; however, it is the most recent discovery of 2014 (Mount Kitty 1) that is potentially of the most interest in the region. Figure 11 highlights basin locations.

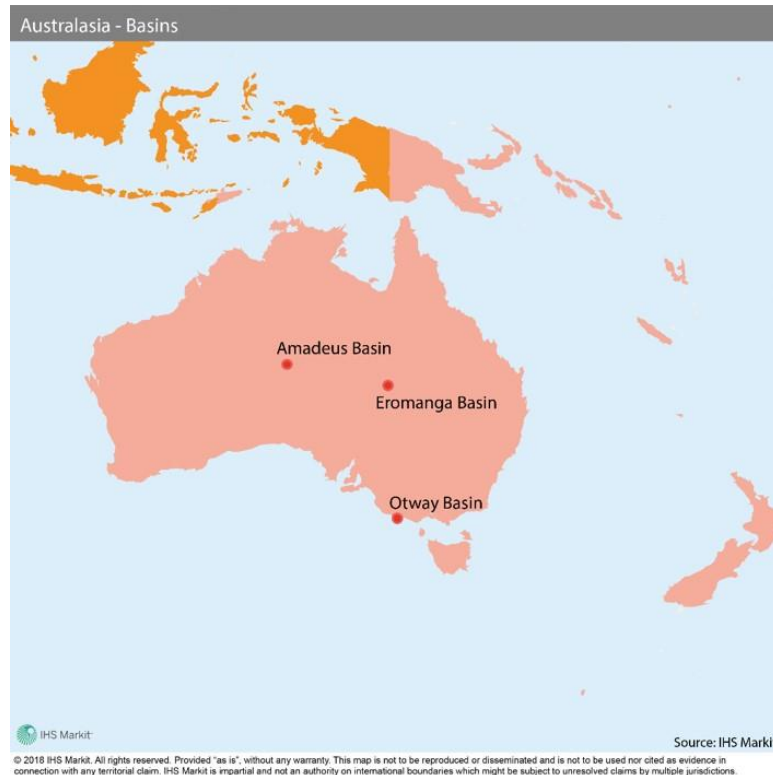


Figure 11. Image showing the location of basins in the Australasia region that contain fractured basement discoveries

Amadeus Basin

The Proterozoic basement structural play was discovered by Mount Kitty 1 in 2014. The well primarily targeted gas, condensate and helium within the Heavitree Formation. Sidewall cores confirmed that the Heavitree Quartzite was absent and that gas flows were actually from fractured granitic basement. Image logs indicated the extensive nature of fractures, which is typical of many structures in the Amadeus Basin.

The discovery itself is not on commercial production but flow rates from the well from granitic basement at a depth of approximately 2,150 m reached a maximum of 530 Mcfg/d of gas. At the time of writing, the Mount Kitty 1 discovery is under appraisal.

Helium generated via radiogenic decay within basement forms an important element of the play (9% at Mount Kitty 1), potentially enhancing the economics of discovered accumulations.

Two structural 'plays' have been described by Ambrose & Heugh [32] that are fractured basement structural play. The first occurs where Gillen Formation source rocks onlap a basement palaeohigh ('Fractured basement Play') while the second occurs where hydrocarbons are trapped within imbricate thrust sheets ('Thrust Belt Play') which was represented in the Mount Kitty 1 discovery. The source and seal for both plays are the same, the only difference being the structural configuration and potential migration pathways.

Cooper Eromanga

A discovery of note is the Sturt oil discovery. In 1988, Sturt 6 discovered, within a fault block, significant oil in fractured Mooracoochie Volcanics of Early Cambrian age. Net oil pay of approximately 6 m was mapped in the felsic tuffs (upper basement). The discovery was commercially productive with cumulative production from 1990 to 2002 from the Patchawarra/Mooracoochie Volcanics interval totaling 72,860 bo.

The 1990 gas discovery, Lycosa 1 flowed gas from several tests in the fractured metasediments (anticlinal structure) within the Cambrian Dullingari Group.

The Warburton – Cooper – Eromanga Basin contains a further basement associated play, the Basement Unconformity Play. This play has one gas discovery associated with it in the basin, the Farina Field. The weathered basement zone (weathered porosity) was discovered by well Farina 1 in 1992. It encountered just over a 1 m of net gas pay. It tested around 0.4 MMcfg, with minor amounts of heavy oil also being recovered.

Otway Basin

The basement play in the Otway basement was discovered by well Kalangadoo 1 in 1965. It encountered significant gas shows over an approximate 115 m interval within a tilted basement fault block. During testing, the well flowed predominantly CO₂ gas at a maximum rate of 2.8 MMcfg/d from steeply dipping arenaceous sediments of Paleozoic age.

8. NORTH AMERICA

USA

There are a small number of relatively minor fields producing from basement rocks in the US. The most noteworthy are along the Central Kansas Uplift in Kansas. Scattered production exists from volcanics in Colorado, Arizona and Nevada but they are local anomalies with little further success to date. Figure 12 shows the location of basins with fractured basement accumulations.



Figure 12. Locations of basins in North America that host fractured basement discoveries

Alaska

The McArthur River field is located in the Cook Inlet Basin, Alaska and is thought to have produced (on test) 180,000 bo from Jurassic metamorphosed marine volcanoclastics and tuffites of the Talkeetna Formation (discovered in 1990). This volume represents less than 1% of the total oil produced from the McArthur field up to the end of 2013 [33] and the discovery has yet to be appraised [34].

California

There are five fields in California producing from fractured basement rocks (Figure 13). The Edison, Playa del Rey, El Segundo and Wilmington fields produce from fractured Jurassic schists within the California Continental Borderland Basin and the Great Valley Basin. In the Salinas Basin, hydrocarbons are produced from a fractured sandstone basement within the Santa Maria Valley field.

At the El Segundo field, in the east, production is from a basal schist conglomerate; and in the west from a Jurassic fractured schist. Oil has been tested to up to 4,500 bo/d with 27° API crude [15]. The Wilmington field is the third largest oil field in America in terms of cumulative production (2.8 Bbbl) and 22 MMbbl is from fractured basement [14]. Oil production from the Edison field basement reservoir is reported to be in the region of 20 MMbbl [14].

Kansas

Oil is produced from fractured quartzites. Within the Central Kansas Uplift there are more than 10 small basement oil fields. The oil is predominantly found in fractures within the Pre-Cambrian quartzite and granite. Specific fields include: Orth (first drilled in 1926 and has three actively producing wells), Ringwald (1948) and Silica (1915) situated in Rice County; Kraft-Prusa (discovered in 1900, 21 wells targeted the Pre-Cambrian but only two are currently active), Beaver (1934), Bloomer (1900), Trapp (1900) (one well producing), Eveleigh (1944) and Heinz (1938) all situated in Barton County. Additionally, Hall-Gurney (1930) and Gorham (1924) of Russell County have previously produced hydrocarbons from a biotite rich granite. Each of these fields are small oil pools containing approximately 150,000 bo/well.

Nevada

Within the Eastern Great Basin Province, the Eagle Spring field produces from crystalline rocks –four wells have produced from Oligocene fractured volcanics and currently, two are active.

Oklahoma

Five wells exist within the Hardeman-Hollis Basin, the Amarillo Uplift, and the Anadarko Basin which have historically produced from granite in Oklahoma. The wells are located within five different fields namely: Altus, Altus East, Lake Creek, Liberty and Willow Northeast. The first producing field was the Altus Field (initially drilled in 1935) however these wells are currently inactive.

Pennsylvania

Within the Appalachian Foreland Basin two wells targeted the fractured Silurian Tuscarora quartzite. Both of these wells are located within the Devils Elbow Field but only one is active. The wells have cumulatively produced approximately 2,900 bbl of oil and over 4.5 MMcf of gas. Hydrocarbons were first produced from this formation in 1980.

Texas

It is reported within the Gulf Coast Basin, the Ouachita Thrust Belt and the Bend Arch-Fort Worth Province that oil is produced from basalts, chlorites and serpentinites within the following fields: Thrall (three wells), Chapman, Yoast (21 wells, two of which are active), Dale (at

least one well) and Lytton-Springs (31 wells - 16 currently active). The Thrall oil field was discovered in 1914 and identified oil within serpentinite rocks.



Figure 13. Locations of fractured basement discoveries in North and Latin America (red circles). The turquoise dots indicate significant finds

Utah

In the Utah Great Basin Province there are four wells that have historically produced hydrocarbons from tertiary basalts but at the Rozel Point field they are all inactive. Oil from the basalts was first produced in 1967.

Wyoming

There are 11 wells in Wyoming that have produced from Pre-Cambrian basement rocks. The wells are distributed over three basins, the Green River and Big Horn Basins and the Central Wyoming Overthrust. A total of eight wells are currently active all within the Green River Basin (Lost Soldier and Wertz fields). The Lost Soldier field first produced from the Pre-Cambrian in 1983 and is currently producing minor amounts and has low future potential. Cumulative production from the eight wells is approximately 605,500 bbl.

9. LATIN AMERICA

Brazil

In the Sergipe-Alagoas Basin (Figure 14), the basement play is reported in seven fields, including the Aruari field (discovered 1986), the Carmopolis field (discovered 1963) and the Riachuelo field (discovered 1961). Reservoirs are in highly fractured metamorphic rocks located in horst-type features.

In the Campos Basin, the Badejo (1976), Linguado (1978) and Trilha (1983) fields have Neocomian fractured volcanic basement - the Lower Cretaceous basalts of the Cabiunas Formation is oil producing. These igneous rocks have usually negligible permeability, but where affected by fractures, they may have developed brecciated zones with interconnected porosity [35]. In December 1982, three wells were producing from the Cabiunas Formation at the Badejo field, where combined rates of 5,160 bo/d were reported. Additionally, one well produced at a rate of 2,200 bo/d.



Figure 14. Locations of basins that host fractured basement discoveries in Latin America

Chile

In Chile, the fractured basement play is only observed at the Punta Baja field, which was discovered in 1952 and the Lago Mercedes fields, discovered in 1992. Both fields are situated in the Austral Sub-Basin of the Magallanes Basin. The reservoir consists of Permo-Triassic fractured granites in an overthrust structure. Combined resources/reserves for the two fields amounts to approximately 15 Bcf of gas and 50 Mbo. This basement reservoir is assumed to be productive at Punta Baja and appraisal is ongoing at Lago Mercedes.

Cuba

In Cuba there are oil discoveries in fractured serpentinite. These include the Bacuranao-Cruz Verde field (1955), the Camarioca field (discovered 1971), the Cantel field (discovered 1982), the Guanabo field (discovered 1968), the Jarahueca field (discovered 1943), the Motembo field (developed 1930-45), the Penas Altas field (discovered 1956) and the Santa Maria del Mar field (discovered 1955); all are located in the North Cuban Province.

Venezuela

There are six fractured basement finds in Venezuela. Four are located in the Maracaibo Basin. One of which, the Totumo field, was abandoned in 1947. Two fields are non-developed discoveries in the Falcon Basin. Production from the Pre-Cretaceous basement section is considerable, particularly in the La Paz-Mara area of the Maracaibo Basin [14].

The Caribbean Petroleum Company was the first to discover oil in the Venezuelan basement with the Totumo discovery in 1915. After the completion of two wells and work on a third, the company suspended its activities in 1915. The field was reactivated in 1928 by the Rio Palmar Oil Fields Corporation who completed ten wells in the basement between 1928 - 1929. The whole field was finally abandoned in 1947 having produced approximately 150,000 barrels of 22° API oil.

In Venezuela, basement production is entirely from the Maracaibo Basin; at La Concepcion field (discovered in 1925) approximately 7 MMbo is thought to be recoverable from the basement reservoir. By 1959, at the near-by Mara field (discovered in 1945) 46 wells had been drilled to the Paleozoic granitic basement reservoir. Reserves in this field are estimated at roughly 110 MMbo. The La Paz Basement which was discovered in 1953, has approximately 350 MMbo reservoirized in its Pre-Cretaceous Structural basement play.

10. EUROPE

Norway

As of 2018, basement on the Norwegian Continental Shelf (NCS) has largely been under-explored. Despite the fact that numerous indications of hydrocarbons have been reported in wells dating as far back to the 1960s the play received little attention. The very first well drilled on the NCS in 1966 (8/3-1) was drilled 50 m into basement but it wasn't until recently that this play was proven here. Work surrounding fractured basement plays on the NCS has been focused on the Utsira High. The first indication of the basement potential in this area was proven by exploration well 16/1-4, drilled in 1993. The well encountered gas/condensate in the upper part of the Pre-Devonian basement section at a depth of approximately 1,865 m.

Almost two decades later in 2007, exploration well 16/2-3 was drilled on the Ragnarrock prospect to check the presence of hydrocarbons in the basement and to test its permeability and productivity. The well was drilled 9 m into basement rock to a total depth (TD) of around 1,900 m but only encountered dead oil stains in the upper 7 m. Appraisal well 16/2-4 followed later in the same year encountering oil and gas in basement rocks however, a series of small scale tests showed limited flow properties.

Work to delineate this new play continued in 2009 with exploration well 16/1-12, drilled to target the Luno South prospect. The well proved oil in weathered and faulted/fractured granitic basement beneath a thin, 20 - 30 cm, early Cretaceous conglomerate. The weathered and fractured basement showed moderate reservoir characteristics with an average porosity of 9% and an average permeability of 1 mD.

Drilling continued in 2011 with exploration well 16/1-15 proving a 45 m oil column in weathered and porous /fractured basement. Top of basement was encountered at 1,920 m. The well was subsequently tested and flowed oil at a rate of 650 bo/d. Following the test, the Norwegian Petroleum Directorate confirmed that it was the first successful full-scale production test of a fractured basement reservoir on the NCS. In other words, a new play model had been defined. The basement pay is now part of the Edvard Grieg field, which commenced production in 2015.

A second production test was performed in basement rocks in 2015 when 16/1-25 was drilled to appraise the 2009 Luno South discovery. The well encountered a 30 m gross oil column in porous granitic basement and flowed oil at a rate of 265 b/d.

The basement play on the Utsira High is now proven by the Edvard Grieg in the East Shetland Basin (Figure 15), Edvard Grieg South, Ragnarrock, Cliffhanger North, Rolvsnes and 16/1-4 discoveries. This play may be found in other sub-basins of the Horda Platform but as yet it is unproven.

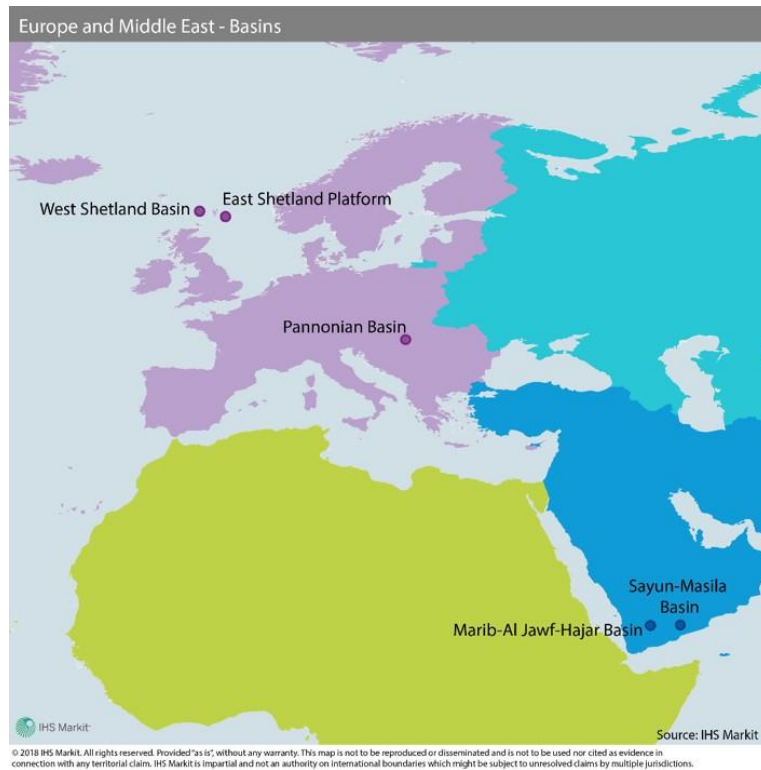


Figure 15. Image showing location of basins with fractured basement discoveries in Europe (pink region)

UK

The Lewisian Basement play in the UK Continental Shelf (UKCS), has until recently, been relatively under explored despite its potential. The Basement play in the West of Shetland was first encountered in 1974 when the Lancaster structure was originally drilled. Well 205/21-1A targeted the Mesozoic sediments overlying the Basement but actually encountered traces of oil over a 75 m section in the Pre-Cambrian Basement. At the time, the potential of this as a reservoir was dismissed. Further drilling in 1977 resulted in the discovery of the giant shallow Paleozoic Clair field (Figure 16). The field's main reservoir is of Devonian/Carboniferous age. However, well 206/7-1 also penetrated a 200 m oil column in the fractured Lewisian Basement. Oil density was 23° API and flowed approximately 965 b/d. This was followed by an appraisal well which tested the basement via a 530 m horizontal section. After acidification, production rates from the basement were reported at 2,110 bo/d from an interval with five fracture zones. Production from the Clair field commenced in February 2005 and up to 2016 has produced over 100 MMbo from the Clair Group - Lewisian Complex reservoir.

Following on from these two successes a series of basement discoveries were made in the West of Shetlands. Typhoon proved the presence of hydrocarbons in 1981 and Whirlwind (operated by Hurricane) in 1999. The company is now focusing mainly on developing the basement play in this area, and in October 2016 it completed testing the Lancaster discovery. Results from a horizontal sidetrack proved that with an electric submersible pump (ESP) flow rates of 14,500 bo/d were achievable. The well was suspended as a future producer with first production expected in 2019. Hurricane had further success in December 2016 when it discovered Lincoln. The company believes Lincoln to be an analogue of Lancaster, with the two structures separated by a sealing fault. Lincoln could contain in excess of 550 MMbo. As of August 2018, alongside developing Lancaster, Hurricane is focusing on the Warwick prospect which is expected to be an extension of the Lincoln discovery.

The East Shetland Platform also has hydrocarbons in a basement play. In 1990 the Cairngorm prospect was found to be hydrocarbon bearing by Marathon. Exploration well 16/3a-11Z encountered oil in a fractured granite reservoir and upon testing, the well flowed 40° API oil

at an approximate rate of 2,000 b/d. Appraisal drilling took place in 2008 and 2013, the results of which concluded that a great deal of uncertainty remained on recovery potential and more information was required on the fault/fracture distribution.

Hungary, Croatia, Serbia

Pannonian Basin

The Pannonian Basin is built-up from microplates enclosed by the Carpathians, the Alps and the Dinarides. It covers Hungary, the north-eastern part of Croatia, the north-western part of Romania, the north of Serbia and some small areas in Austria, Slovakia and Bosnia Herzegovina. The highly fragmented basement, composed mainly of metamorphic rocks, has developed through a series of complex tectonic events throughout the Jurassic and Cretaceous.

The arrival of significant volumes of sediment in the Neogene triggered faster subsidence, resulting in the formation of basement uplifted highs separated by deep trenches. The deepest are the Mako Trench and the Bekes Basin. Fractured basement plays an important role in the petroleum system of the basin. It serves as a pathway for the hydrocarbons from deep trenches, where they are generated and overpressured. This explains one characteristic of the basin: most fields lie above Palaeozoic highs with Pannonian reservoirs usually forming curved arches over them.

Exploration and testing of the fractured basement in the Hungarian Pannonian Basin began in the late fifties. In 1959, the exploration well Nagykoros Del 1 tested up to 28 MMcf/d of gas from granite. The gas was of poor quality and the well was abandoned. Between 1959 and 1963, tests were conducted in the quartzite and granite of the Battonya field in 16 wells. Flows up to roughly 4 MMcfg/d with minor condensate or up to 300 bc/d with minor gas were measured. The field is still producing.

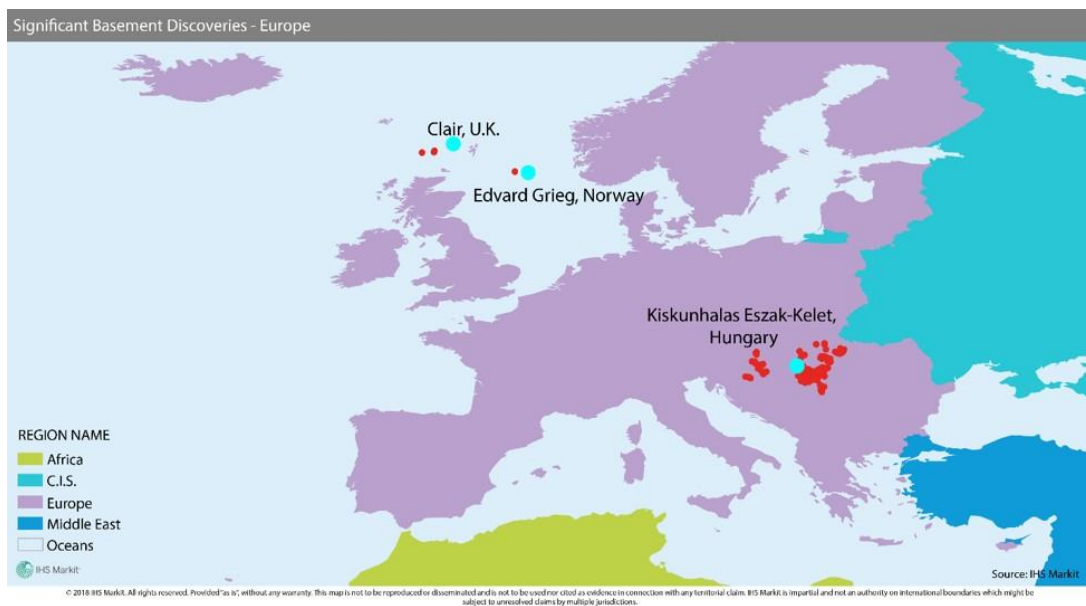


Figure 16. Image showing the location of fractured basement fields in Europe (red circles), turquoise dots indicate significant finds

In total, more than 300 wells had tests in the fractured basement, most of them before 2000. The biggest gas flows were measured in the Sarkadkeresztur field in 1982 with up to 85 MMcfg/d and 300 bc/d coming from the metamorphic rocks. In 1980, the Szeghalom field tested 50 MMcfg/d and over 300 bc/d from the metamorphic basement. The biggest oil flows were measured in the Kiskunhalas Eszak-Kelet field in 1974 with almost 1,400 bo/d streaming from gneiss. The Kiskundorozsma field recorded 1,100 bo/d in 1992 from the mica schist basement.

According to studies carried out in Hungary, the quality of basement rocks as reservoirs is highly variable and depends mainly on the rock type which influences preferred fracture orientation, the extent of the fractures and the fracture connectivity.

Many basement discoveries also exist in Croatia (e.g., Sumecani discovered in 1948, currently shut-in), Romania including the Nadlac field, which was discovered in 1979 and the Zimandu Nou field discovered in 1990 and Serbia (e.g., the Kikinda field).

11. Synthesis

11.1. Discoveries

This analysis shows that hydrocarbon in basement reservoir discoveries exist in just 29 countries (Figure 17). Globally, there are more than 640 discoveries. Africa is a frontier area with only 27 discoveries; the same applies to the Middle East with only 24, all of which are situated in Yemen. The centre of development for fractured basement plays is the Far East (50%), over 260 fields are located in the region with China hosting most (> 160). This is followed by Europe (19%), the C.I.S. (dominated by Russia, 15%), North America (4%), Latin America (3%), Africa (3%) and the Middle East (3%) solely represented by Yemen, and finally Australasia (< 1%) (rounding errors).

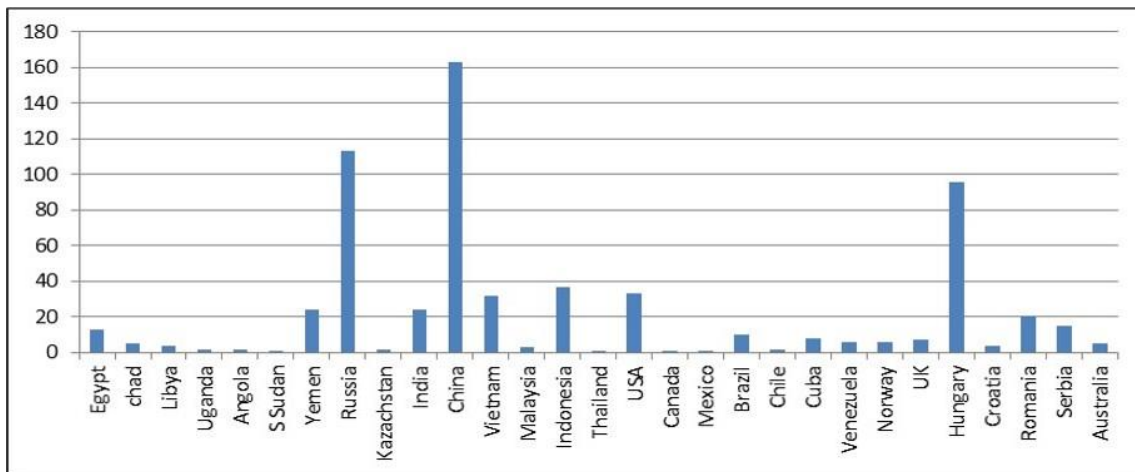


Figure 17. Approximate number of basement finds per country with number producing

11.2. Estimated ultimate recovery

The EUR (2P/2C) associated with these discoveries are at best rough estimates. The total discovered recoverable volume amounts to roughly 15,000 MMboe or ca. 0.001 % of global EUR (BP (2016) and IHSM (2016)).

Most of these volumes (Figure 18) are located in the Far East (56%), followed by Europe (19%), the C.I.S. (9%), Africa (7%), Latin America (5%), Middle East (3%), North America (1%) and Australasia (< 1%). The discoveries are clearly dominated by single large fields. The bulk of reserves are currently located in the Far East; the largest volumes are found in Vietnam and China.

11.2.1. Largest fields

The average field contains some 22 MMboe (average of volumes / fields) of recoverable oil and gas. However, volumes across the globe show a large range and a dominance of a few large fields (Figures 5, 8, 10, 13 and 16).

11.2.2. Number of productive fields

Approximately 220 fields (Figure 21) have produced from the basement. The majority (86 fields) are located in the Far East (39%). This is followed by Europe (21%), CIS (14%), North

America (11%), Africa (7%), Latin America (4%) and the Middle East with 8 previously productive fields (4%). Australasia has no production at present (last production from 1 field in 2002). Please refer to Figure 17.

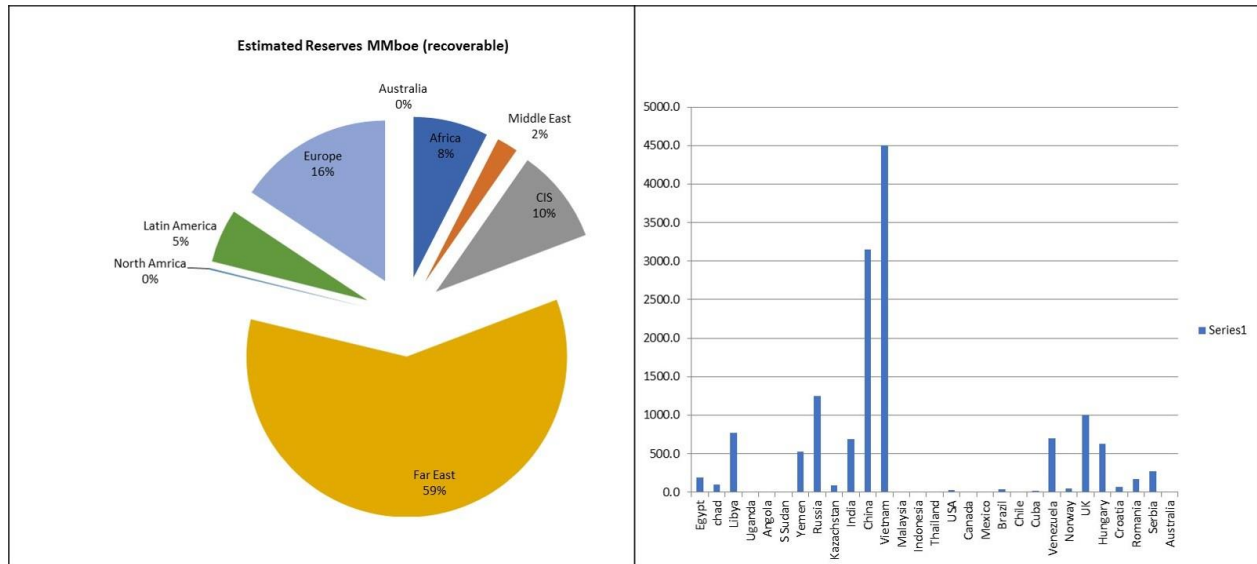


Figure 18. Pie chart showing estimated recoverable reserves (EUR) per region and country (MMboe) (bar chart)

11.2.3. Maximum production rates

Maximum production is highly variable (Figure 19). The architecture and properties of the fracture network are significant controls on well deliverability. Reported well rates vary between 10 bo/d to 30,000 bo/d. This range likely reflects fracture intensity and connectivity. This synthesis suggests that the play has significant exploration potential and warrants a re-look at producing assets to unlock its full capacity. Please note that there are gaps due to unreported data.

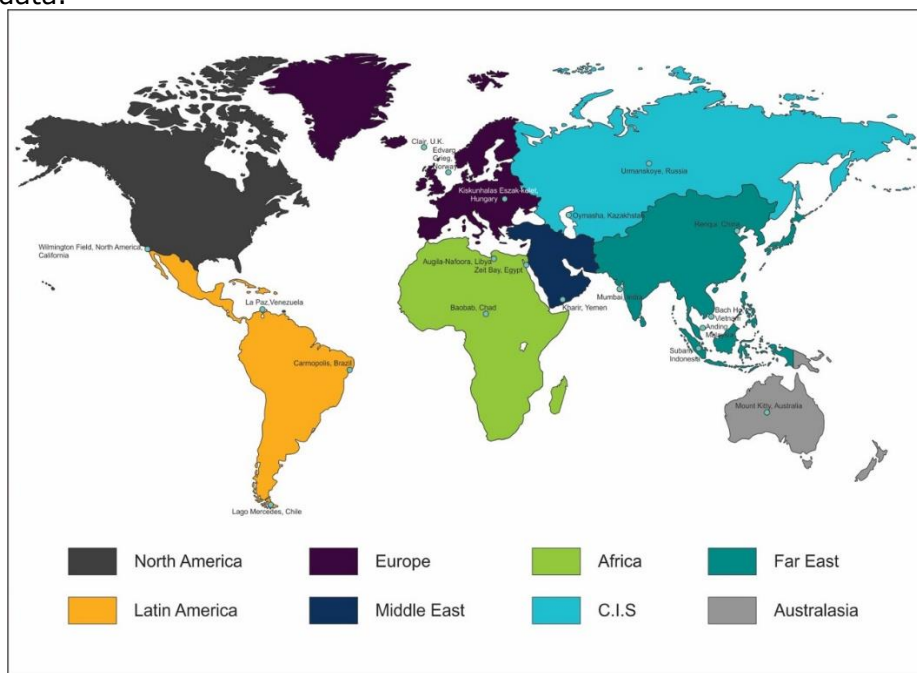


Figure 19. Maximum individual well rates for selected countries

12. Petroleum system

Components of the basement petroleum system resemble conventional plays (Figure 20).

12.1 Seal and source

Source and top seal are typically the same lithology, mostly organic rich claystone or marl onlapping and draping the reservoir. Because there is no source underneath the reservoir, lateral or downward charge or invoked (Figure 20).

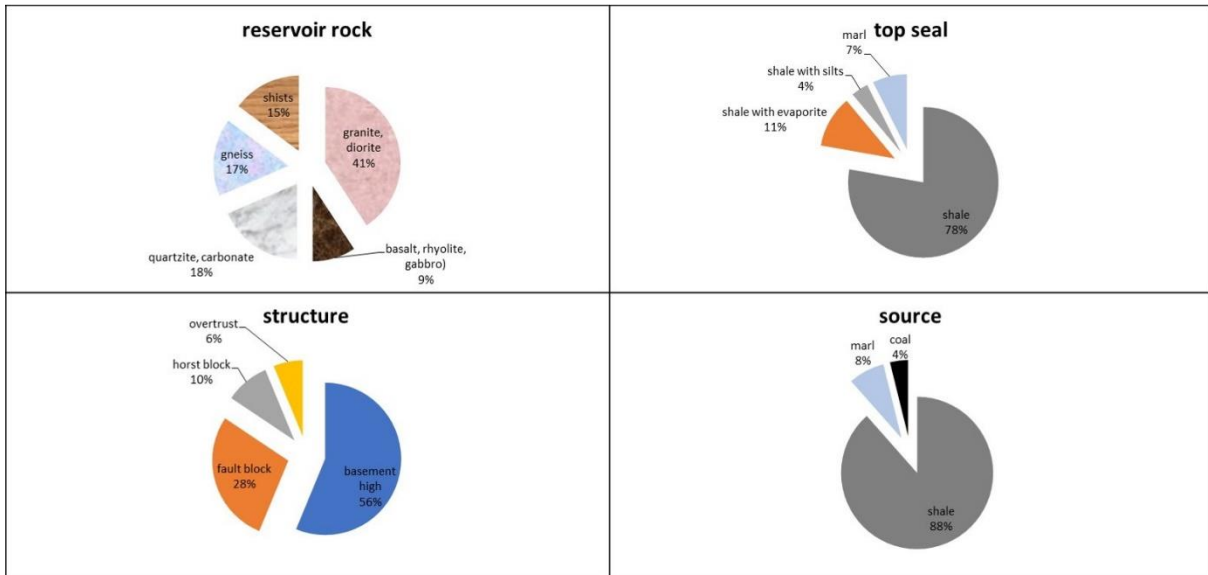


Figure 20. Common lithologies of reservoir, source and seal and nature of structure for fractured basement plays from selected global examples

12.2. Reservoir

The reservoir is mostly provided by brittle magmatic intrusiva. The most commonly encountered lithology is granite, with porosity and permeability associated with fractures that can be solution enlarged. Other common reservoir types included effusive magmatic (basalt, thuff) or metamorphic rocks such as gneiss, quartzite or marble. Less common are pelitic metamorphic rocks.

12.3. Structure

Hydrocarbons are stored in structural highs, most commonly fault blocks or buried hills.

Acknowledgements

The authors gratefully acknowledge the support from IHSM. Thanks to Belinda Spiteri for assistance with Figures (3- 16) and to Jeremy Benton for resource advice.

References

- [1] North FK. Petroleum in Basement Rocks. AAPG Bulletin, 1990; 66: 1597-1543.
- [2] Trice R. Basement exploration, West of Shetlands: progress in opening a new play on the UKCS. In: S. J. C. Cannon, & Ellis, D. (eds) Hydrocarbon Exploration to Exploitation West of Shetlands. Geological Society, London, Special Publications, 2014; 397: 81-105
- [3] Rodriquez K, Intawong A, Hodgson N, Paton D, and Birch P. Fractured basement - an overlooked play type with significant potential from a global seismic database. First Break, 2017; 35: 77-82.
- [4] Du Hung N, Van Le H, & Vu H. Hydrocarbon geology of Cuu Long Basin-offshore Vietnam. 2003, Extended Abstract presented at the AAPG International Conference, Barcelona, Spain.

- [5] Gutmanis JC. Basement reservoirs – A review of their geological and production characteristics. IPTC 13156. 2010. Hydrocarbon Production from Fractured Basement Formations. GeoScience Limited, Version 9
- [6] Cuong TX, and Warren JK. Bach Ho field, a fractured granitic basement reservoir, Cuu Long Basin, Offshore SE Vietnam: A 'buried-hill' play. *Journal of Petroleum Geology*, 2009; 32 (2): 129-156.
- [7] IHS Markit International E&P Database. detailed database capturing past and present worldwide E&P activities. 2016, 2017, 2018, with over 13,000 E&P data attributes, International Exploration and Production Database (IRIS21) is the most comprehensive and reliable dataset available to oil and gas industry professionals today.
- [8] IHS Markit Enerdeq Browser. Enerdeq Browser provides a single point of access to critical IHS Markit North American content. Using a set of mapping, reporting, and analysis tools, Enerdeq Browser allows users to download, query and process over 5 million Well completions and over 2 million Production entities, Interpreted Formation Tops, Rig Activity and Permits, 2D/3D Seismic, Land and Lease, Pipeline and Facilities, and Spatial information. 2016, 2017, 2018
- [9] Powers S. Reflected buried hills and their importance in petroleum geology. *Economic Geology*, 1922; 17(4): 233-259
- [10] Dake CL, and Bridge J. Buried and resurrected hills of central Ozarks. *AAPG Bulletin*, 1932; 16(7): 629-652.
- [11] Landes KK, Amoroso JJ, Charlesworth LJ, Heany F, and Lesperance PJ. Petroleum resources in basement rocks. *AAPG Bulletin*, 1960; 44: 1682-1691.
- [12] P'an Ch-H. Petroleum in basement rock. 1982, *AAPG Bulletin*, 1982; 66(10):1597-1643.
- [13] Petford N, and McCaffery KJW. Hydrocarbons in crystalline rocks., Special Publication of the Geological Society of London. The Geological Society 2003, 242 p.
- [14] GeoScience Limited. Hydrocarbon production from fractured basement formations. 2015 Version 11.
- [15] Koning T. Fractured and Weathered Basement Reservoirs: Best Practices for Exploration and Production – Examples from USA, Venezuela, and Brazil. 2013, AAPG Annual Convention, Poster Paper Presentation. Abstract volume.
- [16] Nguyen TBN, Dang TQC, Bae W, Phung HT, & Lee W-K. A Review of Geological Characteristics and Improved Oil Recovery for a High Temperature Fractured Basement Reservoir, Vietnam, 2014, *Energy Sources, Part A: Recovery, Utilization, and Environmental Effects*, 2014; 36(17): 1895-1912,
- [17] Salah MG, and Alsharhan AS. The Pre-Cambrian basement: a major reservoir in the rifted basin, Gulf of Suez. *Journal of Petroleum Science and Engineering*, 1998; 19: 201-222. Elsevier Science B. V., Amsterdam, Netherlands.
- [18] Zahran I, and Askary S. Basement reservoir in Zeit Bay oil field, Gulf of Suez. *Bulletin AAPG*, 1988; 72(2): 261.
- [19] Younes AI, Engelder T, and Bosworth W. Fracture distribution in faulted basement blocks: Gulf of Suez, Egypt. Structural geology in reservoir characterization. Geological Society of London Special Publications, 1998; 127: 167-190.
- [20] Lirong D, Xiaodong W, Jingchun W, Jianlin L, Renchong W, and Suhong Z. Characteristics of granitic basement rock buried-hill reservoir in Bongor Basin. *Chad. Acta Petrolei Sinica (Shiyou Xuebao)*, 2015; 36(8)_ 897-904.
- [21] Lirong D, Shrivastava C, Chuanshu D, Jingchun W, Hammond N, Anoliefo C, Lei D, and Siddick M. Understanding the interplay of fractures, stresses & facies in unconventional reservoirs - case study from Chad granites. 76th EAGE Conference & Exhibition 2014, Amsterdam RAI, The Netherlands, 16-19 June 2014, 1-5. European Association of Geoscientists & Engineers (EAGE).
- [22] Zheng CM. A new exploration method for buried-hill oil fields, the Liaohe depression. China, in Wagner, H. C. and others, eds., *Petroleum resources of China and related Subjects*. 1988, Houston, Texas, Circum-Pacific Council for Energy and Mineral Resources Earth Science Series, 1988; 10: 251-262
- [23] Neff P. The Habban Field and the Fractured Basement Play in Yemen. Presentation, AAPG ICE, Turkey, 2014.
- [24] Legrand N, de Kok J, Neff P, and Torsten C. Recovery mechanisms and oil recovery from a tight, fractured basement reservoir, Yemen. 2010, SPE 133086.

- [25] Zhai GM, and Zha QH. Buried-hill oil and gas pools in the in the North China basin, in Halbouty. M.T., ed., The deliberate search for the subtle trap. 1982, American Association of Petroleum Geologists Memoir, 1982; 32: 317-335.
- [26] Zhao X, Jin F, Wang Q, Han C. Exploration and discovery of subtle deep buried hill and buried hill inner-curtain hydrocarbon reservoir in Jizhong Sag. China Petroleum Exploration, 2014; 19(1): 10-21.
- [27] Gao R, Zhao Z, Qiao H, Yuan X. The Frontier Petroleum Exploration in China: Exploration of Subtle Oil and Gas Reservoirs in Bohai Bay Basin (V.3). Petroleum Industry Press 2001, Beijing, China. 1-231.
- [28] Li X, Yan W, Cui Z, Guo B. Prospecting potential and targets of buried hill oil and gas reservoirs in Bohai Bay Basin. Petroleum Geology & Experiment (Shiyou Shiyuan Dizhi), 2012; 34 (2): 140-144, 152.
- [29] Koning T, Darmono FX. The Geology of the Beruk Northeast Field, Central Sumatra: Oil Production from Pre-Tertiary Basement Rocks. Proceedings 13th Indonesian Petroleum Association Annual Convention, 1984; 13(1): 385-406. Indonesian Petroleum Association, Jakarta, Indonesia.
- [30] Liew KK. Structural development at the west-central margin of the Malay Basin. Geol. Soc. Malaysia, Bull. 1994; 36: 67-80.
- [31] Leo, C., T., A. Exploration in the Gulf of Thailand in deltaic reservoirs, related to the Bongkot Field. In: Fraser, A. J., Matthews, S. J., and Murphy, R. W., eds., Petroleum Geology of South-east Asia. 1997, Geological Society Special Pub., no. 126, 77-87.
- [32] Ambrose G, and Heugh J. Fractured Basement Hydrocarbon Plays and 'Buried Hill' Plays in Central Australia. CTP Technical Note, 2011; 11.07.15, 1-16.
- [33] Hite DM, and Stone DM. A history of oil and gas exploration, discovery and future potential: Cook Inlet Basin, South-Central Alaska. AAPG Memoir, 2013; 104: 1-35.
- [34] Hunter WA, Waugaman J, Schmitt DA, Frankforter M, and Schwartz KM. The geology and development of McArthur River Oil field, Trading Bay Unit, Cook Inlet, Alaska. 2011, AAPG Search and Discovery Article, 90125.
- [35] Mohriak WU, Mello MR, Dewey JF, and Maxwell JR. Petroleum geology of the Campos Basin, offshore Brazil. Geological Society of London Special Publications, 1990;50: 119-141.
- [36] Koning T. Fractured and weathered basement reservoirs - an overlooked high risk but potentially high reward oil & gas objective in West Africa. Petroleum Geoscience of West Africa Margin, 2014, 31 March to 2 April, London (U.K.), 84-86. Geological Society of London, London, United Kingdom.
- [37] Adam HZ. Pre-Cambrian fractured basement reservoirs as a new unconventional oil resource in the Melut rift basin, southeastern Sudan. AAPG GEO 2010 Middle East Geoscience Conference & Exhibition, Innovative Geoscience Solutions - Meeting Hydrocarbon Demand in Changing Times 7-10, March 2010, - Manama, Bahrain, 1.
- [38] Jiang Y, Ye T, Zhang S, Liu H. Enrichment characteristics and main controlling factors of hydrocarbon in buried hill of Bohai Bay Basin. Journal of China University of Petroleum (Edition of Natural Science), 2015; 39(3): 20-29.
- [39] Nelson R. Geological analysis of naturally fractured reservoirs. Gulf Professional Publishing 1985. 332pp.

To whom correspondence should be addressed: Dr. Michael C. Pöppelreiter, South East Asia Carbonate Research Laboratory (SEACaRL), Universiti Teknologi Petronas, 31750 Tronoh, Perak, Malaysia, E-mail: m.poppelreiter@Shell.com

Multiple Point Statistics Carbonate Facies Modelling Workflow Using Core Data and Spectral Decomposition Attributes: A Case Study from TX Field in Central Luconia Province, Malaysia

Grisel Jiménez Soto^{1*}, Mirza Arshad Beg¹, Michael C. Pöppelreiter², Khaidir Rahmatsyah³

¹ South East Asia Carbonate Research Laboratory, Department of Geosciences, Universiti Teknologi PETRONAS

² Shell Kuwait

³ Baker Hughes Netherlands

Received May 6, 2020, Accepted August 6, 2020

Abstract

Building static models in carbonate environments proved to be complex due to the multi-dimensional nature of poro- perm-systems (karst to microporosity) and biological growth architecture complex geometries imprint at a different scale from um to km. In addition, the presence of multiple erosions or lack of deposition the interpretation in the stratigraphic columns makes the development of a modelling workflow challenging using the traditional method as variogram-based algorithms that mostly ignore important geological information.

A 100 km² of 3D seismic data, 3 wells logs, 2 core well logs, and selective modern carbonate analog were integrated to define a set of carbonate geological "shapes" calibrated with core linked with facies to bring sedimentary facies architectural realism using Multiple Point Statistics geomodelling technique. This methodology, a good first pass approximation to build a meaningful facies model where depositional facies can be mapped and captured at various scales both vertically and laterally using the input data with relevant contribution and weight.

Keywords: Central Luconia; Middle Miocene; Carbonates; Spectral Decomposition; Carbonate facies; Reef rim; Karst; 3D seismic geobodies extraction; Multiple-point statistics.

1. Introduction

In the past 25 years, there has been a significant development in the computing power and software capability which has led to progressively improve a range of modelling techniques, however, despite all these efforts facies architecture and its distribution is often poorly understood and hence its representation in 3D digital models can be related to large uncertainties.

Isolated carbonate platforms are common carbonate environments of deposition throughout the Phanerozoic. They were especially abundant during the Palaeozoic. Our present understanding of build-up distribution, and the ability to better predict their location, is hampered by the fact that maps of build-ups rarely show evidence of spatial organization of petrophysical properties, at the contrary, they often appear chaotic [1].

Typically, in Luconia carbonate reservoirs, the reservoir heterogeneity arises from differences in porosity/permeability, which are marked by diagenetic overprint and/or meteoric dissolution resulting in Reservoir Rock Types (RRTs) with different petrophysical properties, therefore one of the first challenges for property modelling is to identify the depositional facies.

This study proposes an integrated modelling workflow divided into four steps and using a wide range of data from core to satellite image scale. Seismic attributes interpretation, geomorphology and core-facies seismic analysis were carried out to produce a depositional seismic model using Multiple Point Statistics method in a heterogeneous reservoir in "TX" platform in offshore Luconia province, Malaysia, a unique geologically location where facies and depositional facies are still visually distinct in the core.

2. Geological background

Central Luconia province is located in offshore Sarawak, Northwest Borneo, Malaysia, with an aerial extent of 45,000 km², over 250 isolated carbonate build-ups have aggraded mainly from a Middle Miocene substrate [2]. Global and regional Middle Miocene events provide an imprint to internal facies distribution, lateral and vertical heterogeneity in porosity type and distribution.

The Central Luconia province is a relative paleo high which dips gently NW ward towards a regional lineament, the West Baram line. The province is subdivided structurally into a number of regional highs and lows that are further partitioned into localized extensional horsts and grabens trending systematically SSW-NNE, while compressional structures mostly trend WSW-ENE [3].

The overall architecture of build-ups seems to be determined by four major processes: the rate of skeletal carbonate production, subsidence, sea-level fluctuations, and the supply of clastic material from the Borneo deltas [4]. Observed trends, in general revealed that carbonate build-ups seem to have died earlier and are thinner (<500m) in the south, while they lived gradually longer, are thicker (up to 3000m) and reached higher in the stratigraphy towards the north [5-9].

The platforms experienced several phases of evolution in response growth and architecture of the platforms were controlled by a relative constant subsidence rate over the province (based on relatively uniform platform thicknesses of about 1200 m), and the interplay with eustatic sea-level fluctuations and the monsoonal wind system of the middle Miocene affecting the area [9].

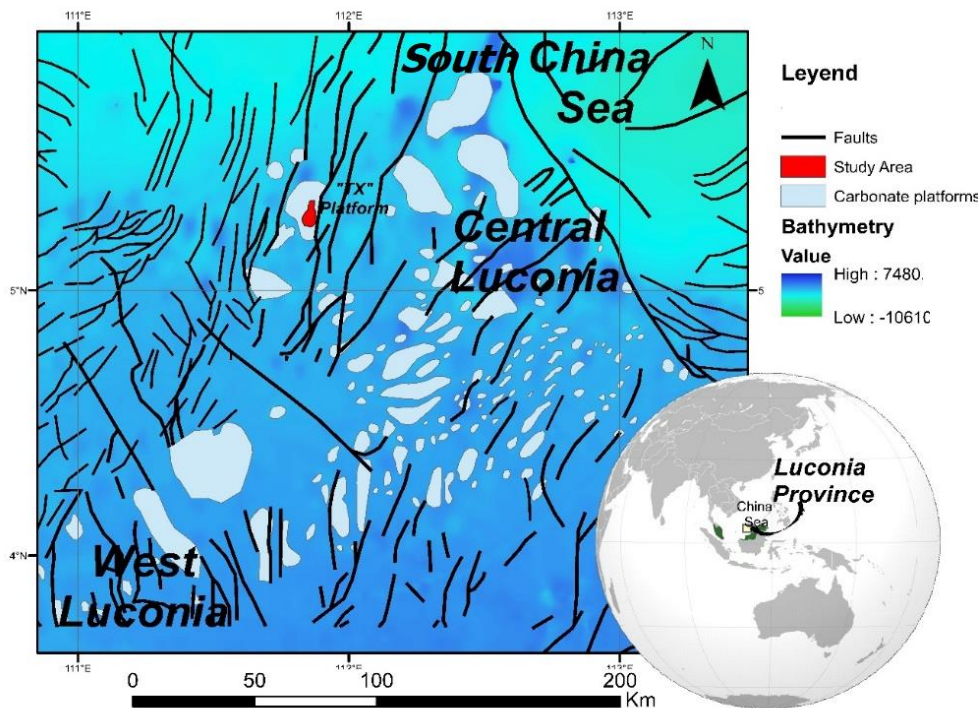


Figure 1. Bathymetric map of the South China Sea, with major structural lineaments (black lines), superimposed with the Miocene carbonate build-ups distributed in Luconia Province. The red polygon shows the location of the "TX" platform

The study field is located in the Northwestern Luconia province and is one of the seven stratigraphic culminations on a major mega platform (30 km x 50 km large). The TX platform is approximately 280 km NNW of Bintulu. The carbonate build-up has experienced an aggradation phase followed by a backstepping phase during a series of third-order sea-level cyclicity in the middle Miocene [9].

3. Dataset and methodology

The subsurface data used for this study comprises three pre-stack time migrated 3D seismic surveys tied to 3 wells that cover an area of approximately 96 km². The well data accessed included wireline logs which include core description information from TX-2 (1713 MD) and TX-3 (1875MD). TX-3 core data was used for calibrating the stratigraphic markers with the seismic stratigraphy. Google Earth satellite images of a modern carbonate build-up located in Tun Sakaran Marine Park, Malaysia were used to develop the conceptual model and training image for MPS simulation. The proposed workflow methodology using MPS includes the following four steps.

3.1. Integrated seismic-core log calibrated geocellular grid

3.1.1. Seismic geomorphology and seismic attributes

The seismic data consist of a pre-stack time cube covering the entire "TX" platform. The data comprise two surveys acquired in 1991 and 1992 for a total of 245 km, the grid spacing is 300 m. The dominant frequency in the carbonate platform averages around 30 Hz, average acoustic velocity averages around 2900 m/s.

Well to seismic ties were completed by establishing a reasonable correlation between the seismic and synthetic seismograms by adjusting T-D functions through stretch and squeeze. In both wells the top of the carbonate sequence is associated with an apparent decrease in density. Also in both wells, the first noticeable reflector of the reverse polarity synthetic originates near the top of the carbonate.

A neural network methodology is applied for seismic interpretation in PaleoscanTM [10] in order to create a number of stratigraphy consistent horizon slices through the "TX" platform. This methodology created a node network for every peak, trough, and zero-crossing. It then calculates the best correlation coefficients between two seismic traces, which results in the minimization of the 'time' of correlation. This correlation was modified and calibrated with nine manually interpreted horizons in the "TX" platform. Then a calculation of a 3D Relative Geological Time model (RGT) was applied using an intra - and extrapolated version of the correlation cube.

To extract the geobodies and define thin horizon stack layers, spectral decomposition (SD) with short-time Fourier transform (STFT) method attribute was applied to 'decompose' the original seismic wavelet into its individual low (Hz 16), mid (33 Hz), and high (46 Hz) frequency components. We use the blending of the red-green-blue (RGB) colour model to identify the delineate the geobodies and seismic facies.

3.1.2. Core and well logs data

Wireline logs are available from three vertical wells: density, porosity, permeability and, lithofacies logs were used for log correlation to identify lateral variations, vertical facies distribution and establish a comprehensive correlation of cross-sections along with the dip and strike directions of the platform. Furthermore, the correlation was used to create a depositional trend map to run MPS simulation. Core data and well data description is used to create upscaled facies logs for MPS simulation.

3.2. Training image

A training image (TI) is a 3D conceptual model that provides a representation of the full range of shapes and dimensions expected in the modeled platform. The properties in the TI grid can be facies properties, porosity, grain size, or other reservoir properties. It is under the assumption that the TI has the same multiple-point statistics and contains the same complexity of the geological features of the area of interest, or in other words, assumed stationary [11].

Google Earth provided high-resolution image input to develop Tis from modern carbonates build-ups [12-13] a selected modern analog satellite image was used for the comparative metric analysis of main depositional facies environments. These interpreted images were processed and converted into a 3D grid by defining the number of cells in JewelSuiteTM.

3.3. Auxiliary variable or trend map

The objective to generate a 3D auxiliary variable is to create a trend containing information about facies dimensions and relationships among facies. In this step, horizons and seismic facies, seismic attributes were used to delineate the geobodies of seven 3D depositional facies: Deep Lagoon, Shallow Lagoon, Proximal Reef (Lagoon), Reef Rim, Upper Talus, and Lower Talus.

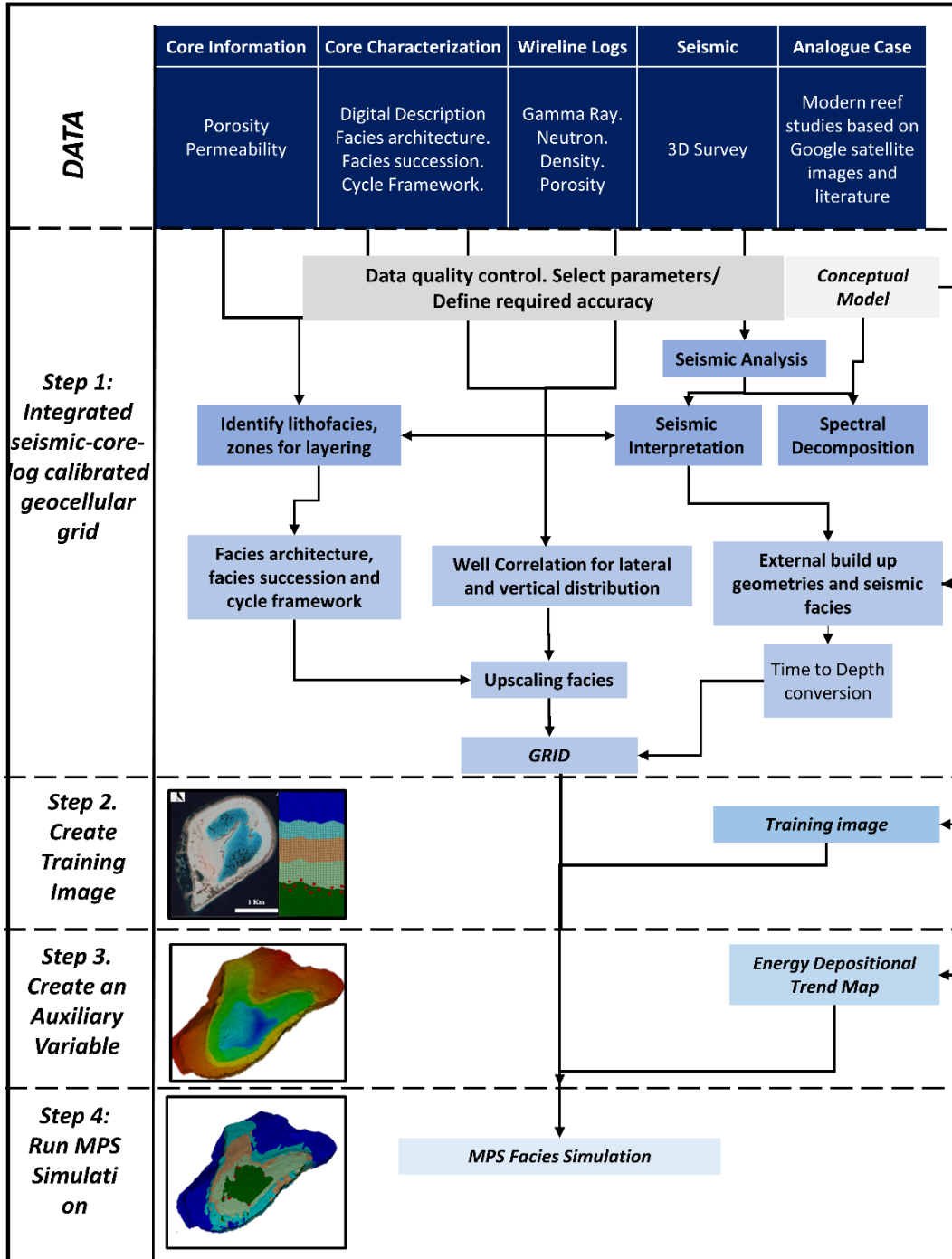


Figure 2. Proposed workflow methodology using MPS facies modelling. The basic data include geological information, seismic survey, well data and satellite images

3.4. Simulate depositional facies population using the trend map and training image

An MPS simulation using the TI and auxiliary variable run at this late stage. This technique is inspired by the object-based modelling method. The resulting continuous training image was eventually transformed to match a target property histogram to generate an MPS Simulation in cross-section and maps and to match facies regions.

4. Results and discussion

4.1 Integrated seismic-core-log calibrated geocellular grid

4.1.1. Seismic expression

The seismic interpretation of site survey data demonstrates the 'TX platform' comprises parallel-layered stratigraphy. The eastern margin is rimmed by a high energy organic reef non-continuous and often chaotic reflectors. Erosion and faulting, combined with depositional thinning, limit the buildup to the west and north.

The identification of major flooding surfaces, sequences boundaries was carried out combining seismic expression, seismic geomorphology, well and core data. Four main zones were identified. Three main reservoir porous zones delimited by two flooding surfaces or tight layers calibrated with the deepest cored and wireline logs well TX-3 (Figure3)

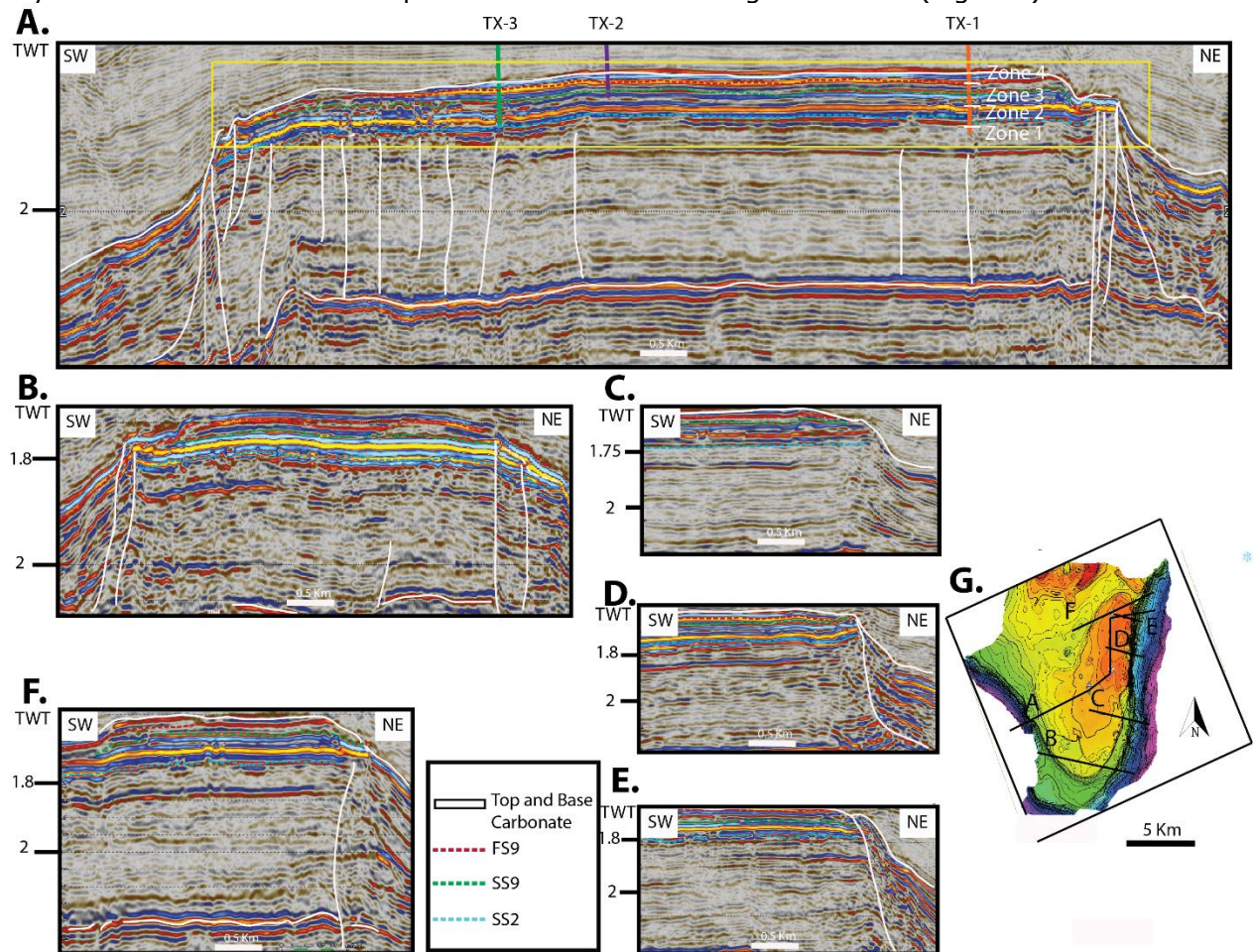


Figure 3. A. Arbitrary multiregional line interpreted northeast to southwest arbitrary covering the 3 study wells. B, C, D, E showing eastern arbitrary seismic lines showing the seismic character of the talus distribution and reef rim geometries. F. Arbitrary line displaying the seismic character of the Northern part of the build-up. G. The insert map shows the locations of the arbitrary lines

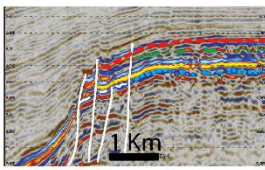
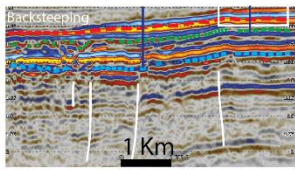
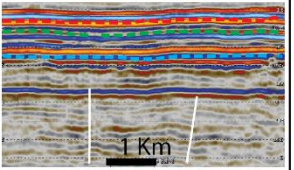
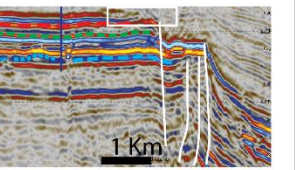
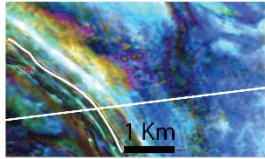
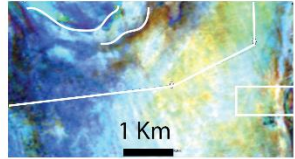
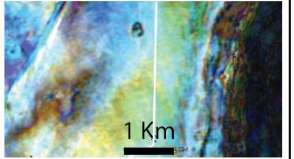
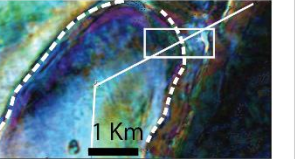
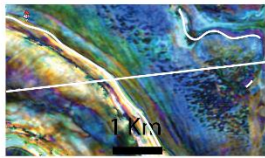
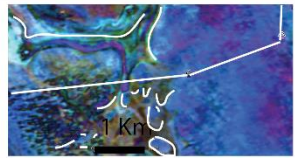
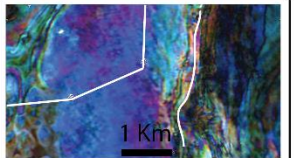
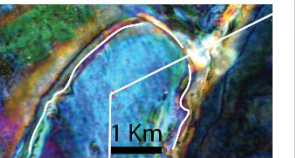
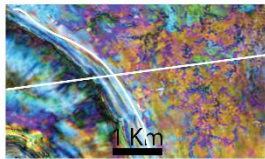
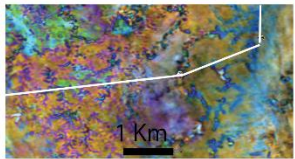
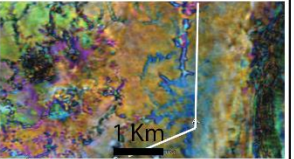
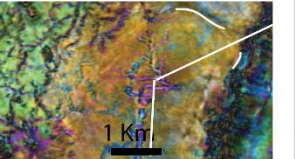
	Leeward SW 4	3	2	1 Windward NE
2D Seismic expression				
FS9				
Architecture	FS9 interval is not present in this interval, but the reef margin and talus has chaotic seismic expression	Reflectors are nearly parallel and are abruptly cradled due to the Backstepping process which reduce the size of the platform.	Parallel facies character observed over most of the zone. Reflectors are nearly parallel and with extensive development.	Sharp angle talus in the windward zone is present. Sharp geometries at the margin of the reef are present and continuous.
Dimensions	Azimuth: N70 °W. Rim with max: 0.54 Km. Rim with min: 0.4 Km Rim continuity: Partially. Talus angle: 35°	Lagoon extension: Dip Lagoon Zone: slightly dip towards the west..	Rim with max: 0.2 Km Rim with min: 0.15 Km Lagoon extension: Dip Lagoon Zone: Nealy parallel reflectors.	Azimuth: N30°E Rim with max: 0.5 Km. Rim with min: 0.3 Km. rim continuity: Present. °Talus angle: 45°
Stratigraphy		Protected environment with low energy, characterized with lithofacies in TX-2 and TX-3 wells.	Protectal lagoonal environment dominated by mud supported carbonates. Lithofacies in core in TX2 and TX3 wells evidence restricted sea water circulation.	Reefoidal environment with continuous organic belt characterized by a large spectrum of grain size and reef debris.
SS7				
Architecture	The zone is characterized by an abrupt disrupted of the reflectors to the east and a minor loss of continuity	Reflectors appear to track primary lithologic breaks, enhanced to some degree by subsequent preferential leaching and related diagenesis.	Parallel facies character observed over most of the zone. Reflectors are nearly parallel.	Reef rim margin belt is present as an abrupt reflector in the eastern margin. The former seismic foreereef slope is chaotic. Seismic data reflects faulting and local erosional truncation in the eastern margin.
Dimensions	Azimuth: N75 °W. Rim with max: 0.5 Km. Rim with min: 0.45 Km Rim continuity: Partially. Talus angle: 35°	Lagoon extension: Dip Lagoon Zone: slightly dip towards the west.. Patch average reef diameter: 0.8 Km.	Rim with max: 0.4 Km Rim with min: 0.25 Km Lagoon extension: Dip Lagoon Zone: Nealy parallel reflectors.	Azimuth: N30°E Rim with max: 0.6 Km. Rim with min: 0.3 Km. Rim continuity: Present. °Talus angle: 45°
Stratigraphy	Sharp angle talus in leeward side and abrupt faulting development.	Patch reef development with possible erosional or diagenetic influence.	Protected lagoonal environment dominated by mud supported carbonates. Lithofacies in core in TX2 and TX3 wells evidence restricted seawater circulation.	Reefoidal environment with continuous organic reef belt is present. The margin east present faulting development.
SS2				
Architecture	Abrupted and disrupted reflectors due to the faulting development. An increase in dendritic pattern is present from East to the West.	Chaotic reflectors and increase of dendritic pattern development.	Chaotic reflectors with an increase of dendriti pattern development.	Chaotic reflectors with dendritical pattern in map view .
Dimensions	Azimuth: N70 °W. Rim with max: No visijle. Rim continuity: Partially. Talus angle: 35° Dendritic pattern frequency 70%	Rim with max: No visibile. Lagoon extension: No visibile. Dendritic pattern frequency: 80%	Rim with max: No visibile. Lagoon extension: No visibile. Dendritic pattern frequency: 50%	Azimuth: N30°E Rim with max: No visibile. Rim continuity: No visibile. °Talus angle: 45° Dendritic pattern frequency: 10%
Stratigraphy	Sharply angle talus in the foreereef. Karstification process development in the backreef zone.	Karstification development.	Karstification development.	Early development of karstification process.

Figure 4. Seismic expression and different morphological features of the "TX" platform. For modelling purposes, three main intervals were selected to describe architecture, dimensions, and stratigraphy of internal seismic facies distribution. FS9 interval (Tight layer), SS7, and SS2 Karst interval

The first characteristic reflector of reverse polarity synthetic is originated near the top of Zone 4 which is interpreted as the Top of Carbonate with an abruptly lower gamma-ray response. Below the top of the carbonate, horizon FS9 with a higher density (2.5 g/cm³) and lower porosity (less than 5%) response was calibrated with core information of argillaceous and mud dominated facies indicating a transgressive event which was correlated and matched among the three available wells. In the northern part of the platform, a sharp talus is observed with a slope of ~45° and azimuth of N30°E, in the middle part of FS9 parallel reflectors are observed and near the western part and abrupt change in slope due to the back stepping event which reduces the platform in 80%. (Figure 5)

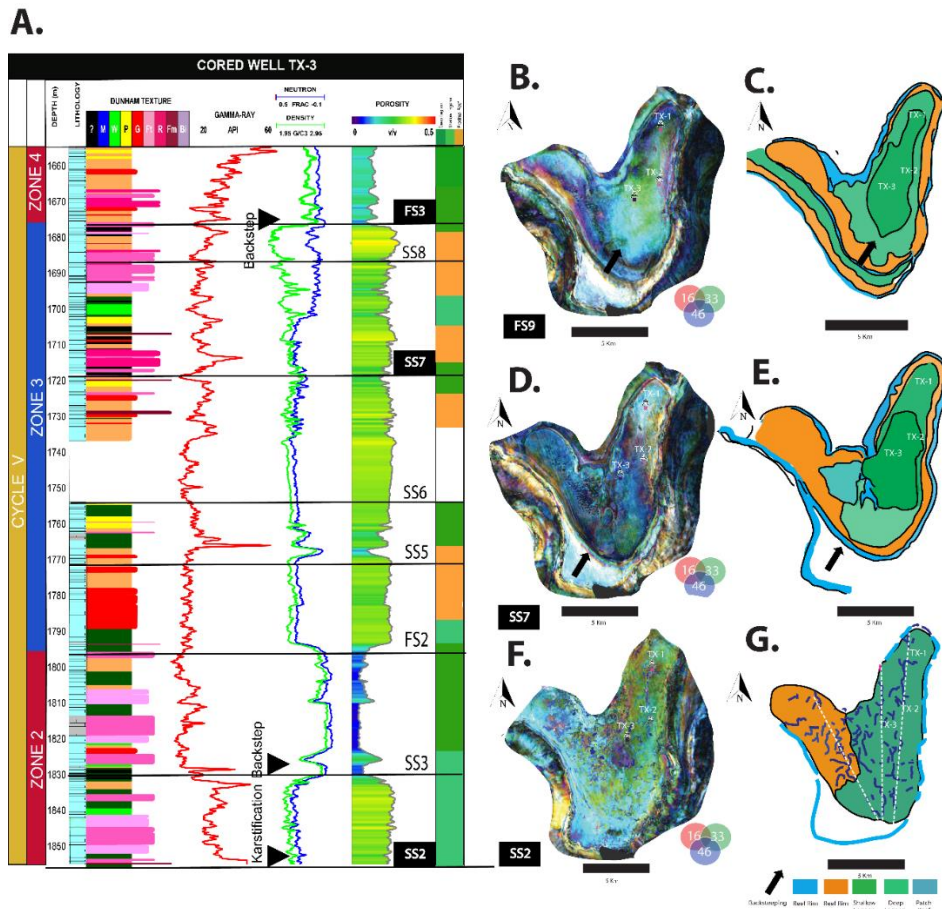


Figure 5. A. Well –Core-Seismic correlation of TX-3 well. The three selected intervals were used to define the trend maps for modelling. B, C correspond to FS9 is the Flooding interval with backstepping evidence in SD maps. D, E, corresponds to SS7 interpreted as an aggradational interval. F, G, corresponds to SS2 with a karst interval with dendritically pattern features

Zone 3 is made by horizons SS8 and SS7, which were fully cored in both wells. In TX-2 and TX-3 with lower density and higher porosity response is present. The lithology is characterized by mud dominated packstone interpreted as lagoon depositional setting. In the western part of the build-up, reflectors appear to break to track primary lithological break with a patch reef and a broader internal late-growth build-up.

Zone 2 ties very well to the horizon FS2 which calibrated with the core is interpreted as a flooding interval and which roughly correlates among the wells, similar to horizon FS9 argillaceous and mud dominated facies indicates flooding interval. Higher density and lower porosity log response at this interval are present. Below FS2, at horizon SS2 the reflectors appear to track primary lithological breaks and enhanced preferential diagenesis with dendritic pattern development due to the karstification events.

4.1.2. Core-spectral decomposition seismic-facies calibration

Spectral decomposition (SD) is a common geophysical method for mapping by its spectral content. This technique was applied to highlight the stratigraphic features and extracting the reef architectural elements such as reef rim belt and dendritically karst patterns. The dominant frequency of the seismic data is measured approximately at 30 Hz. The processing Discrete Fourier Transform (DFT) and the Red-Green-Blue (RGB) colour blended maps are used in a horizon stack of more than 100 horizons. The three frequency ranges are 16Hz, 33Hz, and 46Hz.

Based on the seismic horizon stack and amplitude four different seismic facies were defined in the study. Some of these facies which covered the well location area are correlated with core and wireline logs (Figure 6).

The proposed facies are:

- **Seismic Facies 1 (SF1):** The facies are discontinuous, strong high amplitude strength reflections, and based on comparative sedimentology with the modern analog is interpreted as a reef rim belt. No wells correlation is possible as no wells have drilled the area.
- **Seismic Facies 2 (SF2):** The facies are continuous parallel with moderate amplitude values. The well and core data were used to interpret these facies with good lateral connectivity of a low to moderate energy of the lagoon environment.
- **Seismic Facies 3 (SF3):** The facies consists of abrupt reflectors in the southern region of the platform in interval SS7 and SS6. No wells correlation is possible as no wells have drilled the area, but using the modern analog similar patch reef geometries are present in the lagoon setting.
- **Seismic Facies 4 (SF4):** The facies consists of discontinuous, moderate high amplitude reflections. Well and core data correlates with relatively higher energy in a proximal reef setting.
- **Seismic Facies 5 (SF5):** The facies consists of abrupt and higher amplitudes values with dendritic patterns interpreted as karst features.

4.1.3. 3D seismic – stratigraphy core correlation

Carbonates build-ups margin can show progradational, aggradational, and retrogradational stacking patterns, depending on the balance among the carbonate production and accumulation rates [14]. These processes are encrypted in the external build-up morphology and internal seismic geometries and can provide when calibrated with core and well-exposed build-ups, templates for digital modelling [1].

The Spectral seismic attributes applied in horizon stack cube allowed to correlate with core data for stratigraphic events identification:

Flooding tight layer interval (FS9)

The tight intervals are present with lower amplitudes values on seismic. Log reading interpretation with low Gamma Ray (20-40 API), high density ($\sim 2.3 \text{ g/cm}^3$), and lower porosity ($\sim 18\%$) (Figure X). FS9 is available core and thin sections description is mainly composed of argillaceous limestones, well-preserved foraminifera, and red algae.

The main pore types observed are micropores observed in red algae and rarely observed mouldic porosity. External morphology evidences a size reduction of 20% of the platform area. The flooding interval is interpreted as a drowning event which implies backstepping. In the northern part of the platform, sharp angle talus with a continuous reef rim (SF1) is present and in the southern part, two parallel reef rim is observed evidence of reduction on the size of the platform. (Figure 7).

Agradational Porous layer (SS7)

The porous layers SS5, SS6, SS7, and SS8 are considered with good reservoir potential. From core information, they are mainly composed of coral-dominated grainstone and coral-dominated floatstone indicating a porosity $\sim 23\%$. The poretypes are mouldic and vuggy porosity. Seismic geomorphology allowed to recognize clearly the presence of a continuous reef

rim belt (SF1), lagoon (SF2), and patch reefs (SF3) features on the western side of the platform which is recognized by their chaotic seismic signature in assumed sedimentary conditions of higher accommodation space. (Figure 8)

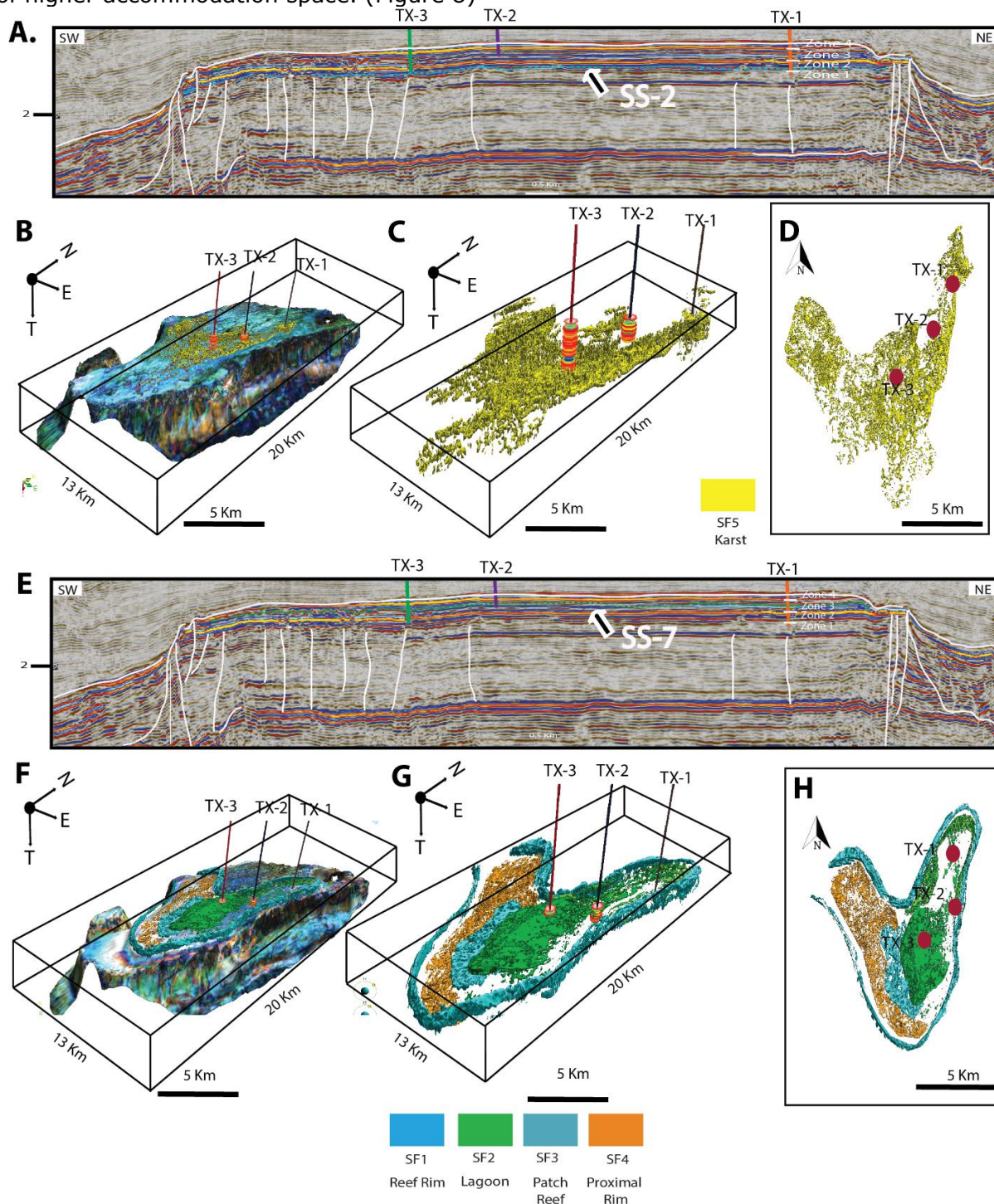


Figure 6. A) Well –Arbitrary line-oriented northeast to southwest showing the location of the SS2 interval used as a reference for geobodies extraction. B) Three-dimensional karst geobodies extraction at SF2 horizon and below Zone 1. C) Map view of SF2 karst distribution. E) Well –Arbitrary line-oriented northeast to southwest showing the location of SS7 interval used for geobodies extraction F) Three-dimensional reef geobodies extraction at SS7 horizon and below Zone 2. G) Three-dimensional reef geobodies extraction at SS7 horizon and below Zone 2. H) Map view of reef seismic facies

Progradational Karst Layer (SS2)

Extensive karstification is present in the upper part of the platform. Karst in seismic is characterized by discontinuous to chaotic seismic facies. This pattern correlates with chalkified limestone with mouldic and abundant vuggy pores in core samples and thin sections [15].

Based on seismic SD attributes at the interval, FS2 has identified dendritic karst (SF5) pattern range in size from 2 km to 15 km and its presence may be influenced by the presence of pre-existing faults of zone 1. This interval was developed during a sub-aerial exposure where dissolution generated various geomorphic features, including large-scale cave systems. (Figure 9). Photomicrograph of FS2 interval, blue areas are epoxy-impregnated porosity. Packstones with large connecting vugs.

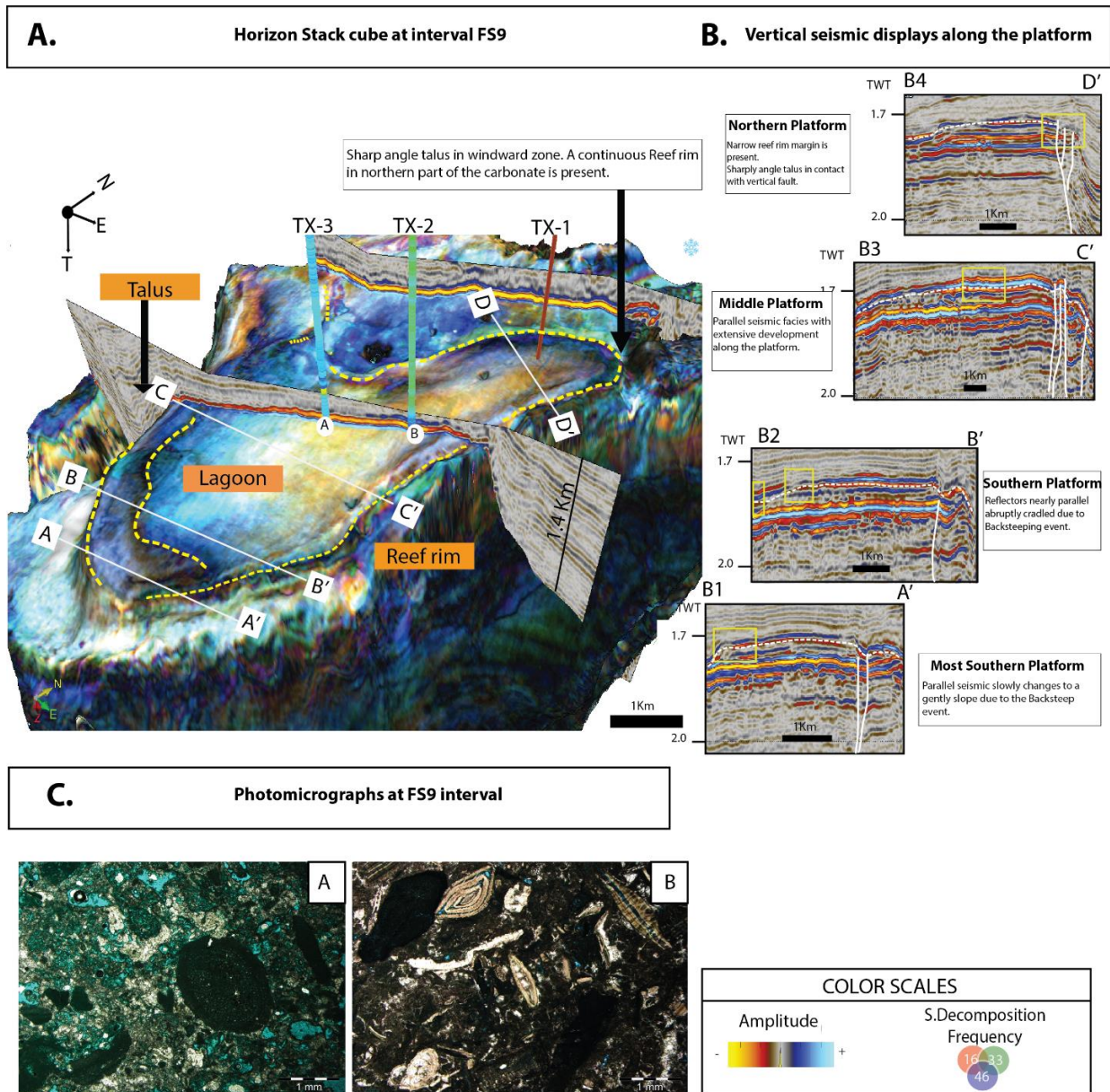


Figure 7. A. Cube display of SD attribute in horizon stack at FS9 interval B1, B2, B3 Vertical seismic displays along with the platform where the less negative amplitude highlights the flooding interval. C1,

C2 Photomicrographs at FS9 interval with foraminifera packstones to wackestones dominated facies with microporosity and less than 10% of porosity and permeability of 0.4 mD

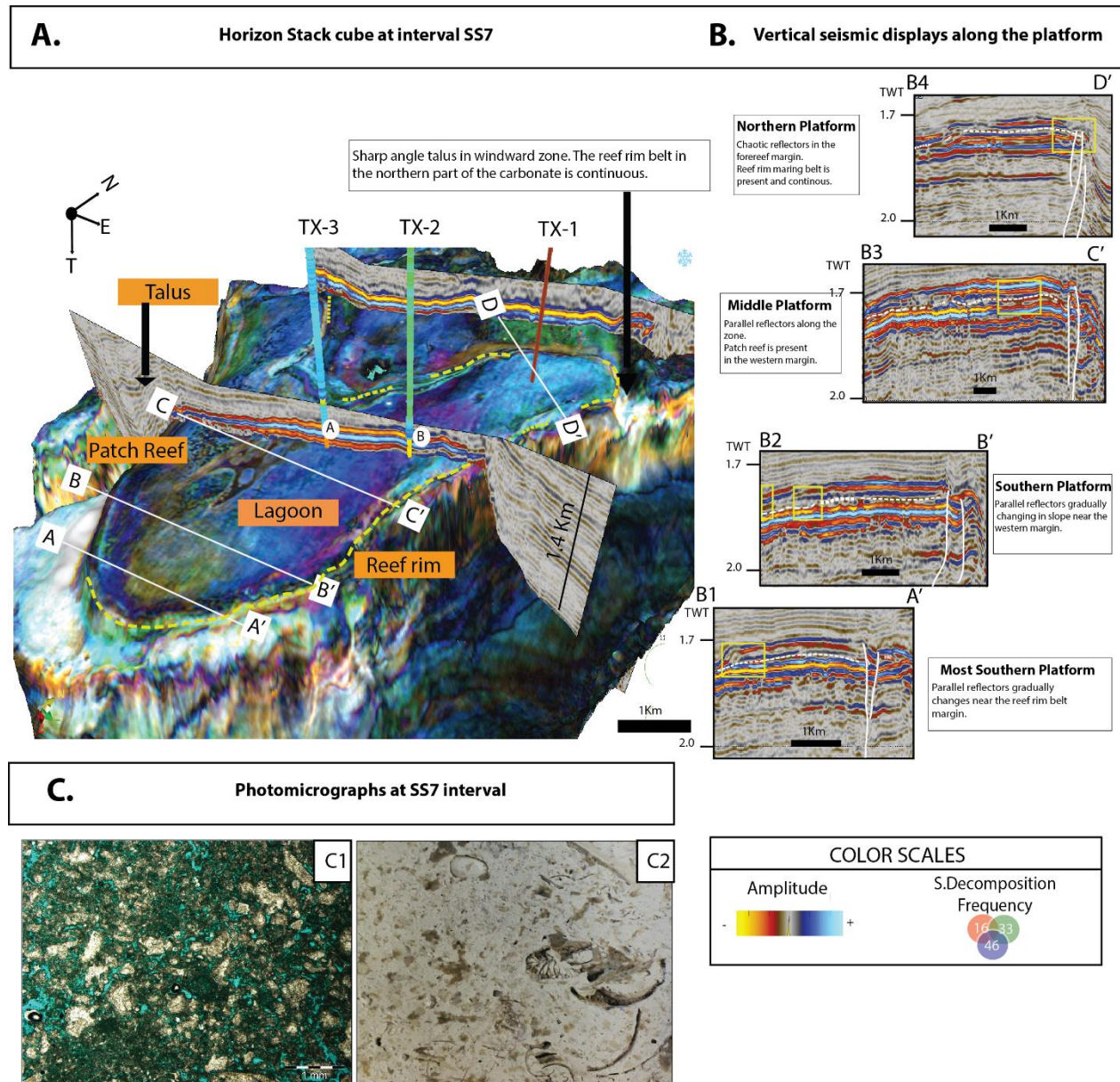


Figure 8. A. Cube display of SD attribute in horizon stack at SS7 interval B1, B2, B3, B4 Vertical seismic displays along with the platform where the less negative amplitude highlights the aggradational interval. C1, C2 Photomicrographs at SS7 interval with coral-dominated grainstone and coral-dominated floatstone with mouldic dominant poretypes and porosity of 28% and permeability of 42 Md

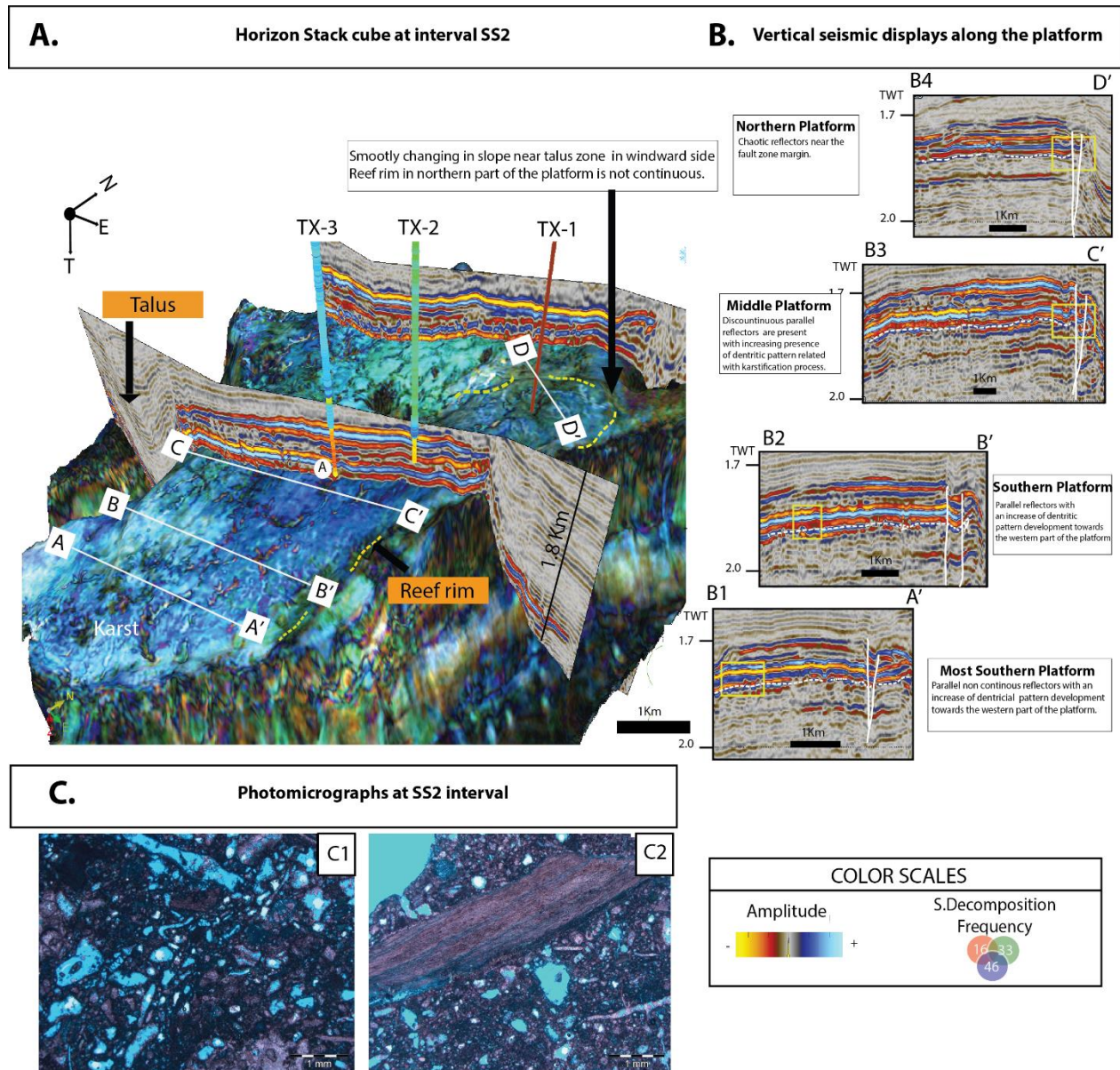


Figure 9. A. 3D Cube display of SD attribute in horizon stack at FS9 interval B1,B2,B3,B4E) Vertical seismic displays along with the platform where the most positive amplitude highlights the karst interval. C1, C2 Photomicrographs at SS2 interval with packstones to wackestones dominated facies with vuggy dominant porotype and porosity of 30% and average kh of 62 mD

4.2. Training image

Open source satellite imagery from Google Earth was used to select a modern carbonate build-up to understand 2D lateral facies architecture. For this work, a modern build-up selected from Tun Sakaran Marine Park in Malaysia. This site includes seven main isolated carbonate platforms: Gaya, Selakan, Kapikan, Mantabuan, Church reef, Maiga, and Sibuan, previously studied and mapped by [16]. The area is situated 7.5 km east of Semporna, and it is surrounded by deep water ranging in depth between 60 m off the western edge of the study area.

The Church reef platform is the fifth largest platform in the Tun Sakaran Marine Park with an area of 4 km² and contains a few patch reefs and is surrounded by carbonate sand shoals. (Figure 10). The geospatial image was imported in JewelSuiteTM and was processed and converted into the 3D GSLIB format grid file by defining several cells. A previous facies map by

Chalabi, 2012 [14] allowed to recognize four main zones: reef complex, carbonate sand shoal shallow lagoon, and deep lagoon and to (Figure 10A).

The analogue based on comparative sedimentology allowed to establish the lateral facies relationship TI grid (Figure 10B). Such comparison identified a lateral facies rule for a second Ti construction. In this new TI, the lateral relationship is defined and two new facies described in the core were added: Proximal reef and patch reef features.

In the MPS simulations, the main objective is not to reproduce the identical geological patterns or geometries in the TI, but to generate similar features, then is advisable to create a simple TI which may reflect simple facies relationships.

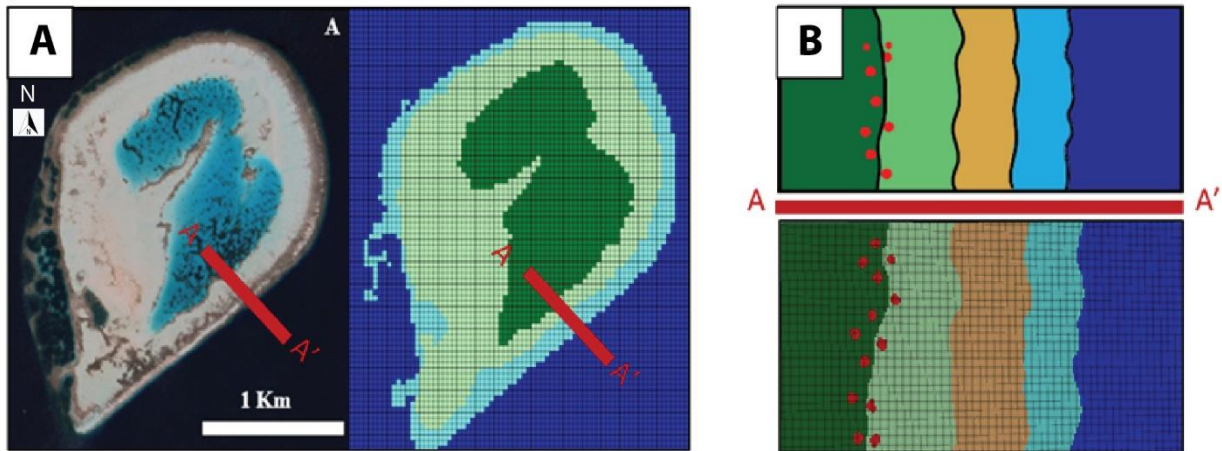


Figure 10. A. Training images in GLSIB format of Church Reef platform (B) Lateral segment of the platform

4.3. Auxiliary variables based on seismic geobodies extraction

An auxiliary variable is a 3D grid property that is defined in both the training image and simulation model and describes the presence of a trend without explicitly referring to any conventional condition [17].

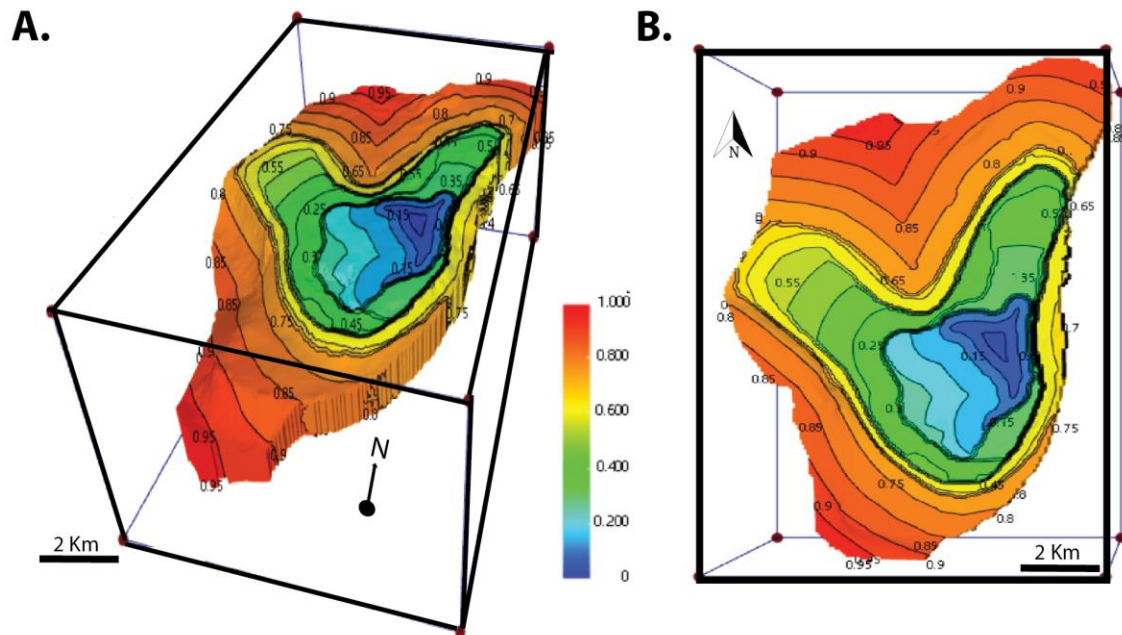


Figure 11. A. 3DAuxiliary variable cube representation B. 2D map of the energy trend map

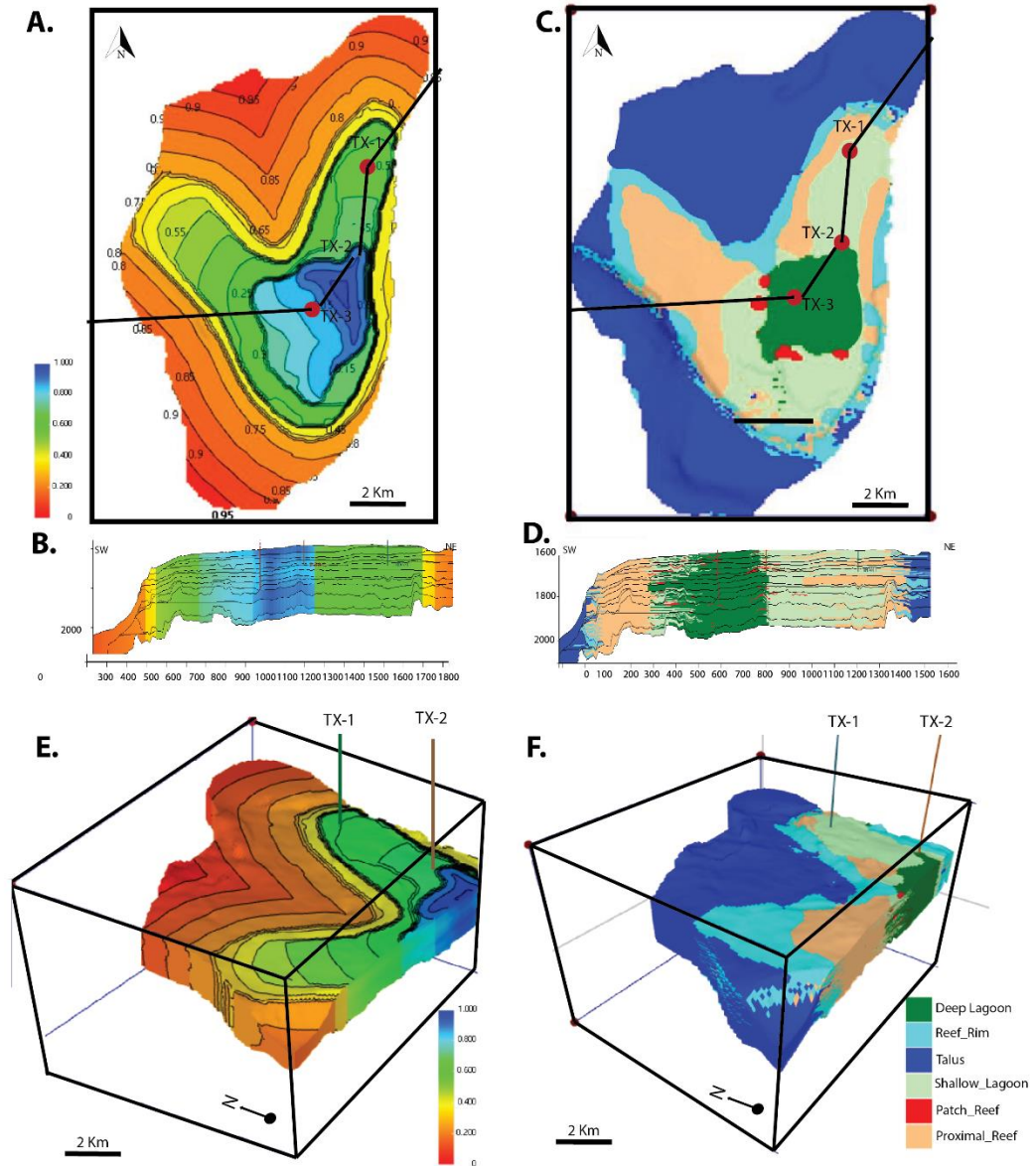


Figure 12. A. 3D energy trend model as an auxiliary variable for MPS simulation B. Northeast to the south-western cross-section of the energy trend map C. MPS 3D facies model of "TX" platform D. North-east to a south-western cross-section of the facies model. E. Western to Eastern cross-section of the 3D energy trend F. Western to Eastern cross-section of the 3D facies model

Depositional and sequence-stratigraphic models suggest that modern and ancient carbonate platforms should have a well-stratified internal character, representing the development of distinct depositional elements generated by the interaction of various relative sea level, climatic, and diagenetic controls. Some depositional models suggest that carbonate platforms consist of high-energy deposits (reefs or sand shoals) at margins and protected interior lower-energy lagoonal deposits, possibly containing small patch-reef bodies [14].

For the modelling purposes and honor the facies distribution a 3D trend was created to simulate the sedimentary energy expected in "TX" platform. Values from 0 to 0.5 are expected to develop sedimentary depositional corresponding to the deep, shallow lagoon (SF2) and proximal reef (SF4). Values from 0.5 to 0.8 are expected to develop the reef rim belt (sf1)

which may represent the high energy of deposit and finally, values from 0.8 to 1 are expected to be the talus and open marine facies.

4.4. MPS simulation

The final simulation grid using the workflow (Figure 8) is capable to create a simple 3D consistent carbonate pattern from very simple training images and one auxiliary variable. The 3D trend has been conditioned to SD results and geobodies extraction (soft data) and core and well data (hard data) to create a representative 3D facies distribution grid. The following facies distribution matched with depositional setting interpreted in TX-1 and TX-2 wells. (Figure 12)

- Deep Lagoon and Proximal reef are modeled in the most interior part of the platform and they matched with TX-1 and TX-2 sedimentary core description.
- Reef Rim: The reef rim belt is modeled in a continuous way based on SD seismic geometries extraction, however, no wells have been drilled the reef rim. The windward northern side shows clearly a continuous rim while in the leeward a non-continuous reef belt is present.
- Patch Reef is modeled on the western side of the "TX" platform. No available wells have been drilled on this side of the platform.

This model can be used as an input for the porosity model and later for flow modelling simulation purposes.

5. Concluding remarks

The MPS method proved to create a simple model combining object-based concepts from the comparative sedimentology of a modern carbonate and ancient platform. This comparison assisted to provide a training image which provides simple facies lateral relationship and seismic geobodies to create an auxiliary variable or trend maps to handle non-stationarity in both TI and simulation model. The proposed workflow includes the following steps:

Step 1: Integrated Stratigraphic core – logs calibration with seismic attributes and geomorphology

Step 2: Create a training image or set of training images with sufficient geological information to provide facies neighbourhood patterns.

Step 3: Create an Auxiliary Variable or Trend Map to handle one or more trends.

Step 4: Simulate depositional facies with 2D training images and 3D auxiliary variables.

The workflow proposed in this work is general and can potentially be used as an input for different sedimentary settings and used for reservoir simulation stages. The simple model can also help to improve the general understanding of reef rim growth patterns and diageneses karst behavior.

Acknowledgements

The authors acknowledge the full support of the South East Asia Carbonate Research Laboratory (SEACARL) at Geoscience Department, Universiti Teknologi PETRONAS (UTP) to complete this study. We acknowledge PETRONAS's Malaysian Petroleum Management for providing the data and allowing the publication of this work. We also are grateful to the following software companies for providing academic licenses: Elilis for providing PaleoScan™ and Baker Hughes for JewelSuite™.

References

- [1] Elvebakk G, Hunt DW, Stemmerik L. From isolated build-ups to build up mosaics: 3D seismic sheds new light on upper Carboniferous–Permian fault controlled carbonate buildups, Norwegian Barents Sea. *Sedimentary Geology*, 2002; 152(1–2): 7–17.
- [2] Warrlich G, Adams E, Ryba A, Tam T, Ting K, Tang H. What matters for flow and recovery in carbonate gas reservoirs: Insights from the mature Central Luconia Province, offshore Sarawak, Malaysia. *AAPG Bulletin*, 2019; 103(3): 691–721.
- [3] Koša E. Sea-level changes, shoreline journeys, and the seismic stratigraphy of Central Luconia, Miocene-present, offshore Sarawak, NW Borneo. *Marine and Petroleum Geology*, 2015; 59: 35–55.

- [4] Epting M. The Miocene carbonate build-ups of central Luconia, offshore Sarawak. In A. W. Bally (Ed.), Atlas of seismic stratigraphy (pp. 168–173). AAPG 1989 (Tulsa). Studies in Geology.
- [5] Ho KF. Stratigraphic framework for oil exploration in Sarawak. Geol. Soc. Malays. Bull., 1978; 10: 1e13.
- [6] Epting M. Sedimentology of Miocene carbonate buildups, central Luconia, offshore Sarawak. Buletin Persatuan Geologi Malaysia, Bulletin Geological Society of Malaysia, 1980; 12: 17–30.
- [7] Epting M. The Miocene carbonate buildups of central Luconia, offshore Sarawak. In A. W. Bally (Ed.), Atlas of seismic stratigraphy (pp. 168–173). AAPG 1989(Tulsa). Studies in Geology
- [8] Doust, H. Geology and exploration history of offshore central Sarawak. In M. T. Halbouty (Ed.), Energy resources of the Pacific region (pp. 117–132). AAPG 1981, (Tulsa), Studies in Geology.
- [9] Vahrenkamp VC, David F, Duijndam P, Newall M, and Cravello P. Growth architecture, faulting, and karstification of a Middle Miocene carbonate platform, Luconia Platform, offshore Sarawak, Malaysia, Chapter 15 in Eberli, G.P., Masafiero, J.L., and Sarg, J.F.R., (eds.), Seismic imaging of carbonate reservoirs and systems, AAPG Memoir, 2004; 81: 329-350.
- [10] Pauget F, Lacaze S, Valding T. A global approach in seismic interpretation based on cost function minimization. SEG Technical Program Expanded Abstracts 28(1):2592-2596, <https://doi.org/10.1190/1.3255384>.
- [11] Pyrcz M, and Deutsch CV. Geostatistical Reservoir Modelling. Oxford University Press 2014, ISBN 13: 978-0199731442.
- [12] Jimenez G, Pöppelreiter M, Rahmatsyah K. Non stationarity training images from modern carbonate analogues for MPS modelling in Central Luconia Province. National Geoscience Conference 2019. Kota Kinabalu.
- [13] Jimenez G, Arshad B, Pöppelreiter M, Rahmatsyah K. Features extraction from carbonate modern platforms satellite imagery using Computer Vision. Petroleum and Coal, 2020; 62(3): 899-906.
- [14] Burgess PM, Winefield P, Minzoni M, Elders C. Methods for identification of isolated carbonate buildups from seismic reflection data. AAPG Bulletin, 2013; 97(7): 1071-1098.
- [15] Yusliandi A, Sautter B, Pöppelreiter M. The Various Controls on the Platform Architecture of Carbonate Build-ups in The Central Luconia Province, Offshore Sarawak. Petroleum and Coal, 2019; 61(6): 1425-1437.
- [16] Chalabi A, Pierson B, Talib J. Remote Sensing Analysis of Recent Carbonate Platforms, East of Sabah: Potential Analogues for Miocene Carbonate Platforms of the South China Sea. Indonesian Journal of Geology, 2012; 7(3): 123-135.
- [17] Riou J, Hocker C. Practical recommendations for Successful Application of the MPS Facies Modelling Method. Abu Dhabi International Petroleum Exhibition and Conference 2015. SPE-177675-MS.

To whom correspondence should be addressed: Dr. Grisel Jiménez Soto, South East Asia Carbonate Research Laboratory, Department of Geosciences, Universiti Teknologi PETRONAS, Malaysia, E-mail: jimenezsotogrisel@gmail.com

Combustion Characteristics and Decomposition Kinetics of Melon Seed Husks Based on the Distributed Activated Energy Model

Bemgba B. Nyakuma^{1*}, Olagoke Oladokun¹, Tertsegba J-P. Ivase², Moses I. Ayoosu³, Jamila Baba Ali⁴, Samuel Moveh⁵, Yakudu A. Dodo⁶

¹ School of Chemical and Energy Engineering, Faculty of Engineering, Universiti Teknologi Malaysia, 81310 Skudai, Johor, Malaysia

² Bio-Resource Development Centre, National Biotechnology Development Agency, Makurdi, Benue State, Nigeria

³ Faculty of Built Environment and Surveying, Universiti Teknologi Malaysia, 81310 Skudai, Johor, Malaysia

⁴ Department of Polymer and Textile Engineering, Faculty of Engineering, Ahmadu Bello University, Samaru Zaria, Kaduna State, Nigeria

⁵ School of Mechanical Engineering, Faculty of Engineering, Universiti Teknologi Malaysia, 81310 Skudai, Johor Bahru, Malaysia

⁶ Faculty of Engineering and Built Environment, Universiti Sains Islam Malaysia (USIM), 71800 Nilai, Negeri Sembilan, Malaysia

Received May 6, 2020; Accepted September 21, 2020

Abstract

This paper examined the thermal decomposition kinetics of melon seed husks (MSH) under multi-heating rates and non-isothermal oxidative conditions by thermogravimetric analysis (TGA), temperature profile characteristics (TPCs), and the distributed activated energy model (DAEM). The thermal analysis resulted in 95.06 – 95.77% mass loss (M_L) and 4.01 – 4.94% residual mass (R_M). The TPCs indicated that the midpoint (T_{mid}), endpoint (T_{end}), peak drying and peak devolatilization temperatures (I and II) increased with incremental heating rates except for the ignition (T_{ons}). In addition, the changes in temperature and heating rates significantly influenced the thermal behaviour, degradation mechanisms, and TPCs as evident in TG/DTG plots. Kinetic analyses indicated the activation energy (E_a) and frequency factor (A) also fluctuated significantly during TGA. The values of E_a were from 46.53 kJ/mol to 533.82 kJ/mol, whereas A was from 3.62 min⁻¹ to 1.68 × 10⁵¹ min⁻¹ with average values of 215.56 kJ mol⁻¹ and 8.85 × 10⁴⁹ min⁻¹, respectively. Overall, the MSH displayed high thermal reactivity during thermal and kinetic analyses. Hence, combustion is a potentially practical route for the valorisation of MSH into clean energy for a sustainable environment.

Keywords: Combustion; Kinetic analysis; Melon seed husks; Activated energy; DAEM.

1. Introduction

Melon seed (*Citrullus colocynthis*, L.) otherwise called *Egusi* is an important perennial cash crop extensively cultivated in Nigeria. It is a yearly, monoecious and herbaceous non-creeping plant of the *Cucurbitaceae* family that survives in the tropics, subtropics, temperate or parched regions worldwide [1]. With an oil content of 45-60%, the melon seed is commonly consumed as food, condiment or processed into a vegetable oil termed melon seed oil (MSO) in many parts of Nigeria and West Africa [2-3]. Over the years, MSO has become a vital vegetable oil and feedstock for biodiesel production, cosmetics, fine chemicals, and traditional medicines [4-8]. As a result, the demand for melon seeds and its rich oil has increased significantly, resulting in the cultivation of over 500,000 tonnes of the crop annually [9].

Typically, the extraction of oil from melon seed generates MSO, seed cake, and the outer seed coat called the husks or shells [1]. The seed cake is currently utilised as an essential

source of protein, carbs, and minerals for animal feeds and food supplements for humans [10]. However, the melon seed husk (MSH) is discarded as wastes in dumpsites, open pits or landfills. Other known disposal strategies include utilisation as cooking fuel, organic manure, mulching material, biochar feedstock and bio-herbicides [11-15]. Over the years, the low efficiencies of the outlined waste disposal and management strategies have resulted in MSH accumulation in the environment. Hence, the open-air burning of MSH has soared over the years, thereby resulting in airborne pollution with aggravated risks to human health and safety in the affected areas. Therefore, more sustainable approaches are required to effectively address the current and impending problems arising from the poor disposal and management of MSH.

Given its lignocellulosic nature, the valorisation of MSH through biomass conversion technologies is proposed as an efficient approach to effectively dispose and manage the growing stockpiles of MSH. Previous studies have examined the thermal conversion of MSH under pyrolysis conditions [9, 16-17]. The study by Nyakuma [17] examined the solid biofuel potentials of MSH as feedstock for clean energy and power generation. The thermal and kinetic properties were also examined under non-oxidative (pyrolysis) conditions using thermogravimetric analysis (TGA).

In a separate study, Nyakuma [9] examined the bioenergy potential along with the physicochemical and thermodynamic fuel properties of MSH as feedstock for pyrolysis. The findings indicate that MSH has a high energy content, heating value, and combustible elements for thermochemical conversion into clean energy. However, the limitations of the non-oxidative nature, product selectivity, and distribution of pyrolysis products require further investigation of the potential of MSH as solid biofuel feedstock. Since current energy conversion processes and infrastructure in biomass power plants are based on pulverised combustion, it is expedient to explore the oxidative thermal conversion of MSH for future applications.

Therefore, this study seeks to examine the oxidative thermal properties of MSH as a potential feedstock for combustion in future biomass power plants. In addition, the thermal degradation and kinetic behaviour of MSH will be examined through the Distributed Activated Energy Model (DAEM). To the best of the authors' knowledge, there is currently no publication on the oxidative thermal analysis and combustion kinetics of MSH in the literature. Hence, this study presents novel insights into the bioenergy potential of MSH during combustion for future clean energy generation.

2. Experimental

In this study, the melon seed husks (MSH) examined were purchased from a popular market in Kaduna State, Nigeria. Next, the MSH was characterised to determine its physiochemical (ultimate and proximate) and calorific fuel properties, as reported in our previous studies in the literature [9, 16-17]. Based on the results, MSH can be effectively utilized as feedstock for thermochemical energy conversion through pyrolysis, gasification or combustion.

In this study, the thermal and kinetic characterisation of the MSH was examined under oxidative thermal conditions for combustion applications. Therefore, the thermal properties of MSH were examined through thermogravimetric analysis (TGA). The tests were performed under non-isothermal conditions by heating 8 mg of the pulverised MSH sample in an alumina crucible from 30°C to 800°C at different heating rates 10°C/min, 20°C/min, and 30°C/min using the Shimadzu TG-50 (Japan) thermal analyser. During TGA, the furnace was purged with air at a flow rate of 20 ml/min to flush out the evolved gases. In the end, the mass loss (%) was computed as a function of temperature to determine the thermogravimetric (TG, %) and derivative (DTG, %/min) plots, presented in Figures 1 and 2.

Next, the thermal degradation behaviour of MSH was examined to determine the temperature profile characteristics (TPCs) using the Shimadzu TA Workstation thermal analysis software. Hence, the onset (ignition) (T_{ons}), midpoint (T_{mid}), endpoint (T_{end}), and devolatilization peak (T_{max}) temperatures were computed along with mass loss (M_L) and residual masses (R_M) under oxidative (combustion) conditions during TGA. Based on the TG plots, the degrees of conversion (α) of MSH were determined at the various corresponding temperatures to compute the kinetic parameters; activation energy (E_a) and frequency factor (A) using the distributed activation energy model (DAEM). The model was proposed by Vladimir Vand in 1943 [18]

and has since been successfully adapted to characterise the kinetic changes occurring in thermally degrading components during TGA. Based on DAEM, the devolatilization of thermally reacting species can be described by the equation:

$$1 - \frac{V}{V_\infty} = \int_0^\infty \Phi(E_a, T) f(E_a) dE_a \tag{1}$$

Where the terms V , V_∞ , $\Phi(E_a, T)$, $f(E_a)$, and A represent the total volatiles changed at the time, t ; efficient fuel volatile content; temperature-dependent activation energy E_a ; normalised activation energy distribution curve for the irreversible first-order reactions and frequency factor, respectively. By applying the Arrhenius relation, which accounts for the effects of heating rate (β) on the change in volatiles, the mathematical relation for DAEM can be deduced as expressed by the relation;

$$\ln\left(\frac{\beta}{T^2}\right) = \ln\left(\frac{AR}{E_a}\right) + 0.6075 - \frac{E_a}{RT} \tag{2}$$

Hence, the activation energy, E_a , and frequency factor, A , can be deduced from the slope and intercept of the fitted linear curve, respectively.

3. Results and discussion

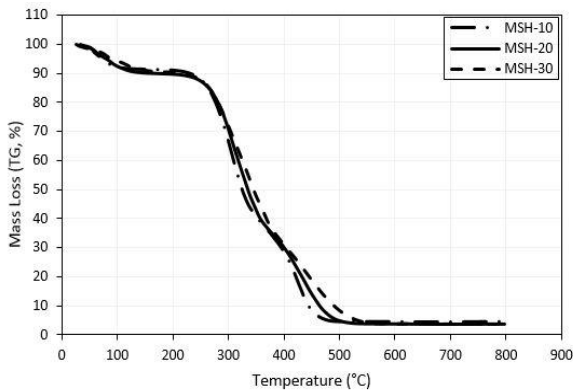


Figure 1. Plots for oxidative TG analysis of MSH

Figure 1 presents the thermogravimetric (TG) plots for the oxidative thermal analysis of MSH. As stated earlier, the TG analysis aims to examine the thermal degradation behaviour of MSH under non-isothermal oxidative conditions, which simulates the combustion of the fuel under multiple heating rates. As observed, the TG plots exhibited a downward sloping trend from the left to the right of Figure 1 with increasing temperature at the various heating rates adopted in this study. The trend indicates that the higher temperatures thermally degraded MSH during TGA under the oxidative conditions

examined in this study. The observed trend could be ascribed to the thermal degradation of the lignocellulosic components (lignin, cellulose and hemicellulose) in MSH into evolved flue gases, char, and ash.

Similarly, the change in heating rates affected the rate of thermal degradation of MSH. As observed, there was a shift in the TG plots to the right-hand side of Figure 1 as the heating rates increased from 10°C/min to 30°C/min. Although the shapes and forms of the TG plots for all the heating rates remain unchanged, the rate of thermal degradation and corresponding temperature profile characteristics (TPCs) were significantly modified. This observation could be ascribed to the thermal lag that occurs during multiple heating rate degradation of biomass materials [19-20]. As a result, the plots shifted to the right-hand side or higher temperatures as observed from the TPCs presented in Table 1.

Table 1 TG TPCs for Oxidative Thermal Analysis of MSH

°C/ min	T_{ons} , °C	T_{mid} , °C	T_{end} , °C	M_L , %	R_M , %
10	259.39	321.32	388.86	95.06	4.94
20	256.86	332.34	412.59	95.99	4.01
30	249.99	342.77	444.39	95.77	4.23

The TPCs computed for MSH in this study include; onset (T_{ons}), midpoint (T_{mid}), and end-point (T_{end}), temperatures along with mass loss (M_L) and residual masses (R_M). As observed

in Table 1, the onset (T_{ons}) temperature decreased from 259.39 °C to 249.99°C. However, the midpoint (T_{mid}) increased from 321.32°C to 342.77°C, whereas the endpoint (T_{end}) temperature increased from 388.86°C to 444.39°C. Lastly, the mass loss (M_L) and residual mass (R_M) were in the ranges; 95.06% to 95.99% and 4.01% to 4.94%. The results indicate that the change in heating rates significantly affected the TPCs for MSH during TGA.

Next, the thermal degradation mechanism was examined through the DTG plots presented in Figure 2. As observed, the thermal degradation of MSH resulted in three sets of DTG peaks in the range from RT to 200 °C and 200°C to 600°C during TG analysis.

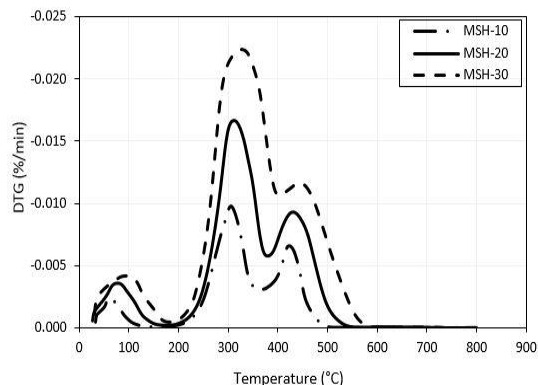


Figure 2 Plots for oxidative DTG analysis of MSH

The first set of peaks below 200°C could be ascribed to drying and loss of low molecular weight volatile compounds. The second set of DTG peaks observed between 200°C and 600°C could be attributed to the devolatilization of major organic compounds during TGA. However, this primary devolatilization stage was characterised by two sets of peaks denoted as devolatilization peak temperatures I and II, which occurred in two different range of temperatures (I = 200°C to 400°C and II = 400°C to 600°C) during TGA. Table 2 presents the temperature profile characteristics of the MSH based on the DTG in Figure 2.

Table 2. DTG TPCs for Oxidative Thermal Analysis of MSH

Heating Rate °C/min	Peak Drying Temp. (°C)	Peak Devolat. Temp. I (°C)	Peak Devolat. Temp. II (°C)
10	60.46	305.34	423.77
20	76.88	310.75	500.34
30	94.02	327.51	446.33

As observed, the peak drying temperatures increased from 60.46°C to 94.02°C, whereas the peak devolatilization temperatures I increased from 305.34°C to 327.51°C and peak devolatilization temperatures II were in the range 423.77°C to 500.34°C. The findings show that the thermal degradation of the MSH occurred in three stages under oxidative (combustion) conditions. These include; drying, devolatilization, and lastly, char combustion characterised by the long tailing observed after 600°C for all heating rates during TGA. The findings indicate that MSH is thermally reactive and can be efficiently degraded under the conditions examined in this study. To further examine the thermal reactivity of MSH during combustion, its kinetic properties were computed through the governing equations of the DAEM Model detailed in section 2 [18].

3.1. Kinetics

The DAEM model proposed by Vladimir Vand in 1943 [18] was adopted to examine the kinetic parameters; activation Energy (E_a) and frequency factor (A) for MSH during the oxidative thermal degradation or combustion process. The kinetic parameters were determined for different degrees conversion from $\alpha = 0.05$ to 0.95 (increments $\Delta = 0.05$). Consequently, the E_a and A were computed from the slopes and intercepts of the DAEM Equation. As observed, the activation energy (E_a) was in the range from 46.53 kJ/mol to 533.82 kJ/mol, whereas the frequency factor ranged from 3.62 min⁻¹ to 1.68 × 10⁵¹ min⁻¹ based on the R² of 0.86 to 1.00. The findings indicate that the kinetic parameters for the oxidative or combustion of MSH fluctuated significantly during TGA.

Table 3. Computed kinetic parameters for Oxidative Thermal Analysis of MSH

(a)	R ²	(E _a)	(A)
0.05	0.9140	46.53	9.25×10 ⁰¹
0.10	0.9855	533.82	1.68×10 ⁵¹
0.15	0.9564	298.15	2.30×10 ²⁴
0.20	0.9959	260.41	9.05×10 ¹⁹
0.25	0.9949	263.92	6.92×10 ¹⁹
0.30	0.9837	235.32	6.02×10 ¹⁶
0.35	0.9835	218.25	7.95×10 ¹⁴
0.40	0.9998	176.34	6.40×10 ¹⁰
0.45	0.9847	152.33	2.76×10 ⁰⁸
0.50	0.9937	148.88	8.49×10 ⁰⁷
0.55	0.9386	125.80	4.39×10 ⁰⁵
0.60	0.9133	190.78	8.68×10 ¹⁰
0.65	0.8908	367.35	6.51×10 ²⁴
0.70	0.9753	346.49	1.81×10 ²²
0.75	0.9974	290.20	1.67×10 ¹⁷
0.80	0.9365	142.58	3.32×10 ⁰⁵
0.85	0.9518	114.62	1.46×10 ⁰³
0.90	0.9637	96.71	4.28×10 ⁰¹
0.95	0.8582	87.12	3.62×10 ⁰⁰

Based on the findings, the average values of E_a and A for MSH were; 215.56 kJ/mol and $8.85 \times 10^{49} \text{ min}^{-1}$. Furthermore, the lowest (46.53 kJ/mol) and highest (533.82 kJ/mol) E_a values were observed at $a = 0.05$ and $a = 0.10$, respectively. This indicates that MSH is highly reactive at $a = 0.05$, which resulted in a rapid fluctuation of the kinetic parameters, as observed during the analysis. Hence, it can be reasonably surmised that MSH is a potentially practical feedstock for thermal conversion through combustion due to its high thermal reactivity. However, this submission requires macro-scale reactor tests to effectively observe its thermal degradation and reactivity for large scale combustion applications.

4. Conclusion

The study presented findings on the thermal decomposition kinetics of MSH under non-isothermal, oxidative, and multiple heating rate conditions. The thermal degradation and kinetic behaviour of MSH were examined through thermogravimetric analysis (TGA), the temperature profile characteristics (TPCs), and the distributed activated energy model (DAEM). The findings showed that the variation in temperature and heating rates significantly influenced the thermal behaviour, degradation mechanisms, and TPCs as observed in the shape, size and orientation of the TG and DTG plots. Lastly, the kinetic analysis indicated that MSH is highly thermally reactive as evident in its rapidly fluctuating kinetic parameters; activation energy (E_a) and frequency factor (A) during the thermal and kinetic analyses. Overall, the results showed that combustion is a potentially practical route for the valorisation of MSH.

Acknowledgement

The authors gratefully acknowledge the support of Universiti Teknologi Malaysia (UTM), University Industry Research Laboratory (UIRL) and its staff for the technical assistance during the experiments.

References

- [1] Oluba O, Ogunlowo Y, Ojieh G, Adebisi K, Eidangbe G, and Isiosio I. Physicochemical properties and fatty acid composition of *Citrullus lanatus* (Egusi Melon) seed oil. *Journal of Biological Sciences*, 2008;8(4): 814-817.
- [2] Ogunsua A, and Badifu G. Stability of purified melon seed oil obtained by solvent extraction. *Journal of Food Science*, 1989; 54(1): 71-73.
- [3] Bankole S, Osho A, Joda A, and Enikuomehin O. Effect of drying method on the quality and storability of egusi melon seeds (*Colocynthis citrullus* L.). *African Journal of Biotechnology*, 2005; 4(8): 799-803.
- [4] Bankole S, Ogunsanwo B, Osho A, and Adewuyi G. Fungal contamination and aflatoxin B1 of 'egusi' melon seeds in Nigeria. *Food Control*, 2006; 17(10): 814-818.
- [5] Mabaleha M, Mitei Y, and Yeboah S. A comparative study of the properties of selected melon seed oils as potential candidates for development into commercial edible vegetable oils. *Journal of the American Oil Chemists' Society*, 2007; 84(1): 31-36.
- [6] Giwa S, Abdullah LC, and Adam NM. Investigating "Egusi" (*Colocynthis citrullus* L.) seed oil as potential biodiesel feedstock. *Energies*, 2010; 3(4): 607-618.
- [7] Chen P-H, Chen G-C, Yang M-F, Hsieh C-H, Chuang S-H, Yang H-L, Kuo Y-H, Chyuan J-H, and Chao P-M. Bitter melon seed oil-attenuated body fat accumulation in diet-induced obese mice is associated with cAMP-dependent protein kinase activation and cell death in white adipose tissue. *The Journal of Nutrition*, 2012;142(7): 1197-1204.
- [8] Ekpa OD, and Isaac IO. Fatty acid composition of melon (*Colocynthis vulgaris* Shrad) seed oil and its application in synthesis and evaluation of alkyd resins. *IOSR Journal of Applied Chemistry*, 2013; 4(4): 30-41.
- [9] Nyakuma BB. Bioenergy Potential of Melon Seed Husks. *Lignocellulose*, 2017; 6(1): 15-22.
- [10] Ugwumba C. Allocative efficiency of 'egusi' melon (*Colocynthis citrullus* L.) production inputs in Owerri west local government area of Imo State, Nigeria. *Journal of Agricultural Sciences*, 2010; 1(2): 95-100.
- [11] Okieimen F, and Onyenkpa V. Removal of heavy metal ions from aqueous solutions with melon (*Citrullus vulgaris*) seed husks. *Biological Wastes*, 1989; 29(1): 11-16.
- [12] Giwa A, Bello I, Oladipo M, and Adeoye D. Removal of cadmium from waste-water by adsorption using the husk of melon (*Colocynthis citrullus* L.) seed. *International Journal of Basic and Applied Sciences*, 2013; 2(1): 110-123.
- [13] Madu P, and Lajide L. Physicochemical characteristics of activated charcoal derived from melon seed husk. *Journal of Chemical and Pharmaceutical Research*, 2013; 5(5): 94-98.
- [14] Giwa A, Olajire A, Adeoye D, and Ajibola T. Kinetics and thermodynamics of ternary dye system adsorption on to melon (*Colocynthis citrullus* L.) seed husk. *Chemical Science International Journal*. 2015; 7-25.
- [15] Olajire A, Giwa A, and Bello I. Competitive adsorption of dye species from aqueous solution onto melon husk in single and ternary dye systems. *International Journal of Environmental Science and Technology*, 2015; 12(3): 939-950.
- [16] Nyakuma BB. Pyrolysis kinetics of Melon (*Colocynthis citrullus* L.) seed husk. arXiv preprint arXiv. 2015; 1506.05419.
- [17] Nyakuma BB. Thermogravimetric and Kinetic Analysis of Melon (*Colocynthis citrullus* L.) Seed Husk Using the Distributed Activation Energy Model. *Environmental and Climate Technologies*, 2015; 15(1): 77-89.
- [18] Li L, Wang G, Wang S, and Qin S. Thermogravimetric and kinetic analysis of energy crop Jerusalem artichoke using the distributed activation energy model. *Journal of Thermal Analysis and Calorimetry*, 2013; 114(3): 1183-1189.
- [19] Nyakuma BB, Ahmad A, Johari A, Tuan TA, Oladokun O, and Aminu DY. Non-Isothermal Kinetic Analysis of Oil Palm Empty Fruit Bunch Pellets by Thermogravimetric Analysis. *Chemical Engineering Transactions*, 2015; 45: 1327-1332.
- [20] Oladokun O, Ahmad A, Abdullah T, Nyakuma B, Bello A-H, and Al-Shatri A. Multicomponent Devolatilization Kinetics and Thermal Conversion of *Imperata cylindrica*. *Applied Thermal Engineering*, 2016; 105: 931-940.

To whom correspondence should be addressed: Dr. Bemgba B. Nyakuma, School of Chemical and Energy Engineering, Faculty of Engineering, Universiti Teknologi Malaysia, 81310 Skudai, Johor, Malaysia, E-mail: bbnyax1@gmail.com

Vaclav Smil's Perspective on Fossil Fuels and Renewable Energy: A Review

Anil Kumar Vinayak, Anand V. P. Gurumoorthy*

School of Chemical Engineering, Vellore Institute of Technology, Vellore – 632014, Tamil Nadu, India

Received May 8, 2020; Accepted September 21, 2020

Abstract

Increasing pace of development coupled with higher standards of living and exponential population growth in recent years have increased the energy demand substantially worldwide. A considerable portion of these energy demands are met by fossil fuels. However, energy derived from fossil fuels release large amounts of greenhouse gases that possess many detrimental effects such as changes in weather patterns and extreme meteorological conditions. A transition to cleaner energy sources is, therefore, highly desired. There has been numerous advancements in achieving this objective but the pace of transitioning towards cleaner alternatives has been quite sluggish. However, grandiose predictions have been made towards the integration and pervasive usage of these alternative sources. In this paper, we examine these type of predictions and present the reality of the situation through the perspective of Vaclav Smil.

Keywords: Vaclav Smil; Fossil fuels; Renewable energy; Energy transition.

1. Introduction

Sustainable energy generation and greener alternatives have been the center of academic interest with substantial leaps to its integration in modern society being predicted. The world population currently stands at around 7.7 billion which is a significant increase compared to the meagre value of 2.5 billion in 1950 and at this rate, the population is bound to surpass the 10 billion mark by 2050. This explosive growth in population comes with increased energy demand and estimates show that there will be a 35% rise in energy consumption by 2035 [1]. Bulk of this energy demand will be supplied by fossil fuels and a 25% increase in its consumption by 2035 is predicted [1]. The rise in fossil fuels usage will be followed by an increase in greenhouse gas emissions, particularly carbon dioxide, and this has been agreed by the majority of the scientific community to bring forth drastic climate change all over the world. The International Energy Agency's 450 scenario aims to limit the concentration of CO₂ to 450 ppm in an attempt to limit the global average temperature increase to 2°C. The current concentration of CO₂ in the atmosphere is estimated to be above 400 ppm and it would require a tremendous reduction in CO₂ emissions to achieve this scenario [1].

As mentioned earlier, there will be a rise of 35% in energy consumption by the year 2035. For the 450 scenario to take effect, there should be a drop of CO₂ emissions by 35% in the same time frame. This paradox is called the Energy Equation and solving it will be the prime factor that will determine the way energy will be used in the future [2]. However, fossil fuels still measured up to 86% of the world's primary energy in 2015 and the progress made is quite sluggish when compared to its share 25 years prior, which stood at 90% [3].

2. Vaclav Smil's perspective of the future

There exists a wide array of alternatives that have been proposed in lieu of fossil fuels. Scientist and interdisciplinary researcher, Vaclav Smil believes that "We are a fossil fueled civilization, and we will continue to be one for decades to come as the pace of grand energy

transition to new forms of energy is inherently slow” [16]. He counters the common energy expectations and dispels myths on the subjects by giving specific evidence and sound reasoning.

The sub-sections below details his perspective on these alternatives and his supported opinion of the next energy transition.

2.1. Electric vehicles

Most of the countries import oil from OPEC nations and are, therefore, directly affected by the oil price fluctuations caused by the decisions of this international cartel. This provides the prime incentive to ensure the use of an electric car in addition to the fossil fuel emission. Since the commercial introduction in 1897 of the electric cars, the technology used has changed, however, their mass usage seems to have been postponed to date with each coming decade being touted as the generation of electric vehicles [4]. The commercial failures of electric cars or hybrids such as the Chevrolet Volt and Tesla’s Model S and project flops such as the Renault-Nissan alliance which aimed to command 10% of the world car market share by 2020, indicates that the common use of electric cars is still an unfeasible reality [4].

The primary factor hindering the commercial use of an electric vehicle is the price of the car which makes it inaccessible to the majority of the public. For instance, the highly anticipated Tesla Roadster has a base selling price of \$200,000 in the US (as on 2019). The next challenge is the base infrastructure involved to run these vehicles smoothly. High density charging stations need to be set up prior to the retail distribution of electric vehicles. The final point of contention, as per Smil, is that the energy source for the electric energy required to run these cars will come from non-renewable sources which would not result in primary energy savings and reduction of carbon emissions which defeats the purpose of the introduction of electric vehicles. The viability in terms of energy source can be achieved if the base sources are renewable and Smil states that it is only practical after a period of 50 years [4].

Smil argues that another impediment to the prevalence of electric vehicles is the battery used in electric vehicles. Efficient and higher capacity batteries are the only solutions to bring electric vehicles into the mainstream market. The current candidate is Lithium-ion battery but it comes with its own set of challenges. Idle discharge followed by battery degradation are the main concern. A Li-ion battery is expected to have a life of 2 to 3 years which pales in comparison to the 10 year mark of other car components. Furthermore, the degradation is dependent on temperature where “at the freezing point and at 100 percent charge, degradation is about 6 percent after one year; at 25°C it is 20 percent; and at 40°C it is 35 percent.” Therefore, electric vehicle would not be realistic choice in the warmer regions where the population densities are comparatively higher. Smil claims that the above mentioned factors and potential for improvements in the efficiency of internal combustion (IC) engines would make a transition towards electric vehicles a gradual process unlike popular predictions [4].

2.2. Solar and wind

Solar energy seems to be the most optimistic solution to combat the use of fossil fuels. However, Smil states that the reality is far from it. Solar energy harnessed via photovoltaic cells seems to have garnered the most attention with positive trends in the production of these cell being forecasted by Moore’s law [5]. Although it is true that the cost of producing photovoltaic cells have reduced considerably, the capital investment required (including batteries, inverters, and frames) as well as the labor costs to set up a system to convert solar energy to electrical energy is tremendous and would thus dissuade consumers from employing it. Moreover, the intermittency of solar energy and low energy densities would further delay its extensive use (1000 to 2000 W/m² for coal while only 6 to 10 W/m² for concentrated solar power) [6]. In addition to this, the materials used to manufacture photovoltaic cells require rare earth metals like neodymium, dysprosium, terbium and europium whose mining results in severe environmental repercussions such as land and water pollution with China, the biggest exporter of rare earth metals, cutting back on its exports due to these concerns [7]. The dumping of hazardous chemicals used in manufacture of solar panels in developing countries have also resulted in public outcry and therefore strips off the “clean” energy tag of solar panels.

Smil points out that the primary factors limiting wind power are same as that of solar: energy density, intermittency and capacity integration. Another significant hurdle is the land area required for the installation of wind turbines as each turbine requires a space of 5 to 10 rotor diameters from the adjacent turbine in order to mitigate excessive wake interference [4]. The maximum attainable power per unit area at the moment from wind farms stands at around 10 W/m² on land and 15 W/m² offshore. Secondary factors that limit the building of wind farms include aesthetics, noise and disruptions to bird and bat life [4]. Moreover, wind turbines are manufactured using steel and iron extraction from ore is highly dependent on fossil fuels as coke is required thereby making the technology dependent on fossil fuels.

2.3. Biofuels

Biofuels have been around for a while and it has been used in hybrid vehicles and aircrafts as means of transportation fuel. Lower carbon emissions, renewability and relative inexpensiveness is what prompted interest in biofuels and paved the way for further research into it. However, Smil counters that there are numerous limitations to biofuel that makes its broader use quite difficult. The major problem is the land area required to cultivate the plants needed to be turned into biofuels. The biofuel with the highest productivity (Brazilian ethanol from sugarcane) has a meagre power density of just 0.45 W/m² and the land required for producing this transportation ethanol would sum up to 600 million hectares which is equivalent to about 40% of the world's cultivated area [4]. Moreover, it has been found that in 2015 the global productions of biofuel amounted to a meagre 75Mtoe which just amounts 1.8% of the energy extracted from crude oil per year [3]. This is highly impractical. Moreover, the net energy return of biofuels is quite bleak. Mass production of biofuel plants like corn and cane will result in negative environmental effects like soil erosion and have economic implications such as food shortages due to arable land being used for cane and corn cultivation. Moreover, due to necessary use of fertilizers in growing corn, biofuel from corn is definitely not carbon neutral [8]. Smil does consider the possibility of third-generation biofuels like algae to mitigate the constraints of land area for cultivation but does not collate it with his arguments presently.

Another option that has been suggested is to use the stalk, stem and leaves of the corn to produce cellulosic ethanol. However, the process has its own set of limitations. The enzymatic hydrolysis to convert cellulose to glucose is very difficult as the number of organisms that can perform the hydrolysis is small and is limited to certain bacteria and fungi not easily found on the earth's crust. In addition, cellulase, the enzyme required for hydrolysis has no dedicated production plants and even if the six demonstration plants funded by the U.S. Department of Energy were to enter operation, the combined capacity would only equate to 0.1% of transportation fuel in the U.S. [4]. Therefore, Smil argues that this option is also not applicable in a larger scale.

2.4. Nuclear power

Nuclear power is a contentious energy source with its fair share of detractors primarily due to political rather than scientific reasons. The "zero carbon energy" promise of nuclear power and large energy densities are the hook that draws attention to it as an alternative power source. From a financial perspective, the cost of commissioning a nuclear power plant is massive albeit the energy generation being relatively inexpensive. Moreover, public perception towards nuclear energy has always been negative with the recent nuclear disasters such as the Fukushima Daiichi nuclear disaster further undermining its popularity [9]. The generation of nuclear waste, exposure of personnel involved to radiation and its weaponizing potential are some of the major arguments against nuclear power. Experts argue that a focus on nuclear energy is a necessity as it is the only low-carbon footprint fuel source that has energy potential at the gigawatt-level scale. This is an example where government policy and public perception are the limiting factors for the proliferation of the energy source [4].

As per the energy equation discussed in the introduction, CO₂ concentrations should be kept at 450 ppm in order to limit the increase in atmospheric temperature by 2°C. However, industrial expansion shows no signs of slowing down which eliminates reducing the rate of

emissions as a viable option. Therefore, the focus has shifted towards carbon sequestration methods. These include capturing CO₂ within basalt layers; extraction from air using a liquid sorbent; large scale industrial carbon capture by scrubbing.

Smil believes carbon capture to be a very ineffective solution. The price of electricity generation would rise as carbon capture require the use of equipment such as electrostatic precipitators which have high capital and running costs. As per reports by the Intergovernmental Panel on Climate Change (IPCC), the cost of operating a pulverized coal-fired power plant could raise by about 44 to 74% [4]. Furthermore, the energy requirement for operating carbon capture systems is very high and Smil believes that it would “erase half a century of efficiency gains in electricity generation” [4]. Another potent problem is the storage after carbon capture. CO₂ leaks could occur and this could lead to adverse effects such changes in the soil pH and release of toxic substances due to changes in acidity. Moreover, carbon capture and storage is at its fledgling stage and the ramifications of the process are not fully understood yet.

Large scale industrial carbon capture and sequestration was a proposed solution and considered as a better alternative to carbon dioxide extraction from the air. However, Smil points out that sequestering even a meagre 15% of CO₂ emissions would requiring the creation of an entirely new industry which does not provide any monetary returns and would need several decades to set up. The scale of the whole process is a tremendous undertaking. For instance, more than 4.8 billion tons (about 15% of 2008 emissions) of CO₂ need to be stored every year and this would require infrastructure encompassing compression, storage and transport where the annual volume throughput would be about 1.3 to 2.2 times the annual volume throughput of the crude oil industry worldwide [4]. Smil puts forth this argument as the major drawback of industrial carbon sequestration and concludes that this option will not become economically realistic in the near future.

3. Pace of energy transition

Smil defines an energy transition as “the time that elapses between the introduction of a new primary energy source and its rise to claiming a substantial share of the overall market” [6]. From Smil’s justifications, it is evident that a drastic energy transition in the direction of renewable energy is not realistic. Even if an innovative spurt brings forth a working technology, the widespread use of it in order to spur an energy transition would take longer due to existing infrastructure. An example of this is China’s \$300 billion investment (from 2001 to 2008) on coal based electricity generation which would require at least 35 years to break even [6]. Convincing the abandonment of such large scale investments in favor of transitioning towards renewables would be highly unlikely and would subsequently hinder the pace of integration of renewables. Add to this the increased extraction of coal in India and rise in exports from Indonesia indicates that the bulk of the electricity generation will be from coal. In the case of the United States, 50% of the US electricity comes from coal-fired power plants and 20% from nuclear stations while energy derived from renewable sources stand at less than 2.5% [4]. Thus, a transition from coal is highly unlikely. As per the studies done on the timelines of established technological products, a period of 30 to 40 years is required for complete commercialization of a new technology if it were to come into existence [10]. Claims made by the adherents of Moore’s law such as former American Vice President Al Gore that the demand for renewable energy would reduce its cost while a solar revolution is imminent are also unsubstantiated [11]. All in all, the actual pace of the energy transition will be very slow. The predictions usually made with respect to this usually stems from wishful thinking and sociopolitical factors (Gore’s claims) rather than substantiated evidence [12-13]. Furthermore, predictions pertaining to global energy shifts show that renewable energy might surpass each individual fossil fuel use but the cumulative sum of all fossil fuels will exceed that of renewable sources (refer graph below) [14].

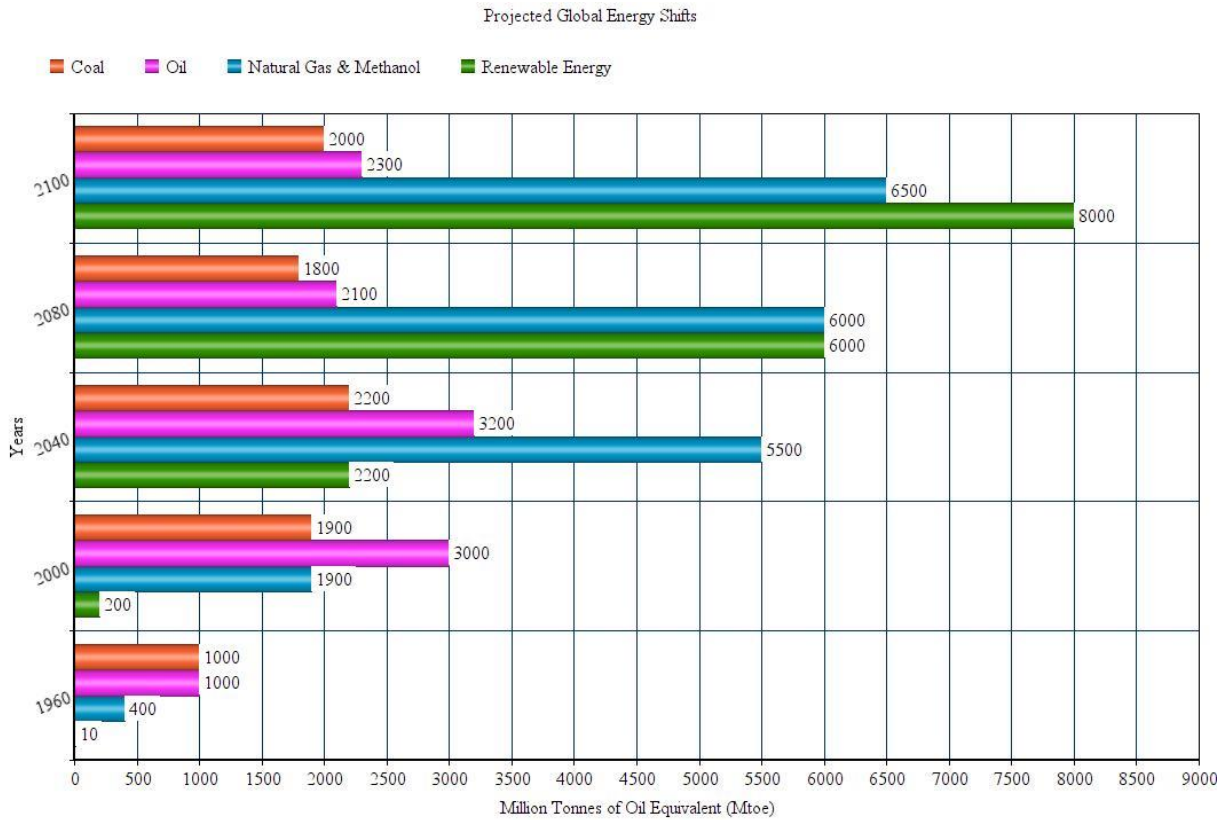


Figure 1 The Graph depicts the past usage of energy sources in Mtoe and the projected use of each energy source in the future. The global energy shifts indicate the rise in usage of renewable energy, however, the sum of all fossil fuel sources always exceeds that of renewable sources [14]

As per the historical trend, coal and oil took 60 years to achieve 50% and 40% of the global energy supply respectively [15]. Smil believes that the next energy transition will be dominated by natural gas which took 60 years to reach 25% of world energy supply with renewables contributing to less than 5% of world supply. As per the table below, natural gas is apt as its carbon content is minimal which results in lower CO₂ emissions as opposed to traditional fossil fuels like coal and gasoline (56 kgCO₂/GJ for natural gas and 95 and 70 kgCO₂/GJ for coal and gasoline respectively) [16]. There is renewed global interest in natural gas and techniques like fracking are gaining popularity, especially in America.

Table 1. Amount of CO₂ released by each fossil fuel [16]

Fuel type	Amount of CO ₂ released in kgCO ₂ /GJ	Fuel type	Amount of CO ₂ released in kgCO ₂ /GJ
Natural Gas	56	Diesel	75
Coal	95	Heavy Fuel Oil	77
Gasoline	70	Solid Biofuels	110

4. Natural gas – The future

As mentioned in the previous section, natural gas releases the least amount of carbon dioxide with respect to its fossil fuel counterparts therefore making it a better alternative to traditional fossil fuels like coal, diesel and gasoline. Moreover, there exists numerous years of hydrocarbon extraction expertise and state of the art computerized and automated technology which makes the extraction of natural gas a very systematic process with minimum risk. The refining of natural gas is simpler as operations such as denitrification and desulphurization is not required to be carried out due to its compositions which results in cost reduction when compared to traditional fuels like crude. Moreover, natural gas processing is mostly concerned

with separation of undesirable material as opposed to its liquid counterpart which requires complex processing techniques involving high temperatures and pressures as well as expensive catalysts [16]. There has also been significant increase in the extraction of nonconventional gas such as shale, gas from tight sands and coal bed methane especially in the United States. It is worth mentioning that 73% of natural gas production the US was derived from non-conventional sources in 2012 and this is a large jump from the 18% production in 1990 [16]. From an economic point of view, improvements in the LNG transportation infrastructure would ensure higher rates of market penetration for natural gas. For instance, in the United States alone there are 3 million miles of mainline transporting natural gas [17]. This strengthens Smil's reasoning that natural gas could be the potential player in the upcoming energy transition.

5. Alternative perspectives

To lend perspective to Smil's conclusions, alternative projections of Industrialist Vincent Petit and Academic Sir David J. C. MacKay are included below. Vincent Petit's opinion is one of optimism, particularly in terms of solving the energy equation, while Mackay maintains one that is in support of Smil's perspective albeit being slightly more generous with the renewable energy transition.

5.1. Vincent Petit

According to Vincent Petit, the energy equation can be cracked by utilizing certain acute strategies. He states that increasing the end use efficiency of sectors such as industries, buildings and transportation would result in savings of about 25% of the total final energy consumption in the coming 20 years [2].

One-third of the energy consumption worldwide is attributed to the industry sector and equals about 2400 Mtoe of energy per year [2]. The bulk of this is utilized by electro-intensive industries such as petrochemical and iron and steel. Large portion of the energy requirement is for heat generation and this results in significant amounts of wastage to the environment. Petit says that reducing the heat loss and optimizing its use would be an effective strategy which would result in minimizing the fossil fuel requirement [2]. Better insulation and automated controls would optimize the heating process and using superior catalysts would reduce the heat input requirement for chemical processes to occur. In non- electro intensive industries, high efficiency motors would help cut down energy requirement. The above solutions coupled with carbon capture systems is Petit's solution to reduce CO₂ emissions in industry [2].

As per the International Energy Agency, 20% of the energy used in buildings could be saved with almost 2800 Mtoe of energy being consumed in 2010 [1]. Improving thermal insulation, optimizing equipment efficiency and appliances' consumption and by adjusting the energy requirement in particular zones depending on time and occupancy could save up to 60% of energy in buildings [2]. The transportation sector provides numerous possibilities for energy savings. In 2010, about 2400 Mtoe of energy was consumed by the transportation sector [2]. Innovations in motorizing technologies, aerodynamic designs and using lightweight materials could lead to higher energy efficiencies. Additionally, increased usage of public transportation, providing incentives for carpooling and utilizing work-at-home modes of employment would contribute to improving energy efficiency in the transportation sector [2].

Another sector where energy is wasted is during electricity generation where the conversion to usable form is significantly low. The ratio of primary energy requirement to transportable electricity is 3:1 which indicates that the electricity generation process is highly inefficient [2]. Therefore, to increase the efficiency, the process variables such as temperature and pressure should be optimized in addition to the system elements like ventilation systems, pumps, etc. Optimizing as mentioned above will improve the efficiency but not by a substantial amount. The alternative is to use other sources such as nuclear energy and renewable energy which are further discussed below.

The market growth of nuclear energy is stated to be within the range of 1.3 to 3.8% which is among the highest growth rates in comparison to other energy sources [2]. At present, most of the nuclear reactors use Uranium 235 and Plutonium 239 which drives the fission reaction.

There is ongoing research on nuclear breeder reactors which is estimated to produce 60 times more energy than a traditional reactor. The goal of these reactors is to reduce the waste produced while generating 300 times more electricity than current technologies [2]. This could have significant implications on the energy equation.

The other viable alternative, as per Petit, is renewable energy. It is abundantly available and clean. When compared with oil reserves, two-thirds of wind energy and 4% of solar energy are the equivalent [2].

Amongst the renewable energy sources, solar energy seems to be the most promising. Estimates show that about 26,000TW of solar power could be captured to produce electricity [1]. Also, the scale of production of photovoltaic modules, the key component of the cell that converts radiation into electricity and which forms the bulk of the initial investment cost, have increased while the production costs have come down primarily due to production practices by China which has resulted in increased competitiveness of solar cells. This could well be the solution to tackle the detrimental effects spurred on by the usage of fossil fuels such as the increase in carbon dioxide emissions (about 70% in the last 70 years). As of now, production capacity from solar energy stands at around 132 GW with a rise to 1720 GW by 2030 and above 4670 GW by 2050 as per the predictions by International Energy Agency [7]. The goal by then is that 16% of the global energy production will be from solar power.

Utilizing the above strategies of increasing end use efficiency and the integration of renewable energy seems to be the key to cracking the energy equation. The theoretical primary energy saving potential is about 8900 Mtoe [2]. The primary challenge for achieving this is to minimize the end use consumption. With increasing the rate of implementation of the above methodologies, Petit posits that the energy equation can be solved.

Petit's predictions are based more on undue optimism rather than technical progress and innovation as shown by Smil's justifications in the earlier sections.

5.2. Sir David J. C. MacKay

Sir David J. C. Mackay was a British academic whose book "*Sustainable energy - without the hot air*" provides a qualifying perspective to Smil while presenting a more realistic perspective than Vincent Petit. He has based his predictions on a case study of the UK. Mackay surmised that the average consumption is 125kWh/d per person in the UK [18]. As indicated in the graph below, he compares his estimates to that of other agencies and further modifies his results after public consultation to come to the subdued conclusion that current renewable energy resources in the UK can only generate 18 kWh/day per person [18]. This is significantly lower than the demand and depicts a live limitation of renewables.

Another significant hurdle towards a renewable transition is the cost. The UK's current consumption stands at 300 GW. To replace this equivalent with renewables, an input of £300 billion would be required. This is an enormous amount and a better perspective can be obtained by comparing it with the current market value of energy consumption in UK which totals to an approximate £130 billion per year [18]. Therefore, a renewable transition would be an economic disaster.

Another obstacle is the tackling of lulls and slew. Lulls are extended periods of time with smaller renewable energy production and slews are supply or demand changes in the short run. Given the intermittency of renewable sources, this is a very relevant issue. Proposed solutions include pumped storage and energy imports, however, these are plagued with high investment costs, lack of infrastructure and land shortages. This coupled with larger population densities makes the transition towards renewables all the more difficult [18].

The arguments of David MacKay and Vaclav Smil strike hard because they analyze renewable energy in terms of their power densities (see table below). Based on their analysis they conclude that investments in renewable energy to replace fossil fuel sources will need to be country-sized.

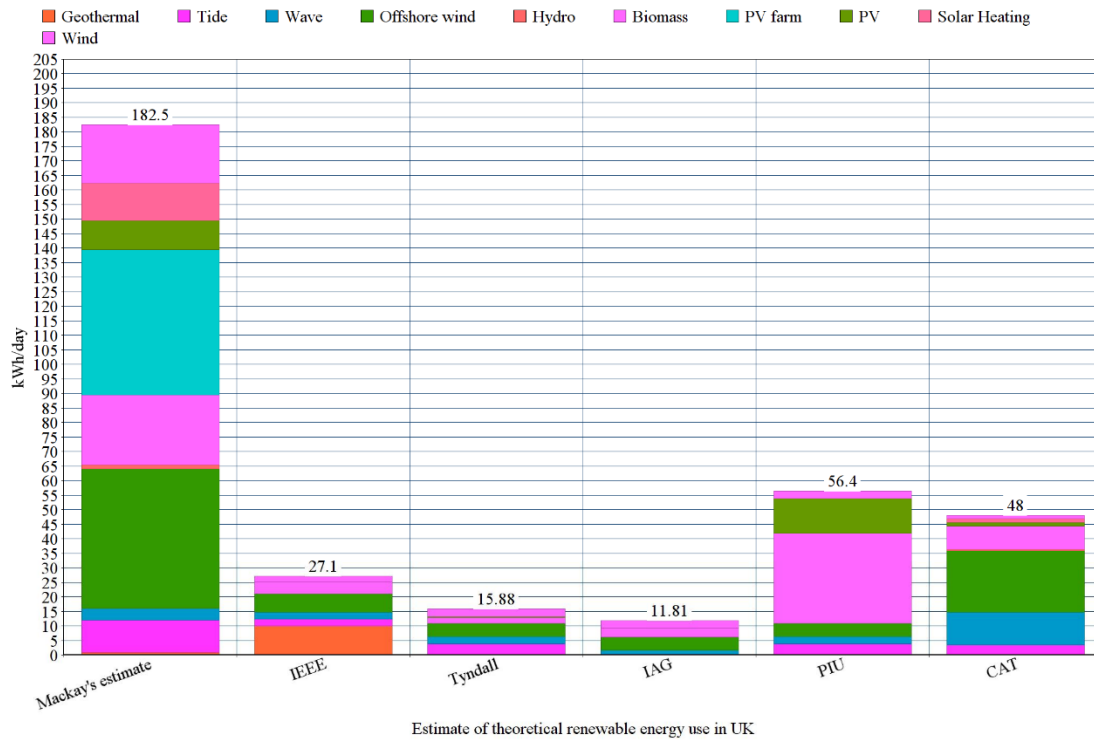


Figure 2. Estimates of theoretical or practical renewable resources in the UK, by the Institute of Electrical Engineers (IEEE), the Tyndall Centre, the Interdepartmental Analysts Group (IAG), the Performance and Innovation Unit (PIU); and the proposals from the Centre for Alternative Technology's (CAT) "Island Britain" plan for 2027 against that of Mackay [18]

6. Conclusion

In this paper, we review Vaclav Smil's perspective on fossil fuels and renewable energy. We started off with the Energy Equation (Energy Conundrum as we prefer to call it) which states that while the IEA proposes a drop of CO₂ emissions by 35% by the year 2035, actually there will be a rise of 35% in energy consumption in the same time frame. We have looked at several 'solutions' to tame the energy equation such as electric vehicles, solar and wind, biofuels, carbon sequestration and storage, etc. While Smil is not against renewable solutions and actually predicts the eventual dominance of renewable energy, he points out why the solutions are unrealistic and unfeasible in the present time.

Vaclav Smil's views on renewable energy offer a pessimistic outlook on its prospects albeit being backed by sound reasoning. Smil's arguments often find themselves in the crosshairs of individuals like Vincent Petit who back the renewable energy revolution as a potent solution for the problems caused by fossil fuels. However, Petit's models rely on optimistic projections whose assumptions have been countered by Smil. Moreover, the efficiency adjustments that have been suggested by Petit as a way of improving the existing energy sources are yet to be proved effective. David MacKay, on the other hand, provides the pragmatic perspective to view Smil's work. He supports Smil's arguments and provides data to lend credibility although he does believe that renewable energy can be integrated to a greater level into the current infrastructure. MacKay's careful optimism and Petit's outright optimism showcases the depth of the contentious topic of renewable energy and thus defines the perspective that Smil states.

We have also discussed the pace of energy transitions. The pace would not accelerate exponentially as adherents of Moore's law maintain. The pace would be gradual as Smil posits and it may take more than 50 years to wean ourselves away in considerable measure from fossil fuels.

References

- [1] IEA (2012), World Energy Outlook 2012, OECD Publishing, Paris.
<https://doi.org/10.1787/weo-2012-en>.
- [2] Petit V. Energy Transition: An Overview of the True Challenge of the 21st Century. Springer 2017, ISBN 978-3-319-50292-2.
- [3] Smil V. Energy and Civilization: A History. MIT Press 2017, ISBN: 9780262035774.
- [4] Smil V. Energy Myths and Realities: Bringing Science to the Energy Policy Debate. AEI Press 2010, ISBN-13: 978-0844743288.
- [5] Norris D, and Aydil E. Getting Moore from Solar Cells. *Science*, 2012; 338(6107): 625–626.
- [6] Smil V. Energy Transitions: History, Requirements, Prospects. Praeger 2010, ISBN: 978-0-313-38177-5. 178.
- [7] Jefferson M. Closing the gap between energy research and modelling, the social sciences, and modern realities. *Energy Research & Social Science*, 2014; 4: 42–52.
- [8] Giampietro M, and Mayumi K. The Biofuel Delusion: The Fallacy of Large Scale Agro-Biofuels Production. Taylor and Francis 2009, eBook ISBN9781849770200.
- [9] Kim Y, Kim M, and Kim, W. Effect of Fukushima Nuclear Disaster on the Global Public Acceptance of Nuclear Energy. *Energy Policy*, 2013; 61(C): 822-828.
- [10] Gross R, Hanna R, Gambhir A, Heptonstall P, and Speirs J. How long does innovation and commercialisation in the energy sectors take? Historical case studies of the timescale from invention to widespread commercialisation in energy supply and end use technology. *Energy Policy*, 2018; 123: 682–699.
- [11] Smil V. Moore’s Curse and the Great Energy Delusion. American Enterprise Institute 19 Nov. 2008.
<http://www.aei.org/publication/moores-curse-and-the-great-energy-delusion/>.
- [12] Jefferson M. Renewable and low carbon technologies policy. *Energy Policy*, 2018; 123: 367–372.
- [13] Smil V. Global Energy: The Latest Infatuations. *American Scientist*, 2011; 99(3): 212.
- [14] Podobnik B. Global Energy Shifts: Fostering Sustainability in a Turbulent Age. Temple University Press, 2006.
- [15] Smil V. The Long Slow Rise of Solar and Wind. *Scientific American*, 2013; 310(1): 52–57.
- [16] Smil V. Natural gas: Fuel for the 21st century. Chichester, West Sussex: Wiley Blackwell 2015, ISBN:1119012864.
- [17] U.S. Energy Information Administration- EIA-Independent Statistics and Analysis. Natural Gas Pipelines- U.S. Energy Information Administration (EIA),
<https://www.eia.gov/energyexplained/natural-gas/natural-gas-pipelines.php>.
- [18] MacKay DJC. Sustainable Energy-without the Hot Air. UIT Cambridge 2009, ISBN 978-0-9544529-3-3.

To whom correspondence should be addressed: professor Anand V. P. Gurumoorthy, School of Chemical Engineering, Vellore Institute of Technology, Vellore – 632014, Tamil Nadu, India, E-mail: anand.g@vit.ac.in

Utilisation of Sweet Potato (*Ipomoee batatas*) and Rice Husk (*Oryza sativa*) Starch Blend as a Secondary Viscosifier and Fluid Loss Control Agent in Water-based Drilling Mud

Queendarlyn A. Nwabueze^{1*}, Joshua O. Ighalo^{2,3}

¹ Department of Petroleum and Gas Engineering, Faculty of Engineering, University of Lagos, Nigeria

² Department of Chemical Engineering, Faculty of Engineering and Technology, University of Ilorin, Nigeria

³ Department of Chemical Engineering, Nnamdi Azikiwe University, P. M. B. 5025, Awka, Nigeria

Received May 13, 2020; Accepted August 21, 2020

Abstract

The drilling mud plays an important role in ensuring the success of any drilling operation as it remove cuttings from the wellbore regions. The viscosity of the drilling mud must be constantly monitored and adjusted during drilling to enable it suspend the cuttings when mud circulation is halted. Starch is frequently applied in drilling fluid technology due to its solubility in water, viscosity and water retention capacity. This study evaluated the use of sweet potato (*Ipomoee batatas*) and rice (*Oryza sativa*) husk starch blend as a viscosifier and fluid loss control agent in water based drilling mud. The mud samples were prepared according to the API 13B-1 specifications. The rheological and fluid loss tests were also according to the API 13B-1 specifications. The plastic velocity, yield point and gel strength of the drilling mud increased with increasing starch content (0 – 8g). From the study of temperature effects (25 – 80°C), higher temperatures were detrimental to the mud's plastic viscosity and had a positive effect on yield point and gel strength. This shows a clear positive effect of the starch blend as a viscosifier. The starch blend was also shown to reduce mud fluid loss by 8% due to its water retention capacity.

Keywords: Drilling mud; Viscosifier; Rheology; Fluid loss control; Starch.

1. Introduction

Drilling is considered to be an important aspect of any oil and gas sector due to the fact that it creates access to the hydrocarbons underground [1]. For a drilling operation to be carried out successfully, a drilling fluid with appropriate specifications needs to be used [2]. To enable penetration rates at a faster pace, majority of wells are drilled with clear water until a considerable depth is attained where the hole conditions would determine if a drilling fluid with special properties is required [3]. The basic function of the drilling fluid is to remove cuttings from the wellbore regions to the surface [4]. For the fluid to remove cuttings effectively, the fluid has to have a good measure of viscosity [5]. The viscosity of the drilling fluid must be continuously monitored and adjusted during the course of drilling in order for the mud to achieve the designed requirements [6]. Water based mud has a variety of applications due to its ease of formulation [3]. There are different types of water based mud namely; inhibitive, non-inhibitive and polymer water based mud [7]. Polymer-water based mud was used for the Purpose of this research.

Polymer fluid generally comprises of small amounts of bentonites that would improve viscosity, reduce cuttings dispersions and also help in well bore stabilization through the process of encapsulation. Additives should be added to drilling fluids to preserve and evaluate the drilling fluid properties [8]. In contemporary times, several polymers mostly natural polymers e.g. starch, synthetic or modified polymers are used for controlling fluid loss and enhancing viscosity in the oil and gas industry [9-11]. Starch is frequently applied in drilling fluid technology

in modified forms because it is soluble in water [11]. Starch is frequently applied as an effective colloid due to its ability in increasing the viscosity of drilling fluids and the vital role it plays in the reduction of loss of the drilling fluids due to its swelling capacity and its ability to increase its volume (as a result of free space water absorption).

Starch comprises of amylose and amylopectin polysaccharides, the amylose contained in starch swells up aiding in fluid control loss [12]. Sweet potato (*Ipomoea batatas*) is an important food crop cultivated in Africa with Nigeria being the highest producer having an annual production output of 3.56 million tonnes [13]. Sweet potato starch is a polysaccharide polymer and the amylose present in sweet potato enables its starch to portray unique characteristics such as improving viscosity and reducing fluid loss [14]. Rice (*Oryza sativa*) starch is amongst the varieties of cereal starch with well-known characteristics [15]. Starch is the main component of rice and accounts for about 80% of its total constituents [16]. Rice has a high amylose content which enhances its pasting abilities and also its capacity to retain water [15].

In recent years, the substitution of locally produced materials for imported drilling fluid additives have been reported. Ademiluyi, Joel [17] indicated that the filtration control properties of local materials were better than their imported counterparts and yielded better results. Egun and Achadu [18] revealed that cassava starch improves the water retention capacity of drilling fluids. A study was conducted by Igbani, Peletiri [19] on improving the density of drilling fluid using cassava starch, and the results were positive. The study by Olatunde, Usman [1] and Udoh and Okon [4] indicated that some local materials such as soda ash, sweet potato and Gum Arabic have the capacity to act as a good substitute for imported additives. It was observed by Saboori, Sabbaghi [20], that core-shell nano composites can serve as a good substitution to control mud cake thickness whilst preserving other mud properties. The use of starch from rice husk and sweet potato is unreported and scarcely studied in open literature. This study attempts to fill this gap in knowledge. This study is important as viscosifiers used in the oil and gas industry in Nigeria are very expensive and not always available. Nigeria has the capacity to formulate water based drilling fluids from local materials but little research has been conducted to investigate the potential of using starch derived from a combination of sweet potato and rice husk to formulate a drilling fluid that would serve as a secondary viscosifying agent and a fluid control agent. Therefore, it is of utmost importance to investigate the basic characteristics of the combination of sweet potato and rice husk to formulate a drilling mud that will perform the same functions as the imported additives. This study is aimed at appraising the performance of a combination of sweet potato and rice husk blend as a viscosifier and fluid loss control agent in water based drilling mud.

2. Methodology

2.1. Preparation of sweet potato and rice husk starch granules

A local variety of sweet potato (*Ipomoea batatas*) called "Dan Izala" was used for this experiment. Sweet potato tubers weighing 10 kg were flaked and cut into uneven smaller shapes, the reduced slices of sweet potato were then thoroughly washed and soaked using distilled water. The soaked potato was then ground using an electric grinder to yield a paste. Distilled water was used to dilute the paste and then it was discharged into a cloth and it was then firmly squeezed whilst the filtrate was collected. The filtrate was left to settle for 30 h and the water suspended was removed while the starch settled at the base of the wooden container. The moist starch was spread on a large metallic tray and sundried for 15 days. The sample was then oven dried at 80°C for 12 h. The starch was ground and sieved through mesh size 0.425 mm. The sweet potato then underwent the process of pre-gelatinization to a temperature range of about 60°C–80°C in order to break the amylose-amylopectin chains affecting its solubility in water. The rice (*Oryza sativa*) husk was carefully sorted out to remove the stones and other particles and weighed to be about 5 kg. The husk was washed using distilled water and sun dried for 10 days. The dried husk was then pulverized to powder using an electric grinder. It was then sieved with a sieve of mesh size 0.425 mm. The sweet potato flour was then mixed with the rice husk powder using an electric mixer to form a mud flour (denoted as SPRH) to be used in the study.

2.2. Preparation of the water based mud samples

The methodology applied in this study abided by the API 13B-1 [21] standard for preparation of and evaluation of drilling fluid. The ratio of 350 ml distilled water to 22.5 g of bentonite were used for every system setup according to the API specification for drilling fluid preparation. For the study, Bentonite of about 112.5 g was mixed with 1750 mL of distilled water. About half of the total volume of water was poured into a container after which the bentonite was added. The resulting mixture was then stirred thoroughly using a hand-held mixer for about 5 minutes. Subsequently, the left over water was then added and the mixture was stirred thoroughly until there were no visible lumps. Five samples of the bentonite mud were used for the study, one of which was a control sample without the addition of the SPRH flour. 2g, 4g, 6g and 8g of the SPRH flour were added to the bentonite mud to prepare the remaining four samples. All four samples were vigorously stirred using a hand-held mixer until there were no visible lumps of the SPRH flour. The test analysis was carried out following the 16 hours of the aging process at room temperature.

2.3. Test of rheology and fluid loss

The two main properties that play a significant role in determining the viscosity properties of good drilling fluids are plastic viscosity (PV) and yield point (YP). The plastic viscosity, yield point, gel strength of approximately 10 seconds and 10 minutes were carefully recorded at structural dial readings of 600 rpm, 300 rpm, 200 rpm, 100 rpm, 60 rpm, 30 rpm and 3 rpm as specified in API 13B-1 [21] for measurement of drilling fluid properties. Following the completion of the experiments at 25°C, thermos-cup was used to heat the mud samples at 40°C, 60°C and 80°C after which the test was repeated. Equations 1 and 2 were used to compute the viscosity properties of the developed mud [22]. Equation 1 was applied to calculate the plastic viscosity (PV) in mPa.s.

$$PV = \theta_{600} - \theta_{300} \quad \text{Eqn. 1}$$

Equation 2 was applied to calculate the yield point (YP) in kg/m²

$$YP = \theta_{300} - PV \quad \text{Eqn. 2}$$

where θ_{600} is the 600 rpm dial reading and θ_{300} is the 300 rpm dial reading.

Following the completion of the rheology test, the fluid loss was determined by pouring the control and the bentonite mud with distinctive weights of SPRH starch into the API filter press mud cell. The pressure was then increased to 100 psi as recommended in API 13B-1.

3. Results and discussion

The analysis of the results from the experiments carried out were compared to the control bentonite, including previous works done by other researchers. The range of numerical values for estimating the quality of the properties of water based drilling mud which is very fundamental to ensuring a successful drilling operation is outlined in Table 1. The dial readings, estimated plastic viscosities, yield point values, gel strength at a time value of 10 seconds and 10 minutes of mud samples with distinct concentrations (0g, 2g, 4g, 6g, 8g) of SPRH flour at different temperatures of 25°C, 40°C, 60°C and 80°C min SI units are illustrated in Table 2. An outline of how the fluid loss from the different experimental samples increased with time is also depicted in Table 3. The filter cake measurements at the completion of the fluid loss test is outlined in Table 4.

Table 1. API Standard Range of Numerical Values Specifications for Drilling Grade Bentonite

Mud Properties	Specification (SI units)	(Oilfield units)
Plastic viscosity (PV)	<65 (mPa.s)	<65 (cP)
Yield point (YP)	73.5-220.5 (kg/m ²)	15-45 (lb/100ft ²)
Gel strength @ 10 seconds	14.7-98	3 - 20 (lb/100ft ²)
Gel strength @ 10 minutes	39.2 - 147 (kg/m ²)	8 - 30 (lb/100ft ²)
API Fluid loss	15.0 ml (max)	15.0 ml (max)

Table 2. The results for PV, YP, Gel Strength and Dial Readings of the Samples of Mud gotten from the Laboratory Test

Sample	Parameter	Temperature			
		25°C	40°C	60°C	80°C
WBM + 0g SPRH	θ_{600}	24	27	24	25
	θ_{300}	20	22	20	22
	PV (mPa.s)	4	5	4	3
	YP (Kg/m ²)	77.3	71.8	77.8	82.1
	Gel Strength @ 10secs (Kg/m ²)	15.8	15.8	18.7	40.9
	Gel Strength @ 10mins (Kg/m ²)	54.8	62.9	77.5	94.2
WBM + 2g SPRH	θ_{600}	27	25	28	32
	θ_{300}	22	20	24	28
	PV (mPa.s)	5	5	4	4
	YP (Kg/m ²)	76.7	76.7	92.8	108.5
	Gel Strength @ 10secs (Kg/m ²)	28.5	35.6	54.3	79.2
	Gel Strength @ 10mins (Kg/m ²)	67.4	76.7	104.9	142.7
WBM + 4g SPRH	θ_{600}	25	27	32	35
	θ_{300}	20	24	28	31
	PV (mPa.s)	5	3	4	4
	YP (Kg/m ²)	94.7	106.9	119.3	104.8
	Gel Strength @ 10secs (Kg/m ²)	37.1	29.6	38.5	85.1
	Gel Strength @ 10mins (Kg/m ²)	76.3	86.1	96	145
WBM + 6g SPRH	θ_{600}	33	38	33	38
	θ_{300}	25	33	26	31
	PV (mPa.s)	8	5	7	7
	YP (Kg/m ²)	101.4	126.2	126.2	135.7
	Gel Strength @ 10secs (Kg/m ²)	39.2	56.1	69.8	99
	Gel Strength @ 10mins (Kg/m ²)	84.1	115.9	106.3	168.2
WBM + 8g SPRH	θ_{600}	39	36	34	39
	θ_{300}	31	30	29	34
	PV (mPa.s)	8	6	5	5
	YP (Kg/m ²)	104.7	115.2	138.6	151.9
	Gel Strength @ 10secs (Kg/m ²)	50.2	61.8	72.4	90.2
	Gel Strength @ 10mins (Kg/m ²)	83.7	120.1	132.3	157.6

Table 3. Results for the Fluid Loss Test

Time (mins)	Fluid loss (mL)				
	0g SPRH	2g SPRH	4g SPRH	6g SPRH	8g SPRH
1	1	1.4	1.6	1.4	1.4
3	3.2	2.8	3.2	3	3
5	4.6	4.4	4.2	4.8	4.8
7	5.2	5.2	5.8	5.6	5.6
9	6.4	6.8	6.8	6.3	6.6
10	7.1	7.4	6.8	6.8	6.8
11	7.4	7.4	7	7.2	7.4
13	8.6	8.4	8.2	8	7.8
15	9	8.4	8.2	8.2	8.2
17	9.4	9	8.8	9.2	9.2
19	10	9.4	9.4	9.4	9.6
20	10.4	10	9.6	10	10
21	11	10.2	10	10.4	10
23	11.4	11	10.6	10.8	10.8
25	12.2	11.6	11.6	11.2	11.6
27	12.6	11	10.8	11.6	11.6
29	13	12.6	11.8	12.6	12.6
30	13.2	12.3	12	12.2	12.2

Table 4. Measurement of the filter cake

Mud sample with SPRH starch granules	Thickness of the filter cake (mm)
0g of SPRH starch	2
2g of SPRH starch	2
4g of SPRH starch	3
6g of SPRH starch	3
8g of SPRH starch	3

3.1. The effect of SPRH starch on mud plastic viscosity

There is an increase in the PV of a water based drilling fluid in response to an increase in its solid content. However, the PV of a water based drilling mud decreases with an increase in temperature. It can be observed from Figure 1 that at a temperature of 25°C, an increase in the SPRH flour concentration led to an increase in the PV of the drilling mud samples, by that performing as a secondary viscosifying agent. Contrastingly, as the temperature of the drilling mud increased from 25°C to 80°C, a decrease in PV was observed. The plastic viscosity of the 8g concentration of SPRH flour mud decreased steadily with its temperature increasing. The latter’s pattern aids in reducing the suspension of molecules in the drilling mud while the drilling operation is ongoing.

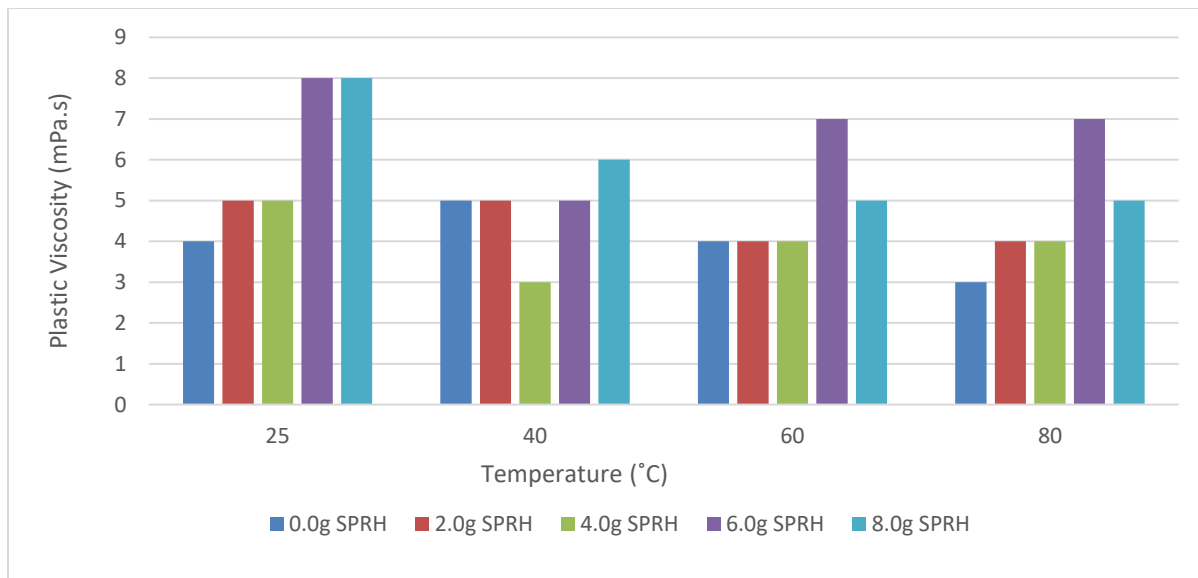


Figure 1. Plastic viscosity of the SPRH composition at different temperature

In 2g SPRH starch flour concentration, it was observed that the PV was decreased with the temperature increasing from 25°C to 40°C. Although, no further increase in plastic viscosity was observed when the mud temperature was increased to 80°C. A similar pattern was observed for the mud sample with 4g of SPRH starch except that an increase in the temperature of the mud to 80°C comparatively resulted in an increase in the plastic viscosity. A decrease in the plastic viscosity of the mud sample having 6g of SPRH starch flour was observed as the temperature increased starting from 25°C and the temperature stabilized between 60°C and 80°C.

The decrease in the plastic viscosity of the mud sample emanates from the basis that, when the temperature of the mud sample is increased, it brings about a decrease in the liquid phase of the drilling mud and causes a thermal degeneration of starch as a result of the dissociation of the polymer chains present in starch. This pattern was also observed in previous studies by Ademiluyi, Joel [17] and Akintola and Isehunwa [23] albeit for other viscosifier types. When the plastic viscosity is low, it indicates that the mud has the capacity of speeding up the rate of drilling because the mud flowing out of the bit has a low viscosity. Typically, alterations in the

temperature affected the plastic viscosity of the mud because it is an important factor of viscosity. Taking into account, the rheological analysis of the water based fluid that is depicted in Figure 1, the results gotten for plastic viscosity were found to be in approved ranges required for successful drilling operations. This confirms that the drilling mud developed with a combination of sweet potato and rice husk flour can adequately carry cuttings to the wellbore surface with slight alterations.

3.2 The Effect of SPRH starch on mud yield point

The yield point can be seen as a determinant of the attractive forces present in a drilling mud that is under specified flow. The yield point is commonly seen as the force of attraction in colloidal particles or fragments present in drilling fluids. An increase in temperature and contaminants present in drilling muds (i.e., CO₂, salt, anhydrites and other particles) during the process of drilling results to an increase in the yield point of water-based mud. With increasing SPRH concentrations, the yield point noticeably increased from 25°C to 80°C due to water loss through the process of evaporation. Evaporation results from the increased temperature during the process of thickening the drilling mud.

It can be closely observed in Figure 2 that the temperature and concentration of SPRH granules have symbolic aftermaths on the yield point of the drilling mud. Essentially, the yield point also illustrates the capacity of the drilling mud in carrying cuttings to the wellbore surface. If the yield point of a drilling fluid is low, the drilling fluid will flow rapidly and the cuttings will be left in the wellbore. The performance observed in correlation to the resulting effects of temperature on the yield point of the drilling mud apparently indicates verge limits in which further addition of SPRH starch granules would lead to negative consequences on the properties that affects the yield point of a drilling mud. This can be attributed to the fact that a high yield point will amount to a high pressure loss during mud circulation. On the other hand, assuming the yield point of the mud is on a high level, it notifies the mud engineer that in order to use a mud of that attributes, a higher pumping pressure needs to be applied to enable the mud flow properly, this is earnestly required in the oil & gas industry.

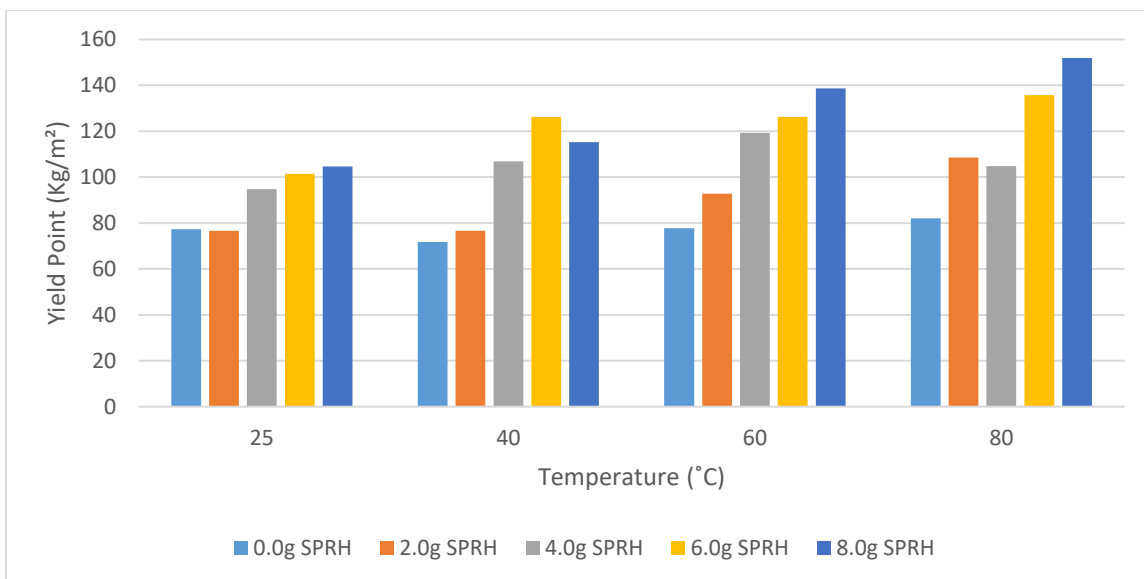


Figure 2. Yield point of SPRH starch mud compositions at different temperature

3.3. The effect of SPRH starch on mud gel strength

It can be observed from Figure 3 that all the samples of drilling mud with SPRH starch exhibited the same temperature trend, the gel strength of the mud were directly proportional to its weight, and increasing with increasing temperature. At a temperature of 40°C, the mud sample having 4g of SPRH starch granules was observed to have decreased for the 10 seconds

gel strength. With regards to the 10-minute gel strength illustrated in Figure 4, the drilling mud samples with SPRH starch granules composition was found to have a similar trend of increase according to increased temperature. Although at a temperature of 80°C of mass 6g and 8g SPRH starch granule mud, 168.2 and 157.6 kg/m² were recorded respectively which is not acceptable for a successful drilling operation.

This pattern is associated to the degrading of the polymer bonds present in the mud samples when the temperature increased from a level of 25°C to 80°C. It can be concluded from the analysis gotten from the experiments carried out, that temperature had a very high effect on the gel strength of the drilling mud samples. The gel strength plays a vital role in determining the properties of the drilling fluid because it increases the capacity of the drilling mud to suspend the colloidal particles when the process of mud circulation is stopped. In a scenario where the gel strength of the mud is high, a high pressure pump will be required to enable the dissociation of the fixed bonds after the mud has previously stopped circulation.

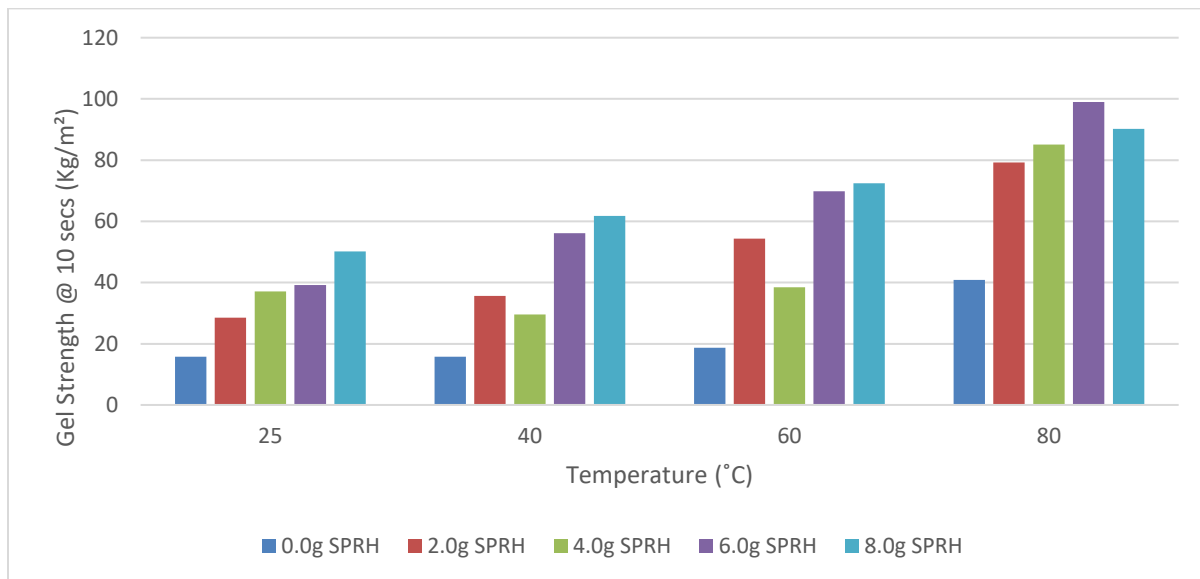


Figure 3. Ten seconds gel strength of SPRH starch mud compositions vs temperature

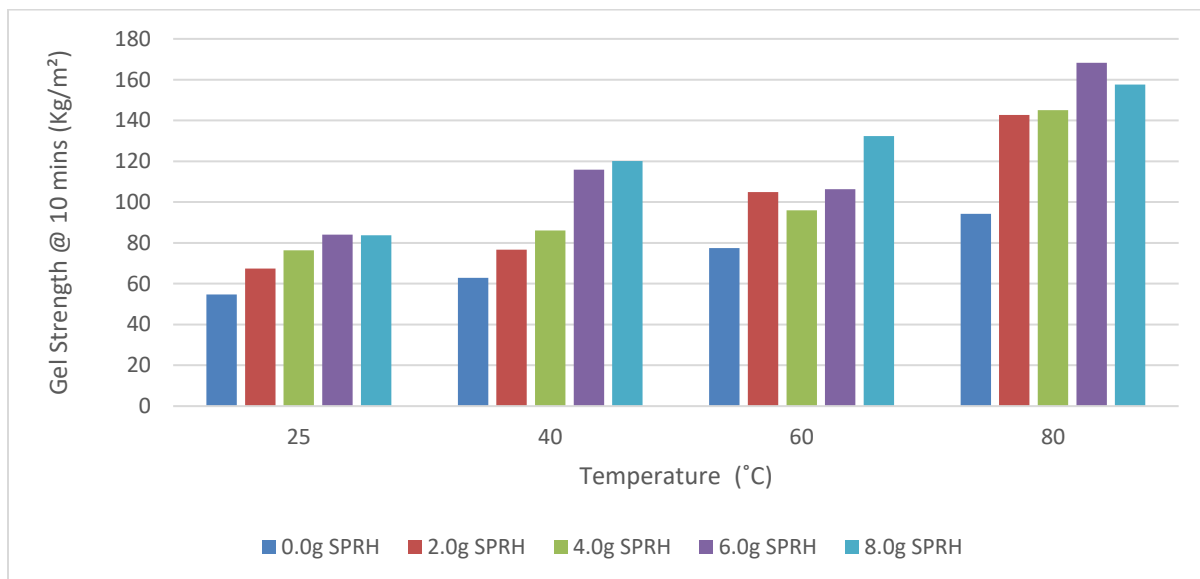


Figure 4. Ten minutes gel strength of SPRH starch mud compositions vs temperature

3.4. The effect of SPRH Starch on mud fluid loss

The correlation between fluid loss with time for SPRH compositions is illustrated in Figure 5. The fluid loss pattern differs from 1 min to 3 min with various volumes of SPRH starch granules. It was observed from Figure 5 that the fluid loss sample increased directly with time, although the 8g of SPRH starch granules contained in the drilling mud exhibited a marginally lower fluid loss than the set-out control bentonite (0g SPRH Starch granules). Furthermore, the mud sample having 2g concentration of SPRH flour at a lower time period of about (1-3 mins) recorded a lower value of fluid loss. This behaviour can be attributed to the high percentage of amylose present in sweet potato as stated in a similar project executed by [4]. The ratio of fluid loss can be considerably decreased by increasing the mass of SPRH starch granules in the drilling mud. It was observed using a filter cake that when the concentration of SPRH starch granules was increased, the thickness of the cake increased from 2 mm to 3 mm resulting in a thinner cake. A thinner cake is more desirable in drilling operations as it reduces the risk of pipe sticking hazards [20].

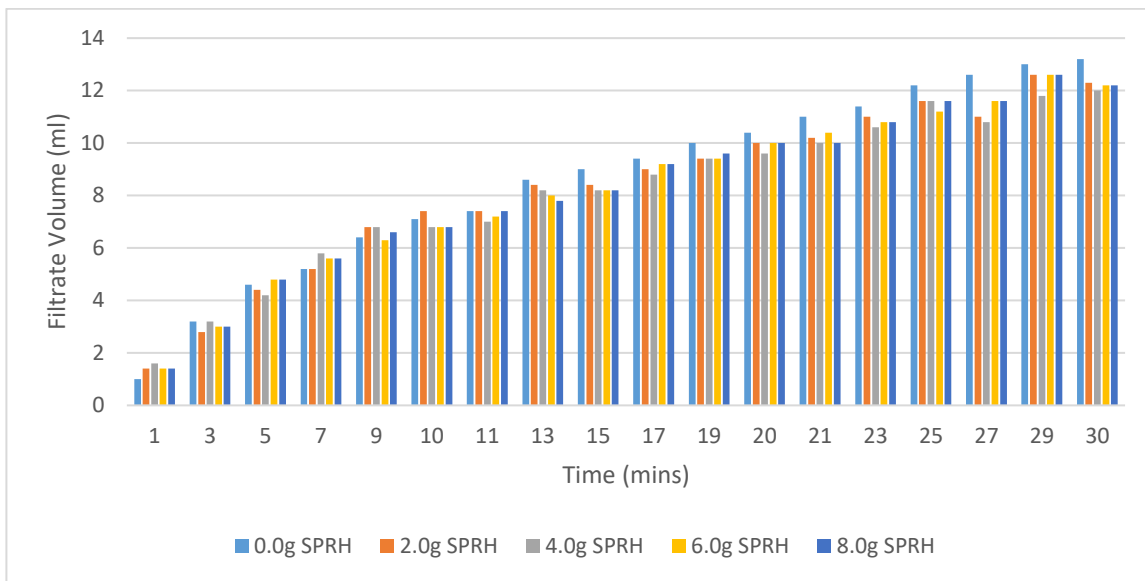


Figure 5. Filtration Loss of the Samples of Mud vs Time

3.5. Rheogram

It can be clearly deduced from Figures 6 - 9 that when the quantities of the SPRH starch granules is increased, there is a corresponding increase in their distinctive viscosities leading to an increase in the shear stress of the drilling mud. It can also be clearly deduced from the graphical representations that the pattern of the curves of the different samples illustrates the characteristics of non-Newtonian fluids. The basic crystalline compound contained in the granular starch is amylopectin. The disparity in the percentage of amylopectin and amylose present in starch alters the rheological nature of the starch. The gelling behaviour of starch is controlled by its amylose components.

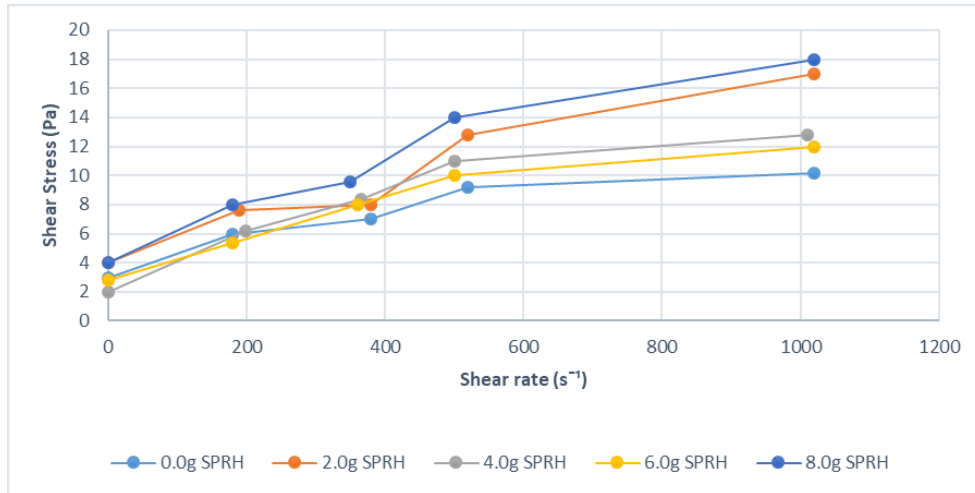


Figure 6. Rheogram illustrating the fluid behaviour at a temperature of 25°C

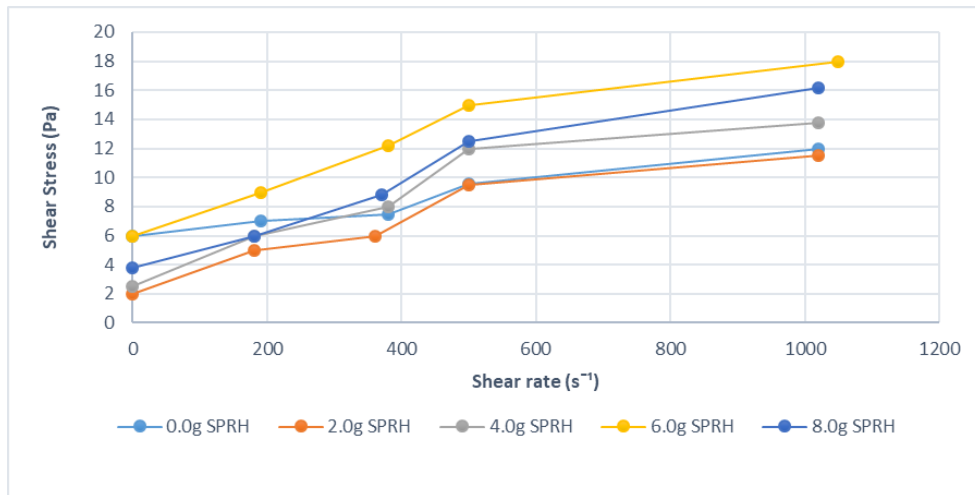


Figure 7. Rheogram illustrating the fluid behaviour at a temperature of 40°C

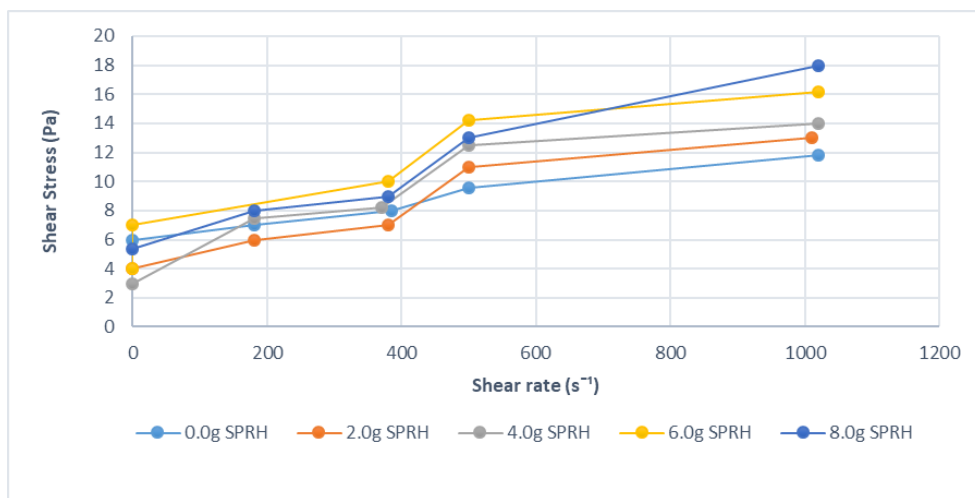


Figure 8. Rheogram illustrating the fluid behaviour at a temperature of 60°C

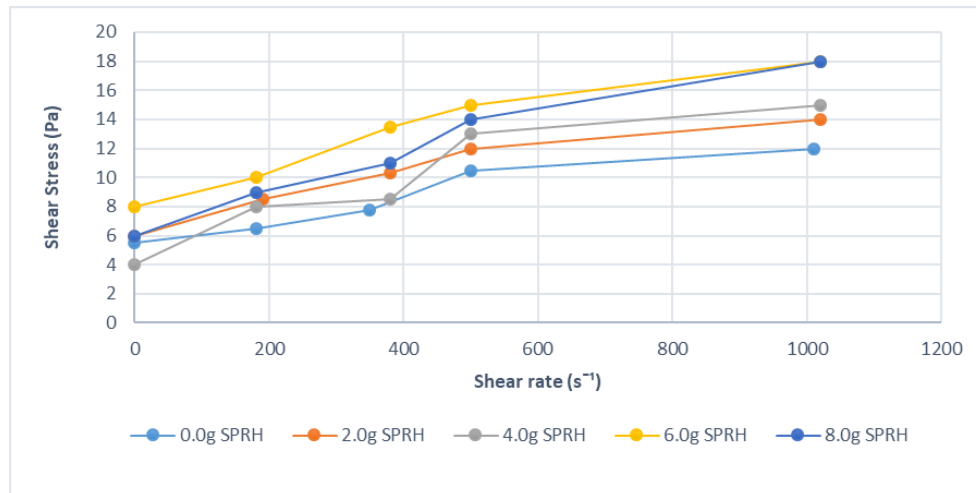


Figure 9. Rheogram illustrating the fluid behaviour at a temperature of 80°C

4. Conclusion

This study investigated sweet potato (*Ipomoe batatas*) and rice (*Oryza sativa*) husk starch blend as a viscosifier and fluid loss control agent in water based drilling mud. The plastic viscosity, yield point and gel strength of the drilling mud increased with increasing starch content. This showed a clear positive effect of the starch blend as a viscosifier. The decrease in the plastic viscosity of the mud sample with temperature is because higher temperatures brings about a decrease in the liquid phase of the drilling mud and causes a thermal degeneration of starch. From the study of temperature effect (25 – 80°C), higher temperatures were detrimental to the mud plastic viscosity and had a positive effect on yield point and gel strength. Several specific conclusions were drawn from the study.

1. The PV of the drilling mud sample with SPRH blend ranged from 3-8 mPa.s, which is ideal because it enables the drilling mud to carry cuttings to the well bore.
2. The yield point values of the drilling mud samples were in the ranges of 71.8- 151.9 kg/m² which is favourable for a successful drilling operation.
3. The samples of mud having concentrations of SPRH blend exhibited a greater gel strength than that of the control sample (0g SPRH Blend). Except for the 6g and 8g concentration of SPRH blend at a temperature of 80°C for the gel strength of 10 mins.
4. The SPRH starch blend at the different experimented concentration had a significant effect on the swelling capacity of the water based drilling mud as a result the viscosity of the drilling mud was significantly increased.
5. The introduction of the SPRH starch blends with concentration ranging from 2g to 8g affected the thickness of the filter cake leading to a thin filter cake with a thickness range of 2mm - 3mm, therefore resulting in an appropriate decrease in fluid loss by about 8%. This affirmed the basis that continuous increase in the concentration of the SPRH starch blend would significantly decrease fluid loss

Furthermore, the starch blend was also shown to reduce fluid loss from the drilling mud. The viscosifier was also shown to improve the viscosity of the drilling mud. The drilling mud also revealed the usual rheological characteristics of non-Newtonian fluids. This study has successfully utilised sweet potato and rice husk starch blend as a viscosifier and fluid loss control agent in water based drilling mud.

Disclosure statement

No potential conflict of interest was reported by the authors.

Acknowledgement

The authors would like to sincerely thank the technical staff at the Drilling Fluid Laboratory in the Department of Chemical and Petroleum Engineering at the University of Lagos.

List of symbols

<i>PV</i>	<i>Plastic Viscosity</i>	<i>YP</i>	<i>Yield Point</i>
<i>Rpm</i>	<i>Revolutions per minute</i>	Θ_{600}	<i>600 RPM dial reading</i>
<i>SPRH</i>	<i>Sweet Potato and Rice Husk</i>	Θ_{300}	<i>300 RPM dial reading</i>
<i>WBM</i>	<i>Water Based Mud</i>		

References

- [1] Olatunde AO, Usman MA, Olafadehan OA, Adeosun TA and Ufot OE. Improvement of rheological properties of drilling fluid using locally based materials. *Petroleum & Coal*. 2012; 54.
- [2] Al-Nimer A, Al-Wabari A, Al-Fuwaies O, Saleh A-yA and Bubshait A. An Innovative Manganese Tetroxide/CaCl₂ Water-Based Drill-In Fluids for HT/HP Wells. *SPE Latin America and Caribbean Petroleum Engineering Conference*. 2014.
- [3] Dankwa OK, Opoku Appau P and Tampuri M. Performance Evaluation of Local Cassava Starch Flour as a Secondary Viscosifier and Fluid Loss Agent in Water Based Drilling Mud. *Ghana Mining Journal*. 2018; 18: 68 - 76.
- [4] Udoh FD and Okon AN. Formulation of water-based drilling fluid using local materials. *Asian Jr of Microbiol Biotech Env Sc*. 2012; 14.
- [5] Neff JM. Composition, environmental fates, and biological effects of water based drilling muds and cuttings discharged to the marine environment: A synthesis and annotated bibliography. Battelle, Duxbury, MA: Petroleum Environmental Research Forum (PERF) and American Petroleum Institute, 2005.
- [6] Okumo I and Isehunwa SO. Prediction of the Viscosity of a Water - Base Mud treated with Cassava Starch and Potash at varying Temperatures using Factorial Design. *Nigeria Annual International Conference and Exhibition*. 2007.
- [7] Asgharzadeh Shishavan R, Hubbell C, Perez H, Hedengren J and Pixton D. Combined rate of penetration and pressure regulation for drilling optimization by use of high-speed telemetry. *SPE Drilling & Completion*. 2015; 30: 17-26.
- [8] Annis MR and Smith MV. *Drilling Fluids Technology*. Exxon Company, USA, 1974.
- [9] Nasiri A, Valizadeh M, Norouzi H and Hemmati M. Investigating the Effect of Polythin and Polydrill on the Properties of Drilling Fluids. *Journal of Petroleum Science and Technology*. 2012; 2: 37-42.
- [10] Loong WSS. Development of drilling fluid system using carboxymethyl cellulose (cmc) for high temperature-high pressure (HTHP) applications. *Faculty of Chemical & Natural Resources Engineering*. Malaysia: Universiti Malaysia Pahang, 2012.
- [11] Samavati R, Abdullah N, Tahmasbi Nowtarki K, Hussain SA and Awang Biak DR. The Prospect of Utilizing a Cassava Derivative (Fufu) as a Fluid Loss Agent in Water Based Drilling Muds. *International Journal of Chemical Engineering and Applications*. 2014; 5.
- [12] Harry TF, Joel OF, Ademiluyi FT and Oduola K. Performance Evaluation of Local Cassava Starches with Imported Starch for Drilling Fluid. *American Journal of Engineering Research*. 2016; 5.
- [13] Eleazu CO and Ironua C. Physicochemical composition and antioxidant properties of a sweetpotato variety (*Ipomoea batatas* L) commercially sold in South Eastern Nigeria. *African Journal of Biotechnology*. 2013; 12: 720-7.
- [14] Eutamene M, Benbakhti A, Khodja M and Jada A. Preparation and Aqueous Properties of Starch-grafted Polyacrylamide Copolymers. *Starch-Stärke*. 2009; 61: 81-91.
- [15] Wani AA, Singh P, Shah MA, Schweiggert-Weisz U, Gul K and Wani IA. Rice starch diversity: Effects on structural, morphological, thermal, and physicochemical properties—A review. *Comprehensive Reviews in Food Science and Food Safety*. 2012; 11: 417-36.
- [16] Vandeputte G and Delcour J. From sucrose to starch granule to starch physical behaviour: a focus on rice starch. *Carbohydrate polymers*. 2004; 58: 245-66.
- [17] Ademiluyi T, Joel OF and Amuda AK. Investigation of local polymer (cassava starches) as a substitute for imported sample in viscosity and fluid loss control of water based drilling mud. *ARPN Journal of Engineering and Applied Sciences*. 2011; 6.
- [18] Egun IL and Achadu MA. Comparative performance of Cassava Starch to PAC as Fluid Loss Control Agent in Water Based Drilling Mud. *Discovery*. 2013; 3.
- [19] Igbani S, Peletiri SP and Egba SU. A Study on the Individual Impact of Cassava Starch and Hydroxyl Propyl-Modified Starch on Mud Density. *International Journal of Engineering Trends and Technology* 2015; 29.

- [20] Saboori R, Sabbaghi S, Kalantariasl A and Mowla D. Improvement in filtration properties of water-based drilling fluid by nanocarboxymethyl cellulose/polystyrene core-shell nanocomposite. *Journal of Petroleum Exploration and Production Technology*. 2018.
- [21] 13B-1 AR. Recommended Practice for Field Testing Water-based Drilling Fluids. API 4th Edition, 2009.
- [22] Caenn R, Darley HCH and Gray GR. Composition and properties of drilling and completion fluid. 7th ed. Houston, Texas, USA: Gulf Publishing, 2017.
- [23] Akintola AS and Isehunwa SO. Temperature and Time-Dependent Behaviour of a Water Base Mud Treated with Maize (*Zea mays*) and Cassava (*Manihot esculanta*) Starches. *Journal of Scientific Research & Reports*. 2015; 5: 591-7.

To whom correspondence should be addressed: Dr. Queendarlyn A. Nwabueze, Department of Petroleum and Gas Engineering, Faculty of Engineering, University of Lagos, Nigeria, E-mail: queendarlene268@gmail.com

Performance Characteristics of *Parkia biglobosa* as Fluid Loss Control Agent in Aqueous Mud System

Nnaemeka Uwaezuoke *, *Ibuchukwu S. Onwukwe*, *Chinwuba K. Igwilo*, *Ugochukwu I. Duru*, *B. Obah*

Department of Petroleum Engineering, Federal University of Technology, P.M.B. 1526, Owerri, Nigeria

Received May 20, 2020; Accepted September 21, 2020

Abstract

Recent trend in the use of biomaterials in oilfield applications involves minimum refining and purification. The effectiveness of *Parkia biglobosa* as fluid loss control additive in aqueous based mud was tested according to API standard. The effect of temperature on the formulation was determined to identify any deviation due to presence of the material in the formulation. At 8ppb concentration used, 3.6mL fluid loss and 1.1mm filter cake thickness were recorded; compared with 8mL and 0.8mm, and 5.4mL and 0.8mm of *Pleurotus* and PAC respectively. Both fluid loss and filter cake thickness increased with increase in temperature. A low-flat discontinuous gel was observed at elevated temperatures which is desirable. Other drilling fluid rheological parameters were not adversely altered by the presence of the material, even at elevated temperature conditions. The biodegradable material was found to be suitable as fluid loss agent, both in effectiveness and environmental consideration since it is biodegradable, and might reduce cost of formulation since minimum processing is required.

Keywords: *Aqueous mud; Fluid loss control; Parkia biglobosa; PAC UL.*

1. Introduction

One of the most important functions of the mud is to wall the hole with an impermeable cake [1]. This prevents formation damage and provides borehole stability. Filter cake formation is directly related to fluid loss property of the mud, and represents fluid interaction with borehole wall under prevalent temperature and pressure conditions [2]. It is usually determined under static or dynamic conditions of fluid flow [3], and API fluid loss tests [4] are static tests and are commonly used. The soft surface layers of the static cake are not found in dynamic cake since its surface is eroded due to shear stress from the hydrodynamic force of mud stream.

A lot of materials have been published on fluid loss control both in water and oil based mud formulations, and the use of natural polymers for oilfield operations can be traced back to the 1930s. Recent trend in the use of green materials involves minimization of refining and purification processes, contrary to extraction, fractionation and other chemical and physical treatments previously used [5].

The fundamental theory of static filtration has been presented [3]. For a unit volume of stable solids suspension through a substrate; x = volume of filtrate, then $1-x$ volumes of cake is deposited on the substrate, Q_c =volume of cake, Q_w =volume of filtrate, and h =cake thickness;

$$\frac{Q_c}{Q_w} = \frac{1-x}{x} \quad (1)$$

$$h = \frac{1-x}{x} Q_w \quad (2)$$

$$\text{From Darcy's law; } \frac{dq}{dt} = \frac{kP}{\mu h} \quad (3)$$

where k =permeability (darcies); P =differential pressure (atm.); μ =viscosity of filtrate (cP); q =filtrate volume (cm³); A =area of filtrate; t =time (sec.); and q_0 =spurt loss or zero error.

Substituting and integrating;

$$Q_w^2 = \frac{2kP}{\mu} * \frac{x}{1-x} t \tag{4}$$

$$Q_w^2 = \frac{2kP}{\mu} * \frac{Q_w}{Q_c} t \tag{5}$$

$$Q_w^2 = \frac{2kPA^2}{\mu} * \frac{Q_w}{Q_c} t \tag{6}$$

For a given pressure [6];

$$Q_w - q_o = A\sqrt{(Ct)} \tag{7}$$

where: $C = \frac{2kP}{\mu} * \frac{Q_w}{Q_c}$ (8)

Equation (6) is the fundamental equation that governs fluid loss under static conditions. The filter cake permeability can be determined from Equation (6);

$$k = Q_w Q_c \frac{\mu}{2tPA^2} \tag{9}$$

With standard API laboratory fluid loss tests and using pressure (100psig), time (30min) and filter cake area of 7-in²;

$$k = Q_w Q_c \mu * 1.99x * 10^{-5} \text{ md} \tag{10}$$

In the wellsite, the filter cake is measured manually and Eq. (6) takes the form;

$$k = \frac{Q_w h \mu}{2tPA} \tag{11}$$

and, with h given in millimeters;

$$k = Q_w h \mu * 8.95 * 10^{-3} \text{ md} \tag{12}$$

Nonetheless, the mechanism of fluid loss control by the use of say bentonite, which lay platelets like packs of cards on the wellbore wall to control fluid loss, is different from that of biomaterials such as polymers that bridge on the flow channels due to their deformable cells [7]. Organic materials impart filter cake due to the ability of their hydrolyzed cells to deform, and due to small size that fit into and tend to plug the pore spaces in the formation adjacent the wellbore. However, with increase in solid concentration, fluid losses decreases and filter cake increases [3]. The impermeable layer should be flexible and thin. Ultimately, loss of the aqueous phase from the mud system into the formations due to positive differential pressure is reduced. Filter cake thickness in the range of 1/32 (0.8mm) to 2/32 (1.6mm) of an inch would be desirable, with an upper limit of 3/32" (2.4mm) not expected to be exceeded, high-pressure high-temperature tests inclusive. Spurt loss is usually observed in all the cases. It is determined by extrapolation to time zero of the plot of fluid loss against square root of time [8]. This is because it is after the spurt loss that fluid loss becomes proportional to the square root of time.

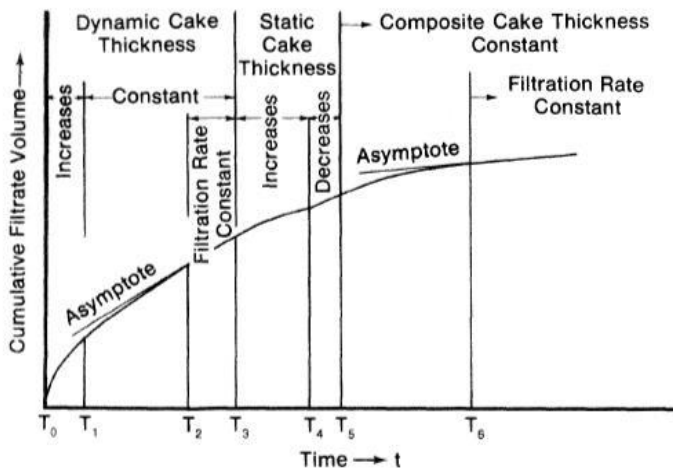


Figure1. Relative static and dynamic filtration in the wellbore [3]

For dynamic filtration, an illustration of the stages is shown (Figure 1). The filtration rate decreases and the filter cake thickness increases from time T₀ to T₁, while the filter cake thickness remains constant and filtration rate continues to decrease from time T₁ to T₂. The filtration rate is thus;

$$Q = \frac{k_1(\tau/f)^{-v+1}}{\mu\delta(-v+1)} \tag{13}$$

where k₁=filter cake permeability at 1 psi; τ=shear stress exerted by the mud stream; f=coefficient of internal friction of the cake's surface layer; δ=thickness of the filter cake subject to erosion; and (-v+1) = a function of cake compressibility.

Experimental evaluation of performances of fluid loss additives under varying conditions is not new. Results of fluid loss rates in aqueous system using commercial agents such as carboxymethyl cellulose, polyacrylate and starch under dynamic conditions have been presented, and did not even conform to API fluid loss test rankings in terms of effectiveness [9].

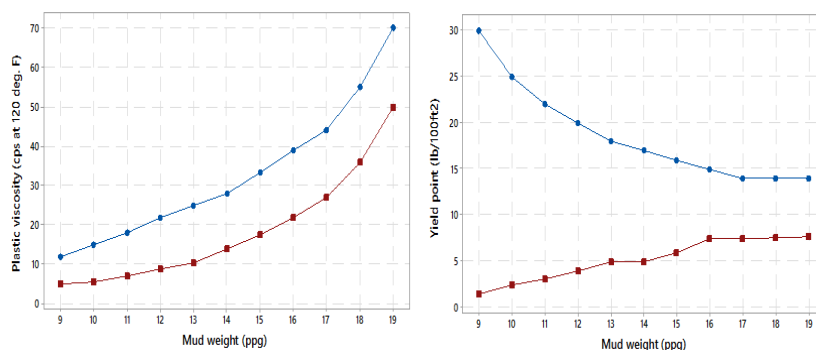


Figure 2. Acceptable ranges of PV and YP for a given mud weight [10]

Similarly, studies on effects of temperature on mud properties, which include fluid loss, are not new. The need to correct viscometric readings taken at surface temperatures to downhole circulation temperatures has been identified over six decades ago. A study on the effect of temperature on the flow properties of some water-based muds has been conducted [11]. Though recommended ranges of plastic viscosity and yield point for aqueous based muds have been presented (Figure 2), research has found that plastic viscosity and apparent viscosity decrease with an increase of temperature. However, the curves were not linear, and did not appear to follow any definite trends or patterns. Yield point data showed much more scattering. Several authors have presented their reports on the effect of temperature on mud properties [12-14]. Also, the study of fluid loss properties (plastering property) on muds has been carried out over seven decades ago [15]. Increase in fluid loss with increase in temperatures was reported.

The effect of temperature on gel strength was also presented within the same period [16]. Temperature affected gel strength, but to a certain degree depended on the mud type. Effects of temperature on biomaterial mud formulations with *Mucuna solanica* and *Brachystegia eurycoma* have been shown to be consistent with earlier research findings [17]. Also, reproducible properties of non-Newtonian liquids have been achieved by the use of polymers such as CMC and Xanthan gum [18]. Generally, rheological parameters determination is in accordance with the technique recommended and applied in previous works [19-20].

2. *Parkia biglobosa*

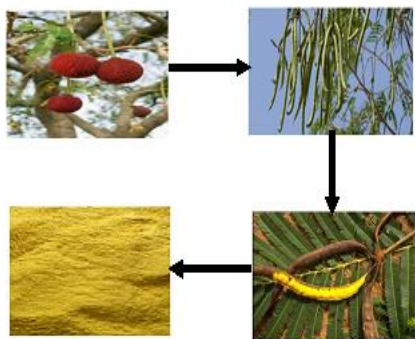


Figure 3. *Parkia biglobosa* pods are pink in the beginning and dark brown when fully mature

This is a perennial deciduous tree of the Fabaceae family found in South-Eastern part of Nigeria in West Africa and other African countries. The pods are 30-40 centimeters long on average, and can contain up to 25 seeds. The leaves are alternate and bipinately compound, about 30-40 centimeters long and bears up to 17 pairs of pinna. Also, the fluorescence is on drooping peduncle, biglobose and showy in red colour like an electric bulb (Figure 3). The seeds are embedded in yellowish pulp, with crude fibre and carbohydrate. The proximate analysis, mineral composition, physico-chemical analysis, reproductive biology, economic potential and taxonomy have been shown in detail in previous studies [21-25].

2.1. Summary of *Parkia biglobosa* fruit pulp characterization

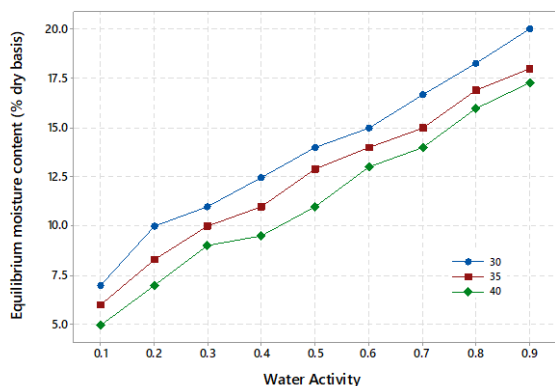


Fig. 4. Adsorption moisture sorption isotherms of *Parkia biglobosa* flour at 30, 35 and 40°C [27]

Literature reveals that it has a proximate composition of 30.0% protein, 15.0% fat, 4.0% crude fiber, 2.0% ash and 49.0% carbohydrate [26]. Also, the pulp contains more carbohydrates than the seeds, but less crude fiber. It has a hydrogen ion concentration (pH) of 5.22. It is the insoluble dietary fiber from the crude fiber that is essential for fluid loss control. Strong associative forces in the starch granules known to be responsible for viscosity stability have been reported. The adsorption moisture sorption isotherms at 30, 35 and 40°C have also been presented (Figure 4) [27]. Most biological products follow the sigmoid curve.

They are known to be rich in flavonols, hence, the ability to act as anticancer factors, anti-inflammatory agents, antioxidants, and regulate different cellular signalling pathways. Their chemical structure and representations are shown (Figure 5; Figure 6). Similarly, the solubility and swelling patterns of *Parkia biglobosa* and *Zea mays* starches compare favourably (Figure 7; Figure 8). The photomicrograph is shown (Figure 9).

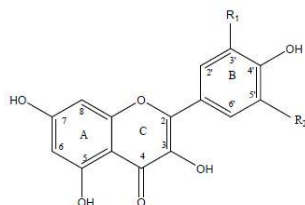


Figure 5. Chemical structure of flavonols [28]

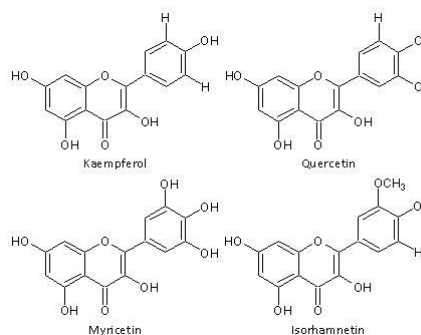


Figure 6. Flavonols represented by glycosides [28]

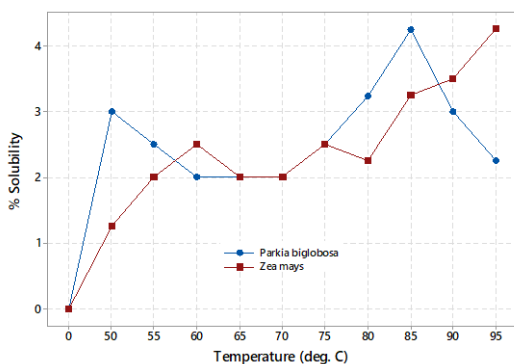


Figure 7. Percent solubility pattern of *Parkia biglobosa* and *Zea mays* starches [29]

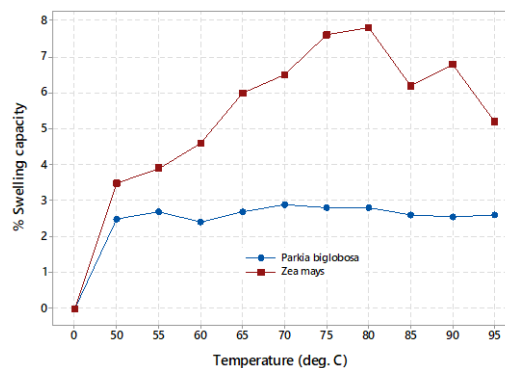


Figure 8. Percent swelling pattern of *Parkia biglobosa* and *Zea mays* starches [29]

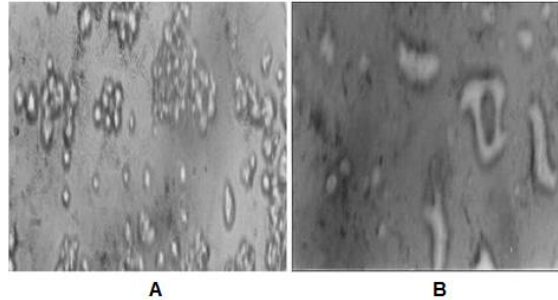


Figure 9. Photomicrograph of *Zea mays* (A) and *Parkia biglobosa* (B) starches [29]

2.2. PAC UL

PAC UL is a cream coloured low viscosity polymer. It is a free flowing powder with specific gravity in the range of 1.5-1.8 and pH of 6.5-8.0. It is used as fluid loss control additive in salt water, KCl, seawater and fresh water muds. It is environmentally acceptable and resists bacterial attack; hence, biocides might not be necessary when used in a formulation. Its temperature limit of application is 250°F.

3. Materials and method

Parkia biglobosa fruit pods were plucked from a tree in Abia State, Nigeria during the March/April fruiting season of 2019. The fruit pods (10kg) were sorted and cleaned of extraneous materials and manually split. The yellow pulps and the seeds were removed from the hulls. It was sun dried at 29 +/- 1.5°C for 4 days and pounded with a pestle in a mortar. The pulps were separated and milled in a hammer mill (Model RLA 201 – 800014, UK) and the powder was sieved with BS sieve 200mm (0.15mm aperture) to fine sized particles for quality assurance. The processed flour was packed in high density polyethylene (HDPE, 0.77mm thickness) bags, heat sealed with a sealing machine. A relative humidity of 75% was reported. It was stored in a refrigerator ready for use when required in the preserved unrefined form [5]. The American Petroleum Institute recommended test procedures for oil and gas well aqueous based drilling fluids were used. The mud formulation is presented in Table 1. Two other mud formulations with *Pleurotus* and PAC UL as fluid loss control agents were used as control samples. *Mucuna solannie* and *Brachystegia eurycoma* have been used in mud formulations where they exhibited predictable characteristics [30].

Table 1 Raw materials used for the formulation of drilling mud sample

Raw material	Quantity	Function(s)
Water	233.35	Base fluid
Potassium chloride	20	Inhibitor
Caustic soda	0.25	pH control
<i>Mucuna solannie</i>	6	Viscosifier
<i>Brachystegia eurycoma</i>	6	Mild Viscosifier
<i>Parkia biglobosa</i>	8	Fluid loss agent
XCD polymer	1	Rheology
Barite	75.4	Weighing agent

4. Results and discussion

4.1 Results

Presented are the observations in the fluid loss test performed according to American Petroleum Institute (API) recommended procedures. Figure 10 and Figure 11 show variations of fluid losses and filter cake thicknesses with additive concentration and temperature effect on rheological properties, respectively.

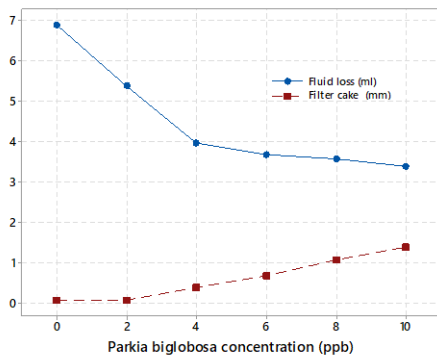


Figure 10. Fluid loss and filter cake thickness variation with concentration

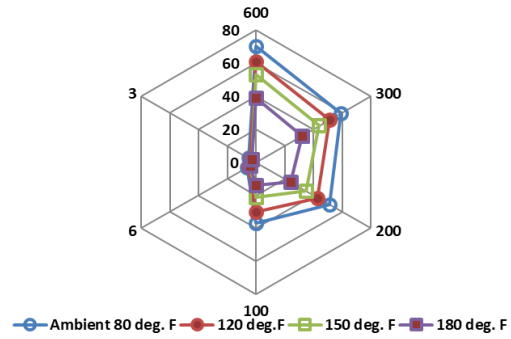


Figure 11. Effect of temperature on rheological properties at 8ppb concentration

Table 2 presents the observed effects of temperature on the fluids rheological parameters, particularly the effect on the gel strength in the presence of *Parkia biglobosa*. Similarly, the type of gel and the effect of time on the fluid loss are presented in Figure 12 and Figure 13 respectively. Figure 13 highlights the effect of temperature on the spurt loss.

Table 2. Effect of temperature on other rheological parameters at 8ppb concentration

Parameter	Ambient 80°F	120°F	150°F	180°F
Fluid loss (mL)	3.6	3.9	4.2	4.3
Filter cake (mm)	1.1	1.2	1.21	1.4
10sec./10min. gel strength (lb/100ft ²)	5/6	4/5	4/4	3/4
YP (lb/100ft ²)	4	3	2	2
PV (cP)	11	10	9	7

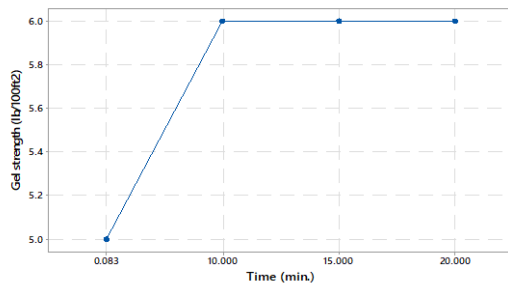


Figure 12. Gel strength characteristics at 80°F (low-flat gel)

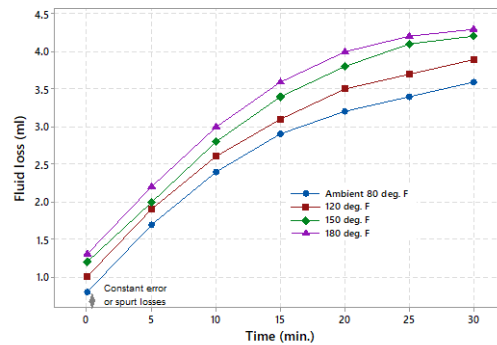
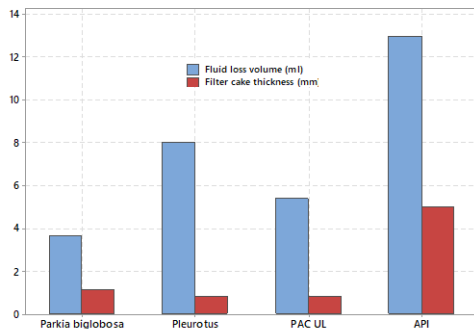


Figure 13. Relation of fluid loss to time



A summary of the comparison of the performance of the *Parkia biglobosa* additive in the fluid loss experiment with other additives used to prepare muds in the same quantity is shown as Figure 14.

Figure 14. Fluid loss and filter cake values at 80°F mud weighted with barite

4.2. Discussion

The density of the weighted mud was 9.4ppg. As the additive concentration increased, fluid losses decreased and filter cake thickness increased (Figure 10) [3]. The rheological properties increased with decrease in temperature (Figure 11). The 10 sec. gel strengths are within the range recommended by API standard, whereas the YP and PV values fall below the range (Table 2). However, the YP and PV values are acceptable for the measured mud weight (Figure 1). The yield point presented in Table 2 decreased with temperature, though the estimated values could vary, and depends on the method of calculation applied [19]. It showed that *Parkia biglobosa* is not expected to appreciably alter the expected yield point values of the water-based mud formulation from the green material. A low flat gel was also observed (Figure 12). Spurt loss is also temperature dependent (Figure 13). The effect of temperature on the fluid loss is due to the effect on filtrate viscosity. At 8ppb concentration used, 3.6ml fluid loss and 1.1mm filter cake thickness were recorded; compared with 8ml and 0.8mm, and 5.4ml and 0.8mm of *Pleurotus* and PAC respectively. Both fluid loss and filter cake thickness increased with increase in temperature (Figure 14). The material is biodegradable and therefore environmentally friendly, though biocide might be required to retard bacterial activity.

5. Conclusion and recommendation

The fluid loss and filter cake values are within the recommended API static test values. The fluid loss control capacity of *Parkia biglobosa* might be attributed to the insoluble dietary fiber [26] and starch contents [29] that plugged the pore spaces and created an external bridge. The mud exhibited similar trends in fluid loss property with increase in fluid loss with temperature, and the use of biomaterials in mud formulations is a recent trend [5, 31-32]. High temperature gelation was not observed, since low-flat or discontinuous gelling was only obtained even at elevated temperature conditions (Table 2; Figure 12). These are gels that do not appreciably alter with time. Pumping of the mud might not be difficult if drilling is interrupted. The pH of 5.22 would inhibit microbial activities to some extent in any mud formulation.

Recommended treatment for *Parkia biglobosa* is from 6 to 12ppb, with an expected optimum concentration of 10ppb, since increase in temperature increases fluid loss. The recommended concentration of *Parkia biglobosa* is 10ppb, so that the API recommended filter cake thickness will not be exceeded. However, the effect of the fluid loss additive on the aged mud was not considered. It is recommended that further test be carried out on aging mud at lower concentrations.

References

- [1] Gatlin C. Petroleum Engineering Drilling and Well Completions, Prentice-Hall Inc., Englewood Cliffs, N.J., 1960: 74.
- [2] Hussain R. Well Engineering and Construction. Elsevier Science Publishers B.V, Amsterdam, the Netherlands, 2002: 290.
- [3] Darley HCH, Gray GR. Composition and Properties of Drilling and Completion Fluids, Fifth Edition, Butterworth-Heinemann, Wildwood Avenue, Woburn, MA (1988): 282-320.
- [4] American Petroleum Institute, Recommended practice for field testing water-based drilling fluids, Fourth Edition, ANSI/API RP 13B-1, 2009.
- [5] Adewole JK, Muritala KB. Some applications of natural polymeric materials in oilfield operations: a review. Journal of Petroleum Exploration and Production Technology, 2019; 9: 2297-2307.
- [6] Larsen DH. Determining the filtration characteristics of drilling muds. Petrol. Eng., 1938; 42: 44-46.
- [7] Skalle P. Drilling Fluid Engineering. Pal Skalle & Publishing ApS (2010): 98-100.
- [8] Bourgoyne AT, Millheim KK, Chenevert ME, Young FS. Applied Drilling Engineering, Second Edition, SPE, Richardson, Texas, 1991: 46.
- [9] Krueger RF. Evaluation of drilling-fluid filter-loss additive under dynamic conditions Journal of Petroleum Technology, 1963; SPE, 15 (1).
- [10] Heriot-Watt University Drilling Engineering Handbook, Available from Institute of Petroleum Engineering, Heriot-Watt University (2010): 368-369.

- [11] Srini-Vasan S, Gatlin C. The effect of temperature on the flow properties of clay-water drilling muds. Society of Petroleum Engineers, 1958; 10 (12). <https://doi.org/10.2118/975-G>.
- [12] Bartlett LE. Effect of temperature on the flow properties of drilling fluids Society of Petroleum Engineers, 1967: <https://doi.org/10.2118/1861-MS>.
- [13] <https://doi.org/10.2118/933112-G>.
- [14] McMordie Jr. WC, Bennett RB, Bland RG. The effect of temperature and pressure on the viscosity of oil-base muds Society of Petroleum Engineers, 1975; 27(07): <https://doi.org/10.2118/4974-PA>
- [15] Byck HT. Effect of temperature on plastering properties and viscosity of rotary drilling muds. Society of Petroleum Engineers, 1940; 136 (01): <https://doi.org/10.2118/940165-G>.
- [16] Routh BI, Craft BC. Effect of temperature on the gel strength of some gulf coast drilling muds Society of Petroleum Engineers, 1938; 1(03): <https://doi.org/10.2118/938082-G>.
- [17] Uwaezuoke N, Igwilo KC, Onwukwe SI, Obah B. Effects of temperature on Mucuna solanmie water-based mud properties. International Journal of Advanced Engineering Research and Science, 2017; 4(1): 1-10.
- [18] Escudier MP, Gouldson IW, Pereira AS, Pinho FT, Poole RJ. On the reproducibility of the rheology of shear-thinning liquids Journal of Non-Newtonian Fluid Mechanics, 2001; 97; 99-124.
- [19] Uwaezuoke N, Igwilo KC, Onwukwe SI, Obah B. Optimization of Mucuna solanmie mud rheological parameters. Journal of Petroleum Engineering and Technology, 2017; 7(1): 15-26.
- [20] Igwilo KC, Odo JE, Uwaezuoke N, Ihedilionye GS, Nwaneri PC. Optimization and modeling of the rate of penetration in an extended reach drilling process Pet Coal, 2020; 62(2): 299-308.
- [21] Orwa C, Mutua A, Kindt R, Jamnadass R, Anthony S. Agroforestry Database: a tree reference and selection guide, Version 4.0, World Agroforestry Centre, Kenya (2009).
- [22] National Research Council, Lost Crops of Africa, 2, the National Academies Press, Washington, DC (2006).
- [23] Sina S, Traoré SA. Parkia biglobosa (Jacq.) R.Br. ex G.Don., Wageningen, Netherlands (2002).
- [24] Hopkins HC. The taxonomy, reproductive biology and economic potential of Parkia (Leguminosae: Mimosoideae) in Africa and Madagascar. Bot. J. Linnean Soc., 1983; 87 (2): 135-167.
- [25] Femi-Ola TO, Ajibade VA, Afolabi A. Chemical composition and termicidal properties of Parkia biglobosa (Jacq) Benth. Journal of Biological Sciences, 2008; 8 : 494-497: <https://doi.org/10.3923/jbs.2008.494-497>
- [26] Gernah DI, Atolagbe MO, Echegwo CC. Nutritional composition of the African locust bean (Parkia biglobosa) fruit pulp. Nigerian Food Journal, 2007: 25(1):190-196: <https://doi.org/10.4314/nifoj.v25i1.33669>
- [27] Akubor PI. Processing, Utilization and storage properties of locust bean. (Parkia biglobosa) fruit pulp, Ph.D dissertation, University of Nigeria, Nsukka, 2007.
- [28] Bhagwat S, Haytowitz DB, Holden JM. Nutrient Data Laboratory, U.S. Department of Agriculture, 2014; Retrieved April 13, 2019, from: https://www.ars.usda.gov/ARSUserFiles/80400525/Data/Flav/Flav_R03-1.pdf
- [29] Ihegwuagu N, Omojola MO, Emeje MO, Kunle OO. Isolation and evaluation of some physico-chemical properties of Parkia biglobosa starch. Pure Appl. Chem., 2009; 81 (1): 97-104: <https://doi.org/10.1351/PAC-CON-08-01-21>
- [30] Uwaezuoke N, Onwukwe SI, Igwilo KC, Obah B. Biopolymer substitution and impact on cuttings transport of a lightweight water-based drilling fluid Journal of Petroleum Engineering and Technology, 2017; 7(2): 54-64.
- [31] Nareh'ei MA, Shahri MP, Zaman, M. Rheological and filtration loss characteristics of colloidal gas aphron based drilling fluids Journal of the Japan Petroleum Institute, 2012; 55(3):182-190.
- [32] Igwilo KC and Zaka B. Evaluation of rheological properties of Detarium Microcarpum, Brachystegea eurycoma using Herschel-Buckley model and their commercial availability. Journal of Petroleum and Gas Engineering, 2014; 5(2): <https://doi.org/10.5897/JPG2014.0191>

To whom correspondence should be addressed: Dr. Nnaemeka Uwaezuoke, Department of Petroleum Engineering, Federal University of Technology, P.M.B. 1526, Owerri, Nigeria, E-mail: nnaemeka.uwaezuoke@futo.edu.ng

Intellectual Training-System of the Process of Catalytic Cracking of Heavy Oils

*Galina Y. Nazarova, Vyacheslav A. Chuzlov, Emiliya D. Ivanchina, Elena N. Ivashkina, Uljana N. Kopycheva, Irena O. Dolganova**

Tomsk Polytechnic University, Lenin Avenue, 30, 634050, Tomsk, Russia

Received May 26, 2020; Accepted September 23, 2020

Abstract

A description of a process that depends on a set of parameters is a complex set of functional dependencies. The system is intellectual, because it is based on the actual data on the operation of industrial processes and devices of chemical technology. These data are analyzed, conclusions and recommendations are made. The physico-chemical model is a software-implemented main unit of this system, which includes calculations on the equations of material and thermal balances of hydrocarbon transformations.

Keywords: *Mathematical modelling; Oil refining; Training system; Catalytic cracking; Physico-chemical model.*

1. Introduction

In the field of catalytic processes of hydrocarbon processing, the integration of Sciences is associated with the transition to system analysis and problem solving using intellectual computer systems as complex systems that combine databases and knowledge bases, as well as program codes built on the basis of predictive models [1-2].

Today in the world, the development of catalytic cracking technology provides a significant proportion of gasoline, diesel fractions and light olefins [3-4]. The development and introduction of the latest designs of catalytic cracking units for the processing of various types of raw materials and modern catalysts provided a significant increase in yield and an improvement in the quality of cracking products during the process of becoming [3,5-13].

At the same time, the technology of catalytic cracking is difficult from the point of view of forecasting and optimal control of a chemical technological object [12,14], the reactor unit includes two interconnected and continuously operating devices that implement the "operation – regeneration" cycle. The effective management of industrial installations requires the introduction of an intellectual training-system, which allows to solve the problem of control and increase the level of knowledge and skills of the engineering and technical personnel of the plant.

The aim of the work was the creation of an intellectual training-system of catalytic cracking of heavy oils. Intellectual system can be used as a computer simulator for training technical personnel to the laws of the catalytic cracking process and research aimed at:

- Forecasting and planning of the optimal mode of operation of the industrial plant, taking into account the basic physical and chemical laws of the catalytic cracking process, as well as research on the effect of technological parameters on the composition and quality of products;
- Improvement of knowledge, skills and competencies of personnel in order to increase the degree of readiness of personnel of technological installations and testing of actions in the detection of malfunctions and emergency and emergency situations.

2. Object of research

The feedstock is characterized by a broad fractional composition of 320–544°C with density of 900–917 kg/m³. The products of the catalytic cracking are:

- Gasoline fraction (fr. IBP–215°C) directed to redistillation unit of gasoline;
- Gas products: unsaturated gas with a high content of C₃–C₄ hydrocarbons intended for gas fractionation unit after purification from sulfur compounds and fuel gas used as the furnaces fuel after purification from hydrogen sulphide;
- Light catalytic gas oil (fraction 195–350°C) used for the diesel fuel production;
- Heavy fractions: catalytic gas oil (fraction 350–420°C) used as the coking feedstock and slops (fraction > 420°C) directed to the reactor in order to maintain the coke load;
- Coke burned out during the catalyst regeneration and providing the heat balance of the “reactor-regenerator” system (Fig. 1).

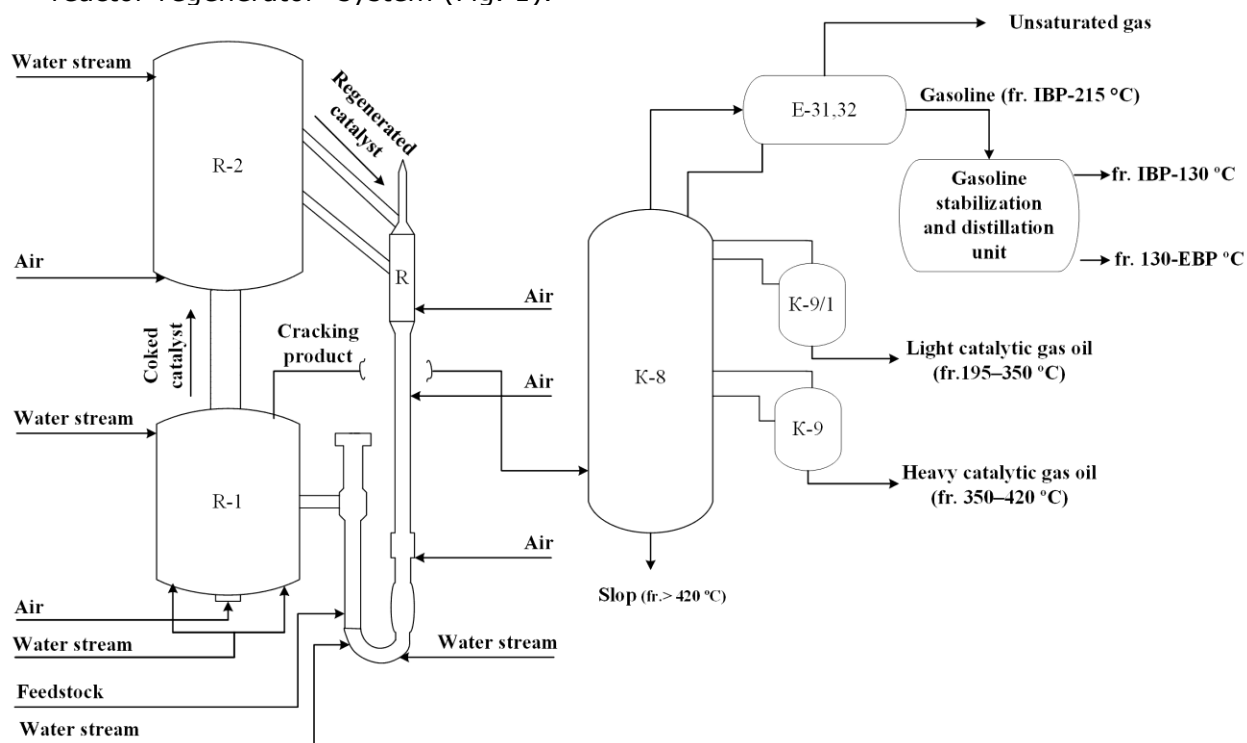
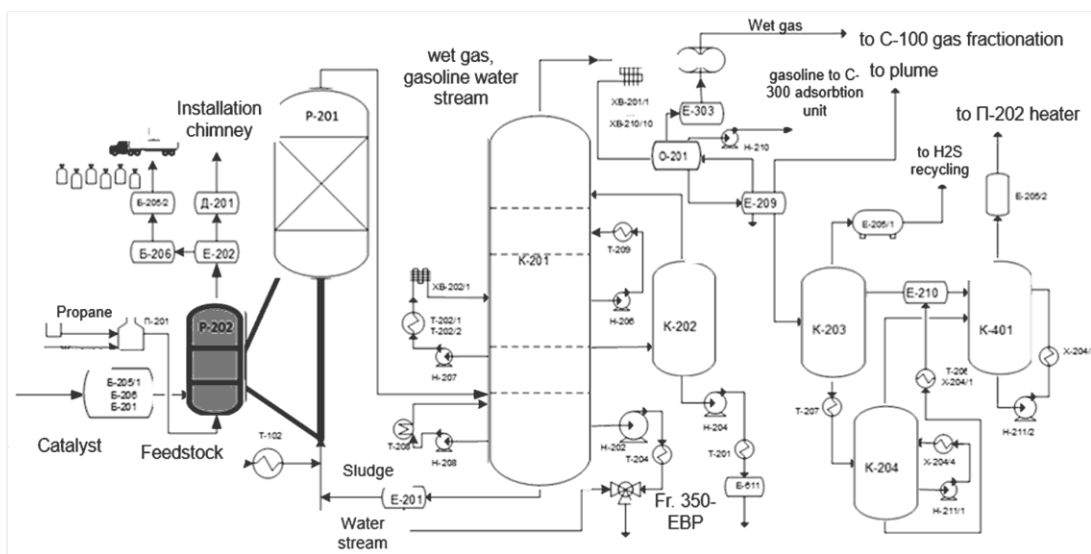


Fig. 1. Process flow diagram of a catalytic cracking unit

System of technological modelling of oil processing includes mathematical model of the of processing of hydrocarbon raw materials is building on the basis of physical and chemical laws of transformation of individual components, as well as taking into account the unsteadiness of industrial processes caused by the dynamic change in the hydrocarbon composition of the processed raw materials, as well as the deactivation of the catalytic systems used [15].

Subject area – a set of processes and devices of chemical technologies, information about which is accumulated in the intellectual system. The computer modelling system has an accessible and user-friendly interface (Fig. 2).



Problem	Reasons	Recommendations
The fluidized catalyst bed temperature in P-202 regenerator is increased. The difference in temperature between the setting zone and fluid bed is increased. The pressure change between P-201 and P-202 is changed (pos. FV2193). The catalyst level in P-202 regenerator is decreased (pos. LIRA2104, LIF).	<ol style="list-style-type: none"> 1. The intensive CO oxidation in the setting zone or the collection chamber. 2. Reducing the sludge consumption in the P-201 reactor (pos. FIRCA). 3. Reducing the temperature in the reactor P-201 reactor (pos. TIRCA). 4. Reducing the feedstock consumption to P-201 reactor (reduction of t). 5. Increasing the catalyst circulation ratio. 	<ol style="list-style-type: none"> 2.1. To restore the sludge consumption to P-201 reactor by valve pos. FV2193.

EXIT

Fig. 2. The program working window

3. Cases for training of engineering personnel of the catalytic cracking industrial unit of oil raw materials

Case 1. The effect of temperature changes on the material balance of the process

It is necessary to determine how the yields of products (gasoline fraction, light catalytic gas oil, heavy catalytic gas oil, fatty gas (gas and reflux) and coke will change when the process temperature changes (operating temperature range for section C-200 of the industrial unit KT-1/1 – 475-535°C, for the industrial unit i 43-103 – 490-525°C, according to the technological regulations).

The studies were carried out using a computer training system "Catalytic cracking", which allows to calculate the group composition of the flow after the reactor unit, the individual composition of gasoline from different units, as well as the outputs of products from the catalytic cracking (Fig. 3).

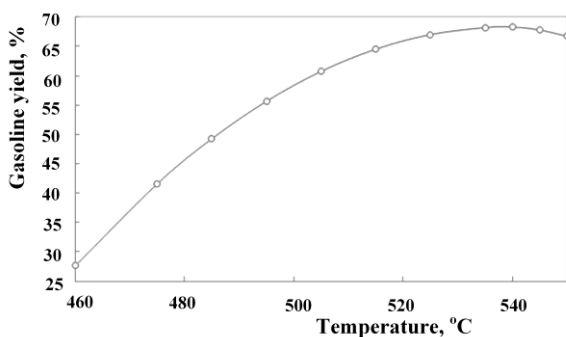


Fig. 3. The dependence of the gasoline and wet gas yields from the process temperature

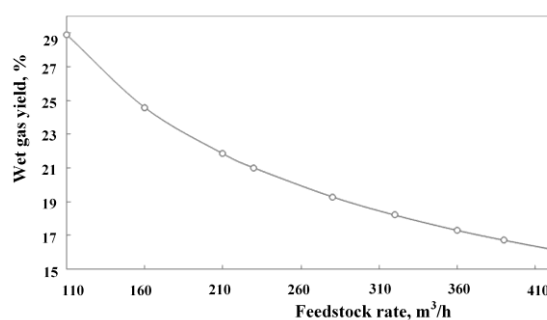


Fig. 3. The dependence of the wet gas yields from the feedstock rate

Case 2. The effect of raw material consumption on the material balance of the process

It is necessary to determine to determine how to change the yields of products (gasoline, light catalytic gas oil, heavy catalytic gas oil, wet gas (gas and reflux) and coke) for a change in the consumption of raw materials (working range of changes of consumption of raw materials 130-420 m³/h, according to the technological regulations) (Fig. 4).

Case 3. The influence of raw material composition and temperature on the material balance of the process

It is necessary to determine the temperature of the process necessary to maintain the yield of gasoline fraction at the level of a 59.42% and the octane number 91.98, changes in the composition of the *raw material 1 in 2*. The compositions of raw materials are given and the parameters of the process mode are given in the tables. The parameters of the technological mode must be maintained at a constant level (Tab. 1).

Table 1. Initial data for model-based calculations

The parameters of the technological mode		
Raw material consumption, m ³ /h		378.22
Slops consumption, m ³ /h		9.23
Density g/cm ³		0.90
Total steam flow to the reaction zone, kg/h		7898.04
Temperature at the separator outlet, °C		521.40
Reactor inlet temperature, °C		303.70
Pressure, kg/cm ²		1.44
The compositions of raw materials for the calculation in case 3 and 4.		
Hydrocarbon group	Raw material 1, wt. %	Raw material 2, wt. %
Saturated hydrocarbons	69.32	58.00
Aromatic hydrocarbons	27.68	38.00
Resins	3.00	4.00

Case 4. Study of the influence of the composition and consumption of raw materials on the material balance of the process

The parameters of the technological mode are presented in Tab. 2.

Table 2. The parameters of the technological mode according to the case 4

Component	Raw material 1		Raw material 2	
	Flow rate, t/h	Yield, %	Flow rate, t/h	Yield, %
Unstable gasoline	163.74	59.42	155.68	56.50
Light catalytic gasoil	30.95	11.23	35.03	12.72
Heavy catalytic gasoil	22.96	8.33	26.81	9.73
Wet gas	47.70	17.31	44.03	15.98
Coke	10.20	3.70	13.98	5.07

Raw material 1 of catalytic cracking mainly consists of paraffin and naphthenic hydrocarbons (69.32 % by weight.), the content of resins and aromatics is lower (30.68 % by weight.). The yield of unstable gasoline on favorable raw materials is 59.42 % and its RON is 91.98. On unfavorable raw materials, which mainly consists of aromatic hydrocarbons and resins – 42 % by weight. (RON – 90.24).

If we go to the conventional units, which are defined as the product of the octane number of gasoline output, it is possible to conditionally assess the economic efficiency of forecasting the composition and quality of products. For favorable *raw materials 1*, this indicator 5465.45, and adverse raw material 5098.56.

4. Conclusions

The following results were obtained:

Reduction of capital and operating costs, due to forecasting and planning of the optimal operation mode of the industrial plant and formulations of mixing of commercial products, taking into account the basic physical and chemical properties, as well as research on the effect of technological parameters on the composition and quality of products using the simulator – 2-3%.

Improved knowledge, skills and competencies of staff, use of software to enhance the speed of response personnel of process plants with detection of faults and emergency situations (the use of the simulator as a data source) – 1 %; improved quality of personnel training technological peculiarities and regularities of the plant and as a consequence.

Increase in the depth of orientation and degree of readiness for emergency situations – 1 %; high degree of readiness for the implementation of the plan of localization and liquidation of emergency situations, based on knowledge of the sources and causes of emergency situations, a step-by-step analysis of their development and analysis of the actions of production personnel for localization and elimination of emergency situations, worked out with the use of computer simulators (reducing the risk of emergency situations and, respectively, reducing the cost of equipment restoration and downtime) – 5%.

Acknowledgements

The research was supported by Tomsk Polytechnic University within the framework of Tomsk Polytechnic University Competitiveness Enhancement Program. The research was also supported by RSCF grant №19-71-10015.

References

- [1] Dolganova I, Ivanchina E, Ivashkina E, Dolganov I. Comment on "Sulfonation of alkylbenzene using liquid sulfonating agent in rotating packed bed: Experimental and numerical study". *Chem. Eng. Process. Process Intensif.*, 2018; 123: 45–46.
- [2] Ivanchina ED, Dolganov IM, Chuzlov VA, Belinskaya NS. Intensification of flow blending technology in the production of motor fuels by the method of mathematical modelling. *Chem. Eng. Process. Process Intensif.*, 2017; 122: 415–424.
- [3] Ivanchina ED, Kirgina MV, Chekantsev NV, Sakhnevich BV, Sviridova EV, Romanovskiy RV. Complex modeling system for optimization of compounding process in gasoline pool to produce high-octane finished gasoline fuel. *Chem. Eng. J.*, 2015; 282: 194–205.
- [4] Lappas AA, Iatridis DK, Papapetrou MC, Kopalidou EP, Vasalos IA. Feedstock and catalyst effects in fluid catalytic cracking - Comparative yields in bench scale and pilot plant reactors. *Chem. Eng. J.*, 2015; 258: 140–149.
- [5] Ren XH, Bertmer M, Stapf S, Demco DE, Blümich B, Kern C, Jess A. Deactivation and regeneration of a naphtha reforming catalyst. *Appl. Catal. A Gen.*, 2002; 228: 39–52.
- [6] Hou X, Qiu Y, Zhang X, Liu G. Analysis of reaction pathways for n-pentane cracking over zeolites to produce light olefins. *Chem. Eng. J.*, 2017; 307: 372–381.
- [7] Gerzeliev IM, Dement'ev KI, Khadzhiev SN. Effect of catalyst and feedstock modification with ultrafine molybdenum disulfide particles on the performance characteristics of catalytic cracking. *Pet. Chem.*, 2015; 55: 481–486.
- [8] Duan A, Li T, Niu H, Yang X, Wang Z, Zhao Z, Jiang G, Liu J, Wei Y, Pan H. Synthesis of a novel zeolite W and application in the catalyst for FCC gasoline hydro-upgrading. *Catal. Today*, 2015; 24: 163–171.
- [9] Chen S, Fan Y, Yan Z, Wang W, Liu X, Lu C. CFD optimization of feedstock injection angle in a FCC riser. *Chem. Eng. Sci.*, 2016; 153: 58–74.
- [10] Berry TA, McKeen TR, Pugsley TS, Dalai AK. Two-dimensional reaction engineering model of the riser section of a fluid catalytic cracking unit. *Ind. Eng. Chem. Res.*, 2004; 43: 5571–5581.
- [11] Baudrez E, Heynderickx GJ, Marin GB. Steady-state simulation of Fluid Catalytic Cracking riser reactors using a decoupled solution method with feedback of the cracking reactions on the flow. *Chem. Eng. Res. Des.*, 2010; 88: 290–303.

- [12] Sa'idi M, Mostoufi N, Sotudeh-Gharebagh R. Modelling and optimisation of continuous catalytic regeneration process using bee colony algorithm. *Can. J. Chem. Eng.*, 2013; 91: 1256–1269.
- [13] Kolesnikov IM, Frolov VI, Borzaev KK, Glotov AP, Kardashev SV. Mathematical Modeling of the Catalytic Cracking of Oil Sludge that has Been Subjected to Electromagnetic Activation. *Chem. Technol. Fuels Oils*, 2016; 51: 663–672.
- [14] Das AK, Baudrez E, Marin GB, Heynderickx GJ. Three-dimensional simulation of a fluid catalytic cracking riser reactor. *Ind. Eng. Chem. Res.*, 2003; 42: 2602–2617.
- [15] Nazarova GY, Shafran TA., Ivashkina EN., Dolganova IO. Modelling of regeneration process of zeolite-containing cracking catalysts. *Pet. Coal*, 2018; 60: 1283-1290.

To whom correspondence should be addressed: Dr. Irena O. Dolganova, Tomsk Polytechnic University, Lenin Avenue, 30, 634050, Tomsk, Russia, E-mail: dolganovaio@tpu.ru

Optimum Conditions for the Catalytic Cracking of Palm Oil from Empty Fruit Bunch over Dolomite in a Continuous Reactor

Phasatorn Khunoad¹, Phorndranrat Suchamalawong², Kittiphop Promdee^{3,5*}, and Tharapong Vitidsant^{4,5*}

¹ Program for Petrochemical and Polymer Science, Faculty of Science, Chulalongkorn University, Bangkok, 10330, Thailand

² Interdisciplinary Program of Environmental Science, Graduate School, Chulalongkorn University, Bangkok, 10330, Thailand

³ Department of Environmental Science, Academic Division, Chulachomklao Royal Military Academy, Nakhon Nayok, 26001, Thailand

⁴ Department of Chemical Technology, Faculty of Science, Chulalongkorn University, Bangkok 10330, Thailand^f

⁵ Center of Fuels and Energy from Biomass, Chulalongkorn University, Saraburi 18110, Thailand

Received May 18, 2020; Accepted September 21, 2020

Abstract

This research evaluates the effectiveness of cracking palm oil from an empty fruit bunch (EFB) over dolomite in a continuous reactor and used the 2k factorial design to investigate the influence of parameters, such as reaction temperature (380-460°C), feed rate of palm oil (3-9 mL/min), nitrogen gas flow rate (50-150 mL/min), and the amount of catalyst (30-60% by reactor volume) that affected the yield of organic liquid product (OLP) and diesel-like fraction. OLP was obtained and analyzed by using distillation simulation gas chromatography and gas chromatograph mass-spectrometry to identify the structure of liquid fuels. An analysis from the design-expert program demonstrated that the optimum conditions for the catalytic cracking of PEFB on dolomite in continuous reactor were: a temperature of 460°C, feed rate of palm oil 8.96 mL/min, nitrogen gas flow rate of 50.04 mL/min, and the amount of catalyst 60% (v/v), which yielded the highest diesel-like fraction of 66.12%wt and a liquid yield of 57.93%wt. The physicochemical analysis of OLP resulted in a heating value of 45.20 MJ/kg and acidity value of 0.35 mgKOH/g.

Keywords: Catalytic cracking; Empty fruit bunch (PEFB); Dolomite; Organic liquid product (OLP).

1. Introduction

Biodiesel is bio-renewable and environmentally-friendly fuel that can be made from triglyceride in animal fats or vegetable oils by a trans-esterification reaction with alcohols, such as methanol and ethanol, using a homogeneous base or acid catalysts [1-7]. Nevertheless, these systems of homogeneous catalysis have many disadvantages since a purification process is required to remove these catalysts from the end products. In this regard, glycerol as a by-product has proven to be difficult to remove and requires an immense amount of water to do so. Therefore, the catalytic cracking of triglycerides represents an alternative way to produce biofuel with fewer complications and less use of resources. In addition, the process also has lower production costs, lower equipment costs, and compatibility with existing infrastructure and feed stock flexibility [8-11], which result in final products that have a composition similar to diesel fuel [12-15].

With regard to the raw materials used in this research, the empty fruit bunch (EFB) is a commonly available biomass waste residue generated from the palm oil industries in Thailand and other locations, particularly in Southeast Asia [16-19]. The EFBs are often incinerated at the plant site, which causes air pollution. The successful conversion of these waste materials to

produce biofuels may, therefore, provide environmental, as well as additional financial benefits. Dolomite ($\text{CaMg}(\text{CO}_3)_2$) is a mineral that consists of calcium carbonate and magnesium carbonate, which has low toxicity, low cost, and high basicity. It is a naturally abundant mineral in many areas of Thailand. Currently, this mineral is mostly used for cement manufacturing and landfill due to its low cost, low toxicity, high basicity, and environmentally-friendly properties. The material was chosen for this experiment in light of the extent of its successful application in biodiesel production, as reflected in numerous existing literature [20].

The objective of this research was to investigate the optimum conditions for the production of biofuel through the catalytic cracking of palm oil from empty fruit bunches (EFB) on dolomite in continuous reactor. The experiments were designed to study the effect of different types of catalysts and other factors such as the reaction temperature, feed rate, nitrogen gas flow rate, and the amount of catalysts on the liquid yield and diesel fraction from obtained biofuel.

2. Methodology

2.1. EFB preparation and characterization

The EFB used in this study as the feedstock was obtained from Southern Palm (1978) Company Limited in Thailand. The palm oil sample was filtered through filter paper to remove solid impurities and was heated to 100-110°C for 10 minutes to remove moisture prior to its use in cracking. The thermal decomposition of sample was evaluated by thermo-gravimetric analysis (TGA) carried out by a Setaram LABSYS EVO thermogravimeter at a ramping rate of 20°C/min in an argon atmosphere.

2.2. Catalyst preparation and characterization

The dolomite, which will be the experiment's catalyst, was obtained from L S M (1999) Company Limited in Thailand. The dolomite was dried in the oven at 110°C for 2 hours to remove all surface moisture and calcined at 600°C for 1 hour in a muffle furnace to remove impurities and left to cool to room temperature.

The X-ray diffraction (XRD) was performed by a Bruker AXS D8 Discover. The samples were scanned from 5 to 70°. The diffractograms were analyzed using the standard JCPDS files. Elemental analysis was performed by an AXIOS PW-4400 fluorescence spectrometer. Morphological study was carried out by a JOEL JSM-5800LV scanning electron microscope. The instrument was operated at 15 kV acceleration voltages. Prior to analysis, samples were coated with a thin film of gold to make them conductive. The N_2 adsorption and desorption isotherms were measured by a Micromeritics ASAP 2020 instrument. Pore size distributions of the samples were determined from the isotherms by the Barrett-Joyner-Hallenda (BJH) method. All samples were dried in the oven at 110°C overnight before the adsorption measurement.

2.3. Catalytic cracking reaction

The cracking of palm oil from EFB was conducted in a continuous reactor 3 L (Biodiesel reactor unit, model no. Bio-3401) from HIRO Company Limited in Japan. The dolomite as catalyst was loaded over quartz wool and placed in the horizontal furnace. The temperature was monitored by a thermocouple positioned in the center of catalyst bed. Nitrogen gas as a carrier gas was passed through the reactor throughout the reaction. The reaction temperature was in the range of 380 to 460°C. The palm oil was fed using a rotary pump (Iwaki Metering Pump model no. LK-22VSH-02). Once a stable state was reached in the reactor, the liquid product (organic and aqueous fractions) was collected in a liquid sampler, while the gaseous products were collected in a gas-sampling tube. The process run time for each experiment was 5 hours.

The gaseous product was analyzed using column (Molecular sieve packed columns) over gas chromatograph (Agilent 7820A), equipped with thermal conductivity detector (TCD). The OLP was analyzed by gas chromatograph simulated distillation (GC SimDist) using a capillary glass column (100% dimethylpolysiloxane stationary phase, J&W Scientific, DB-HT-SIMDIS, 5 m length \times 0.53 mm diameter \times 0.15 μm film thickness) over gas chromatograph (Agilent

7890A), equipped with flame ionization detector (FID). The OLP contains a large number of components of hydrocarbon compounds.

Consequently, the composition of liquid product was defined according to the boiling range of petroleum products in three categories, that is gasoline fraction (273.15-473.15 K), kerosene fraction (473.15-523.15 K), and diesel fraction (523.15-643.15 K). The liquid product identification and composition determination were performed on a GC Agilent series 7890A with a Agilent mass selective detector of series 5975C using a capillary glass column (J&W Scientific, 100% dimethylpolysiloxane stationary phase, HP-5MS, 30 m length × 0.25 mm diameter × 0.25 μm film thickness). The yield of organic liquid products was calculated using the following equation:

$$\text{Yield (wt\%)} = \left(\frac{\text{Obtained Product(g)}}{\text{PEFB Feed(g)}} \right) \times 100\% \quad (1)$$

2.4. 2⁴ Factorials design

Table 1. 2⁴ factorials design containing five central points

Run	Code factors			
	A	B	C	D
1	-1	-1	-1	-1
2	+1	-1	-1	-1
3	-1	+1	-1	-1
4	+1	9	-1	-1
5	-1	3	+1	-1
6	+1	3	+1	-1
7	-1	9	+1	-1
8	+1	9	+1	-1
9	-1	3	50	+1
10	+1	3	50	+1
11	-1	9	50	+1
12	+1	9	50	+1
13	-1	3	+1	+1
14	+1	3	+1	+1
15	-1	9	+1	+1
16	+1	9	+1	+1
17	0	0	0	0
18	0	0	0	0
19	0	0	0	0
20	0	0	0	0
21	0	0	0	0

3. Results and discussion

3.1. Oil characterization

The fatty acid composition was determined by gas chromatography simulation distribution (standard method D2887). The analysis of the EFB's boiling point before catalytic cracking was determined by DGC standard ASTM D2887, as shown in Table 2. The EFB was mainly composed of long residue at 84.50% whereas the quantity of diesel was 15.50%. The EFB cannot be directly used in engines and requires further processing to improve its quality. The catalytic pyrolysis process breaks down the large molecules to smaller hydrocarbon molecules. The OLP created from pyrolysis has similar properties to generic diesel oil and benzene oil, as well as other physical and chemical properties that are similar to petroleum diesel oil.

The composition of the EFB was determined in the terms of different types of fatty acids as represented in Table 3. The result showed that the majority proportion (43.07%) of palmitic acid (C16:0) was saturated, while 39.72% oleic acid (C18:1) was an unsaturated fatty acid.

Table 2. The distribution of palm oil from empty fruit bunch, as analyzed by gas chromatography simulation distribution (DGC)

Boiling point	Composition	Recovery (wt%)
IBP-200	Naphtha (C ₅ -C ₁₂)	0.00
200-250	Kerosene(C ₁₂ -C ₁₅)	0.00
250-370	Diesel(C ₁₅ -C ₃₃)	15.50
370-FBP	Long residue(>C ₃₃)	84.50

Table 3. Composition of fatty acid of EFB

Fatty acid composition, g/100 g		
Lauric acid	C12:0	0.30
Myristic acid	C14:0	0.90
Pentadecanoic acid	C15:0	0.05
Palmitic acid	C16:0	43.07
Hepadecanoic acid	C17:0	0.12
Stearic acid	C18:0	4.38
Arachidic acid	C20:0	0.36
Behenic acid	C22:0	0.08
Lignoceric acid	C24:0	0.10
Total saturated fatty acid		49.36
Palmitoleic acid	C16:1	0.15
Oleic acid	C18:1	39.72
Cis-9, 12-Octadecadienoic acid	C18:2	9.96
Cis-9, 12, 15-Octadecatrienoic acid	C18:3	0.31
Cis-11-Eicosenoic acid	C20:1	0.14
Nervonic acid	C24:1	0.14
Total unsaturated fatty acid		50.42
Unidentified peak		0.24

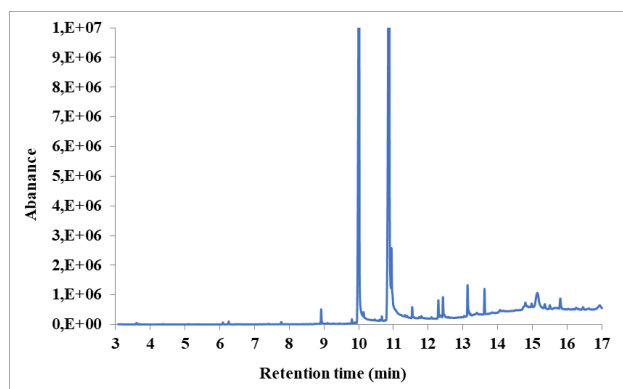


Figure 1 GC-MS Chromatograms of palm oil from EFB

The chemical compound of the EFB was analyzed by gas chromatograph-mass spectrometry. Figure 1, shows the chromatogram of the EFB sample. For the purpose of clarity, the solvent peaks (carbon disulfide) are not shown. The n-hexadecanoic acid (palmitic acid, C₁₆:0) appears at a retention time of 10.015 min, followed by 9-Octadecenoic acid (oleic acid, C₁₈:1), which appeared at a retention time of 10.879 min and octadecanoic acid (stearic acid, C₁₈:0) peak appears at a retention time of 10.946 min, as shown in Table. 4. The large peaks of GC-MS chromatogram, mostly shows carboxylic acid, while small peaks show other groups. The EFB is a source of hydrocarbons C₁₆-C₁₈ atoms, which is similar to the number of carbon atoms of diesel produced from petroleum distillation.

A thermal analysis of the EFB's decomposition temperature was also performed. The TGA curves of the EFB are shown in Figure 2 and demonstrate the fact that the EFB begins to thermally decompose at approximately 155°C, while the high temperature of decomposition is 440°C, at a heating rate of 20°C/min from 25 to 600°C, under the inert gas (argon) atmosphere. Consequently, the decomposition temperature range of 380 to 460°C was chosen for the cracking of the EFB.

Table 4. The chemical compound of EFB

Retention time (min)	Name	Formula chemical	Area (%)
10.015	n-Hexadecanoic acid	C ₁₆ H ₃₂ O ₂	34.88
10.145	Octadecanoic acid	C ₁₈ H ₃₄ O ₂	0.98
10.877	6-Octadecenoic acid	C ₁₈ H ₃₄ O ₂	48.15
10.947	Octadecanoic acid	C ₁₈ H ₃₄ O ₂	6.33
12.291	9-Octadecenal, (Z)-	C ₁₈ H ₃₄ O	0.79
13.617	Squalene	C ₃₀ H ₅₀	0.90
14.792	Benzo[h]quinoline, 2,4-dimethyl-	C ₁₅ H ₁₃ N	0.92
15.135	Cyclotrisiloxane, hexamethyl-	C ₆ H ₁₈ O ₃ Si ₃	3.95
15.798	2-Ethylacridine	C ₁₅ H ₁₃ N	0.67

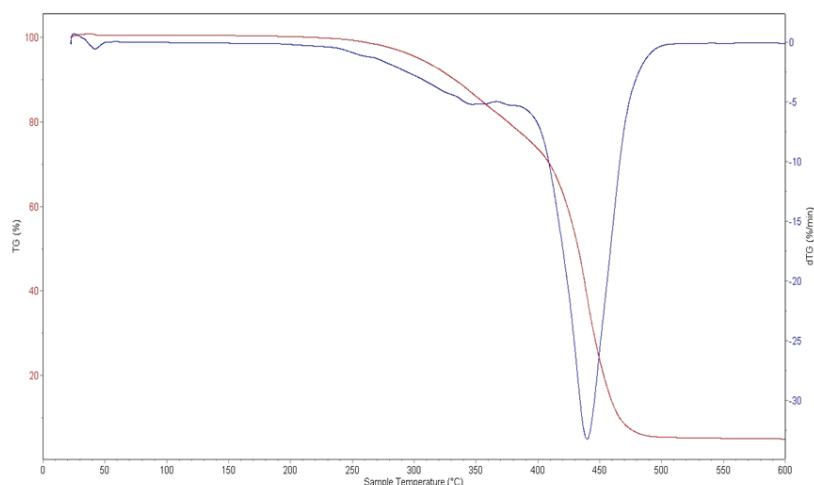


Figure 2 Thermal decomposition analysis of PEFB by thermogravimetric analyzer

3.2. Catalyst characterization

3.2.1. X-ray Fluorescence (XRF)

The catalyst used in this study was powdered dolomite. Its chemical composition, as determined through X-ray fluorescence (XRF) analysis, is as follows: CaO 59.80%, MgO 33.5%, SiO₂ 0.39%, Fe₂O₃ 0.23%, Al₂O₃ 0.19% and Others 5.89%. The XRF analysis result can be seen in Table 5. It is observed that the CaO content in the dolomite is higher than MgO content. Calculations by stoichiometry on the XRF analysis showed that the dolomite consisted of 59.80 wt% CaO and MgO 33.50 wt%.

Table 5. Chemical composition of dolomite

Compound	Concentration (wt%)
Calcium (CaO)	59.80
Magnesium (MgO)	33.50
Silica (SiO ₂)	0.39
Iron (Fe ₂ O ₃)	0.23
Aluminium (Al ₂ O ₃)	0.19
Other	5.89

3.2.2. X-ray powder diffraction (XPD)

Figure 3 shows the X-ray Powder Diffraction (XPD) patterns of the raw dolomite and calcined dolomite at 800°C. It can be seen that CaO, MgO, Mg(OH)₂ and Ca(OH)₂ is present in the raw dolomite. A decarbonation occurs with the increase in calcination temperature, which leads to the transformation of CaMg(CO₃)₂ to CaO, MgO and carbonate phase of CaCO₃ or calcite. The diffraction peak intensities of MgO increased relatively after calcination and the

peak of calcium hydroxide ($\text{Ca}(\text{OH})_2$) and magnesium hydroxide ($\text{Mg}(\text{OH})_2$) disappears in an XPD analysis of calcined dolomite.

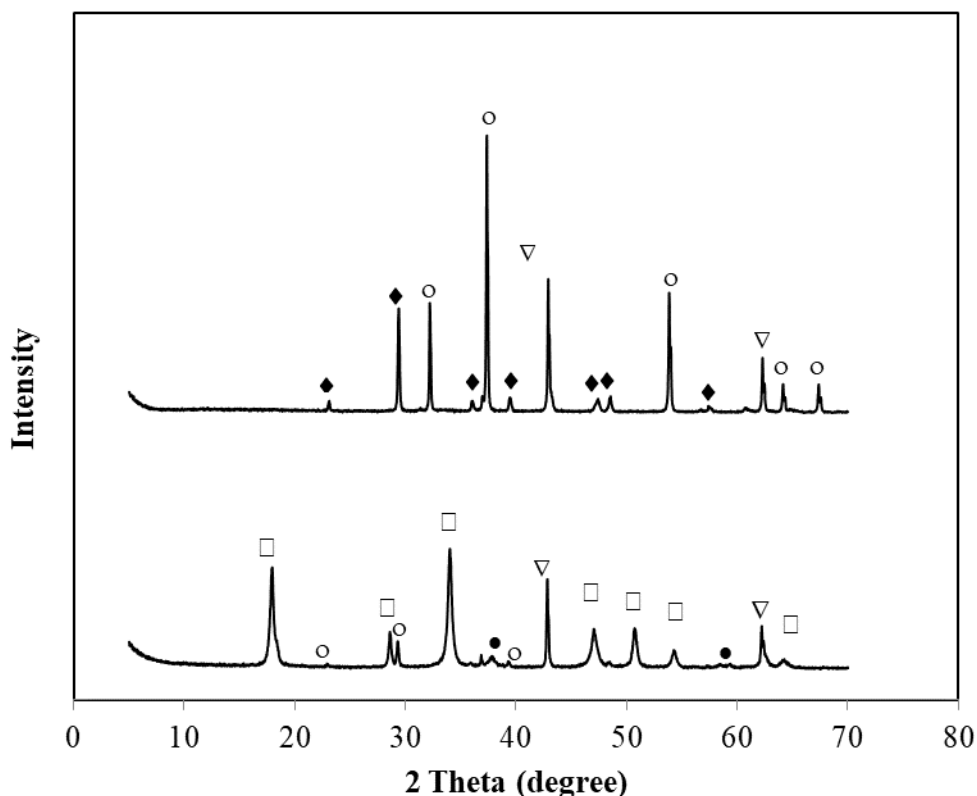


Figure 3. XPD pattern of dolomite (a) raw dolomite and (b) calcined dolomite at 800°C , symbol: (●) $\text{Mg}(\text{OH})_2$, (□) $\text{Ca}(\text{OH})_2$, (◆) CaCO_3 , (▽) MgO , and (○) CaO

3.2.3. BET surface area measurement

The surface areas of the raw dolomite and calcined dolomite were determined through the nitrogen adsorption method and the BET equation, as shown in Table 6. The maximum activity was obtained with the catalyst calcined at 800°C for 2 hours. Table 6 shows the specific surface area and porosity of the dolomite. Decarbonation by the calcination of the dolomite produces MgO and increases its specific surface area. Thus, the BET surface area of raw dolomite $8.00 \text{ m}^2\text{g}^{-1}$ was significantly increased to $19.95 \text{ m}^2\text{g}^{-1}$ after thermal treatment at 800°C . The dolomite also saw increases in pore volume and diameter.

The thermal decomposition of dolomite occurs via a system involving a number of reactions that are still being debated in existing literature. When performed in vacuum or in an inert atmosphere, this is also a one-step reaction leading to the mixture of magnesium or calcium oxides. When it takes place in air or in the presence of CO_2 , it occurs as a two-step process. Thus, the phenomenon that occurs during the thermal decomposition of fresh dolomite can be expressed as follows:

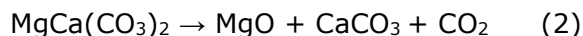


Table 6. Specific surface area and porosity of examined dolomite

Sample	Specific surface area ($\text{m}^2 \text{g}^{-1}$)	Total pore volume ($\text{cm}^3 \text{g}^{-1}$)
Raw dolomite	8.00	0.01
Calcined dolomite	19.95	0.10

3.2.4. SEM analysis

The results of the SEM analysis is shown in Figure 4. Changes in the morphology of the dolomite were observed as a result of recrystallization when undergoing calcination. The SEM image of the raw dolomite clearly shows that it had a wide range of particles sizes in random shapes and may display a macropore or almost non-porous structure. The microstructure of calcined dolomite has a porous surface, the particle size decreased due to cracking large particles from the decarbonation of dolomite (chemical equation 1-2). This phenomenon is caused by the release of CO₂ from the dolomite grain and it proves that the dolomite calcinations reaction originated on the surface of dolomite.

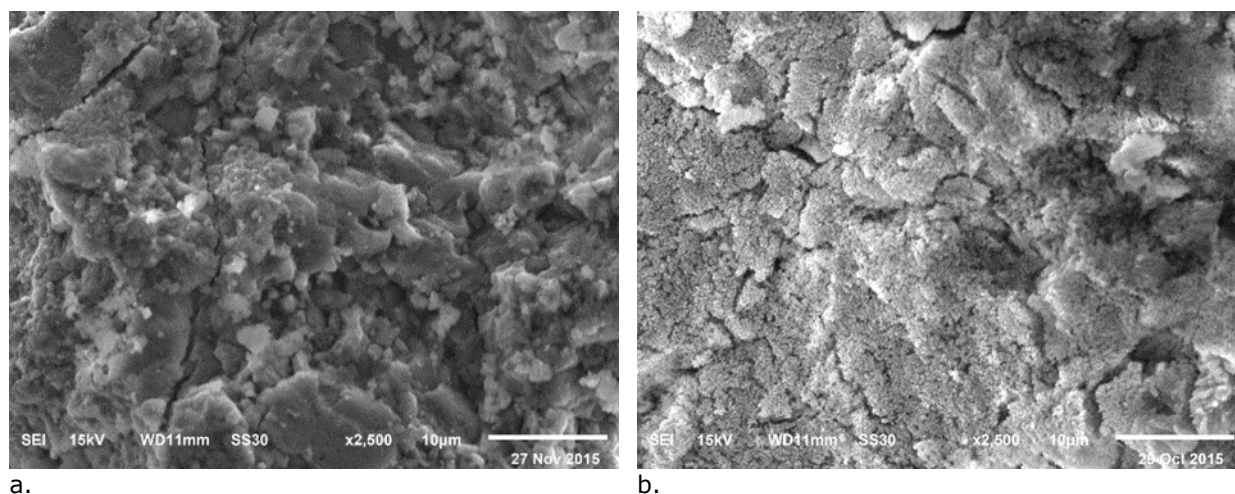


Figure 4. Electron micrograph of raw dolomite (a) and calcined dolomite (b) at 2500x magnification

3.3. Yield liquid

Table 8 shows the highest yield of liquid and diesel-like fuel that can be obtained from the catalytic cracking of palm oil from the EFB. The important operating variables affecting the liquid yield and product distribution were: reaction temperature, feed rate, flow rate of the carrier gas, and the amount of catalyst. A 2^k factorial design with three process variables where each containing three levels, namely low (-1), central (0), and high level (+1) was used. Table 7 presents the 2^k full factorial design with the operating range of each variable. The total number of experiments conducted was 16, where five experiments were repeated at the central level of each factor to check their reproducibility and experimental error.

The results show that higher temperatures and lower feed rates gave higher yields of gaseous product, while low reaction temperatures and high feed rate deactivated the catalyst [21-29]. The conversion of EFB, yield of OLP and yield of diesel-like fraction at different reaction are presented in Table 8. It shows that the OLP varied in the range of from 7.08 to 65.76 wt%. The OLP increased steadily with the increase in the reaction temperature due to higher cracking rates. The diesel-like fraction varied in the range of 47.50 to 74.35 wt%.

Table 7. Code factor and factor level of variable of cracking of palm oil from empty fruit bunch on dolomite in continuous reactor

Factor	Factor code	Level			Unit
		Low (-1)	Central point (0)	High (+1)	
Reaction temperature	A	380	420	460	°C
Feed rate of palm oil	B	3	6	9	mL/min
Flow rate of carrier gas (N ₂)	C	50	100	150	mL/min
The amount of catalyst	D	30	45	60	%v/v of reactor volume

Table 8. Experimental matrix and response obtained based on Design of Experiment

Run	Code factors				OLP yield (wt%)	Diesel fraction yield (wt%)
	A	B	C	D		
1	-1	-1	-1	-1	36.25	63.13
2	+1	-1	-1	-1	63.70	59.07
3	-1	+1	-1	-1	42.29	58.38
4	+1	9	-1	-1	65.76	56.25
5	-1	3	+1	-1	34.36	59.50
6	+1	3	+1	-1	55.58	57.82
7	-1	9	+1	-1	36.55	51.25
8	+1	9	+1	-1	63.14	47.50
9	-1	3	50	+1	28.20	74.35
10	+1	3	50	+1	53.84	67.81
11	-1	9	50	+1	30.40	71.88
12	+1	9	50	+1	61.68	66.13
13	-1	3	+1	+1	26.87	70.63
14	+1	3	+1	+1	51.62	63.44
15	-1	9	+1	+1	7.08	61.57
16	+1	9	+1	+1	59.19	62.25
Repeated trial						
17	0	0	0	0	42.87	49.38
18	0	0	0	0	37.01	48.75
19	0	0	0	0	39.69	49.13
20	0	0	0	0	33.79	50.62
21	0	0	0	0	40.86	48.73

3.4 Results of 2^k factorial design

3.4.1. Variables affecting the percentage of oil yield

To confirm the significance of variables on the percentage of oil yield, the 2^k factorials design was used to determine the effect of four operating parameters: reaction temperature (A), flow rate of oil (B), flow rate of carrier gas (C) and the amount of catalyst (%v/v) of reactor volume (D). The variables' significance was assessed using an analysis of variance (ANOVA).

Since several variables were studied, the conditions that significantly affected the product distribution had to be identified statistically. Figure 5 shows the half normal plot of the effect of reaction temperature (A), flow rate of oil (B), flow rate of carrier gas (C) and the amount of catalyst (%v/v) of reactor volume (D) were significant variables for OLP. Therefore, the ANOVA, was performed at 95% level of confidence for designed experiments using the Design-Expert software (version 6.0.6). The value of Prob > F for the models is less than 0.05, indicating that the model is significant and shows that the terms in the model has a significant effect on the response.

Table 9 shows the summary of the results obtained. It found that the reaction temperature (A), flow rate of oil (B), flow rate of carrier gas (C) and the amount of catalyst (%v/v) of reactor volume (D) have a value Prob > F less than 0.05 and implies that these variables affect the yield of OLP. Figure 6 shows the normal plot of residuals of OLP, the correlation coefficient for the OLP was 0.96. The data on OLP yield fits the normal distribution and contains no outliers.

Table 9. ANOVA result for the 2k factorials design of OLP

Source	Sum of Squares	Degree of freedom	Mean Square	F value	Prob > F value
Model	6160.75	4	1540.19	248.70	<0.0001
A	5504.37	1	5504.37	888.82	<0.0001
B	182.84	1	182.84	29.52	<0.0001
C	79.10	1	79.10	12.77	<0.0012
D	394.45	1	394.45	63.69	<0.0001
Residual	191.98	31	6.19		
Total	6586.43	36			

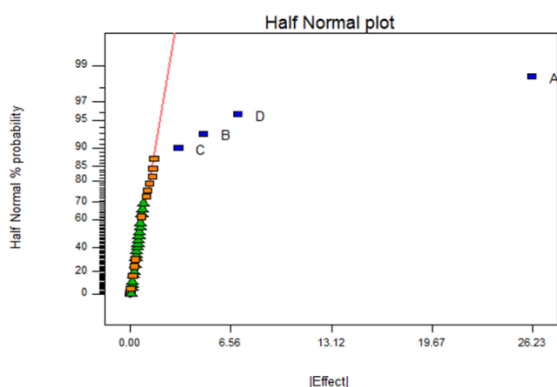


Figure 5. Half Normal probability plot of percentages yield of OLP

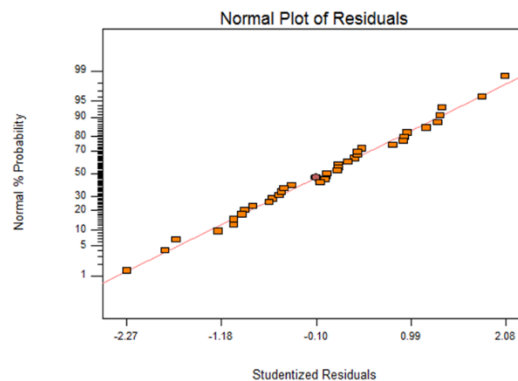


Figure 6. Normal probability plot versus studentized residuals of OLP

3.4.2. Variables affecting the percentage of diesel-like fraction yield

Figure 7 shows a half normal probability plot of the effect of reaction temperature (A), flow rate of oil (B), flow rate of carrier gas (C), the amount of catalyst (%v/v) of reactor volume (D), reaction temperature-the amount of catalyst (%v/v) of reactor volume of reaction interaction (AD), flow rate of oil-flow rate of carrier gas of reaction interaction (BC), and reaction temperature-flow rate of carrier gas-the amount of catalyst (%v/v) of reactor volume (ACD). It indicates that these variables are factors that affect the percentage yield of diesel products.

Table 10 shows the ANOVA results, which found that the reaction temperature (A), flow rate of oil (B), flow rate of carrier gas (C), the amount of catalyst (%v/v) of reactor volume (D), reaction temperature-the amount of catalyst (%v/v) of reactor volume of reaction interaction (AD), flow rate of oil-flow rate of carrier gas of reaction interaction (BC), and reaction temperature-flow rate of carrier gas-the amount of catalyst (%v/v) of reactor volume of reaction interaction (ACD) have a value Prob>F less than 0.05 percent and implies that these variables affect the yield of diesel products.

Figure 8 shows the normal plot of residues. The obtained data on diesel product was tested for normalcy to determine if the data obtained from the experiment is suitable for further statistical evaluation. It was determined that the percentage of diesel is approximately a straight line with $R^2 = 0.97$ and data on diesel product fit the normal distribution, while containing no outliers.

Table 10. ANOVA result for the 2k factorials design of diesel fraction

Source	Sum of Squares	Degree of freedom	Mean Square	F value	Prob > F value
Model	1608.63	7	229.80	164.18	<0.0001
A	92.24	1	92.24	65.90	<0.0001
B	180.83	1	180.83	129.19	<0.0001
C	201.55	1	201.55	143.99	<0.0001
D	1027.29	1	1027.29	733.91	<0.0001
AD	5.96	1	5.96	4.26	0.0485
BC	74.82	1	74.82	53.45	<0.0001
ACD	25.94	1	25.94	18.53	0.0002
Residual	39.19	28	1.40		
Total	2201.09	36			

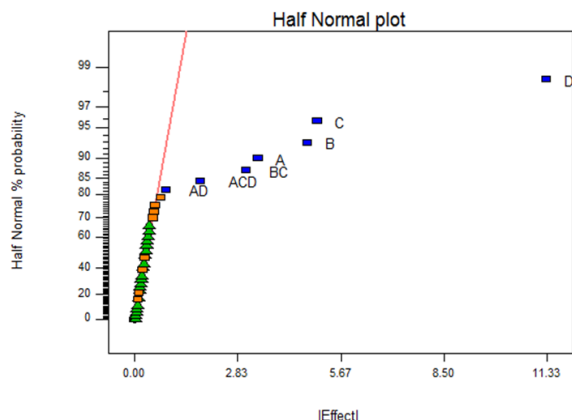


Figure 7. Half Normal probability plot of percent-ages yield of diesel-like fraction from the cracking of EFB on dolomite in continuous reactor

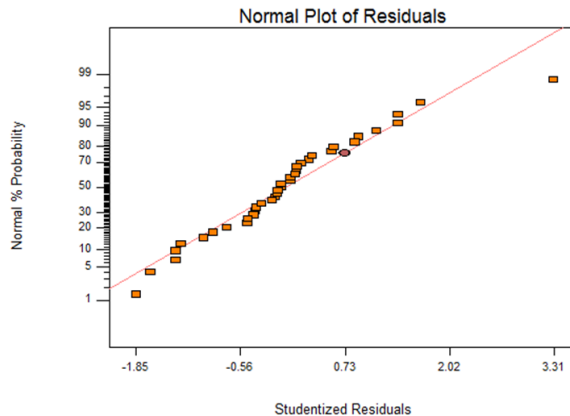


Figure 8. Normal probability plot versus studentized residuals of diesel fraction

3.5. Optimum conditions according to the Design-Expert 6.0.10 program

Table 11 shows an analysis from Design-Expert 6.0.10 program. According to the program, the optimum condition for catalytic cracking of palm oil from EFB on dolomite in continuous reactor is as follows: a temperature of 460°C, feed rate of palm oil 8.96 mL/min, nitrogen gas flow rate of 50.04 mL/min, and the amount of catalyst 60% (v/v). This gave the highest diesel-like fraction of 66.12%wt, whereas liquid yield was 57.93%wt. The desired criteria are summarized in Table 12, which shows that the values obtained from program and experiment yielded the same optimum condition.

Table 11. Optimization criteria

Name	Goal	Lower Limit	Upper Limit	Unit
Temperature	is in range	380	460	°C
Feed rate of palm oil	is in range	3	9	mL/min
Flow rate of carrier gas	is in range	50	150	mL/min
Catalyst	is in range	30	60	%v/v
Liquid yield	maximize	25.95	66.75	%wt
Diesel yield	maximize	47.5	75.57	%wt

Table 12. Optimum conditions from Design-Expert Program

Factor	Condition from program	Condition from experiment
Reaction temperature (°C)	460.00	460.00
Feed rate of palm oil (mL/min)	8.96	9.00
Flow rate of carrier gas (mL/min)	50.04	50.00
The amount of catalyst (v/v% reactor volume)	60.00	60.00
OLP (wt%)	59.73	61.68
Diesel fraction (wt%)	66.12	66.13

3.6. Properties of the biofuel

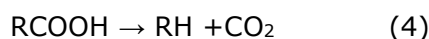
The elemental composition of the palm oil from the EFB (PEFB) and pyrolysis oils from triglyceride materials both with and without the dolomite are shown in Table 13. The analysis of the PEFB found that the following elemental contents: carbon, hydrogen, nitrogen, and oxygen (by reference) were 59.30, 12.00, 0.04 and 28.66% respectively. The analysis of the OLP shows that the carbon, hydrogen, nitrogen and oxygen (by reference) were 76.50, 12.80, 0.03 and 10.67% respectively. The presence of oxygen in OLP is lower than that of the oils from the PEFB. The decreasing of percentage of oxygen corresponded to the increase of the

heating value [30-34]. Normally, the effect of decreasing percentage of oxygen is that the heating value increases.

Table 13. Elemental analysis of the bio-oil

Oil	C	H	N	O*
PEFB	59.30	12.00	0.04	28.66
Non-catalyst	70.90	11.90	0.09	17.11
OLP	76.50	12.80	0.03	10.67

The total acid and heating value of PEFB and OLP were measured by potentiometric titration (ASTM D664), as shown in Table 14. The acid value of OLP is lower than the PEFB, decreasing from 54.44 to 0.35 mgKOH/g. The acid value was quite low when the catalyst contained MgO. These phenomena of decarboxylation of fatty acids to hydrocarbons were catalyzed by MgO, as shown in Equation 4 [1].



The heating value was determined for the catalytic cracking products and presented in Table 14. The heating value of OLP is higher than PEFB, increasing from 39.25 to 45.20 MJ/kg. It was observed that the OLP has characteristics similar to those of petroleum fuels.

Table 14. Acid and heating values of OLP

Oil	Acid value (mgKOH/g)	Heating value (MJ/kg)
PEFB	54.44	39.25
OLP	0.35	45.20

The chemical composition of OLP produced at optimum operating condition was analyzed by gas chromatograph-mass spectrometry and presented in Figure 9. The OLP produced can be classified into hydrocarbons, alcohols, phenol, esters, aldehydes, ketones, carboxylic acids, and other ester. GC MS analysis matches each peak observed in the chromatogram with a substance peak stored in the reference library. The result of the analysis is presented in Table 15. The GC-MS chromatograms large peaks mostly show aromatic, aliphatic and cyclic hydrocarbons while small peaks shows other groups.

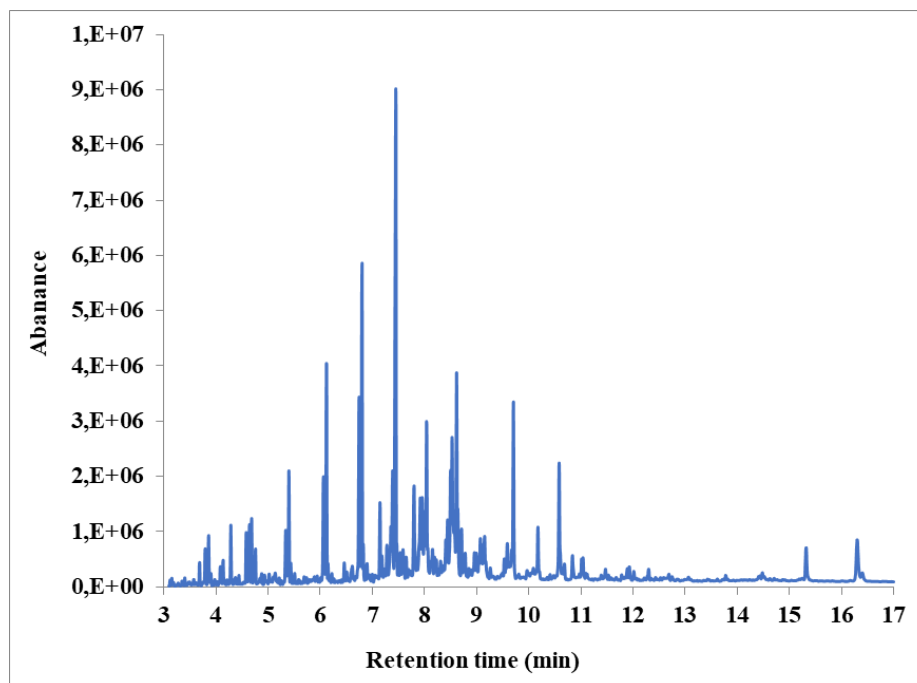


Figure 9. GC-MS Chromatograms of OLP

Table 15. The chemical compound in the oil yield product of cracking of PEFB on dolomite in continuous reactor

Time (min)	Name	Formula chemical	Area (%)
3.117	3-Nonene	C ₉ H ₁₈	0.06
3.147	2-Cyclopenten-1-one, 2-methyl-	C ₆ H ₈ O	0.09
3.182	cis-2-Nonene	C ₉ H ₁₈	0.04
3.269	Bicyclo[2.2.2]octane, 2-methyl-	C ₉ H ₁₆	0.05
3.343	Cyclohexane, propyl-	C ₉ H ₁₈	0.06
3.399	2-Cyclopenten-1-one, 3,4-dimethyl-	C ₇ H ₁₀ O	0.10
3.468	Cyclopentene, 1-butyl-	C ₉ H ₁₆	0.07
3.490	Cyclohexanone, 2-methyl-	C ₇ H ₁₂ O	0.08
3.568	Cyclohexene, 1-propyl-	C ₉ H ₁₆	0.09
3.681	Phenol	C ₆ H ₅ OH	0.28
3.763	2,4-Hexadienoic acid, ethyl ester (Ethyl sorbate)	C ₈ H ₁₂ O ₂	0.11
3.789	1-Decene	C ₁₀ H ₂₀	0.43
3.854	Decane	C ₁₀ H ₂₂	0.67
3.897	4-Decene	C ₁₀ H ₂₀	0.13
3.971	2-Decene, (Z)-	C ₁₀ H ₂₀	0.09
4.019	1-Tridecyne	C ₁₃ H ₂₄	0.05
4.132	D-Limonene	C ₁₀ H ₁₆	0.35
4.210	2-Cyclopenten-1-one, 2,3-dimethyl-	C ₇ H ₁₀ O	0.10
4.279	Phenol, 2-methyl-	C ₇ H ₈ O	0.73
4.348	Benzene, butyl-	C ₁₀ H ₁₄	0.08
4.435	Phenol, 3-methyl-	C ₇ H ₈ O	0.13
4.530	Cyclooctane, methyl-	C ₉ H ₁₈	0.09
4.578	1-Undecene	C ₁₁ H ₂₂	0.70
4.639	Undecane	C ₁₁ H ₂₄	0.85
4.678	5-Undecene	C ₁₁ H ₂₂	0.76
4.730	Phenol, 2,6-dimethyl-	C ₈ H ₁₀ O	0.14
4.752	5-Undecene	C ₁₁ H ₂₂	0.44
4.838	Cyclodecene, (Z)-	C ₁₀ H ₁₈	0.18
4.873	Cyclopentene, 1-butyl-	C ₉ H ₁₆	0.18
4.929	Phenol, 2-ethyl-	C ₈ H ₁₀ O	0.13
4.951	Cyclohexane, 2-propenyl-	C ₉ H ₁₆	0.06
5.016	Phenol, 2,3-dimethyl-	C ₈ H ₁₀ O	0.19
5.042	Cyclopentene, 1-pentyl-	C ₁₀ H ₁₈	0.06
5.064	8,10-Dodecadien-1-ol, (E,E)-	C ₁₂ H ₂₂ O	0.06
5.107	Cyclohexanol, 1-ethynyl-	C ₈ H ₁₂ O	0.19
5.133	Benzene, pentyl-	C ₁₁ H ₁₆	0.31
5.211	4-Methylphenyl acetone	C ₁₀ H ₁₂ O	0.09
5.246	Phenol, 3,5-dimethyl-	C ₈ H ₁₀ O	0.06
5.332	1-Dodecene	C ₁₂ H ₂₄	0.84
5.397	Dodecane	C ₁₂ H ₂₆	1.46
5.432	3-Dodecene, (Z)-	C ₁₀ H ₂₀	0.28
5.467	Phenol, 2,3,6-trimethyl-	C ₉ H ₁₂ O	0.06
5.506	2-Dodecene, (Z)-	C ₁₂ H ₂₄	0.17
5.584	Z-1,6-Undecadiene	C ₁₂ H ₂₀	0.07
5.606	Phenol, 2,3,5-trimethyl-	C ₉ H ₁₂ O	0.06
5.684	Phenol, 2-ethyl-4-methyl-	C ₉ H ₁₂ O	0.13
5.731	1-Tridecene	C ₁₃ H ₂₆	0.17
5.792	1,E-8,Z-10-Tridecatiene	C ₁₃ H ₂₂	0.12
5.818	p-Aminotoluene	C ₇ H ₉ N	0.05
5.840	2,4-Dodecadiene, (E,Z)-	C ₁₂ H ₂₂	0.07
5.883	Bicyclo[6.4.0]dodeca-9,11-diene	C ₁₂ H ₁₈	0.18
5.090	Phenol, 2-ethyl-4-methyl-	C ₉ H ₁₂ O	0.07
5.935	Benzene ethanol, .beta.-methyl-	C ₉ H ₁₂ O	0.14
6.004	Phenol, 2,3,4,6-tetramethyl-	C ₁₀ H ₁₄ O	0.12
6.056	1-Tridecene	C ₁₃ H ₂₆	1.59
6.117	Tridecane	C ₁₃ H ₂₈	2.97
6.143	3-Tridecene, (Z)-	C ₁₄ H ₂₈	0.24
6.217	2-Tridecene, (E)-	C ₁₄ H ₂₈	0.17
6.260	1H-Imidazole, 2-ethyl-	C ₅ H ₈ N ₂	0.08
6.455	Cyclopentane, (2-methylpropyl)-	C ₁₉ H ₁₈	0.33
6.503	Cyclopentene, 1-octyl-	C ₁₃ H ₂₄	0.21
6.642	1-Methyl-2-n-hexylbenzene	C ₁₃ H ₂₀	0.10
6.676	Cyclopentane, (2-methylpropyl)-	C ₉ H ₁₈	0.16
6.741	2-Tetradecene, (E)-	C ₁₄ H ₂₈	2.85

Time (min)	Name	Formula chemical	Area (%)
6.798	Tetradecane	C ₁₄ H ₃₀	4.62
6.819	3-Tetradecene, (Z)-	C ₁₄ H ₂₈	0.43
6.893	3-Tetradecene, (Z)-	C ₁₄ H ₂₈	0.27
6.941	Naphthalene, 1,6-dimethyl-	C ₁₂ H ₁₂	0.25
6.993	Cyclotetradecane	C ₁₄ H ₂₈	0.17
7.075	8-Hexadecyne	C ₁₆ H ₃₀	0.26
7.140	Cyclopentane, decyl-	C ₁₅ H ₃₀	1.08
7.179	Cyclopentene, 1-octyl-	C ₁₃ H ₂₄	0.48
7.275	Cyclohexene, 1-octyl-	C ₁₄ H ₂₆	0.69
7.353	Cyclopentadecane	C ₁₅ H ₃₀	1.44
7.383	1-Pentadecene	C ₁₅ H ₃₀	1.81
7.444	Pentadecane	C ₁₅ H ₃₂	9.24
7.491	1-Octadecyne	C ₁₈ H ₃₄	0.24
7.582	(1S)-(+)-Menthyl chloroformate	C ₁₁ H ₁₉ ClO ₂	0.85
7.643	Cyclohexane, (1-methylpropyl)-	C ₁₀ H ₂₀	0.47
7.726	Cyclohexene, 1,6-dimethyl-	C ₈ H ₁₄	0.33
7.795	n-Nonylcyclohexane	C ₁₅ H ₃₀	2.19
7.851	Cyclohexadecane	C ₁₆ H ₃₂	0.33
7.916	Cyclohexene, 1-nonyl-	C ₁₅ H ₂₈	2.33
7.955	Z-8-Hexadecene	C ₁₆ H ₃₂	1.56
7.994	Cetene	C ₁₆ H ₃₂	1.47
8.037	Hexadecane	C ₁₆ H ₃₄	2.36
8.059	Z-8-Hexadecene	C ₁₆ H ₃₂	0.51
8.116	Cyclopentane, (2-methylpropyl)-	C ₉ H ₁₈	0.41
8.189	Cyclopentene, 5-hexyl-3,3-dimethyl-	C ₁₃ H ₂₄	0.52
8.224	6-Methyl-bicyclo[4.2.0]octan-7-ol	C ₉ H ₁₆ O	0.37
8.259	Cyclodecanol	C ₁₀ H ₂₀ O	0.26
8.302	Trans-1-methyl-2-nonyl-cyclohexane	C ₁₀ H ₂₀	0.48
8.341	1-Methyl-2-methylenecyclohexane	C ₈ H ₁₄	0.36
8.441	Pentadec-7-ene, 7-bromomethyl-	C ₉ H ₃₁ Br	1.02
8.497	8-Heptadecene	C ₁₇ H ₃₄	2.15
8.528	8-Heptadecene	C ₁₇ H ₃₄	2.98
8.571	E-14-Hexadecenal	C ₁₆ H ₃₀ O	1.09
8.614	Heptadecane	C ₁₇ H ₃₆	3.12
8.636	E-14-Hexadecenal	C ₁₆ H ₃₀ O	1.19
8.705	8-Heptadecene	C ₁₇ H ₃₄	0.81
8.848	2-Methyl-Z-4-tetradecene	C ₁₅ H ₃₀	0.30
8.926	7-Octadecyne, 2-methyl-	C ₁₉ H ₃₆	0.21
8.952	Heptadecane, 2-methyl-	C ₁₈ H ₃₈	0.55
8.991	Cyclohexane, 2-propenyl-	C ₉ H ₁₆	0.72
9.039	5-Octadecene, (E)-	C ₁₈ H ₃₆	0.41
9.069	9-Octadecene, (E)-	C ₁₈ H ₃₆	0.71
9.087	9-Octadecene, (E)-	C ₁₈ H ₃₆	0.59
9.148	Octadecane	C ₁₈ H ₃₈	1.26
9.169	E-15-Heptadecenal	C ₁₇ H ₃₂ O	0.40
9.260	Cyclopentadecanone, 2-hydroxy-	C ₁₅ H ₂₈ O ₂	0.33
9.299	(R)-(-)-14-Methyl-8-hexadecyn-1-ol	C ₁₇ H ₃₂ O	0.24
9.395	7-Pentadecyne	C ₁₅ H ₂₈	0.22
9.473	Z,E-3,13-Octadecadien-1-ol	C ₁₈ H ₃₄ O	0.22
9.525	cis-11-Tetradecen-1-ol	C ₁₄ H ₂₈ O	0.37
9.559	1-Heneicosanol	C ₂₁ H ₄₄ O	0.22
9.585	9-Nonadecene	C ₁₉ H ₃₈	0.90
9.629	Z-5-Nonadecene	C ₁₉ H ₃₈	0.21
9.672	Hexadecane	C ₁₆ H ₃₄	0.68
9.702	2-Heptadecanone	C ₁₇ H ₃₄ O	2.69
9.772	1-Eicosene	C ₂₀ H ₄₀	0.15
9.806	Hexadecanoic acid, methyl ester	C ₁₇ H ₃₄ O ₂	0.18
9.963	13-Tetradecen-1-ol acetate	C ₁₆ H ₃₀ O ₂	0.44
10.045	1,19-Eicosadiene	C ₂₀ H ₃₈	0.20
10.084	Cyclopropanoethanal, 2-octyl-	C ₁₉ H ₃₆ O	0.46
10.171	Octadecan-4-one	C ₁₈ H ₃₆ O	1.14
10.348	7-Heptadecyne, 1-chloro-	C ₁₇ H ₃₁ Cl	0.11
10.405	Eicosane	C ₂₀ H ₄₂	0.17
10.578	Z,E-3,13-Octadecadien-1-ol	C ₁₈ H ₃₄ O	2.36
10.639	Octadecane	C ₁₈ H ₃₈	0.28
10.682	2-Nonadecanone	C ₁₉ H ₃₈ O	0.32

Time (min)	Name	Formula chemical	Area (%)
10.834	Oleic Acid	C ₁₈ H ₃₄ O	0.66
10.934	2-Dodecen-1-yl(-)succinic anhydride	C ₁₆ H ₂₆ O ₃	0.14
10.968	3,4-Octadiene, 7-methyl-	C ₉ H ₁₆	0.14
11.012	6-Octadecenoic acid	C ₁₈ H ₃₄ O ₂	0.37
11.094	Docosane	C ₂₂ H ₄₆	0.11
11.116	9-Octadecenoic acid, (E)-	C ₁₈ H ₃₄ O ₂	0.17
11.467	1-Tricosene	C ₂₃ H ₄₆	0.36
11.528	1-Chloroeicosane	C ₂₀ H ₄₁ Cl	0.09
11.571	.beta.-Piperidinopropiophenone	C ₁₄ H ₁₉ NO	0.08
11.887	Pyrrolidine, 1-(1-oxopentadecyl)-	C ₁₉ H ₃₇ NO	0.27
11.926	Benzene, 1-fluoro-4-methoxy-	C ₇ H ₇ FO	0.26
12.347	Eicosane	C ₂₀ H ₄₂	0.05
13.058	10-Nonadecanone	C ₁₉ H ₃₈ O	0.06
14.406	Cyclotrisiloxane, hexamethyl-	C ₆ H ₁₈ O ₃ Si ₃	0.10
14.432	Cyclotrisiloxane, hexamethyl-	C ₆ H ₁₈ O ₃ Si ₃	0.09
15.243	Silane, chlorodiethylheptyloxy-	C ₁₁ H ₂₅ ClOSi	0.09
16.396	13H-Dibenzo[a,i]carbazole	C ₂₀ H ₁₃ N	0.32

Figure 10 shows the concentration of CO₂, indicating that a significant fraction of oxygen from triglyceride fatty acid in palm oil was converted to CO₂ and short chain hydrocarbon molecules were generated. A possible reason for this phenomenon is that the higher temperature accelerated the thermal cracking and hence changing the long chain of hydrocarbon molecules to middle hydrocarbon and light hydrocarbon molecules [35-43]. Therefore light hydrocarbon molecules were thermally and catalytically cracked, converting them into gaseous product.

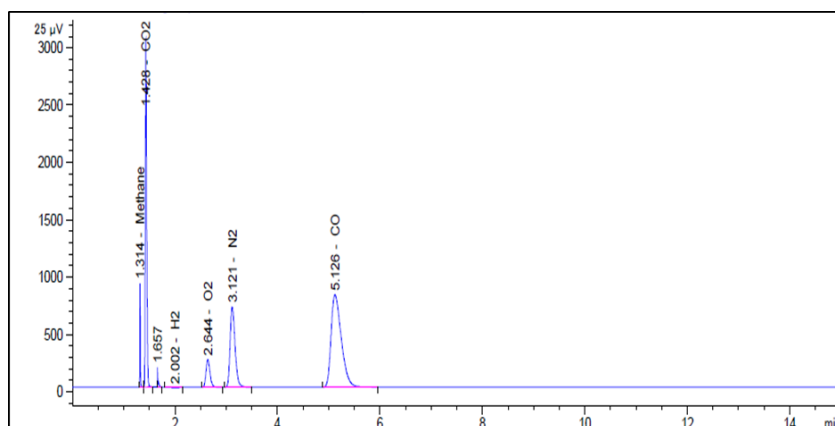


Figure 10. GC chromatograph of gas products from cracking of Palm oil from EFB on dolomite in continuous reactor

4. Conclusion

This research aimed to discover variables that significantly affect the catalytic cracking process of PEFB over dolomite in a continuous reactor and to find the optimum condition that will produce the maximum yield of organic liquid products (OLP) and diesel-like fraction. Using the 2^k factorial design, the researchers investigated the effects of reaction temperature, feed rate of palm oil, nitrogen gas flow rate and the amount of catalyst (v/v% by reactor volume) on the yield of OLP and diesel-like fraction, where the liquid products were obtained and analyzed by using distillation simulation gas chromatography and gas chromatograph mass-spectrometry to identify the structure of liquid fuels.

An analysis from a design-expert program indicated that the optimum conditions for the catalytic cracking of PEFB on dolomite in a continuous reactor were the following: a temperature of 460°C, feed rate of palm oil 8.96 mL/min, nitrogen gas flow rate of 50.04 mL/min, and the amount of catalyst 60% (v/v). These conditions led to the highest yield of diesel-like fraction of 66.12%wt and a liquid yield of 57.93%wt. It was found that basic catalyst gave a product with relatively low acid value. The results demonstrate that biofuel from catalytic cracking of PEFB has characteristics similar to those of petroleum fuels.

Acknowledgments

The authors wish to express their gratitude to Southern Palm (1978) Company Limited and Chulalongkorn University's Endowment Ratchadaphiseksomphot Fund for their financial support of this project.

References

- [1] Tani H, Hasegawa T, Shimouchi M, Asami K, Fujimoto K. Selective catalytic decarboxy-cracking of triglyceride to middle-distillate hydrocarbon. *Catalysis Today*, 2001; 164(1): 410-414.
- [2] Ulf S, Ricardo S, Rogério MV. Transesterification of vegetable oils: A review. *Journal of the Brazilian Chemical Society*, 1998; 9(1): 199-210.
- [3] Le TT, Kenj, O, Luu VB, Yasuaki M. Catalytic technologies for biodiesel fuel production and utilization of glycerol: A review. *Catalysts*, 2012; 2: 191-222.
- [4] Goyal G, Kuhn JN, Philippidis GP. Light alkene production by cracking *Picochlorum ocellatum* microalgae using aluminosilicate catalysts. *Biomass and Bioenergy*, 2018; 108: 252-257.
- [5] Ch Luadthong, P Khemthong, W Nualpaeng, K Faungnawakij. Copper ferrite spinel oxide catalysts for palm oil methanolysis. *Applied Catalysis A: General*, 2016; 525: 2016, 68-75.
- [6] Heuchel M, Reinhardt F, Merdanoğlu N, Klemm E, Traa Y. Co-catalytic cracking of n-decane and 2-ethylphenol over a variety of deactivated zeolites for the conversion of fossil- and bio-based feeds in Co-FCC. *Microporous and Mesoporous Materials*, 2017; 2017: 59-68.
- [7] Alipour R, Esfahani M, Osmieri L, Specchia S, Yusup S, Tavasoli A, Zamaniyan A. H₂-rich syngas production through mixed residual biomass and HDPE waste via integrated catalytic gasification and tar cracking plus bio-char upgrading. *Chemical Engineering Journal*, 2017; 308: 578-587.
- [8] Venkateswarulu TC, Cherukuwada V, Kodali VP, John DB, Ranganaha Reddy A, Indira M, Venkatanarayana A. A renew on methods of transesterification of oils and fats in bio-deisel formation. *International Journal of Chemtech Research*, 2010; 6(4): 2568-2576.
- [9] Santillan-Jimenez E, Loe R, Garrett M, Morgan T, Crocker M. Effect of Cu promotion on cracking and methanation during the Ni-catalyzed deoxygenation of waste lipids and hemp seed oil to fuel-like hydrocarbons. *Catalysis Today*, 2018; 302: 261-271.
- [10] Huiyan Z, Rui X, He H, Gang X. Comparison of non-catalytic and catalytic fast pyrolysis of corncob in a fluidized bed reactor. *Bioresource Technology*, 2009; 100(3):1428-34.
- [11] Itthibenchapong V, Srifa A, Kaewmeesri R, Kidkhunthod P, Faungnawakij K. Deoxygenation of palm kernel oil to jet fuel-like hydrocarbons using Ni-MoS₂/γ-Al₂O₃ catalysts. *Energy Conversion and Management*, 2017; 134: 188-196.
- [12] Galeano JD, Mitchell DA, Krieger N. Biodiesel production by solvent-free ethanolysis of palm oil catalyzed by fermented solids containing lipases of *Burkholderia contaminans*. *Biochemical Engineering Journal*, 2017; 127: 77-86.
- [13] Jung YH, Park HM, Park Y-Ch, Park K, Kim KH. Efficacy of pretreating oil palm fronds with an acid-base mixture catalyst. *Bioresource Technology*, 2017; 236: 234-237.
- [14] Wheeldon I, Christopher P, Blanch H. Integration of heterogeneous and biochemical catalysis for production of fuels and chemicals from biomass. *Current Opinion in Biotechnology*, 2017; 45: 127-135.
- [15] Alzate CAC, Toro JCS, Peña ÁG. Fermentation, thermochemical and catalytic processes in the transformation of biomass through efficient biorefineries. *Catalysis Today*, 2018; 302: 61-72.
- [16] GY Chen, R Shan, B-B Yan, J-F Shi, S-Y Li, Ch-Y Liu. Remarkably enhancing the biodiesel yield from palm oil upon abalone shell-derived CaO catalysts treated by ethanol. *Fuel Processing Technology*, 2016; 143: 110-117.
- [17] Shahbaz M, Yusup S, Inayat A, Patrick DO, Ammar M. The influence of catalysts in biomass steam gasification and catalytic potential of coal bottom ash in biomass steam gasification: A review. *Renewable and Sustainable Energy Reviews*, 2017; 73: 468-476.
- [18] Sudiyani Y, Styarini D, Triwahyuni E, Sembiring KC, Aristiawan Y, Abimanyu H, Han MH. Utilization of biomass waste empty fruit bunch fiber of palm oil for bioethanol production using pilot – scale unit. *Energy Procedia*, 2013; 32: 31-38.
- [19] Somrat K, Kongkaew L. 2011. Renewable energy from palm oil empty fruit bunch. *Renewable Energy from Palm Oil Empty Fruit Bunch*, Renewable Energy - Trends and Applications, Dr. Majid Nayeripour (Ed.), ISBN: 978-953-307-939-4.
- [20] Boonyawan Y, Parncheewa U, Buppa P. Hydration-dehydration technique for property and activity improvement of calcined natural dolomite in heterogeneous biodiesel production: Structural transformation aspect. *Applied Catalysis A: General*, 2011; 395: 87-94.

- [21] Nongbe MC, Ekou T, Ekou L, Yao KB, Le Grogne E, Felpin F-X. Biodiesel production from palm oil using sulfonated graphene catalyst. *Renewable Energy*, 2017; 106: 135-141.
- [22] McIntosh RM, Sharp JH, Wilburn FW. The thermal decomposition of dolomite. *Thermochimica Acta*, 1990; 165: 281-296.
- [23] Shan R, Shi J, Yan B, Chen G, Yao J, Liu Ch. Transesterification of palm oil to fatty acids methyl ester using K_2CO_3 /palygorskite catalyst. *Energy Conversion and Management*, 2016; 116: 142-149.
- [24] Korkut I, Bayramoglu M. Ultrasound assisted biodiesel production in presence of dolomite catalyst. *Fuel*, 2016; 180: 624-629.
- [25] Rapagnà S, Gallucci K, Foscolo PU. Olivine, dolomite and ceramic filters in one vessel to produce clean gas from biomass. *Waste Management*, 2018; 71: 792-800.
- [26] Yoosuk B, Udomsap P, Puttasawat B. Hydration-dehydration technique for property and activity improvement of calcined natural dolomite in heterogeneous biodiesel production: Structural transformation aspect. *Applied Catalysis A: General*, 2011; 395(1-2): 87-94
- [27] Quitete CPB, Souza MMVM. Application of Brazilian dolomites and mixed oxides as catalysts in tar removal system. *Applied Catalysis A: General*, 2017; 536: 1-8.
- [28] Qian H, Kai W, Hongde X. A novel perspective of dolomite decomposition: Elementary reactions analysis by thermogravimetric mass spectrometry. *Thermochimica Acta*. 2019; 676: 47-51.
- [29] Charusiri W, Vitidsant T. Upgrading bio-oil produced from the catalytic pyrolysis of sugarcane (*Saccharum officinarum* L) straw using calcined dolomite. *Sustainable Chemistry and Pharmacy*, 2017; 6: 114-123.
- [30] Otsuka T. Recent studies on the decomposition of the dolomite group by thermal analysis. *Thermochimica Acta*, 1986; 100: 69-80.
- [31] Pinthong Ch, Phoopraintra P, Chantiwas R, Pongtharangkul T, Chenprakhon P, Chaiyen P. Green and sustainable biocatalytic production of 3,4,5-trihydroxycinnamic acid from palm oil mill effluent. *Process Biochemistry*, 2017; 63: 122-129.
- [32] da Conceição LRV, Carneiro LM, Rivaldi JD, de Castro HF. Solid acid as catalyst for biodiesel production via simultaneous esterification and transesterification of macaw palm oil. *Industrial Crops and Products*, 2017; 89: 416-424.
- [33] Wheeldon I, Christopher P, Blanch H. Integration of heterogeneous and biochemical catalysis for production of fuels and chemicals from biomass. *Current Opinion in Biotechnology*, 2017; 45: 127-135.
- [34] Yang H, Chen Zh, Chen W, Chen Y, Wang X, Chen H. Role of porous structure and active O-containing groups of activated biochar catalyst during biomass catalytic pyrolysis. 2020: 210: 118646.
- [35] Ivan-Tan ChT, Islam A, Yunus R, Taufiq-Yap YH. Screening of solid base catalysts on palm oil based biolubricant synthesis. *Journal of Cleaner Production*, 2017; 48: 441-451.
- [36] Poosumas J, Ngaosuwan K, Quitain AT, Assabumrungrat S. Role of ultrasonic irradiation on transesterification of palm oil using calcium oxide as a solid base catalyst. *Energy Conversion and Management*, 2016; 120: 62-70.
- [37] Zhang B, Zhang L, Yang Zh, He Zh. An experiment study of biomass steam gasification over NiO/Dolomite for hydrogen-rich gas production. *International Journal of Hydrogen Energy*, 2017; 42: 76-85.
- [38] Boot-Handford ME, Virmond E, Florin NH, Kandiyoti R, Fennell PS. Simple pyrolysis experiments for the preliminary assessment of biomass feedstocks and low-cost tar cracking catalysts for downdraft gasification applications. *Biomass and Bioenergy*, 2018;108: 398-414.
- [39] Kannaiyan S, Madhavan VR, Rajagopal S, Jayabalan A. An experimental analysis on tar cracking using nano structured Ni-Co/Si-P catalyst in a biomass gasifier-based power generating system. *Applied Thermal Engineering*, 2016; 97: 13-21.
- [40] Promdee K, Vitidsant T. Preparation of Biofuel by Pyrolysis of PlantMatter in a Continuous Reactor. *Theoretical and Experimental Chemistry*, 2013; 49: 126 – 129.
- [41] Khuenkaeo N, MacQueen B, Onsree T, Daiya S, Tippayawong N, Lauterbach J. Bio-oils from vacuum ablative pyrolysis of torrefied tobacco residues. *RSC Advances.*, 2020; 10: 34986-34995.
- [42] Promdee K, Vitidsant T. Bio-oil synthesis by pyrolysis of Cogongrass (*Imperata cylindrica*). *Chemistry and Technology of Fuels and Oils*, 2013; 49: 287 – 292.
- [43] Auersvald M, Macek T, Schulzke T, Staš M, Šimáček P. Influence of biomass type on the composition of bio-oils from ablative fast pyrolysis. *Journal of Analytical and Applied Pyrolysis*, 2020; 150: 104838.

To whom correspondence should be addressed: Dr. Tharapong Vitidsant and Dr. Kittiphop Promdee, Center of fuels and Energy from Biomass, Chulalongkorn University, Saraburi 18110, Thailand, E-mail: nuumensci@gmail.com

Investigating the Impact of PVT Analysis Errors on Material Balance Calculations for Oil Reservoirs

A. Ragab¹ and E. M. Mansour²

¹ Reservoir Engineering Department, Agiba Petroleum Company, Cairo, Egypt

² Production Department, Egyptian Petroleum Research Institute, Cairo, Egypt

Received April 29, 2020; Accepted July 29, 2020

Abstract

Original hydrocarbons in place calculations using material balance equation are sensitive to the input data uncertainty, these inputs are production data, pressure data, and PVT data. In literature, most of research done to study the effect of input data uncertainty are focused on the production data uncertainties, but for the effect of PVT data uncertainty on MB calculations are rarely considered. This paper discusses the impact of PVT data uncertainty on MB calculations for volumetric oil reservoirs. In this work, the MB calculations for volumetric oil reservoirs are investigated versus PVT data errors. Synthetic errors are introduced into reservoir fluid properties that are used as inputs for the MBE such as oil formation volume factors, solution gas oil ratio, and bubble point pressure the amount synthetic errors introduced to all PVT parameters were $\pm 5\%$ and $\pm 10\%$ in order to account for typical PVT laboratories errors. The MB calculations were performed for different three volumetric oil reservoirs using the erroneous PVT data and the resulting OOIP values are compared to the base case of each reservoir. The average relative errors observed in the calculated OOIP for sample-01 from errors introduced to all PVT parameters $\pm 5\%$ and $\pm 10\%$ were -1%, -7%, 18%, 36%, respectively. In case for Sample-02 the relative errors for the same introduced errors were -16% and -20%, 21%, and 44%, respectively, while, in Sample-03 the relative errors were -26%, -44%, 31%, and 81%, respectively.

Keywords: Obomkpa coal; Organic macerals; Vitrinite; Pyrolysis; Combustion; Nigeria.

1. Introduction

Characterization of the reservoir is a vital step earlier before conducting any studies for reservoir simulation. This step is required to detect uncertainty range in reservoirs [1]. The material balance equation is a simple, efficient, and important tool for reservoir engineers [2]. Material balance methods are still usually used in analyzing performance of reservoirs and evaluation the OGIP and OOIP. The MB calculations require reservoir pressure, production, and PVT data in order to build a well-calibrated MB model that can be used for estimate the OHIP (oil and/or gas), identify the reservoir drive mechanism and its indices and predict the future performance of the reservoir pressure/production [3]. If any one of these input data has inaccuracies or errors, it will effect automatically on the output of the material balance equation [4]. The data quality of each input parameter for MBE is a vital concern. Usually, the oil and gas production data are measured inaccurate as the oil and gas company's revenues are based on these data [5]. However, the reservoir pressure measurements are quite limited and in some cases are questionable due to reservoir heterogeneities, some averaging procedures are used to compute the reservoir pressure history [6]. Reservoir pressure uncertainties and their effects on MB calculations have been investigated by many different researchers and well documented. Also, PVT data can be uncertain, due to the absence of a representative fluid sample for PVT analysis, sampling cost, and uncertainty of measurements or obtained data. Therefore in case of the absence of the experimental measurements, using empirical correlations instead for MB calculations is necessary [7]. Mc-Ewen used a statistical method to get

straight line equation through the origin thereby isolating the uncertainty in the dependent variable with minimum square fitting method was used to get results [8]. L. Mattar and R. McNeil presented method to evaluation original gas-in-place (OGIP). This method involves cumulative production versus a p/z plot of the flowing pressure. A straight line was drawn over the pressure data and at that time, a parallel line also was drawn over the reservoir pressure to get the original gas-in-place. [9]. Heather and Robert decided the uncertainty comes from some causes such as incomplete data sets, measurement errors, and mathematical model errors. error type can be reduced by using human effort and other perfect tools, but it will never be removed [10].

This paper will investigate the deviations of OOIP calculated by MBE against the introduced errors into all PVT data of three different reservoirs. For these different cases, the pressure and production data are assumed to be measured in an accurate manner and only the uncertainty of PVT data is considered.

2 Case Studies

Three reservoirs located in the Western Desert of Egypt were used in the MB calculations. These reservoirs are oil reservoirs contained different oils and the solution gas drive (depletion drive) is the dominant drive mechanism and no secondary recovery method is applied upon the study time. PVT data for each reservoir are acquired from the PVT laboratory analysis. Using the MBAL tool of the PETEX package is used to build the material balance models for each reservoir. The first reservoir contains black oil which has low gas-solution ratio (R_s) about 272 SCF/STB, 25 °API, and 1.2 oil formation volume factor (B_o). The second reservoir is containing a volatile oil which has gas-solution ratio (R_s) about 1,312 SCF/STB, 33 °API, and 1.7 oil formation volume factor (B_o), while the third one is containing more volatile oil which has gas-solution ratio (R_s) about 3,390 SCF/STB, 41 °API, and 2.7 oil formation volume factor (B_o). All of these reservoirs pressure went below the bubble point pressure (P_b) as per reservoir pressures measurements.

3. Methodology

The general material balance equation for an oil reservoir can be written in the following expression [11]:

$$F = N E_t + W_e$$

$$F = N_p (B_o - (B_g * R_s)) + B_g (G_p - G_i) + (W_p - W_i) B_w$$

$$E_t = (B_o - B_{oi}) + (R_{si} - R_s) B_g + m B_{oi} \left(\frac{B_g}{B_{gi}} - 1 \right) + (1 + m) B_{oi} \left[\frac{S_{wc} C_w + C_f}{1 - S_{wc}} \right] (P_i - P)$$

where, F : The underground withdrawal (RB), N : Original oil in place (STB), and E_t : The total expansion term of an oil and its dissolved gas, gas cap, connate water, and pore volume compaction.

The above equation explained the general material balance equation and its parameters which mainly pressure, production and PVT data [12]. There are many computer programs are used to perform the different calculations for the different forms of material balance equations that could be used according to the reservoir type (oil and/or gas) [13]. The work started with building the MBAL models of each reservoir using the base case PVT data, then using PVT cell in PVT lab in order to introduce synthetic errors in each PVT sample that used to test the impact of such errors on the OOIP estimated from MBE. The new PVT data sets were used to recalculate the MBE which resulted in a new OOIP estimation. The relative errors percentage for the different cases are calculated using the following equation;

$$\% \text{ error} = \frac{\text{trial value} - \text{base value}}{\text{base value}}$$

where, **trial value**; is the new calculated OOIP using the erroneous PVT data and **base value**; is the calculated OOIP using the original PVT data [14].

The original PVT parameters and the erroneous data are plotted on the plot for each parameter; the data for Reservoirs 01, 02 and 03 were summarized in Table 1, and the oil forma-

tion factor curves are shown in Figure 1, and the gas in solution ratio curves are shown in Figure 2. For Reservoir 02, the data summary is tabulated in Table 1, and the oil formation factor curves are shown in Figure 3, and the gas in solution ratio curves are shown in Figure 4. For Reservoir 03, the data summary is tabulated in Table 1, and the oil formation factor curves are shown in Figure 5, and the gas in solution ratio curves are shown in Figure 6.

Table 1. Summary for reservoirs 01,02, and 03

parameter	units	Reservoir 01	Reservoir 02	Reservoir 03
Reservoir pressure	psi	5,165	4,892	2,551
Reservoir temperature	°F	282	271	199
Rsi	SCF/STB	3,392	1,312	272
°API		41	32.7	25
Y _{gas}		1	0.89	1.02
CO ₂	Mole%	6	3.6	0.6
H ₂ S	Mole%	0	0.0	0.0
Bubble point	psi	3,392	4,452	1,015

Table 2. Models results for reservoirs 01, 02, and 03 MBAL

PVT data error	Reservoir 01		Reservoir 02		Reservoir 03	
	OOIP	Relative error	OOIP	Relative error	OOIP	Relative error
10%	10.7	-7%	14.8	-20%	4.7	-44%
5%	11.4	-1%	15.6	-16%	6.2	-26%
0%	11.5	0%	18.6	0%	8.4	0%
-5%	13.6	18%	22.5	21%	11.0	31%
-10%	15.7	36%	26.8	44%	15.2	81%

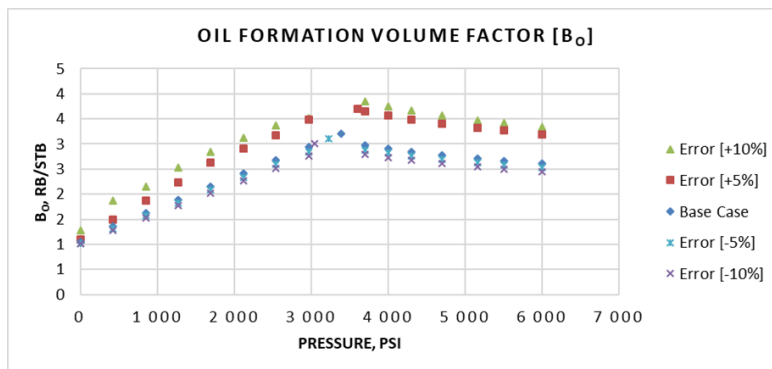


Figure 1. Oil formation volume factor for Reservoir 01; [Base case and erroneous PVT]

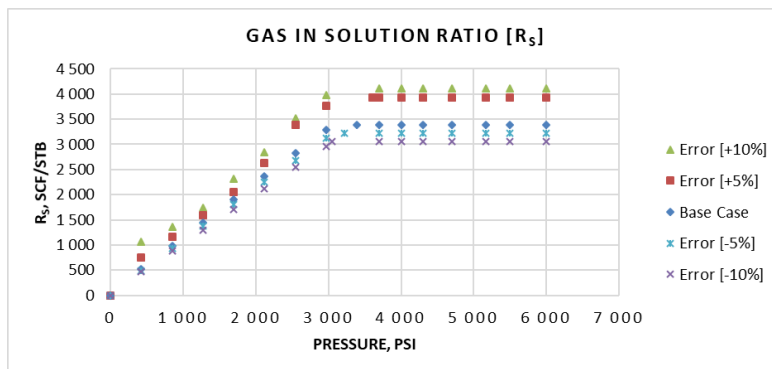


Figure 2. Gas in solution ratio for Reservoir 01; [Base case and erroneous PVT]

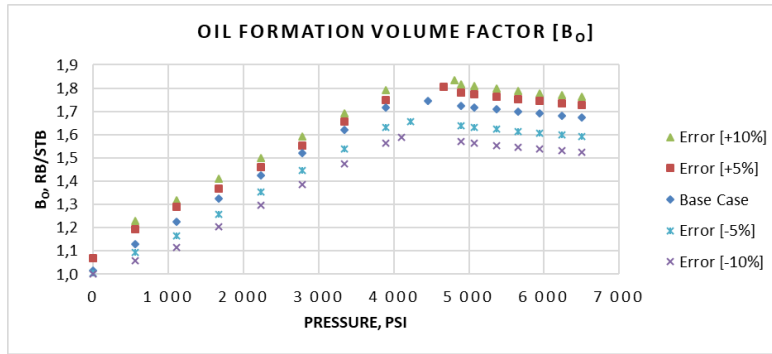


Figure 3. Oil formation volume factor for Reservoir 02; [Base case and erroneous PVT]

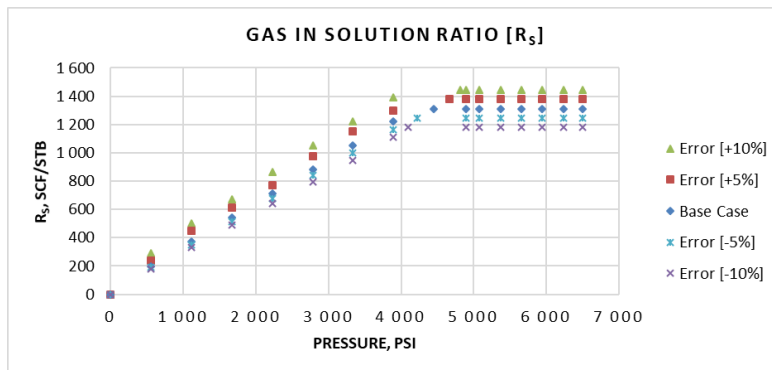


Figure 4. Gas in solution ratio for Reservoir 02; [Base case and erroneous PVT]

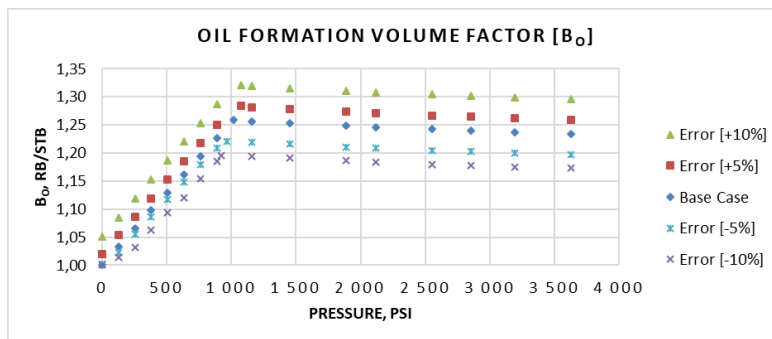


Figure 5. Oil formation volume factor for Reservoir 03; [Base case and erroneous PVT]

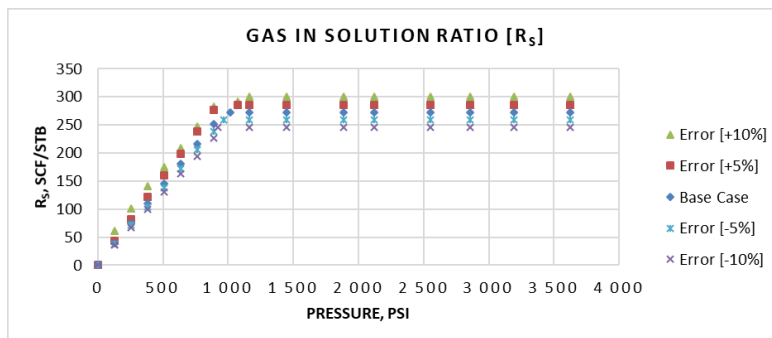


Figure 6. Gas in solution ratio for Reservoir 03; [Base case and erroneous PVT]

3. Results and discussion

3.1. For reservoir 01

It is a solution gas drive reservoir located in the Western Desert of Egypt, its initial pressure of 5,165 psi, the reservoir fluid is volatile oil as the B_o is greater than 2.0 RB/STB and the R_{si} is greater than 3,000 SCF/STB with an oil gravity up to 41°API. The average reservoir porosity is 10% and 20% initial water saturation. The reservoir was put on production in January 2008 and producing till now under the primary recovery. The OOIP as calculated from the base case model of MBAL is 11.5 MMSTBO and the reservoir has produced about 2.2 MMSTBO which about 19% recovery factor up to date of calculation. The introduced errors in all PVT parameters resulted in errors in the calculation of OOIP. Table 2 summarizes the MBAL results of the base model and introduced error models. We observed that the positive errors in PVT data resulted in lower calculated OOIP (+10% introduced error gives -7% relative error), on the other hand the negative errors resulted in higher calculated OOIP (-10% introduced error gives +36% relative error), which indicates the negative errors have larger impact than the positive ones.

3.2. For reservoir 02

It is a solution gas drive reservoir located in the Western Desert of Egypt, its initial pressure of 4,892 psi, the reservoir fluid is less volatile than Reservoir 01 as the B_o is about 1.6 RB/STB and the R_{si} is 1,250 SCF/STB with an oil gravity up to 33°API. The average reservoir porosity is 12% and 32% initial water saturation. The reservoir was put on production in August 2011 and producing till now under the primary recovery. The OOIP as calculated from the base case model of MBAL is 18.6 MMSTBO and the reservoir has produced about 1.03 MMSTBO which about 5.5% recovery factor up to date of calculation. The introduced errors in all PVT parameters resulted in errors in the calculation of OOIP. We observed that the positive errors in PVT data resulted in lower calculated OOIP (+10% introduced error gives -20% relative error), on the other hand the negative errors resulted in higher calculated OOIP (-10% introduced error gives +44% relative error), which indicates the negative errors have larger impact than the positive ones.

3.3. For reservoir 03

It is a solution gas drive reservoir located in the Western Desert of Egypt, its initial pressure of 2,552 psi, the reservoir fluid is black oil as the B_o is about 1.17 RB/STB and the R_{si} is 270 SCF/STB with an oil gravity up to 25°API. The average reservoir porosity is 12% and 32% initial water saturation. The reservoir was put on production in November 2014 and producing till now under the primary recovery. The OOIP as calculated from the base case model of MBAL is 8.4 MMSTBO and the reservoir has produced about 0.54 MMSTBO which about 6.4% recovery factor up to date of calculation. The introduced errors in all PVT parameters resulted in errors in the calculation of OOIP. We observed that the positive errors in PVT data resulted in lower calculated OOIP (+10% introduced error gives -44% relative error), on the other hand, the negative errors resulted in higher calculated OOIP (-10% introduced error gives +81% relative error), which indicates the negative errors have larger impact than the positive ones.

The general observation from the three reservoirs that the black oil is more sensitive for PVT data as its models have the highest errors in the calculated OOIP on both sides positive and negative introduced errors. In Figure 7, the resulted errors in the calculated values OOIP are plotted versus the introduced errors in PVT data and Figure 8 shows the calculated OOIP against the introduced errors in PVT data.



Figure 7. Relative errors in calculated OOIP vs. introduced errors in PVT data

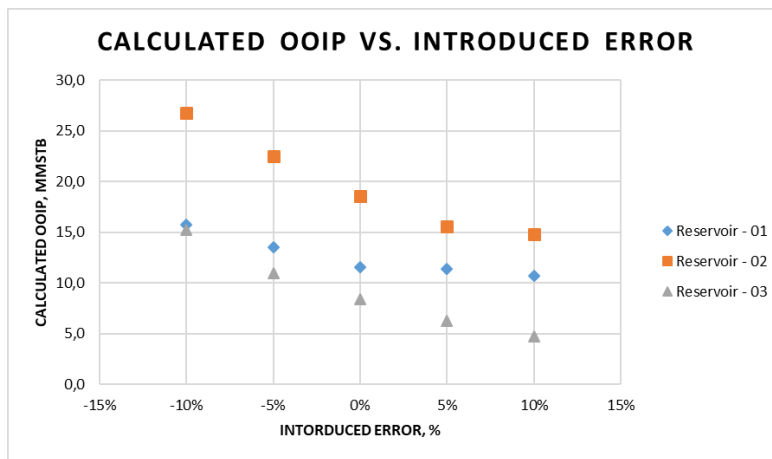


Figure 8 Calculated OOIP vs. introduced errors in PVT data

4. Conclusion

According to the work done in this research, the impact of PVT data errors on the calculated OOIP using MBE can be significant in all types of reservoir fluids and became badly on black oil reservoirs such as Reservoir 03 in this work. The PVT data should be calibrated with the production and pressure data (comparing the R_{si} from PVT analysis with the producing GOR) in order to make sure all of these data are in an agreement with each other which will help to reduce the uncertainties of the calculations of the MBE. In Figure 7, the resulted errors in the calculated values OOIP are plotted versus the introduced errors in PVT data and Figure 8 shows the calculated OOIP against the introduced errors in PVT data. The reservoir engineer should have a good understanding of the MBE assumptions, limitations, and calculations techniques and apply these concepts in order to get the best results of the MBE.

Nomenclature

PVT	Pressure-Volume – Temperature relationship
MB	Material Balance
MBE	Material Balance Equation
$OOIP$	Original Oil In-Place
$OHIP$	Original hydrocarbons In-Place
B_o	Oil Formation Volume Factor, RB/STB
B_{oi}	Initial Oil Formation Volume Factor, RB/STB
W_e	Water Influx, RB
N_p	Produced Oil Volume, STB

B_g	Gas Formation Volume Factor, CF/SCF
B_{gi}	Initial Gas Formation Volume Factor, CF/SCF
G_p	Produced Gas Volume, SCF
G_i	Injected Gas Volume, SCF
W_p	Produced Water Volume, BBL
W_i	Injected Water Volume, BBL
B_w	Water Formation Volume Factor, RB/STB
R_{si}	Initial Gas In Solution Ratio, SCF/STB
M	Gas Cap volume to Oil volume
S_{wc}	Connate Water Saturation, fraction
C_w	Water Compressibility Factor, psi^{-1}
C_f	Formation Compressibility Factor, psi^{-1}
P_i	Initial Reservoir Pressure, psi
P	Average Reservoir Pressure, psi
GOR	Gas To Oil Ratio, SCF/STB
MMSTBO	Million Stock Tank Barrel of Oil

Reference

- [1] Dmour HN, Bageri MS, and Kinawy MM. Investigating the Effect of Input Data Uncertainties in Material Balance Calculations for Hydrocarbon Reservoirs. *Journal of Industrial and Intelligent Information*, 2014; 2(4): 289-296.
- [2] Mansour E, Dessouky SM, Batanoni MH, Mahmoud MR, Frag AB, El-Dars F. Modification proposed for SRK equation of state. *Oil and Gas Journal*, 2012; 110(6): 78-91.
- [3] Imo-Jack O, and Emelle C. An Analytical Approach to Consistency Checks of Experimental PVT Data. in SPE Nigeria Annual International Conference and Exhibition. 2013. Society of Petroleum Engineers.
- [4] Esor E, Dresda S, and Monico C. Use of material balance to enhance 3D reservoir simulation: A case study. in SPE Annual Technical Conference and Exhibition. 2004. Society of Petroleum Engineers.
- [5] Ojo K, Tiab D, and Osisanya SO. Dynamic material balance equation and solution technique using production and PVT data. *Journal of Canadian Petroleum Technology*, 2006; 45(03):.
- [6] Ojo K, Tiab D, and Osisanya SO. Dynamic Material Balance Equation and Solution Technique Using Limited Pressure Data. in Canadian International Petroleum Conference. 2004. Petroleum Society of Canada.
- [7] Mansour EM, Farag AB, El-Dars FS, Desouky SM, Batanoni MH, Mahmoud MRM. Predicting PVT properties of Egyptian crude oils by a modified Soave–Redlich–Kowng equation of state. *Egyptian Journal of Petroleum*, 2013; 22(1): 137-148.
- [8] Dobbyn A, and Marsh M. Material balance: A powerful tool for understanding the early performance of the Schiehallion Field. in Offshore Europe. 2001. Society of Petroleum Engineers.
- [9] Aly MAEE. Reservoir characterization from material balance results analysis. in International Oil Conference and Exhibition in Mexico. 2007. Society of Petroleum Engineers.
- [10] Vega Riveros GL, Saputelli LA, Patino Perez JL, Chacon A, Solis R. Reserves Estimation Uncertainty in a Mature Naturally-fractured Carbonate Field Located in Latin America. in OTC Brasil. 2011. Offshore Technology Conference.
- [11] Caldwell RH, and Heather DI. Characterizing uncertainty in oil and gas evaluations. in SPE Hydrocarbon Economics and Evaluation Symposium. 2001. Society of Petroleum Engineers.
- [12] Ireke IU, and Princewill M. Impact of PVT Correlations on Reserve Estimation: Reliability and Qualitative Analysis. in SPE Nigeria Annual International Conference and Exhibition. 2017. Society of Petroleum Engineers.
- [13] Garcia CA, and Villa JR. Pressure and PVT Uncertainty in Material-Balance Calculations. in Latin American & Caribbean Petroleum Engineering Conference. 2007. Society of Petroleum Engineers.
- [14] Stephen AG, Bergman DF, Dodd T, Kriel W. PVT Data Quality: Round Robin Results. in SPE Annual Technical Conference and Exhibition. 2008. Society of Petroleum Engineers.

To whom correspondence should be addressed: A. Ragab, Reservoir Engineering Department, Agiba Petroleum Company, Cairo, Egypt, E-mail: aragab89@outlook.com

Estimation of Original Oil in Place Using Pickett's and Buckle's Plots, Offshore Niger Delta, Nigeria

Agbasi E. Okechukwu^{1*}, Etuk E. Sunday², Abdulaziz M. Abdulaziz³, Joseph I. Namdie², Robert W. Ubong⁴

¹ Department of Physics, Michael Okpara University of Agriculture, Umudike, Nigeria

² Department of Physics, University of Uyo, Uyo, Nigeria

³ Mining, Petroleum, and Metallurgical Engineering Department, Faculty of Engineering, Cairo University, Giza 12316, Egypt

⁴ Department of Physics, Akwa Ibom State University, Ikot Akpaden, Mkpato Enin, Nigeria

Received May 22, 2020; Accepted September 23, 2020

Abstract

Quick look analysis was performed in five (5) wells across a depobelt in the Niger Delta region, Nigeria using lithology (gamma), porosity (sonic, neutron and density) and saturation (resistivity) logs to infer six possible hydrocarbon plays. These plays showed good hydrocarbon saturation with a thickness between 11ft (3.35m) and 120ft (36.58m) that occur at a depth from 6223.5ft (1896.93m) to 11216.5ft (3418.79m). The average estimated porosity falls between 21.8% to 33.7% and the average volume of shale reported between 0.072 to 0.187, indicating sandstone reservoirs with good porosity. Water saturation was then estimated using Archie and modified Archie's equations from Pickett's plot. The original oil in place (OOIP) derived from Archie's (445.299 bbl. to 1488.735 bbl.) and Pickett's (150.120 bbl. to 1290.596 bbl.) techniques were compared showing a percentage difference between 5.30% to 86.28%. Archie's equation overestimated the original oil in place (OOIP) values across the reserves in the study area. Porosity exponent from Pickett's was between 1.74 to 2.09 as compared to Archie's constant of 2. The variation of the porosity exponent across the study area is attributed to the variations in shape of grains and pores, type of grain, pore system and overburden pressure. This influence is clearly seen from the Buckle's plot, which was used to delineate the variation using Buckle's number, and subsequently compared with the standard values for sandstones. This study highlighted the importance of porosity exponent and apparent formation water resistivity for estimation of water saturation, formation factor and in consequence the reserves.

Keywords: Buckle's Plot; Pickett's Plot; Niger Delta; Original Oil in Place.

1. Introduction

According to Adebayo *et al.*, [1], the application of Archie's equation is used to determine the formation factor F , where the formation factor of rock is defined as the ratio of rock resistivity when 100% saturated by brine, R_o , to the brine water resistivity, R_w [2-3]. According to Archie [4], the value of the formation resistivity factor (F) for any given rock sample will remain essentially constant for a wide range of formation water resistivity (R_w) measured in reservoir rocks. In routine formation evaluation, the primary goal typically involves reasonable determination to the OOIP. Archie's parameters a , m and n are normally set respectively to the default values of 1, 2 and 2 in the carbonate reservoirs and 0.62, 2.15 and 2 in the sandstone reservoirs with the water saturation exponent (n) equals 2 only in a water-wet homogeneous reservoir [5]. However, in heterogeneous reservoirs the water saturation exponent (n) typically varies from 20 in highly oil-wet reservoir to 2 in considerably water-wet reservoir conditions [6-7]. The wettability represents an important parameter in partial water saturation of the core sample [8-9].

Oil discoveries was aided by geologist, geophysicist and petroleum engineers (as well as some sort of good luck), all of the assessments of the volume of hydrocarbon reserves were made using data from petrophysical measurements together with a set of relationship that originated with Archie's water saturation equation [4]. Archie's equation presents a relationship between electrical resistivity of a rock to its porosity and the fractional water saturation of the pore space [10]. These are used to calculate the hydrocarbon saturation of the reservoir rock from which the reserves are inconsequence calculated. Archie's equation contains two exponents, porosity exponent (m) and saturation exponent (n), the conductivity of the hydrocarbon saturated rock is highly sensitive to changes in both exponent [11].

Determination of Archie's parameters is very important, as determination of recoverable hydrocarbon in a place is the main goal of the formation evaluation process [12-13]. The common practice in formation evaluation is to held Archie's parameter constant in sandstone reservoirs [14-15]. Pickett plot (Resistivity-Porosity Relationship) technique is utilized for calculating reservoir petrophysical exponents [16]. This plot shows a useful model for putting together the petrophysical parameters including water saturation, permeability, capillary pressure, pore throat radii and height above free water level [17-18]. This technique highlights Pickett's plot as one of the most important plots for reservoir evaluation, where several keys of geological and reservoir engineering parameters are evaluated in one plot. Estimation of petrophysical exponents greatly affect the estimation of water saturation and consequently reservoir productivity, therefore it is important to accurately evaluate these exponents [19-20]. Porosity exponent is affected by several influences including shape of grains and pores, types of grains, pore system etc. [21-23], this influences lead to the use of Buckle's ploy to confirm the porosity exponent values.

In 2018, there were approximately 1.73 trillion barrels of oil in the world, enough to secure energy supply for another 50 years since the world uses 95 million barrels per day [24]. Nigeria has 37,062 million of barrels as 2018 reserves [24].

Even a tiny uncertainty in a saturation exponent of 2, say 0.01, (*i.e.* 0.5 % or 2 ± 0.01) would result in an error in the reserve calculations of about USD ± 254.36 billion [25]. When $n = 2 \pm 0.01$ is considered, a change of ± 0.3245 % in hydrocarbon saturation is calculated, allowing a change in global reserves to be recalculated. However, the degree to which we can carry out the real calculations does not match this precision. Uncertainty in input parameters of representative seismic and petrophysical parameters together with the difficulties of heterogeneity and anisotropy in the real calculations have uncertainty in the order of $\pm 20-40$ % [25].

It is interesting that the uncertainty in reserve estimate is controlled by a choice of petrophysical exponent and constant. This work demonstrates a statistical analysis of such uncertainty and highlights the result of error propagation in reserve estimate. In addition, the statistical approach allows a comparative study on the effect of Archie's derived exponent and estimated exponent on reserve estimate.

2. Geology of the study area

The Niger Delta Province includes Nigeria, Cameroon and the Equatorial Guinea. This province is situated in the Gulf of Guinea with one petroleum system, identified so far, and designated in Nigeria as the Tertiary Niger Delta (Akata-Agbada) petroleum system [26]. Tuttle [27] outlined the formation of the Niger Delta at a rift triple junction related to the opening of the southern Atlantic started in the Late Jurassic and continued up to the Cretaceous. The proper delta is developed in the Eocene with accumulating sediments over 10 kilometres thick. The primary source rock is the upper Akata Formation, marine-shale facies of delta with possibly a contribution from interbedded marine shale of the lower most Agbada Formation [26].

The Niger Delta covers an aerial stretch over 70,000 km² within the Federal Republic of Nigeria, representing about one-fourteenth of the total land mass of the country. The Niger Delta Province remains the youngest of three depositional cycles leading to the development of the coastal sedimentary basin of Nigeria with three stratigraphic subdivisions, namely the Benin Formation, the Agbada Formation and the Akata Formation [28].

Lithologically, the upper portion of the Niger Delta Province (Benin formation) is mainly sandstone while the middle Agbada formation comprises an intervening unit of alternating sandstone and shale with the lower Akata formation, predominantly shale [29]. According to Short and Stauble [30], three units extending across the entire delta are related to the present outcrops and environments of deposition and represent prograding depositional facies that are distinguished mostly based on sand-shale ratios.

Tuttle *et al.*, [27] investigated the hydrocarbon potential of the Niger Delta and indicated that the Niger Delta petroleum is produced from sandstone and unconsolidated sands predominantly in the Agbada Formation that are controlled by depositional environment and depth of burial. In 1999, the Niger Delta Province of Nigeria was estimated to hold recoverable oil and gas of approximately 35 billion barrels (bbl.) of oil and 94 trillion standard cubic feet (ft³) of gas.

3. Methodology

This work uses five well log data in the Niger Delta Region, Nigeria with six potential oil and gas reservoirs were identified. Log data include Gamma Ray, Compensated Neutron, Sonic, Resistivity (Deep) and Density logs.

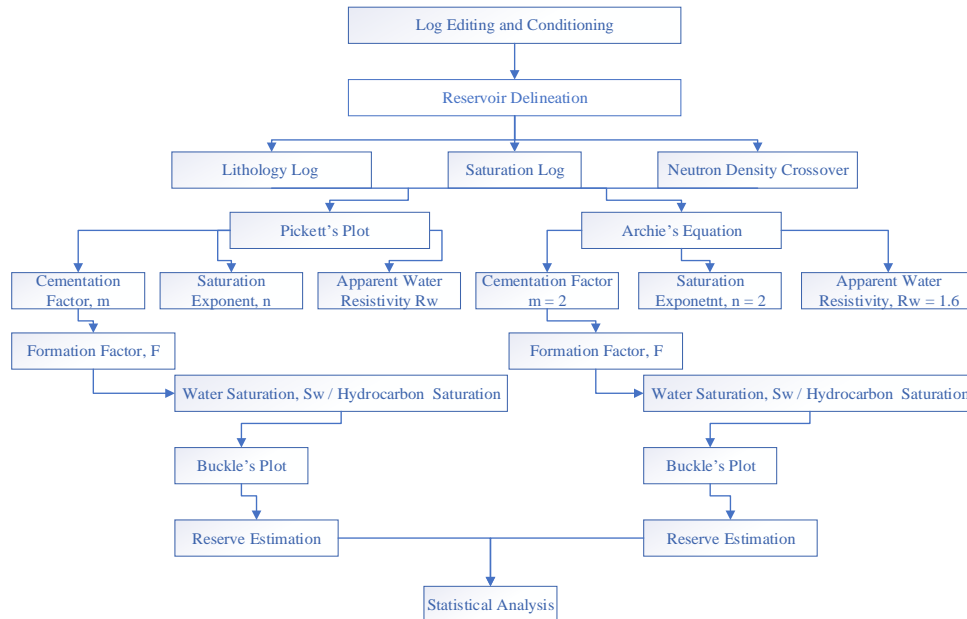


Fig. 1. A flowchart for Reserve Estimation from Pickett's plot and Archie's Equation

Original oil in place (OOIP) and original gas in place (OGIP) refer to the total volume of hydrocarbon stored in a reservoir prior to production. Volumetric estimates of OOIP and OGIP are based on a geological model that geometrically describes the volume of hydrocarbons in the reservoir.

One basic volumetric equation is

$$OOIP = \frac{7758Ah\phi(1-S_w)}{B_{oi}} \quad (1), \text{ or}$$

$$OOIP = \frac{7758V_b\phi(1-S_w)}{B_{oi}} \quad (2)$$

where, N = OOIP (STB); 7758 = conversion factor from acre-ft to bbl; A = area of reservoir (acres) from map data; h = height or thickness of pay zone (ft) from log and/or core data; V_b = bulk reservoir volume; φ = porosity (decimal) from log and/or core data; S_w = connate water saturation (decimal) from log and/or core data; B_{oi} = formation volume factor for oil at initial conditions (reservoir bbl/STB) from lab data; a quick estimate is B_{oi} = 1.05 + (N × 0.05), where N is the number of hundreds of ft³ of gas produced per bbl of oil [for example, in a well with a GOR of 1000, B_{oi} = 1.05 + (10 × 0.05)].

Pickett plots [31-32], have been long recognized as very useful technique in log interpretation. In Pickett's method, a resistivity index, "I", and water saturation, "S_w" are calculated from log-log plots of true (in some cases apparent) resistivity versus porosity or response of a porosity tool. This technique not only gives estimation of water saturation (S_w), but also helps in determination of Formation water resistivity (R_w), Cementation factor "m", and matrix parameters for porosity logs (Δt_{ma} and ρ_{ma}). The Pickett method is based upon the observation that true resistivity (R_t) is a function of porosity, water saturation (S_w), and cementation factor "m". The Pickett cross plot developed by plotting porosity values with deep resistivity values on two-by- three cycle log-log paper. The theory of this plot started with Archie's equation, as follows:

$$S_w = I^{-\frac{1}{n}} \tag{3}$$

$$I = \frac{R_t}{R_o} = \frac{R_t}{F \times R_w} \tag{4}$$

$$F = \frac{a}{\phi^m} \tag{5}$$

Equations 3, 4 and 5 can be combined to yield.

$$R_t = \frac{aR_w}{\phi^m} (I) \tag{6}$$

$$R_t = \frac{aR_w}{\phi^m} (S_w^{-n}) \tag{7}$$

If the logarithm with base 10 has been taken, the equation [31] leads to:

$$\log R_t = \log(aR_w) - \log(\phi^m) + \log I \tag{8}$$

$$\log R_t = \log(aR_w) - m \log(\phi) + \log I \tag{9}$$

This is the equation of a straight line, on log -log paper, can be written in the form:

$$y = mx + b \tag{10}$$

According to equation 9, a plot of log R_t vs. log φ can be drawn in a straight line with a negative slope controlled by "m", where m = 1/slope. The slope is determined manually by measuring a distance on the R_t axis (in cm) and dividing it by the corresponding distance on the porosity axis. The value of (aR_w) is derived from the intercept of such a line with the porosity axis at φ = 1.

Using this convention, the intercept is equated directly with R_w, and the slope of m becomes an average estimate of cementation factor within the reservoir.

Calculations of water saturation from either the Archie equations or the Pickett plot when combined with porosity give values which describe the volume of water and hydrocarbon as a fraction of either pore space or the total rock volume. The bulk volume of water (BVW) is a useful measurement controlled by both pore size and possible position in the hydrocarbon column, and can improve predictions of fluid productivity.

Buckles, [33] made an extensive numerical analysis of reservoir measurements and concluded that the quadrilateral hyperbolic function was a good first-order approximation to real field data. Low values of C (Buckle's number) reflected large average pore sizes, as a direct consequence of a control by internal surface area. The quantity C, is simply the irreducible bulk volume of water (BVW_i) which will be effectively a constant, provided that there is a limited range in pore size. Zones with comparable pore size that have higher values of bulk water volume should be the water-cut or totally water-bearing. When computed for a field or a reservoir, the characteristic value is often known as the "Buckles number".

Pickett, [32] had recognized that reservoir zones at irreducible water saturation tend to lie on a steeper linear trend, whose intercept with the water line reflected the grain- or pore-size. This observation reflects the fact that the hyperbolic relationship of:

$$C = \phi \times S_w \tag{11}, \text{ can be linearized to}$$

$$\log S_w = \log C - \log \phi \tag{12}$$

Substituting the Archie equation solution for water saturation and rearranging, the relationship becomes:

$$\log R_t = \log(aR_w) - n \log C + (n - m) \log \phi \tag{13}$$

Equation 13 describes a line on the Pickett plot with a slope of $(n - m)$ and an intersection with the water line at a porosity corresponding to the water line.

4. Results of analysis

Results of petrophysical analysis for six (6) potential reservoirs from five (5) wells in a field in of the Niger Delta Region are presented with log panels and cross plotting. A cross plot of Pickett’s and Buckle’s was generated from constants of Archie’s equation and Pickett’s plot for all potential reservoirs. A summary of petrophysical results for each reservoir is presented in Table 1 and showing minimum and average values of gamma ray, neutron, density, sonic, resistivity, porosity and volume of shale at a given depth interval and net pay zone. Table 2 presents the minimum and average values of bulk volume of water, hydrocarbon and water saturation, and Buckle’s Number for Pickett’s and Archie’s values for each identified reservoir in the well(s).

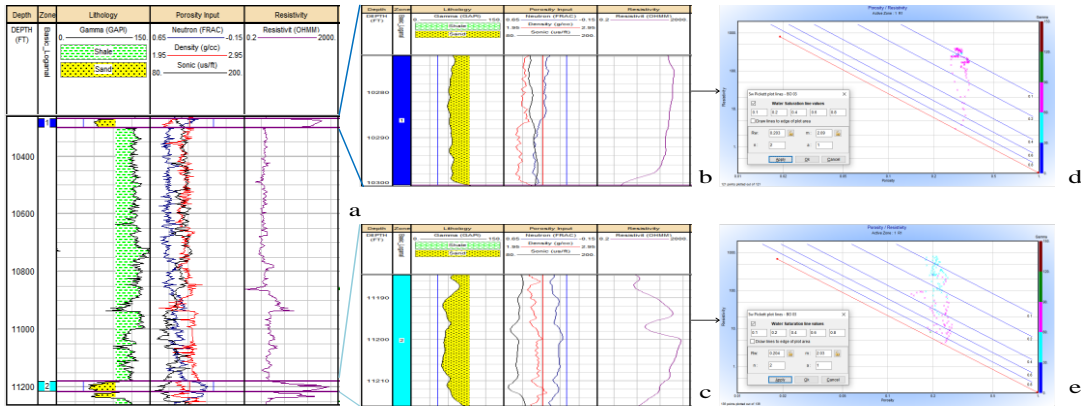


Fig. 2 (a) Basic log view for sand units in well A01 (b) Reservoir A01 R1 (c) Reservoir A01 R2 (d) Pickett’s plot for A01 R1 (e) Pickett’s plot for A01 R2

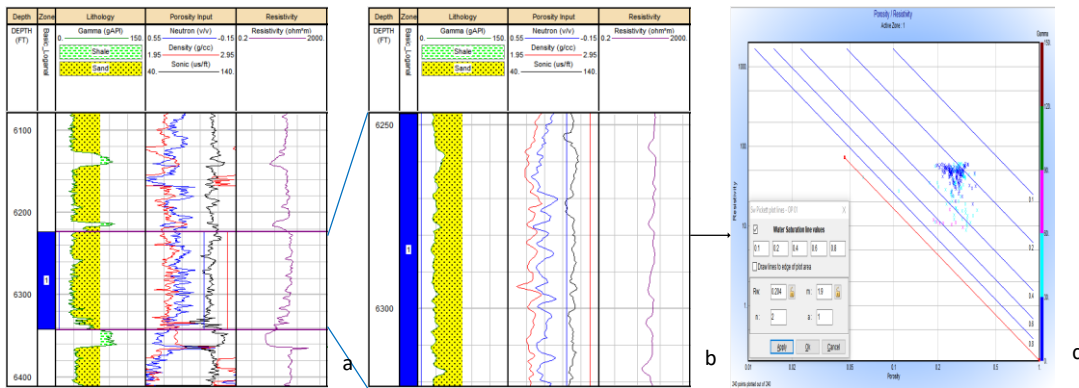


Fig. 3. (a) Basic log view for sand units in well A02 (b) Reservoir A02 R1 (c) Reservoir Pickett’s plot for A02 R1

Well A01 show two distinct Petro-facies within the reservoir’s interval, were identified between 10270 – 10300ft and 11182.75 – 11216.5ft, Well A01 shows a sandstone sequence with various thick shale bed. Reservoirs A01 R1 and A01 R2 have a mean gamma ray value of 64.897 and 61.68gAPI, mean resistivity value of 215.825 and 195.687 ohmm respectively. A distinct Petro-facies within the interval 6233.5 – 6343ft, was identified in Well A02 and shows a sandstone sequence with various thick shale bed. A02 R1 has a mean gamma ray value of 31.775gAPI, mean resistivity value of 40.916 ohmm. Well A03 shows a distinct Petro-facies w (9269.5 – 9289ft) within Well A03 of sandstone sequence with various thick shale bed. The reservoir A03 R1 has a mean gamma ray value of 28.262gAPI and mean resistivity value of 1.639 ohmm. Well A04 show a sandstone interval between 8904 – 8914.5ft, with a shaly sequence of various thick sand sequence. Reservoir A04 R1 has a mean gamma ray

value of 74.006 gAPI, and a mean resistivity value of 13.143 ohmm. Petrophysical analysis on well A05 detected one reservoir at interval 9402.5 - 9438ft. Well A05 show a shaly sequence with various thick shale sequence with a mean gamma ray value of 35.026 gAPI and mean resistivity value of 197.963 ohmm. The net pay zone in all the reservoirs is between 11 – 120 ft indicating a viable economical hydrocarbon potential.

Table 1. Basic log values for two identified reservoirs in well A01, A02, A03, A04 and A05

		Curve	Gamma	Neutron	Density	Sonic	Resistivity	Porosity	Volume of shale
		Units	gAPI	frac	g/cc	us/ft	ohmm	Dec	Dec
A01 R1	Top:10270ft Bottom:10300 Net:30.25	Min	58.369	0.244	2.077	111.612	2.963	0.26	0.133
		Max	89.48	0.407	2.215	123.314	391.928	0.343	0.389
		Mean	64.897	0.332	2.143	116.677	215.825	0.303	0.187
A01 R2	Top:11182.75 Bottom:11216.5 Net:34	Min	49.122	0.146	2.2	84.758	4.056	0.143	0.056
		Max	93.083	0.3	2.408	106.852	788.237	0.267	0.419
		Mean	61.68	0.206	2.286	98.074	195.687	0.218	0.16
A02 R1	Top: 6223.5ft Bottom: 6343ft Net: 120ft	Min	21.062	0.106	2.023	88.743	8.915	0.062	0.104
		Max	78.881	0.422	2.538	123.9	61.126	0.374	0.488
		Mean	31.775	0.29	2.199	111.032	40.916	0.267	0.175
A03 R1	Top: 9269.5ft Bottom: 9289ft Net: 20ft	Min	17.739	0.325	1.936	112.86	1.522	0.283	0
		Max	35.358	0.421	2.185	128.949	2.048	0.434	0.121
		Mean	28.262	0.373	2.095	120.531	1.639	0.337	0.072
A04 R1	Top: 8904ft Bottom 8914.5ft Net 11ft	Min	69.774	0.139	1.852	100.969	2.031	0.313	0.36
		Max	84.63	0.37	2.121	116.153	25.389	0.475	0.448
		Mean	74.006	0.21	1.951	107.812	13.143	0.416	0.385
A05 R1	Top: 9402.5ft, Bottom: 9438.5ft, Net: 36.5ft	Min	22.628	0.079	2.009	87.804	4.355	0.18	0.051
		Max	72.436	0.247	2.337	99.165	804.01	0.386	0.287
		Mean	35.026	0.119	2.113	92.737	197.963	0.322	0.11

Table 2. Mean bulk volume of water, water and hydrocarbon saturation values in well A01, A02, A03, A04 and A05

		Archie's	Pickett's			Archie's	Pickett's
A01 R1	BVW	0.03	0.045	A03 R1	BVW	0.247	0.306
	Sw	0.099	0.149		Sw	0.736	0.911
	Sh	0.901	0.851		Sh	0.264	0.089
A01 R2	BVW	0.046	0.068	A04 R1	BVW	0.11	0.157
	Sw	0.208	0.304		Sw	0.285	0.404
	Sh	0.792	0.696		Sh	0.715	0.596
A02 R1	BVW	0.054	0.071	A05 R1	BVW	0.049	0.065
	Sw	0.206	0.273		Sw	0.18	0.239
	Sh	0.794	0.727		Sh	0.82	0.761

Table 1 shows the minimum, maximum and mean values of lithology log (gamma), saturation log (resistivity), porosity log (neutron, density and sonic), porosity and volume of shale values. The porosity values are seen to decrease with depth, while the volume of shale

(18.7%, 16.0%) values confirms with the gamma ray (64.897 gAPI, 61.680 gAPI) values as high values indicates sand units in both reservoirs in well A01. For well A02, the volume of shale (mean 17.5%) confirms with the gamma ray (mean 31.755gAPI) as high sand units in the reservoir. The volume of shale (mean 7.2%) confirms with the gamma ray (mean 28.262 gAPI) as high sand units in both of the reservoir in well A03. For well A04, the volume of shale (mean 38.5%) confirms with the gamma ray (mean 74.006gAPI) as high sand units in the reservoir. The volume of shale (mean 11.0%) values confirms with the gamma ray (mean 35.026gAPI) values as high sand units for the reservoirs in well A05.

The Pickett's plot (Figures 2d, 2e and 3c) is a crossplot of resistivity against porosity, with water saturation lines of 0.1, 0.2, 0.4, 0.6 and 0.8. At 100% porosity the intercept on the Resistivity axis is the apparent formation water resistivity (R_w) while the slope of the crossplot is the porosity exponent (m), assuming saturation constant (n) equal 2 and tortuosity (a) equals 1. The values of apparent formation water resistivity (R_w) is 0.204 for most of the reservoirs in the study area, exception of reservoir A03 R1. The estimated porosity exponent (m) are 2.03 for A01 R1 and 2.09 for A01 R1, 1.90 for A02 R1, 1.72 for A03 R1, 1.99 for A04 R1 and 1.89 for A05 R1.

Table 2 shows the mean bulk volume of water, water and hydrocarbon saturation for Archie's equation and Pickett's plot for all the reservoirs in the study area. For well A01, Buckle's plots for these reservoirs was plotted using the calculated water saturation from Archie's equation and Pickett's plot. Porosity range of 21.8 – 30.0% are corresponding to water saturation of 9 – 20.8% (Archie's equation) and 14.9 – 30.4% (Pickett's plot). Most of the plotted points cluster around Buckle line of 0.02 – 0.04, representing coarse to medium grain sandstone. For well A02, Buckle's plots for this reservoir was plotted using the calculated water saturation of Archie's equation and Pickett's plot. Porosity of 26.7% corresponded to water saturation of 20.6% (Archie's equation) and 27.3% of (Pickett's plot). Most points clustered around Buckle lines of 0.06 – 0.08, indicating fine grain sandstone. For well A03, Porosity of 33.7% is equivalent to water saturation of 73.6% (Archie's equation) and 91.1% (Pickett's plot) and the data points clustered around Buckle lines above 0.18, characterizing very fine grain sandstone. In well A04, Porosity of 41.6% calculated water saturation of 28.5% of (Archie's equation) and 40.4% (Pickett's plot). Most of the points are clustered around Buckle line of 0.08, representing fine grain sandstones. For well A05, Buckle's plots for this reservoir was plotted using the calculated water saturation from Archie's equation and Pickett's plot. Porosity range of 32.2% corresponding to 18.0% of water saturation (Archie's equation) and 23.9% of water saturation (Pickett's plot) of water saturation. Most of the points are clustered around Buckle line of 0.02, which represent coarse grain sandstones.

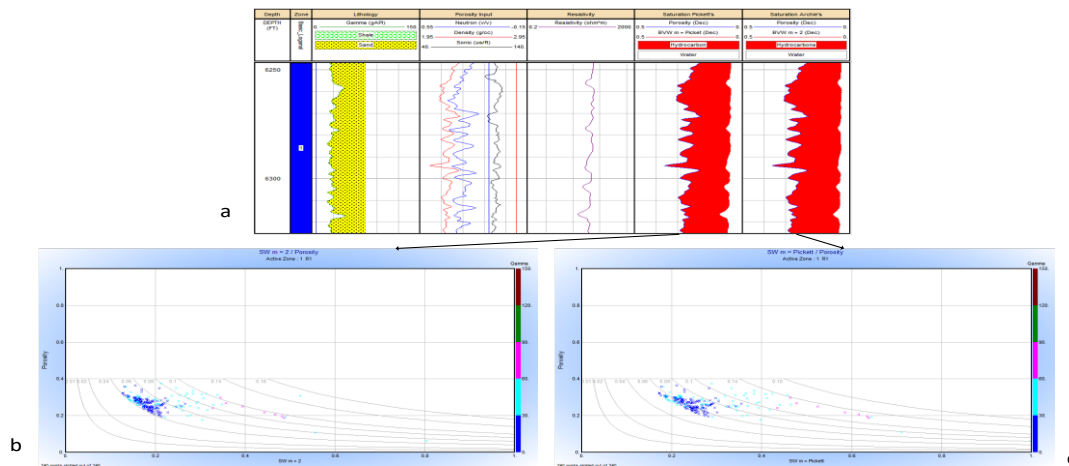


Fig. 4 (a) Comparative plot of saturation calculated from Archie's and Pickett's exponent, A02 (b) Archie's Buckle plot A02 (c) Pickett's Buckle plot A02

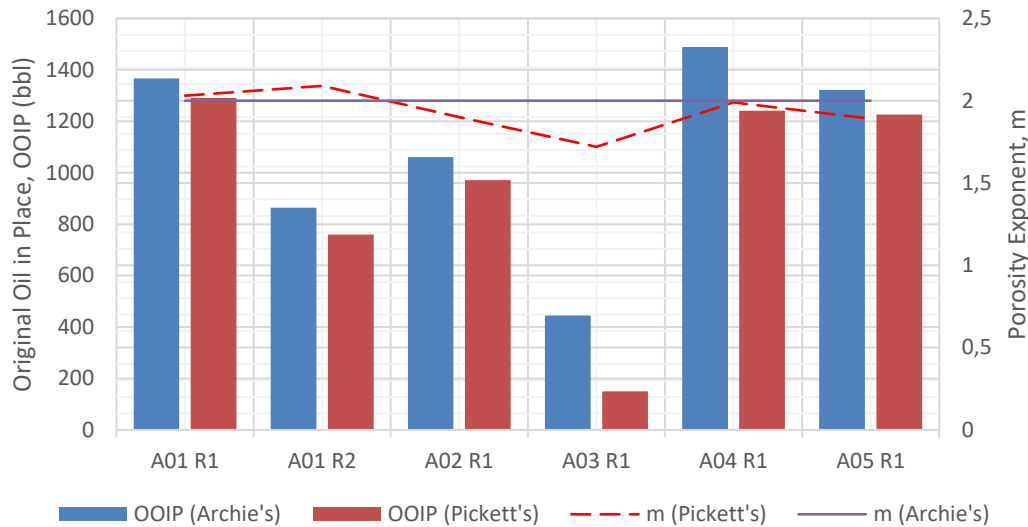


Fig. 5. Histogram of Original Oil in Place calculated from Pickett's and Archie's cementation exponent and line plot for Pickett's and Archie's cementation exponent

In the five wells, porosity exponent ranged from 1.72 to 2.09, and the apparent formation water resistivity for the zones reported 0.204 Ohm.m, except for interval A03 R1 that showed 0.208 Ohm.m. The thickness of these reservoirs is highly variable and ranged from 11ft in well A04 R1 to 120ft in well A02 R1. The lowest correlation (33.71%) is encountered in Reservoir interval A03 R1 where m exponent recorded the lowest m value (1.72) from Pickett plot, with corresponding Archie's m of 2.00. Low reserves estimate in this reservoir (150.12 bbl) demonstrated the role of the cementation exponent on reserve calculations where the reservoir had high porosity value of 33.7%. This high variation in the estimated OOIP in A03 R1 between Archie's and Pickett's techniques (66.29%) is symptomatic of the fine grain facies as confirmed by the Buckle's number above 0.18. In this zone, Archie's equation and the Pickett's in-situ cementation exponents were matchable as indicated by the values of m that fell within 1.8 – 2.0 for water and hydrocarbon saturation estimation [34]. However, the Pickett's m value may be more representative to the changes in the reservoir facies.

For example, in well A01, Archie exponent yielded a Buckle's number of 0.02 (which is indicative of coarse grain sandstone) but Pickett's plot predicted a value of 0.04 indicative of medium size grain sandstone. Therefore, for reservoirs in the study area, there is a close relationship between Archie's exponent (m) and Pickett's exponent values.

Generally, in all wells, Archie equation overestimated the OOIP compared to Pickett plot with the minimal differences (5%) reported in most wells while the largest difference (300%) is encountered in well A03 (Figure 5). Similarly, the cementation exponent (m) is almost matchable in most wells (A01, A04, A05) but significantly different in well A03 (Figure 5).

5. Conclusion

Six (6) reservoirs from five (5) wells in the Niger Delta region, Nigeria was used to evaluate reserves from Archie's and modified Archie's equation. Quick look method was used to delineate the reservoirs. The reservoirs showed good accumulation of hydrocarbon with a thickness of 11ft (3.35m) – 120ft (36.58m) found within a depth of 6223.5ft (1896.93m) – 11216.5ft (3418.79m).

Pickett's plot was employed to estimate porosity exponent, m (1.72 to 2.09) using in-situ logs, also apparent formation water resistivity (R_w) (0.204 – 0.208). The in-situ values were used to calculate water saturation and original oil in place. The results were then compared with results from Archie's water saturation equation, and this comparison shows that the Archie's equation overestimated the calculation of water saturation across the depobelt with the percentage between 5.55% to 68.53%.

The Buckle's plot was used to confirm the calculated Archie's water saturation values. Buckle's number from the Buckle's plot was obtained from each of the reservoirs, reservoir A01 R1 with 5.55% difference in OOIP between Archie (1366.424bbl) and Pickett's (1290.596bbl) having a very close relationship between the Buckle's number of Archie (0.02, coarse grain) and Pickett's (0.04, medium grain). While the reservoir with the highest percentage difference 68.53% (A03 R1) of OOIP between Archie's (445.299bbl) and Pickett's (150.12 bbl.), the Buckle number from Archie (0.18, extremely fine grain) and Pickett (above 0.18, extremely fine grain).

The porosity exponent (m) exhibits wide variation from interval to interval in the same medium (well A01). In-situ logs with the help of Pickett's and Buckle's plot have been used to estimate porosity exponent, apparent formation water resistivity and Buckle's number that was used to estimate original oil in place (OOIP) across the reservoir in the study area.

Nomenclature

A	area of reservoir from map data
a	tutorisity
Bo_i	formation volume factor for oil at initial conditions
BVW	bulk volume of water
BVW_i	irreducible bulk volume of water
C	buckle's number
F	formation factor
h	height or thickness of pay zone
I	resistivity index
n	saturation exponent
m	porosity exponent
OOIP	Original Oil in Place
OGIP	Original Gas in Place
R_t	true resistivity
R_w	formation water resistivity
S_w	water saturation
S_H	hydrocarbon saturation
V_b	bulk reservoir volume
V_{sh}	volume of shale
ϕ	porosity

References

- [1] Adebayo AR, Al-Yousef HY, Mahmoud M. Determination of Archie's saturation exponent for CO₂ sequestration in carbonate reservoirs Society of Petroleum Engineers. #172354SPE. Nigeria Annual International Conference and Exhibition, 5 – 7 August 2014, Lagos, Nigeria.
- [2] Bassiouni Z. Theory, Measurement, and Interpretation of Well Logs. Society of Petroleum Engineers. Richardson, Texas. 1994.
- [3] Hamada GM Al-Awad MNJ, Almalik MS. Log Evaluation of Low – Resistivity Sandstone Reservoirs. SPE Permian Basin Oil and Gas Recovery Conference, 15- 17 May 2001, Midland, Texas. doi:10.2118/70040-MS
- [4] Archie GE. The electrical resistivity logs as an aid in determining some reservoir characteristics. Trans. AIME 1942; 146: 54–67.
- [5] Schlumberger. Log Interpretation Principles / Applications. Schlumberger Educational Services, Houston, Texas. 1987.
- [6] Donaldson EC, Siddiqui TK. Relationship between the Archie saturation exponent and wettability. SPE Form. Evaluation 198; 4: 359–362
- [7] Melani LH, Vidal AC, Filho IM, Schuab FB. The Impact of Archie's Parameters in the Calculation of Water Saturation for Carbonate Reservoir. SEG. Campos Basin, Brazil. 2015.
- [8] Alotaibi MB, Azmy R, Nasr-El-Din HA. Wettability challenges in carbonate reservoirs. Society of Petroleum Engineers. SPE #129972SP Improved Oil Recovery Symposium, 24–28 April, 2010, Tulsa, Oklahoma, USA.
- [9] Glover PWJ. A generalized Archie's law for n phases, Geophysics, 2010; 75: E247–E265, <https://doi.org/10.1190/1.3509781>.

- [10] Agbasi OE, Inyang NJ, Ibut J. Estimation of Water Saturation in Niger Delta Nigeria Using Wire-Line logs. IOSR-JAP. 2013; 3(4): 66 – 71.
- [11] Glover PWJ. What is the cementation exponent? A new interpretation, Lead. Edge. 2009; 28: 82 –85, <https://doi.org/10.1190/1.3064150>.
- [12] Panda A, Darous C, Al-Kindi Z, Akram A, Kriplani S. A specific approach to petrophysical evaluation in a complex carbonate reservoir SPE# 183097 Abu Dhabi Int. Petroleum Exhibition & Conf. 7–10 November, 2016, Abu Dhabi, UAE.
- [13] Akpabio I, Ibuot JC, Agbasi OE, Ojo OT. Petrophysical Characterization of eight wells from Wire-line Logs, Niger Delta Nigeria. Asian J. Appl. Sci. 2014; 2(2): 105 – 109.
- [14] Dewan JT. Essentials of Modern Open-Hole Log Interpretation. PennWell Books. Tulsa, USA. 1983.
- [15] Hilchie D. Reservoir Description Using Well Logs. Douglas W. Hilchie Inc., USA SPE 13346. 1984.
- [16] El-Khadragy AA, Ghorab MA, Shazly TF, Ramdan M, El-sawy MT. Using of Pickett's plot in determining the reservoir characteristics in Abu Roash Formation, El-Razzak oil field, North Western Desert, Egypt. Egypt. J. Pet. 2014; 23: 45 – 51
- [17] Aguilera R. Incorporating capillary pressure, pore throat aperture radii, height above free-water table and Winland r35 values on Pickett plots. AAPG Bulletin. 2001; 86(4): 605–620.
- [18] Mohamed SE, Bassem SN. Determining the porosity exponent m and lithology factor a for sandstones and their control by overburden pressure: A case study from the Gulf of Suez, Egypt. AAPG Bulletin. 2018; 102(9): 1893 – 1910
- [19] Wafta M, Nurmi R. Calculation of saturation, secondary porosity, and producibility in complex Middle East carbonate reservoirs: Society of Petrophysicists and Well Log Analysts 28th Annual Logging Symposium, June 29–July 2, 1987, p. 1–24, London, UK.
- [20] Agbasi OE, Akankpo AO, Essien UE. Estimation of Reservoir Potentials of Two Wells in Niger Delta Region, Nigeria. J. Geosci. Geom. 2017; 5(2): 87 – 95.
- [21] Akankpo AO, Umoren EB, Agbasi OE. Porosity Estimation Using Wire-Line Log to Depth in Niger Delta, Nigeria. IOSR-JAGG. 2015; 3(4): 31 – 38.
- [22] Salem HS. Determination of porosity, formation resistivity factor, Archie cementation factor, and pore geometry factor for a glacial aquifer: Energy Sources, 2001; 23(6): 589–596.
- [23] Agbasi OE, Igboekwe M, Chukwu G, Etuk SE. Discrimination of Pore Fluid and Lithology of a Well in X Field, Niger Delta, Nigeria. Arab. J. Geosci. 2018; 11(11).
- [24] U.S. Energy Information Administration. Country Analysis Brief: 2018. Nigeria.
- [25] Glover PWJ. A new theoretical interpretation of Archie's saturation exponent. Solid Earth, 2017; 8: 805-816.
- [26] Inyang NJ, Okwueze EE, Agbasi OE. Detection of Gas Sands in the Niger Delta by Estimation of Poisson's Dampening-Factor (PDF) Using Wireline Log Data, Geosciences. 2015; 5(1): 46 – 51.
- [27] Tuttle MLW, Charpentier RR, Brownfield ME. The Niger Delta petroleum system: Niger Delta province, Nigeria, Cameroon, and Equatorial Guinea, Africa. USGS. 1999.
- [28] Inyang NJ, Akpabio OI, Agbasi OE. Shale Volume and Permeability of the Miocene Unconsolidated Turbidite Sand of Bonga Oil Field, Niger Delta, Nigeria. Int. J. Adv. Geosci. 2018; 5(1): 37– 45.
- [29] Okoli EA, Agbasi OE, Onyekwu SO, Etuk SE. Crossplot analysis of rock properties from well log data for gas detection in X-field, coastal swamp depobelt, Niger Delta Basin. J. Geosci. Eng. Env. Tech. 2018; 3(4): 180–186
- [30] Short KC, Stubble AJ. Outline of geology of Niger Delta. AAPG Bulletin. 1967; 91: 761-779.
- [31] Pickett GR. A Review of Current Techniques for Determination of Water Saturation from Logs. J. Pet. Technol. 1966; 18: 1425–1433.
- [32] Pickett GR. Pattern recognition as a means of formation evaluation, paper A, in 14th Annual Logging Symposium Transactions: Society of Professional Well Log Analysts, 1973; A1-A21.
- [33] Buckles RS. Correlation and Averaging Connate Water Saturation Data. J. Can. Petrol. 1965; 9: 42 – 52.
- [34] Doveton HJ. Principles of mathematical petrophysics, Oxford University Press, 2014. New York, USA.

To whom correspondence should be addressed: Agbasi E. Okechukwu, Department of Physics, Michael Okpara University of Agriculture, Umudike, Nigeria, E-mail: agbasi.okechukwu@gmail.com

Quantitative Microfacies Study of Miocene Carbonate, Central Luconia, Sarawak

*Shamsimah Rahman**, *Haylay Tsegab*

South East Asia Carbonate Research Laboratory, Geosciences Department, Universiti Teknologi PETRONAS

Received May 12, 2020; Accepted September 21, 2020

Abstract

A thorough qualitative and quantitative interpretation has been made on carbonate sediments from Central Luconia, using microfacies study paired with published geological reports. In this study, the relationship between depositional environments and diagenetic alteration of EX Field, located in the southwest of Central Luconia Province, offshore Sarawak were investigated using core description and microfacies study. Seven facies (F1-F7) were identified from EX-2 and EX-3 wells based on the lithology, texture, fossil assemblages and depositional environment. Each of the facies has been diagenetically altered extensively by micritization, cementation, neomorphism, dolomitization, compaction, and fracturing. Carbonate typically has calcite, dolomite and occasionally other mineral such as pyrite and clay especially those that formed in high sea level/ transgressive unit. The presence of clay mineral during deposition has influenced the diagenetic alteration of the EX Field. A geochemical and stable isotope analysis would provide more information on the pore fluid.

Keywords: *Facies; Porosity; Lagoon; Thin section.*

1. Introduction

Cenozoic carbonates are one of the primary targets for petroleum exploration in the South East Asia region [1-3]. Massive hydrocarbon production was coming from the Miocene carbonate in which more than 200 carbonate build-ups have been mapped out [4]. Due to the increase in the importance of oil and gas recovery and the growing realization that the Luconia carbonate reservoirs are more heterogeneous than assumed in the past, it is important to understand the facies distribution, which directly controls the reservoir properties. With more than 40 TSCF of gas initially in place and over 30 TSCF ultimate recovery, the Central Luconia represents about 40% of the total non-associated gas reserves in Malaysia [5].

Eight major stratigraphy cycles, from Oligocene to Holocene, are regionally distinguished in Central Luconia [1]. Each cycle is bounded by thin transgressive unit at the base [6]. Late Eocene Cycles I and II are dominated by non-marine to marine clastic. The Late Early Miocene Cycle III contains abundant marine shales with thin layers of sandstones and limestones [5]. There are thicker packages of limestones at the top layer of Cycle III in the form of lenses. Cycle IV is dominated by the extensive blankets of limestone bank deposits up to 300-meter-thick in the structurally elevated areas [5]. The carbonate sediments stack-up during this cycle classically were referred to as the Megabank stage [7].

During the Middle to early Late Miocene, the entire shelf was an open marine and Cycle V started to develop. The development of Cycle V was referred to as the pinnacle stage [8-9]. The pinnacle stage is characterized by a thick vertical carbonate deposition, which reaches up to 500 m but the areal extent was reduced [9]. Episodic, small shallow water lagoons may occur during the pinnacle stage [10]. Skeletal component rich carbonates continued to develop in structurally elevated areas producing individual buildups up to 20 km in length and 1.5 km thick [10]. Uplift and erosion were reported at the end of Cycle V. This study attempts to investigate the relation between the depositional environment and diagenetic alteration using well logs, core description and microfacies analysis from EX-2 and EX-3 well of Cycle V. Well

understood depositional environment and diagenesis alterations of the carbonate platforms will dictate the reservoir facies delineation and modeling to predict the carbonate reservoir in the subsurface.

2. Geological setting

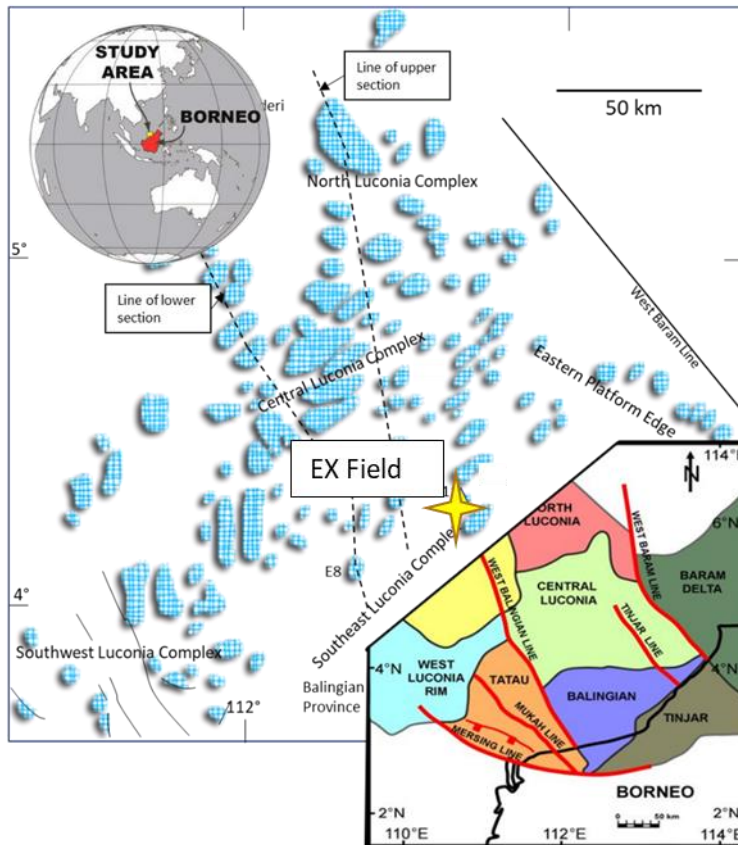


Figure 1. EX Field located in southwestern region of Central Luconia, offshore of Borneo (Modified from [12])

Central Luconia is highly affected by the opening of South China Sea [5]. During Late Cretaceous to Eocene, Luconia continental block is rifted from South China towards the Borneo Block [12]. The proto South China Sea or also known as Rajang Sea is subducted under the Borneo continental block [12]. During Late Eocene to Early Oligocene age, a complete closure of the proto south China Sea caused the collision between the Luconia microcontinental block with the Borneo Block producing the Rajang Mountain [12]. Recent study based on seismic lines proved that the Central Luconia experienced extension during Middle Miocene and followed by compressional period for most of Middle to Late Miocene. The extensional event during Middle Miocene time is supported through age dating of the tilted syn-rift carbonate at the base of half-graben [13]. The entire Sarawak Basin was affected by NW-SE trending right lateral fault movement, which created the faulted blocks with same trending [14]. Central Luconia has been rotated in a counter-clockwise direction and bounded by dextral-wrench movement along West Balingian line, Mukah Line, Igan-Oya line and others [14]. Central Luconia was a depressional region bounded by uplifted regions created basin edges in south, southwest and southeast during the extension and isostatic readjustment episode. The basin near to the uplifted area, the eastern side, was filled with clastic, while for the rifted western margin part was characterized by extensive carbonate development [14]. According to Epting [1], the overall carbonate growth in Central Luconia was influenced by four major processes: (i) the rate of carbonate producing organism, (ii) subsidence rate, (iii) relative sea level fluctuation, (iv) influx of terrigenous material from onshore of Borneo.

Central Luconia is located about 100 to 300 km from the present coastline of Sarawak and covers an area of 45 000 km² [11]. It is part of the seven geological provinces in offshore of Sarawak. The Central Luconia Province is bounded by North Luconia Province in northern area, Balingian Province in southern area, West Baram line in the eastern area, and West Balingian Line in western area (Fig. 1). The size of carbonate platform in Central Luconia ranged from a couple of km² up to more than 200 km² [11].

Based on $87\text{Sr}/86\text{Sr}$ data [4], Luconia platform growth correlates with a period of sea level highstand during Middle Miocene correspond to the Supercycle TB2 and cycles 2.3- 2.6 on the global sea level curve [15]. The deeper carbonate interval has been dated using Sr isotopes to about 18 Ma and the demise of Luconia platforms coincides with a major eustatic sea level drop at the end of Middle Miocene (boundary TB2-TB3) and the onset of Borneo tectonism [4].

The EX Field is located in the southwest of Central Luconia, 80 km north of Bintulu town. The present top carbonate depth is 1500 m deep with gas column of 520 m [9]. The age of the EX field ranges from Middle Miocene until Late Miocene [1], which implies for over 5 Ma years of deposition [9]. EX Field was first discovered in 1971 with a wildcat well named EX-1, followed by two vertical appraisal wells named as EX-2 and EX-3 [7]. No core was preserved in well EX-1, while there are 292 m and 286 m length cores from EX-2 and EX-3 wells, respectively. The architecture of the platform can be subdivided into two, "Megabank" structure with thickness of approximately 170 m and pinnacles structure with thickness 340 m and was divided by a thick deep marine deposits [9] (Fig. 2). Beneath Cycle IV and Cycle V carbonate lies a thick succession of mixed carbonates and siliciclastic of Cycle III.

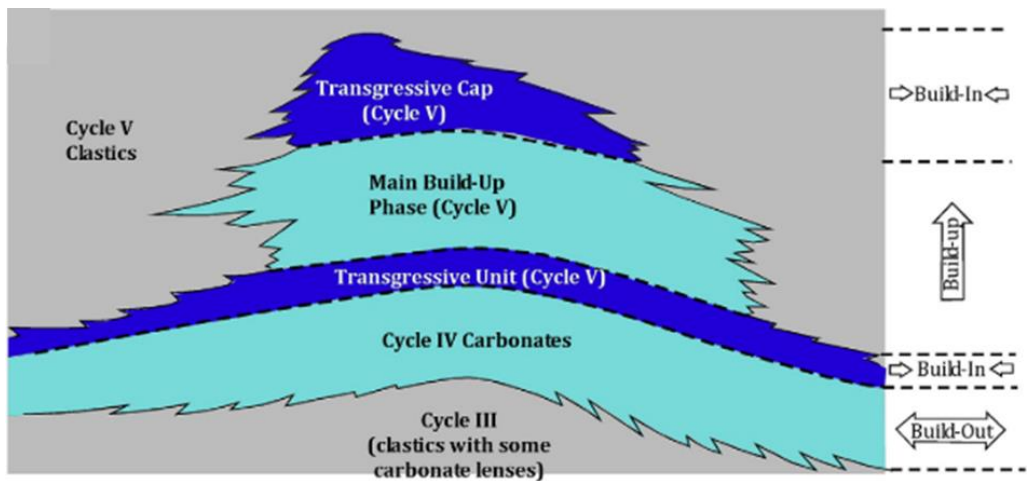


Figure 2 The architecture of EX Field showing the Megabank and pinnacle structure (after [7])

3. Methodology

3.1. Facies analysis

Core description has been used to identify the lithology, texture and skeletal assemblages. The length of core for EX-2 is 292 m and EX-3 is 286 m. 124 thin sections from EX-2 and 68 thin sections from EX-3 were used for microfacies study. The thin sections are impregnated with blue epoxy dye to ease the porosity recognition. The thin section study helps to gain more information on texture, benthic foraminifera assemblages and porosity. Carbonate depositional texture has been described based on Dunham's Classification [16] and Klován [17].

3.2. Lithofacies association

The facies were grouped into 5 facies association, in accordance to their depositional environment which are forereef, reefoid, reefoid- backreef, backreef- lagoon and lagoon environment. These facies associations were based on lithology, texture, fossil assemblages and depositional environment.

4. Results

4.1. Facies and Facies Association of EX Field

Generally, EX Field is characterized by thick limestone from top to bottom, with dolomitic interval in the middle. The most common carbonate skeletal components in EX Field are red algae, planktonic foraminifera, bivalve, brachiopod, bryozoan, massive corals, echinoid and

benthic foraminifera (*Amphitesgina* sp., *Operculina* sp., *Sorites* sp., *Cycloclypeus* sp., *Lepidocyclina* sp., *Miogypsina* sp., *Miogypsinoides* sp., miliolids and uniserial foraminifera). The range of porosity is from 5% to 25%.

Four main lithology were distinguished in the EX Field: limestone, dolomite, argillaceous limestone, dololime and shale (Fig. 3). The largest fraction of the core consists lithologically thick carbonate succession in both EX-2 and EX-3 wells. The carbonate section consists mainly of limestone and dolomite, with a small portion of dololime. The limestone is composed of massive, structureless bed and well cemented, with minor rubble section. The top of both EX-2 and EX-3 were covered by a shaly interval. The same shaly interval was found in the middle of the section. The shaly interval is interpreted as a transgressive unit for the field, which marked the rise of sea level during the time of deposition. And This transgressive unit marked the division of Cycle IV and Cycle V carbonate succession (Fig. 2).

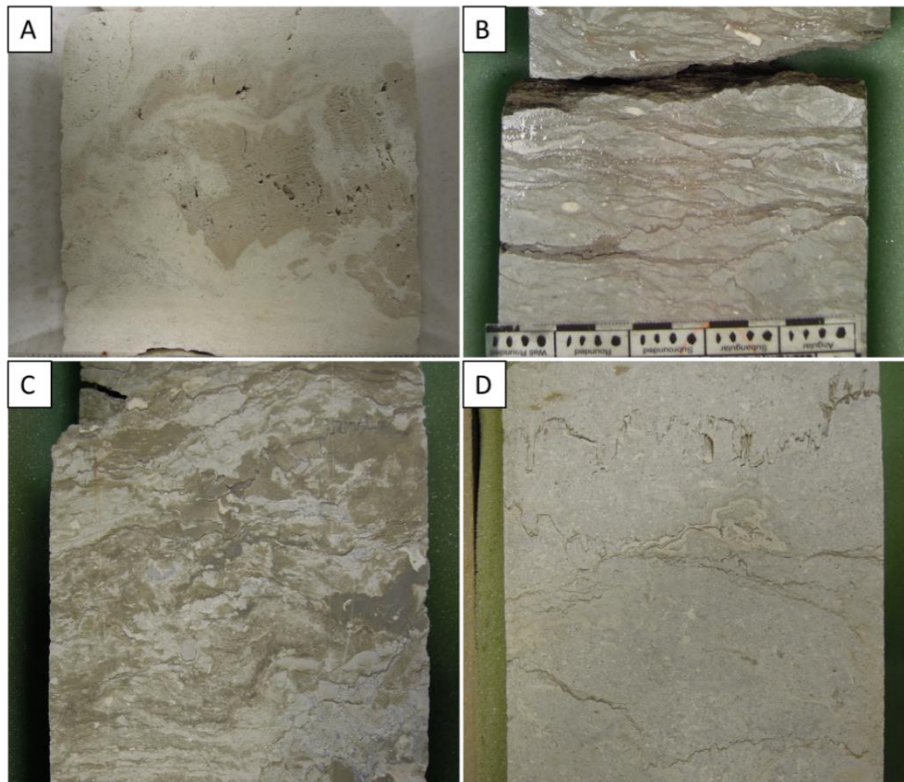


Figure 3. Different type of lithology in EX Field, [A] Dololime; [B] Argillaceous Limestone; [C] Dolostone; [D] Limestone

There are seven facies division from microfacies study on well EX-2 and EX-3 (Fig. 4), namely, F1: Foraminiferal- Red Algal Packstone; F2: Dolomitic Red Algal Wackestone- Floatstone; F3: Coral Framestone; F4: Red Algal-Bioskeletal Grainstone- Rudstone; F5: Red Algal Wackestone- Packstone; F6: Cycloclypeus- Lepidocyclinid Rudstone; and F7: Coral- Red Algal Rudstone. Each of the different facies has been interpreted based on its skeletal and benthic foraminifera assemblages (Fig. 5).

F1 (Foraminiferal- Red Algal Packstone) is dominantly limestone and dololime, characterized by packstone, with rare floatstone and grainstone. 17 thin sections from EX-2 and 18 thin sections from EX-3 are grouped into F1 facies. Common components found are red algae, benthic foraminifera (*Sorites* sp., *Austrotrillina* sp., *Lepidocyclina* sp., miliolid), echinoid, bivalve, brachiopod and fragment of massive coral. Planktonic foraminifera, gastropod, bryozoan, benthic foraminifera (*Cycloclypeus* sp. and *Amphitesgina* sp.) are uncommon. The depositional environment is interpreted as lagoon.

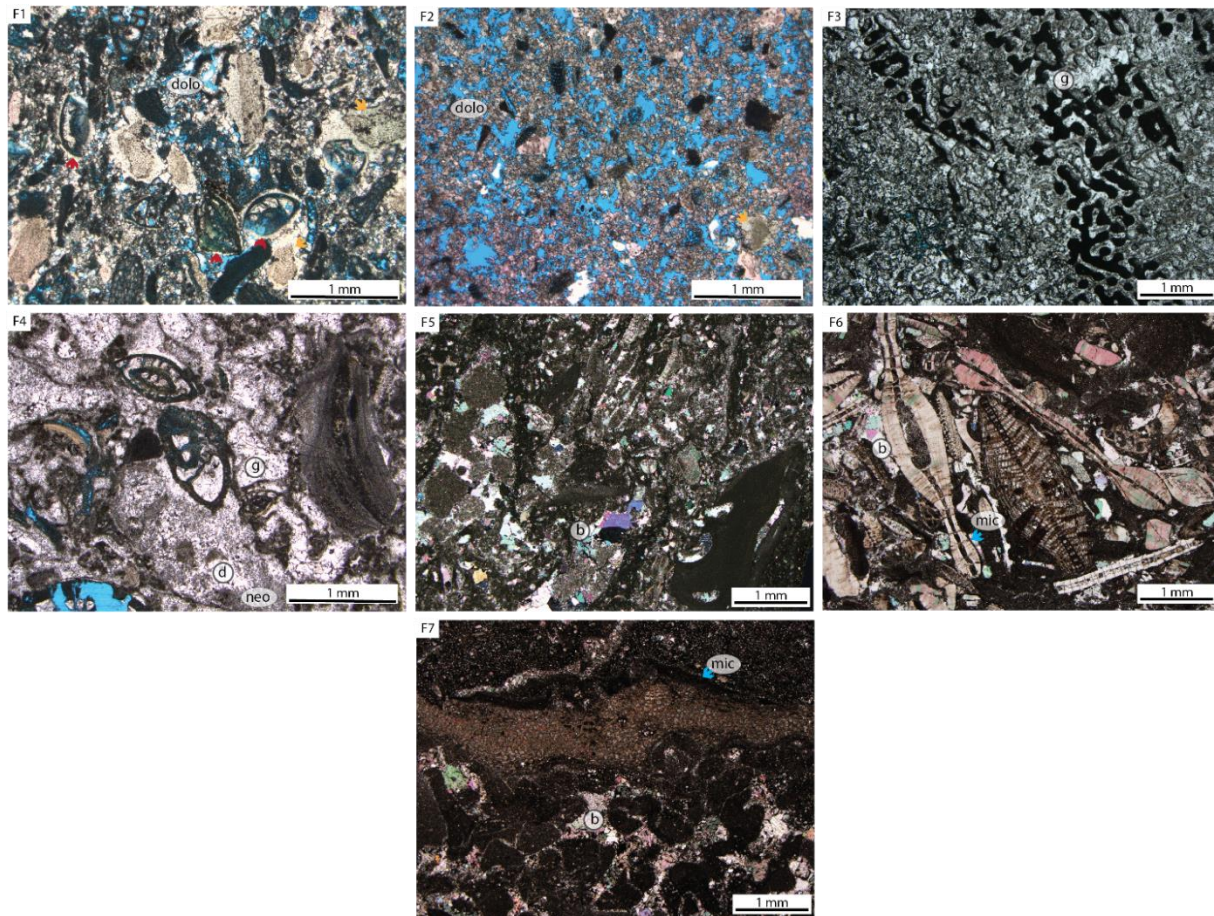


Figure 4. Microfacies of EX Field. F1 shows a dolomite facies with packstone texture. It has high number of benthic foraminifera (*Operculina* sp.), with isopachous rim cement surrounding the grain (red arrow). The overgrowth cement is seen on echinoid plate (orange arrow); F2 shows the dolomitic- mudstone texture of microfacies, where only red algae and echinoid with overgrowth cement (orange arrow) can be seen on the section. This section has high porosity (>20%), contributed by the intercrystalline porosity; F3 shows the massive coral that is heavily crystallized by granular (g) cement; F4 shows a clean rudstone- textured limestone, cemented by granular and drusy, with microspar cement (neomorphism); F5 shows a limestone in wackestone to packstone texture with coarse blocky cement (b) that filled the interparticle space; F6 shows abundance of benthic foraminifera, with no porosity observed. The grains are enveloped by the micritic rim (mic); F7 shows the rudstone texture of coral and encrusting foraminifera

F2 (Dolomitic Red Algal Wackestone- Floatstone) is lithologically of dolomite and dolomite, with mudstone and floatstone textures. It consists of mainly red algae with occasional occurrence of echinoid and benthic foraminifera (*Operculina* sp.). The presence of dolomite and mainly red algae suggested that the depositional environment for F2 is lagoon. There are 39 thin sections from EX-2 and 19 thin sections from EX-3 are F2 facies.

Facies F3 (Coral Framestone) is only recorded from EX-3 showing massive coral in the thin sections, observed only in two thin sections. The massive coral is mostly crystallized and interpreted as reefoid environment.

F4 (Red Algal-Bioskeletal Grainstone- Rudstone) lithology facies is characterized by grainstone-rudstone texture. 17 thin sections from EX-2 and 7 thin sections of EX-3 are categorized as F4 facies. F4 mainly contain red algae, benthic foraminifera (*Operculina* sp., *Sorites* sp., *Austrorillina Howchini*, *Lepidocyclina* sp, miliolid), massive coral fragment and brachiopod. Less common skeletal component found in the F4 are bryozoa, bivalve, biserial foram and encrusting foram. F4 is interpreted as backreef-lagoon depositional environment.

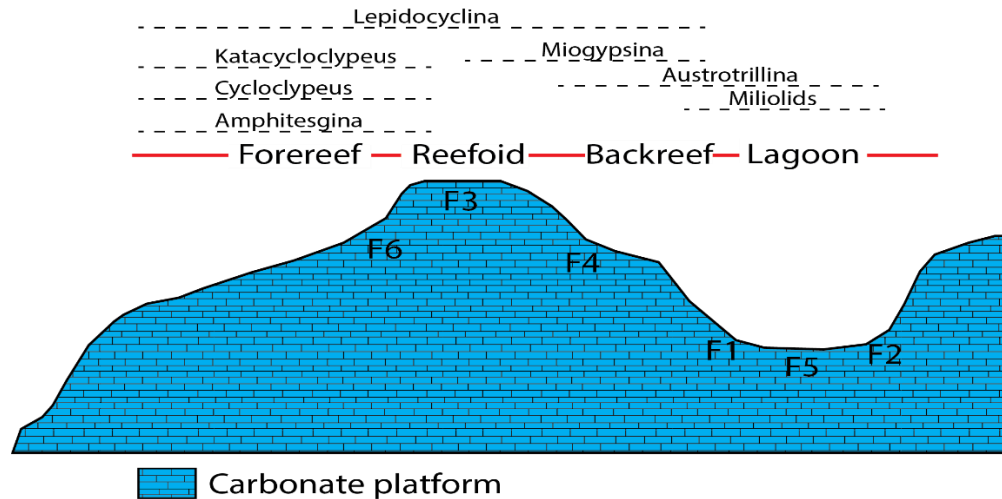


Figure 5 The interpreted facies with its depositional environment for EX Field

F5 (Red Algal Wackestone- Packstone) has limestone and dolomite lithology; and it is wackestone textured. It mainly consists of red algae, echinoid, benthic foraminifera (*Sorites* sp., *Operculina* sp., *Lepidocyclina* sp., *Amphitesgina* sp., miliolid), gastropod and skeletal debris. The skeletal present suggesting a lagoon depositional environment for F5 facies. F5 facies is identified on 21 thin sections of EX-2 and 2 thin sections of EX-3.

F6 is characterized by heavily diverse benthic foraminifera in rudstone textured limestone. The benthic foraminifera include *Cycloclypeus* sp., *Katacycloclypeus* sp., *Miogypsina* sp., *Lepidocyclina* sp., *Operculina* sp. and *Amphitesgina* sp. Other components include red algae, echinoid, bryozoan and massive coral fragment. The foraminifera suggesting a slightly deep marine/ forereef environment for the facies. There are 13 thin sections from EX-2 and 8 thin sections from EX-3 that are classed into F6 facies.

Lastly, F7 (Coral- Red Algal Rudstone) is limestone in lithology and is identified by its rudstone- packstone texture. It is dominated by coral, red algae, benthic foraminifera (*Operculina* sp., *Amphitesgina* sp., *Sorites* sp., *Textularia* sp. and encrusting foram), planktonic foram and brachiopod. F7 is interpreted as reefoid- backreef depositional environment. F7 facies can be seen in 16 thin sections from EX-2 and 11 thin sections from EX-3.

4.2. Diagenetic alteration on carbonates

The carbonate sediments from EX field has undergone extensive diagenetic alteration, affecting the porosity evolution. The diagenesis processes include micritization, cementation, dissolution, dolomitization, compaction and fracturing. Micritization is the earliest diagenetic alteration that affected most of the sediments of the EX field. There are 108 thin sections out of 124 from EX-2 and 53 out of 68 thin sections from EX-3 field that were affected by micritization. Micritization is recognized by its dark rim that surrounded the grain or skeletal on thin section (Fig. 4: F6; F7).

The cementation diagenetic process reduces porosity within the sediments. The cement morphologies found in EX sediment are fibrous, isopachous/ bladed cement, drusy, blocky, granular and overgrowth (Fig. 4: F1; F2; F4; F5; F6; F7). The cements in the EX are developed in both intraparticle and interparticle pores as well as in fractures. Different generation of cementation can be seen from the microfacies study, ranging from marine, meteoric and burial environment. Bladed/ isopachous cement is fairly distributed among all facies, except its low occurrence in F2 (Fig. 6). Granular and drusy cement is found to be high in F5, and lowest in F2. The difference between granular and drusy is in the size of the cement, where drusy cement have equant to bladed cement that increases in size towards the center. Overgrowth cement is found to be the highest in F1 and the lowest in F5 while blocky cement is highly recorded in F2 facies, and low occurrence in F3 facies.

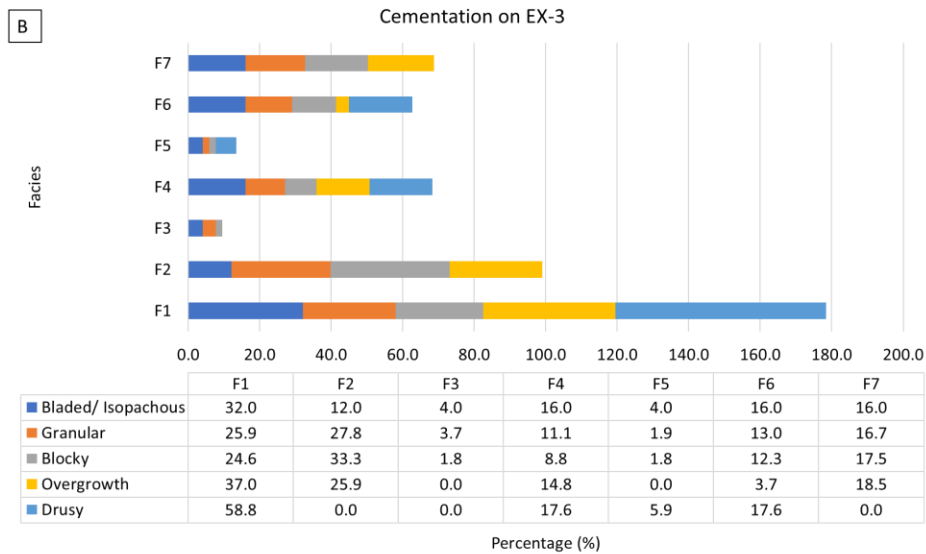
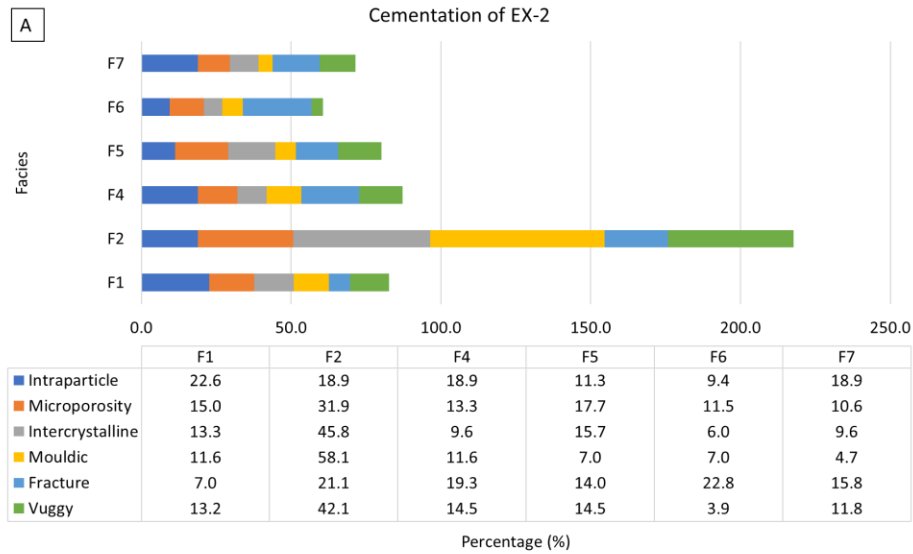


Figure 6. Bar chart of different cement morphologies on EX-2 (Chart A) and EX-3 (Chart B). The highest cementation is found from F1 for both well

Mechanical and chemical compaction processes is noted in the carbonate sediments of the EX well. (Fig. 7). Mechanical compaction is identified by the close packing between the grains, which led to concavo-convex contact as well as sutured contact while chemical compaction is recognized by the presence of insoluble seams, such as stylolite and horsetail pressure solution (Fig. 7).

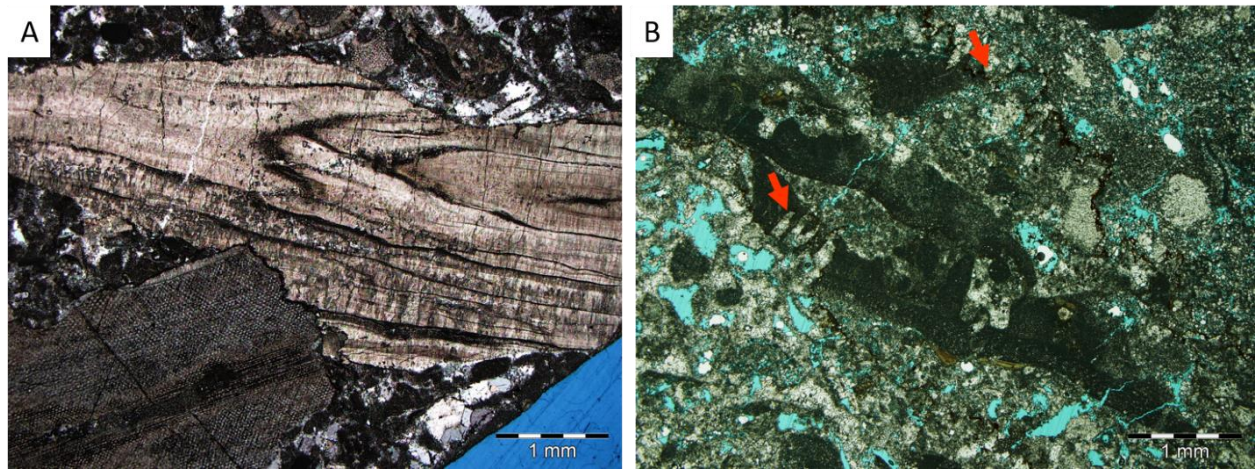


Figure 7 The compaction in EX-3 sediments. [A] mechanical compaction caused a sutured contact between the grain. [B] The chemical compaction caused induced the formation of stylolite (red arrow) with moldic, vuggy and fracture porosity

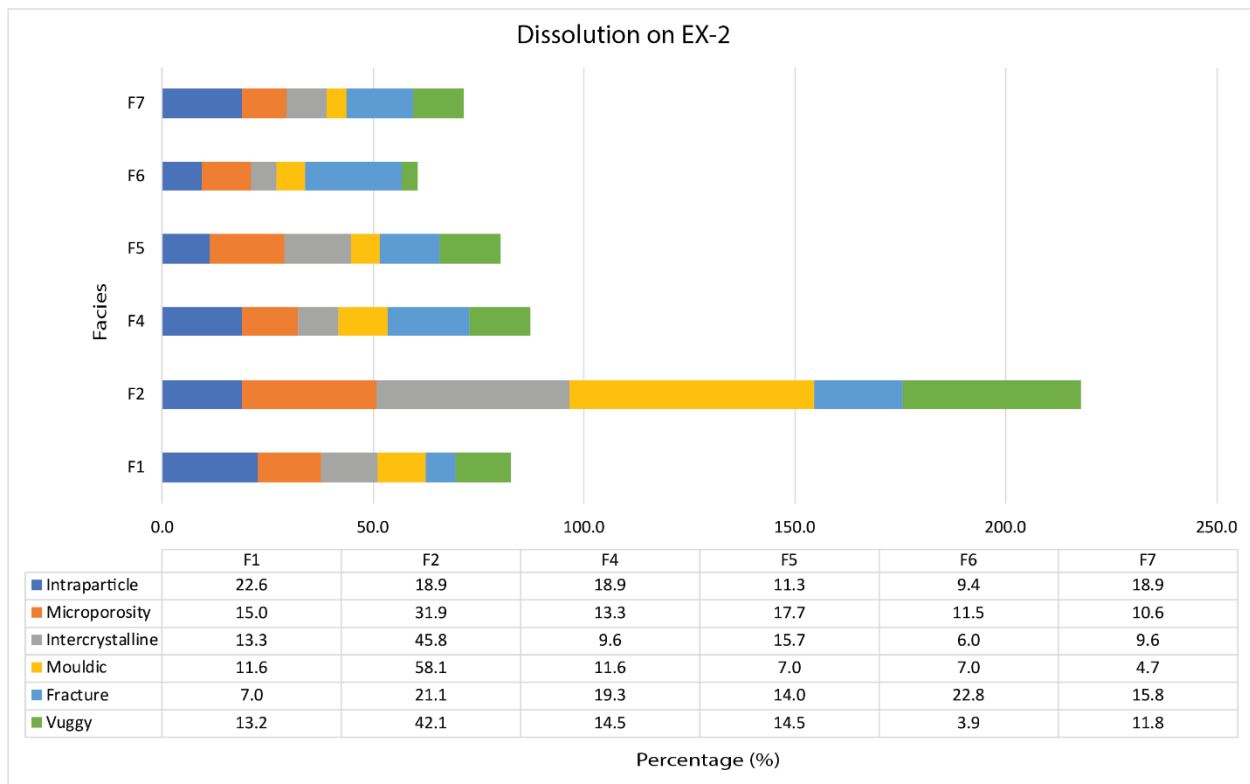


Figure 8. Bar chart for dissolution on EX-2 sediments in accordance of different facies. Highest porosity is found to be in F2 while the lowest is from F6

Dissolution process played an important role in increasing the reservoir quality in the EX field. Porosities in the EX sediments include intraparticle, mouldic, vuggy, fracture (Fig. 7B), micropore (Fig. 4: F1) and intercrystalline (Fig. 4: F2). The highest porosity is recorded from F2 facies, ranging between 10% to 25%. The mentioned facies has the highest occurrence of microporosity, intercrystalline, vuggy and mouldic porosity (Fig. 8). Meanwhile the lowest porosity is recorded from F6, which is interpreted as transgressive unit in EX Field, suggested by its foraminifera assemblages and as tight unit (Fig. 5D). It is a tight unit, with a very low porosity (<5%).

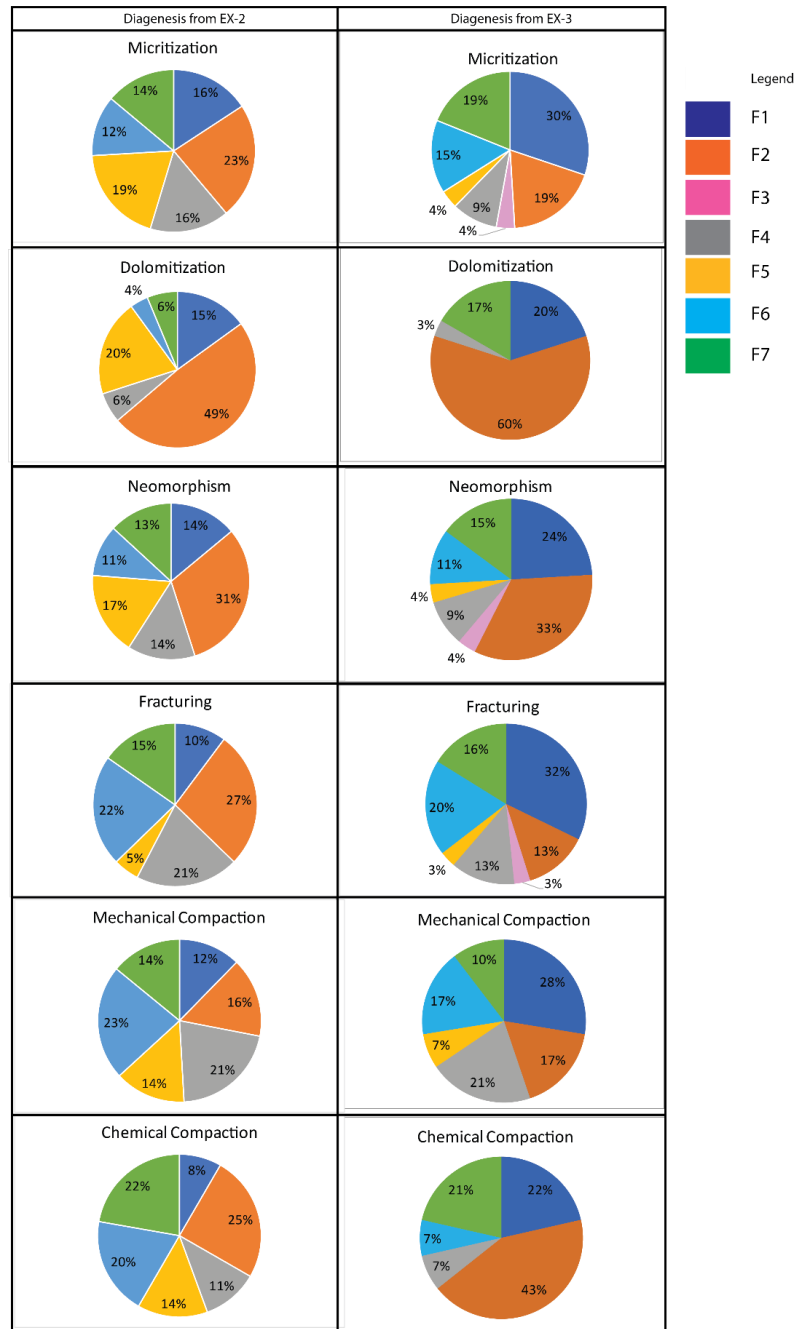


Figure 9. The comparison of diagenesis on difference facies type, from EX-2 and EX-3

Dolomitization is one of the diagenetic processes that occurred in the EX field. Dolomitization is particularly abundant in F2 (Fig. 4: F2). The process has significantly increased the porosity of the field, from intercrystalline porosity. The dolomites in the studied field are found to be both fabric- preserving and fabric destroying dolomites. The dolomite developed in micritic sediments as well as washed sediments. The shape of dolomite crystal found are planar euhedral and subhedral, as well as nonplanar anhedral which is more common in micrite- rich sediments. The planar dolomite (euhedral and subhedral) typically formed in both shallow and deep burial diagenetic zone, where the crystals undergo faceted growth with planar interfaces [18].

5. Discussion

5.1. Influence of depositional environment on diagenetic processes

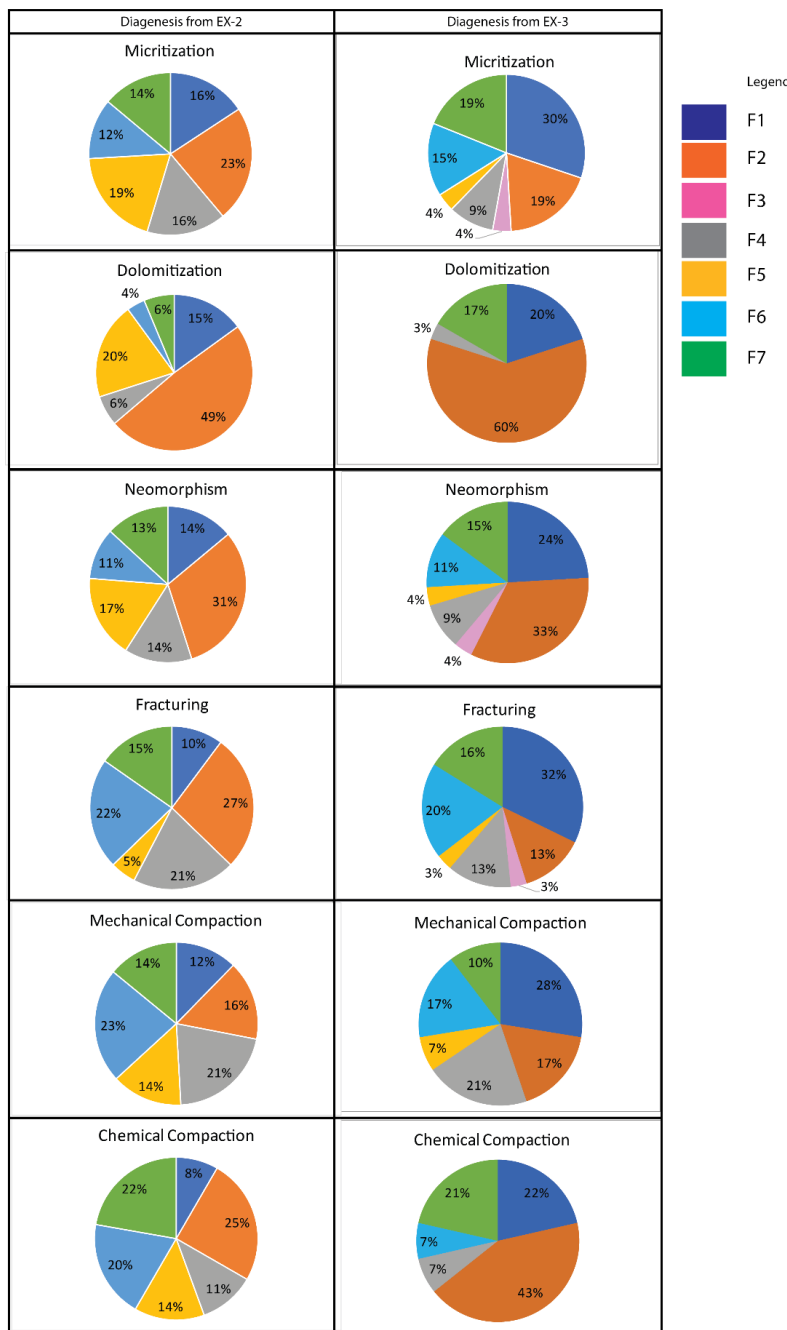


Figure 9 The comparison of diagenesis on difference facies type, from EX-2 and EX-3

Different type of cement morphology has a different distribution on EX sediments. The cement morphology was highly influenced by the fluid flow, mineral saturation and the number of nuclei and the evolution of crystal growth patterns [21]. Factors that control cementation can be: 1) the reprecipitation of the dissolve carbonate phase within sediments and 2) the reprecipitation of dissolve aragonite and calcite from subaerial surface [22]. The bladed or isopachous cement has been associated with marine phreatic environment and considered as

Fluid origin and fluid flow in sedimentary basins have a very important influence on various diagenetic alteration processes [19]. The depositional environment is imperative in providing the fluid flow that can promote the diagenesis. The occurrence of each diagenesis on different facies has been plotted in a series of pie chart in Figure 9. Micritization occurred on all facies regardless of its depositional environment.

Based on microfacies studies, most of sediments from lagoonal facies, F1, F2 and F5 were affected by dolomitization (Fig. 9). This suggest that in the lagoonal facies of EX field, the fluid was rich with magnesium ion and the magnesium ion could be originated from minerals that existed in lagoonal area [18,20]. In subsurface environment, aided with sufficient temperature, the pore water can become dolomitizing solution.

early cement or eogenetic cement [19, 21,23], while blocky cement can form in both marine and meteoric phreatic environment [21]. The occurrence of bladed cement is observed in all facies, suggesting its formation may not be affected by any depositional environment factor. Granular cement and drusy cement are seen to be high in mud-supported lagoonal facies. Granular and drusy cement are associated with meteoric phreatic zone [23]. Overgrowth cement has higher occurrence in lagoon environment. The overgrowth cement is typically observed on echinoderms showing a single calcite crystal on each grain, producing a poikilotopic fabric [23].

For dissolution, the highest porosity is found in dolomitic facies (F2), which is mainly contributed by the intercrystalline, mouldic and vuggy porosity. The solubility of a grain increases with increasing percentage of magnesium in a crystal structure [24], which explains the finding in this study.

Compaction diagenetic process typically starts with mechanical compaction, in which sediments were compressed and lithified together during burial. As the overburden increase with time, this led to chemical compaction within the sediments. Compaction has significantly reduced the porosity in the carbonate succession. mechanical compaction is observed in all of the facies but it is significantly high in the backreef- lagoon facies. Chemical compaction was also observed in all facies, with an abundance from lagoonal environment (F1 and F2) and reefoid- backreef environment (F7). The response of compaction varies with the pore fluid geochemistry, temperature, clay content and amount of overgrowth cement at grain contact [25]. The sediments that are rich in clay may have assisted the chemical compaction to occur. This is due to the locally smaller contact area existed in clay rich region which induced a locally greater rate of chemical compaction [25].

6. Conclusion

There are four different sub-depositional environments that have been interpreted for the EX Field, which are lagoon, lagoon- backreef, backreef- reefoid, reefoid and slightly deep marine. Each of the different facies has undergone substantial diagenesis process which led to creation and destruction of porosities. A good reservoir property (what counts as a good reservoir property?) is seemed to be developed in the reefal to lagoonal setting, while the deeper marine facies has very low porosity and has been interpreted as transgressive unit. Most of the skeletal grains were dissolved and cemented in most of the thin section. In the tight zone, the skeletal grains have commonly preserved their original fabric. Presence of clay in the studied platform is believed to have aided the dolomitization and chemical compaction of the sediments, while for the other diagenesis processes, the reasons remained unclear. The linkage between depositional environment and diagenetic environment is still vague for EX field where geochemistry and stable isotope might aid in enhancing the understanding of the pore fluid.

Acknowledgement

We would like to thank to PETRONAS for allowing us to use the data for this research. We are also grateful to South Eastasia Carbonate Research Laboratory (SEACARL) for providing facility for the study. This project was supported by YUTP Grant (0153AA-H08).

References

- [1] Epting M. Sedimentology of Miocene Carbonate Buildups, Central Luconia, Offshore Sarawak. Geological Society of Malaysia. 1980; 12(12): 17–30.
- [2] Fulthorpe CS, and Schlanger SO. Paleo-Oceanographic and Tectonic Settings of Early Miocene. The American Association of Petroleum Geologists Bulletin, 1989; 6(6), 729–756.
- [3] Doust H, and Sumner HS. Petroleum systems in rift basins – a collective approach in Southeast Asian basins. Petroleum Geoscience, 2008; 13(2), 127–144.
- [4] Vahrenkamp VC. Miocene carbonates of the Luconia province, offshore Sarawak: implications for regional geology and reservoir properties from Strontium-isotope stratigraphy. Geological Society of Malaysia Bulletin, 1998; (42): 1–13.
- [5] Ali MY, and Abolins P. (1999). Central Luconia Province. In The Petroleum geology and resources of Malaysia. p.665.
Available at: https://books.google.com.my/books/about/The_Petroleum_geology_and_resources_of_M.html?id=KXFQAQAAIAAJ.

- [6] Ho KF. Stratigraphic Framework for Oil Exploration in Sarawak. *Bulletin of the Geological Society of Malaysia*, 1978; 10: 1–13.
Available at: <http://www.gsm.org.my/products/702001-101287-PDF.pdf>.
- [7] Rankey EC, Schlaich M, Mokhtar S, Ghon G, Al, SH, and Poppelreiter M. Seismic architecture of a Miocene isolated carbonate platform and associated off-platform strata (Central Luconia Province, offshore Malaysia). *Marine and Petroleum Geology*, 2019; 102: 477–495.
- [8] Kosa E, Warrlich G, and Loftus G. Wings, mushrooms, and Christmas trees: The carbonate seismic geomorphology of Central Luconia, Miocene-present, offshore Sarawak, northwest Borneo. *Am. Assoc. Pet. Geol. Bull.*, 2015; 99(11): 2043–2075.
- [9] Warrlich G, Tabener C, Asyee W, Stephenson B, Esteban M, Boya-Ferrero M, Dombrowski A, and Van Konijnenburg, J.-H. (2010). The Impact of Postdepositional Processes on Reservoir Properties: Two Case Studies of Tertiary Carbonate Buildup Gas Fields in Southeast Asia (Malampaya and E11). In *Cenozoic Carbonate Systems of Australasia*. pp.99–127.
- [10] Tabener C, and Esteban M. Geological Review of the E11- F13 Carbonate Complex: Petrological and Geochemical Analysis for E11-F13 Carbonate Complex. in *Unpublished Internal Report*, Shell International Exploration and Production B. V., RIJSWIJK, 2003
- [11] Koša E. Sea-level changes, shoreline journeys, and the seismic stratigraphy of Central Luconia, Miocene-present, offshore Sarawak, NW Borneo. *Marine and Petroleum Geology*, 2015; 59: 35–55.
- [12] Madon M. Geological setting of Sarawak. The petroleum geology and resources of Malaysia, 1999; 275–290.
- [13] Sim D, and Jaeger G. (2006). Tectonostratigraphy and trap styles of the Half-Graben sub-province in West Luconia , offshore Sarawak. *Geological Society of Malaysia Bulletin*, 2006; 49: 107–110.
- [14] Kob MRC, and Ali MY. (2006). Regional Controls on Carbonate Developments in Central Luconia, Offshore Sarawak. In *PGCE*. p.2006.
- [15] Haq BU, Hardenbol J, and Vail PR. Mesozoic and Cenozoic chronostratigraphy and cycles of sea-level change. *Sea-level Chang. an Integr. approach*, 1988; February: 71–108.
- [16] Dunham RJ. Classification of Carbonate Rocks According to Depositional Textures. in *Classification of Carbonate Rocks--A Symposium*, 1962.
- [17] Embry AF, and Klován EJ. The Upper Devonian stratigraphy of northeastern Banlts Island has. *Bull. Can. Pet. Geol.*, 1971; 19(4): 1971.
- [18] Al-Awadi M, Clark WJ, Moore WR, Herron M, Zhang T, Zhao W, Hurley N, Kho D, Montaron B. and Sadooni F. Dolomite: perspectives on a perplexing mineral. *Oilfield Review* 2009; 21(3): 32–45.
- [19] Liu J, Li Z, Cheng L, and Li J. Multiphase Calcite Cementation and Fluids Evolution of a Deeply Buried Carbonate Reservoir in the Upper Ordovician Lianglitag Formation, Tahe Oilfield, Tarim Basin, NW China. *Geofluids*, 2017; 2017: Article ID 4813235.
- [20] Mason GM, and Surdam RC. Carbonate mineral distribution and isotope-fractionation: An approach to depositional environment interpretation, Green River Formation, Wyoming, U.S.A. *Chemical Geology*, 1992; 101(3–4): 311–321.
- [21] Moore CH. Carbonate reservoirs: Porosity and diagenesis in a sequence stratigraphic framework, Amsterdam: Elsevier B.V. 2001.
- [22] Steinen RP. Phreatic and Vadose Diagenetic Modification of Pleistocene Limestone: Petrographic Observations from Subsurface of Barbados , West Indies. *AAPG Bulletin*, 1974; 58(6): 1008–1024.
- [23] Scholle PA, and Ulmer-scholle DS. Cements and Cementation. In G. V. Middleton, ed. *Encyclopedia of Sediments and Sedimentary Rocks* 2003. pp.110–118.
- [24] Anderson LG. (2013). Carbonate Dissolution. In J. Harff, M. Meschede, S. Petersen, & J. Thiede, eds. *Encyclopedia of Marine Geosciences*. Dordrecht: Springer Netherlands, pp.1–4. Available at: https://doi.org/10.1007/978-94-007-6644-0_46-1.
- [25] Dewers T, and Ortoleva P. Formation of Stylolites, Marl/Limestone Alternations, And Dissolution (Clay) Seams by Unstable Chemical Compaction Of Argillaceous Carbonates. *Developments in Sedimentology*, 1994; 51(C): 155–216.

To whom correspondence should be addressed: Dr. Shamsimah Rahman, South East Asia Carbonate Research Laboratory, Geosciences Department, Universiti Teknologi PETRONAS, Malaysia,
E-mail: nor_17008599@utp.edu.my

Grid Adaptation of Multiphase Fluid Flow Solver in Porous Medium by OpenFOAM

*L. Sugumar, Abhishek Kumar, and Suresh Kumar Govindarajan**

Reservoir Simulation Laboratory, Petroleum Engineering Programme, Department of Ocean Engineering, Indian Institute of Technology – Madras, Chennai, India

Received June 10, 2019; Accepted September 29, 2020

Abstract

The focus of the present work is to develop the two-phase immiscible and incompressible fluid flow solver for porous medium using the object-oriented (C++) Open Source Computational Fluid Dynamics (CFD) toolbox known as OpenFOAM. The reason for choosing the OpenFOAM framework is first elaborated by looking into the history of the programming concepts used in the development of numerical simulators. The scopes and limitations of the existing solvers in the OpenFOAM for the porous medium are looked in detail for identifying the elements of adding any new features to it. The pressure-saturation formulation is the mathematical approach adopted in this present study. In the immiscible two-phase flow, both the wetting phase saturation and the non-wetting phase pressure are solved implicitly using the IMPSAT (IMPLICIT in Pressure and SATuration) numerical formulation. Additionally, the coupled effect of IMPSAT with Adaptive Mesh Refinement (AMR) technique and the specialized two-dimensional Adaptive Mesh Refinement (2DAMR) technique for 2D problems are investigated. The superiority of using 2DAMR over the existing default hex-mesh cutter algorithm is quantified. The numerical solution is validated with standard Buckley-Leverett semi-analytical solution for one dimension and two-dimension problems. Also, the developed solver is tested for the three-dimensional case.

Keywords: *Two-phase; CFD; Pressure-Saturation; IMPSAT; AMR; Buckley-Leverett.*

1. Introduction

The usage of the proprietary closed source software for porous medium numerical simulations usually attracts a hefty annual licensing cost to the company. At the same time, the end-user is not provided access to the source code of the software for customization or new implementation. Moreover, every new module or additional features are made available by request from the vendor at some additional cost. As a matter of fact, the substantial intellectual contents in the commercial closed source software are primarily inspired or developed from the basic research work conducted by educational and research institutions and made available in the open literature. Scientific Free and Open-Source Software (FOSS) for numerical simulation also do exist along with proprietary commercial software. An inquisitive mind engaged in scientific research always wants to explore and so closed source software is definitely a detriment and FOSS is the only solution. The effects to embrace scientific FOSS for Porous Medium simulation at least among the educational and scientific research community spread across the globe opens the door wider for innovation and reproducible research. With time and collective community-driven quality research, FOSS in the porous medium numerical simulation could be a preferred option to consider over the proprietary commercial software even by the industries. Some of the existing FOSS for porous medium applications are OpenGeoSys (OGS) [1], PFLOTRAN [2], OPM-FLOW, DUMUX [3].

Looking at the history of the development of numerical simulators for the porous medium there is an obvious shift from the functional programming language (FORTRAN, C) to the object-oriented programming (OOP) language (C++) in creating numerical simulators. Tradi-

tionally FORTRAN and C are the preferred programming language, especially among the scientific community. The major drawback of it is first the modeled PDEs are to be numerically discretized and then segregated in terms of components before starting the process of coding. The fate of any functional programming language is to rely heavily on the low-level of programming by performing the four basic mathematical operations (+, -, *, /) on individual floating-point values and arrays. Implementing any new models or validating any new numerical technique was challenging and painstakingly slow even to the well-experienced programmer. The continuous advancement in computer hardware technology bolstered by the research in numerical techniques, linear algebra, data structures, and algorithms equipped us with the necessary infrastructure to solve more and more complex problems. So, the numerical simulators have grown increasingly sophisticated and become even tougher now to handle it in terms of functional programming languages like FORTRAN and C. Initially, there was a strong hesitation among the scientific community to adapt to the object-oriented programming language like C++, fearing the code execution overhead incurred by OOP will impair the performance of a numerical simulator. It was all true that in the mid-1990s, a typical benchmark test proved that the performance of FORTRAN was 1.2 to 10 times faster than C++. But things got changed after 2000, better optimizing C++ compiler emerged and it had improved functionality in the area of vector code generation. The new programming techniques introduced later in C++ like expression template and template meta-program performed optimizations like loop fusion and algorithm specialization. The OOP language like C++ is very expressive and with its powerful functionality of abstraction, it enables the flexible design of algorithms in high-level syntax for the mathematical constructs. At the same time, the benchmark results conducted in 2005 are convincing to believe that C++ runtime performance at the worst can be matched with the functional programming language like FORTRAN while substantially reducing the design and building time of that application [4].

The numerical solution for PDE can be obtained from one of the three numerical methods, (1) finite-difference method (FDM), (2) finite-volume method (FVM), and (3) finite-element method (FEM). The finite-difference is old and simple of all three. It is based on the truncated Taylor's series expansion of the derivatives for the differential form of governing PDE. So, it has the restriction of application only to the Cartesian grid. The approach gets complicated when applying to the curvilinear grid and it can't be applied to the unstructured grid which is essential to capture the irregular reservoir topology. While the finite element and finite volume method relies on the integral form of PDE, they can be naturally applied on the unstructured grid. The finite element method is complex and highly mathematical. The governing PDE is not solved directly in the finite element method and rather it undergoes the rigorous mathematical treatment of the weighted residual method in order to get the weak form of the PDE which is then solved. It is not very intuitive to use the finite element method (FEM) to fluid flow problems. The finite element method is convenient and intuitive for finding the stress distribution of the physical system since it deals with local and global stiffness matrices in its method for finding the numerical solution. In the Finite volume method, the divergence term of the volume integrated PDE is converted into a surface integral by applying the Gauss divergence theorem. Then it is computed as the summation of fluxes through the control surface enclosing the finite-sized control volume. Since two adjacent finite-sized control volumes share a common face (control surface) between them, the flux entering one control volume through the common face is the same as the flux leaving the adjacent control volume. So, the finite volume method has an inherent conservativeness property in it. Also, the formulation of finite volume on the computational domain discretized as polyhedral cells is very simple and easy, unlike finite element formulation. It is just a systematic and repeated application of conservation laws on each and every cell of the discretized CFD domain.

Initially, there was a need for many FOSS groups with specific and individual objectives since it is very laborious to build a numerical simulator in a functional programming language like FORTRAN. Even after adapting to object-oriented programming like C++, they failed to appreciate the scope to build a quality software framework to regroup the fragmented FOSS groups and co-exist within it. Most of the existing FOSS for the porous medium numerical

simulator is not build on a quality software framework. The existing DUNE framework is not successful since there is no sense of connecting between the modeled mathematical PDEs and the syntax of the programming language used to code and solve it. Moreover, it is a finite element based which is less charming compared to finite volume for CFD simulations. Another important aspect is it failed to attract more users and developers even after a decade ever since its first release in 2007. Individual groups of FOSS developers not into the quality software framework are more susceptible to lose their focus of research, by often doing the redundant work of reinventing the wheel to meet their short-term goal. Therefore, the need of the hour is the quality software framework for developing FOSS for porous medium numerical simulation preferably using the finite volume formulation.

In OpenFOAM, the current IMPES solver for multiphase flow in the porous medium doesn't have the Adaptive Mesh Refinement (AMR) technique implemented and tested in it. Additionally, there is no specialized mesh cutter algorithm for solving the two-dimensional problem. The default hex mesh cutter algorithm for the three-dimensional problem is a computational overhead when applied for a two-dimensional problem. The present study focuses on using a 2D hex-mesh cutter algorithm with the AMR technique in FVM based OpenFOAM for multiphase fluid flow in porous media. The developed and validated IMPSAT solver is first tested for the static grid. Necessary modification is made to the native IMPSAT solver first to equip it with the default AMR capability of the hex-mesh cutter algorithm (IMPSAT-AMR). Then, the 2D hex-mesh cutter algorithm is developed and tested with an IMPSAT solver for 2D problems. The IMPSAT-AMR solver is tested for a two-phase air-water system.

2. Methodology

2.1. OpenFOAM framework for porous numerical simulator

Unlike, the other open-source simulator like OpenGeoSys, PFLOTRAN, OPM-Flow, DuMux which are solely developed for some specific porous medium application, OpenFOAM [5] is not intended for any specific application and it is designed and developed with an insight of generic toolkit for solving PDE by finite volume method. The conservation laws of continuum mechanics are precisely expressed in the mathematical sense with the help of Partial Differential Equations (PDE). The best part of OpenFOAM is all its effort to retain the same PDE representation while computationally solving the continuum mechanics problems by using the high-level syntax of object-oriented programming. For example, if one intends to solve the transient heat conduction equation which is represented as parabolic PDE $\frac{\partial T}{\partial t} - K \left(\frac{\partial^2 T}{\partial x^2} \right)$. It can be achieved simply by calling the below high-level syntax in OpenFOAM.

```
solve(fvm::ddt(T)-kappa*fvm::laplacian(T))
```

So obviously there is a strong sense of connection between the mathematical representation of the physical model and the syntax of the programming language used to represent it in the numerical simulator. It additionally checks the dimensional homogeneity of the PDE intended to solve. There is a dissociation between the implementation and interface. Now, the research into mathematical modeling & simulation is completely diversified with advancement into numerical schemes (QUICK scheme, Upwind scheme, GMRES, etc). Thus, it permits the scope for any user to participate at different levels according to their own level of interest and knowledge in physics and programming. The choice of using OpenFOAM as a black-box CFD application or as a platform for research code is left to the individual. It has been successfully used for Large-Eddy Simulation (LES) of external aerodynamic flows [6], realistic wave generation, and interaction on the coastal structure [7], turbo machinery application [8], mass transfer in oxide cells [9].

2.2. Treatment of porous medium in OpenFOAM

As of now, there are no devoted solvers and dedicated boundary conditions for modeling the multiphase porous medium application at the macro scale even in the latest official release of OpenFOAM. But in situations like airflow through the straight or angled duct with porous

plug in its path acting like filters or flow conditioners, the airflow effects in the porous plug are modeled effectively by marking the cell zones of porous plug and adding the additional viscous and inertial resistance by Darcy-Forchheimer relation in the N-S momentum equation [10]. Penalizing the momentum equation only in the region of porous plug and solving the normal momentum equation at the other remaining free space. There exist two types: (1) implicit porous treatment and (2) explicit porous treatment. The implicit porosity treatment is more robust and is opted if (1) the pressure drop is large, (2) porous substance is more anisotropic, and (3) its axis is not aligned with global coordinates. The explicit porosity treatment is preferred for a simple flow condition. The modeling of the multiphase flow in the porous medium essentially involves concepts like phase saturation, relative permeability, and capillarity effect. Horgue *et al.* [10] started a new chapter in OpenFOAM for multiphase fluid flow in a porous medium by developing an open-source toolbox considering all the essential elements mentioned above and published his work. The developed toolbox includes (1) Dedicated IMPES (Implicit Pressure Explicit Saturation) solver for incompressible and immiscible two-phase porous medium flow, (2) The special boundary condition for treating the phase velocity in the porous medium, (3) The porous medium two-phase flow relative permeability models and capillarity models. In OpenFOAM, the current IMPES solver for multiphase flow in the porous medium doesn't have the Adaptive Mesh Refinement (AMR) technique implemented and tested in it. Additionally, there is no specialized mesh cutter algorithm for solving the two-dimensional problem. The default hex mesh cutter algorithm for the three-dimensional problem is a computational overhead when applied for a two-dimensional problem. Therefore, an AMR technique with a 2D hex-mesh cutter algorithm has been used herein OpenFOAM for multiphase fluid flow in porous media. This part should contain sufficient detail so that all procedures can be repeated. It can be divided into subsections if several methods are described.

2.3. Pressure-Saturation formulation

Choosing the two primary unknowns as wetting phase saturation S_b and non-wetting phase pressure p_a results in the system of improved characteristics with reduced coupling and non-linearity behavior. The following is the system of governing equation in S_b and p_a

$$\frac{\partial}{\partial t}((1 - S_b)\phi) + \nabla \cdot \left[-\frac{Kk_{ra}}{\mu_a} (\nabla p_a - \rho_a g) \right] = Q_a \quad (1)$$

$$\frac{\partial}{\partial t}(S_b\phi) + \nabla \cdot \left[-\frac{Kk_{rb}}{\mu_b} (\nabla p_a - \nabla p_c(S_b) - \rho_b g) \right] = Q_b \quad (2)$$

where K is the absolute permeability of the porous medium; p_c is the capillary pressure which depends on saturation S_b and ϕ is the porosity of the medium.

Adding the equation (1) and (2) results as

$$\frac{\partial}{\partial t}(S_b\phi + \phi - S_b\phi) + \nabla \cdot \left[-\frac{Kk_{ra}}{\mu_a} (\nabla p_a - \rho_a g) - \frac{Kk_{rb}}{\mu_b} (\nabla p_a - \nabla p_c(S_b) - \rho_b g) \right] = Q_a + Q_b \quad (3)$$

$$\nabla \cdot [(M_a + M_b)\nabla p_a] = -\nabla \cdot (M_a\rho_a g + M_b\rho_b g - M_b \frac{\partial p_c}{\partial S_b} \nabla S_b) + Q_a + Q_b \quad (4)$$

Rewriting the equation (2) by substituting the $\nabla p_c = \frac{\partial p_c}{\partial S_b}$

$$\phi \frac{\partial}{\partial t}(S_b) + \nabla \cdot \left[-\frac{Kk_b}{\mu_b} \left(\nabla p_a - \frac{\partial p_c}{\partial S_b} \nabla S_b - \rho_b g \right) \right] = Q_b \quad (5)$$

$$\phi \frac{\partial}{\partial t}(S_b) + \nabla \cdot \left[-M_b \nabla p_a + M_b \frac{\partial p_c}{\partial S_b} \nabla S_b + M_b \rho_b g \right] = Q_b \quad (6)$$

The equations (4) & (6) form the set of governing equations for Pressure-Saturation formulation [11-12].

2.4. IMPSAT (IMplicit in Pressure and SATuration) method

This method is also called as Sequential Fully Implicit (SFI) method. Unlike the IMPES method where the divergence term ($\nabla \cdot (-M_b(S_b^n)\nabla p_a^n)$) is at the n-th time step, in this method, it is solved by the inner newton's iterative correction for each time step. Though it results in extra computational cost but gives more numerical stability as compared to the IMPES method. The more details of the IMPSAT method can be found in [13].

$$T(S_b^{v+1}, S_b^v, u_b^{v+1}) := \phi \frac{S_b^{v+1} - S_b^v}{\Delta t} + \nabla \cdot (u_b^{v+1}) = f^v(Q_b, M_b, p_c, \rho_b) \quad (7)$$

where $u_b^{v+1} = -M_b(S_b^{v+1}) \nabla p_a^{v+1}$

$$P(S_b^v) := -\nabla \cdot (M_a(S_b^v) + M_b(S_b^v)) \nabla p_a^{v+1} = f_p^v(Q_b, M_b, p_c, \rho_b) \quad (8)$$

3. Problem definition

3.1. One-Dimensional case for validation

In order to first test the IMPSAT solver and then its AMR capability, the standard one-dimensional case of Buckley and Leverett [14] for the air-water system is considered for the 1D reservoir domain. The respective equation for the radial Buckley-Leverett flow is as follows [15]

$$\frac{\partial S_b}{\partial t} + \frac{1}{r} \frac{\partial}{\partial r} (r f_b(S_b, r)) = 0 \quad (9)$$

Here 'r' is defined as the radial distance from the point of injection in the circular domain and S_b is the wetting phase saturation. Since the flow is incompressible $f_b(S_b, r) = f_b(S_b)/r$. So, the above equation (9) is written as

$$\frac{\partial S_b}{\partial t} + \frac{1}{r} \frac{\partial}{\partial r} (f_b(S_b)) = 0 \quad (10)$$

$$\frac{\partial S_b}{\partial t} + \frac{1}{r} \frac{\partial f_b(S_b)}{\partial S_b} \frac{\partial S_b}{\partial r} = 0 \quad (11)$$

The information about reservoir properties, fluid properties, and Relative permeability model used is listed in Table 1. The obtained numerical result is validated against the standard Buckley-Leverett semi-analytical solution as in Fig. 1.

Table 1. Information of (a) Reservoir properties, (b) Fluid properties, and (c) Relative permeability model [10]

(a) Reservoir properties		
Length of reservoir	1 m	
Porosity	0.5	
Permeability	$1 \times 10^{-11} \text{ m}^2$	
Production rate	$1 \times 10^{-7} \text{ m}^3/\text{sec}$	
(b) Fluid properties		
Fluid	$\rho \text{ (kg/m}^3\text{)}$	$\mu \text{ (Pa.s)}$
Water	1000	1×10^{-3}
Air	1	1.76×10^{-5}
(c) Relative permeability mode		
	power coefficient m	
Brooks and Corey [16]	3	
van Genuchten [17]	0.5	

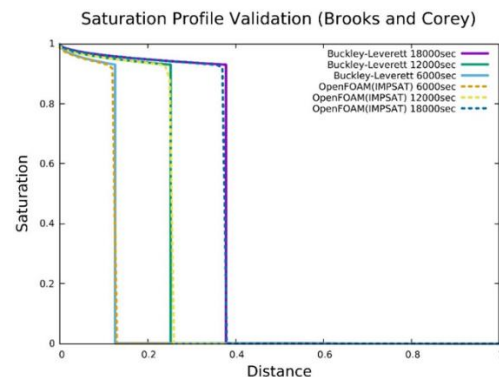


Fig. 1 Validation of Water Saturation with Buckley-Leverett (Air-Water) [14]

3.2. Two-dimensional case for validation

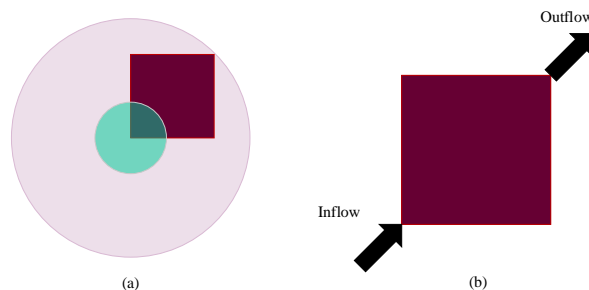


Fig. 2 Water Flooding for diagonal Injection and Extraction Well

Consider the case as shown in Fig. 2 where the water phase is pumped in from the left lower corner into the domain saturated with oil. Doing so will displace the oil to the right upper corner production well because the sides of the domain are impermeable. So, the principal flow direction will be the diagonal of the domain.

The water saturation line profile is examined along the diagonal line $(x, y), x = y$, for the considered case computed in OpenFOAM

with the fine-scale semi-analytical numerical result of the radial Buckley-Leverett flow [18]. It is described as a scenario where the water phase is being pumped into the center of a circular domain.

Huber and Helmig [15] adopted the above approach of validating the special case of diagonal well two-dimensional problem by radial Buckley-Leverett flow semi-analytical solution as shown in Fig. 2(a) and 2(b). The initial condition used by Huber and Helmig is uniform saturation of $S_b=0$ inside the domain and the results are compared at 0.075 PVI (pore volumes injected). The pore volume injected is given by $PVI = \frac{(injectionrate \times time)}{(volume \times porosity)}$.

In OpenFOAM, the computational domain of dimension $1m \times 1m \times 2.83cm$ is considered and the porosity of it is 0.5. The injection well is located at the lower-left corner. All the walls of the domain are impermeable except a patch on the top right corner of 10cm. The injection well strength is $1 \times 10^{-6} m^3/sec$.

To validate with Huber and Helmig, the above-considered case in OpenFOAM has to be simulated until 1061 seconds to compare the saturation profile at 0.075 PVI. Fig. 3(a) shows the saturation profile at 0.075 PVI for a two-dimensional case. The quantitative validation on the diagonal line from the injection well to the producer well is shown in Fig. 3(b). The numerically simulated results of the IMPSAT solver developed in OpenFOAM are in good comparison with Huber and Helmig.

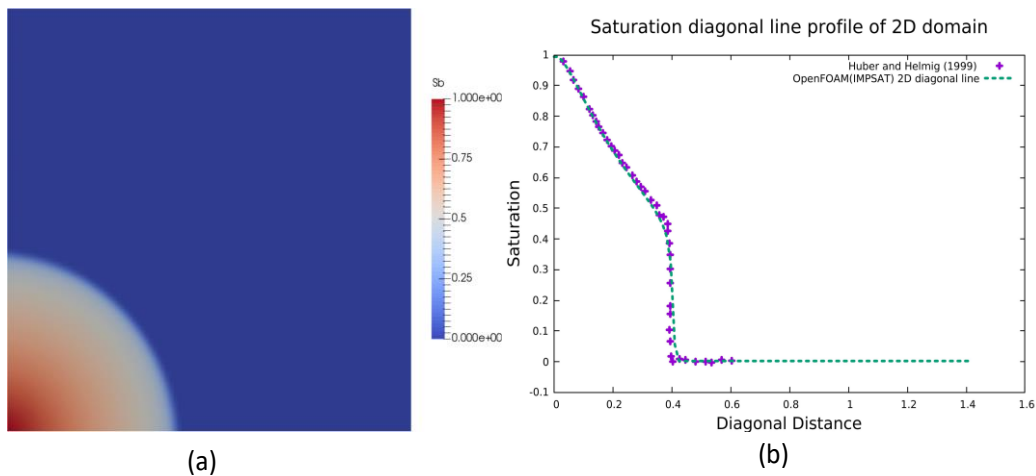


Fig. 3. (a) Water Flooding at the instance of 0.075 PVI, (b) 2D Diagonal line validation at the instance of 0.075 PVI

4. Results and discussion

4.1. Grid independent study

The domain of the water injection configuration along with its boundary conditions (BCs) used in this present work is shown in Fig. 4(a). A non-uniform grid has been generated with fine cells towards the injection well location in X-direction. It results in slightly clustered grids in the X direction whereas equal and uniform grids are generated in the Y direction as shown in Fig. 4(b). The computational grid is generated by using *blockMesh* utility.

Grid independence study is to be conducted by taking into consideration four different mesh configurations as listed in Table 2. The water is injected at the rate of 1 liter/sec from the injection well. The simulated numerical results are post-processed in *Paraview*.

Table 2. Three mesh configuration for grid independence study

Grid	X-Direction	Y-Direction	Total Cells
Very coarse	40	20	800
Coarse	80	40	3200
Medium	160	80	12800
Fine	240	120	28800

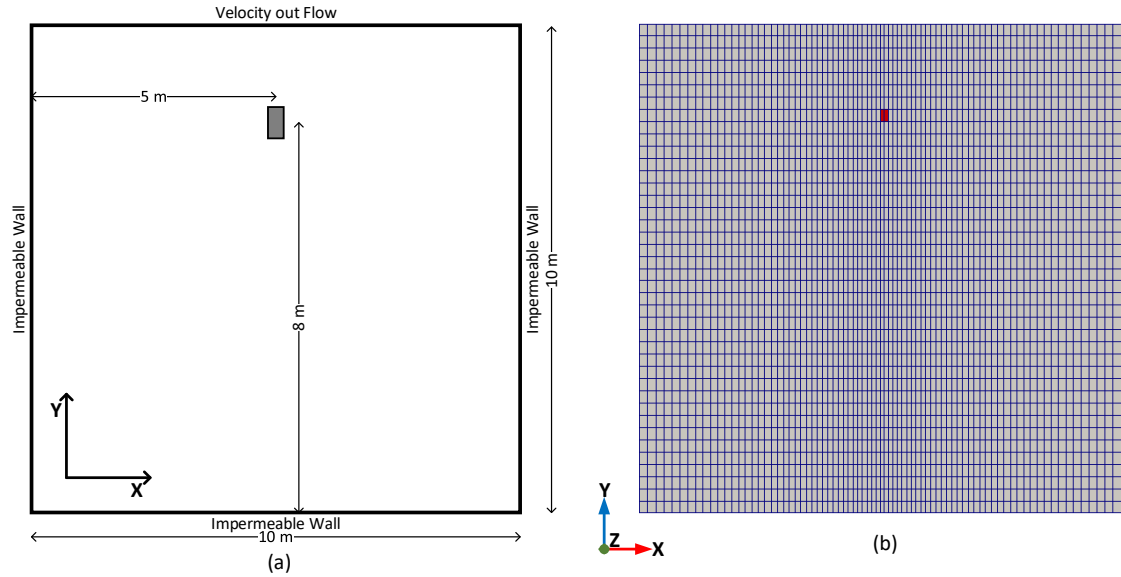


Fig. 4. (a) Computational domain and (b) Computational grid with injection well location

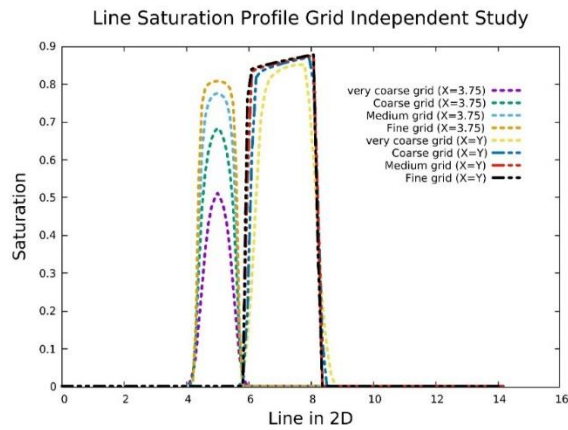


Fig. 5 Grid Independent Study of Saturation on line profiles of 2d domain

It can be inferred from Fig. 5 by the saturation line profile compared for all four-grid configuration (very coarse grid, coarse, medium, fine) over $X=Y$ and $X=3.735$ of the domain shown in Fig. 4(a). The variation in the saturation is very minimum for the medium and fine grid as can be seen in Fig. 6. The medium grid configuration arrives at the converged saturation profile with lesser computing time as compared to the fine grid. In CFD for the multiphase fluid, the mass balance of the system can be easily verified from the saturation contour profile, and at all times its value is $0 < S_b < 1$. The same is inferred in the present case.

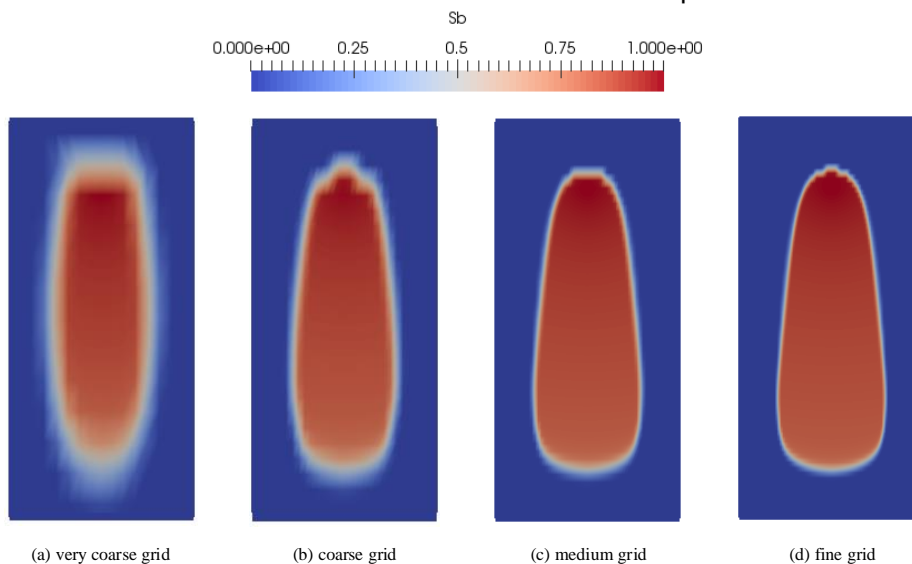


Fig. 6. S_b contour for a very coarse, coarse, medium and fine grid

4.2. Need for 2D hex-mesh cutter

The default hex-mesh cutter engine shipped with OpenFOAM is efficient in handling only three-dimensional mesh. The reason for it could be that OpenFOAM is geared to solve all the problems in 3D by default. In order to solve 2D problems, first, the 3D mesh is created with only one cell in the third dimension and then it is instructed that the boundary patches normal to the third dimension to be specified as 'empty' in the boundary file of the simulation control settings. So, those faces in that boundary patches marked as empty won't participate in the total control volume flux calculation process with its associated cell and therefore it requires no solution on those 'empty' boundary patches. When the default hex-mesh cutter engine is applied to 2D mesh it starts to create the cells unnecessarily in the third dimension also and because of it the solution is in no way going to improve at all. It is only a mere computational overhead to refine the cells in the third dimension for the 2D mesh. It is wise to make the necessary modification in the existing hex-mesh cutter engine and create a specialized 2D hex-mesh cutter engine to enable the handling of 2D mesh more efficiently.

4.3. D Hex-Mesh cutter refinement algorithms

The 2D hex-mesh cutter engine is very similar to that of the default 3D hex-mesh cutter engine with a slight difference. One extra information about the normal axis to the empty boundary patches is to be given for this new engine. The process of 2D hex-mesh cutter refinement is very descriptive in Fig. 7. The new cell center point is not created in the current 2D hex-mesh cutter engine.

- (1) As the first step here, the new points are created on the face center of the empty boundary patches of the candidate cell for refinement as in Fig. 7(b).
- (2) Then, the next step is to loop for the edges on the faces of the empty boundary patch and create a new point at its mid-point. This is shown in Fig. 7(c).
- (3) Four new faces are created on the empty boundary patches of the chosen cell as in Fig. 7(d).
- (4) The remaining four faces which don't have the face center are divided into two faces as in Fig. 7(e).
- (5) The last step is to create the four new internal faces as in Fig. 7(f).

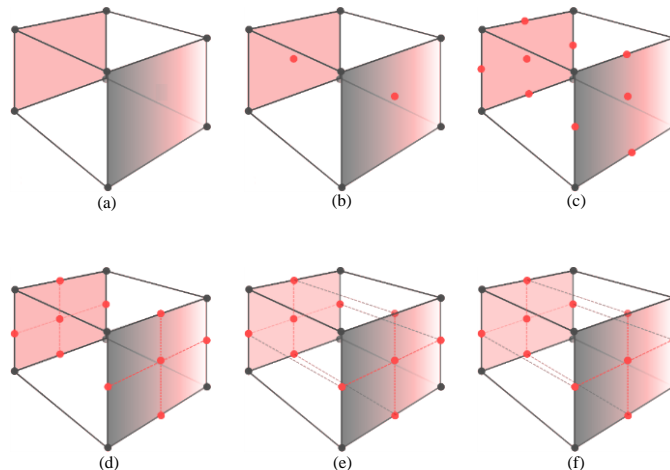


Fig. 7 The Process of Hex-mesh cutter Refinement algorithm

The coarsening process and the solution field mapping are done in the same way as discussed for the default 3D hex-mesh cutter engine.

4.4. Testing the AMR-IMPSAT Solver

The developed and validated IMPSAT solver is first tested for the static grid. Now here, the necessary modification is made to the native IMPSAT solver first to equip it with the default

AMR capability of the hex-mesh cutter algorithm (IMPSAT-AMR). Then, the 2D hex-mesh cutter algorithm inspired by the work of Ahmad Baniabedalruhman [19] is developed and tested with an IMPSAT solver for 2D problems. The IMPSAT-AMR solver is tested for both multiphase air-water and water-oil system in the following sections.

4.4.1. AMR in multiphase air-water porous system

The details of the case like domain size, boundary conditions, and injection well strength areas are given in Fig. 4(a). The numerical simulation is performed on the dynamic grid. The value of the S_b field is used as the criterion to check whether a cell requires refinement or coarsening. Obviously, it could only be a natural choice for the following reasons.

- (1) Hex-mesh cutter engine in OpenFOAM necessitates a scalar field as adaptation criterion and S_b comes under the scalar field category.
- (2) The range of solution of the water saturation field S_b is well known and it always honors the relation $S_{b, min} < S_b < S_{b, max}$.
- (3) The key functions in the multiphase flow of the porous system computation like relative permeability and capillary functions are related to water saturation field S_b .

The range of the S_b is [0.2; 0.8]. If the S_b value is within this specified range in any cell then it is entitled to the refinement process otherwise it is selected for the coarsening process. The maximum refinement level is chosen to be 2. The refinement interval is specified as 1 which implies that at every time step the adaptation criterion is checked to carry out the mesh modification process. The maximum cell limitation for the refinement process is kept as 400000 cells which may not be achieved during the entire simulation time and so the adaptation process is always on. First, a very coarse mesh of 800 cells is given as initial base mesh to start with for:

- (1) The default IMPSAT-AMR of OpenFOAM which is referred to in this work as AMR2D3D
- (2) The specialized IMPSAT-2DAMR which is referred to in this work as AMR2D2D.

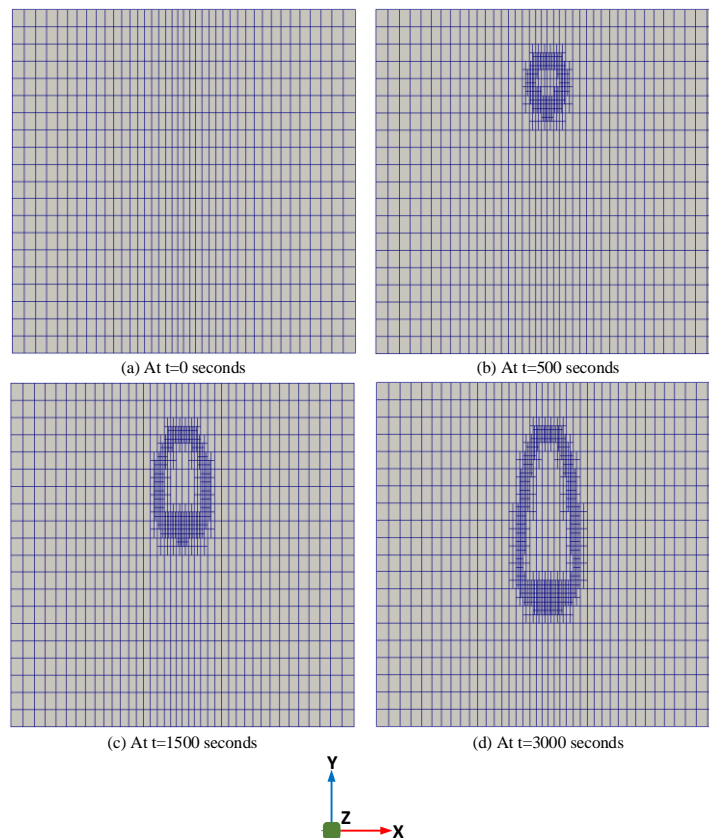


Fig. 8. The grid adaptation process at different time instances for both AMR2D3D and AMR2D2D

The grid adaptation process for both AMR2D3D and AMR2D2D is shown in Fig. 8 for different time instances such as $t=0$ sec, $t=500$ sec, $t=1500$ sec, and $t=3000$ seconds. There is no difference in both of the processes in the view as shown in Fig. 8. The distinct difference between the AMR2D3D and AMR2D2D solver's result is noticed in the adapted grid cut-view in Fig. 9.

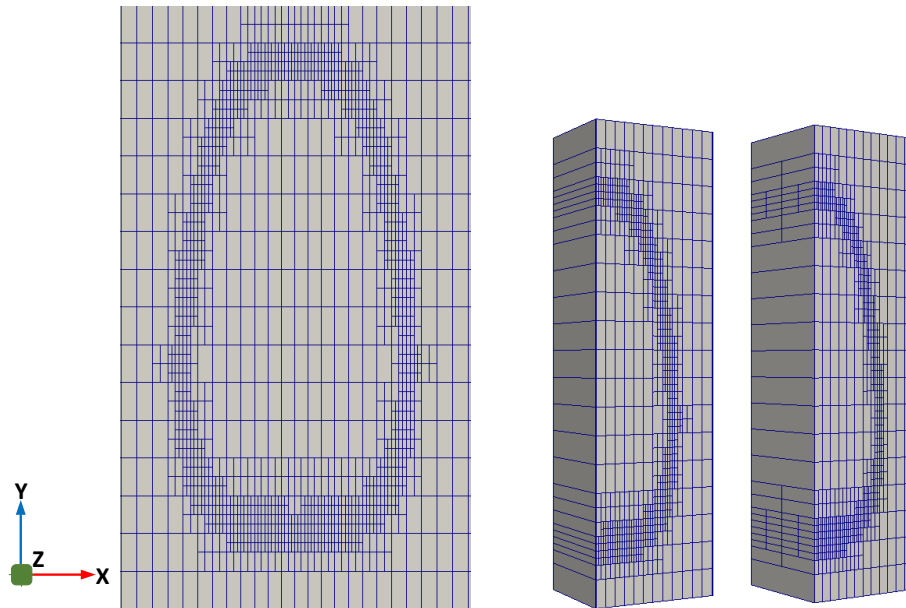


Fig. 9. The zoom-in view of the adaptive grid for AMR2D2D and AMR2D3D

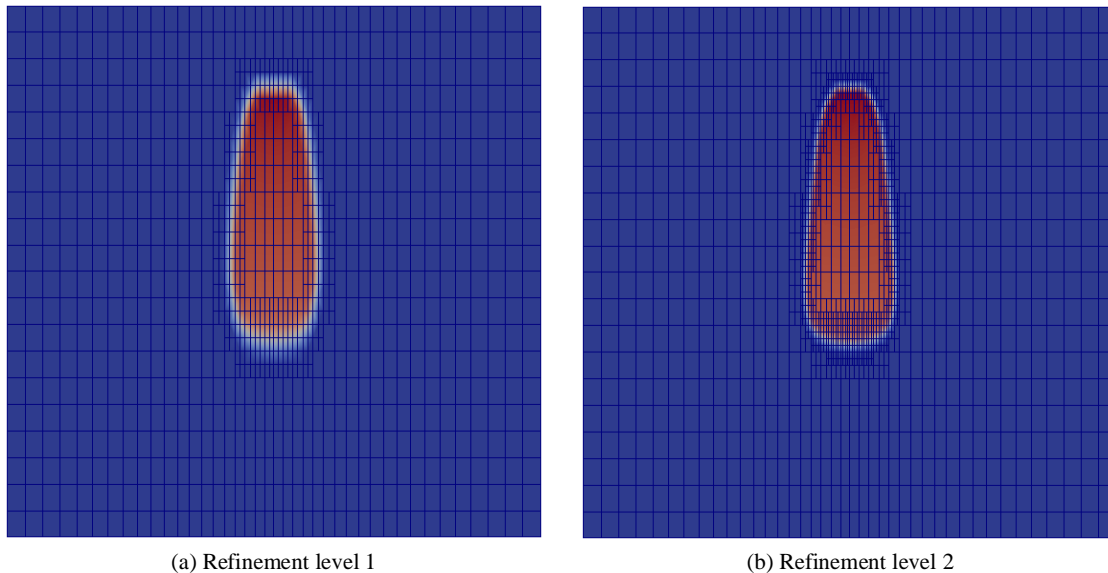


Fig. 10. Refinement level comparison S_b contour with a grid superimposed

The results of both AMR2D3D & AMR2D2D is compared both quantitatively and qualitatively with fine static grid (28,800 cells) solution. The qualitative comparison is as shown in Fig. 10. It can clearly be seen from Fig. 10 that the interface is captured more precisely for computation set with refinement level 2 over level 1. The quantitative comparison is done at three sampling line profiles such as $x=y$, y -axis, and $x=3.75$ m as shown in Fig. 11(a). The slight variation is observed in the quantitative plot at the sampling line profile of $x=3.75$ m.

The comparison of the time history of the adapted cells for both AMR2D3D and AMR2D2D is plotted in Fig. 11(c) and its inferences are listed below.

(1) Both the processes start with 800 cells as the initial grids at time $t=0$ seconds.

- (2) The general increasing trend is observed in both the processes until the end of simulation of 3000 seconds.
- (3) At any given instance, after $t=0$ seconds, the number of adapted grids for the AMR2D3D process is more than the AMR2D2D process.
- (4) At the end of 3000 seconds simulation time, the number of grid cells in AMR2D2D is just 1500 cells while the number of grid cells in AMR2D3D is 3400. The AMR2D2D process takes slightly less than 50% number of grid cells as compared to AMR2D3D.
- (5) The initial high slope of the curves for both the processes from $t=0$ seconds to $t=200$ seconds is indicative of the fact that the particular phase is only with the refinement process. After that, both the coarsening and refinement processes are taking place.

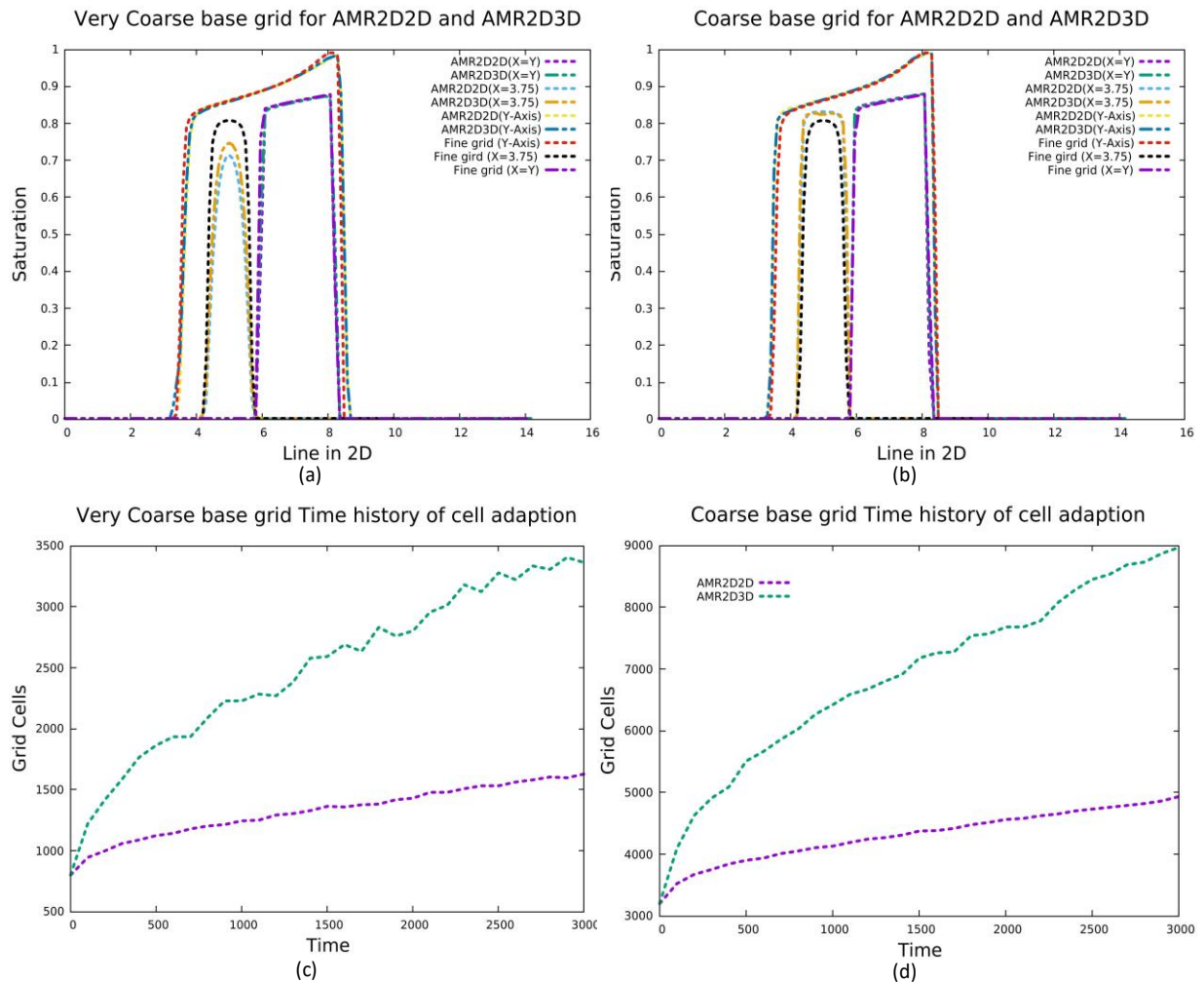
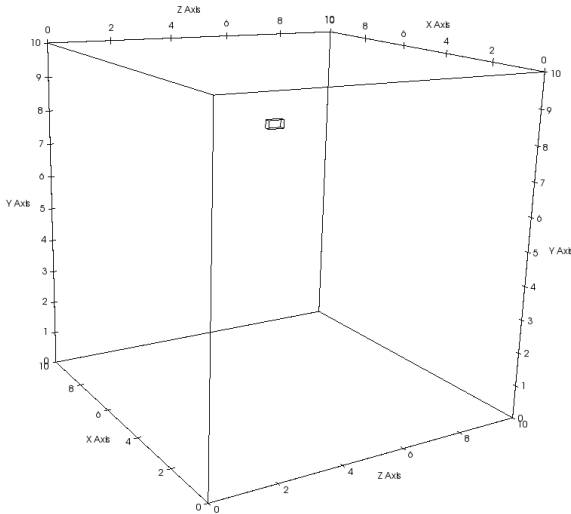


Fig. 11. Comparing S_b on line profiles for AMR2D2D, AMR2D3D with (a) very coarse base grid of 800 cells, (b) coarse base grid of 3200 cells, and; Time history of Adapted cells in AMR2D2D and AMR2D3D with (c) very coarse base grid, and (d) coarse base grid

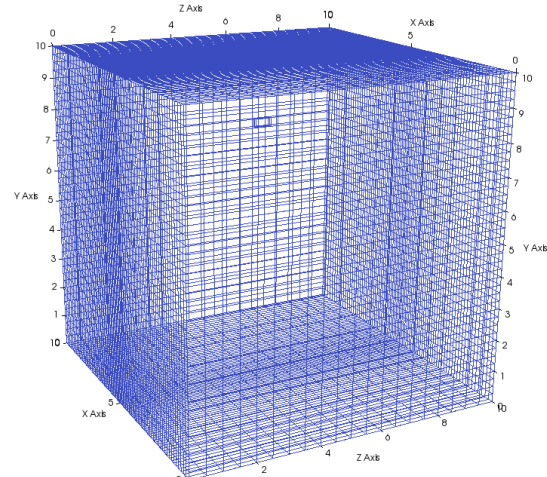
As compared to the static grid process, AMR2D3D is far better since for static grid computation 28,800 cells are used whereas for the AMR2D3D process it took only 3400 cells. The static grid computation took 8.5 times more grid cells than AMR2D3D and 19.2 times more than AMR2D2D. The marked superiority of AMR2D2D is distinctively clear with the above information. As there is a practice of grid-independent study for arriving at the quality computational mesh assertively for the static grid, in a similar way, the whole above set of procedures is repeated for both AMR2D3D and AMR2D2D solver for another coarse base grid of 3200 cells as initial cells. The quantitative comparison is shown in Fig. 11(b) respectively. The time history of refined cell details for both AMR2D3D and AMR2D2D is plotted in Fig. 11(d). The slight

variation observed in the quantitative plot at the sampling line profile of $x=3.75$ m in the former case is also not recognizable here. The aspect regarding the total computational time for all the above cases is studied separately and elaborately in the later section under performance study.

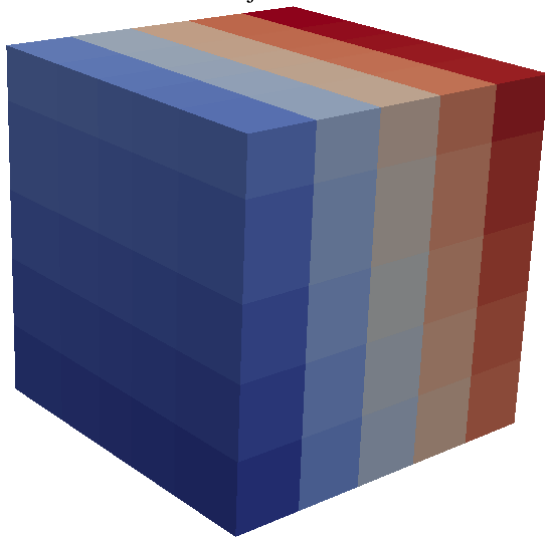
4.4.2. Comparison of static grid versus AMR for 3D case



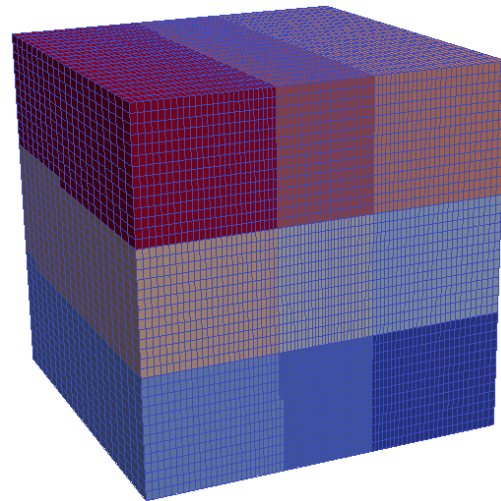
(a) The sketch of physical domain 10m×10m×10m and injection well



(b) The view of the CFD wireframe mesh



(c) Parallel computing 125 CPU domains for water flooding with grid adaptation



(d) Parallel computing 9 CPU domains for water flooding without grid adaptation

Fig. 12. The physical domain for the 3D case with wireframe mesh and domain decomposition of parallel computing CPUs for AMR and static grid computations

The advantages of the AMR technique and its effects are realized much better when a three-dimensional case is solved. In this pursuit, the previous 2D case of 10m×10m domain is converted into the three-dimensional case by taking the third dimension also to be 10 m. So, the dimension of the 3D domain is 10m×10m×10m as shown in Fig. 12 (a). The injection well is placed at (5m, 8m, 4.75m) and its injection rate is 1 liter/second. The front, back, right, left and bottom wall is chosen to be impermeable wall boundary condition. The top boundary is given as a velocity outflow boundary condition. The number of grids in x, y, and z directions

are 80 cells, 40 cells, and 20 cells respectively. The view of CFD wireframe mesh is shown in Fig. 12 (b). The same CFD mesh is given for both IMPSAT and IMPSAT-AMR solvers. In order to solve the grid adaptation process of IMPSAT-AMR solver by parallel computing, 125 processors are engaged. The domain decomposition for 125 processors is shown in Fig. 12 (c). Since the static grid computation by IMPSAT solver is less computationally intensive only 9 processors are engaged. In Fig. 12 (d) shows the domain decomposition details of the CFD mesh assigned to the nine processors.

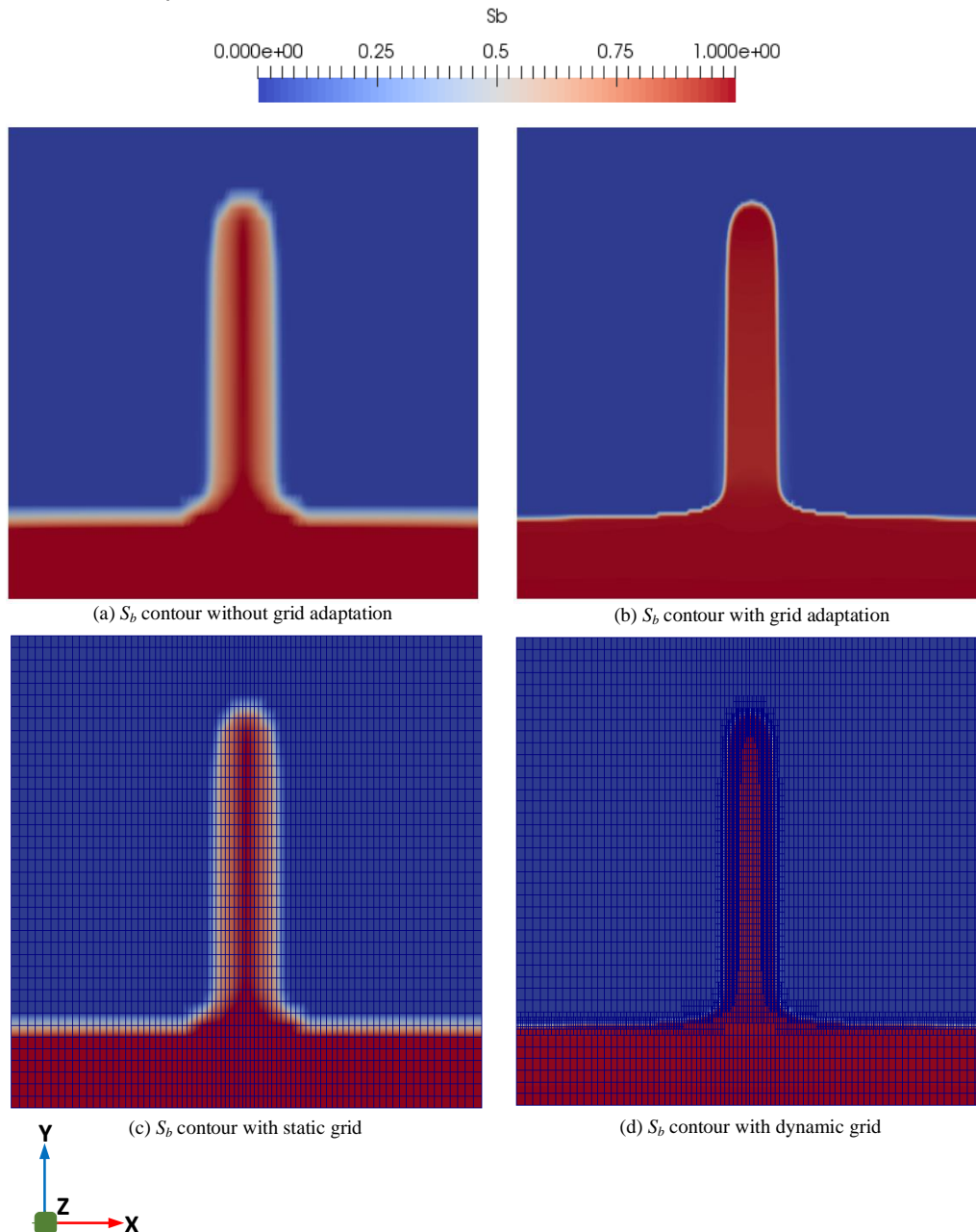


Fig. 13 The saturation contour S_b comparison at $t=3000$ seconds at $Z=0$ plane

The total simulation time is set as 1,06,000 seconds. The saturation contour is compared for with and without grid adaptation processes at two-time instances such as $t=3000$ seconds and $t=1,06,000$ seconds as shown in Fig. 13 and 14 respectively. From the result in Fig. 13 and 14, it can be inferred that the adaptive mesh refinement process captures the air and water interface more precisely. The errors incurred by artificial diffusion due to insufficient

mesh points are addressed by AMR. At any instance in time, the AMR process uses the optimal number of grid points just with the simple concept of adapting and coarsening the mesh at where and when it is required. The volume contour of S_b at 1,06,000 seconds is shown in Fig. 14 and it gives a clear 3D picture of artificial diffusion in the static grid process. The initial mesh size of 64,000 cells at 0 seconds in the AMR process has increased to 1,19,622 cells and 1,76,966 cells at 3000 seconds and 1,06,000 seconds respectively.

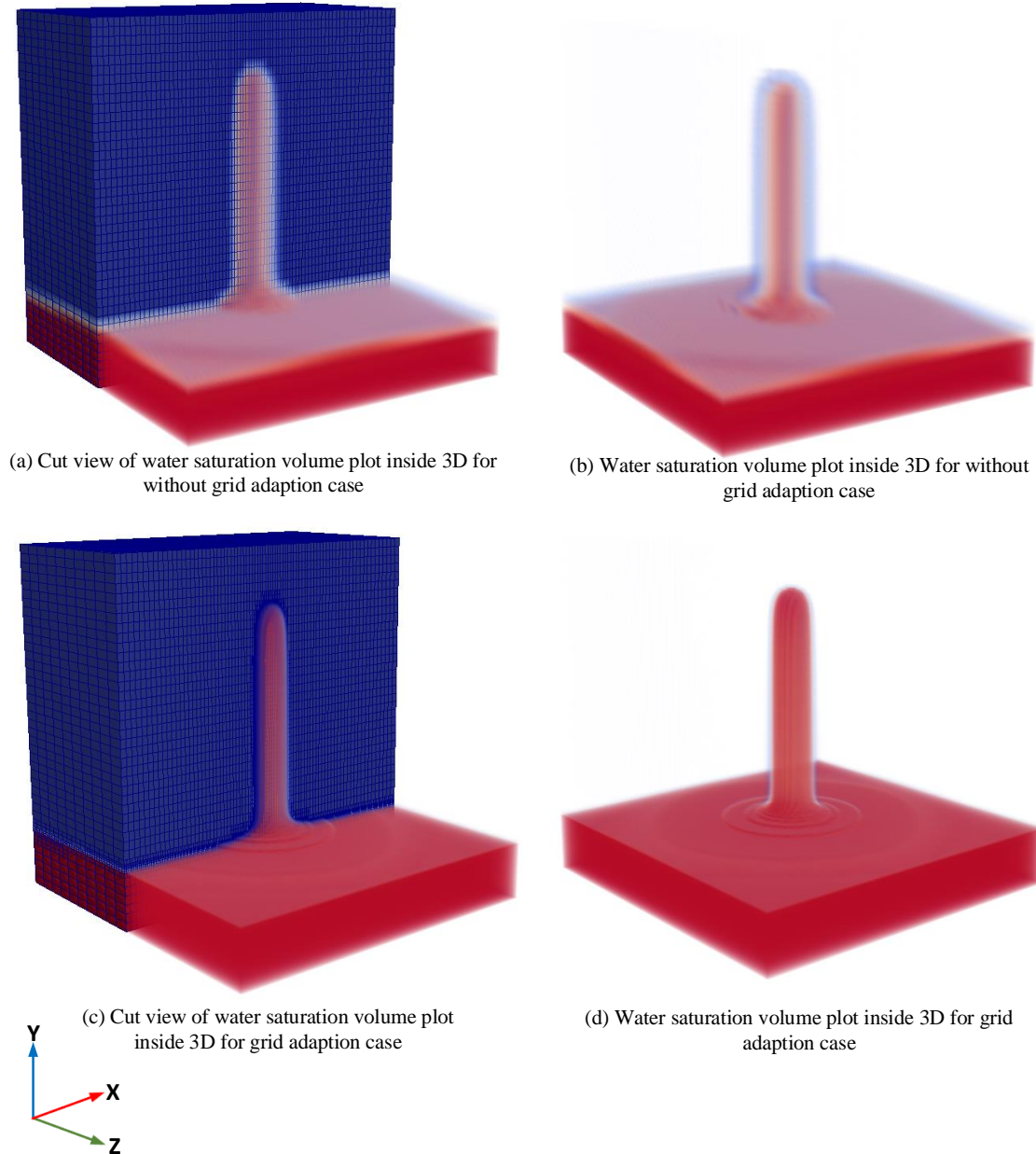


Fig. 14 S_b volume plot at $t=106000$ seconds

5. Conclusion

The developed IMPSAT solver in this paper is validated with literature and its fidelity is tested with a variety of different test cases which includes two dimensional and three-dimensional cases. The IMPSAT solver is implemented with default AMR capability and also with a specialized 2D AMR engine. The developed solver is compared with the static grid and the superiority of AMR2D2D is clearly been shown as compared to the AMR2D3D or the static grid process in terms of the number of cells used. It appears that the adaptive mesh refinement

process captures the air and water interface more precisely. The errors incurred by artificial diffusion due to insufficient mesh points are addressed by AMR. And thus, the AMR process uses the optimal number of grid points just with the simple concept of adapting and coarsening the mesh at where and when it is required. It is concluded that the specialized 2D AMR engine outperforms the existing default AMR for 2D cases in terms of both computational time and runtime memory. The MPI (Message Passing Interface) capability of the developed solver is also tested for the 3D case. The future work can focus on using the present solver for improving the assessment for viscous fingering during the enhanced oil recovery.

Symbols

a	<i>non-wetting phase</i>
b	<i>wetting phase</i>
i	<i>phase</i>
K	<i>absolute permeability of the porous medium</i>
k_{ri}	<i>relative permeability of phase i</i>
M_i	<i>mobility of phase i</i>
p_i	<i>pressure of phase i</i>
p_c	<i>capillary pressure</i>
ρ_i	<i>density of phase i</i>
ϕ	<i>porosity of the medium</i>
μ_i	<i>viscosity of phase i</i>
Q_i	<i>source term</i>
r	<i>radial distance from the point of injection</i>
S_i	<i>saturation of phase i</i>

References

- [1] Kolditz O, Bauer S, Bilke L, Böttcher N, Delfs JO, Fischer T, Görke UJ, Kalbacher T, Kosakowski G, McDermott CI, Park CH. OpenGeoSys: an open-source initiative for numerical simulation of thermo-hydro-mechanical/chemical (THM/C) processes in porous media. *Environmental Earth Sciences*, 2012; 67(2): 589-599.
- [2] Lichtner PC, Hammond GE, Lu C, Karra S, Bisht G, Andre B, Mills RT, Kumar J, Frederick JM. PFLOTRAN Web page. Los Alamos National Laboratory, location: Los Alamos, NM [Available at <http://www.pflotran.org>]. 2019.
- [3] Flemisch B, Darcis M, Erbertseder K, Faigle B, Lauser A, Mosthaf K, Müthing S, Nuske P, Tatomir A, Wolff M, Helmig R. DuMux: DUNE for multi-{phase, component, scale, physics,...} flow and transport in porous media. *Advances in Water Resources*, 2011; 34(9): 1102-1112.
- [4] Veldhuizen TL, Jernigan ME. Will C++ be faster than Fortran?. In *International Conference on Computing in Object-Oriented Parallel Environments 1997 Dec 8* (pp. 49-56). Springer, Berlin, Heidelberg. https://doi.org/10.1007/3-540-63827-X_43
- [5] Weller HG, Tabor G, Jasak H, Fureby C. A tensorial approach to computational continuum mechanics using object-oriented techniques. *Computers in physics*, 1998; 12(6): 620-631.
- [6] Lysenko DA, Ertesvåg IS, Rian KE. Large-eddy simulation of the flow over a circular cylinder at Reynolds number 3900 using the OpenFOAM toolbox. *Flow, turbulence and combustion*, 2012; 89(4): 491-518.
- [7] Higuera P, Lara JL, Losada IJ. Simulating coastal engineering processes with OpenFOAM®. *Coastal Engineering*, 2013; 71: 119-34.
- [8] Beaudoin M, Jasak H. Development of a generalized grid interface for turbomachinery simulations with OpenFOAM. In *Open source CFD International conference 2008 Dec 4* (Vol. 2). Berlin.
- [9] Novaresio V, García-Camprubí M, Izquierdo S, Asinari P, Fueyo N. An open-source library for the numerical modeling of mass-transfer in solid oxide fuel cells. *Computer Physics Communications*, 2012; 183(1): 125-146.
- [10] Horgue P, Soulaire C, Franc J, Guibert R, Debenest G. An open-source toolbox for multiphase flow in porous media. *Computer Physics Communications*, 2015; 187: 217-226.
- [11] Adler PM, editor. *Multiphase flow in porous media*. The Netherlands: Kluwer Academic Publishers; 1995 Nov 30.
- [12] Baer J. *Dynamics of fluids in porous media*. America Elsevier Publishing Company. 1972.
- [13] Jenny P, Lee SH, Tchelepi HA. Adaptive fully implicit multi-scale finite-volume method for multi-phase flow and transport in heterogeneous porous media. *Journal of Computational Physics*, 2006; 217(2): 627-641.

- [14] Buckley SE, Leverett M. Mechanism of fluid displacement in sands. Transactions of the AIME, 1942; 146(01): 107-116.
- [15] Huber R, Helmig R. Multiphase flow in heterogeneous porous media: A classical finite element method versus an implicit pressure–explicit saturation-based mixed finite element–finite volume approach. International Journal for Numerical Methods in Fluids, 1999; 29(8) :899-920.
- [16] Brooks RH, Corey AT. Properties of porous media affecting fluid flow. Journal of the irrigation and drainage division, 1966; 92(2): 61-90.
- [17] Van Genuchten MT. A closed-form equation for predicting the hydraulic conductivity of unsaturated soils 1. Soil science society of America journal, 1980; 44(5): 892-898.
- [18] Blunt M, Rubin B. Implicit flux limiting schemes for petroleum reservoir simulation. Journal of Computational Physics, 1992; 102(1): 194-210.
- [19] Baniabedalruhman, A. Dynamic meshing around fluid-fluid interfaces with applications to droplet tracking in contraction geometries. PhD Thesis. Michigan Technological University, 2015.

To whom correspondence should be addressed: professor Suresh Kumar Govindarajan, Reservoir Simulation Laboratory, Petroleum Engineering Programme, Department of Ocean Engineering, Indian Institute of Technology – Madras, Chennai, India, E-mail: gskumar@iitm.ac.in

Palynostratigraphy and Lithostratigraphy of Ha-001 Well, Shallow Offshore, Western Niger Delta, Nigeria

Olubusayo A. Olatunji¹, Edward A. Okosun², Usman S. Onoduku², And Yahya B. Alkali²

¹ Department of Earth Sciences, Faculty of Science, Adekunle Ajasin University, Akungba-Akoko, Ondo State, Nigeria

² Department of Geology, Faculty of Physical Sciences, Federal University of Technology, Minna, Niger State, Nigeria

Received June 15, 2019; Accepted September 30, 2020

Abstract

The sedimentary intervals from HA-001 well have been analyzed for palynological and sedimentological studies with the aim of generating biozonation, maturation and paleoenvironmental results. Seventy-six ditch cutting samples within the depth intervals of 750 -11610 ft were analyzed. There were few to common recoveries of sporomorphs. Sedimentological inferences were derived from the integration of wire line logs, lithologic characteristic and distribution of index accessory minerals which include ferruginous materials, glauconite, pellets, carbonaceous detritus, shell fragments and pyrites plus minor mica flakes. The lithofacies sequences that characterise the HA-001 well intervals include alternating sand and shale units which suggest rapid shoreline progradation deposited in coastal deltaic to shallow marine settings. The entire interval essentially tested the Benin and the Agbada Formation. The grain increases essentially from fine to medium grained, occasionally coarse to granule-sized at the basal part of the well, to dominantly coarse to pebble-sized, occasionally medium to fine-grained at the upper part. Two (2) palynostratigraphic zones of *Cyperaceaepollis* sp. - *Nymphaeaepollis clarus*, and *Stereisporiles* sp. were established for the well using the International Stratigraphic Guide. The two (2) zones are assemblage range biozones and Late Miocene age was assigned to the interval based on the stratigraphic age range of diagnostic markers such as *Psilatricolporites crassus*, *Echitriletes plicenicus*, *Elaeis guineensis*, *Corylus* sp. and *Zonocostites ramonae*. Thermal maturity on the basis pollen and spores colours indicated maturity to late degree of maturation.

Keywords: Sporomorphs; Lithofacies; Formation; Biozone and Maturation.

1. Introduction

The demands for petroleum worldwide have been steady over the years if not increasing. Hence, the integration of various geological methods such as palynological, sedimentological and paleoenvironmental analyses are needed for the development of hydrocarbon exploration in the offshore Niger delta. The occurrence of hydrocarbon in Niger delta basin has increased the interest of many researchers in the geologic structure as well as petroleum aspects of the basin. The discovery of commercial deposits of hydrocarbon in 1956 began the establishment of the Niger delta as a world-class petroleum province [1]. The science of petroleum exploration and production is multi-disciplinary with each discipline complementing the other. One of these disciplines is palynology. Palynology is a term coined by [2] and was derived from the Greek word, Palynein which means, "to sprinkle, to spread around". Thus, there is need for intensive research of Niger Delta Basin in order to have the understanding of the stacking pattern of the lithofacies and geologic ages respectively

The aim of this work is to carry out palynological and lithofacies analyses of the strata penetrated by HA-001 well in order to produce the palynostratigraphic zonation using the

international stratigraphic procedures as well as assigning ages, inferring the paleoenvironment of deposition and determining the maturation of the well interval for the purpose of hydrocarbon exploration.

2. Study area

The study area lies within the Niger delta basin. HA-001 well lie within latitude 4° 09' 10.9" N and longitudes 6° 14' 1.8" E within the shallow offshore area, western Niger delta, Nigeria. The names of the wells have been coded by Shell Production and Development Company due to proprietary reasons. The location of the wells is shown in Figure 1.

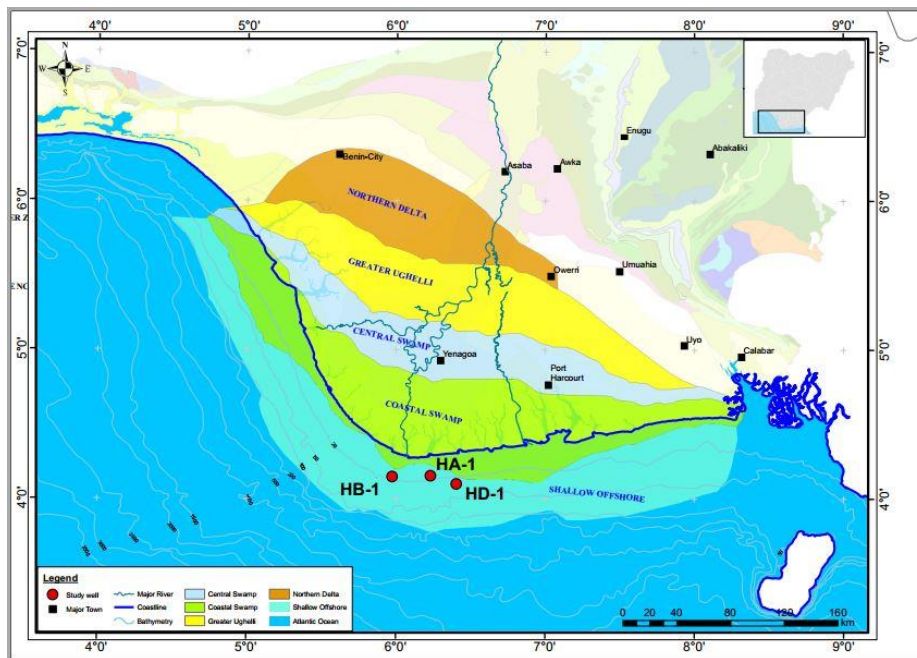


Figure 1. Location of H-wells, shallow offshore depobelt, Niger Delta, Nigeria (modified from [3-4]).

2.1. Geology of Niger delta

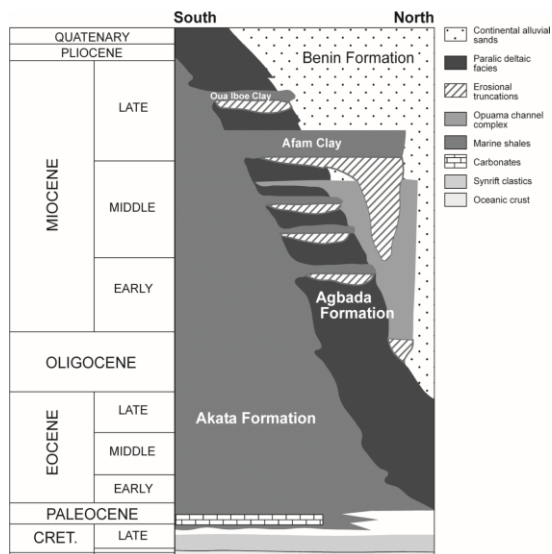


Figure 2. Stratigraphy of the Formations of the Niger Delta [12]

From the viewpoint of size and thickness of sediments, the Niger delta is the most important sedimentary basin in Nigeria. Again, the region is also the most important from the economic standpoint as its petroleum reserves supply a large part of the country's foreign exchange earnings.

The Niger delta covers a land mass in excess of 105,000 km² [5]. It is an arcuate shaped [6-7], and a prograding high energy constructive lobate delta [8]. The sedimentary basin consists of three Formations (Figure 2). These are; Akata, Agbada and Benin Formations. Akata Formation ranges from Paleocene to Recent age. Deposition started in Agbada Formation during the Eocene while Benin Formation experienced deposition during the Oligocene. The Akata Formation is made up mainly of open marine and pro-delta dark shales with lenses of siltstones and sandstones [9].

The Agbada Formation comprises shales, siltstone and sandstone [10]. Benin Formation is made up of indurated sandstones, minor shales, coals and gravels [11].

3. Materials and methods

A total of seventy six (76) ditch cutting samples from HA-001 well and wireline logs were made available by Shell Production and Development Company (SPDC), Nigeria. The well samples which were got from intervals of 750 – 11600 ft were analyzed for their sporomorphs contents and sedimentological analyses through observation under the microscope. The other materials used are; beakers, weighing balance, liquid soap, brush, hot plate, potassium chlorate, 5 and 10 micron sieves, digital sonifier, water, pipette, cover slip, slide, optical adhesive, label, gloves and glass vial. Laboratory procedures involving samples preparation and analyses were carried out at Crystal Age Limited, Lagos, Nigeria.

The standard acid palynological techniques were employed. Ten grammes of each sample were taken through numerous processes to extract the palynomorphs contents from the embedding sediments. The samples were first treated with 10% HCl inside a fume cupboard to remove the carbonates. Neutralization with distilled water was done after 40% HF was added to the sample and placed on a shaker for a period of 24 hours to enable the dissolution of the silicates. After these, the HF was decanted and neutralization with distilled water was carried out to remove fluoro-silicates compounds produced as a result of HF reaction. Brason sonifier 250, which is an electric device, was used to sieve and separate the remaining silicate clay and mud and heavy minerals from the organic matter. A cover slip of 32 mm by 22 mm was placed on the hot plate; a stirrer was then used to stir the residue for even distribution and to transfer some quantity of the residue to the cover slip on the hot plate and then left to dry. The cover slip was then placed on the labelled glass slide with few drops of Canada balsam used as the mounting medium. The glass slide was then left to dry. This process was used for each sample.

The prepared slides for palynomorphs were studied, identified and counted under alight transmitted Olympus CX41 microscope using magnifications of x25 and x40 with relevant literature for description based on size, shape, structure, aperture and sculpture [13-25]. The specimen name and the distribution were recorded on the analysis sheet while those palynomorphs with non-distinguishable features due to either fungal/bacterial attack, corrosion etc. were recorded as indeterminate pollen or spore. Photographs of the palynomorphs were also taken using the attached Olympus DP12 digital camera.

Lithologic description was achieved through the physical examination of the samples and also by feeling between fingers. Fissile samples were observed to be shale while samples with fine to coarse grained sizes are the sandstone units. The lithologic description was made possible by the gamma ray and resistivity logs because high and low values of gamma ray and resistivity logs denote shale and sandstone lithologies, respectively [26]. The paleoenvironmental interpretation of the sedimentary sections was carried out with the framework of the identified lithofacies sequence [27] and [28]. The process was aided by combination of lithologic, textural and wireline log data. Also, the presence of index accessories minerals further helped in the analysis.

4 Results and discussion

4.1. Palynostratigraphic zonation and biochronology of HA-001 well

Two (2) assemblage biozones were recognised in the study namely the *Cyperaceaepollis* sp. – *Nymphaeaepollis clarus* assemblage zone (750-9750 ft) and the *Stereisporites* sp. assemblage zone (9750-11510 ft). These were further divided into two (2) subzones namely; *Nymphaeaepollis-Echitriletes pliocenicus* subzone (750-3750 ft) and *Cyperaceaepollis-Elaeis guineensis* subzone (3750-9750 ft) These assemblage biozones were correlated with the *Echitri-colporites spinosus* palynological zones of [15] and the P860, P850-P840 and P830 palynological subzones of [29]. Thus a Late Miocene age is interpreted for the HA-001 well (750-11510 ft) Figure 3. Details of the biozones were discussed below.

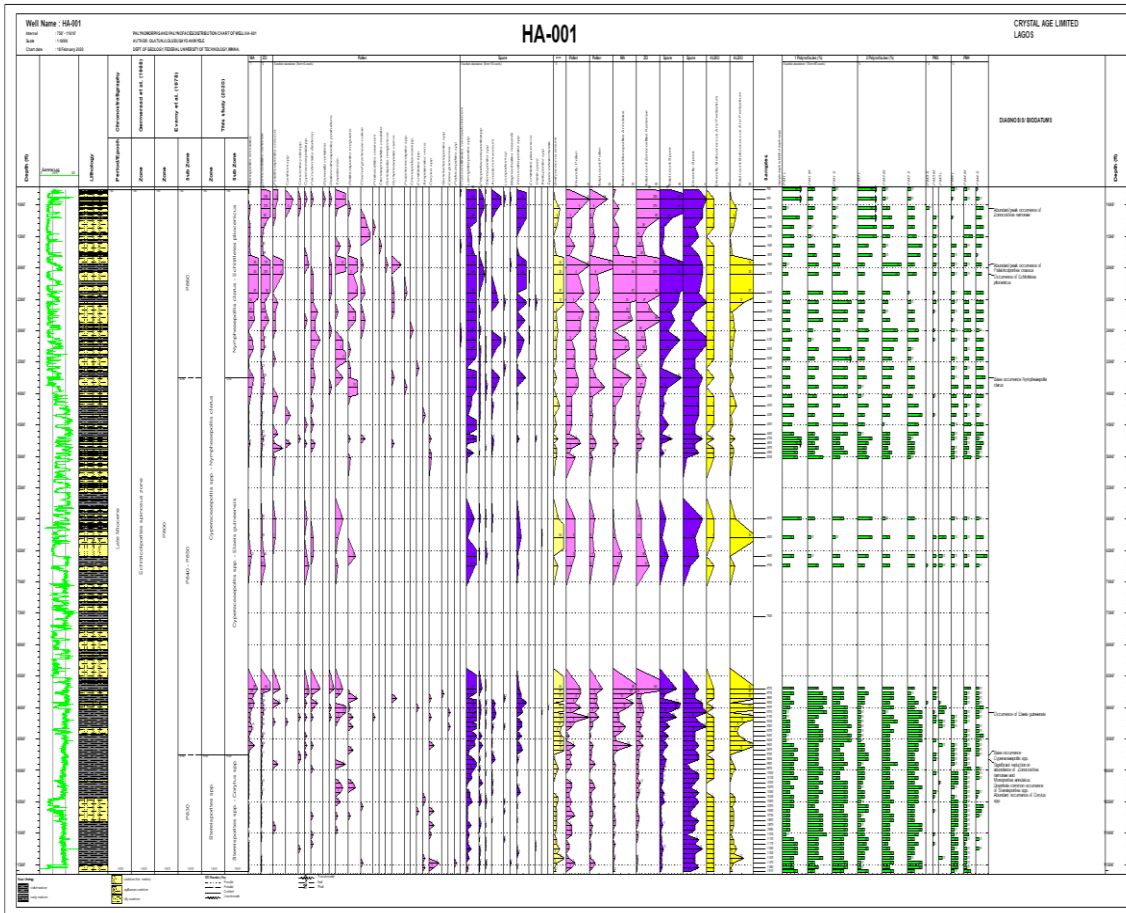


Figure 3. Palynomorphs distribution chart of well HA-001

Cyperaceapollis sp - Nymphaepollis clarus Assemblage Zone

Depth: 750-9750 ft; Age: Late Miocene

Comparable palynological zone: *Echitricolporites spinosus* zone of [15] P860 and P850-P840 palynological subzones of [29].

This biozone is characterised by the palynoflora assemblage of marker species such as *Cyperaceapollis* sp, *Nymphaepollis clarus*, *Echitriteles pliocenicus* and *Elaeis guineensis*. The stratigraphic significant range of key marker species *Cyperaceapollis* sp. and *Nymphaepollis clarus* lie within this assemblage zone. The occurrence of *Cyperaceapollis* sp., at the 900 ft of the well suggests that its actual top of the zone is stratigraphically higher than first sample analysed at 750 ft.

The lower limit is defined by the base occurrence of *Cyperaceapollis* sp. marked at 9750 ft. This zone is further characterised by the abundant occurrences of *Zonocostites ramonae*, *Monoporites annulatus*, *Laevigatosporites* sp., *Pachydermites diderixi* and *Psilatricolporites crassus*. Two (2) subzones are recognised within this assemblage zone and discussed below:

Nymphaepollis clarus - Echiniletes pliocenicus subzone

Depth: 750-3750 ft; Age: Late Miocene (Messinian-Tortonian).

This is the youngest subzone recognised in the study. The base of the subzone is defined by the base occurrence of *Nymphaepollis clarus* identified at 3750 ft. The *Nymphaepollis clarus* subzone is further characterised by the abundant occurrence of *Zonocostites ramonae*, *Verrucatosporites* sp. and *Retitricolporites irregularis*, rare occurrence of *Numulipollis neogenicus*, fairly abundant *Monoporites annulatus* and common occurrence of *Sapotaceae* and

Nympheaepollis clarus. This subzone correlates with the *Echitricolporites spinosus* palynological zone of [15] and the P860 subzone of [29].

Cyperaceaepollis - Elaeis guineensis subzone

Depth: 3750-9750 ft.; Age: Late Miocene (Tortonian).

The top of this subzone is marked by the base occurrence of *Nympheaepollis clarus* at 3750 ft. The base is marked by the base occurrence of *Cyperaceaepollis* sp. defined at 9750 ft.

The occurrence of *Elaeis guineensis*, rare occurrence of *Aletesporites* sp. and *Retibrevitricolporites obodoensis*, reduced abundance of *Verrucatosporites* sp. and rare occurrence of *Acrostichum aureum* also characterised this subzone. This subzone correlates with the *Echitricolporites spinosus* palynological zone of [15] and the P850-P840 (undifferentiated) subzone of [29].

Stereisporites sp. Assemblage Zone

Depth: 9750-11510 ft; Age: Late Miocene (Tortonian).

Echitricolporites spinosus zone of [15], P830 palynological subzones of [29].

This Assemblage zone is characterised by the occurrences of marker species such as *Stereisporites* sp., *Corylus* sp., low records of *Pachydermites diderixi* and *Canthiumidites* sp.

The top of the zone is marked at 9750 ft by the base occurrence of *Cyperaceaepollis* sp., while the base occurrence of *Stereisporites* sp. which marks the base of the zone was not recognised as at the last sample analysed. As such, the base is stratigraphic deeper than the last sample analysed.

The zone is further characterised by the significant reduction the *Zonocostites ramonae* and *Monoporites annulatus*, moderate records of *Corylus* sp., common occurrence of *Stereisporites* sp., and lower records of *Pachydermites diderixi* compared to the higher zones. Some of the recovered pollen and spores from the studied well are shown in Figure 4.

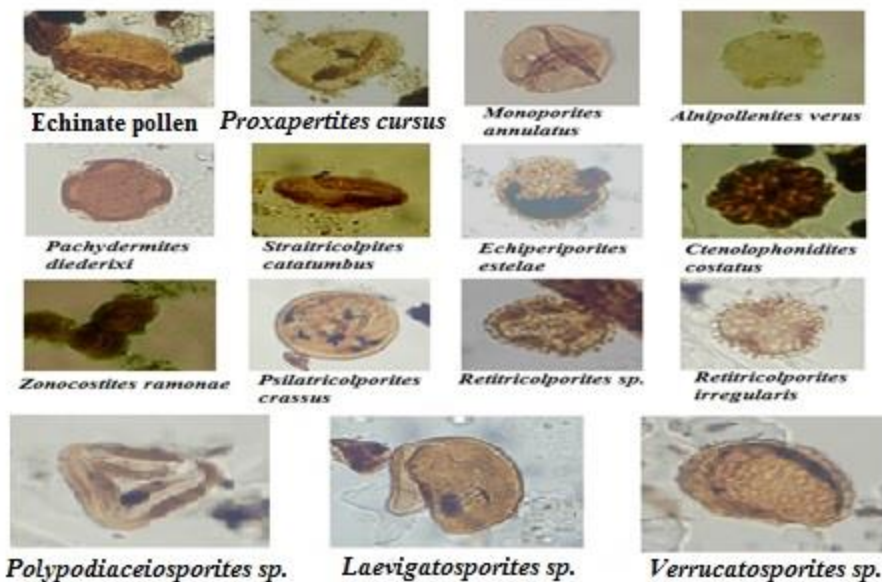


Figure 4. Some of the pollen and spores recovered from well HA-001 (x400)

4.2. Lithologic description and sedimentological analysis

Sedimentological attributes are derived from the integrations of wire line log motifs and textural/ lithologic attributes, the distribution of index accessories as well as our knowledge of the mutual juxtaposition of Niger delta sub-environments. Textural characteristics and the distribution of index accessory minerals, according to [30-31]; allowed the division of the entire intervals within the three well into Continental Benin Formation and Agbada Formation. The lithologic subdivision of the well is shown in the Table 1.

Table 1. Lithostratigraphic subdivision of HA-001 well

Interval (ft)	Formation	Lithofacies Sequence	Lithological Characteristic
750 – 1,800	BENIN	CONTINENTAL	-Predominantly sands with minor shale intercalations. -Sands are predominantly quartzose, slightly feldspathic, pebbly to fine-grained. -Sands are generally poorly-sorted. -Sand/ Shale ratio of approximately 90:10.
1,800– 3,750		TRANSITIONAL PARALIC	-Predominantly sands with occasional shale intercalations -Sands are predominantly quartzose, slightly feldspathic, fine to granule-sized with occasional pebbles. -Sands are generally moderately to poorly sorted -Sand/ Shale ratio of 80:20.
3,750- 8,250	AGBADA	PARALIC	-Heterogenous sequence of alternating sand and shale/ silt units. -Sands are predominantly quartzose, slightly feldspathic, fine to medium, occasionally coarse to very coarse-grained. -Sands are generally poorly to well sorted. -Sand/ Shale ratio of approximately 60:40.
8,250- 11,600		MARINE PARALIC	-Predominantly shale with relatively thin sands. -Sands are quartzose, fine to medium-grained, occasionally coarse to granule-sized. -Sands are poorly to moderately well sorted. Sand/ Shale ratio of approximately 25:75.

4.2.1. Marine paralic/paralic lithofacies sequence of HA-001 well (11500 – 3750 ft)

This interval is essentially a heterogeneous sequence of alternating sand and shale/ siltstone units. The regular pattern of sand and shale/siltstone intercalations permits easy recognition (on logs) of six halloccycles (third-order cycles) or sub-cycles of sedimentation within the marine paralic and paralic sequences. Each of these sub-cycles commences with a relatively thick marine shale/silt and progressively shallows into fluviomarine /fluviatile sands, based on the signatures of the gamma ray log and sand to shale ratio [30-31].

4.2.2. The marine paralic lithofacies sequence (11500 – 8250 ft)

The marine paralic lithofacies sequence has thick shale units. The sand/shale ratio is approximately 25:75 [30-31]; two (2) Depositional halloccycles (subcycles A and B) were identified based on the signature of the gamma ray log. Each halloccycle consists of underlying predominantly shaly (transgressive) phase, overlain by a thick sandy (regressive) phase. These halloccycles are:

(i) Subcycle A: (11500 – 10450 ft)

This is the lowermost section of the analyzed interval and it is composed of a monotonously shaly lower section (11,500 – 10,850 ft), overlain by a stack of sands (10,850 – 10,450 ft.). The shale is brownish grey to grey, silty, platy to flaggy, occasionally blocky and moderately hard to hard. The sands are quartzose, very fine to medium- grained, occasionally coarse to

very coarse-grained and granular; angular to rounded, and moderately to poorly-sorted. Ferruginous materials, carbonaceous detritus, mica flakes, shell fragments and glauconite pellets characterized the sequence. The monotonously shaly character of the lower section and the presence of shell fragment and glauconite pellets are consistent with low energy, shallow marine settings.

The amplified sand unit of the upper section of the sub cycle (10850 – 10450 ft) consisting of a stack of sands exhibiting upward coarsening profile indicative of a barrier bar build-up, probably deposited during progradational episode. This is further confirmed by the mixture of carbonaceous detritus, mica flakes and glauconite pellets [27].

(i) Subcycle B: (10450 – 8250 ft)

This 2200 ft thick subcycle is composed of hemipelagic shale with silty sand intercalations (10450 – 8500 ft), overlain by a sandy section (8500 – 8350 ft). It constitutes the top of the marine paralic lithofacies sequences. The shale/ siltstone is brownish grey to dark grey, silty, platy to flaggy, occasionally blocky and moderately hard to hard. Lithologically, the sands are quartzose, fine to medium – grained, occasionally coarse to very coarse –grained, sub angular to surrounded and moderately sorted. Ferruginous materials, carbonaceous detritus, glauconite pellets and mica flakes occurring in varying abundances constitute the accessory minerals suite of this subcycle. Also one spot occurrence of shell fragments was recorded at sample interval 9150 ft. The predominantly shaly/silty character of the lower part of the sub-cycle and the presence of glauconite pellets, ferruginous materials and shell fragments suggest deposition in a low energy, oxygenated, shallow marine settings [27]. The stack of sands over intervals 10300 – 10160 ft and 9450 – 9340 ft exhibiting upward coarsening grain-size profiles are probably of barrier bar origins. Elsewhere within the shales are fining upward and symmetrical sands interpreted as tidal channels and offshore bars respectively.

The typical multiserrate cylinder-shaped log character coupled with the regular carbonaceous detritus and glauconite pellets may suggest subaqueous channel deposits of the lower deltaic plain for the sandy upper part (8500 – 8250 ft).

4.2.3. The paralic lithofacies sequence (8250 – 7800 ft)

This lithofacies sequence directly overlies the marine paralic sequence. This interval is essentially a heterogenous sequence of alternating sand and shale/ mudstone units [30-31]. The sand/ shale ratio is approximately 60:40. Four (4) depositional subcycles were differentiated within this sequence, based on the signature of Gamma Ray Log. These are:

(i) Subcycle C (8250 – 7800 ft)

This interval is made up of a thin shaly base (8250 – 8100 ft) with minor sand intercalations, overlain by a more sandy section (8100 – 7800ft). Non-availability of ditch cutting samples for this interval restricted interpretation only on the wire-line log evidence. The subtle symmetrical sands occurring over interval 8200 – 8150 ft are most likely to be of offshore bar origin [28]. The amplified sand unit of the upper section (8100 – 7800 ft) of this sub-cycle consisting of multiple stacks of well-developed sands exhibiting cylinder - shaped grain-size profile is interpreted as distributary channel deposits.

(ii) Subcycle D: (7800 – 6200 ft)

This subcycle is composed of a thick shale unit (7800 – 6400 ft) with several silty sand intercalations, overlain by a sandy interval (6400 – 6200 ft). Like subcycle C discussed above, the ditch cutting samples were not recovered, except for intervals 6750 – 6200 ft. The shale is grey, brownish grey to dark grey, platy to flaggy and moderately hard. The sands are milky white to smoky, predominantly quartzose, slightly feldspathic, very fine to medium-grained, occasionally coarse/very coarse grained, moderately to moderately well-sorted and sub-angular to sub-rounded. Rare to common carbonaceous detritus, mica flakes, rare ferruginous materials glauconite pellets were recorded. The log character of the sands within the shale unit vary from symmetrical, crescentic and cylinder-shaped motifs, probably interpreted as offshore bars, channel overbank lobes and subaqueous channels. The Gamma Ray Log motifs of the upper section (6400 – 6200 ft) is a hybrid sand units of multiserrate cylinder with minor

bells and are most probably subaqueous channel-tidal channel associations [28]. This is corroborated by the presence of carbonaceous detritus and glauconite pellets. The gradual absence of shell fragments shows that the depositional environment probably deepened from base to top [27].

(iii) Subcycle E (6200 – 4700 ft)

This interval is composed of alternating sand and shale interbeds. The basal section (6200 – 5570 ft) is essentially shaly with few sand breaks, grading upwards into a predominantly sandy sequence (5570 – 4770 ft). The shale is grey, brownish grey to brown, platy to flaggy, occasionally blocky and moderately soft to hard. The sands are milky white, predominantly quartzose, slightly feldspathic, fine to medium-grained, occasionally coarse to very coarse-grained, moderately to poorly sorted and sub-angular to sub-rounded. This subcycle recorded an increase in the abundance of accessory minerals carbonaceous detritus, shell fragments, glauconite pellets and ferruginous materials. They occur regularly in rare to common quantities.

The crescentic, funnel and symmetrical-shaped log motifs of the sands within the shaly lower section, coupled with the present of glauconite pellets and shell fragments may suggest these are channel overbank lobes, barrier bar and offshore bar deposits. These criteria indicate marine deposition in close proximity to the ancient shoreline [30].

The bell, serrate/ slightly serrate cylinder-shaped log motifs by the sands occurring over the upper section (5570 – 4700 ft), are interpreted as tidal channel and subaqueous channel deposits. Supportive of this deduction is the occurrence of carbonaceous detritus and glauconite pellets. The appearance of shell fragments may also suggest an infilling of the channel to shallower depth. This subcycle holds a total of 100 ft net hydrocarbon sands at intervals 6070 – 6030 ft, 5710 – 5680 ft and 4730 – 4700 ft.

(iv) Subcycle F (4700 – 3750 ft)

This is composed of alternating beds of sands and shales with a lower thick shale section (4700 – 4200 ft.) with few sand breaks, overlain by a more sandy sequence (4200 – 3750 ft). It constitutes the top of the paralic lithofacies sequence. Lithologically, the sands are milky white to smoky, predominantly quartzose, slightly feldspathic, fine to medium-grained, occasionally coarse to very coarse-grained, moderately to poorly sorted and sub-angular to sub-rounded. The shale is grey, dark grey to brown coloured, silty, platy to flaggy, occasionally blocky and moderately hard to hard. The accessory mineral suites are mostly shell fragments, mica flakes, carbonaceous detritus ferruginous materials and glauconite pellets in decreasing order of abundance. These criteria indicate deposition in the lower deltaic plain environment. The crescentic-shaped motif occurring over interval (4560 – 4500 ft) is interpreted as channel overbank lobes. The amplified sand unit occurring over the interval 4420 – 4350 ft exhibiting a subtle upward coarsening grain-size profile is most likely to be of barrier bar origin. The underlying high gamma shale bed is interpreted as a barrier foot [10]. Elsewhere in the shale lower section, symmetrical-shaped sands occur and are most probably offshore bar deposits.

The serrate cylindrical with overall coarsening upward Gamma Ray log motifs of the upper section (4200 – 3750 ft) may suggest subaqueous channel and barrier bar deposits respectively. This is corroborated by the present of glauconite pellets and carbonaceous detritus [30]. Sediments of this subcycle are believed to have been laid down in an inner shelf to coastal deltaic settings. Also the trend of increasing abundance of shell fragments from the bottom to the top of this subcycle could be attributed to progressive shallowing of the environment.

4.2.4. The transitional paralic lithofacies sequence (3750 – 1800 ft)

This is composed of alternating sequence of sands (20 – 150 ft. thick) and relatively thinner shales (10 – 100 ft thick). The sequence exhibit a sand/shale ratio of approximately 80:20. The sands are predominantly quartzose, slightly feldspathic; fine to medium; occasionally coarse to granule-sized and pebbles, moderately to poorly sorted and sub-angular to rounded. The shale is grey, dark grey to reddish brown, platy to flaggy and moderately soft to moderately hard. Index accessories are dominated by carbonaceous detritus, shell fragments and ferruginous materials. Rare glauconite pellets and mica flakes are recorded with one spot occurrence of pyrites at interval 2400 ft. This suggests deposition in a high energy, subwave, suboxic to anoxic, deltaic environment [27].

The sand/ shale alternation of the sequence suggest frequent interchanging high and low depositional energy regimes which might have resulted from a frequently shifting depositional axis on a gently subsiding passive continental margin. However, the higher proportion of sand and the ubiquitous occurrence of carbonaceous detritus suggest that it was deposited under a generally higher energy regime than the underlying paralic Sequence and definitely represent an environment proximal to the underlying paralic/marine paralic sequence within a general deltaic environment.

The sand bodies exhibiting the funnel-shaped motifs over this sequence are proposed to be of barrier bar origin. The other sand bodies showing cylinder and cylinder on funnel-shaped motifs are suggested to be of subaqueous channel and subaqueous channel-barrier bar association origin. The shales interbedded with the sands are suspected to be of interdistributary/prodelta origin [30].

The alternation of high and low energy regime is probably related to the well documented frequent shift of depositional axis in the Niger delta.

4.2.5. The continental lithofacies sequence (1800 – 750 ft)

This consists predominantly of poorly sorted pebbly to fine-grained sands with minor shale intercalations. The sequence exhibit a sand/ shale ratio of approximately of 90:10. The base is always defined by a major shift of resistivity to the left, probably marking the bottom of fresh water. (Resistivity log for this sequence is unavailable).

On gamma ray log the sands (10 – 250 ft thick) exhibit cylinder and funnel-shaped motifs. The sequence is very rich in accessory minerals dominated by shell fragments, carbonaceous detritus, mica flakes and ferruginous materials with glauconite pellets restricted to intervals 1800 – 1050 ft. The aforementioned criteria suggests that the sediments of this sequence are probably distributary channel and distributary mouth bar deposits of the upper deltaic plain in close proximity to the lower deltaic plain [30]. The increase in sand- percentage suggests relative shallowing or tremendous shallow water clastic influx. The depositional environment probably shallowed from base to top.

4.3. Thermal maturity of miospores in HA-001 well

Microscopic study of dispersed organic matter under transmitted light during the 70s increased ideas in recognizing the actual relation between the physical properties of dispersed organic particles and petroleum potential. The composition of pollen and spores and the degree of thermal alteration of sedimentary rocks based upon changes in colour of miospores have been used in the oil industries in determining the level of organic maturation and hydrocarbon source rock potential.

A thermal alteration scale of [32] and Spore colour index chart of [33] (Figure 5) were adopted for this study. Palynological analysis is a fast, efficient and reliable method of determining hydrocarbon maturation level.

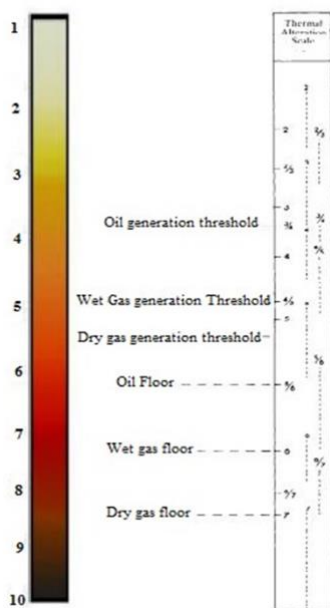


Figure 5. Relationship between thermal alteration and spore colour indices of [32] and [33] based on threshold of oil generation

4.4. Organic maturation levels for miospores in HA-001 well

Thermal Alteration Scale: Ranges between 4/5 – 5/6 (4/5 – 5/6) [32]. Palynomorph colours: Ranges from light -medium brown to medium-dark brown [33]. Degree of Maturation: Ranging from maturity degree to late degree of maturation (Figure 6).

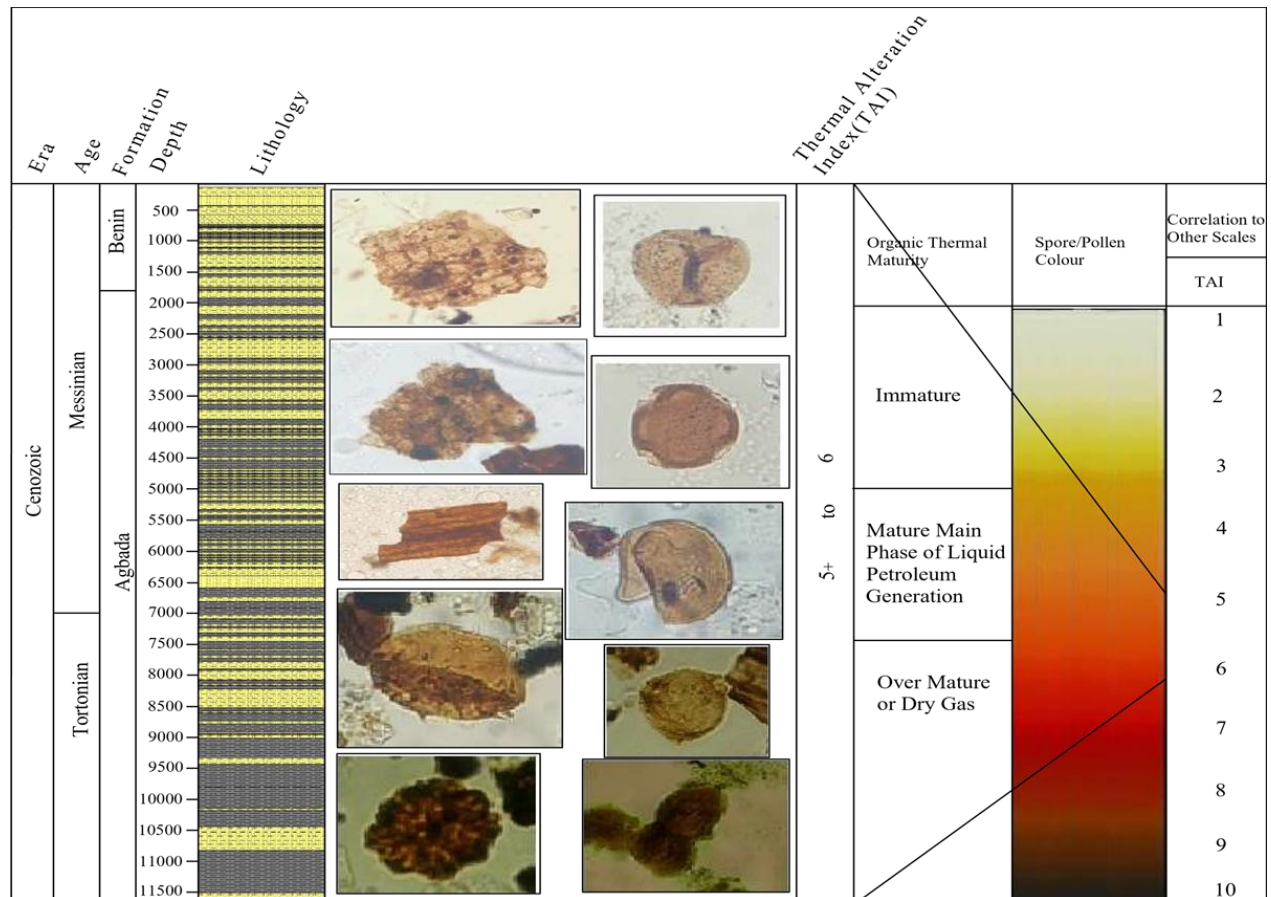


Figure 6. Miospores and organic thermal maturation of HA-001

5. Conclusions

Palynostratigraphic and lithostratigraphic analyses were carried out on the sedimentary intervals of HA-001 well using ditch cutting samples and wireline logs provided by Shell Production and Development Company. Seventy-six (76) ditch cutting samples within the depth intervals of 750 – 11,610 ft in the well were analysed. The standard palynological method of sample preparation and sedimentological analyses were employed.

The stratigraphic age range of the recovered diagnostic marker species indicates Late Miocene age for the studied intervals. *Nymphaepollis clarus* has been assigned Late Miocene age in Nigeria [29]. *Cyperaceapollis* sp. and *Elaeis guineensis* have not been reported earlier than Late Miocene age [29] and [15] and they are Late Miocene markers. The recovery of the diagnostic marker species from the intervals of the studied wells gave the indication that the stratigraphic interval were deposited during the Late Miocene. Two palynostratigraphic zones each were established in the well using the international stratigraphic guide. *Cyperaceapollis* sp. – *Nymphaepollis clarus* and *Stereisporites* zones were established in HA-001 well. *Nymphaepollis clarus* – *Echitriletes pliocenicus* and *Cyperaceapollis* sp. – *Elaeis guineensis* sub-zones were established for the *Cyperaceapollis* sp. – *Nymphaepollis clarus* zone in the well. The two zones are assemblage zones. The subzones and the zone erected in the studied wells are equivalent to P860, P840 – P850 and P830 of [29].

The sedimentological analysis showed lithological alteration of sand and shale units which suggests rapid shoreline progradation. The grain size increases from essentially fine to medium-grained, occasionally coarse-grained at the basal part of the wells, to dominantly fine to medium-grained, occasionally coarse to granule sizes at the upper part. The sands are mostly sub-angular to sub-rounded and generally poorly to well sorted. Index minerals and accessories are dominated by ferruginous materials, glauconite pellets, carbonaceous detritus, shell fragments and pyrites with irregular occurrences of mica flakes. The lithologic, textural and Gamma Ray Log data indicate that the entire interval studied in the HA-001 well essentially tested the Benin and Agbada Formation.

Thermal maturity of miospores encountered in the well using the thermal alteration scale of [32] and spores colour index chart of [33] indicated early degree of maturation to late degree of maturation. The upper intervals in the well showed early degree of maturation for the miospores and palynomacerals while the lowest interval displayed late degree of maturation. The composition of palynomacerals and the degree of thermal alteration of sedimentary rocks based upon change in colour of miospores have been used in the oil industries in determining the level of organic maturation and hydrocarbon source rock potential.

References

- [1] Kulke H. Nigeria. In Kulke H. ed., Regional Petroleum Geology of the World. part 11, Africa, America, Australia and Antarctica: Berlin, Gebrüder Borntraeger 1995, 143-172
- [2] Hyde HA, and Williams DA. Pollen Analysis Circular 1955; 8: 6.
- [3] Samuel O. Integrated Evaluation of CO₂ Risk in Niger Delta Reservoirs: A Critical Value Driver for HPHT Prospects. SPDC internal unpublished report 2009.
- [4] Oluwajana OA. 2D seismic interpretation and evaluation of Middle Miocene source rocks within Agbada Formation, Coastal Swamp depobelt, Niger Delta Basin, Nigeria. Global Journal of Geological Science, 2019; 17(2): 97-103.
- [5] Avbovbo AA. Tertiary lithostratigraphy of the Niger Delta. American Association of Petroleum Geologists Bulletin, 1978; 62: 259 – 300.
- [6] Allen JRL. Late Quaternary Niger Delta and adjacent areas: Sedimentary Environment and Lithofacies. American Association of Petroleum Geologists Bulletin, 1965; 49: 547–600.
- [7] Short KC, and Stauble AJ. Outline of geology of Niger Delta. American Association of Petroleum Geologists Bulletin, 1967; 51: 761-771.
- [8] Whiteman A. Nigeria: Its Petroleum Geology Resources and Potential, vol. 1 and 2 Graham and Tottman, London 1982, 393, pp.
- [9] Weber KJ, and Daukoru EM. Petroleum Geological Aspects of Niger Delta. Journal of Mining and Geology, 1975; 12: 9 – 22.
- [10] Weber KJ. Sedimentological aspects of oil field in the Niger Delta. *Geologie en Mijnbouw*, 1971; 50: 559 – 576.
- [11] Reijers TJA, Petters SW, and Nwajide CS. The Niger delta basin, sedimentary geology and sequence stratigraphy. In Reijers TJA. (Ed)., Selected chapters on geology, 1996; 100-117.
- [12] Ige OE. (2009). A Late Tertiary Pollen record from Niger delta, Nigeria, International Journal of Botany, 2009; 5: 203-215.
- [13] Erdtman G. Pollen morphology and plant taxonomy–Angiosperms, Almqvist and Wiksell, Stockholm 1952, 539p
- [14] Gonzalez-Guzman AE. A palynological study of the Upper Los Cuervos and Mirador Formations (Lower and Middle Eocene, Tibu area, Columbia). Thesis 1967, Univ. Amsterdam, 68p
- [15] Germeraad JH, Hoppings CA, and Muller J. Palynology of Tertiary Sediment from Tropical areas. Review of Palaeobotany and Palynology, 1968; 6(3&4): 189-348.
- [16] Knaap WA. A montane pollen species from the Upper Tertiary of the Niger Delta. Journal of Mining and Geology, 1971; 6: 23 – 29.
- [17] Legoux O. Quelques especes de pollen caracteristiques du Neogene du Nigeria. Bull. Cent.Rech.Explor.Elf.Aquit.,1978; 2: 265–317.
- [18] Adegoke OS, Jan du Chene RE, Agumanu AE, and Ajayi PO. Palynology and age of the Kerri-Kerri Formation, Nigeria. Rev. Esp. Micropaleontol., 1978; 10(2): 267-283.
- [19] Jan du Chene RE, Onyike MS, and Sowunmi MA. Some new Eocene pollen of the Ogwashi-Asaba Formation Southeastern Nigeria, Rev. Esp. Micropal., 1978; 10(2): 285-322.
- [20] Salard – Cheboldaeff M. Quelques grains de pollen peripores Tertiares de Cameroon, Rev. Micropaleont., 1975; 17(4): 182 – 190.

- [21] Salard – Cheboldaeff, M. A propos de la microflore cryptogamique Tertiaire de basin sedimentaire coties du Cameroon, *Rev. Micropaleont.*, 1976; 18(2): 97–116.
- [22] Salard – Cheboldaeff M. Sur la palynoflore Maestrichtienne et Tertiaire du basin sedimentaire littoral du Cameroun, *Pollen et Spores*, 1978; 20: 215 – 260.
- [23] Salami MB. Some Late Cretaceous and Early Tertiary Pteridophytic spores from the Southern Nigeria Sedimentary Basin. *Rev. E spanola. Micropaleont.*, 1983; 15: 252 – 272.
- [24] Agip. Palynomorphs of Niger Delta. Agip publication 1987, 44 plates.
- [25] Ajaegwu NE, Odoh BI, Akpunonu EO, Obiadi II and Anakwuba EK. Late Neocene to Early Pliocene palynostratigraphy and palaeoenvironments of ANE. 1 well, Eastern Niger Delta. *Nigeria Journal of Mining and Geology*, 2012; 48(1): 31-43.
- [26] Olayiwola MA, and Bamford MK. Petroleum of the Deep: Palynological proxies for paleoenvironment of deep offshore upper Miocene-Pliocene sediments from Niger delta, Nigeria. *Palaeontologia Africana*, 2016; 50: 31-47
- [27] Selley RC. Subsurface Environmental Analysis of North Sea Sediments. *AAPG Bulletin*, 1976; 60(2): 184 – 195.
- [28] Sneider RM, Tinker CN, and Merkel LD. Deltaic Environment, Reservoir Types and their Characteristics. *Journal of Petroleum Technology*, 1978; 1538 – 1546.
- [29] Evamy BD, Haremboure J, Kemerling WA, Molloy FA, and Rowlands PH. Hydrocarbon habitat of Tertiary Niger Delta, *American Association of Petroleum Geologists Bulletin*, 1978; 62: 1–39.
- [30] Selley RC. Concepts and Methods of Subsurface Facies Analysis. *AAPG Education Course Notes. Series*, 1978; 9: 86.
- [31] Durugbo EU, and Uzodimma E. Effects of lithology on palynomorph abundance in wells X1 and X2 from the western Niger delta. Nigeria. *International Journal of Geology, Earth and Environmental Sciences*, 2013; 3: 170-179
- [32] Batten DJ. Palynofacies, Palaeo-environments and Petroleum. *Journal of Micropalaeontology*, 1982; 1: 107 – 114, pp. 1-2.
- [33] Pearson DL. Pollen/Spores colour “standard”, ver. 2. Phillips Petrol 1984, privately distributed.

To whom correspondence should be addressed: Olubusayo A. Olatunji, Department of Earth Sciences, Faculty of Science, Adekunle Ajasin University, Akungba-Akoko, Ondo State, Nigeria,
E-mail: olubusayo.olatunji@aaau.edu.ng

The Coking Properties Quality Prediction of Coal from Steenkool Formation in Bintuni Basin, West Papua, Indonesia

Ahmad Helman Hamdani, Johannes Hutabarat*

Faculty of Geology, University of Padjadjaran, Jl. Raya Bandung-Sumedang Km.21 Jatinangor, 45363, Indonesia

Received June 7, 2019; Accepted September 29, 2020

Abstract

The Pliocene coals from the Steenkool Formation in Bintuni Basin, West Papua were selected and analyzed using proximate, ultimate, and rheological methods to evaluate their coking properties. This study revealed that all coal samples were high-volatile bituminous. The Horna Block coal samples have an average of Simoni's G-value of 0.95; Free Swelling Index of 5.0 and maximum fluidity 18,33 ddpm, therefore that coal samples are classified as a low-plasticity and moderately-coking grade. Although the Menci and Disihu blocks have a similar G value as the coal in Horna Block (i.e. 0.94 -0.96); but because of the low Free Swelling Index value of around 1-3 so it is categorized as weak-coking grade. The CSR and CRI show that all coal samples are meet with the Blast Furnace standards in several countries.

Keywords: Coking coal; Steenkool formation; Proximate analysis; Rheology.

1. Introduction

The Bintuni Basin is one of the sedimentation basins located in West Papua Province, the Indonesian Archipelago which is rich in coal and oil and gas resources. The largest gas project in the Bintuni Basin was developed in the Tangguh area. The Tangguh LNG Project is being developed by BP, and comprises six offshore and onshore gas fields with a total estimated (proven, probable, and possible) reserve of generally 'dry gas' at 24 trillion cubic feet (TCF). The coal found abundantly in the northern part of the Bintuni basin. The main exposed stratum is the Tertiary Pliocene Steenkool Formation. The rock group is a coal-bearing rock group, and the main lithology is sandstone, siltstone, mudstone, and coal seam. However, information about the quality and quantity of coal has not been widely published.

Based on the coal formation process, coal is classified into peat, lignite, sub-bituminous and bituminous to anthracite [1]. Whereas in the industrial sector, coal terminology is based on the type of utilization of coal which depends on the attributes possessed by coal, such as coal caking and non-caking coal.

Non-caking coal is often referred to as thermal coal, also known as steaming coal, which is coal that is usually burned to drive electricity-generating turbines both for meeting public and industrial energy needs (such as the ceramic industry, paper manufacturing, cement industry). While caking coal is categorized as cooking coal, or often also called metallurgical coal; is coal used in the process of making coke which is used in the steel and iron making industry. However, not all coal can function as coking coal; coal can turn into coke only if it is softened into a plastic mass on carbonization, followed by decomposition, swelling, and evolution of gases and finally resolidification while gas is still being developed [2].

Increased demand for coke coal quality by blast furnace operators and increased use of PCI (pulverized coal injection) in the world related to the construction of several blast furnaces for steel processing, which of course requires coal as a paired source in blast furnace technology with pulverized coal injected at the tuyeres and coke as a permeable support. Has led to more

intensive research and development in the case of coking coal, especially an understanding of coal quality for the quality of coke making. The Indonesian archipelago has a lot of coal resources but is limited to cooking coal. Some cooking coal in Indonesia is spread in East Kalimantan in the Pulobalang Formation [3-4], while in Central Kalimantan it is identified in the Batu Ayau Formation [5]. The more intensive research and development in the case of coking coal, especially an understanding of coal quality for the quality of coke making in Indonesia, especially in the Bintuni Basin, is very important to do.

The purpose of coal research of Steenkool Formation in Bintuni Basin, West Papua evaluates the coal proximate, ultimate, and rheology tests about their coking properties (fluidity/plastic properties) in accessing the suitability for metallurgical coke production.

2. Material and methods

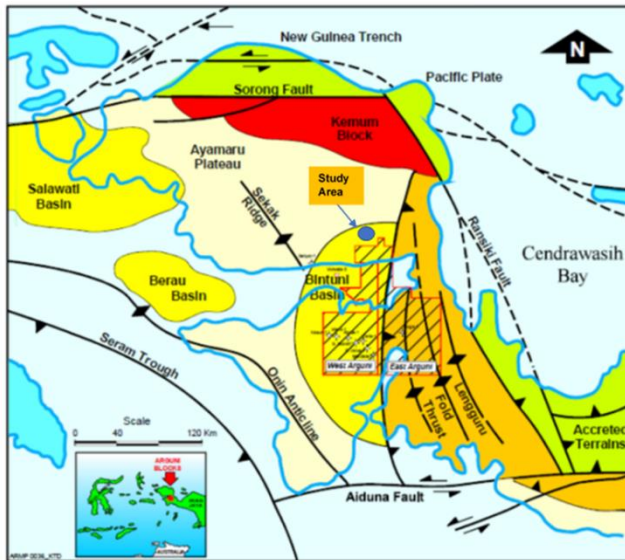


Figure 1. Map of study area in Isim District, West Papua Province, Bintuni Basin

Three coal sampling locations were conducted at Disihu Block, Horna Block and Menci Block, which located in Isim District, West Papua (Fig. 1).

The coal thicknesses ranging from 0.6–3.10 meters. The method of coal sampling is a channel ply sampling/ply by ply. The samples can be taken channel sampling per seam thickness (layer) or ply per ply (if there are parting insertions) [6].

Before being analyzed the coals have to dry to expel moisture and ground into a fine material. Then a fine powder is filtered using a filter size of 0.0250 cm and 0.0425 cm. The airtight plastic bag used for storing a fine powder before a proximate, an ultimate, and a rheology measurement were performed.

2.1. Analysis of proximate and ultimate analysis

The American Society for Testing and Material Standards (ASTM) is used as a reference in the proximate analysis of coal samples [7]; the test was measured moisture, volatile material, fixed carbon, and ash within the sample and was reported as a percentage of the weight of the sample used. ASTM D3173 is used for moisture (IM). To determine a volatile matter (VM) is used the ASTM D3175. The ASTM D3172 is used to measure fixed carbon (FC). For ash and total Sulphur determined by ASTM D3174 and ASTM D4239, respectively.

The ultimate analysis is done to determine the chemical elements in coal; such as carbon (C), hydrogen (H), oxygen (O), sulfur (S), and other elements in coal samples. These variables are measured in percent by weight (% by weight) and are calculated on the basis described as air-dried base. The ASTM D5373 is used to identify a carbon. To determine a hydrogen is used ASTM D5373. For nitrogen identified by ASTM D5373. The ASTM D5142-02 is used to measure a Sulphur. To determined oxygen content is used ASTM D3176

2.2. Ash analysis

To determine the level of basicity index (BI), the component analysis is carried out in ash. The ash composition of coal: SiO_2 , Al_2O_3 , Na_2O , K_2O , CaO , MgO , total Fe as Fe_2O_3 , P_2O_5 , MnO , TiO_2 . The ash chemical components were determined according to the ASTM D6349-13.

2.3. Rheology analysis

The three tests that measure rheological properties are the free swelling index (FSI), Gieseler plastometry (measured the fluidity) and, Ruhr dilatometry (measure the dilatation).

2.3.1. Free swelling index determination

Modified an ASTM D720-67 procedure was used conducted a free swelling index [8]. This test is one of the tests that is often used to find out the potential of coal in the formation of coke. This test also makes it possible to find out its potential quickly. However, this test cannot describe coal as having good or bad potential for coke formation This experiment used a coal sample of 1 gram of coal which was heated in covered silica crucible at a temperature range of 800°C and 820+ 10°C in 1 minute and 820+ 50°C in 1 minute. The value of FSI is obtained by comparing the button coke formed in the crucible with a chart of standard profiles. The FSI value between 1 and 9 in increments of 0.5.

2.3.2. Gieseler plastometry

The Gieseler plastometry test is performed to determine the degree of formation of the coal plasticity phase and what is the maximum temperature of fluidity reached [9-10]. A total of 5 grams of freshly ground coal (< 0,0425 cm) were put into the crucible by pressing using a ballast 1 kg weight ten times. The initial temperature of the test is 350°C with an increase in heating temperature of 3°C per minute. With a constant torque the stirrer will stir the coal. The stirring movement is seen on the dial and measured in dial division per minute (ddpm). When the coal component (coal maceral) begins to enter the plastic zone, due to it experiences less friction when the coal becomes more liquid, the ddpm value will start to increase. When the dial reads read 1 ddpm indicate the initial temperature of softening (°C) was start reading and at a times the reading reaches the maximum value, the temperature read is recorded as the maximum temperature of fluidity (°C). The zero-reading indicated that the measured temperature is the solidification temperature (°C). The plastic range is defined as the difference between the compaction temperature and the initial softening temperature. The maximum speed of the stirrer movement is referred to as maximum fluidity, which the unit measurement is ddpm. The ratio between temperature range and log maximum fluidity is called the Gieseler ratio.

2.3.3. Ruhr dilatometry

In this test, freshly ground coal with a size of 0.0425 cm is moistened and formed into a pencil with a length of 6 cm. Next, a coal pencil is placed in a tub where just above it is placed a sliding-fit steel rod. In a special furnace is placed a tub that is heated at a temperature of 300°C with an increase of 3°C per minute. The dilatometer data point, i. e, softening temperature (°C), maximum dilatation temperature (°C), contraction (%), and dilatation (%) were used to calculate the cooking capacity (G-value).

$$G = \frac{E+V}{2} \times \frac{c+d}{V \times c + E \times d} \quad (1)$$

where: G-cooking capacity; E-softening temperature; V- Maximum dilatation temperature; c- contraction; d-dilatation.

3. Result and discussion

3.1. Proximate analysis

The coals show low moisture content (< 3%), high volatile matter (>40%), high fixed carbon, low ash content (below 10%) and higher calorific values ranging from 7,208 cal/g to 7,930 cal/g. All the coals were classified as the high volatile bituminous coal. The result proximate analysis was tabulated in Table 1.

Table 1. Data from proximate analysis

Location/Sample No	Parameter				
	Moisture (adb)	Ash (adb)	Volatile matter	Fixed carbon	
Horna	D1	2.3	1.1	44.2	52.4
	D2	2.4	1.2	44.1	52.3
Menci	D052	1.9	1.4	45.2	51.5
	D96	1.9	4.2	45.9	47.5
	D211	2.6	6.3	44.7	46.4
Disihu	D22	2.1	1.7	47.2	49.0
	D122	2.8	7.2	44.7	45.3

One of the parameters that must be known in determining the quality of coal for the formation of coke is to measure the moisture content. A large moisture level will form coal particle agglomeration that make pseudo-particles. So, the compacting effect will appear, make a decrease in space between particles and an increase in density. A high moisture content is not useful because it increases operational costs in removing impurities from the furnace and decreasing system capacity [11-12]. For good coking coal, the moisture content should be between 1% and 6% but most of the adequate content is in the range of 3-4%. Based on the moisture content, the coal samples were in value for good coking coal.

The high ash content in coal is disadvantageous because of the negative effect in the form of decreased Blast Furnace efficiency due to the amount of slag that has accumulated in Blast Furnace [13-14]. The good coke quality which indicated by a high CSR and low CRI value is related with lower ash content (<10%). The decreasing coke productivity in the blast furnace is correlated with increased ash in coals. All coal samples in this research area were categorized under low ash content (1.1%–7.2%); therefore, these coal samples have good potential for coke-making.

The performance of the blast furnace is also influenced by the presence of volatile matter (VM) in the coal [15]. The high pressure during the carbonization process due to the high content of VM (> 30.30%), the Blast Furnace should be broken especially in the walls. The best coals for coke making have VM in the range of 27.70% to 30.30% air-dried base (adb). Therefore, all coal samples with a volatile matter content in the range of 44.19%–47.2% are included in the range that is not acceptable for making good metallurgical coke. However, with special treatment, such as the size of coal made smaller (< 0.5 mm), it will cause increased dilatation followed by the release of volatile matter from the matrix [16].

For good coke-making, the coal must have high carbon content, which is expressed in fixed carbon (FC). All coal samples had a high FC content in the range of 46.4% to 52.4% (Fig. 2). The Horna Block coal samples had the highest value (52.4%) with more carbon for coke formation followed by the Disihu Block (49.0%) and Menci Block coal samples (47.5%).

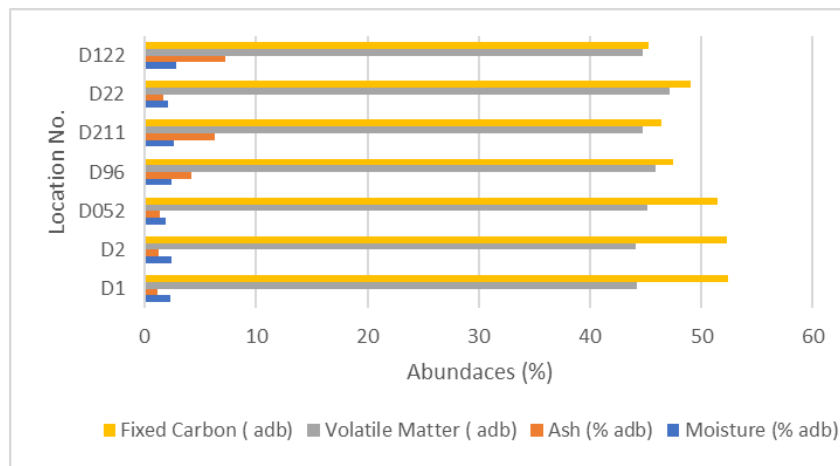


Figure 2. Graph of proximate analyses

3.2. Ultimate analysis

The result of ultimate analysis is demonstrated in Table 2

Table 2. Data from Ultimate Analysis

Location/No.	Elemental Elements (%)					
	Hydrogen	Oxygen	Nitrogen	Carbon	Sulfur	
Horna	D1	5.91	7.53	2.20	82.5	0.80
	D2	5.96	7.08	2.19	82.8	0.81
	D052	5.90	8.37	2.08	81.1	1.17
Menci	D96	5.72	10.02	2.02	77.5	0.72
	D211	5.51	10.45	2.04	75.1	0.62
Disihu	D22	5.83	12.68	1.94	77.63	0.22
	D122	6.06	12.13	1.92	72.22	0.47

The percentage of hydrogen element in coal deposits in the three locations shows that there is no big difference, either between samples in one block or between blocks; as follows Horna Block 5.91% and 5.96%; 5.90%, Menci block 5.72% and 5.51% and Disihu Block 5.83% and 6.06. Similarly, there was no significant difference in the carbon content of coal samples in all blocks in the Isim District. The highest carbon content was found in the Horna Block, while the lowest was found in the Disihu Block (D122). The sulfur in Disihu Block of 0.22% and 0.47% and the Menci coal samples had a value of 0.72%–0.72%, whereas the Horna Block samples more higher contents (0.80%–1.17%) comparing the two locations. The oxygen contents of the coal samples were in the range of 7.08% to 12.68%. The high oxygen content of 12.683% (D22) was found in Disihu Block. In Menci Block and Horna Block samples were smaller as 10.45 % (D211) and 7.53 % (D1), respectively. The lowest value of nitrogen was identified in Disihu Block (1.92 %), while the highest nitrogen content of 2.20 % was detected in the Horna Block. The ultimate analysis of all coal samples shows that all samples contain large amounts of carbon, while other elements such as hydrogen, nitrogen, oxygen, and sulfur are found in smaller amounts. This research found that the content of elemental carbon is quite large in all samples but is in a short-range (Fig. 2).

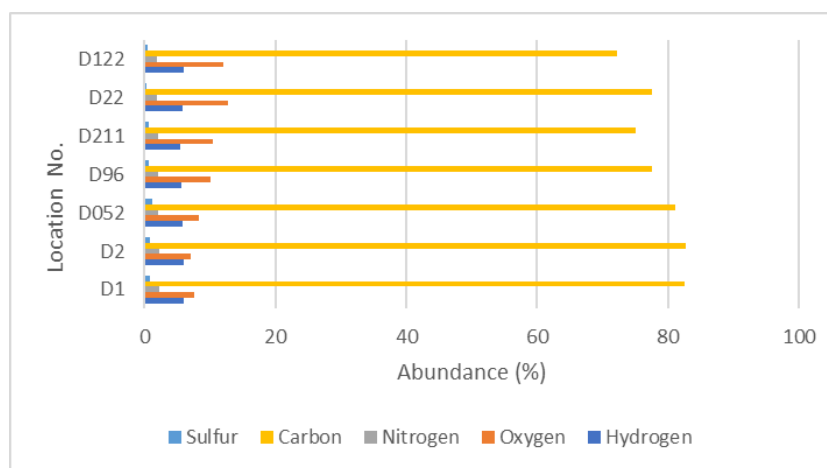


Figure 3. Graph of elemental content of elements in coal

The high carbon content is related to the high volatile matter content [17] as shown in Table 1. Ultimate analysis indicates that all coal samples are categorized as flame coal with good grade characterized by low sulfur content, and can be used for coke making technology [18].

3.3. Ash chemical component analysis

The results of the ash chemical component analysis of all coal samples are shown in Table 3.

Table 3. Data from ash chemical component analysis

Ash	Horna Block			Menci Block		Tisiyu Block	
	D1	D2	D052	D96	D211	D22	D122
SiO ₂	25.61	27.57	32.17	25.65	40.45	48.46	46.59
Al ₂ O ₃	11.67	10.25	12.81	14.86	20.15	23.43	26.14
Fe ₂ O ₃	29.13	30.19	30.57	15.73	9.8	14.86	7.85
TiO ₂	0.62	0.59	0.57	0.57	0.73	0.38	0.79
CaO	7.99	7.66	4.66	10.17	6.13	5.02	3.96
MgO	9.59	8.88	8.09	11.26	7.24	2.18	4.76
K ₂ O	0.32	0.26	1.17	0.74	2.79	0.55	1.79
Na ₂ O	0.89	0.87	0.84	0.97	1.64	0.42	0.35
P ₂ O ₅	0.04	0.04	0.05	0.43	0.06	0.11	0.44

The result of the chemical composition of the ash to obtain coke with the specified Coke Reactive Index (CRI) and CSR (coke strength after reaction with CO₂). The better quality of coke is requirement low CRI and high CSR index. The ash basicity index employed in formula 2 may be denoted by B_b

$$B_b = Na_2O + K_2O + CaO + MgO + Fe_2O_3 / (SiO_2 + Al_2O_3) \quad (2)$$

$$CRI_p = 13.4 - 0.45 (B_b)^2 + 9.35 (B_b) \quad (3)$$

$$CSR_p = 94.23 - 1.275 CRI_p$$

where: B_b-basicity index; CRI_p- predicting CRI; CSR_p - predicting CSR.

Table 4 shows coke quality parameters CRI and CSR, calculated by using basicity index (BI) model, and according to formulas (2) and (3). All coal samples analyzed show low CRI_p (15.78 - 24.51) values and high CSR_p values (62.77- 74.12).

Table 4. Predicting value of CRI and CRS of coal

Location/Sample No.	Bb	Parameter		
		CRI _p	CSR _p	
Horna	D1	1.29	24.68	62.77
	D2	1.27	24.51	62.98
	D052	1.01	22.37	65.71
Menci	D96	0.96	21.96	66.23
	D211	0.46	17.57	71.83
Disihu	D22	0.32	16.35	73.38
	D122	0.26	15.78	74.12
Average			20.46	68.15

3.4. Rheology properties

The results of the FSI, dilatometric properties, and Gieseler test of all coal samples are shown in Table 5. All coal samples from the Horna Block had the highest FSI of 5.5 followed by coal samples from Menci Block and Disihu Block with 3.0 and 2.5, respectively. Based on the British Standard Swelling Number (BSS No.), the Horna Block coal samples are classified as coal of moderate caking power, while the Menci Block and Disihu Block coal samples are classified as coals of weak caking power.

Table 5. Data from rheology test

Parameter	Horna Block			Menci Block		Disihu Block	
	D1	D2	D052	D96	D211	D22	D122
FSI	5.5	5.5	5.5	3.0	1.5	3.0	2.5
ST (°C)	358	369	352	368	376	368	376
MCT (°C)	408	405	402	439	500	429	446
MDT (°C)	440	440	436	438	440	18	1
C (%)	20	25	15	18	28	21	16
T (%)	19	32	28	19	36	17	27
G	0.90	0.95	0.99	0.93	0.96	0.93	0.99
D (%)	-1	7	13	1	8	-4	11
IST (°C)	392	387	304	403	406	456	454

Parameter	Horna Block			Menci Block		Disihu Block	
	D1	D2	D052	D96	D211	D22	D122
MFT (°C)	428	426	432	427	413	459	457
ST	449	449	466	446	436	468	465
MF	13	20	22	2	2	4	4
PR	57	62	162	43	30	12	11
GR	51.17	47.65	113.23	142.84	99.65	19.93	18.27

Remarks:

- | | | | |
|-----|--------------------------------|-----|---------------------------------|
| FSI | : Free Swelling Index | IST | : Initial softening Temperature |
| ST | : Softening Temperature | MFT | : Max. Fluidity Temperature |
| MCT | : Max. Contraction Temperature | ST | : Solidification Temperature |
| C | : Contraction | MF | : Fluidity Temperature |
| D | : Dilatation | PR | : Plastic Range |
| G | : Cookability Factor | GR | : Gieseler Ratio |

The Gieseler plastometric test was shown in Table 5. The rheological characteristic values such as the initial softening, maximum fluid, and re-solidification temperature that have been measured. The Horna coal samples have an average of the initial softening temperature is 361°C, a maximum fluidity between 13 to 22 ddpm and the average of solidified temperature of 451°C. The temperature range between was 57°C to 152°C. The Menci Block coal samples had low maximum fluidity with an average 2 ddpm, range is 30°C and 40°C, the average of maximum fluidity in Disihu is 4 ddpm with plastic range 11°C and 12°C. An adequate range for proper operation of a blast furnace is 750-1,000 ddpm.

To assess the cookability of the coal, the dilatometric test was conducted. This test is used in calculating the cookability factor G-value of Simonis. Referring to the results of the dilatation test, the G-value of each location can be determined; the average G-value for the Horna Block, Menci, and Disihu 0.95, 0.84, 0.96, respectively Based on Simon’s G-range, the values between 0.90–0.99 are classified as medium to strongly coking coals.

3.5. Discussion

The parameters of proximate and ultimate analysis, show that all coal samples were suitable used for coke making technology, except the volatile matter (VM). In this study, all coal samples have VM more than 45% daf. The best coals for coke making have 24–26% dry ash free (daf) volatile matter [19]. The high VM content will produce low maximum fluidity as indicated in the coal samples from this area which in the range of 2-22 ddpm. The Lower fluidity produces weaker bonding during carbonization, making coke susceptibility to damage during transport.

Based on Simon’s G-range, the values between 0.90–0.99 are classified as medium and strongly cooking coals. The coals can be classified as a medium-cooking class. This is also supported by an intermediate FSI value (5.5). It was observed from the various coals tested, that total dilatation values are moderate (17-36%). In the steel industry, the required physical properties of blast furnace coke (Table 6) are the same; namely CRI (coke reactivity index) and CSR (coke strength after reaction with CO₂) [20].

Table 6. The coke reactivity index (CRI) and coke strength after reaction with CO₂ (CSR) from several blast furnace in some country

	European Range [20]	Australian Range [21]	American Range [22]	Japan Range [23]	China Range [24]
CRI	20 -30	17.7	23	< 35	23-24
CSR	> 60	74.1	61	50 - 65	79-71

This study shows that there are differences between various parameters measured in determining coal quality as coke making, however, based on the CSR and CRI in all coals show low CRI values (15.78 – 24.68%) and high CSR values (62.77- 74.12%); indicates that coals in the research area has the potential to be used as a coke-making material as the CRI and CSR parameter value which required in several blasts furnace in various places in the world (Table 6).

4. Conclusion

Although the proximate, ultimate, ash analysis, rheology's parameter, indicated that all coal samples have low-moderate potential to use as making coke. It also supported by the value of CRS and CSR which meets with the Blast Furnace standard criteria in several countries (low CRI and high CSR). Due to low fluidity the coal from Bintuni Basin can't used in coke making alone. To improve the quality of coal in the research area for use in the steel industry, the coal must be blended with other coal with high fluidity, which can make the interaction between coal particle to be strength.

Acknowledgments

The authors are grateful to the funding from the University Padjadjaran Research Programme of the Academic Leadership Grant (ALG) of the year 2018. The authors also would like to acknowledge the Dean of the Faculty of Geology for their support to establish this article.

References

- [1] Francis W and Peters MC. Fuels and Fuel Technology. 1980 Pergamon Press. Oxford.: 716
- [2] Ward CR. Coal geology, In: Encyclopedia of Physical Science and Technology. 2002: 45-76.
- [3] Tanggara D, Amijaya DH, Surjono SS. Evaluation of coking properties bituminous medium volatile coal, Batu Ayau Formation, Kutai Basin, Central Kalimantan. in IOP Conf. Ser.: Earth Environ. Sci. 2018; paper 212 012032: 1-11
- [4] Daulay B, Santoso B, Nining SN. Evaluation of Selected High Rank Coal in Kutai Basin, East Kalimantan Relating to Its Coking Properties. Indonesian Mining Journal 2015; 18: 1-10, 2015
- [5] Nas C and Hindartan. The Quality of Central Kalimantan Coking Coals. Kalimantan Coal and Mineral Resources. in Proceeding MGEI-IAGI. 2010; 1-11.
- [6] Thomas L. Coal Geology (2nd ed). Wiley-Blackwell John Wiley & Sons, Ltd. England. 2013.
- [7] American Society for Testing and Material (ASTM, Annual book of ASTM standard: Petroleum products, lubricants and fossil fuels.1992.
- [8] Mazmuder B. Coal Science and Engineering. Woodhead Publishing India. 2012.
- [9] Guelton N. The prediction of the Gieseler characteristics of coal blends. Fuel, 2017; 209: 661-673.
- [10] Vega M, Díaz F, Barriocanal E. Modification of coking properties due to oxidation. Effect of relative humidity. Journal of Material Research and Technology, 2019; 8(2): 1663-1673.
- [11] Tafadzwa M, Daniel M. M, Harold J. A. Influence of coal properties on the performance of fixed bed coal-burning braziers. Journal of Energy in Southern Africa. 2017; 28(2); 40-51.
- [12] Henrique BM, Guilherme LE, Amaral ARV, Marina CC. Influence of moisture and particle size on coal blend bulk density. REM, Int. Eng. J., 2019; 72 (2): 18-26.
- [13] Saini MK and Srivastava PK. Effect of Coal Cleaning on Ash Composition and its Fusion Characteristics for a High-Ash Non-Coking Coal of India. International Journal of Coal Preparation and Utilization, 2016; 36: 1-11, 2016
- [14] Bryant GW, Browning GJ, Emanuel H, Gupta SK, Gupta RP. The fusibility of blended coal ash. Energy Fuel, 2000; 14: 316-325.
- [15] Shalini G. Assessment of Low-Volatile Poor Caking Indian Coal for Coke Making. International Journal of Coal Preparation and Utilization, 2017; 37: 33-43.
- [16] Das B, Nag D, Dash PS. Effect of Grinding on Chemical and Coking Properties of a Highly Volatile Bituminous Coal and Its Size Fractions. International Journal of Coal Preparation and Utilization, 2018; 38: 355-360.
- [17] Ryemshak SA, Jauro A, Chindo IY, Ekenam EO. Pre-heating and partial briquetting technique for production of coke from binary blend of local coal and bitumen. International Journal of Engineering and Advanced Research Technology, 2016; 1: 7 -12.
- [18] Ryemshak SA, Jauro A, Putshaka JD, Sore RM. Ultimate Analysis of some Nigerian coal: Ranking and Suitable Application, International Journal of Engineering and Applied Sciences, 2016; 3: 31-35.
- [19] Arslan V. Kemal M. The effects of inert matters and low volatile coal addition on the plasticity of high volatile Zonguldak coals. The Journal of The South African Institute of Mining and Metallurgy, 2006; 106 (3): 199-204.
- [20] Ghosh B, Sahoo BK, Chakraborty B, Manjhi KK, Das SK, Sahu JN, & Varma AK. Influence of coke structure on coke quality using image analysis method. Int. J. Coal Sci. Technology, 2018; 5(4): 473-485.

- [21] Leonard DC, Bonte L, Dufour A, Ferstl A, Raipala K, Scmole P, Schoone P, Verduras JL, Willmers RR. Coke quality requirements of European blast furnace engineers. (joint EBFC-Paper). Proc. 3rd European Cokemaking Cong., CRM-VDEh, Gent, Belgium, pp. 1– 10.
- [22] Horrocks KRS, Cunningham RB, Ellison JF, Nightingale RJ. Coke quality at BHP Steel Port Kembla. Proc. 4th European Coke and Ironmaking Cong., ATS-RM. 2000; 1: 167–173.
- [23] Poveromo JJ. Operational considerations for high-level blast furnace fuel injection. Proc. 55th Ironmaking Conf., ISSAIME. 1996; 79– 92.
- [24] Nishioka K. History and future of the Japanese cokemaking technology. J. Japan. Inst. Energy, 2000; 79(876): 284– 298
- [25] Zheng JL, Zhang JL, Yang TJ. Low Carbon Operation of Super-Large Blast Furnaces in China. ISIJ International, 2015; 55 (6). 1146–1156
- [26] Lin MF, Hong MT. The effect of coal blends fluidity on the properties of Coke. Fuel, 1986; 65: 307–311.

*To whom correspondence should be addressed: professor Ahmad Helman Hamdani, Faculty of Geology, University of Padjadjaran, Jl. Raya Bandung-Sumedang Km.21 Jatinangor, 45363, Indonesia,
E-mail: ahmad.helman@unpad.ac.id*

Fuel Characterisation of the Physicochemical, Thermal and Kinetic Properties of Corn Cob Biomass Wastes for Potential Energy Recovery

Victor O. Otitolaiye¹, Yakubu A. Dodo², Zainab T. Jagun³, Faizah M. Bashir⁴, Lawrence P. Moveh⁵, Samuel-Soma M. Ajibade⁶, Samuel Moveh⁷, Bemgba B. Nyakuma^{8*}

¹ Department of Health Safety and Environmental Management, International College of Engineering and Management, Seeb, Sultanate of Oman

² Department of Architecture, Faculty of Architecture and Engineering, Istanbul Gelisim University, 34310 Istanbul, Turkey

³ Faculty of Built Environment and Surveying, Universiti Teknologi Malaysia, 81310 Skudai, Johor, Malaysia

⁴ Department of Interior Design and Decoration, College of Engineering, University of Hail, 55417 Hail, Kingdom of Saudi Arabia

⁵ Faculty of Engineering and Built Environment, Universiti Sains Islam, Bandar Baru Nilai, 71800 Nilai, Negeri Sembilan, Malaysia

⁶ Department of Computer Science, Faculty of Computing, Universiti Teknologi Malaysia, 81310 Skudai, Johor, Malaysia

⁷ School of Mechanical Engineering, Faculty of Engineering, Universiti Teknologi Malaysia, 81310 Skudai, Johor, Malaysia

⁸ BNG Consulting, Taman Sri Pulai Perdana, 81110 Skudai, Johor, Malaysia

Received May 26, 2019; Accepted September 29, 2020

Abstract

This study presents insights into the solid biofuel properties of corn cob biomass (CCB) wastes for sustainable energy recovery. The physicochemical, thermal, and kinetic properties of CCB were characterised through ultimate, proximate, heating value, and thermogravimetric (TGA) analyses. Results showed that CCB contains high carbon (41.88 wt.%), hydrogen (6.33 wt.%), volatile matter (68.21 wt.%), and higher heating (15.70 wt.%) values for potential energy recovery. However, the high ash (16.56 wt.%) content could pose bed agglomeration, fouling, and sintering problems during high-temperature conversion. Thermal analysis resulted in 55.84%–59.51% loss of mass and residual mass of 40.49%–44.17%. Kinetic analyses revealed that CCB is highly reactive as characterised by the average activation energy, $E_a = 134.58$ kJ/mol and pre-exponential factor, $k_0 = 2.53 \times 10^{08}$ /min. In conclusion, CCB is a potentially practical feedstock for sustainable energy recovery through thermochemical conversion.

Keywords: Biofuel characterisation; Physicochemical properties; Thermokinetics; Corn cobs.

1. Introduction

The valorisation of agricultural biomass wastes is gaining significant traction worldwide. Over the years, the quest to reduce the overdependence of global economies on fossil-based fuels such as petroleum and coal has prompted the transition to cleaner alternatives [1]. The utilization of agricultural biomass wastes for energy, chemicals, and fuels is considered carbon neutral with potential benefits for human health, safety, and the environment [2-3]. Researchers posit that the transition to clean energy technologies such as biomass will enhance the diversification of the world's energy mix and reduce the long term impacts of global warming and climate change [4-5]. Therefore, the potential of valorising various agricultural biomass waste streams such as wheat straw [6-7], soybean stalk/straw [8-9], oil palm wastes [10-11], rice

husks and other biomass into biofuels, bioenergy and biomaterials have been widely explored in the literature.

However, the valorisation of agricultural biomass wastes requires analyses of their intrinsic physical, chemical, thermal, kinetic and thermodynamic properties [12-13]. Hence, prospective agricultural biomass wastes are typically subjected to extensive characterisation and assessment through ultimate, proximate, and calorific analyses to determine the elemental (CHNSO-carbon, hydrogen, nitrogen, sulphur and oxygen contents in wt.%), chemical fuel properties (moisture, volatiles, ash, and fixed carbon), and higher heating value (HHV) [14]. The thermal and kinetic analyses of prospective agricultural biomass wastes are also examined through thermogravimetric analysis (TGA) [15]. TGA provides comprehensive data on the thermal behaviour, degradation mechanism, and temperature profile characteristics (TPCs) of prospective biomass feedstock [16-17]. Based on literature reviews, the valorisation of agricultural biomass wastes is typically accomplished by biochemical and thermochemical technologies such as digestion, fermentation, torrefaction, pyrolysis, gasification, and combustion [18-19]. However, lack of data on the outlined characteristics of potential feedstock biomass could severely hamper the design, development, and scale-up of future bioenergy and biofuel conversion systems.

Therefore, this study seeks to characterise the solid biofuel properties of corn cob biomass (CCB) wastes through physicochemical, thermal, and kinetic analysis for sustainable energy recovery. Previous studies in the literature have examined the biochemical conversion and pre-treatment of CCB through hydrolysis, saccharification, ultrasonic treatment, and extraction [20-22]. Other studies have examined the thermochemical conversion of CCB through gasification [23-24], and combustion [25-27]. Therefore, it is envisaged that this study will provide insights into the biofuel properties of CCB and present comprehensive data for sustainable energy recovery through pyrolysis.

2. Experimental

2.1. Physicochemical analysis

The physicochemical properties of CCB were elucidated through ultimate, proximate, and calorific analyses to determine its elemental, chemical fuel, and heating values. The ultimate analysis was carried out using an elemental analyser (Model: vario MACROCUBE, Germany) to determine the composition of carbon, hydrogen, nitrogen, and sulphur contents based on the ASTM D5291-16 technique. The proximate analysis was performed by thermogravimetric (TG) analysis to determine the moisture (M), volatile matter (VM), ash (AC) and fixed carbon (FC). The TG Analyser (Model: Shimadzu TG-50, Japan) was employed to determine the M and VM by heating a known mass of the sample at 105°C and 950°C in nitrogen gas (N₂) at a flow rate of 100 mL/min for a hold time of 11 minutes. The ash (A) was determined in an air atmosphere at 950°C. The calorific analysis was performed using an isoperibol oxygen bomb calorimeter (IKA C200, USA) located at the School of Mechanical Engineering, Universiti Teknologi Malaysia (UTM, Skudai Malaysia) to compute the higher heating value (HHV). Each test was performed at least twice to ensure accuracy and precision of the results presented in Table 1.

Table 1. Physicochemical fuel properties of CCB

Analysis	Fuel property	Symbol (Unit)	Corn Cob Biomass
Ultimate	Carbon	C (wt.%)	41.88
	Hydrogen	H (wt.%)	6.33
	Nitrogen	N (wt.%)	0.79
	Sulphur	S (wt.%)	0.14
	Oxygen	O (wt.%)	50.86
Proximate	Moisture	M (wt.%)	9.44
	Volatile Matter	VM (wt.%)	68.21
	Ash	A (wt.%)	16.56
	Fixed Carbon	FC (wt.%)	5.79
Calorific	Higher Heating Value	HHV (MJ/kg)	15.70

2.2. Thermal analysis

The thermal properties of CCB were examined by thermogravimetric (TG) analysis based on the non-isothermal and multiple heating rate programs of the TG analyser (Model: Shimadzu TG-50, Japan). For each TGA experiment, approximately 13.5 mg of CCB (particle size below 250 μm) was weighed in an alumina crucible before heating from 25 $^{\circ}\text{C}$ to 700 $^{\circ}\text{C}$ based on the multiple heating rates of 10 $^{\circ}\text{C}/\text{min}$, 20 $^{\circ}\text{C}/\text{min}$, 30 $^{\circ}\text{C}/\text{min}$ under nitrogen (N_2) gas flow rates of 100 mL/min. The aim of the process was to simulate the non-isothermal thermal degradation of CCB under the non-oxidative conditions typical of pyrolysis.

On completion, the furnace of the TG analyser was cooled to room temperature using an automatic air blower. The TG data was then analysed using the thermal analysis software (Shimadzu TA-60WS) to determine the mass loss and derivative of the mass loss, which were plotted against temperature ($^{\circ}\text{C}$) to deduce the TG (%) and DTG (%/min) plots in Figures 1 and 2. Subsequently, the temperature degradation profiles for each heating rate during TGA were determined to understand the thermal behaviour and degradation mechanism. The temperature degradation profiles deduced from the TG plots in this study were; Onset temperature (T_o), Midpoint temperature (T_m), Endpoint temperature (T_e), Loss of Mass (L_M) and Residual Mass (R_M). However, the temperature degradation profiles deduced from DTG were; peak drying temperature (T_{DRY}), peak devolatilization temperature I (T_{DV1}) and peak devolatilization temperature II (T_{DV2}).

2.3. Kinetic analysis

The kinetic parameters for the non-oxidative thermal degradation of CCB were examined based on the Kissinger kinetic model (KKM). In principle, the governing equations of KKM are based on the peak decomposition temperatures derived from the DTG plots of multiple heating-rate thermal degradation of materials such as the CCB examined this study. The central concept is derived from the Arrhenius relation for thermally degrading carbon materials described as follows;

$$k(T) = k_o \exp\left(-\frac{E_a}{RT}\right) \quad (1)$$

From Eq. 1, the terms $k(T)$, k_o (/min), E_a (kJ/mol), and R (J/mol K) represent the temperature-based rate constant, pre-exponential factor, activation energy, and ideal gas constant, respectively. Hence, the thermal decomposition of CCB based on the multiple heating rates, non-oxidative, and non-isothermal decomposition could be described as;

$$\frac{d\alpha}{dT} = \frac{k_o}{\beta} \exp\left(-\frac{E_a}{RT}\right) f(\alpha) \quad (2)$$

From Eq. 2, the term β symbolises the heating rates (10, 20, and 30 $^{\circ}\text{C}/\text{min}$), whereas the reaction function for the CCB thermal decomposition model is described by $f(\alpha)$. Hence, the governing equations for the KKM can be subsequently deduced by separating and integrating the variables in Eq. 2 to derive the relation in Eq. 3;

$$\ln\left(\frac{\beta}{T_x^2}\right) = \ln\left(\frac{k_o R}{E_a}\right) - \ln\left(\frac{E_a}{RT_x}\right) \quad (3)$$

Consequently, the peak decomposition terms namely; peak drying temperature (T_{DRY}), peak devolatilization temperature I (T_{DV1}), and peak devolatilization temperature II (T_{DV2}) derived from the DTG plots were substituted for T_x in Eq. 3. The kinetic parameters; activation energy (E_a) and pre-exponential factor (k_o) for the drying (T_{DRY}) and devolatilization (T_{DV1} and T_{DV2}) of CCB during TGA were deduced.

3. Results and discussion

3.1. Physicochemical properties

The physicochemical properties of potential biomass are crucial to determining its potential for bioenergy recovery [28]. Numerous studies have employed various techniques to examine the solid bioenergy and biofuel properties of different biomass feedstock [29]. In this study, the physicochemical properties of corn cob biomass (CCB) are examined based on ultimate,

proximate, and calorific analyses. Table 1 shows the elemental composition, chemical fuel properties, and higher heating value of CCB in as received (a.r.) basis.

The results indicate that CCB contains carbon, hydrogen, nitrogen, sulphur, oxygen, along with moisture, volatile matter, ash, fixed carbon, and higher heating value in various proportions. The high carbon and hydrogen content observed in CCB indicates it has good potential for energy recovery, despite the high oxygen content. Typically, high oxygen content could result in over oxidation of biomass feedstock during thermal conversion producing high ash and mineral matter along with low heating value flue gases [19]. However, the low moisture content (< 10%) indicates CCB does not require additional treatment or conditioning such as drying, which is an energy-intensive and costly process during biomass energy recovery [30]. The volatile matter was also found to be sufficiently high (> 65%), which indicates CCB has high condensable and non-condensable fractions, which are crucial to enhancing product yield and distribution during biomass conversion. Furthermore, high VM ensures good ignitability and thermal conversion particularly for gasification and combustion [31]. The ash content was considerably high (> 5%), whereas the fixed carbon was within the acceptable limits [13]. The high ash content of CCB could present operational and technical challenges due to bed materials agglomeration, fouling, or sintering during thermochemical conversion [32-33]. Lastly, the heating value of CCB (HHV = 15.70 MJ/kg) was found to be within the range from 14 MJ/kg to 20 MJ/kg typically reported for biomass [34]. Based on its physicochemical properties CCB is a potentially good feedstock for energy recovery through thermochemical conversion.

3.2. Thermal properties

The thermal properties of CCB were analysed by thermogravimetric analysis (TGA) to determine its thermal behaviour, decomposition mechanism, and temperature degradation profiles. The TG and derivative TG plots for the non-oxidative, non-isothermal, and multiple heating rate thermal decompositions of CCB are shown in Figures 1 and 2. The TG plots for CCB are characteristic of thermally decomposing carbonaceous materials with progressive loss of mass observed during TGA. The plots indicate that the non-isothermal incremental change in temperatures from 25°C to 700°C along with the variation of the heating rates from 10°C/min to 30°C/min significantly influenced the thermal decomposition of CCB during TGA.

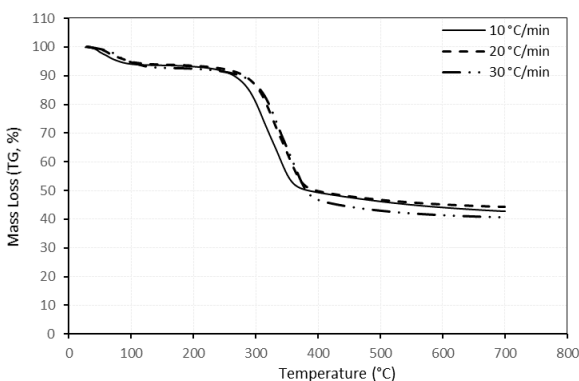


Figure 1. TG plots for thermal decomposition of CCB

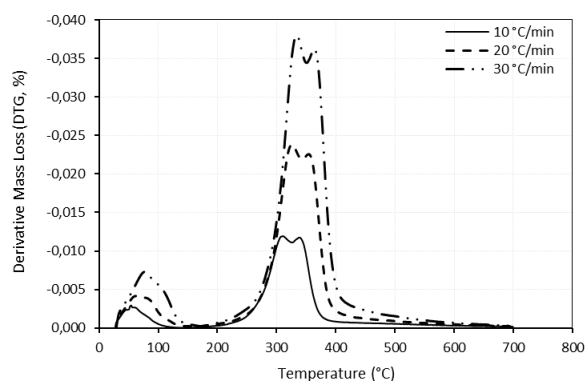


Figure 2. DTG plots for thermal decomposition of CCB

As observed, the TG plots shifted from right to left with increasing heating rate during TGA. According to numerous authors in the literature [30, 35-36], the shifts can be ascribed to the thermal-time lag that causes delayed degradation of biomass decomposition and transforms the degradation temperature profiles. Hence, the extent of the shifts on the TG plots and the thermal properties of CCB were examined as presented in Table 2.

Table 2. TG-Degradation temperatures for CCB

Heating Rate (°C/min)	Onset temperature (T_o , °C)	Midpoint temperature (T_m , °C)	Endpoint temperature (T_e , °C)	Loss of mass (L_M , %)	Residual mass (R_M , %)
10	262.15	317.22	372.72	57.23	42.77
20	278.42	331.71	385.81	55.84	44.17
30	287.70	338.90	395.24	59.51	40.49

As observed, the TG based degradation temperature profiles; onset (T_o), midpoint (T_m), and endpoint (T_e) temperatures for CCB increased with increasing heating rates from 10°C/min to 30°C/min during TGA. The onset (T_o) temperatures increased from 262.15°C to 287.70°C indicating the ignition of CCB increased by 25.55°C with an increase in the heating rates. Likewise, the midpoint (T_m) temperatures increased from 317.22°C to 338.90°C signifying the rise in the heating rates resulted in a 21.68°C increase in the T_m . Lastly, the endpoint (T_e) temperatures also increased from 372.72°C to 395.24°C or by 22.52°C with rising heating rates from 10°C/min to 30°C/min during TGA. Hence, it can be reasonably surmised that the variation in the heating rates exerted a higher influence on the onset (T_o), compared to the endpoint (T_e), and lastly midpoint (T_m) temperatures in decreasing order. On the other hand, the loss of mass was in the range of 55.84% to 59.51%, whereas the residual mass was from 40.49% to 44.17%. On average the onset temperature (T_o), midpoint temperature (T_m), and endpoint temperature (T_e), loss of mass (L_M) and residual mass (R_M) for CCB degradation are; 276.09 °C, 329.28 °C, 384.59 °C, 57.52% and 42.48%.

The analysis of the derivative TG or DTG plots was examined to understand the decomposition mechanism of CCB during TGA. Figure 2 shows the DTG plots for CCB at different heating rates based on non-isothermal heating under non-oxidative conditions.

The DTG plots for each heating rate displayed two sets of endothermic peaks. The first set of small-sized peaks can be observed from 25 °C to 150°C, which signifies the loss of mass due to surface-bound moisture (drying) and low molecular weight (partial devolatilization). However, the second set or peaks can be observed between 150°C and 425°C, which signifies the mass loss due to holocellulose and lignin degradation during TGA [37-39]. Furthermore, the mass loss in this range is typically ascribed to the loss of volatile matter, hence the term devolatilization. Further analysis of the devolatilization peaks revealed the presence of two humps denoted as peak devolatilization temperatures I (T_{DV1}) and II (T_{DV2}) for the heating rates. Table 3 presents the characteristic peak temperatures for drying and devolatilization at T_{DV1} and T_{DV2} .

Table 3. DTG-Degradation temperatures for CCB

Heating Rate (°C/min)	Peak drying temperature (T_{DRY})	Peak devolatilization temperature I (T_{DV1})	Peak devolatilization temperature II (T_{DV2})
10	54.53	310.90	339.45
20	62.59	326.31	353.87
30	77.66	333.58	363.49

Similarly, the findings indicate that higher heating rates shifted the degradation parameters to higher temperatures during TGA. From Table 3, it can be observed that peak drying temperature (T_{DRY}) increased by 23.13°C from 54.53°C to 77.66°C with the increase in heating rate from 10°C/min to 30°C/min. Likewise, the peak devolatilization temperature I (T_{DV1}) increased but by 22.68°C, whereas the peak devolatilization temperature II (T_{DV2}) was by 24.04°C from 310.90°C and 339.45°C, respectively. Typically, the mass loss at the peak devolatilization temperatures I (T_{DV1}) and II (T_{DV2}) are attributed to the thermal degradation of hemicellulose and cellulose during TGA [38-39].

3.3. Kinetic properties

The Kissinger kinetic model (KKM) was employed to examine the kinetic parameters; activation energy (E_a) and pre-exponential factor (k_o) for CCB based on the drying (T_{DRY}) and devolatilization (T_{DV1} and T_{DV2}) stages during TGA. Based on Eq 1-3, the terms $\ln\left(\frac{\beta}{T_x^2}\right)$ were plotted against $\left(\frac{1}{T_x}\right)$, whereby the values of E_a and k_o were determined from the slope and intercept of the plots, respectively. Therefore, the kinetic plots for the drying and devolatilization stages (T_{DV1} and T_{DV2}) are presented in Figures 3-5.

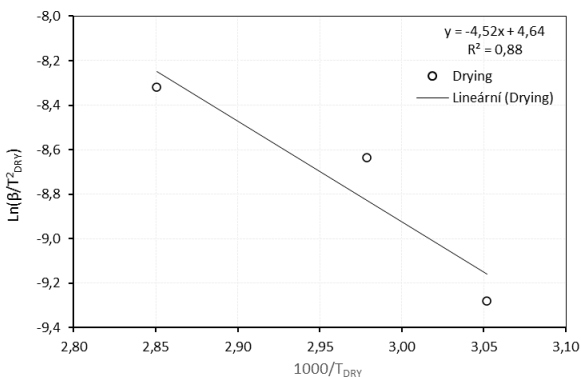


Figure 3. Kissinger kinetic plots for drying of CCB

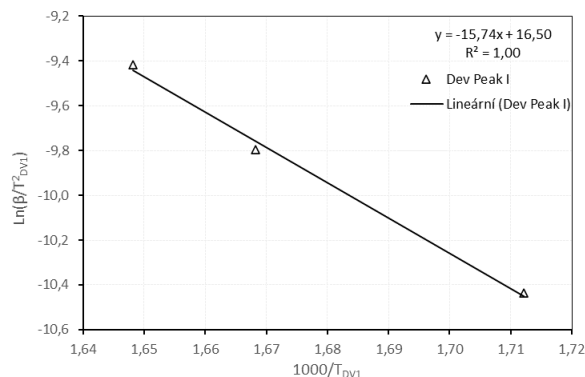


Figure 4. Kissinger kinetic plots for CCB devolatilization at T_{DV1}

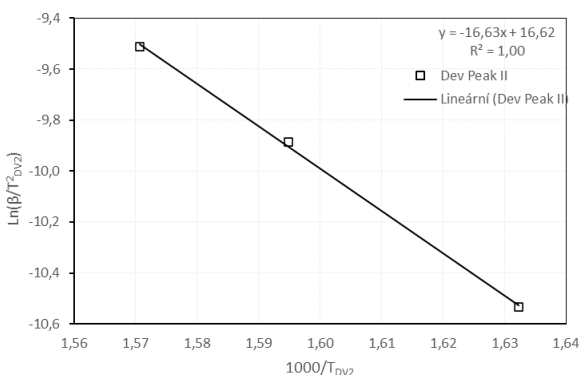


Figure 5. Kissinger kinetic plots for CCB devolatilization at T_{DV2}

Based on the slope and intercept of the plots in Figures 3-5, the kinetic parameters for the thermal degradation of CCB under non-oxidative and non-isothermal conditions were examined. Therefore, the activation energy required for drying CCB was computed as $E_a = 37.61$ kJ/mol, with the pre-exponential factor, $k_o = 4.71 \times 10^{02}$ /min. For the devolatilization at the peak decomposition temperature 1 (T_{DV1}), the computed activation energy was $E_a = 130.89$ kJ/mol with the pre-exponential factor, $k_o = 2.32 \times 10^{08}$ /min. Lastly, for devolatilization at the peak

decomposition temperature 2 (T_{DV2}), the activation energy was computed as $E_a = 138.27$ kJ/mol with the pre-exponential factor, $k_o = 2.75 \times 10^{08}$ /min.

On average the E_a and k_o for the devolatilization process was 134.58 kJ/mol and 2.53×10^{08} /min. In comparison, the kinetic parameters of CCB are lower than oil palm empty fruit bunch pellets (144.30 – 146.63 kJ/mol) [28], cornstalk (206.40 kJ/mol), oak (236.20 kJ/mol), and sawdust (232.60 kJ/mol) [40] as reported in the literature. Hence, the kinetic parameters indicate that CCB is highly reactive despite the mass loss (55.84% – 59.51%) and residual mass (40.49% – 44.17%) during TGA.

4. Conclusion

The study examined the physicochemical, thermal, and kinetic properties of corn cob biomass (CCB) wastes as potential solid biofuel for sustainable energy recovery. The characterisation analyses revealed that CCB has the requisite fuel properties such as high carbon, hydrogen, volatile matter, and higher heating values for energy recovery through thermochemical conversion. However, the high ash content could pose potential problems such as bed materials agglomeration, fouling, and sintering during high-temperature conversion. The thermal and kinetic analyses revealed that CCB is highly reactive with the average values of $E_a =$

134.58 kJ/mol and $k_o = 2.53 \times 10^{08}$ /min deduced for the devolatilization process and the mass loss (55.84% – 59.51%) and residual mass (40.49% – 44.17%) during TGA. Overall, the findings indicate that CCB is a potentially viable feedstock for sustainable energy recovery through thermochemical conversion.

References

- [1] Chu S and Majumdar A. Opportunities and challenges for a sustainable energy future. *Nature*, 2012; 488(7411): 294.
- [2] Ragauskas AJ, Williams CK, Davison BH, Britovsek G, Cairney J, Eckert CA, Frederick WJ, Hallett JP, Leak DJ, and Liotta CL. The path forward for biofuels and biomaterials. *Science*, 2006; 311(5760): 484-489.
- [3] Suman S and Gautam S. Biochar Derived from Agricultural Waste Biomass Act as a Clean and Alternative Energy Source of Fossil Fuel Inputs. *Energy Systems and Environment*, 2018: 207.
- [4] Meinshausen M, Meinshausen N, Hare W, Raper SC, Frieler K, Knutti R, Frame DJ, and Allen MR. Greenhouse-gas emission targets for limiting global warming to 2 C. *Nature*, 2009; 458(7242): 1158.
- [5] McGlade C and Ekins P. The geographical distribution of fossil fuels unused when limiting global warming to 2 C. *Nature*, 2015; 517(7533): 187.
- [6] Schnitzer M, Monreal, CM, and Powell EE. Wheat straw biomass: A resource for high-value chemicals. *Journal of Environmental Science and Health, Part B*, 2014; 49(1): 51-67.
- [7] Tsegaye B, Gupta P, Balomajumder C, and Roy P. Optimization of Organosolv pretreatment conditions and hydrolysis by *Bacillus* sp. BMP01 for effective depolymerization of wheat straw biomass. *Biomass Conversion and Biorefinery*, 2020: 1-15.
- [8] Martelli-Tosi M, Assis OB, Silva NC, Esposto BS, Martins MA, and Tapia-Blácido DR. Chemical treatment and characterization of soybean straw and soybean protein isolate/straw composite films. *Carbohydrate polymers*, 2017; 157: 512-520.
- [9] Khomina V, Trach I, Semenyshyna I, Koberniuk O, Mudryk K, Jewiarz, M, Wróbel M, and Styks J, Potential of Soybean Straw in Ukraine and Solid Biofuel Production, in *Renewable Energy Sources: Engineering, Technology, Innovation*. 2020; Springer. p. 163-170.
- [10] Nyakuma BB, Ahmad A, Johari A, Abdullah TA, Oladokun O, and Alkali H. Fluidised Bed Gasification and Chemical Exergy Analysis of Pelletised Oil Palm Empty Fruit Bunches. *Chemical Engineering Transactions*, 2017; 56(1): 1159-1164.
- [11] Abdullah N and Sulaiman F, The Oil Palm Wastes in Malaysia, in *Biomass Now-Sustainable Growth and Use*. 2013; InTech Open Publishers. p. 75-93.
- [12] Nyakuma BB. Bioenergy Potential of Melon Seed Husks. *Lignocellulose*, 2017; 6(1): 15-22.
- [13] Vassilev SV, Baxter D, Andersen LK, and Vassileva CG. An overview of the Chemical Composition of Biomass. *Fuel*, 2010; 89(5): 913-933.
- [14] Cai J, He Y, Yu X, Banks SW, Yang Y, Zhang X, Yu Y, Liu R, and Bridgwater AV. Review of physicochemical properties and analytical characterization of lignocellulosic biomass. *Renewable and Sustainable Energy Reviews*, 2017; 76: 309-322.
- [15] Cai J, Xu D, Dong Z, Yu X, Yang Y, Banks SW, and Bridgwater AV. Processing thermogravimetric analysis data for isoconversional kinetic analysis of lignocellulosic biomass pyrolysis: Case study of corn stalk. *Renewable and Sustainable Energy Reviews*, 2017; 82(3): 2705-2715.
- [16] Oladokun O, Ahmad A, Abdullah TT, Nyakuma BB, Al-Shatri A, and Bello A. Modelling multi-component devolatilization kinetics of *Imperata cylindrica*. *Chemical Engineering Transactions*, 2015; 45: 919-924.
- [17] Carrier M, Loppinet-Serani A, Denux D, Lasnier J-M, Ham-Pichavant F, Cansell F, and Aymonier C. Thermogravimetric analysis as a new method to determine the lignocellulosic composition of biomass. *Biomass and Bioenergy*, 2011; 35(1): 298-307.
- [18] Baska, C, Baskar S, and Dhillon RS. Biomass conversion: The interface of biotechnology, chemistry and materials science. 2012.
- [19] Basu P. Biomass Gasification, Pyrolysis and Torrefaction: Practical Design and Theory. 2018; 2: 530.
- [20] Xu Q-Q, Zhao M-J, Yu Z-Z, Yin J-Z, Li G-M, Zhen M-Y, and Zhang Q-Z. Enhancing enzymatic hydrolysis of corn cob, corn stover and sorghum stalk by dilute aqueous ammonia combined with ultrasonic pretreatment. *Industrial Crops and Products*, 2017; 109: 220-226.
- [21] Sewsynker-Sukai Y and Kana EBG. Simultaneous saccharification and bioethanol production from corn cobs: Process optimization and kinetic studies. *Bioresource Technology*, 2018; 262: 32-41.

- [22] Sewsynker-Sukai Y, Suinyuy TN, and Kana EBG. Development of a sequential alkalic salt and dilute acid pretreatment for enhanced sugar recovery from corn cobs. *Energy Conversion and Management*, 2018; 160: 22-30.
- [23] Du C, Wu J, Ma D, Liu Y, Qiu P, Qiu R, Liao S, and Gao D. Gasification of corn cob using non-thermal arc plasma. *International Journal of Hydrogen Energy*, 2015; 40(37): 12634-12649.
- [24] Biagini E, Barontini F, and Tognotti L. Gasification of agricultural residues in a demonstrative plant: Corn cobs. *Bioresource technology*, 2014; 173: 110-116.
- [25] Chyang C-S, Duan F, Lin S-M, and Tso J. A study on fluidized bed combustion characteristics of corncob in three different combustion modes. *Bioresource technology*, 2012; 116: 184-189.
- [26] Chaivatamaset P, Sricharoon P, and Tia S. Bed agglomeration characteristics of palm shell and corncob combustion in fluidized bed. *Applied Thermal Engineering*, 2011; 31(14-15): 2916-2927.
- [27] Várhegyi G, Mészáros E, Antal MJ, Bourke J, and Jakab E. Combustion kinetics of corncob charcoal and partially demineralized corncob charcoal in the kinetic regime. *Industrial & engineering chemistry research*, 2006; 45(14): 4962-4970.
- [28] Nyakuma BB, Wong S, Oladokun O Non-oxidative thermal decomposition of oil palm empty fruit bunch pellets: fuel characterisation, thermogravimetric, kinetic, and thermodynamic analyses. *Biomass Convers Biorefinery*.2019; pp 1.20.
<https://doi.org/10.1007/s13399-13019-00568-13391>.
- [29] Nudri NA, Bachmann RT, Ghani WAWAK, Sum DNK, and Azni AA. Characterization of oil palm trunk biocoal and its suitability for solid fuel applications. *Biomass Conversion and Biorefinery*, 2020; 10(1): 45-55.
- [30] Nyakuma BB, Ahmad A, Johari A, Tuan TA, Oladokun O, and Aminu DY. Non-Isothermal Kinetic Analysis of Oil Palm Empty Fruit Bunch Pellets by Thermogravimetric Analysis. *Chemical Engineering Transactions*, 2015; 45: 1327-1332.
- [31] Basu P. *Biomass Gasification and Pyrolysis: Practical Design and Theory*. 2010.
- [32] Mettanant V, Basu P, and Butler J. Agglomeration of biomass fired fluidized bed gasifier and combustor. *The Canadian Journal of Chemical Engineering*, 2009; 87(5): 656-684.
- [33] Ninduangdee P and Kuprianov VI. A Study on Physical and Chemical Changes in the Bed Material during Long-Term Combustion of Oil Palm Residues in a Fluidized Bed of Alumina Sand. *Energy Procedia*, 2015; 79: 865-870.
- [34] Vassilev SV, Vassileva CG, and Vassilev VS. Advantages and Disadvantages of Composition and Properties of Biomass in comparison with Coal: An overview. *Fuel*, 2015; 158: 330-350.
- [35] Słopiecka K, Bartocci P, and Fantozzi F. Thermogravimetric analysis and kinetic study of poplar wood pyrolysis. *Applied Energy*, 2012; 97: 491-497.
- [36] Oladokun O, Ahmad A, Abdullah T, Nyakuma B, Bello A-H, and Al-Shatr, A. Multicomponent Devolatilization Kinetics and Thermal Conversion of *Imperata cylindrica*. *Applied Thermal Engineering*, 2016; 105: 931-940.
- [37] Nyakuma BB. Thermogravimetric and Kinetic Analysis of Melon (*Citrullus colocynthis* L.) Seed Husk Using the Distributed Activation Energy Model. *Environmental and Climate Technologies*, 2015; 15(1): 77-89.
- [38] Burhenne L, Messmer J, Aicher T, and Laborie M-P. The effect of the biomass components lignin, cellulose and hemicellulose on TGA and fixed bed pyrolysis. *Journal of Analytical and Applied Pyrolysis*, 2013; 101: 177-184.
- [39] Skreiberg A, Skreiberg Ø, Sandquist J, and Sørum L. TGA and macro-TGA characterisation of biomass fuels and fuel mixtures. *Fuel*, 2011; 90(6): 2182-2197.
- [40] Sun WG, Zhao H, Yan HX, Sun BB, Dong SS, Zhang CW, and Qin S. Pyrolysis Characteristics and Kinetics of Jerusalem artichoke Stalk Using Thermogravimetric Analysis. *Energy Sources, Part A: Recovery, Utilization, and Environmental Effects*, 2012; 34(7): 626-635.

To whom correspondence should be addressed: Dr. Bemgba B. Nyakuma, BNG Consulting, Taman Sri Pulai Perdana, 81110 Skudai, Johor, Malaysia, E-mail: bbnyax1@gmail.com

A comparative Approach to Differentiate Between the Amount of Rock Cuttings Generated in ERD and Conventional Drilling

Sameer Younus¹, Hussein El Gburi², Mohamed Halafawi², Lazăr Avram²

¹TAQA Global, Iraq

²Petroleum-Gas University of Ploiesti, Romania

Received June 17, 2019; Accepted September 30, 2020

Abstract

Extended Reach Drilling is one of the drilling techniques that is used to drill horizontal wells to very long distances. These types of wells have many applications and advantages over conventional drilling techniques. The paper concentrates on one of the environmental advantages of ERD wells over conventional drilling. Since an oil and gas well can generate thousands of barrels of drill cuttings, it is important to know how much cuttings will be generated per well. What is the calculation method, and what are the parameters involved in cuttings amount generation. Additionally, the article compares the amount of drill cuttings generated in both ERD wells and conventional drilling. An accurate drilling technique is used to calculate the amount of cuttings generated while drilling both types of wells. The factors and parameters control the amount of cuttings generation is explained and showed how ERD project minimizes the amount of cuttings. A mathematical method is used to determine the amount of cuttings generated per each section of well drilled. Parameters involved in drilling cuttings calculation are explained. M-16 ERD well of Wytch Farm and a real conventional well from Iraq are used to calculate the amount cuttings generated. The total amount of cuttings generated during drilling deeper sections is bigger, although they have small diameters. For M-16 ERD well, the larger amount of cuttings appeared during drilling 12.25" hole section while it appeared in the conventional well during drilling 17.5" hole section.

Keywords: ERD; Rock cuttings; Comparative study; Wellbore trajectory; Factors influencing cuttings waste .

1. Introduction

An extended reach well is considered as a special type of long radius horizontal well in which the ratio of the measured depth (MD) is twice the true vertical depth (TVD). ERD assists in facilitating drilling into potential reservoirs situated in environmentally sensitive fields, which have very sharp rules not favorable for setting up a rig there. With ERD (Extended Reach Drilling), a drilling rig can be set 10 kilometers from the sensitive area. ERD patterns generally are deep (MD), with long horizontal displacements between the surface location and the bottom of the hole. ERD is one of the techniques that oil companies apply to effectively drill wells to long distances, from onshore to offshore locations. The amount of extended reach drilling is getting increasing day by day. This is due to the fact that using ERD techniques has many advantages over conventional drilling methods. ERD has many applications that improve environmental efficiencies. Some of these applications are; It reduces environmental footprint in offshore environments, It limits drilling operation effects on the environment, It reduces underwater noise and other activities, It eliminates interaction with the marine environment while drilling from land to oceans, It decreases the need for installing the number of platforms needed to develop an offshore field, this is due to the fact then, multiple wells can be drilled in the same platform, thus eliminating the number of platforms. In many papers and textbooks, the environmental benefits of drilling an ERD well are extensively explained. Environmental consideration has been one of the most important aspects of well engineering and design. Recently, many papers and articles are published about extended reach wells. Existing

extended reach technologies have been reviewed and summarized. Principles and mathematics of ERD, horizontal, and directional drilling have been presented [1-11]. An overview of the drilling issues is provided, and the completion issues as relevant for a gas production well are examined [12]. Woodside Offshore Petroleum Company presented and studied the drilling extended reach wells in the Northwest Shelf in Australia [13]. The development of multilateral wells and long reach wells has been explained on how to maximize recovery for many oil fields [14]. Three main principles on the design of ERD well trajectory were studied by optimizing the build section within nine types of shapes [15]. The results illustrated that sideway curves, curvature reducing curves, and circular arc are better than others. Additionally, the obtained results are essential guidelines for the design of ERD trajectory. Moreover, a hole cleaning program of a ERD field was developed by Amoco UK over the course of three ERD wells. This program proved its effectiveness in cleaning the hole as well as increasing drilling progress [16].

Applications of ERD Oil companies have always searched for new techniques and new development in drilling methods to best exploit oil and gas reserves, for that they spend millions of dollars on technical researches and development projects to find the most economical and convenient ways to drill oil and gas wells. The applications and benefits of ERD wells encouraged drilling engineers to further develop techniques to drill such challenging wells. This helped oil companies to reach extremely difficult and critical geological targets. Below lists some of the applications and benefits of ERD wells:

- Used to drill oil and gas wells in complex and challenging environments such as the Arctic
- Drilling wells from a location on land to the oil and gas under the ocean, example in Russia, Sakahlin-1 project
- Guiding the wellbore to the extreme distance in the pay zone, which increases the recovery of hydrocarbon and it is dramatically increasing production rate and reservoir drainage
- Reducing environmental footprint and, in offshore applications and It limits our presence in the marine environment
- Reducing underwater noise and other activities
- Eliminating interaction with the marine environment while drilling from land to oceans by using ERD techniques
- Reducing cost for developing the field and minimizes impacts on the marine environment by decreasing the number of platforms needed because it uses a single structure to develop a field
- Drilling and producing the reservoir from a remote location

Obviously, most of these papers concentrate on operational aspects and drilling efficiencies of these types of wells. There are little, if not any, publications about the environmental benefits of extended reach wells, especially drill cuttings waste minimization. Therefore, this paper tries to compare the amount of cuttings generated per well for each ERD well project and a conventional well. The paper also tries to demonstrate how much cuttings can be generated per drilling and oil and gas well. How an ERD project minimizes the amount of environmental damage by decreasing drilling waste generation. How these amounts of cuttings are calculated, and what are the parameters involved in drilling waste calculations. What are the factors that control the amount of waste generation?

Furthermore, this article is shedding light on one of the most important applications of extended reach drilling, which it is the amount of cuttings generated while drilling a specific well. With the rise of the environmental protection movement, the petroleum industry has placed greater emphasis on minimizing the environmental impact of its operations [17]. Both Governments and International oil companies are always trying to develop drilling techniques that best serve the environment and, at the same time, cost-effective.

2. Cuttings Amount Determination

A typical well can generate several barrels of fluid and cuttings per foot of hole drilled. In 1992, the number of hole feet drilled was 115,903,000 in the USA. If we consider an average hole size of 12 ¼ hole size with zero access and zero porosity, this will give an amount of 16,895,953 bbl of cutting generation per year in USA [17]. This is a huge amount of cuttings

to be treated and environmentally disposed. Therefore, the basic mathematics of cuttings amount calculation requires a straightforward equation that is simple, easy to understand, and use. Normally these kinds of calculations are performed while planning oil and gas wells to estimate the open hole size, amount of cement plug needed to cement a portion of open hole, hole volume for drilling fluids, well-killing operation in case of a well kick and amount of cuttings that will be generated while drilling of each open hole section. In order to determine the amount of cuttings generated while drilling oil and gas wells, the following equations are used.

$$V_c(bbl) = \left[\frac{(D_h)^2}{1029.4} \right] \cdot L \tag{1}$$

$$V_c(bbl) = \left[\frac{(D_h)^2}{1029.4} \right] L (1 - \emptyset) \tag{2}$$

Another factor to be considered while calculating the amount of cuttings generation is the access size of the open hole. While drilling oil and gas wells the size of the hole is over-gauged in most of the cases by an amount that can be estimated either by experience while drilling the same section in the area or by using wire line method technology called caliper log. For the sake of simplicity, in this paper, an average amount of 15% is added to actual hole size. The equation for calculating amount of cutting will have another parameter.

$$V_c(bbl) = 1.15 \left[\frac{(D_h)^2}{1029.4} \right] L (1 - \emptyset) \tag{3}$$

where: V_c is volume of cuttings in bbl; D_h is diameter of the hole, normally drilling bit size in inches; L is length of section drilled in feet; \emptyset is porosity of the rocks drilled; 1.15 is 15% extra hole size added to the original hole size.

First, for the sake of simplicity, the amount of porosity will not be integrated to the equation, but later correct values of porosity will be used to have better results. The amount of cuttings generation will be calculated for each section of the hole drilled.

3. Field study data

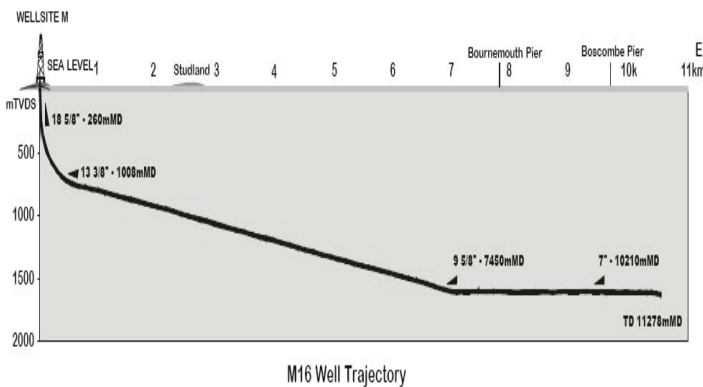


Figure 1. Actual Trajectory of 11-km ERD Well at Wytch Farm [18]

Two wells are used to do the comparative study in order to differentiate between the amount of rock cuttings generated in ERD and conventional drilling. The first well (M-16 well) is one of the most common well profile for an ERD project used for Wytch Farm which once it was a world record for longest ERD well. In order to calculate the amount of waste generated in ERD and actual well profile (Figure 1) of Wytch Farm M-20 was used for better demonstration. The second well is

selected from Iraq. It is a conventional well which is drilled in the northern Iraq. The well scheme is shown in Figure 2. Details of both wells are presented in Tables 1 and 2.

Table 1. Actual Well scheme of 11-km ERD Well at Wytch Farm [18]

Depth, ft	Hole Size, in	Casing Size, in
0 – 853	24	18 5/8
853 – 3307	16	13 3/8
3307 – 15585	12 1/4	9 5/8
15585 – 37003	8 1/2	7

Table 2. Actual well scheme of conventional well

Depth, ft	Hole Size, in	Casing Size, in
0 – 100	30 Conductor mostly hammered	
100 – 2625	26	20
2625 – 7218	17 1/2	13 3/8
7218 – 9843	12 1/4	9 5/8
9843 – 11484	8 1/2	7

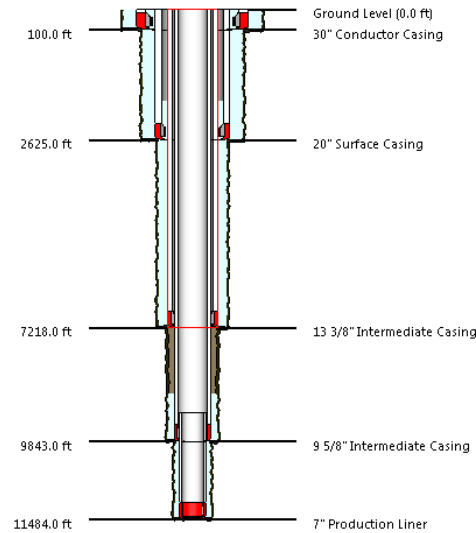


Figure 2. A typical well scheme for a conventional well

4. Amount of cuttings generated in the ERD well and the conventional well

The amount of cuttings for the M-16 ERD well and the conventional well is determined and appeared in Tables 3 through 4 and Figures 3 through 4.

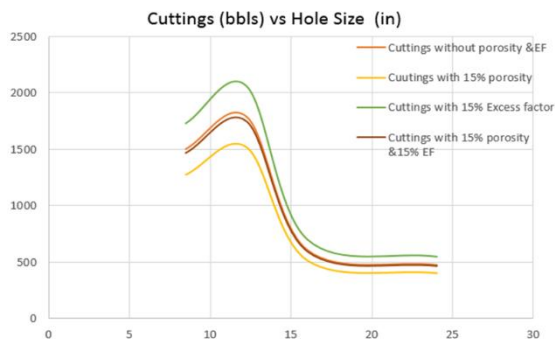


Figure 3. Amount cuttings generated in M-16 ERD well

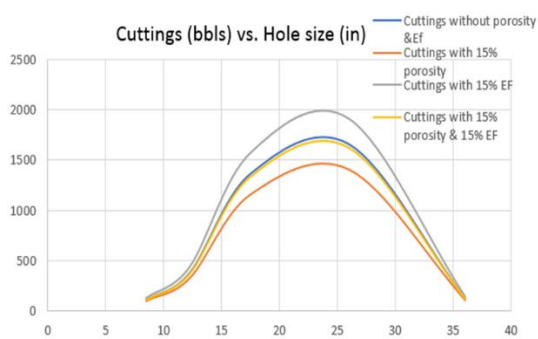


Figure 4. Amount cuttings generated in conventional well

The porosity and the excess factor are taken 15 % as a good indication for good porosity and washouts. It is found that the amount of cuttings generated for the ERD well and the conventional well are 4381, and 3648 bbls, respectively. This means the amount of waste which damages the environment for ERD is more than that of conventional drilling. However, the calculated amount of cuttings generated is not accurate; it needs some details to be considered, like the porosity of the rocks and hole washouts. Since the underground rocks are porous and not solid rocks only. This means that the fraction of rocks which it is hallow should be estimated and integrated to the equation to have a more precise amount of cuttings calculations. Therefore, the calculations are repeated including 15% for porosity, and excess factor. It is clear that the resulted values will be lower than that calculated without porosity and higher than that calculated without excess factor. The total amount of cuttings generated while drilling the ERD well and the conventional well are 5038, and 4196 bbls respectively with including only 15% excess factor and these amounts are higher than that of determined including 15% porosity, 15% porosity and 15% excess factor, or without both of them (Tables 3&4). For M-16 ERD well, the bigger amount of cuttings appeared during drilling 12.25" hole section while it appeared in the conventional well during drilling 17.5" hole section. Due to

long hole in deeper sections, the total amount of cuttings generated during drilling these sections is bigger although they have small diameters (Figures 3&4).

Table 3. Calculations of cuttings amount generated in M-16 ERD well

Depth, ft	Hole size, in	Casing size, in	Volume of cuttings, bbl	Volume of cuttings with 15% EF, bbl	Volume of cuttings with 15% porosity, bbl	Volume of cuttings with 15% porosity & 15% EF, bbl
0 - 853	24	18 5/8	477.295512	548.8898	405.7012	466.5564
853 - 3307	16	13 3/8	610.281718	701.824	518.7395	596.5504
3307 - 15585	12 1/4	9 5/8	1789.84591	2058.323	1521.369	1749.574
15585 - 37003	8 1/2	7	1503.25481	1728.743	1277.767	1469.432
		Total	4380.67794	5037.78	3723.576	4282.113

Table 4. Calculations of cuttings generated in a conventional well

Depth, ft	Hole size, in	Casing size, in	Volume of cuttings bbl	Volume of cuttings with 15% EF, bbl	Volume of cuttings with 15% porosity, bbl	Volume of cuttings with 15% porosity & 15% EF, bbl
0 - 100	36	30	125.898582	144.7834	107.013794	123.0659
100 - 2625	26	20	1658.15038	1906.873	1409.42782	1620.842
2625 - 7218	17 1/2	13 3/8	1366.43312	1571.398	1161.46815	1335.688
7218 - 9843	12 1/4	9 5/8	382.663748	440.0633	325.264186	374.0538
9843 - 11484	8 1/2	7	115.176073	132.4525	97.8996624	112.5846
		Total	3648.3219	4195.57	3101.07361	3566.235

5. How ERD well reduces cuttings amount?

The above values are based on comparing one ERD well with a conventional well only. However, drilling one extended reach well might eliminate drilling several wells to penetrate the same reservoir vertically Figure 5.

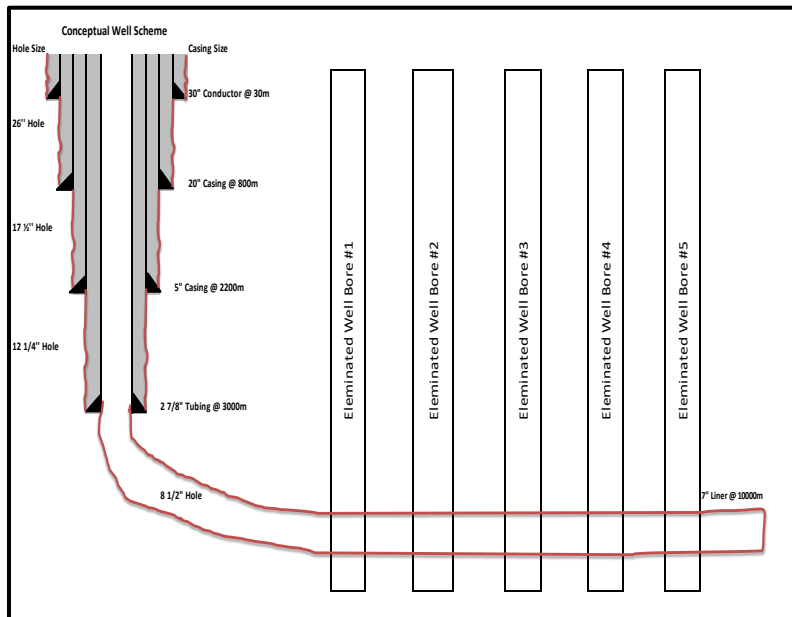


Figure 5. Conceptual Well Scheme for an ERD Project

Because the ERD well penetrates through the reservoir section horizontally for very long distances, thus drilling of several vertical wells to penetrate the reservoir section will not be

needed. EDR wells might generate more drilling cuttings than conventional wells if it is compared with a single well. However, in reality, if it is compared on field level, they generate much less drilled cuttings than a conventional well. This is due to the fact that to penetrate a specific reservoir at any targeted depth. Figure 5 tries to demonstrate how an ERD project in a specific field decreases the amount of drilled cuttings. Clearly, one ERD well will penetrate the same reservoir with 5 targets that can be drilled with 5 conventional wells. Additionally, the actual well trajectory shown in Figure 4 proves the same concept. Therefore, one ERD well saves the environment at least from 70% of the drilling cuttings generated from the 5 vertical wells passing through 5 targets: NRQ 255 6H-1, NRQ 255 6H-2, NRQ 255 6H-3, NRQ 255 6H-4, and NRQ 255 6H-5.

The drilling ERD well on field level will reduce the amount of wells needed to penetrate the same reservoirs in the field vertically by drilling multiple wells. This proves that the amount of cuttings that can be generated in the field by drilling ERD wells is much more less than the amount of cuttings that will be generated by drilling multiple vertical wells.

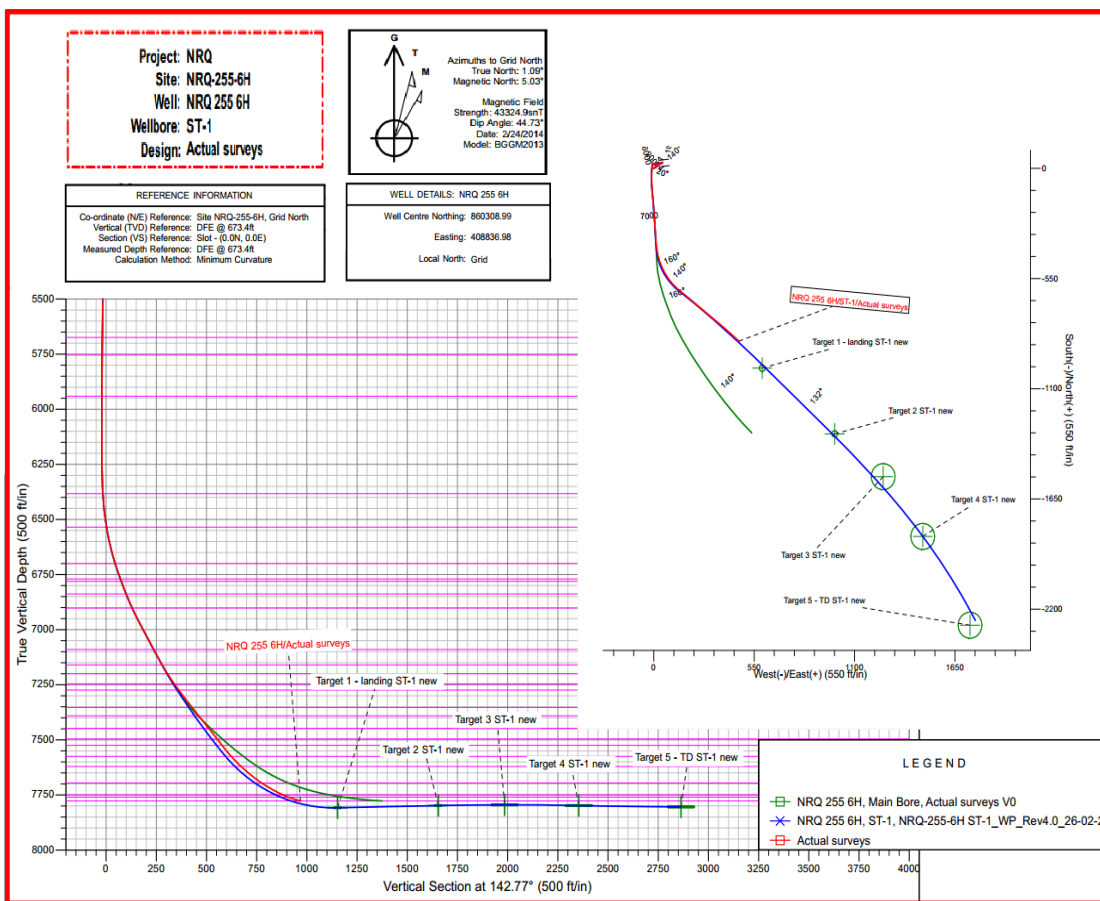


Figure 6. Actual horizontal well trajectory- the planned versus the reality [10]

6. Factors affect the actual hole size and amount of cuttings generation

There are several factors that control the actual hole size drilled, that is why, after drilling each hole size, a special logging tool called caliper logging is run down the hole so as to measure the actual hole size. The amount of cuttings generated per each section of the well depends on these factors. The factors are listed below:

- Type of drilling fluid which it is used to drill the well, normally synthetic drilling fluids system give a gauged hole, thus it produces less amount of cuttings. Meanwhile water based drilling fluid systems give bigger size of hole and more cuttings generation.

- Drilling bit gauge, if the drill bit is under gauge the hole size will be smaller, thus produces less cuttings
- Type of rocks and geological formation drilled, if the rocks are sloughing shale the hole size will become bigger and the number of cuttings generated will be more. Meanwhile if the geological formations are solid dolomite or limestone the hole size will be same as drilling bit.

7. Conclusion and results insights

The amount of waste generated per well is different from one well to another, there are many factors involved in waste generation percentage. Both ERD well drilling technique and conventional drilling was compared to prove that drilling ERD wells have an environmental advantage over conventional drilling in terms of drilling cuttings generation amount. Using ERD well might decrease the need for drilling several wells to access a targeted reservoir. It means that it eliminates need of drilling several wells Figures 5&6, which in turn decreases the need to drilling the very top hole sections several times. Normally drilling top hole section generates more drill cuttings, this is due to the fact that surface holes are bigger in size.

References

- [1] Azar JJ, Samuel RG. Drilling Engineering, PennWell Corporation 2007, ISBN-13: 978-15937 00720.
- [2] Mitchell BJ. Advanced Oil Well Drilling Engineering Handbook and Computer Programs, USA Library of Congress, 1974 to Mitchell Engineering, 10th edition, 1st revision, July 1995.
- [3] Bourgoyne AT, Millheim KK, Chenevert ME, Young FS. Applied Drilling Engineering. SPE text series, Volume II, 1991
- [4] Hossain ME, Al-Majed AA. Fundamentals of Sustainable Drilling Engineering., Scrivener Publishing LLC., Wiley, Canada, 2015.
- [5] Adams NJ, Charrier T. Drilling Engineering: A Complete Well Planning Approach, PennWell Publishing Company 1985, ISBN-10: 0878142657.
- [6] Rabia H. Well Engineering and Constructions. Entrac Consulting 2002, ISBN: 0954108701.
- [7] Mitchell RF, Miska SZ. Fundamentals of Drilling Engineering. SPE Textbook Series No. 12, ISBN: 978-1-55563-207-6.
- [8] Rădăcină D, Halafawi M, Avram L. Casing Wear Prediction In Horizontal Wells. Petroleum and Coal Journal, 2020; 62(2): 395-405.
- [9] Tahair M, Halafawi M, Wiercigroch M, Avram L. Optimum Well Trajectory Design Based on Numerical Optimization Method PSO Algorithm and Wellbore Stability. Petroleum and Coal Journal, 2020; 62(1): 114-128.
- [10] Halafawi M, Avram L. Wellbore Trajectory Optimization For Horizontal Wells: The Plan Versus The Reality. Journal Oil Gas Petrochem Science, 2019; 2(1):49-54.
- [11] Halafawi M, Avram L. Trajectory Optimization for Drilling Long Horizontal Wells. The International Scientific Conference dedicated to oil and gas researches entitled "The Exploration and Exploitation oil and gas reservoir: present and perspectives" published by Petroleum-Gas University of Ploiesti Bulletin, Technical Series, 71 (1): 72-79, 2019.
- [12] Mason D, Hey O, Kramer H. Extended Reach Well Completion and Operational Considerations. OTC8569, Offshore Technology Conference, 5-8 May, Houston, Texas, 1997.
- [13] Scott PW, Lintern GA, Embury JE. Drilling Extended-Reach Wells, Northwest Shelf, Australia. SPE23014, SPE Asia-Pacific Conference, 4-7 November, Perth. Australia, 199.
- [14] Aadnoy B. Technology Focus: Multilateral/ Extended-Reach Wells. Journal of Petroleum Technology, SPE-0515-0114-JPT, 67(5), 2015.
- [15] Ma S, Huang G, Zhang J, Han Z. Study on Design of Extended Reach Well Trajectory. SPE50900, SPE International Oil and Gas Conference and Exhibition in China, 2-6 November, Beijing, China, 1998.
- [16] Guild GJ, Wallace IM, Wassenborg MJ. Hole Cleaning Program for Extended Reach Wells. SPE29381, SPE/IADC Drilling Conference, 28 February-2 March, Amsterdam, Netherlands, 1995.
- [17] Reis JC. Environmental control in Petroleum Engineering. PennWell Publishing Company, Houston, Texas, USA, 1996.
- [18] Meader T, Allen F, Riley G. To the Limit and Beyond - The Secret of World-Class Extended-Reach Drilling Performance at Wytch Farm. SPE59204, IADC/SPE Drilling Conference, 23-25 February, New Orleans, Louisiana, 2000

- [19] Hyne NJ. Nontechnical Guide to Petroleum Geology, Exploration, Drilling and Production (2nd edition). PennWell Corporation Tulsa, OK, USA, 2001.
- [20] Mims M & Krepp T. Drilling Design and Implementation for Extended Reach and Complex Wells – Third Edition. K&M Technologies Group, LLC.USA, 2007.
- [21] Moore PL. Drilling Practices Manual. Second Edition. PennWell Publishing Company, Tulsa, Oklahoma USA, 1986.

To whom correspondence should be addressed: Mohamed Halafawi, Petroleum-Gas University of Ploiesti, Romania, E-mail: halafawi@upg-ploiesti.ro

Analysis of Factor Effects and Interactions in a Conventional Drilling Operation by Response Surface Methodology and Historical Data Design

Wilson Fidelis Ekpotu¹, Joshua O. Ighalo^{2*}, King-akanimo Bassey Nkundu³, Precious Ogwo Onu⁴, Adewale George Adeniyi²

¹ Power and Energy Oil Tools Ltd, Port Harcourt, Nigeria

² Department of Chemical Engineering, Nnamdi Azikiwe University, P. M. B. 5025, Awka, Nigeria

³ Ministry of Petroleum Resources, Calabar, Nigeria

⁴ Department of Chemical and Petroleum Engineering, University of Uyo, Uyo, Nigeria

Received June 18, 2020; Accepted September 30, 2020

Abstract

A smooth drilling process can achieve safe and fast well establishment and better investment efficiency. Response surface methodology (RSM) on Design Expert 10.0.1 (Stat Ease Inc., Minneapolis, USA) was utilised for the factor effects and interactions in a conventional drilling operation. The aim of this study was to utilise RSM and historical data design (HDD) was used to model the effect of weight on bit (WOB), hook load and revolutions per minute (RPM) on the rate of penetration (ROP), pressure and torque of drilling. Statistical validation of the data was conducted using Analysis of Variance (ANOVA) Partial sum of squares - Type III. The models for all three responses were statistically significant (at a significance level of $p < 0.05$). At low RPM (80 – 81 Hz) and an intermediate hook load (235 – 240 lb), ROP was observed to be high. It was observed that the torque is optimal anywhere above a hook load of 235 lb. The pressure was highest at high RPM (83 – 85 Hz) and low WOB (8 – 12 lb). From this study, the effects of process factors on drilling parameters have been successfully modelled and investigated.

Keywords: Drilling; Historical data design; Factors; Response surface methodology.

1. Introduction

Drilling activities are some of the most essential processes of oil and gas operations [1]. Ranging from Seismic activities to geological and geophysical survey and then exploration activities, the value chain towards the production of crude oil or natural gas from both conventional and unconventional reservoirs cannot be completed without actively having the drilling phase [2]. In this regards, it is therefore pertinent to know that drilling activities have several factors that affect its effectiveness and efficiency. And therefore a clear understanding of the effects of these numerous parameters on drilling operations will help in ascertaining the planning of the entire drilling programme as the case may be [3].

Egbe and Iturrios [4] stated that the continuous demand for hydrocarbons for multiple purposes has led to the necessity of exploring new ways to develop new or existing oil field to keep up with the ever-increasing demand. However, such a strategy comes with its challenges, like formation pressure heterogeneity and rapid change in formation pressure within the same hole section. Accordingly, Abd Rahman [5] emphasized that managed pressure drilling utilizes an underbalanced mud density which when combined with the annular surface pressure, maintains the overbalance condition at all times with a target bottom hole pressure close to the formation pressure.

Han, Sun [6] observed that drilling is one of the most important aspects of resource development. A smooth drilling process can achieve safe and fast well establishment and better investment efficiency [7]. And an accurate rate of penetration (ROP) estimation can benefit the well planning and prevent unexpected drilling accidents [8]. Many parameters influence

the instantaneous ROP, including formation properties, mud rheology, drill bits, and bit/rock interactions. String vibrations, deformations, and bit fatigue can also affect the rate of bit penetration [9].

Therefore, factors such as the rate of penetration (ROP), revolutions per minute (RPM) of the bit, weight on bit (WOB), hook load, pressure and torque are generally critical to ensuring that drilling operations are carried out with standard international drilling practices.

These variables play a very critical role in ensuring that drilling rate is being improved and can also be a major factor in impeding the ultimate progress of drilling operations if it leads to adverse effects such as wellbore caving in, and an indefinite downhole problem that will trigger more drilling cost and increase downtime which could have been averted [10]. It is worthy of note that these drilling parameters enlisted can be adjusted and recalibrated to suit the formation being drilled offshore or onshore, thus reducing drilling difficulties at different zones and scenarios [11].

The weight on bit (WOB) is the difference of weight force of the part of the drill string below the neutral point and the buoyancy force of drilling mud [12]. Increasing WOB can enhance the rate of drill bit penetration. Nevertheless, increasing WOB may lead to buckling of the drill string. Buckling causes permanent contact of a drill string with the borehole wall and leads to corrosion and failure in both of them [12]. In 1974, Bourgoyne and Young developed a multi regression model to estimate ROP [13]. Weight on bit, rotary speed, bit wear, bit size, hydraulics Formation depth, strength, and over/under balance conditions were used for rate of penetration calculation. Rock/bit interactions, bit properties, fluid properties were also considered in their model [6].

For developing advanced real-time analysis, rate of penetration (ROP) prediction is always one the most key aspects among drilling engineers, because it makes the possibility to optimize drilling parameters to achieve the minimum cost per foot [14]. Moraveji and Naderi [15] emphasized that the prediction and optimization of the penetration rate will be crucial to be able to reduce the cost of drilling operations. However, Cheatham and Nahm [16] specified that overall drilling costs can be reduced in slow drilling formations by increasing ROP. Therefore, this states the role and effect of ROP and specific other drilling parameters in drilling operations.

Generally, according to Jahanbakhshi, Keshavarzi [14], in many studies, factors affecting the ROP have been grouped as follows:

- a) Formation characteristics (e.g. hardness and/or abrasiveness (drillability), underground formations stress, pore pressure, porosity and permeability)
- b) Mechanical factors (e.g. weight on bit, bit type and rotary speed)
- c) Hydraulic factor (e.g. bit hydraulic power, pump pressure, bottom- hole cleaning)
- d) Drilling fluid properties (e.g. mud weight, viscosity, filtrate loss, solid content, yield point, gel strength, mud pH)
- e) Drilling operation (e.g. hole size, equivalent circulating density)

A combination of the above-mentioned factors influencing ROP while some of them are controllable but the others are uncontrollable. Formation as nearly an independent or uncontrollable variable is influenced to a certain extent by hydrostatic pressure. Laboratory experiments indicate that in some formations any increase in hydrostatic pressure cause to increase the formation hardness or reduces its drillability. The bit type selected, i.e., whether a drag bit, diamond bit, or roller cutter bit can somewhat affect the ROP obtainable in a given formation. Also, the mechanical factors of weight on the bit and rotary speed are then linearly related to ROP.

Within the scope of the authors' exhaustive search, Historical Data Design (HDD) on Response Surface Methodology (RSM) have not been employed in factor analysis for drilling operations. To further emphasize on the novelty of this work, Response Surface Methodology has not been used for the analysis of a conventional oil field drilling data such as weight on bit (WOB), hook load, rate of penetration (ROP), revolutions per minute (RPM), pressure and torque. Hence, this work seeks to analyse the factor effects and interactions in a conventional field drilling operation by Response Surface Methodology (RSM) and Historical Data Design (HDD).

2. Materials and methods

2.1. Method

Response surface methodology (RSM) is a group of statistical technique used for modelling and optimisation [17-18]. It can also be used for investigating factor effects and interactions on a process system [19]. In this study, RSM on Design Expert 10.0.1 (Stat Ease Inc., Minneapolis, USA) was utilised for the factor effects and interactions in a conventional drilling operation. The used in the study was on the mechanical parameters for the drilling operation of a conventional oil well. The key factors were WOB, hook load and RPM while the responses were ROP, pressure and torque. There were 999 lines of data for the analysis.

2.2. Data analysis

RSM was used to investigate the effect and interactions between WOB, hook load and RPM on the ROP, pressure and torque in a drilling operation. In this regard, the total force pulling down on the hook that includes the weight of the drill string in air, the drill collars and any ancillary equipment is referred to as the hook load. Similarly, the ROP is the speed at which the drill bit can break the rock under it and thus deepen the wellbore. However, the data analysis was inputted into Design Expert 10.0.1 (Stat Ease Inc., Minneapolis, USA) using the Historical Data Design (HDD). HDD allows the flexibility of specifying the number of factors, number of responses and the number of data lines. It is especially suitable for the analysis of a historical dataset in which these variables are already available and are outside the control of the researcher. Historical data design has been previously utilized for the optimization of biodiesel production [20], machining condition [21], solvent extraction [22], photo-catalysis [23], etc. Statistical validation of the data was conducted using Analysis of Variance (ANOVA) partial sum of squares - type III. The effects and interactions were visualised using both contour plots and surface plots. The variables used in the study is summarised in Table 1.

Table 1. Designation of factors and responses for the study

Designation	Data (x)	Unit	Data band
Factor 1	Revolutions per minute (RPM)	Hz	80 < x < 85
Factor 2	Weight on bit (WOB)	Lb	8 < x < 25
Factor 3	Hook load	Lb	225 < x < 245
Response 1	Rate of Penetration (ROP)	Ft/min	-
Response 2	Torque	Nm	-
Response 3	Pressure	Psi	-

3. Results and discussion

3.1. Statistical validation of the response surface model

Analysis of variance (ANOVA) partial sum of squares - type III was used to validate the research data. The ANOVA tables are shown in the Appendix. From the results, it was observed that all three response surface models were statistically significant (at a significance level of $p < 0.05$). Furthermore, the best fit model for ROP was the response surface sixth model. Response surface fifth model was the best fit for torque while the quartic model was the best fit for pressure. The lack-of-fit was also not significant for all three models which further reinforces the accuracy and suitability of the modelling study. The values on the y-axis of in the response plots for investigating the effects and interactions must be ignored as they are not actually the exact values because the model is a non-hierarchical polynomial regression model (and it excludes hierarchically inferior terms). The plots are chosen in such a way that all factors are discussed and all key factor interactions are highlighted.

3.2. Factor effects and interactions on ROP

In most of the studies, the rate of penetration (ROP) has been considered as the objective function of the optimization process. ROP depends on many factors including well depth, formation characteristics, mud properties, the rotational speed of the drill string, etc. [24]. Zhao,

Noorbakhsh 24 stated that several studies have been conducted to gain a profound insight into the effective parameters on ROP. ROP is affected by several parameters, which can be categorized into controllable and uncontrollable parameters [25].

For developing advanced real-time analysis, rate of penetration (ROP) prediction is always one of the most key aspects among drilling engineers, because it makes the possibility to optimize drilling parameters to achieve the minimum cost per foot. Besides, ROP models can be used to estimate formation drillability by considering the effects of drilling parameters, bits design and bit wear [14]. The effect of WOB and RPM on ROP is shown in Figure 1. It can be observed that when WOB and RPM are low, this results in a low ROP. Similarly, when WOB and RPM are high, a low ROP is also observed. The Weight on Bit (WOB) and Revolutions Per Minute (RPM) are direct factors that can affect the Rate of Penetration (ROP) in a conventional and an unconventional drilling formation because they improve the optimal functionalities of the drill bit that therefore improves the rate at which penetration occurs through the formation. The region of optimality lies adjacent to these two earlier described regions and shown by the red areas on the surface in Figure 1. ROP was observed to the optimum at low RPM (80 – 81 Hz) and high WOB (20 – 25 lb) and high RPM (83 – 85 Hz) and low WOB (8 – 14 lb).

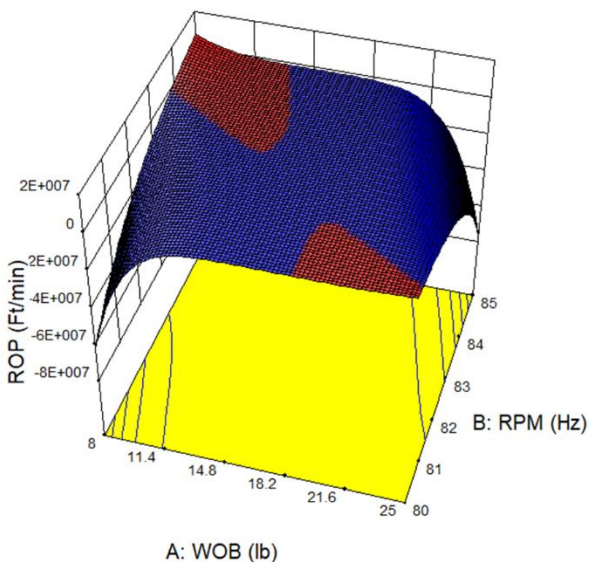


Figure 1. Effect of WOB and RPM on ROP

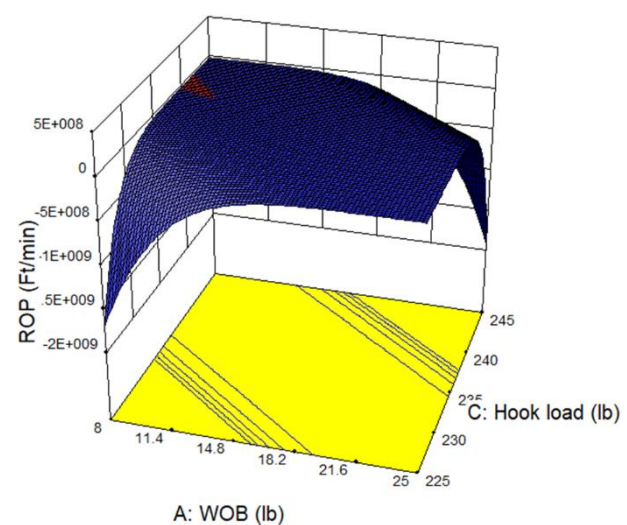


Figure 2. Effect of WOB and hook load on ROP

The RPM and WOB are consistent factors that have seemingly interchangeable effects but same results and as thus they vary are different sections of the formation geometry and specific formation points for this conventional reservoir formation dataset allowed for optimum ROP once one of the active parameters peaked individually, and hence accounting for an optimum ROP at a high WOB and a low RPM and thereafter still optimal at a high RPM and a low WOB. Alum and Egbon [26] stipulated that ROP is mostly obtained real-time and it is often difficult to predict. This is because the factors controlling ROP are numerous and dependent on so many others, also some factors are not complementary (rather they are complex and non-linear) meaning an increase in one may lead to a decrease in the other, the overall effect then reflecting in ROP.

The effect of WOB and hook load on ROP is shown in Figure 2. It can be observed that when WOB and hook load is low, this results in a low ROP. Similarly, when WOB and hook load is high, a low ROP is also observed. The effectiveness of the Rate of Penetration (ROP) is also critically hinged on the Weight of Bit and the hook load as the weight on bit acts as a vertically aligning force that conveys the bit in enabling a penetration increase through the different layers of the formation. Consequently, if the WOB and Hook load are both low, the ROP will gradually decline while also being cushioned by the other parameters. Hence an increased bit

weight can stimulate a maximum penetration rate. The ROP was observed to be optimum at an intermediate hook load (235 – 240 lb) but low WOB (8 – 10 lb).

The effect of RPM and hook load on ROP is shown in Figure 3. The optimal regions can be observed by the red areas on the response surface. At low RPM (80 – 81 Hz) and an intermediate hook load (235 – 240 lb), ROP was observed to be high. The result shows that at a practical intermediate hook load level of between (235 – 240 lb), the ROP (Rate of Penetration) was increased even with the RPM being low, and this is because the variability and non-linear nature of the data set accounts for only an increased ROP when the hook load (a mechanical property) was at an intermediate position at a specific formation interval that generated a low RPM. Furthermore, at high RPM (83 – 85 Hz) and an intermediate hook load (230 – 235 lb), ROP was observed to be high. Alum and Egbon [26], factors controlling ROP (including hook load and RPM) are dependent and are not complementary (rather they are complex and non-linear), and this accounts for the switch between the high and low nature of the RPM and the hook load and their responses on the ROP.

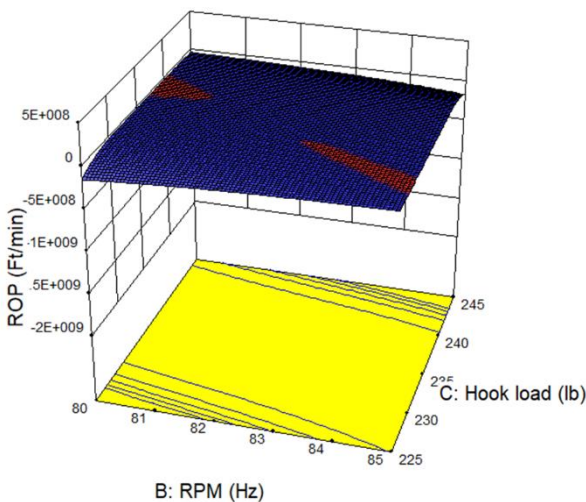


Figure 3. Effect of RPM and hook load on ROP

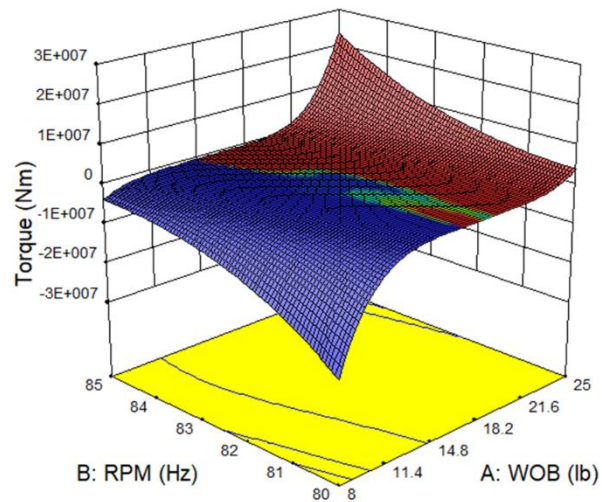


Figure 4. Effect of WOB and RPM on Torque

3.3. Factor effects and interactions on torque

Drilling Torque is a measure of the cumulative force that can directly cause the drill bit to rotate vertically into the formation axis and could also engage angular acceleration as in the case of directional drilling in certain fields. The effect of WOB and RPM on torque is shown in Figure 4. It can be observed that the torque increases with increasing WOB and this is because torque uniquely refers to the rotational equivalent of linear force, which in this case is the twist of the drill bit around a particular formation axis and as such when the WOB and RPM increases the torque also increases proportionally. A synergistic effect of WOB and RPM is observed as the torque becomes quite high at high values of each of the parameters. Torque was optimal anywhere above WOB of 15 lb and was maximum at the highest values of both factors. Schamp, Estes [27] emphasized that the torque required to rotate generally arises from two sources: the frictional resistance between the rotating drill string and the casing or bore-hole and the bit/stabilizer torque. Hence, the frictional resistance between the rotating drill string is a direct reflection of the RPM which is inter-dependent on the WOB.

An increase in Weight-on-bit (WOB) may increase ROP for some time but may lead in faster Bit wear and dulling, which will then reduce ROP in the long run, hence making optimization difficult [26]. The effect of WOB and hook load on torque is shown in Figure 5. A synergistic effect of both factors can be observed as increasing values of both factors increased the torque. Minimal torque was achieved at the least values of WOB and hook load while maximum torque was observed at the highest values of both factors. Therefore, a direct and proportional increase in the Weight-on-bit and the hook load ensures an increase in the drilling torque for the given hole section.

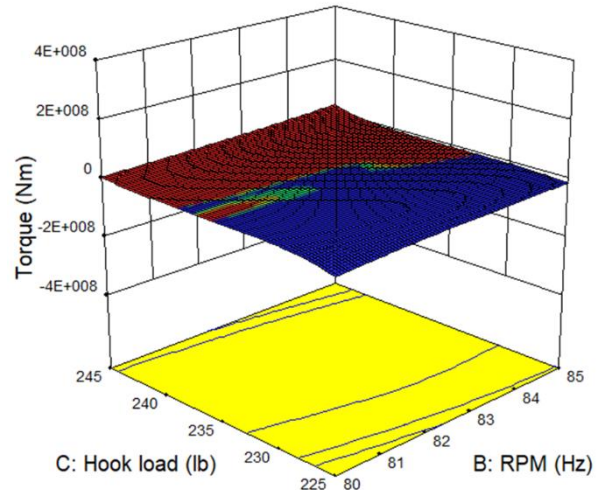
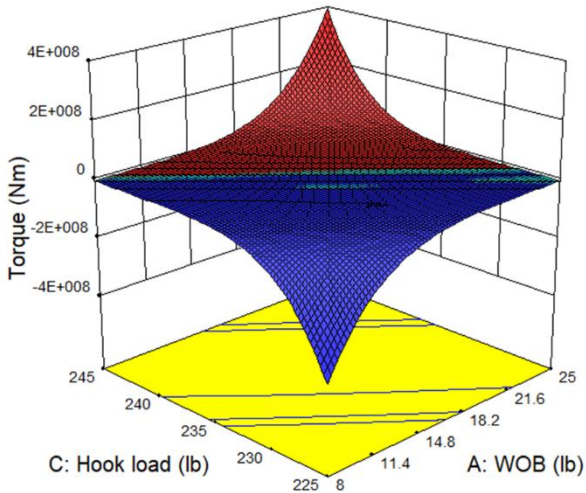


Figure 5. Effect of WOB and hook load on Torque Figure 6. Effect of RPM and hook load on Torque

The effect of WOB and hook load on torque is shown in Figure 6. It can be observed that the torque is optimal anywhere above a hook load of 235 lb. In line with this, optimal drilling torque can only be achieved at an accelerated hook load resident at above 235 lb and beyond given the pre-defined reservoir data set, because the two variables are simply reliant on the forward nature of the other. In this domain, RPM had a minimal interactive effect with WOB as it affects the torque.

3.4. Factor effects and interactions on pressure

Affirmatively, van Riet, Reitsma [28] stated that accurate control over bottom hole pressure during drilling is essential as the industry operates in an increasingly challenging drilling environment. Similarly, in conventional drilling, the downhole pressure is composed of the following two main components:

1. The hydrostatic pressure of the mud column including cuttings (P_{stat}).
2. The hydrodynamic pressure in the annulus induced by various effects such as mud flow or drill pipe movement (P_{dyn}).

Therefore, uncertainties in pore pressure can also lead to an influx of unwanted reservoir fluids into the wellbore [4], and the WOB and RPM will not effectually have a direct impact on the pressure during drilling. The effect of WOB and RPM on pressure is shown in Figure 7. The pressure is observed to be low at high RPM and high WOB. The pressure was also low at low values of both factors. Pressure is a precise parameter in drilling operations and this comes in different forms, and one of those primary forms is the pressure ranging from pumping operations of the drilling fluids through the drill bit nozzles to the mud return rate towards the mud tanks through the annulus, hence WOB and RPM are implicit variables and hence even if pressure is low, the Response Surface methodology represents a non-effect of these parameters on pressure. The region of optimality was observed at the diagonal between these factors. Pressure was highest at high RPM (83 – 85 Hz) and low WOB (8 – 121 lb).

The effect of WOB and hook load on pressure is shown in Figure 8. Pressure is observed in this case to be low at high hook load and high WOB. Pressure was also low at low values of both factors. The critical variable here to be looked out for is the WOB which has an impact on the pressure in this case at both high and low levels as shown by Figure 8. The region of optimality was observed at the diagonal between these factors. These areas are where a factor was kept and the other kept low and vice versa.

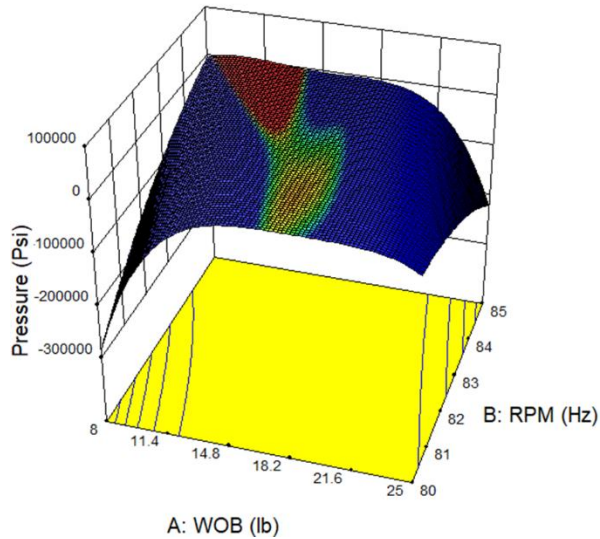


Figure 7. Effect of WOB and RPM on pressure

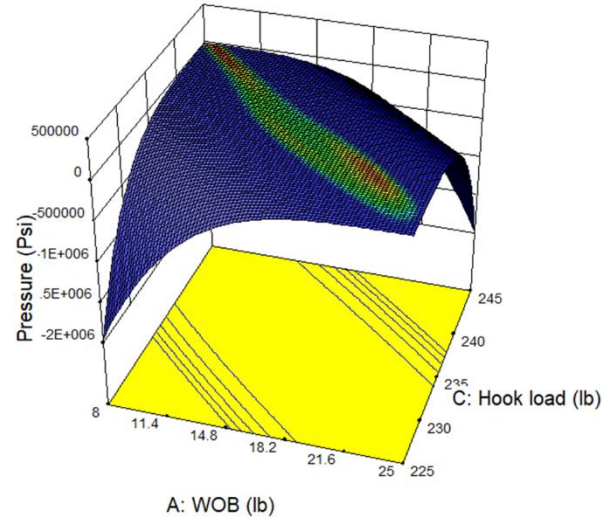


Figure 8. Effect of WOB and hook load on pressure

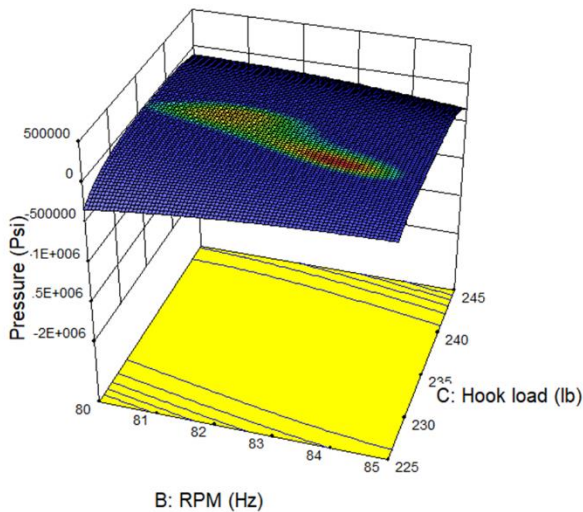


Figure 9. Effect of RPM and hook load on pressure

4. Conclusion

In this study, RSM was used to model the effect of weight on bit (WOB), hook load and revolutions per minute (RPM) on the rate of penetration (ROP), pressure and torque. The models for all three responses were statistically significant (at a significance level of $p < 0.05$). ROP was observed to the optimum at low RPM (80 – 81 Hz) and high WOB (20 – 25 lb) and high RPM (83 – 85 Hz) and low WOB (8 – 14 lb). At low RPM (80 – 81 Hz) and an intermediate hook load (235 – 240 lb), ROP was observed to be high. It was observed that the torque is optimal anywhere above a hook load of 235 lb. In line with this, optimal drilling torque can only be achieved at an accelerated hook load resident at above 235 lbs and beyond given the pre-defined reservoir data set, because the two variables are simply reliant on the forward nature of the other. The pressure was highest at high RPM (83 – 85 Hz) and low WOB (8 – 12 lb). From this study, the effects of process factors on drilling parameters have been successfully modelled and investigated.

Disclosure statement

Conflict of Interest: The authors declare that there are no conflicts of interest. Compliance with Ethical Standards: This article does not contain any studies involving human or animal subjects.

Apendix

ANOVA table for ROP

ANOVA for Response Surface Sixth model						
Analysis of variance table [Partial sum of squares - Type III]						
Source	Sum of Squares	df	Mean Square	F Value	p-value Prob > F	
Model	44147.86	83	531.90	1.92	< 0.0001	significant
A-WOB	402.62	1	402.62	1.46	0.2279	
B-RPM	34.41	1	34.41	0.12	0.7243	
C-Hook load	319.77	1	319.77	1.16	0.2825	
AB	20.68	1	20.68	0.075	0.7846	
AC	1.03	1	1.03	3.731E-003	0.9513	
BC	0.010	1	0.010	3.637E-005	0.9952	
A ²	2.90	1	2.90	0.010	0.9185	
B ²	380.53	1	380.53	1.38	0.2410	
C ²	0.21	1	0.21	7.634E-004	0.9780	
ABC	39.52	1	39.52	0.14	0.7055	
A ² B	47.77	1	47.77	0.17	0.6778	
A ² C	377.31	1	377.31	1.36	0.2430	
AB ²	18.01	1	18.01	0.065	0.7986	
AC ²	398.40	1	398.40	1.44	0.2303	
B ² C	1.96	1	1.96	7.087E-003	0.9329	
BC ²	32.27	1	32.27	0.12	0.7327	
A ³	369.79	1	369.79	1.34	0.2478	
B ³	5.62	1	5.62	0.020	0.8867	
C ³	429.01	1	429.01	1.55	0.2132	
A ² B ²	1.26	1	1.26	4.568E-003	0.9461	
A ² BC	51.80	1	51.80	0.19	0.6652	
A ² C ²	192.97	1	192.97	0.70	0.4037	
AB ² C	6.07	1	6.07	0.022	0.8822	
ABC ²	109.47	1	109.47	0.40	0.5294	
B ² C ²	25.92	1	25.92	0.094	0.7596	
A ³ B	17.72	1	17.72	0.064	0.8002	
A ³ C	163.48	1	163.48	0.59	0.4421	
AB ³	47.10	1	47.10	0.17	0.6799	
AC ³	210.20	1	210.20	0.76	0.3835	
B ³ C	16.00	1	16.00	0.058	0.8100	
BC ³	190.48	1	190.48	0.69	0.4067	
A ⁴	126.61	1	126.61	0.46	0.4988	
B ⁴	335.21	1	335.21	1.21	0.2711	
C ⁴	212.46	1	212.46	0.77	0.3809	
A ² B ² C	264.92	1	264.92	0.96	0.3279	
A ² BC ²	0.86	1	0.86	3.109E-003	0.9555	
AB ² C ²	105.83	1	105.83	0.38	0.5363	
A ³ B ²	463.08	1	463.08	1.67	0.1959	
A ³ BC	4.56	1	4.56	0.016	0.8979	
A ³ C ²	243.67	1	243.67	0.88	0.3481	

ANOVA for Response Surface Sixth model						
Analysis of variance table [Partial sum of squares - Type III]						
Source	Sum of Squares	df	Mean Square	F Value	p-value Prob > F	
Model	44147.86	83	531.90	1.92	< 0.0001	significant
A ² B ³	697.09	1	697.09	2.52	0.1127	
A ² C ³	253.50	1	253.50	0.92	0.3386	
AB ³ C	697.75	1	697.75	2.52	0.1125	
ABC ³	0.32	1	0.32	1.175E-003	0.9727	
B ³ C ²	662.54	1	662.54	2.40	0.1220	
B ² C ³	19.18	1	19.18	0.069	0.7923	
A ⁴ B	17.48	1	17.48	0.063	0.8015	
A ⁴ C	248.65	1	248.65	0.90	0.3432	
AB ⁴	542.51	1	542.51	1.96	0.1616	
AC ⁴	278.90	1	278.90	1.01	0.3155	
B ⁴ C	536.40	1	536.40	1.94	0.1640	
BC ⁴	0.97	1	0.97	3.498E-003	0.9528	
A ⁵	268.93	1	268.93	0.97	0.3243	
B ⁵	930.22	1	930.22	3.36	0.0669	
C ⁵	321.29	1	321.29	1.16	0.2813	
A ² B ² C ²	473.78	1	473.78	1.71	0.1909	
A ³ B ³	403.06	1	403.06	1.46	0.2276	
A ³ B ² C	417.34	1	417.34	1.51	0.2195	
A ³ BC ²	633.34	1	633.34	2.29	0.1305	
A ³ C ³	359.84	1	359.84	1.30	0.2542	
A ² B ³ C	404.02	1	404.02	1.46	0.2270	
A ² BC ³	644.44	1	644.44	2.33	0.1272	
AB ³ C ²	404.28	1	404.28	1.46	0.2269	
AB ² C ³	513.67	1	513.67	1.86	0.1732	
B ³ C ³	403.67	1	403.67	1.46	0.2272	
A ⁴ B ²	354.52	1	354.52	1.28	0.2578	
A ⁴ BC	606.91	1	606.91	2.20	0.1388	
A ⁴ C ²	312.01	1	312.01	1.13	0.2884	
A ² B ⁴	936.22	1	936.22	3.39	0.0661	
A ² C ⁴	410.50	1	410.50	1.48	0.2234	
AB ⁴ C	965.74	1	965.74	3.49	0.0620	
ABC ⁴	646.48	1	646.48	2.34	0.1266	
B ⁴ C ²	961.33	1	961.33	3.48	0.0625	
B ² C ⁴	528.68	1	528.68	1.91	0.1671	
A ⁵ B	561.52	1	561.52	2.03	0.1545	
A ⁵ C	266.91	1	266.91	0.97	0.3261	
AB ⁵	1218.89	1	1218.89	4.41	0.0360	
AC ⁵	463.31	1	463.31	1.68	0.1958	
B ⁵ C	1339.55	1	1339.55	4.84	0.0280	
BC ⁵	646.68	1	646.68	2.34	0.1265	
A ⁶	224.07	1	224.07	0.81	0.3682	
B ⁶	1310.48	1	1310.48	4.74	0.0297	
C ⁶	516.38	1	516.38	1.87	0.1721	

ANOVA for Response Surface Sixth model						
Analysis of variance table [Partial sum of squares - Type III]						
Source	Sum of Squares	df	Mean Square	F Value	p-value Prob > F	
Model	44147.86	83	531.90	1.92	< 0.0001	significant
Residual	2.533E+005	916	276.49			
Lack of Fit	2.530E+005	912	277.37	3.69	0.1031	
Pure Error	300.39	4	75.10			
Cor Total	2.974E+005	999				

ANOVA table for torque

ANOVA for Response Surface Fifth model						
Analysis of variance table [Partial sum of squares - Type III]						
Source	Sum of Squares	df	Mean Square	F Value	p-value Prob > F	
Model	9.156E+007	55	1.665E+006	300.16	< 0.0001	significant
A-WOB	4413.79	1	4413.79	0.80	0.3726	
B-RPM	2.288E+005	1	2.288E+005	41.26	< 0.0001	
C-Hook load	2717.04	1	2717.04	0.49	0.4841	
AB	6895.63	1	6895.63	1.24	0.2651	
AC	23263.34	1	23263.34	4.19	0.0408	
BC	3253.36	1	3253.36	0.59	0.4439	
A ²	15580.77	1	15580.77	2.81	0.0940	
B ²	45548.26	1	45548.26	8.21	0.0043	
C ²	29451.64	1	29451.64	5.31	0.0214	
ABC	11177.77	1	11177.77	2.02	0.1560	
A ² B	8162.82	1	8162.82	1.47	0.2254	
A ² C	43489.58	1	43489.58	7.84	0.0052	
AB ²	401.58	1	401.58	0.072	0.7879	
AC ²	42780.44	1	42780.44	7.71	0.0056	
B ² C	171.37	1	171.37	0.031	0.8605	
BC ²	15000.18	1	15000.18	2.70	0.1004	
A ³	41887.25	1	41887.25	7.55	0.0061	
B ³	12874.67	1	12874.67	2.32	0.1279	
C ³	39926.85	1	39926.85	7.20	0.0074	
A ² B ²	12217.17	1	12217.17	2.20	0.1381	
A ² BC	616.97	1	616.97	0.11	0.7388	
A ² C ²	9535.39	1	9535.39	1.72	0.1901	
AB ² C	13253.81	1	13253.81	2.39	0.1225	
ABC ²	143.68	1	143.68	0.026	0.8722	
B ² C ²	13914.36	1	13914.36	2.51	0.1135	
A ³ B	1610.34	1	1610.34	0.29	0.5901	
A ³ C	7833.75	1	7833.75	1.41	0.2349	
AB ³	26.58	1	26.58	4.792E-003	0.9448	
AC ³	11006.96	1	11006.96	1.98	0.1592	
B ³ C	1037.65	1	1037.65	0.19	0.6654	
BC ³	3.48	1	3.48	6.268E-004	0.9800	
A ⁴	5940.03	1	5940.03	1.07	0.3010	

ANOVA for Response Surface Fifth model						
Analysis of variance table [Partial sum of squares - Type III]						
Source	Sum of Squares	df	Mean Square	F Value	p-value Prob > F	
B ⁴	13807.79	1	13807.79	2.49	0.1149	
C ⁴	12145.10	1	12145.10	2.19	0.1393	
A ² B ² C	22557.69	1	22557.69	4.07	0.0440	
A ² BC ²	17171.73	1	17171.73	3.10	0.0788	
AB ² C ²	20625.16	1	20625.16	3.72	0.0541	
A ³ B ²	23809.92	1	23809.92	4.29	0.0385	
A ³ BC	19370.90	1	19370.90	3.49	0.0619	
A ³ C ²	28630.02	1	28630.02	5.16	0.0233	
A ² B ³	14309.31	1	14309.31	2.58	0.1085	
A ² C ³	29451.54	1	29451.54	5.31	0.0214	
AB ³ C	13588.14	1	13588.14	2.45	0.1179	
ABC ³	15073.13	1	15073.13	2.72	0.0996	
B ³ C ²	12228.13	1	12228.13	2.20	0.1379	
B ² C ³	18060.33	1	18060.33	3.26	0.0715	
A ⁴ B	21463.10	1	21463.10	3.87	0.0494	
A ⁴ C	28194.01	1	28194.01	5.08	0.0244	
AB ⁴	6295.47	1	6295.47	1.14	0.2870	
AC ⁴	30652.84	1	30652.84	5.53	0.0189	
B ⁴ C	3430.41	1	3430.41	0.62	0.4318	
BC ⁴	13273.46	1	13273.46	2.39	0.1222	
A ⁵	28073.01	1	28073.01	5.06	0.0247	
B ⁵	15095.47	1	15095.47	2.72	0.0993	
C ⁵	32121.86	1	32121.86	5.79	0.0163	
Residual	5.235E+006	944	5546.00			
Lack of Fit	5.235E+006	940	5569.60			
Pure Error	0.000	4	0.000			
Cor Total	9.679E+007	999				

ANOVA table for pressure

ANOVA for Response Surface Quartic model						
Analysis of variance table [Partial sum of squares - Type III]						
Source	Sum of Squares	df	Mean Square	F Value	p-value Prob > F	
Model	1.505E+006	34	44274.67	20.40	< 0.0001	significant
A-WOB	3099.83	1	3099.83	1.43	0.2323	
B-RPM	63314.97	1	63314.97	29.18	< 0.0001	
C-Hook load	2880.47	1	2880.47	1.33	0.2496	
AB	102.34	1	102.34	0.047	0.8281	
AC	3004.72	1	3004.72	1.38	0.2396	
BC	1522.91	1	1522.91	0.70	0.4024	
A ²	4400.99	1	4400.99	2.03	0.1547	
B ²	2014.91	1	2014.91	0.93	0.3355	
C ²	2384.03	1	2384.03	1.10	0.2948	
ABC	1153.03	1	1153.03	0.53	0.4662	

A^2B	3410.79	1	3410.79	1.57	0.2103
A^2C	8.92	1	8.92	4.111E-003	0.9489
AB^2	1087.38	1	1087.38	0.50	0.4792
AC^2	102.73	1	102.73	0.047	0.8278
B^2C	7.39	1	7.39	3.404E-003	0.9535
BC^2	224.93	1	224.93	0.10	0.7476
A^3	86.44	1	86.44	0.040	0.8418
B^3	39.22	1	39.22	0.018	0.8931
C^3	160.88	1	160.88	0.074	0.7855
A^2B^2	929.94	1	929.94	0.43	0.5129
A^2BC	1025.96	1	1025.96	0.47	0.4919
A^2C^2	1204.93	1	1204.93	0.56	0.4564
AB^2C	918.62	1	918.62	0.42	0.5154
ABC^2	830.57	1	830.57	0.38	0.5363
B^2C^2	1190.28	1	1190.28	0.55	0.4591
A^3B	1367.92	1	1367.92	0.63	0.4274
A^3C	1235.85	1	1235.85	0.57	0.4506
AB^3	180.06	1	180.06	0.083	0.7734
AC^3	1218.37	1	1218.37	0.56	0.4539
B^3C	336.05	1	336.05	0.15	0.6940
BC^3	667.62	1	667.62	0.31	0.5793
A^4	1367.27	1	1367.27	0.63	0.4275
B^4	17.94	1	17.94	8.265E-003	0.9276
C^4	1240.76	1	1240.76	0.57	0.4497
Residual	2.094E+006	965	2170.04		
Lack of Fit	2.094E+006	961	2179.07		
Pure Error	0.000	4	0.000		
Cor Total	3.599E+006	999			

References

1. Chima CM. Supply-chain management issues in the oil and gas industry. *Journal of Business & Economics Research (JBER)*. 2007; 5.
2. Maxwell S. *Microseismic imaging of hydraulic fracturing: Improved engineering of unconventional shale reservoirs*. SEG Books, 2014.
3. Eren T and Ozbayoglu ME. Real time optimization of drilling parameters during drilling operations. SPE Oil and Gas India conference and exhibition. Society of Petroleum Engineers, 2010.
4. Egbe P and Iturrios C. Mitigating Drilling Hazards in a High Differential Pressure Well Using Managed Pressure Drilling and Cementing Techniques. International Petroleum Technology Conference. Dhahran, Kingdom of Saudi Arabia: International Petroleum Technology Conference, 2020, p. 13.
5. Abd Rahman AM. Optimization of weight on bit during drilling operation based on rate of penetration model. 2011.
6. Han J, Sun Y and Zhang S. A Data Driven Approach of ROP Prediction and Drilling Performance Estimation. International Petroleum Technology Conference. Beijing, China: International Petroleum Technology Conference, 2019, p. 9.
7. Nwabueze QA and Ighalo JO. Production and Economic Analysis of Enhanced Oil Recovery (EOR) by Water Flooding: A case study of Reservoir OB-48 In the Niger Delta Petroleum and Coal, 2020; 62: 103-13.
8. Khakzad N, Khan F and Amyotte P. Quantitative risk analysis of offshore drilling operations: A Bayesian approach. *Safety science*, 2013; 57: 108-17.
9. Ritto T, Soize C and Sampaio R. Robust optimization of the rate of penetration of a drill-string using a stochastic nonlinear dynamical model. *Computational Mechanics*, 2010; 45: 415-27.

10. Smith SA and Comeskey AE. Sustainable wells: maintenance, problem prevention, and rehabilitation. CRC Press, 2009.
11. Jain JR, Ricks G, Ledgerwood L and Phillips A. Mitigating Drilling Dysfunctions and Enhancing Performance with Self-Adjusting Bit Technology: Analytical and Experimental Case Studies. SPE/IADC Drilling Conference and Exhibition. Society of Petroleum Engineers, 2017.
12. Asghar Jafari A, Kazemi R and Faraji Mahyari M. The effects of drilling mud and weight bit on stability and vibration of a drill string. Journal of vibration and acoustics, 2012; 134.
13. Bourgoyne Jr AT and Young Jr F. A multiple regression approach to optimal drilling and abnormal pressure detection. Society of Petroleum Engineers Journal, 1974; 14: 371-84.
14. Jahanbakhshi R, Keshavarzi R and Jafarnezhad A. Real-time Prediction of Rate of Penetration During Drilling Operation In Oil And Gas Wells. 46th US Rock Mechanics/Geomechanics Symposium. Chicago, Illinois: American Rock Mechanics Association, 2012, p. 7.
15. Moraveji MK and Naderi M. Drilling rate of penetration prediction and optimization using response surface methodology and bat algorithm. Journal of Natural Gas Science and Engineering. 2016; 31: 829-41.
16. Cheatham CA and Nahm JJ. Effects of Selected Mud Properties on Rate of Penetration in Full-Scale Shale Drilling Simulations. SPE/IADC Drilling Conference. New Orleans, Louisiana: Society of Petroleum Engineers, 1985, p. 9.
17. Khuri AI and Mukhopadhyay S. Response surface methodology. Wiley Interdisciplinary Reviews: Computational Statistics, 2010; 2: 128-49.
18. Hill WJ and Hunter WG. A review of response surface methodology: a literature survey. Technometrics, 1966; 8: 571-90.
19. Ighalo JO and Adeniyi AG. Factor effects and interactions in steam reforming of biomass bio-oil. Chemical Papers, 2019; 74: 1459-70.
20. Adeniyi AG, Ighalo JO and Odetoye TE. Response surface modelling and optimisation of bio-diesel production from Avocado plant (*Persea americana*) oil. Indian Chemical Engineer, 2020; 62(3): 243-250.
21. Kasim MS. Comparison between Taguchi method and response surface methodology (RSM) in optimizing machining condition. Proceeding of 1st International Conference on Robust Quality Engineering. 2013, p. 60-8.
22. Widyaningsih T, Widjanarko S, Waziroh E, Wijayanti N and Maslukhah Y. Pilot plant scale extraction of black cincau (*Mesona palustris* BL) using historical-data response surface methodology. International Food Research Journal, 2018; 25.
23. Mahmoodi NM, Keshavarzi S and Rezaei P. Synthesis of copper oxide nanoparticle and photocatalytic dye degradation study using response surface methodology (RSM) and genetic algorithm (GA). Desalination and Water Treatment, 2017; 72: 394-405.
24. Zhao Y, Noorbakhsh A, Koopialipoor M, Azizi A and Tahir M. A new methodology for optimization and prediction of rate of penetration during drilling operations. Engineering with Computers, 2019: 1-9.
25. Al-AbdulJabbar A, Elkatatny S, Abdulhamid Mahmoud A, et al. Prediction of the Rate Penetration while Drilling Horizontal Carbonate Reservoirs Using a Self-Adaptive Artificial Neural Network Technique. Sustainability, 2020; 12: 1376.
26. Alum MA and Egbon F. Semi-Analytical Models on the Effect of Drilling Fluid Properties on Rate of Penetration (ROP). Nigeria Annual International Conference and Exhibition. Abuja, Nigeria: Society of Petroleum Engineers, 2011, p. 13.
27. Schamp JH, Estes BL and Keller SR. Torque Reduction Techniques in ERD Wells. IADC/SPE Drilling Conference. Miami, Florida, USA: Society of Petroleum Engineers, 2006, p. 9.
28. van Riet EJ, Reitsma D and Vandecraen B. Development and Testing of a Fully Automated System to Accurately Control Downhole Pressure During Drilling Operations. SPE/IADC Middle East Drilling Technology Conference and Exhibition. Abu Dhabi, United Arab Emirates: Society of Petroleum Engineers, 2003, p. 12.

To whom correspondence should be addressed: Joshua O. Ighalo, Department of Chemical Engineering, Nnamdi Azikiwe University, P. M. B. 5025, Awka, Nigeria, E-mail: oshea.ighalo@yahoo.com

Characterization of Bara Formation coals in Lakhra region, Lower Indus Basin Pakistan: Implication of hydrocarbon generation potential and depositional environment

Zain Gul¹, Wan Hasiah Abdullah², Yousif M. Makeen Ahmed³, Muhammad Jamil¹, Nisar Ahmed¹

¹ Department of Geoscience, Universiti Teknologi PETRONAS. 32610 Seri Iskandar, Perak, Malaysia

² Department of Geology, University of Malaya, Malaysia

³ College of Earth Science, Jilin University, Changchun, China

Received June 26, 2020; Accepted October 15, 2020

Abstract

To date, very little has been published on the organic geochemical and petrological aspects of the Bara formation coals, Southern Indus Basin, Pakistan. To address this, fresh unweathered coal samples were collected from seven different coal mines of the Lakhra coal field and were subsequently analysed and evaluated in detail. Numerous characteristics were assessed i.e. thermal maturity (coal rank), petroleum generation potential, type of organic matter and paleo-depositional environment. Evaluation techniques include proximate analysis, bitumen (soluble organic matter) extraction, fractionation of hydrocarbon yield using liquid column chromatography, Rock Eval, pyrolysis-GC (Py-GC), GC-MS, huminite/vitrinite reflectance and maceral analysis. Based on proximate analysis, the samples are classified as lignite to subbituminous C based on the ASTM standard. This low rank is supported by extracted bitumen and Rock Eval data. Although immature, these Lakhra coals show to possess excellent hydrocarbon generation potential. The distributions of n-alkanes, isoprenoid, hopane and sterane biomarkers further corroborate that these coals are thermally immature for hydrocarbon generation. The probable paleodepositional environment interpreted based on biomarkers and maceral analysis data suggests a waterlogged swamp in a lower delta plain setting that experienced frequent marine influence as indicated by the sub-oxic condition of deposition.

Keywords: Bara Formation Coal; Organic geochemistry; Coal petrology; Thermal maturity; Kerogen type II/III; Paleo-depositional setting; Biomarkers.

1. Introduction

Coal resources has always been in consideration for transport, industry utilization and for other miscellaneous purposes [1-3]. Moreover, due to its organic rich nature its thoroughly been studied for hydrocarbon potential purposes [4-7] and proven that it can be a possible source rock in petroleum system. Thus, Bara Formation consist of large coal reserves and its regionally wide spreads [8-11], due to limited outcrop exposure on the surface, the samples has been collected from underground mines operated by Lakhra Coal Development Company (LCDC) located in small town named Khanote, District Jamshoro and almost 40 km south east to Hyderabad District, Sindh Pakistan Fig. 1C. Based on [10] investigation coal indicates good permeability characterized as subbituminous C to lignite A. Whilst, cleat and fracture investigation good permeability for CBM storage [12]. To date, limited studies has been recorded which established detail hydrocarbon source rock profile. Therefore, in this study we have incorporated organic geochemical and organic petrological analyses in order to assess coal quality, thermal maturity/rank, hydrocarbon generation potential and the paleo depositional condition of Bara Formation coal. This integration of methods is commonly performed in such studies as conducted by previous workers [13-16]. In this current study, the derived data and parameters that were gathered include volatile, moisture, ash, carbon, Rock-Eval pyrolysis data and total organic content (TOC), Kerogen (Py-GC), vitrinite/huminite reflectance (%R_o) and maceral

analysis. Moreover, bitumen extraction and biomarker data were used as supporting evidence for assessment of thermal maturity and depositional environment of the analysed Bara Formation coals.

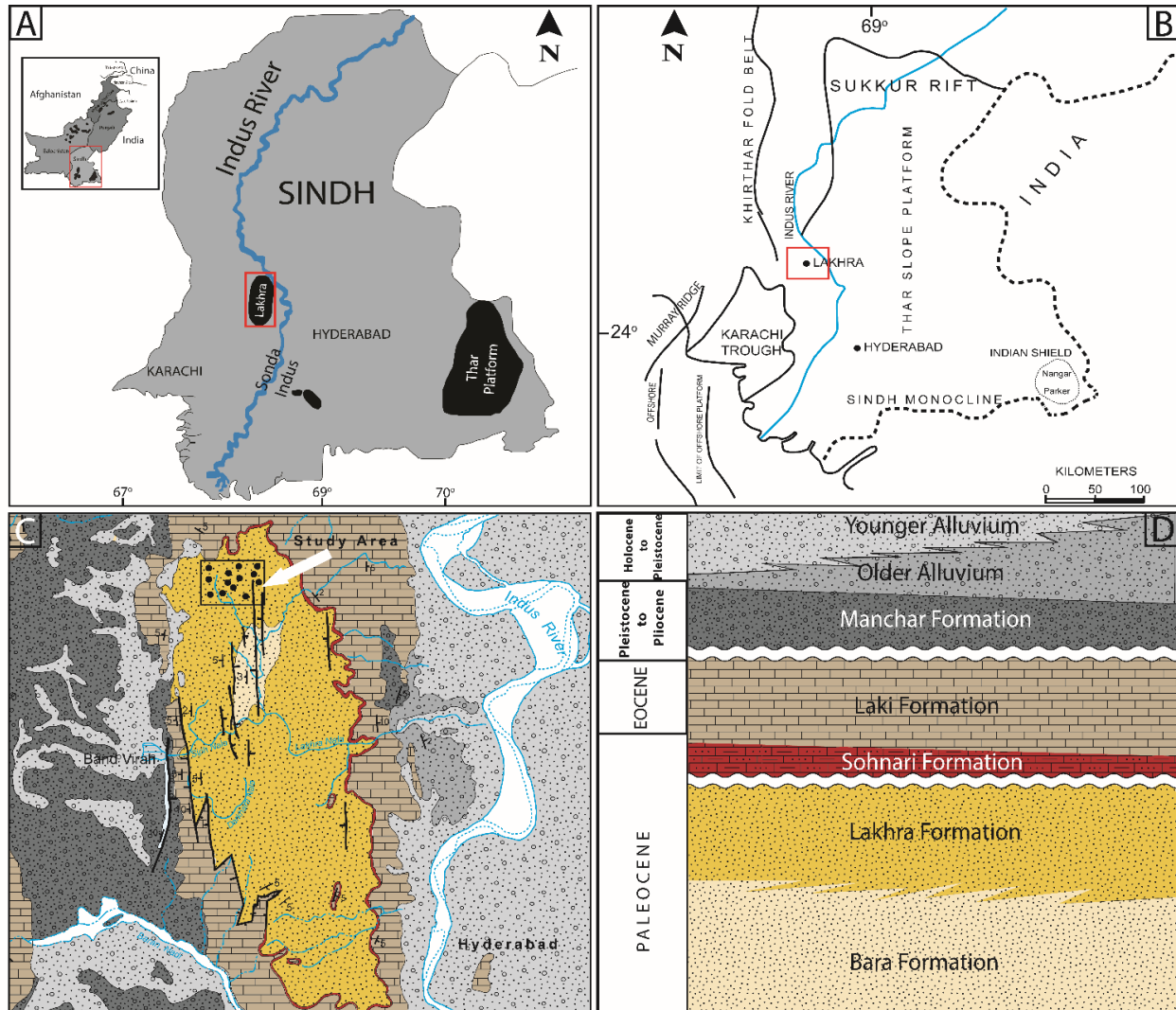


Figure 1. (A) showing location map of the study area, (B) showing structural setting of the southern Indus Basin (modified after [12]). (C) Showing stratigraphic distribution of Lakhra region (modified after [13] and [14]). (D) showing the stratigraphic column of Tertiary sediments of the lower Indus basin within the study area (modified after [15]).

2. Geological settings

The Indus Basin is divided into three parts: Lower/southern Indus Basin, Middle Indus Basin and Upper Indus Basin. Lower Indus basin spreads almost 150,000 square miles with 38,000 ft of vertical sequences composed of Jurassic, cretaceous and tertiary sediments [2,8].

The Lower Indus basin is structurally bounded by Sukkur Rift (Jacobabad-Kandhkot high) in the north. Indian shield in the east (Nangar Parker) and marginal zone (Indian Plate) in the west Fig. 1B. The stratigraphic sequence consists of the rocks from Precambrian to recent age that are mainly dominated by Jurassic, Cretaceous, and Tertiary sediments. In this study, our focus is on Tertiary formations; from top to bottom are Laki, Sohniari, Lakhra and Bara Formation respectively Fig. 1D. The Bara Formation is composed of siliciclastic sediments mainly of claystone, shale, siltstone and having multiple coal seams [19]. The Lakhra Formation rocks shows similar characteristics to Bara Formation, the only difference is noted is the presence

of limestone. Thus, it predominantly consists siliciclastic sediments, initiated with sandstone bed at the base and top part is dominated by limestone often appears as interbedded with siliciclastic materials [10-11].

Lakhra formation is covered widespread sitting at the top of Bara Formation and unconformably overlies the upper Laki limestone. In some parts, Laki limestone is eroded due to post-Ranikot erosion [19] only leaving place to Manchar Formation sitting at the top of Ranikot group formations. Nuttall [21] subdivided the [22]"Laki Series" into 2 units, of which the lower unit, a lateritic claystone, he named the Basal Laki laterite or Sonhari formation, and the upper unit Laki limestone. In outcrops the "Basal Laki laterite" is a highly ferruginous, dark red, maroon, dark brown, and yellowish-brown massive claystone containing concretions of iron oxide, Locally, where the overlying limestone has been stripped off by erosion, the laterite has a duricrust or hardpan on exposed surfaces. On the surface the "Basal Laki laterite" is a wide-spread, very conspicuous lithologic unit in the Lakhra area; even partially exposed outcrops are readily recognizable when viewed in the field from great distances.

No diagnostic fossils have been found in rocks of the "Basal Laki laterite" by which to ascertain its age. Since the laterite is regarded to be the lowermost unit of the Laki Limestone, it is considered early Eocene (Ypresian) in age [21-22]. The Laki Limestone is equivalent to the "Laki Series" of Verdenburg [22] who derived the term from the Laki hill range and village in the western part of the Hyderabad. The formation consists of finely crystalline limestone and very subordinate amounts of claystone or marl. The limestone is light yellowish-gray, white, and light gray, stained yellow to brown, and weathers to light gray. It is a nodular, hard, resistant, massive, and commonly forms cliff. Foraminifera abounds throughout the formation, but most of the megafauna is present in the middle part. [23-24] considered the "Laki Series" to be early Lutetian in age. Later work by [21] shows that the "Laki Series" corresponds to the Ypresian. The youngest rocks in the area are unconsolidated stream, colluvial, and eolian deposits composed of sandstone, siltstone, claystone, and limestone and sandstone pebble and cobble beds. The alluvium is as much as 10 feet thick or more in places and is widespread in the western part. Stream-laid deposits are present in the larger watercourses in the central and eastern parts [19].

3. Sample and methods

A total of seven coal samples were collected from the Bara Formation from seven different coal mines, 2 from block A and 5 from block B of Lakhra coal field, these samples are labeled as per mined identification. The coal is currently been extracted for industry utilization purpose.

The quality of a Lakhra coal was previously studied using the ASTM (American society of testing materials) method [10]. In this current study, the ASTM analysis was performed on all of the seven investigated coal samples. The coal quality of these coals was also analyzed using a thermogravimetric Analyzer (TGA) DTA/DSC TA (Model SDT Q600) on crushed samples to determine fixed carbon, volatile matter, moisture and ash content.

Rock-Eval 6 together with TOC component were performed on crushed samples for pyrolysis analysis. The measured parameter includes, TOC (Total organic carbon), T_{max} (temperature of maximum pyrolysis yield), S_1 (volatile hydrocarbon content, mg HC/g rock), S_2 (remaining Hydrocarbon generating potential) and S_3 (carbon dioxide yield, mg CO_2 /g rock). OI (oxygen index), PI (production index) and HI (hydrogen index) were calculated as suggested by [24].

Approximately 2g of the crushed powdered samples were extracted using Soxhlet apparatus with (93:7) dichloromethane and methanol (CH_3OH) mixture for 72 hours. The extracted organic matter (EOM), also referred to as bitumen, were further fractioned into saturated, aromatic and polar fractions using liquid column chromatography and were developed with petroleum ether, dichloromethane and methanol respectively. For analysis of biomarker distributions, gas chromatography (GC) were performed on saturated fractions using an Agilent 6890N series GC. Aliphatic fractions were dissolved in hexane and analyzed in a GC with a HP-5MS column, and temperate held at 30 min at 300°C. Gas chromatography-mass spectrometry (GC-MS) analysis was carried on a V 5975B inert MSD mass spectrometer together with gas chromatograph and an attached ion source (70 eV ionization, 230°C interface temperature,

100 mA filament emission current). The acquired fingerprints from the GC and GCMS were interpreted for biomarker identification. Pyrolysis gas chromatography (Py-GC) using Frontier Lab Pyrolyser and pyrolysis (at 600°C) were applied on crushed samples to identify kerogen types as described by previous workers [25-26].

Organic petrographic examination including vitrinite reflectance measurement and maceral microscopy were performed on polished block in order to established thermal maturity and maceral content. The analysis was carried out at organic petrographic laboratories of the Department of Geology at University of Malaya. The polished block was prepared by mounting whole rock fragments, using slow setting polyester resin (serfix) mixed with resin hardener and set to dry. The mounted samples were ground flat on diamond lap, using water as lubricant and subsequently polished using silicon carbide paper (P800, P2400 and P4000) grades. Samples were finally polished for highly reflecting surface using finer alumina suspension (1 µm, 0.3 µm and 0.5 µm).

Petrographic analysis was conducted on a LEICA DM6000M microscope and LEICA CTR6000 photometry system equipped with fluorescence illuminators under plane polarized reflected light. Filter system used for analysis are LP425 suspension filter, BP 340-380 excitation filters and RKP 400 dichromatic mirror.

Maceral composition has been identified by counting 1000 points under UV (ultraviolet) and reflected white "light". Vitrinite/huminite reflectance was measured under oil immersion (%Ro) by using DISKUS fossil/Maceral software package.

4. Results

4.1. Proximate analysis and coal rank

The results of the proximate analysis performed in this study shown in Table 1 indicate that the coals are thermally immature based on the fixed carbon contents and volatile matter in the range of 26.17-47.32 and 35.44-53.07 wt% respectively. The measurement of huminite/vitrinite reflectance (%Ro) seems to concur with this interpretation, whereby the %Ro values varies between 0.26 and 0.36%. This is in agreement with values of volatile matter and fixed carbon contents based on ASTM method which indicates that these coals are of sub-bituminous C to Lignite rank.

Table 1. TGA results performed in this study and compared to a previous study based on ASTM method

Analysis	ASTM	Thermogravimetric analyzer						
		LCDC A21	LCDC A33	LCDC B4A	LCDC B27	LCDC B31	LCDC B63	LCDC B39
Moisture %	28	6.41	8.97	2.62	3.36	2.39	28.74	11.34
Volatile matter %	28	51.05	53.07	45.64	52.06	35.44	39.65	43.48
Ash %	15	0.24	0.13	0.09	0.18	9.60	0.11	0.03
Carbon %	39	37.66	37.18	47.32	40.61	26.17	28.20	32.03

4.2. Bitumen extraction: Extractable organic matter (EOM) data

The results from bitumen extraction process were gathered and tabulated. The amount of EOM ranges from 10,528 ppm to 27,453 ppm. Generally, if amount of EOM is greater than 5,000 ppm, it is considered as having a very good hydrocarbon generation potential based on classification by [27]. The concentrations of the EOM are shown in Table 2 and Fig. 2b. The EOM were further fractioned into aliphatic, aromatic and polar compounds Fig. 2a. The recovered aliphatic fractions ranges from 820 to 2,884 ppm with yield of 5.29% to 14.36% for EOM, while aromatic hydrocarbon recovered ranges from 2,869 ppm to 9,272 ppm with yield of 23.56% to 44.31%. The collected NSO compounds were around 5,291 ppm to 17,323 ppm with yield of 50.52% to 62.06%. Fractions from bitumen indicates that the NSO compounds are more dominant than saturated and aromatic, while aromatic hydrocarbons are more dominant compared to saturated hydrocarbon. Previous studies e.g. [21-22,25-26] reported that the abundance of NSO compounds are more common in coal, whereas the dominance of aromatic

over saturated hydrocarbon indicates that the samples are gas-prone or having mixed oil and gas potential.

Table 2. Bitumen extraction and liquid column chromatography data (in ppm)

Coal Field	Sample ID	Bitumen Extraction and chromatographic fraction (ppm of whole rock)					Chromatographic fractions of Bitumen Extraction (EOM wt %)			
		EOM	SAT	ARO	NSO	HC	Sat	Aro	NSO	HC
Lakhra coal field	LCDC A21	17240	1814	6715	8711	5829	10.52	38.95	50.52	49.47
	LCDC A33	27453	1454	9272	16727	10726	5.29	33.77	60.92	39.07
	LCDC B4A	14425	819	6393	7213	7212	5.68	44.31	50.00	49.99
	LCDC B27	28115	1529	9263	17323	10765	5.43	32.94	61.61	38.37
	LCDC B31	10528	1005	4232	5291	5237	9.54	40.19	50.25	49.74
	LCDC B63	12167	1748	2867	7552	4615	14.36	23.56	62.06	37.93
	LCDC B39	22883	2884	6346	13653	9230	12.60	27.73	59.66	40.33

HC = Hydrocarbon fractions (Saturated + Aromatic); NSO = Nitrogen, Sulphur, Oxygen components;
 Aro= Aromatic hydrocarbons; Sat = Saturated hydrocarbons;
 EOM = Extractable organic matter (Bitumen extraction).

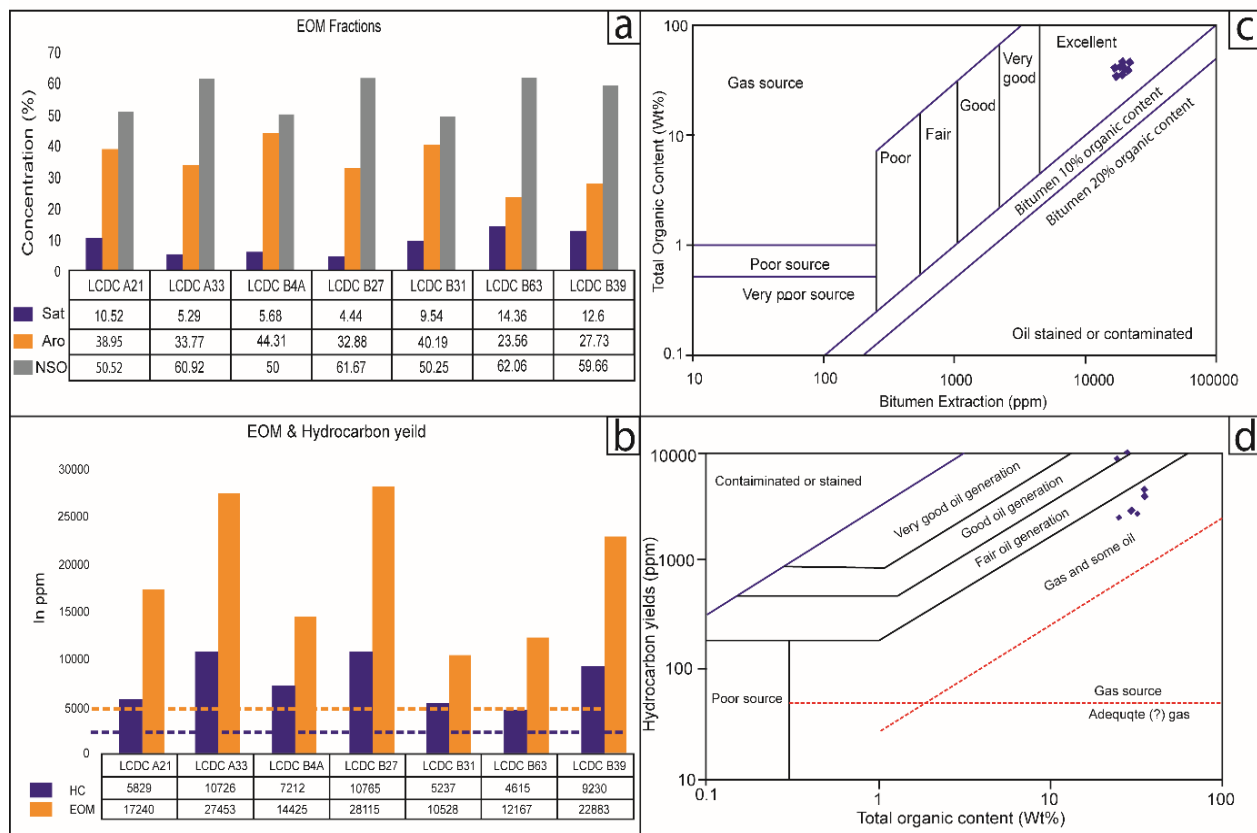


Figure 2. (a) Histogram of fractions concentration from bitumen extraction data, (b) Histogram indicates the amount of extracted Hydrocarbon yield and EOM; lines indicate it has excellent generation potential if exceeds. (c) Hydrocarbon yield versus TOC indicates about quality of the samples (modified after [26]) and (d), TOC versus bitumen (ppm) indicates the generating potential

The combination of saturated hydrocarbon and aromatic hydrocarbons is referred to as hydrocarbon fraction. The amount of hydrocarbon recovered ranges from 4,615 to 10,726 ppm representing yield of 37% to 49% which indicates that the samples possess excellent hydrocarbon generation potentials Fig. 2a. The hydrocarbon generating potential data of the analysed Bara Formation coals were presented in modified plots used by [29] together with classification of [27] Fig. 2 c & d. The plots show that the studied coal samples possess viable source rocks potential with predominantly excellent gas and fairly good oil generation capability.

4.3. Rock Eval 6 and pyrolysis analysis

Rock-Eval pyrolysis and TOC analysis were performed with the purpose to identify the petroleum generation potential, quality and type of organic matter as well as the thermal maturity of the studied samples. As expected for coals, high TOC values were obtained that ranges from 37.89 to 62.75 wt% and is considered to possess excellent petroleum generation potential. Meanwhile, the parameter S_2 that represents free hydrocarbons generated during pyrolysis range from 93.52 to 243.84 which is also useful to evaluate the generation potential of source rocks [25,27-28]. The parameter S_1 represents the volatile hydrocarbon ranging from 1.68 – 5.39 which also indicate excellent hydrocarbon generation potential. S_3 represents the amount of carbon dioxide present in samples. It is also useful in interpreting the coal quality. In addition, T_{max} value which represents the temperature at the point where S_2 peak is at maximum is also determined. The T_{max} values range from 403-429°C thus indicating organic matter is thermally immature for hydrocarbon generation. Hydrogen index (HI) and oxygen index (OI) of the studied samples were calculated and determined to be in the range of 375-213 mg HC/g TOC and 0-20 mg CO_2 /g TOC, respectively Table 3. A diagram of Fig. 3 a & b was based of pyrolysis data, kerogen classification and thermal maturity using the HI versus T_{max} and HI versus OI data shown that the Lakhra coals are dominated by Type II/III kerogens. In this respect, all the analysed samples are generally plotted in the immature organic matter region of mixed Type II/III kerogens. Moreover, by plotting S_2/S_3 versus TOC results and S_2 versus TOC on classified diagram of Fig. 3 c & d suggest the analysed coals are of mixed oil and gas-prone characters with excellent remaining hydrocarbon generating potentials.

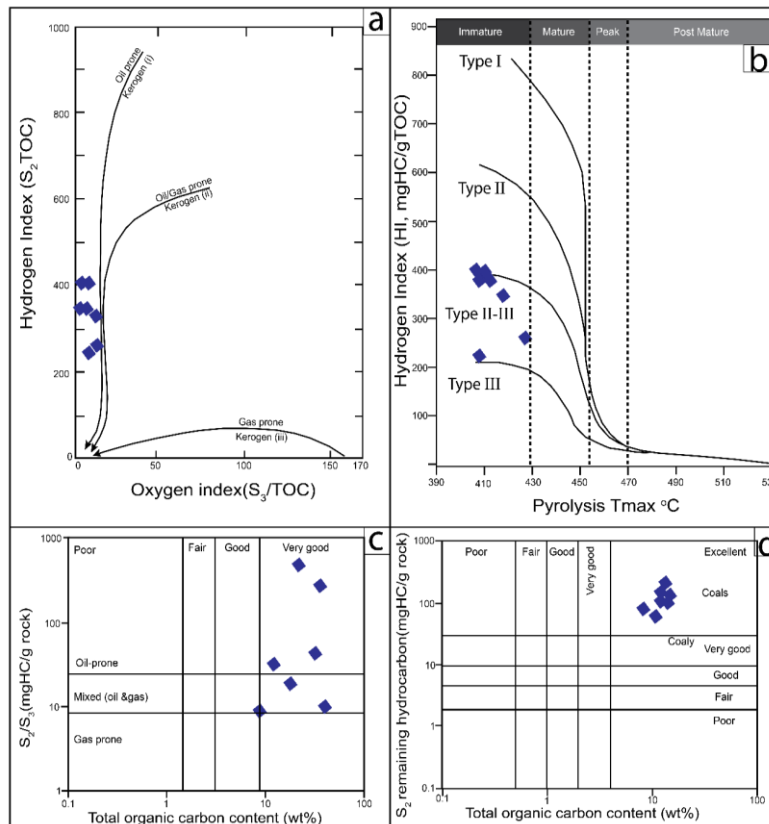


Figure 3. (a) Hydrogen versus oxygen index (OI) indicates kerogen quality, (b) Plot of Hydrogen Index (HI) versus pyrolysis T_{max} indicates thermal maturity of the analysed coal samples from Lakhra coal field (c) Plot of total organic carbon S₂/S₃ versus (TOC) yields showing hydrocarbon generative potential and, (d) Pyrolysis S₂ versus total organic carbon (TOC) plot showing generative source rock potential from coal from Lakhra coal field of the studied coals modified after [26].

Table 3. Results of TOC and Rock Eval pyrolysis analysis with calculated parameters for the Lakhra coal field samples

Coal field	Sample ID	Lithology	Pyrolysis data								
			TOC	S ₁ (mg/g)	S ₂ (mg/g)	S ₃ (mg/g)	Tmax (°C)	S ₂ /S ₃	HI	OI	PI
Lakhra coal field	LCDC A21	Coal	60.46	3.61	212.30	8	417	26.53	351	14	0.02
	LCDC A33	Coal	53.23	3.67	199.73	0.24	404	832.2	375	0	0.02
	LCDC B4A	Coal	62.75	3.81	159.65	10.36	429	15.41	254	17	0.02
	LCDC B27	Coal	60.47	5.39	243.84	0.39	410	625.2	403	1	0.02
	LCDC B31	Coal	37.89	3.35	156.12	4.11	407	37.98	412	11	0.02
	LCDC B63	Coal	53.69	3.66	200.11	2.96	404	67.60	373	6	0.02
	LCDC B39	Coal	43.92	1.68	93.52	8.71	403	10.73	213	20	0.02

TOC: Total Organic Carbon, wt %;

Tmax: Temperature at maximum of S₂ peak;

Hydrogen Index= S₂ X 100/TOC, mg HC/g;

S₂: Remaining HC generative potential, mg HC/g rock;

PI: Production Index = S₁/(S₁ + S₂);

OI: Oxygen Index= S₃ X 100/TOC, mg CO₂/g TOC;

S₃: Carbon dioxide yield, mg CO₂/g rock;

S₁: Volatile Hydrocarbon (HC) content, mg HC/g rock;

4.4. Kerogen pyrolysis (Py-GC)

In addition to Rock-Eval, pyrolysis-GC was performed to verify the kerogen type, because many workers believed that the data from Rock-Eval equipment does not always represent accurate types of hydrocarbon generated from source rocks e.g. [25-26,31-32]. However, it is an additional benefit to have Rock-Eval pyrolysis data as it is commonly used to interpret kerogen types and to some extent, can differentiate the variation between petroleum composition. This characteristic gives a straight forward indication about the hydrocarbon which can be generated from kerogen type during the maturation process [25,33-35].

The Py-GC fingerprints Fig. 4 of the analyzed samples indicate that the studied coal samples possess mixed oil and gas potential as characterized by the dominance of aromatic compounds over n-alkene/alkane doublets. The distributions of these doublets, as expected, concur that the coals are derived from terrestrial sources e.g. [29, 36-39]. The studied samples show that the n-alkane/alkene doublets chains extend beyond C₃₀ which indicates that these coals are aliphatic-rich whilst the abundance of aromatic compounds suggesting a mixed kerogen type (oil and gas-prone). In addition, three pyrolystate components (m, p-xylene, phenol and n-octane) were identified Fig. 5 which indicates a mixture of Type II/III [38-39]. Based on this ternary plot, the majority of the analyzed coal samples fall within the Type II/III kerogen. This is in support of their HI values which ranges from 213 to 403 mgHC/TOC, thus indicates a mixed oil and gas generating potential.

4.5. GC and GC-MS

4.5.1. Distribution of n-alkanes and isoprenoids

The gas chromatography (GC) and gas chromatography–mass spectrometry (GC–MS) analyses were performed on the saturated hydrocarbon fraction of the analyzed coal samples Fig. 4. Ion m/z 85 is used to interpret the distribution of n-alkanes and isoprenoids. Parameters derived from ion m/z 85, are commonly applied in organic geochemistry to recognize the paleo-depositional condition and maturity stage of source rock extracts [37,40-43]. The calculated parameters for the analyzed samples are listed in Table 4. The distribution of n-alkanes and isoprenoids show a bimodal distribution. This distribution also shows odd majority of the heavier members (n-C₂₅₊) which gave moderate to high CPI values in the range of 1.15–1.41. These CPI values >1 would be expected as the Lakhra coal is immature and predominantly consist of terrestrial derived higher plants [43-45]. Isoprenoids, in particular pristane, occur in high relative abundance, with pristane/phytane (Pr/Ph) ratios >1.0 (1.46–2.41) which suggest that these coals were deposited under suboxic conditions [46-48]. Pristane concentrations are generally lower than the closely eluting n-alkane (n-C₁₇) in the analyzed samples see Fig. 5b and Table 5. Meanwhile Pr/n-C₁₇ versus Ph/n-C₁₈ plot that represent relationship between the kerogen type and depositional environment suggested that the analyzed samples were deposited

within a transitional environment, which strongly supports a mixed environment of terrestrial with marine influence as indicated by the bimodal distribution of n-alkanes described earlier.

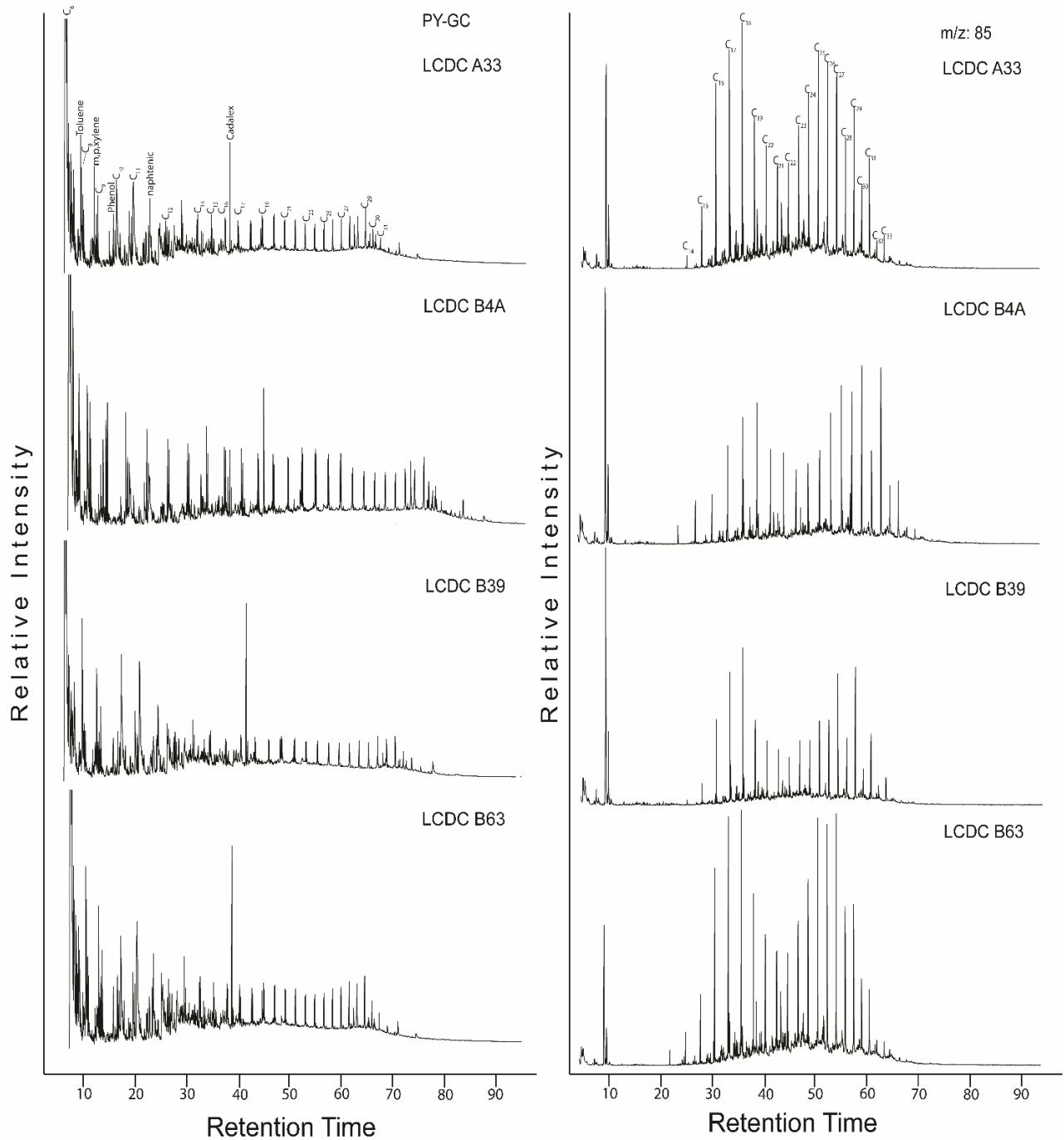


Figure 4. PyGC pyrograms of coal samples LCDC BA33, LCDC B4A, LCDC B39, and LCDC B63 n-alkanes and isoprenoids distribution in m/z 85

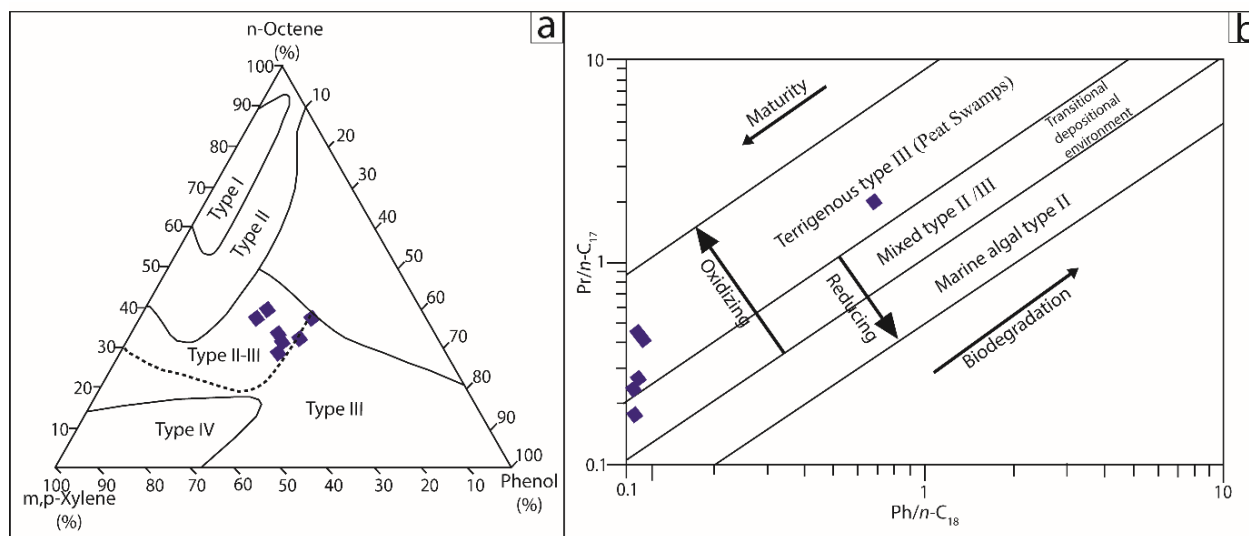


Figure 5. (b) Pr/n-C₁₇ versus Ph/n-C₁₈ plot represents the kerogen type and depositional environment of studied samples (modified after [41]). (a) Calculated parameters from Py-GC (S2) to identify kerogen type (modified after 40-41)

Table 4. Calculated parameters from kerogen pyrolysis (PY-GC)

Sample ID	Percentage %		
	m,p- xylene	phenol	n-octane
LCDC A21	30.76	34.61	34.61
LCDC A33	37.31	31.34	31.34
LCDC B4A	26.38	34.35	39.26
LCDC B27	36.22	33.07	30.70
LCDC B31	37.77	24.44	37.77
LCDC B39	33.52	36.99	29.47
LCDC B63	35.10	26.59	38.29

Table 5. Parameters of n-alkane calculated from ion m/z 85 of the studied samples

Sample ID	Normal Alkanes and isoprenoid ion m/z 85			
	Pr/Ph	Pr/n-C ₁₇	Ph/n-C ₁₈	CPI
LCDC A21	1.62	0.39	0.18	1.08
LCDC A33	1.47	0.21	0.13	1.2
LCDC B4A	2.41	0.44	0.16	1.21
LCDC B27	1.81	0.55	0.29	1.12
LCDC B31	2.15	1.8	0.88	2.38
LCDC B63	1.46	0.16	0.11	1
LCDC B39	1.58	0.27	0.17	1.54

Pr: pristane;

Ph: phytane.

CPI: Carbon Preference Index: $(2[n-C_{23}+n-C_{25}+n-C_{27}+n-C_{29}]/[n-C_{22}+2\{n-C_{24}+n-C_{26}+n-C_{28}\}+n-C_{30}])$.

4.5.2. Triterpanes (m/z 191)

The distribution of triterpanes are characterized by the m/z 191 ion chromatogram Fig. 4 of saturated hydrocarbon fraction. Labelled peaks are as listed in Table 9, and derived parameters are in Table 6. In m/z 191 mass chromatograms, the distribution shows that the Lakhra coal samples are abundant in triterpanes. High abundance of C₂₉ hopanes are generally observed in all studied samples. Among the hopane homologs, the dominance of C₃₁ and the presence of low abundance of homohopane C₃₂ is the indication of sub-oxic environment, which is also supported by the absence of C₃₅ in the homohopanes series [49-50].

Table 6. Parameters of triterpanes and terpanes calculated from m/z 191 fingerprints of the studied samples

Sample ID	Triterpanes and terpanes (m/z191)			C ₃₂ homohopane (22S+22R)
	Ts/(Ts+tm)	Tm/Ts	OI/C30	
LCDC A21	0.04	21.5	0.03	0.33
LCDC A33	0.12	7.33	0.05	0.4
LCDC B4A	0.03	29.5	-	0.2
LCDC B27	0.02	35	0.03	0.3
LCDC B31	0.05	18.5	0.03	0.33
LCDC B63	0.11	8	0.05	0.41
LCDC B39	0.07	12.33	0.10	0.47

Ts: (C₂₇ 18a (H)-22,29,30-trisnorneohopane); Tm: (C₂₇ 17a (H)-22,29,30-trisnorhopane);
 OI/C30: oleanane/C30 hopane

The Tm (C₂₇ 17 a(H)-22,29,30-trisnorhopane) is dominated over Ts (C₂₇ 18a(H)-22,29,30-trisnorneohopane) with Tm/Ts ratio ranging from 8-29 which suggest dominant presence of higher plants [15]. Ts/(Ts+Tm) for the studied samples ranges from 0.032 to 0.12. Ts/(Ts+Tm) is generally a ratio to identify maturity but [52] noted that Ts/(Ts+Tm) it is not always sensitive for quantitative measurement. In the studied samples oleanane is present Fig. 6a which is a strong indicator of occurrence of terrestrial angiosperm plant input in coals of late Cretaceous or younger age [53] The presence of oleanane indicates that the organic matter were effected by marine influence [36]. Moreover for the calculated ratio of C₃₂ 22S/(22R + 22S), according to [54], if C₃₂ 22S/(22S + 22R) homohopane ratio is within <0.3 to 0.5 and with equilibrium of C₂₉ 20S/(20S + 20R) sterane ranges within 0.1 to 0.3 these are considered as thermally immature [55].

4.5.3. Steranes and diasterane (m/z 217)

The distribution of steranes and the diasteranes (C₂₇, C₂₈ and C₂₉) are characterized by the m/z 217 ion chromatograms Fig. 6. Peak labels are listed as in Table 9 and the derived parameters are listed in Table 7. In the m/z 217 mass chromatogram, the regular steranes are dominated by C₂₉ isomers which affirmed that the organic matter input are terrestrially-derived which is closely related to vascular plants [55-57]. The percentage of C₂₇, C₂₈, and C₂₉ steranes of the samples are in the range of 4.9 to 17.2, 15.6 to 60.0, and 32 to 72.1 respectively. The sterane abundance are in the following order: C₂₉ > C₂₈ > C₂₇ and the values are plotted on a ternary diagram of Fig. 7b which indicate the coals, as expected, are derived from higher plants of terrestrial origin. Moreover, this is also supported by the plot of pristane/phytane versus C₂₉/C₂₇ plot Fig. 7c as was previously reported by [37,59-61] indicating the type of organic matter is derived from land pants. The plots of C₂₉ 20S/(20S+20R) and C₂₉ ββ/(ββ + αα) Fig. 17a and Tm/Ts versus C₂₉ 20S/(20S+20R) Fig. 7a and 9d indicate thermal maturity which is strongly in agreement with other results that support thermal immaturity of the analyzed samples.

Table 7. Parameters of steranes calculated from ion m/z 217

Sample Id	C ₂₉ 20S /(20S+20R)	C ₂₉ ββ /(ββ + αα)	C ₂₉ /C ₂₇	C ₂₇ /C ₂₉	Regular steranes		
					C ₂₇ %	C ₂₈ %	C ₂₉ %
LCDC A21	0.08	0.33	5.75	0.1	12.5	15.6	71.8
LCDC A33	0.2	0.30	3.2	0.3	17.2	27.5	55.1
LCDC B4A	0.06	0.25	4.7	0.2	14.7	16.1	69.1
LCDC B27	0.10	0.41	14.6	0.06	4.9	22.9	72.1
LCDC B31	0.11	0.26	3.7	0.2	16	24	60
LCDC B63	0.2	0.45	3.3	0.3	12	48	40
LCDC B39	0.15	0.29	4	0.25	8	60	32

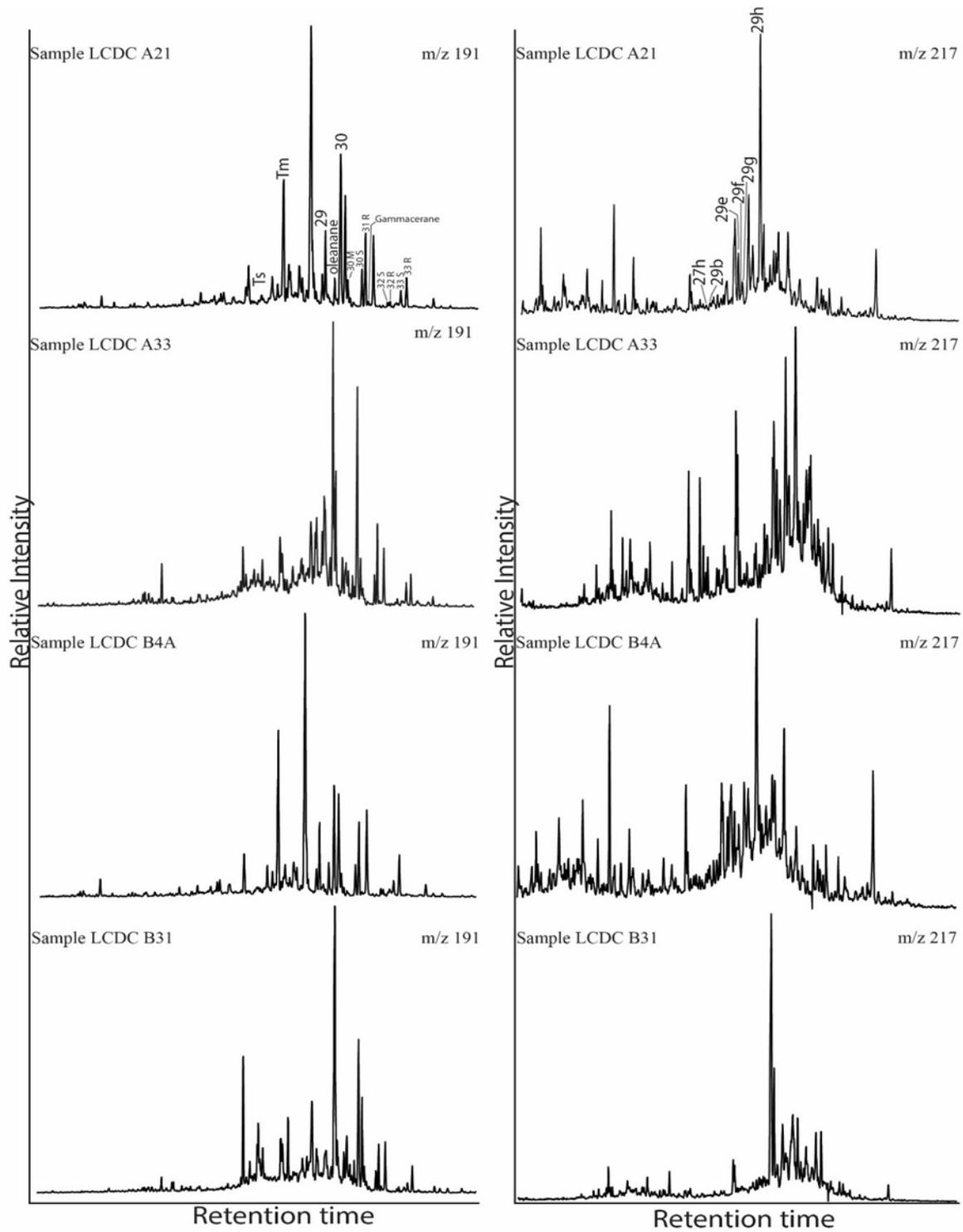


Figure 6. (a) Triterpanes interpreted traces from ion m/z 191 and, (b) Sterane and diasterane traces from ion m/z 217 for LCDC A21, LCDC A33, LCDC B4A and LCDC B31 coal samples

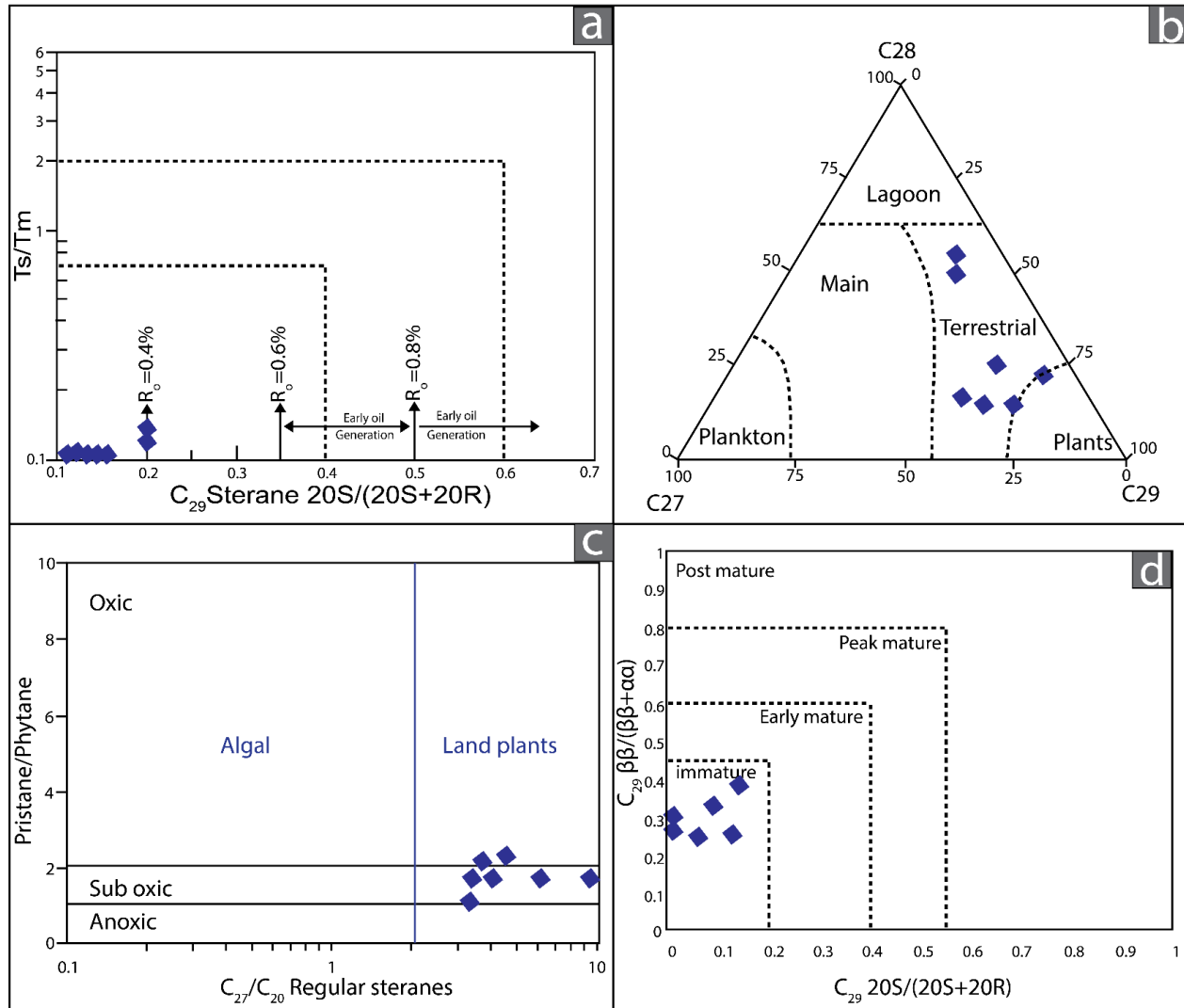


Figure 7. (a) Ts/Tm versus C₂₉ 20S/(20S+20R) and (d) C₂₉ ββ/(ββ+αα) versus C₂₉ 20S/(20S+20R) cross plot showing low maturity of the studied samples (modified after Peters et al., 2005 [50]). (b) the ternary plot representing the dominance of terrestrial drive organic matter deposits based on steranes distribution (after [52]) and (c), Pristane/Phytane versus C₂₉ / C₂₇ indicates the type of organic matter (after [38]).

4.6. Organic petrographic analysis

4.6.1. Huminite reflectance

The reflectance measurements of huminite (ulminite and detrohuminite) are given in Table 8. The measured mean random reflectance of these studied coals varied from 0.26 to 0.32%, indicating the immature nature of the analyzed samples.

4.6.2. Maceral composition

The maceral content of the analyzed coals is presented in Table 8 and examples of macerals present in the studied samples are as shown in Fig. 8. The coal samples are classified as humic coal Fig. 9a and dominated by huminite (82- 92%) with moderate amount of liptinite (5 - 14%), and low amount of inertinite (3 - 4%). TPI and GI values were calculated to indicate depositional environment and plotted on a diagram Fig. 9b that was modified after [62].

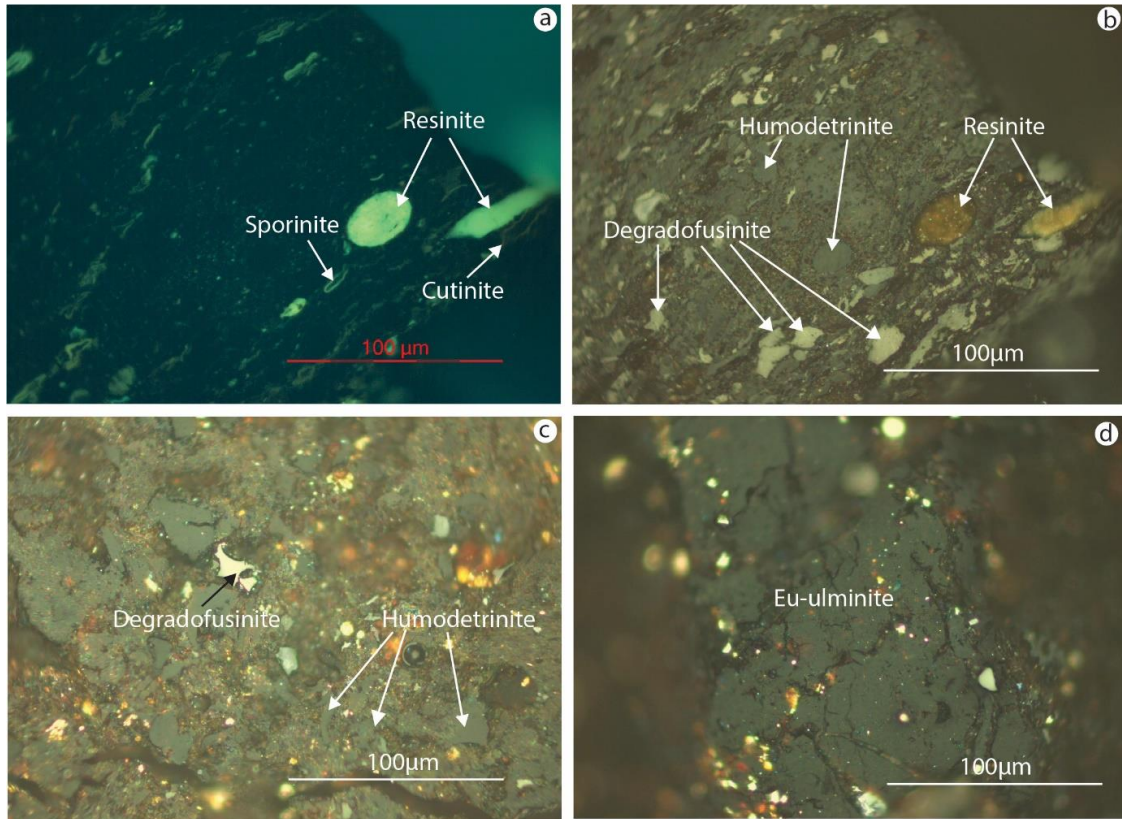


Figure 8. photomicrographs of organic matter assemblages from Bara formation coal samples of Lakhra area as shown under reflected light (b,c,d) and UV light (a) field width = 100 μm. fig (a) showing macerals from liptinite group Resinite, Sporinite and cutinite, (b) showing humodetrinite, resinite and degradofusinite, (c) showing degradofusinite and humodetrinite and, (d) showing eu-ulminite maceral

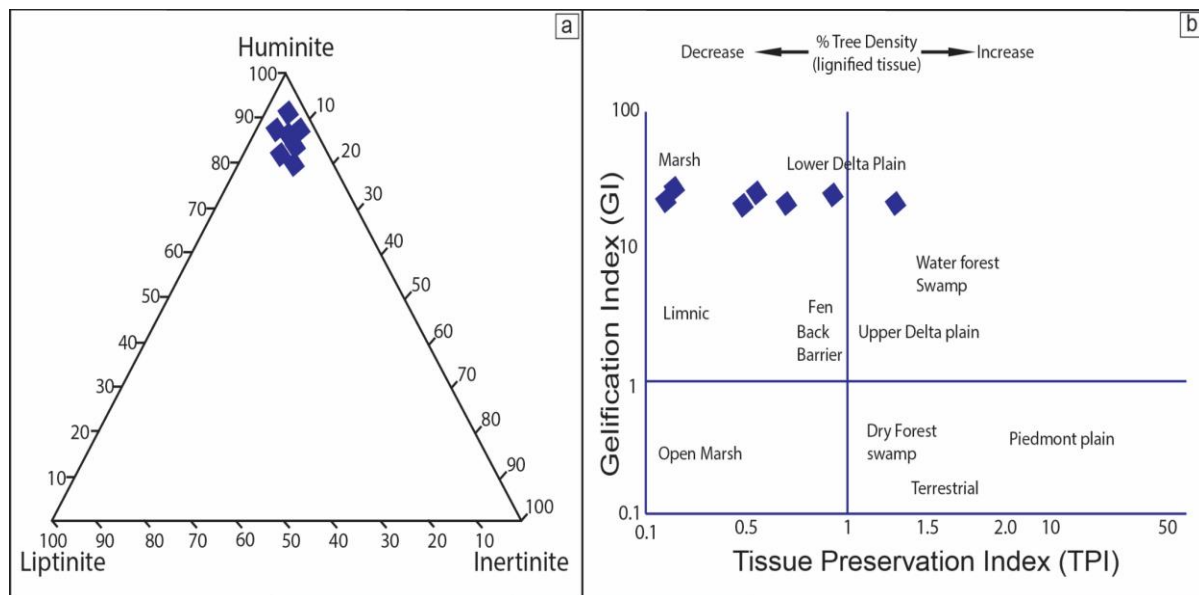


Figure 9. (a) Ternary diagram of maceral group composition (huminite, liptinite, and inertinite) for the analysed Lakhra coals. (b) Diagram of GI versus TPI indicating the paleo depositional environment of the analyzed Lakhra coals modified after (after [58])

Table 8. Huminite reflectance and maceral composition of the analysed Lakhra coals

Sample ID	Ro%	Tx	Huminite %					Liptinite %					Inertinite %			TPI	GI	
			U	Dh	Txu	Total	Sp	Cu	Rs	Ld	Total	df	Sfu	idt	Fg			Total
LCDC A21	0.27	0	40	46	0	86	3	2	4	1	10	1	2	0	1	4	0.91	21
LCDC A33	0.28	0	26	56	0	82	4	3	4	3	14	1	1	1	1	4	0.47	20.5
LCDC B4A	0.32	1	33	57	0	92	2	1	2	0	5	1	2	0	0	3	0.59	30.6
LCDC B27	0.29	0	52	33	1	86	0	3	4	3	10	1	2	0	1	4	0.15	21.5
LCDC B31	0.31	0	45	36	2	83	5	4	3	0	12	2	2	0	1	5	1.25	16.6
LCDC B39	0.26	1	37	49	0	87	1	3	3	1	8	1	2	1	1	5	0.76	17.4
LCDC B63	0.32	11	3	72	2	88	3	2	4	0	9	1	1	0	1	3	0.19	29.3
Total avg %	0.29	1.85	34	50	0.71	86	3	3	4	1	10	1	2	1	1	4	0.61	22.4

R%: Huminite;

Huminite – Tx: textinite; U: ulminite; Dh: Detrohuminite; Txu: textoulminite;

Liptinite – Sp: Sporinite; Cu: Cutinite; Rs: Resinite; Ld: Liptodetrinite;

Inertinite – df: degradofusinite; Sfu: semifusinite; idt: inertodetrinite; Fg: funginite;

TPI: tissue preservation index; = (telohuminite+semifusinite)/(detrohuminite + macrinite + inertodetrinite);

GI: Gelification index; = huminite/inertinite.

a) Huminite group:

Huminite group is the most abundant macerals in the studied coals and ranging from 82 – 92% Table 8. The most abundant maceral being ulminite and detrohuminite. In huminite group, generally ulminite/textinite are known as telohuminite. Meanwhile in the studied coal samples telohuminite and detrohuminite were dominant in huminite group, which indicated the degree of degradation and decomposition of the original peat material [63]. Detrohuminite ranges from 33 to 72% with average around 50% whilst ulminite ranges from 3 to 72%. Textinite occurrence is low in 2 samples (LCDC B4A and LCDC B39) but rather common in sample LCDC B63, whilst it is not present in other samples Table 8.

b) Liptinite group:

The analyzed samples contain significant amount of terrestrial derived liptinite macerals that range from 5 to 14 % with an average of 10% Table 8. The liptinite macerals were identified by their nature of fluorescence in ultraviolet (UV) light. The common liptinite macerals in these coals are sporinite, cutinite, resinite, and liptodetrinite. Resinite is most common and shows yellowish-green fluorescence under UV light Fig. 8a. In reflected “white” light resinite appears as dark gray granular bodies and sometimes it occurs as cell filling in ulminite Fig 8b. Sporinite also shows yellowish-green fluorescence under UV light excitation and is commonly associated with cutinite which fluoresces less intense Fig. 8a. This intense green fluorescence collaborates with the low huminite reflectance data, therefore in support of the thermally immature nature of these organic matters.

c) Inertinite group:

The analysed coal samples from Lakhra coal field also contain inertinite macerals, although low in relative abundance (3 to 5%; Table 8). Identified inertinite macerals include degradofusinite, semifusinite, inertodetrinite and funginite Fig. 8c. Macrinite was also present but rare in occurrence (<1% in the studied coals). The presence of funginite suggests some influence of degradation during deposition of the plant materials that eventually formed these coals.

5. Discussion

5.1. Quality of organic matter

In this study, the type of organic matter was interpreted based on parameters that were obtained by means of organic geochemical and petrological methods. The main parameter used is HI index. According to [27], HI of between 200 to 350 is considered as Type II/III kerogen. The studied coals average HI value is 340, thus they can be considered as Type II/III kerogen. This is interpreted based on the HI versus T_{max} and HI versus OI plots Fig. 3 a & b, which indicates that the organic matter within the studied sample is predominantly of Type II/III Kerogen. This is also in agreement with the results of pyrolysis-GC analyses as shown in the ternary diagram of Fig. 7b, which indicate that the analyzed coal samples are of a

mixture of Type II and III kerogens. The plot of Pr/n-C₁₇ versus Ph/n-C₁₈ Fig. 5b that was modified by [46] also indicates that the organic matter is of Type II/III kerogen that was deposited in a terrigenous depositional setting.

5.2. Hydrocarbon generation potential

To interpret the hydrocarbon generation potential, the classification by [55] is adopted here. The results obtained from the extracted bitumen, and yielded hydrocarbons Table 2 and Fig. 2a show that the coals have excellent generation potential, and this also agrees with the Rock-Eval parameters. The average TOC values for the Lakhra coals is 53 wt%, the average for S₂ is 180.75 and average for S₁ is 3.59 mgHC/g of rock whereby the values of these parameters indicate that the analyzed coals possess excellent hydrocarbon generation potentials. The plot of Fig. 3 c & d further corroborated that the studied coals have excellent hydrocarbon generation potential, and that they can generate significantly more gas with minor oil upon maturation.

5.3. Thermal maturity

The thermal maturity of the Lakhra coal field samples was assessed based on parameters obtained from huminite reflectance, proximate analysis, pyrolysis data and biomarker ratios.

Huminite reflectance (%Ro) of these Lakhra samples range from 0.26% to 0.32% Table 8 indicating that the coalification degree of the analyzed Lakhra coals is of lignite to sub-bituminous C rank.

The results of the proximate geochemical analysis that was carried were compared to the classification based on the ASTM [10]. The volatile matter and fixed carbon content gave higher values, which ranges from 35.44-53.07 and 26.17-47.32 Table 1. These results of the proximate analysis is in agreement with huminite reflectance of these coals i.e. lignite or transitional to sub-bituminous C coal according to ASTM classification by [64].

Production Index (S₁/S₁+S₂) values of the analysed coal samples are 0.02 Table 3. Values of the production index that are less than 0.1 and T_{max} values less than 435°C both indicate thermally immature organic matter [65]. T_{max} values of the Lakhra coals are in the range of 403-429°C, thus they are all immature. To further illustrate the maturity and kerogen type of the organic matter, an HI-Tmax diagram was plotted Fig. 3a which displayed a distribution of mixed Type III and Type II/III kerogen that falls within immature zone. T_{max} values are known to vary with maturity and kerogen type of organic matter [66], although in this case no distinct variation in maturity been displayed.

In immature coals, the dominance of long-chain n-alkanes compared with short-chain n-alkanes, are attributed to terrestrial plants in higher altitudes [63-64]. The CPI values calculated from the analyzed Lakhra coal samples range from 1 to 2.38, with most values being significantly greater than 1 thus also indicate the coals are immature Table 5. Based on GC-MS fingerprints of these Lakhra coal samples, the biomarker parameters lend further support to the immature nature of the analyzed coals. As a consequence of temperature and time of thermal reactions, some biomarkers were transformed. For example, Ts (18a(H)-22,29,30-Trisnorneohopane) is known to be more stable than Tm (17a(H)-22,29,30-Trisnorhopane) thus, the Ts/(Ts+Tm) ratio has been used as an indicator for maturity [62,65]. The Ts/(Ts+Tm) ratio calculated in this study ranges from 0.003 to 0.12, which further implies immature nature of the organic matter. The ratio of 22S/(22S+22R) for C₃₂ are between 0.2 – 0.47 Table 8, also suggesting that the analyzed samples are immature. Based on the m/z 217 mass fragmentogram, the 20S/(20S+20R) sterane and ββ/(ββ+αα) sterane ratios were determined to be 0.06 to 0.2 and 0.25 to 0.45 respectively. According to [54], if the value of 20S/(20S+20R) is equilibrium with values of ββ/(ββ+αα) which is in between the range of 0.005 – 0.2 to 0.2 – 4.5, it represents immaturity Fig 5b, 9d, thus in agreement with other maturity parameters.

5.4. Paleodepositional environment

The depositional environment during the deposition of the peat-forming communities that subsequently formed the Bara Formation coals appears to be in an oxic to sub-oxic condition.

This is as illustrated in the Pr/nC₁₇ versus Ph/nC₁₈ plot of Fig. 5b, which indicates a transitional environment and that the organic matter was mainly derived from terrigenous source dominated by Type II/III kerogen. CPI values also suggest that the analysed coals were deposited under oxic-suboxic condition and is further supported by the bimodal distribution of n-alkanes as well as by relatively low Pr/Ph ratios (1.46–2.41).

Moreover, high Tm/Ts ratio of the coals are also indicative of oxic-suboxic depositional condition [38, 56, 66-67] such as in environments within a lower delta plain or paralic settings. The presence of marine influence as indicated by the occurrence of oleanane, is an important factor in the preservation of organic matter, and thus supports a deposition within a terrestrial environment under suboxic conditions [43, 49]. Marine influence has been reported to be able to help preserve the oil potential of coaly source rocks [73]. It is most probable that marine influence may have contributed to the reasonably well-preserved nature of these Bara Formation coals and thus capable of yielding an excellent amount of extractable organic matter (EOM).

The high abundance of C₂₉ steranes also indicates dominant of terrestrially-derived organic matter that are possibly related to vascular plants [55-57]. The concentration of C₂₇, C₂₈, and C₂₉ steranes as illustrated in a ternary diagram of Fig. 7b, again, as expected, provided further support that the coals were derived from higher plants of terrestrial origin.

As was revealed in the petrographic analysis, the high amount of huminite macerals with the dominance of detrohuminite Table 8, indicates a suboxic depositional condition in peat forming mires and deposition in a waterlogged condition of a wet forest environment [74]. According to [75], detrohuminite is considered to be derived from herbaceous plants and cellulose rich wood, and from poorly preserved big woody plants.

The paleoenvironment of the coal-forming peat has also interpreted using petrographic facies based on Gelification index (GI) and tissue preservation index (TPI) as shown in Fig. 9b which in support, also indicates a deposition within a lower delta plain setting.

Table 9. Ion m/z 191 and ion m/z 217 identified peaks and abbreviation

Peak No.	Compound	Abbreviation
Ion m/z 191		
Ts	18 α (H),22,29,30-trisnorneohopane	Ts
Tm	17 α (H),22,29,30-trisnorhopane	Tm
29	17 α ,21 β (H)-norhopane	C29 hop
Oleanane	1817 α (H)-oleanane	Oleanane
31S	17 α ,21 β (H)-homohopane (22S)	C31 (22S)
31R	17 α ,21 β (H)-homohopane (22R)	C31 (22R)
32S	17 α ,21 β (H)-homohopane (22S)	C32 (22S)
32R	17 α ,21 β (H)-homohopane (22R)	C32 (22R)
33S	17 α ,21 β (H)-homohopane (22S)	C33 (22S)
33R	17 α ,21 β (H)-homohopane (22R)	C33 (22R)
Ion m/z 217		
b	13 β ,17 α (H)-diasteranes20R	Diasteranes
e	5 α ,14 α (H), 17 α (H)-steranes 20S	aaa20S
f	5 α ,14 β (H), 17 β (H)-steranes 20R	a $\beta\beta$ 20R
g	5 α ,14 β (H), 17 β (H)-steranes 20S	a $\beta\beta$ 20S
h	5 α ,14 α (H), 17 α (H)-steranes 20R	aaa20R

6. Conclusions

Organic petrological and geochemical analyses were performed on Lakhra coals of the Bara Formation. Coal rank and petroleum generation potential as well as paleoenvironment were determined and can be concluded as follows:

1. Based on parameters of Rock Eval, kerogen type (Py-GC) & GC-MS it is suggested that the kerogen of these Lakhra coals is of Type II/III. It can also be concluded that the samples are capable of generating significantly more gas and some oil during maturation process. This assumption is also supported by maceral composition as the coals are dominated by

huminite, with low to moderate amount of liptinite. Bitumen extraction (EOM and HC yields) data evaluated in relation to TOC content also indicate the analyzed Lakhra coals to possess fairly good-excellent hydrocarbon generation potential.

2. The thermal maturity assessment based on proximate and huminite reflectance analyses suggest that the Lakhra coals are thermally immature for hydrocarbon generation being of lignite to sub-bituminous C rank. In addition, the pyrolysis T_{max} data and hydrocarbon extraction yields are also in agreement that supports the immature nature of these coals.
3. The paleoenvironmental setting was interpreted as within a lower delta plain that encouraged higher land-plant growth within wet peat swamps while the occurrence of oleanane suggests a presence of marine influence and further support deposition under predominantly sub-oxic conditions. The marine influence may have enhanced the apparent oil-prone nature of these predominantly gas-prone Bara Formation coals.

Acknowledgement

We are highly thankful to Mr. Lalkhan Mastoi, an ex-Managing Director of Lakhra Coal Development company (LCDC) who help to access these remote area mines, by providing their transport with their honorable staff. We cannot forget the help we received from Mr. Ashraf Malah, a Project Director in LCDC who provide his best interest throughout this fieldtrip and during the data collection from mines.

References

- [1] Qian M, Miao X, Xu J. Green mining of coal resources harmonizing with environment. *J China Coal Soc* 2007; 32:1–7.
- [2] Elliott MA. Chemistry of coal utilization. Second supplementary volume. John Wiley and Sons, New York, NY; 1981.
- [3] Wang G, Xu Y, Ren H. Intelligent and ecological coal mining as well as clean utilization technology in China: Review and prospects. *Int J Min Sci Technol* 2019; 29:161–169.
- [4] Levine JR. Coalification: The Evolution of Coal as Source Rock and Reservoir Rock for Oil and Gas. vol. 38. AAPG Special Volumes; 1993.
- [5] Rice DD, Clayton JL, Pawlewicz MJ. Characterization of coal-derived hydrocarbons and source-rock potential of coal beds, San Juan Basin, New Mexico and Colorado, USA. *Int J Coal Geol* 1989; 13:597–626.
- [6] Wilkins RWT, George SC. Coal as a source rock for oil: a review. *Int J Coal Geol* 2002; 50:317–361.
- [7] Petersen HI, Andersen C, Anh PH, Bojesen-Koefoed JA, Nielsen LH, Nytoft HP, Rosenberg P, Thanh L. Petroleum potential of Oligocene lacustrine mudstones and coals at Dong Ho, Vietnam—an outcrop analogue to terrestrial source rocks in the greater Song Hong Basin. *J Asian Earth Sci* 2001; 19:135–154.
- [8] Khokhar Q, Solangi S, Hakro A. D, Abbasi S, Brohi I, Pathan M. Lithofacies of Bara Formation at wadi sawri nala section, northern lakhi range, southern indus basin, Pakistan. *Sindh Univ Res Journal-SURJ Sci Ser* 2014; 46.
- [9] Ghaznavi MI. An overview of coal resources of Pakistan. *GSP, Pre Publ Issue Rec Vol* 2002.
- [10] Simon FO, Khan RA, Landis ER, Hildebrand RT. Chemical and physical characterization of mine samples from Lakhra coal field, South Sind, Pakistan. *US Geological Survey*; 1987.
- [11] Malkani MS. A review of coal and water resources of Pakistan. *J Sci Technol Dev* 2012; 31:202–218.
- [12] Siddiqui I, Solangi SH, Samoon MK, Agheem MH. Preliminary studies of Cleat Fractures and Matrix Porosity in Lakhra and Thar coals, Sindh, Pakistan. *J Himal Earth Sci* 2011; 44:25–32.
- [13] Ayinla HA, Abdullah WH, Makeen YM, Abubakar MB, Jauro A, Yandoka BMS, Abidin NSZ. Petrographic and geochemical characterization of the Upper Cretaceous coal and mudstones of Gombe Formation, Gongola sub-basin, northern Benue trough Nigeria: Implication for organic matter preservation, paleodepositional environment and tectonic settings. *Int J Coal Geol* 2017; 180:67–82.
- [14] Fowler MG, Goodarzi F, Gentzis T, Brooks PW. Hydrocarbon potential of middle and upper Devonian coals from Melville Island, Arctic Canada. *Org Geochem* 1991; 17:681–694.
- [15] Hakimi MH, Abdullah WH, Sia S-G, Makeen YM. Organic geochemical and petrographic characteristics of Tertiary coals in the northwest Sarawak, Malaysia: implications for palaeoenvironmental conditions and hydrocarbon generation potential. *Mar Pet Geol* 2013; 48:31–46.
- [16] Hasiah AW. Oil-generating potential of Tertiary coals and other organic-rich sediments of the Nyalau Formation, onshore Sarawak. *J Asian Earth Sci* 1999; 17:255–267.

- [17] Williams MD. Stratigraphy of the Lower Indus Basin, West Pakistan. 5th World Petroleum Congress. World Petroleum Congress; 1959.
- [18] Jones AG, Manistre BE, Oliver RL, Willson GS, Scott HS. Reconnaissance Geology of part of West Pakistan (Colombo Plan co-operative project conducted and compiled by Hunting Survey Corporation). Gov Canada, Toronto 1960.
- [19] Ghani M., Harbour R., Landis E., Kebblish W. Geology and coal resources of the Lakhra coal field, Hyderabad area, Pakistan. US Geological Survey 1975; No. 75-553.
- [20] Williams MD. 19. Stratigraphy of the Lower Indus Basin, West Pakistan. 5th World Petroleum Congress. World Petroleum Congress; 1959.
- [21] Nuttall WLF. The larger foraminifera of the Upper Ranikot Series (Lower Eocene) of Sind, India. *Geol Mag* 1926; 63:112–121.
- [22] Vredenburg EW. Nummulites douvillei, an undescribed species from Kachh with remarks on the zonal distribution of Indian Nummulites. *Rec Geol Surv India* 1906; 34:79–95.
- [23] Vredenburg EW. A Supplement to the "Mollusca" of the Ranikot Series. Government of India Central publication branch; 1928.
- [24] Espitalié J, Laporte JL, Madec M, Marquis F, Leplat P, Paulet J, Boutefeu A. Méthode rapide de caractérisation des roches mères, de leur potentiel pétrolier et de leur degré d'évolution. *Rev l'Institut Français Du Pétrole* 1977; 32:23–42.
- [25] Dembicki Jr H, Horsfield B, Ho TTY. Source rock evaluation by pyrolysis-gas chromatography. *Am Assoc Pet Geol Bull* 1983; 67:1094–1103.
- [26] Dembicki Jr H. Three common source rock evaluation errors made by geologists during prospect or play appraisals. *Am Assoc Pet Geol Bull* 2009; 93:341–356.
- [27] Peters KE, Cassa MR. Applied source rock geochemistry: Chapter 5: Part II. Essential elements 1994.
- [28] Orem WH, Finkelman RB. Coal formation and geochemistry. vol. 7. 2003.
- [29] Othman R. Petroleum Geology of the Gunnedah-Bowen-Surat Basins, Northern New South Wales: Stratigraphy, Organic Petrology and Organic Geochemistry 2003.
- [30] Bordenave ML. Applied petroleum geochemistry. Technip Paris; 1993.
- [31] Makeen YM, Abdullah WH, Hakimi MH, Elhassan OMA. Organic geochemical characteristics of the Lower Cretaceous Abu Gabra Formation in the Great Moga oilfield, Muglad Basin, Sudan: Implications for depositional environment and oil-generation potential. *J African Earth Sci* 2015; 103:102–112.
- [32] Abbassi S, Edwards DS, George SC, Volk H, Mahlstedt N, di Primio R, Horsfield B. Petroleum potential and kinetic models for hydrocarbon generation from the Upper Cretaceous to Paleogene Latrobe Group coals and shales in the Gippsland Basin, Australia. *Org Geochem* 2016; 91:54–67.
- [33] Eglinton TI, Damsté JSS, Kohnen MEL, de Leeuw JW. Rapid estimation of the organic sulphur content of kerogens, coals and asphaltenes by pyrolysis-gas chromatography. *Fuel* 1990; 69:1394–1404.
- [34] Giraud A. Application of pyrolysis and gas chromatography to geochemical characterization of kerogen in sedimentary rock. *Am Assoc Pet Geol Bull* 1970; 54:439–455.
- [35] Larter SR, Douglas AG. A pyrolysis-gas chromatographic method for kerogen typing. *Phys Chem Earth* 1980; 12:579–583.
- [36] Alias FL, Abdullah WH, Hakimi MH, Azhar MH, Kugler RL. Organic geochemical characteristics and depositional environment of the Tertiary Tanjong Formation coals in the Pinangah area, onshore Sabah, Malaysia. *Int J Coal Geol* 2012; 104:9–21.
- [37] Farhaduzzaman M, Abdullah WH, Islam MA. Depositional environment and hydrocarbon source potential of the Permian Gondwana coals from the Barapukuria Basin, Northwest Bangladesh. *Int J Coal Geol* 2012; 90:162–179.
- [38] Larter SR, Senftle JT. Improved kerogen typing for petroleum source rock analysis. *Nature* 1985; 318:277.
- [39] Abdullah WH, Togunwa OS, Makeen YM, Hakimi MH, Mustapha KA, Baharuddin MH, Sia S-G, Tongkul F. Hydrocarbon source potential of Eocene-Miocene sequence of Western Sabah, Malaysia. *Mar Pet Geol* 2017; 83:345–361.
- [40] Grice K, Schaeffer P, Schwark L, Maxwell JR. Molecular indicators of palaeoenvironmental conditions in an immature Permian shale (Kupferschiefer, Lower Rhine Basin, north-west Germany) from free and S-bound lipids. *Org Geochem* 1996; 25:131–147.
- [41] Zunic WM, Ding S, Durig JR, Cohen AD. Pyrolysis GC/FID/FT-IR, pyrolysis GC/MS, and FT-IR studies of pore water extracts derived from peat samples differing in depositional environments. *J Mol Struct* 1992; 267:371–376.

- [42] Kaur S, Gill JP, Evershed RP, Eglinton G, Maxwell JR. Computerised gas chromatographic–mass spectrometric and high-performance liquid chromatographic analysis of sedimentary benzoporphyrins. *J Chromatogr A* 1989; 473:135–151.
- [43] Traoré M, Kaal J, Cortizas AM. Potential of pyrolysis-GC–MS molecular fingerprint as a proxy of Modern Age Iberian shipwreck wood preservation. *J Anal Appl Pyrolysis* 2017; 126:1–13.
- [44] Bray EE, Evans ED. Distribution of n-paraffins as a clue to recognition of source beds. *Geochim Cosmochim Acta* 1961; 22:2–15.
- [45] Powell TG, McKirdy DM. Relationship between ratio of pristane to phytane, crude oil composition and geological environment in Australia. *Nat Phys Sci* 1973; 243:37.
- [46] Tissot B, Deroo G, Hood A. Geochemical study of the Uinta Basin: formation of petroleum from the Green River formation. *Geochim Cosmochim Acta* 1978; 42:1469–1485.
- [47] Chandra K, Mishra CS, Samanta U, Gupta A, Mehrotra KL. Correlation of different maturity parameters in the Ahmedabad-Mehsana block of the Cambay basin. *Org Geochem* 1994; 21:313–321.
- [48] Didyk BM, Simoneit BRT, Brassell SC t, Eglinton G. Organic geochemical indicators of palaeoenvironmental conditions of sedimentation. *Nature* 1978; 272:216.
- [49] Tissot BP, Welte DH. Diagenesis, catagenesis and metagenesis of organic matter. *Petroleum Formation and Occurrence*. Springer; 1984:69–73.
- [50] Hunt JM. Generation of gas and oil from coal and other terrestrial organic matter. *Org Geochem* 1991; 17:673–680.
- [51] Ramanampisoa L, Radke M, Schaeffer RG, Littke R, Rullkötter J, Horsfield B. Organic-geochemical characterisation of sediments from the Sakoa coalfield, Madagascar. *Org Geochem* 1990; 16:235–246.
- [52] Waples DW, Machiharia T. Biomarkers for geologists 1991.
- [53] Ekweozor CM, Telnaes N. Oleanane parameter: verification by quantitative study of the biomarker occurrence in sediments of the Niger delta. *Org Geochem* 1990; 16:401–413.
- [54] El Diasty WS, Moldowan JM. The Western Desert versus Nile Delta: A comparative molecular biomarker study. *Mar Pet Geol* 2013; 46:319–334.
- [55] Peters KE, Peters KE, Walters CC, Moldowan JM. The biomarker guide. vol. 1. Cambridge university press; 2005.
- [56] Czochanska Z, Gilbert TD, Philp RP, Sheppard CM, Weston RJ, Wood TA, Woolhouse AD. Geochemical application of sterane and triterpane biomarkers to a description of oils from the Taranaki Basin in New Zealand. *Org Geochem* 1988; 12:123–135.
- [57] Huang W-Y, Meinschein WG. Sterols as ecological indicators. *Geochim Cosmochim Acta* 1979; 43:739–745.
- [58] Robinson KM. An overview of source rocks and oils in Indonesia 1987.
- [59] Karavas FA, Riediger CL, Fowler MG, Snowdon LR. Oil families in Mannville Group reservoirs of southwestern Alberta, Western Canada sedimentary basin. *Org Geochem* 1998; 29:769–784.
- [60] Gorter JD. A Marine Source Rock in the Gippsland Basin? 2001.
- [61] Liu B, Zhang G, Mao F, Liu J, Lü M. Geochemistry and origin of Upper Cretaceous oils from the Termit Basin, Niger. *J Pet Geol* 2017; 40:195–207.
- [62] Diessel CFK. On the correlation between coal facies and depositional environments. Proceeding 20th Symposium of Department Geology, University of New Castle, New South Wales. 1986:19–22.
- [63] Hackley PC, Warwick PD, Breland Jr FC. Organic petrology and coalbed gas content, Wilcox Group (Paleocene–Eocene), northern Louisiana. *Int J Coal Geol* 2007; 71:54–71.
- [64] Stach E. Stach’s textbook of coal petrology 1982.
- [65] Merrill RK. Source and migration processes and evaluation techniques 1991.
- [66] Hunt JM. *Petroleum Geochemistry and Geology*. W.H. Freeman; 1996.
- [67] Bechtel A, Sachsenhofer RF, Markic M, Gratzner R, Lücke A, Püttmann W. Paleoenvironmental implications from biomarker and stable isotope investigations on the Pliocene Velenje lignite seam (Slovenia). *Org Geochem* 2003; 34:1277–1298.
- [68] Wang T-G, Simoneit BRT. Organic geochemistry and coal petrology of Tertiary brown coal in the Zhoujing mine, Baise Basin, South China: 2. Biomarker assemblage and significance. *Fuel* 1990; 69:12–20.
- [69] Seifert WK, Moldowan JM. Applications of steranes, terpanes and monoaromatics to the maturation, migration and source of crude oils. *Geochim Cosmochim Acta* 1978; 42:77–95.

- [70] Amijaya H, Schwarzbauer J, Littke R. Organic geochemistry of the Lower Suban coal seam, South Sumatra Basin, Indonesia: palaeoecological and thermal metamorphism implications. *Org Geochem* 2006; 37:261–279.
- [71] Peters KE, Moldowan JM. *The biomarker guide: interpreting molecular fossils in petroleum and ancient sediments* 1993.
- [72] Murray AP, Sosrowidjojo IB, Alexander R, Kagi RI, Norgate CM, Summons RE. Oleananes in oils and sediments: evidence of marine influence during early diagenesis? *Geochim Cosmochim Acta* 1997; 61:1261–1276.
- [73] Sykes R, Volk H, George SC, Ahmed M, Higgs KE, Johansen PE, Snowdon LR. Marine influence helps preserve the oil potential of coaly source rocks: Eocene Mangahewa Formation, Taranaki Basin, New Zealand. *Org Geochem* 2014; 66:140–163.
- [74] Flores D. Organic facies and depositional palaeoenvironment of lignites from Rio Maior Basin (Portugal). *Int J Coal Geol* 2002; 48:181–195.
- [75] Teichmüller M. The genesis of coal from the viewpoint of coal petrology. *Int J Coal Geol* 1989; 12:1–87.

To whom correspondence should be addressed: Zain Gul, Department of Geoscience, University of Technology Petronas, Malaysia, E-mail: zaingulau@gmail.com

Developing an Expert System for Identifying Optimal Pumping Lift Based on Technical, Financial and Components Levels

Mahmoud A. Morsy*¹, Abdel-Alim H. El-Sayed²

¹ General Petroleum Company, Cairo, Egypt

² Mining, Petroleum and Metallurgy Engineering Department, Faculty of Engineering, Cairo University, Cairo, Egypt

Received June 11, 2020; Accepted September 30, 2020

Abstract

Selection of optimum artificial lift system depends basically on reservoir characteristics, fluid properties, well location and geometry, surface facilities, available logistics and feasibility studies. Insightful evaluation of these criteria improves the quality of the decision and its implications. For this large number of conflicting criteria, multi criteria decision making (MCDM) methods are used to clearly show the problem, analyze its dimensions and make optimal decisions. This paper introduces a comprehensive expert system for optimal selection of pumping lift systems based on technical, operational and financial criteria. ES includes four phases; screening inappropriate pumps, determination the components for the acceptable pumps, feasibility analysis and decision optimization. Selection is performed by using technique for order preference by similarity to ideal solution. This ES was developed specifically for the General Petroleum Company, Egypt. It can be considered as a prototype that can be developed to include comprehensively the other artificial lift techniques.

Keywords: TOPSIS; pumping lift selection; expert system; financial evaluation.

1. Introduction

Downhole pump is used to overcome the pressure losses through the conduit of the fluid from its intake to the storage facilities. It is fed by an external source of energy either mechanical, hydraulic or electrical to raise the oil to surface. Positive displacement pump captures a fixed fluid volume and force it to discharge acquiring the required pressure to be raised. While, the dynamic pumps supplies the fluid with kinetic energy which in turn turns into pressure when fluid exits the pump. The evolved pressure raises liquid to surface. Reciprocating rod pump (RRP) and progressive cavity pump (PCP) are of the most common types of downhole positive displacement pumps, while electric submersible pump (ESP) is the most common downhole dynamic pump [1].

2. Selection criteria

Table 1. Selection criteria [1]

Reservoir characteristics	Reservoir pressure, temperature, porosity, permeability, skin factor, drainage area, driving mechanism
Well conditions	Well location, geometry, tubular sizes, depth
Fluid properties	Fluid density, viscosity, composition, content of erosive materials, content of corrosive fluids.
Available logistics	Power sources, servicing equipment, technical support and experienced personnel
Production parameters	Wellhead pressure, surface-facilities pressure, pipelines geometry and condition
Financials	Outflows, including capital expenditure, maintenance, and operating costs, represent expenditures. Inflows, including sold oil revenues and equipment salvage rates, this represent returns.

Selection criteria are classified into reservoir characteristics, well conditions, fluid properties, production parameters, available logistics and financials. Table 1 represents the factors included in each of selection criteria considered in the developed ES [1].

3. Previous expert systems for artificial lift selection procedures

The ES is a computer program that mimics the ability of individuals for decision-making based on their acquired knowledge from the previous experiences. It is composed of two parts; knowledge base and inference engine. The knowledge base is a complex set of experts' knowledge and is represented in the form of "if-then" rules. The inference engine in the ES represents the perception and learning of human-being. The entered data are processed by the inference engine compared to stored knowledge to generate conclusions using logical issues [2].

Valentin *et al.* [2] developed optimal pumping unit system (OPUS). In first stage, the user is asked some questions and based on the answers. Suitability coefficients (SC) are set for each ALS option according to the knowledge base. Suitability coefficients varies between -1 (definitely eliminated option), and 1 (definitely suited option). By using the inference engine, suitability coefficients are compiled to a final result at which the pumping lift system is ranked. Then, technical and financial assessment are performed [2].

In 1994, Espin *et al.* [3] developed a software called SEDLA. It composed of three modules. Module I is a knowledge base including expertise; calculations and theoretical knowledge. Module II is specified for complete design of pump; completion and facility components. Module III provides a financial evaluation based on cost database. SEDLA simulates the experts in evaluating quantitative, qualitative parameters and production problems. Suitability coefficients are set, multiplied by weight of the criteria according to its importance and summed to be ranked.

In 1995, Heinze *et al.* [4] introduced a decision tree to select ALS concentrated on the financial evaluation. The decision tree eliminates the unaccepted options. Then, a technical evaluation is performed for the accepted options. In the last step, a financial evaluation is done to compare among the candidates by determining the net present value (NPV) [4]. Another decision tree was developed by Han-Young Park [5] to screen out the remedial unloading options for gas wells. Ratings are given depending upon a built-in table on the basis of (if) rule. Ratings are got by weight sum model (WSM) and ranked descendingly. Finally, NPV analysis is done for each pump to be ranked [5].

Alemi *et al.* [6] developed an ES for optimal artificial lift selection using a decision-making model called technique for order preference by similarity to ideal solution (TOPSIS). It is based on developing a decision matrix which includes criteria and alternatives. Ratings are filled through the cells presenting the behavior of each alternative against the criterion. The ratings are normalized by TOPSIS model and ideal solution is determined. The ideal solution is an imaginary solution that involves the best values for whole selection criteria. Separation distance of each alternative from the ideal solution is determined. Ranking is performed based on the separation distance from the ideal solution representing the optimal selection. Fatahi *et al.* [7] compared these results to those got by another MCDM method; ELECTRE [7].

Ounsaki *et al.* [8] use machine learning technology to develop a promising tool furnishing the artificial lift selection to adopt the dynamic conditions of matured oil fields. The model is constructed on the patterns and relationships between the inputs, field data, and the outputs (ALS selection). Around 30,000 samples of different production systems were used to build the model. Seventeen attributes are considered in selections [8].

4. Developed multi criteria decision making (MCDM)

As mentioned before, decision-making is a cognitive process resulting in selecting a certain way for action or statement towards situation among several possible options considering desired goals and beliefs appropriate to the decision makers' minds. Critical and complex problems involves both multiple conflicting criteria presented in different units of measurements, and several alternatives to review and take a decision among them. For problems involving uncertainty, complexity and high risk consequences, multi-criteria decision-making (MCDM) methods are developed. MCDM methods are classified into three groups. The priority

method is based on simple numerical analysis for the alternatives depending mainly on the priorities of this criteria while selection, such as weighted sum method (WSM). The distance methods are based on determination of the nearest alternative to the ideal solution, such as technique for order preference by similarity to an ideal solution (TOPSIS). The outranking methods are based on pairwise comparisons among alternatives, such as Elimination Et Choix Traduisant La REalite (ELECTRE) [6-7].

4.1. Technique for order preference by similarity to an ideal solution (TOPSIS)

TOPSIS is based on building a (m × n) matrix in which rows are the alternatives (m) and columns are the criteria (n). It is based on the following steps to determine the best alternative:

1. Normalize each value in the matrix. Find squared alternative responses towards the different criteria (a_{ij}). Then, find the sum of the squared responses for all alternatives for the same criterion. At that juncture, find the square root for this sum, roughly "X_j" for each criterion, Eq. (1). Finally, find the division of each alternative response by "X_j", Eq.(2).

$$X_j = \sqrt{\sum_{i=1}^m (a_{ij})^2} \tag{1}$$

$$r_{ij} = \frac{a_{ij}}{X_j}, \text{ for } i = 1,2,3, \dots, m \tag{2}$$

2. Find t_{ij} using Eq. (3).

$$t_{ij} = r_{ij} * w_j \tag{3}$$

3. Identify the negative-ideal and positive-ideal solutions. For each criterion, the negative-ideal solution t_{worst} is the one with the worst value of (t_{ij}) for all alternatives. While, the ideal solution t_{best} is the one with the best value of (t_{ij}) for all alternatives.
4. For each alternative, find the separation measures between its response and both ideal (S_i^{*}) and negative-ideal (S_i⁻) solutions by Eq. (4 and 5):

$$S_i^* = \sqrt{\sum_{j=1}^n (t_{ij} - t_{best})^2} \tag{4}$$

$$S_i^- = \sqrt{\sum_{j=1}^n (t_{ij} - t_{worst})^2} \tag{5}$$

5. Find for each alternative the relative closeness, C_i, to the ideal solution by Eq. (6 :

$$C_i = \frac{S_i^-}{S_i^- + S_i^*} \tag{6}$$

6. As C_i closes to 0, alternative closes to the positive-ideal solution. Rank the alternatives according to C_i, from the smaller value to the largest one [6].

5. Methodology

The ES is developed to determine the optimal pumping-lift system by analyzing user’s inputs according to a pre-configured database. The research methodology consists of three main parts:

5.1. Optimization problem model

In mathematics, an optimization problem is the problem of finding the best solution from all feasible solutions. The problem model consists of three parts; the design variables, the objective function and the set of constraints. Thus, in order to select pump lift system, design variables used are the criteria that influence selection. Furthermore, it was decided that the objective function is the TOPSIS model and the set of constraints would be the mechanical limits for all pump lift systems (PLSs).

Pumping-lift selection is classified as a multiple objectives optimization problem. This is because multiple criteria are contributed to the selection of optimal PLS. It is challenging to choose a system that satisfies all the criteria. Therefore, TOPSIS decision making method is nominated to reformulate this multiple objectives problem into a single objective problem. TOPSIS-single objective model-is used to determine the closest alternative to the best solution

Twenty-four discrete design variables influence optimal pump selection are given in Table 2. The objective function is TOPSIS alternative closeness to the ideal solution (C_i), Eq. (6). Optimal selection is achieved based on the results of the objective function, where the closest to the positive-ideal solution is the most appropriate choice. The set of constraints for pumps are shown in Table 2.

Table 2. Design variables influencing PLS optimization problem

1. Well Location	2. Gas Liquid Ratio	3. Paraffin Production
4. Measured Pump Depth	5. Aromatics Production	6. Staff Experience
7. Well Deviation	8. Emulsion Production	9. Available Prime Mover
10. Casing Diameter	11. Scale Production	12. Available Servicing Type
13. Dogleg Severity	14. Corrosive Fluid Production	15. PLS Flexibility
16. Desired Gross Rate	17. Fluid Viscosity	18. PLS Reliability
19. Productivity Index	20. Oil Gravity	21. System Efficiency
22. Bottomhole Temperature	23. Abrasives Production	24. Net Present Value

Table 3. PLS screening criteria & mechanical limits

Criteria	RRP	PCP	ESP
Operating vertical depth (ft.)	100 – 16000	2000 – 6000	1000 – 15000
Typical operating rate (BPD)	5 – 5000	5 – 4500	200 – 30000
Operating temperature (° F)	100 – 550	75 – 250	100 – 400
Corrosion handling	Good to Excellent	Fair	Good
Gas handling	Fair to good	Good	Poor to Fair
Solids handling	Fair to Good	Excellent	Poor to Fair
Oil Gravity (°API)	> 8	< 35	> 10
Prime mover	Gas or Electricity	Gas or Electricity	Electricity
Offshore application	Limited	Good	Excellent
Overall system efficiency (%)	45 - 60	45 - 70	35 - 60

5.2. Developed algorithm calculations and database

Developed ES utilizes the basic API calculations, rules of thumb and practice recommendations by GPC engineers to determine the PLSs’ equipment. Database is divided into two main parts; experts’ pump recommendations towards each criteria and equipment list. The entered equipment list is that of current contracts between GPC and vendors. Both experts’ recommendations and equipment list can be modified according to any new developments.

5.3. Phases of the developed ES

Developed ES includes four phases; screening, components selection, financial analysis and PLS optimization decision. Developed ES flowchart is shown in Fig.1.

Technical screening has two stages. The first stage is categorization of the inputs according to Table 4. Categories were determined by taking into account the pumps’ mechanical limits, the experts’ recommendations of choosing PLS and the opinions of the engineers at the GPC. The second stage is to evaluate the performance of each pump for each criterion and rate it from 1 to 5. Pump preferences ratings can be modified according to the admin-users.

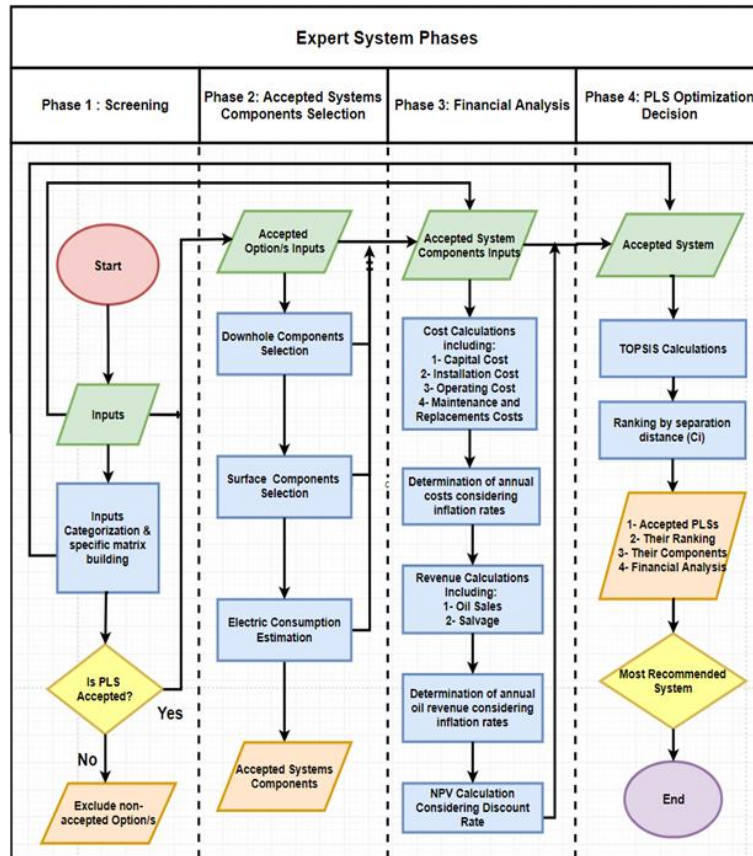


Fig. 1. Developed ES flow diagram

Table 4. Criteria and categories

Criteria	Sub-criteria	
1)	Well location	Onshore, offshore, urban
2)	Well measured depth	Shallow well (<4500 ft.), Intermediate well (4500-6000 ft.), Deep well (6000 to 10000 ft.), Extremely Deep well (>10000 ft.)
3)	Production casing diameter	Conventional, Slim (<6 in.)
4)	Well profile	Vertical (0-20o), Deviated (20-50o), Highly deviated (50-80o), Horizontal (80-90o), Extended reach (80-90o)
5)	Productivity Index	<0.5 bpd/psi, >0.5 bpd/psi
6)	Anticipated gross rate	<200 bpd, 200-1500 bpd, 1500-4500 bpd, >4500 bpd
7)	Dogleg severity	<6 deg. /100 ft., 6-15 deg. /100 ft.
8)	Well temp.	<150 F deg., 150-250 F deg., 250-400 F deg., >400 F deg.
9)	Fluid Viscosity	<200 cp, 200-500 cp, >500 cp
10)	Abrasive solids Production	No or Minor prod. (<0.01%), Moderate (0.01 - 0.1%), Severe (0.1 - 3%), Extremely severe (>3%)
11)	Corrosives production	No Production, Minor, Moderate, Severe
12)	Aromatics production	No or minor production, Moderate, Severe
13)	Emulsion Production	Yes, No
14)	Scale Production	Yes, No
15)	Paraffin production	Yes, No
16)	Fluid API	<15 deg., 15-35 deg., >35 deg.
17)	Gas Liquid Ratio	<500 scf/stb, 500-2000 scf/stb, 2000-3000 scf/stb
18)	Prime mover	Gas engine, Diesel engine, Electric motor or feeder
19)	Staff Experience	Poor, Intermediate, Expertise
20)	Servicing availability	Pulling Unit, Workover Rig, Both

The PLS flexibility, reliability and system efficiency are constants and set according to Table 5. Consequently, any ratings of 1 for any criterion are reflected of pump refusal and screened out the evaluation.

Table 5. PLS flexibility, reliability and system efficiency ratings [9]

Criteria	ESP	PCP	ESPCP	RRP
PLS Flexibility	3	4	3	5
PLS Reliability	3	3	3	5
System Efficiency	55%	60%	60%	50%

Next, both surface and downhole components for acceptable pumps are selected from the database previously entered from GPC's current contract catalogs. The database of pump components are flexibly modified according to available contracts. Financially, revenues and expenditures are determined through the evaluation period and are restored to present to find the net present value (NPV) for each of the accepted pumps.

A specific-case matrix is built which dimensions are $m \times n$, where m is the specified categories by phase 1-step 1, and n is the accepted pumps ratings for each criterion. NPV is also added to the built matrix. TOPSIS is performed to determine the most optimal alternative according to both technical and financial criteria. The rankings of accepted pumps are determined according to the relative separation from the positive ideal solution (C_i).

Two windows are built; one for the admin and the other for the user. The admin's window includes the database of pumps components, experts' preferences and criteria of selection. The user's window is a friendly interface asking the user to enter the required inputs to proceed the ES phases.

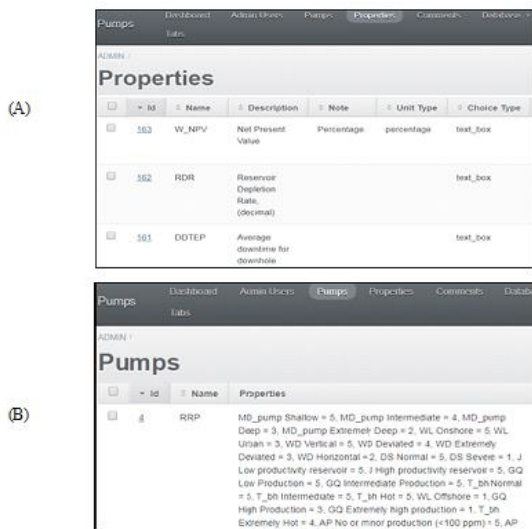


Fig. 2. Admin's window, (A) properties tab & (B) pump preferences

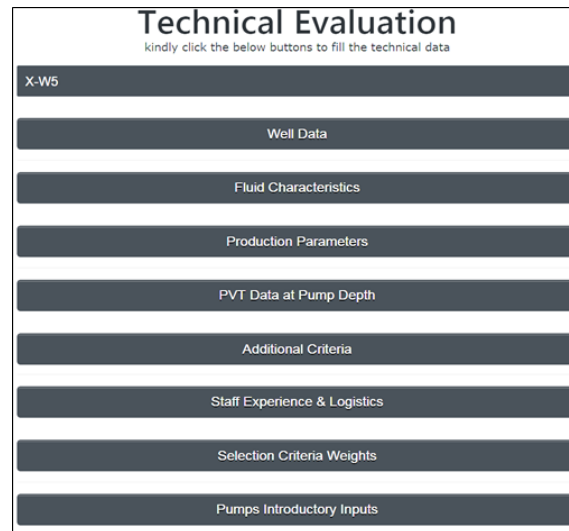


Fig. 3. User's window

Full Assessment For Pumping Lift Systems for X-47 in 2019-07-10					
Phase one : Technical Screening					
	Abb.	ESPCP	ESP	RRP	PCP
Well Location	WL	5	5	5	5
Measured Pump Well	MD_pum	4	4	4	4
Well Deviation	WD	5	5	3	1
Casing Diameter	CSG_ND	5	5	5	5
Dogleg Severity	DS	5	5	5	5
Desired Gross Rate	GQ	4	5	5	4
Productivity Index	J	5	5	5	5

Fig. 4. Sample of phase 1 results

Phase 2 : Components Determination					
Surface Equipment :					
Pumping Unit Designation	C	320	256	144	
NEMA D Motor	150	HP			
Downhole Equipment :					
1-Rod-Characteristics					
Rod Size :		77			
NO. Rods for each size :					
6/8 "		0			
7/8 "		205			
1 "		0			
1 1/8"		0			
Rod Type (Weatherford Nomenclature) :					
		KD			
2-Downhole Pump -Characteristics					
Pump Designation :	30	375	T	HC	20 6 0
Pump Service Material : Corrosive Service					

Fig. 5. Sample of phase 2 results

Phase 3 : Financial Evaluation					
Years	0-1	1-2	2-3	3-4	4-5
Cashflows	1	2	3	4	5
Capital Cost	65684	0	0	0	0
Installation Cost	14500	0	0	0	0
M. & R. Costs per Cashflow	24634				
M.& R. Costs Change Rate (%)	10				
M. & R. Costs After Change Rate	24634	27097	29807	32787	36066
Annual M. & R. After Change Rate	30078				
Operating Cost	1195898				
Operating Cost Change Rate (%)	7				
Operating Cost After Change Rate	1195898	1279611	1369184	1465027	1567578
Annual Operating Cost After Change Rate	1375460				
Salvage Cost After Project Assessment	0	0	0	0	47726
Oil Production Sales	21732000				
Reservoir Depletion Rate (%)	2				
Oil Prices Change Rate (%)	3				
Oil Production Sales After Change Rate	21732000	21936281	22142482	22350622	22560718
Inflow After Rates Of Change	21732000	21936281	22142482	22350622	22608443

Fig. 6. Sample of phase 3 results

Phase 4 : Decision Optimization				
	Abb.	ESPCP	ESP	RRP
Well Location	WL	5	5	5
Measured Pump Well Depth	MD_pump	4	4	4
Well Deviation	WD	5	5	3
Casing Diameter	CSG_ND	5	5	5
Dogleg Severity	DS	5	5	5
Desired Gross Rate	GQ	4	5	5
Productivity Index	J	5	5	5
Bottomhole Temperature	T_bh	4	5	5
Fluid Viscosity	meo_m	5	5	5
Oil Gravity	API	5	5	5
Abrasives Production	AP	5	3	3
Corrosive Fluid Production	CP	3	4	5
Aromatic's Production	ARP	5	5	5
Emulsion Production	EP	5	5	5
Scale Production	SP	5	5	5
Paraffin Production	PP	5	5	5
Gas Liquid Ratio	GLR	5	5	5
Available Prime mover	APM	5	5	5
Staff Experience	SE	2	4	5
Available Servicing type	AST	5	5	5
PLS Flexibility	PF	3	3	5
PLS Reliability	PR	3	3	5
System Efficiency	SE	5	4	3
Net Present Value	NPV	93166021	93871488	89309730
Positive Separation	positiveSep	0.021	0.019	0.022
Negative Separation	negativeSep	0.021	0.019	0.021
ci	ci	0.507	0.501	0.490

The most optimized PLS is : RRP

Fig. 7. Sample of phase 4 results

6. Results validation and discussion

Validating the results of the developed ES takes two main axes. The first is for phase 2, where the results were compared with the results of another approved PLS programs provided by the contracted vendors. The second is for phase 4, where the results are compared with the selections done by GPC for well-designed cases.

Developed ES is applied on 38 wells. Only 13 wells are operating with the optimal PLS. In addition, 16 wells are operated by one of the recommended PLS, but not the most optimal one. Five wells were modified their PLSs. Economically, operating costs were reduced slightly, but the mean time between failures increased which reduced the costs for reproducing the well.

The remaining 9 wells are operating with non-recommended PLSs according to the developed ES. Actually, these 9 wells were nominated to change their PLSs. Changing their PLSs contributes significantly in reducing the well interventions and in magnifying the wells' productivities.

7. Conclusions

Developed ES shows reliable PLS selections when compared to real applications which are well designed. Some wells have very close ES results for multiple PLSs. By practice, it is concluded that we can use any of these alternatives with no issues according to availability and the NPV of each PLS when comparing.

Developed ES show single alternative to be used in some cases from phase 1. Only phase 2 should be performed to determine the components of this system. Using of the developed ES can replace buying of expensive PLS design software licenses and can eliminate probable human errors associated hand calculations.

Acknowledgment

I would like to express my special thanks of gratitude to my supervisor Prof. Dr. Abdel-Alim Hashem El-Sayed for his supervision and encouragement during this research. Many thanks to GPC management and employees who kindly helped me to get through all the administrative procedures during the thesis. Finally, I take the opportunity to express a deep sense of gratitude to all those who have supported me, especially my mother, in my life to get to what I have reached now, and I promise them that I will do my best to be in the position they once expected me.

Nomenclature

ALS	Artificial lift system
API	American petroleum institute
BPD	Barrels per day
C_i	Relative closeness
ELECTRE	Elimination Et Choix Traduisant La REalite
ES	Expert system
ESP	Electric submersible pump
$^{\circ}F$	Degree Fahrenheit
MCDM	Multiple criteria decision making
NPV	Net present value
OPUS	Optimal pumping unit system
PCP	Progressive cavity pump
PLS	Pumping lift system
RRP	Reciprocating rod pump
SC	Suitability coefficient
TOPSIS	Technique for order preference by similarity to an ideal solution
WSM	Weighted sum method

References

- [1] Lake LW, and Clegg JD. Petroleum Engineering Handbook, Vol. 4, Production Operations Engineering, Texas: Society of Petroleum Engineers, 2007.
- [2] Valentin EP, and Hoffman FC. OPUS: An Expert Advisor for Artificial Lift. in 63rd Annual Technical Conference and Exhibition of SPE, Houston, 1988.
- [3] Espin DA, Gasbarri S, and Chacin JE. Expert System for Selection of Optimum Artificial Lift Method. in Latin American/ Caribbean Petroleum Engineering Conference, Buenos Aires, 1994.
- [4] Heinze LR, and Winkler HW. Decision Tree for Selection of Artificial Lift Method. SPE 29510, in Production Operations Symposium, Oklahoma, 1995.
- [5] Park HY. Decision Matrix for Liquid Loading in Gas Wells for Cost/Benefit Analysis of Lifting Options. Texas: Texas A&M University, 2008.
- [6] Alemi M, Jalalifar H, Kamali G, and Kalbasi M. A prediction to the best artificial lift method selection on the basis of TOPSIS model. Journal of Petroleum and Gas Engineering, 2010; 1(1): 009-015, 2010.
- [7] Fatahi E, Jalalifar H, Pourafshari P, and Moradi B. Selection of the Best Artificial Lift Method for One of the Iranian Oil Field Using Multiple Attribute Decision Making Methods. International Journal of Engineering and Technology, 2012; 2(2): 188-193.
- [8] Ounsakul T, Sirirattanachatchawan T, Pattarachupong W, Yokart Y, and Ekkawong P. Artificial Lift Selection Using Machine Learning. IPTC-19423-MS, in International Petroleum Technology Conference, Beijing, 2019.
- [9] Morsy MA. Developing an Expert System for Identifying Optimal Pumping Lift Based on Technical, Financial and Components Levels, Cairo: Cairo University, 2020.

To whom correspondence should be addressed: Mahmoud A. Morsy, General Petroleum Company, Cairo, Egypt, E-mail: mahmoudmorsi10@gmail.com

Modeling of Zeoforming Process Variables Using GMDH Neural Network on Pilot Scale Experiments

Saeed Soltanali, Reza Seif Mohaddecy, Maryam Mashayekhi, Mehdi Rashidzadeh

Catalysis Technologies Development Division, Research Institute of Petroleum Industry (RIPI), Tehran, Iran

Received June 28, 2020; Accepted October 15, 2020

Abstract

In this paper, the group method of data handling (GMDH) networks are applied for modeling the momentous process variables of a bench scale zeoforming. The proposed model can predict the product research octane number (RON), benzene content in the product, liquid recovery (%), coke deposition (%) on the catalyst and sulfur removal conversion (%) by using a grand polynomial correlation which is a function of weight hourly space velocity (WHSV), reactor inlet temperature and reactor pressure. To do such a task, twelve experiments were performed in the bench scale pilot for 1,400 hours. Then, modeling were done by GMDH software.

The results showed that this model can precisely estimate the process variables and product properties. Moreover, it is confirmed that the proposed model is capable of predicting of the product research octane number (RON), benzene content in product, liquid recovery (%), coke deposition(%) on the catalyst and sulfur removal conversion (%) with the average absolute deviation (AAD%) of 0.29% , 0.33%, 0.41%, 0.28% and 3.2% respectively. Moreover, the root means square error (RMSE %) of the mentioned parameters are 0.34%, 0.41%, 0.64%, 0.41% and 3.4%, respectively.

Keywords: Modeling; GMDH; Neural network; Zeoforming; RON; Liquid recovery; Sulfur removal conversion.

1. Introduction

Like typical catalytic reforming, the Zeoforming process converts low-octane hydrocarbons into high-octane gasoline components. *n*-Alkanes are transformed mainly into aromatic hydrocarbons via recombination of olefins formed as a intermediate phase whereas the conversion of *iso*-alkanes and naphthenes takes place on a limited scale [1-2]. In this way the formation of aromatic rings is possible from *n*-pentane and other light *n*-alkanes as well as from *n*-hexane or higher. The Zeoforming process runs with an endothermic heat effect in the presence of catalyst consisting of hydrogen form of zeolite ZSM-5 and a binder Al₂O₃. Contrary to typical reforming [3-8], where the dehydrogenation of naphthenes and dehydrocyclization of *n*-paraffins are the dominating reactions, practically no hydrogen is produced and light hydrocarbons are main by-products only. The Zeoforming process was first developed in the Institute of Catalysis Zeosit in Novosibirsk, Russia and it was investigated on a pilot plant in 1987–1992 [1-2].

On the other hand, developing a black box model, which is exclusively obtained from experimental data, can provide other practical methods in the field of process modeling. These models provide a dynamic relationship between input and output variables and bypass underlying complexity inside the system. Most of these common approaches rely on linear system identification models. The major processes found in chemical engineering are unfortunately nonlinear processes, and previously mentioned approaches fail to respond regarding process nonlinearity. As an alternative to fundamental models, artificial neural networks (ANNs) are a valuable estimate tool, and up to now, numerous applications of ANN models in the engineering area have been reported [9]. ANN can perform better than regression models, and is tolerant to noise in data [10-13]. The increased importance of ANNs arises from their possibility to parallel process of data despite their components are independent of each other [14]. On the

other hand, straightforward theories do not offer adequate precision for estimation of experimental data.

However, ANN's structure contains a massive complicated of equations within its nodes and layers. Furthermore, the arrangement of network is chosen manually or randomly which does not assure the best possible network. As a better alternative, the group method of data handling (GMDH) provides a self-organizing neural network to express the genome of system as well as using the most suitable configuration by means of minimization process. In the other word, the GMDH utilizes feed-forward network whose coefficients are determined using regression together with imitation of self-organizing activity [15]. The algorithm chooses the most suitable polynomial expressions built by combination of two independent variables at a time.

Some artificial neural network models have been developed in the literatures to predict and control parameters in industrial processes such as catalytic reforming unit [16-17]. But based on our literature review, there is no study on using GMDH to model the Zeoforming process. Therefore, the present study is devoted to model the RON of the product, benzene content in product, liquid recovery (%), coke deposition(%) on the catalyst and sulfur removal conversion using GMDH for a pilot scale test of Zeoforming process. To validate the proposed model, several tests were performed with different operating conditions in the Zeoforming pilot plant (about 1440 hrs).

2. Materials and methods

2.1 Process description of the industrial scale Zeoforming unit

A block flow diagram of the industrial scale zeoforming unit is presented in Figure 1.

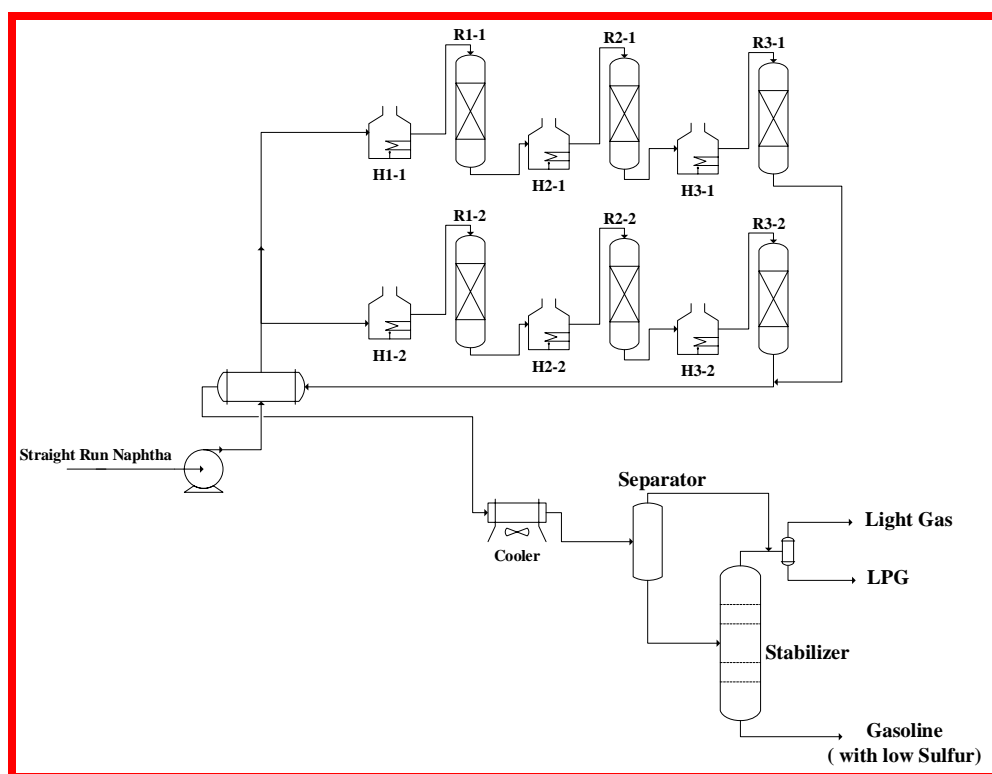


Figure 1. Block flow diagram of the industrial scale Zeoforming unit

The Zeoforming plant has been producing unleaded gasoline component during the last few years. In the conventional Zeoforming plant there are two lines of reactors work alternatively. Both lines consist of three reactors. Each line of reactors works during 7-10 days and then the catalyst is regenerated. The total time of the catalyst work is about one and a half year.

2.2. Experiments in the pilot scale system

The experiments were carried out in a pilot test system, which is licensed by the Research Institute of Petroleum Industry (RIPI). This device can tolerate temperatures and pressures up to 500°C and 70 bar, respectively. The simplified diagram of pilot scale is presented in Figure 2. As can be seen, the temperature along the reactor bed is controlled by use of three thermocouples (TIC 1-3).

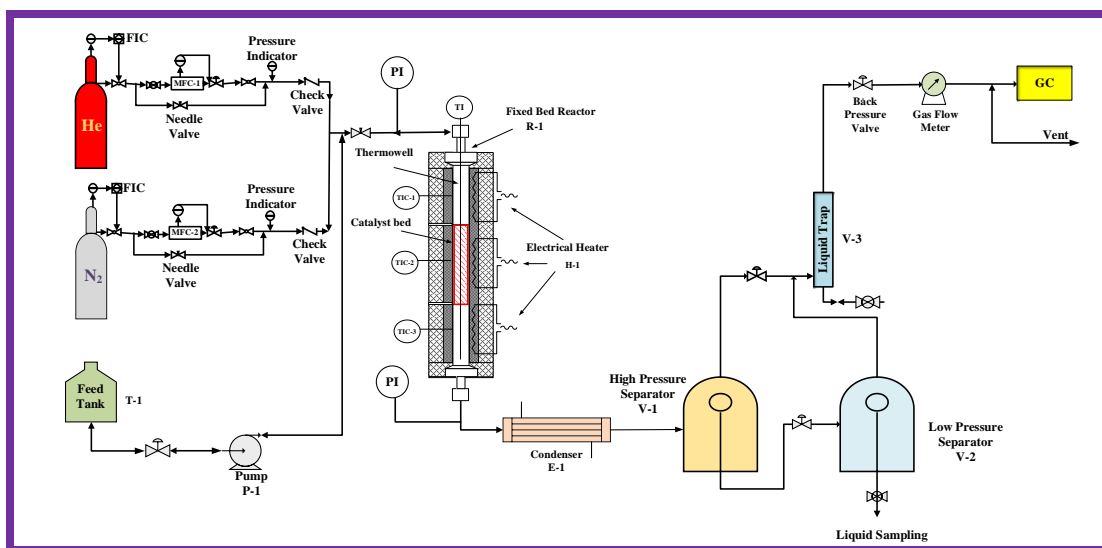


Fig. 2. Schematic diagram of the experimental Zeoforming unit

As can be seen, the feedstock is pumped from the reservoir (T-1) using a piston pump (P-1) to the top of the reactor. Helium and nitrogen gas for purging are sent from their cylinders to the top of the reactor, the flow rate being controlled by mass flow controllers (MFC-1). The unit consists of a stainless steel reactor (internal diameter of 2.2 cm and length of 51 cm), kept at isothermal condition using a three-zone electric furnace. In the reactor inlet, the temperature of inlet feedstock increases to the reaction temperature using the preheating zone of the reactor (zone-1). Reactions are carried out at the following conditions: Temperature of 300-440°C; Pressure of 5-20 bar and WHSV of 1-4. As mentioned, through the bed, there are three thermocouples to control the bed temperature. At the reactor outlet, the reaction effluent is cooled using a water-cooled heat exchanger (E-1). Then, the vapor and liquid phases are separated in a high and low pressure separators (V-1, V-2). After reducing the pressure, the liquid is allowed to flow from the separator to the other flash drum, maintained at atmospheric pressure. The liquid sample is discharged discontinuously into sampling bottles. Finally, the output of gas flow rate was metered by gas-meter and composition of the this stream is determined using an online gas chromatograph (Agilent 8790-A).

The operation conditions for the catalytic activity testing in the pilot and products specifications are shown in Tables 1 and 2.

Table 1. Operation conditions of pilot testing

No.	WHSV h ⁻¹	T Units °C	P bar	No.	WHSV h ⁻¹	T Units °C	P bar
1	1.22	358	5	7	3.61	361	15
2	1.02	400	10	8	3.5	402	5
3	1.2	440	15	9	3.52	440	10
4	2.35	360	10	10	4.02	314	20
5	2.33	400	15	11	3.9	340	17.7
6	2.31	434	5	12	3.01	355	12.5

Table 2. Pilot test products specification

No.	Liquid recovery	Octane number	Coke Deposition	S Conversion	Benzene content
	Units				
	vol /vol	-	%wt	%	%wt
1	55	83.3	1.5	93.3	3.4
2	56	82.7	21.0	39.5	3.9
3	39	67.9	38.0	16.7	8.1
4	71	82.5	9.9	66.7	2.3
5	70	80.4	22.5	39.5	2.0
6	52	85.7	35.0	23.3	4.5
7	82	80.8	2.1	64.3	1.4
8	79	81.9	12.2	69.5	2.0
9	46	84.1	31.8	7.1	4.7
10	84	78.9	8.2	95.7	1.0
11	93	80.7	6.0	48.2	0.8
12	80	80.6	4.2	71.7	2.5

3. GMDH modeling approach for the Zeoforming pilot scale experiments

The basic structure of the brain has been widely employed for various fields such as modeling, control, and pattern recognition. The GMDH, introduced by Ivakhnenko [18], is a hierarchical and learning network structure that provides an effective approach to identify higher order non-linear systems. Its main purpose is the identification of relations in large complex non-linear multidimensional systems as well as their approximation and prediction. In the GMDH network, the part which corresponds to the neuron of a neural network is called the "N-Adaline", and is generally expressed by a polynomial. The N-Adaline is composed of two inputs and one output, and the latter is generated by combinations of two inputs [19]. Inputs, x_i and x_j , are then combined to produce a partial descriptor based on the simple quadratic transfer function as the following:

$$\hat{y}_n = a_0 + a_1x_{i_n} + a_2x_{j_n} + a_3x_{i_n}x_{j_n} + a_4x_{i_n}^2 + a_5x_{j_n}^2 \tag{1}$$

where \hat{y}_n is determined using the least squares method, and coefficients i.e. a_0 to a_5 are determined statistically, and are unique for each transfer function. These coefficients can be thought as analogous to weights found in other types of neural networks. The GMDH topology is usually determined using a layer by layer pruning process based on a pre-selected criterion of what constitutes the best nodes at each level. The traditional GMDH method is based on an underlying assumption that data can be modeled by using an approximation of the Volterra series or Kolmogorov-Gabor polynomial as follows:

$$y = a_0 + \sum_{i=1}^M a_i x_i + \sum_{i=1}^M \sum_{j=1}^M a_{ij} x_i x_j + \sum_{i=1}^M \sum_{j=1}^M \sum_{k=1}^M a_{ijk} x_i x_j x_k \dots \tag{2}$$

where $X (x_1, x_2, \dots, x_M)$ is the vector of input variables, and $A (a_1, a_2, \dots, a_M)$ is the vector of summand coefficients [19].

During constructing GMDH, all combinations of inputs are generated, and sent into the first layer of the network. Outputs from this layer are then classified and selected as input for the next layer with all combinations of the selected outputs, sent into the layer 2. This process is continued as long as each subsequent layer (n+1) produces a better result than layer (n). When layer (n+1) is found to not be as good as layer (n), the process will be stopped. Now, each layer consists of nodes that a pair of inputs is its source.

In GMDH topology, each node produces a set of coefficients (a_i & $i \in \{1,2,3,\dots,5\}$) that are estimated by using training data. Then, the fitness is tested by evaluating the mean square error of the modeled (\hat{y}) and actual (pilot data) (y) values as follows:

$$Error = \sum_{n=1}^N (\hat{y}_n - y_n)^2 \tag{3}$$

To identify the coefficients with the best fit, the partial derivatives of Eq.(3) are calculated with respect to each constant value a_i , and set it equal to zero as follows:

$$\frac{\partial Error}{\partial a_i} = 0 \tag{4}$$

Finally, to compare the modeled and actual values, average absolute deviations (AAD%) and root mean squared error (RMSE) are calculated as follows:

$$ADD\% = \frac{\sum_{i=1}^{N_t=50} \left| \frac{Y_i^{Actual} - Y_i^{modeled}}{Y_i^{Actual}} \right|}{N_t} \tag{5}$$

$$RMSE\% = \sqrt{\frac{\sum_{i=1}^{N_t=50} \left(\frac{Y_i^{Actual} - Y_i^{modeled}}{Y_i^{Actual}} \right)^2}{N_t}} \tag{6}$$

where N_t , Y_i^{actual} , $Y_i^{modeled}$ are the number of test runs, actual variables, and the modeled values.

4. Results and discussion

To build up the GMDH model for the Zeoforming pilot plant, as previous mentioned fourteen test runs with specific operating condition about 1400 hours have been done. These points were included of product research octane number (RON), benzene content in product, liquid recovery (%), coke deposition (%) on the catalyst, sulfur removal conversion (%), temperatures of reactor, Weight hourly space velocity (WHSV), reactor pressure. The corresponding polynomial equations of the proposed models for the growth period are presented in Table 3 to 7. Figures 3 to 7 show the comparison between the measured output variables (pilot data) and the modeled ones using the GMDH network. From these figures, a reasonable agreement can be observed.

Table 3. Nodal expressions for GMDH neural network of product RON

$$\begin{aligned} RON &= 49.025 + A^2 * B * 5.9819e-05 \\ A &= -1412.42 + T * 6.63879 - T * D^2 * 0.0011457 - T^2 * 0.0155909 + T^2 * D * 0.000207261 + ^2 * 0.25228 \\ B &= 70.918 - T * 4.01667 + T * C * 0.0978574 - T * C^2 * 0.000591001 \\ C &= 88.868 - T^2 * P * 4.82775e-06 \\ D &= 199.971 - WHSV * 181.677 + WHSV * T * 0.476092 + WHSV^2 * 30.7452 - WHSV^2 * T * 0.0806093 - T^2 * 0.000805396 \end{aligned}$$

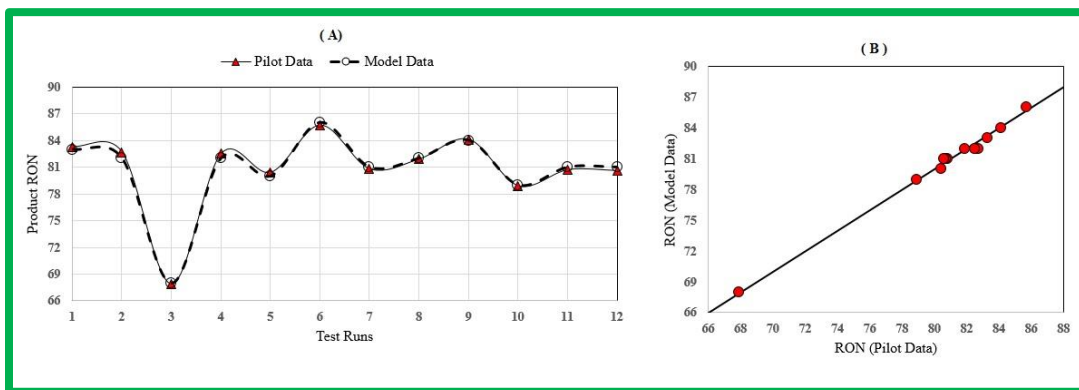


Figure 3. Comparison plots: A) pilot product RON vs. modeled and B) pilot RON product vs. modeled

Table 4. Nodal expressions for GMDH neural network of benzene content in product

$$\begin{aligned} \text{Benzene content} &= 2.44239 + A * 1.4666 - A * B^2 * 0.0383337 + A^2 * B * 0.00157376 - B * 2.64507 + B^2 * 0.535629 \\ A &= 15.2436 - WHSV * 3.56789 + WHSV^2 * C * 0.248011 - C * 4.63411 + C^2 * 0.555185 \\ B &= 4.36356 - P * D * 0.175582 + P * D^2 * 0.0362233 \\ C &= -7.74906 + WHSV * 3.7904 - WHSV * T * 0.0119091 + T^2 * 8.51803e-05 \\ D &= 4.56679 - WHSV * P * 0.121769 + P^2 * 0.015789 \end{aligned}$$

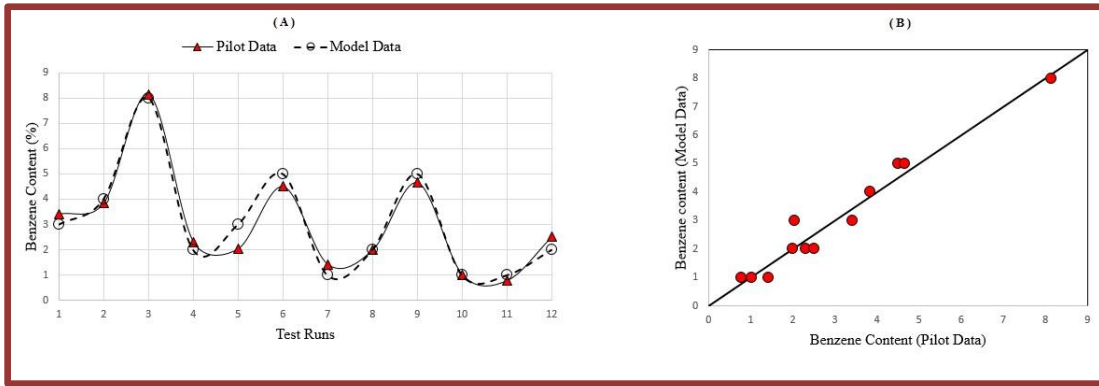


Figure 4. Comparison plots: A) Pilot benzene content in product vs. model data and B) Pilot benzene content in product vs. modeled

Table 5. Nodal expressions for GMDH neural network of coke deposition % on the catalyst

$$\begin{aligned} \text{Coke Deposition} &= -3.32288\text{e-}13 + A*1 \\ A &= -1.66955 - \text{WHSV} * B^2 * 0.00282549 + B * 1.27244 \\ B &= 360.994 - T * 2.10261 + T^2 * 0.00310333 \end{aligned}$$

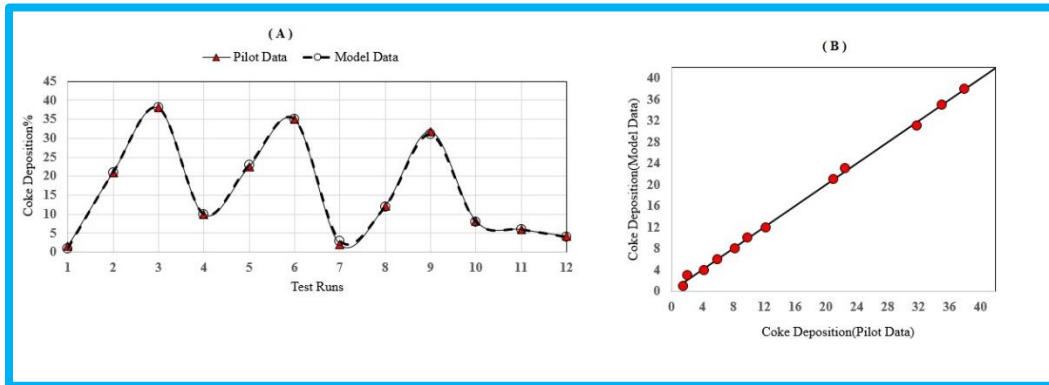


Figure 5. Comparison plots: A) Pilot coke deposition content on the catalyst vs. model data and B) Pilot coke deposition content on the catalyst vs. modeled.

Table 6. Nodal expressions for GMDH neural network of coke deposition % on the catalyst

$$\begin{aligned} \text{Liquid recovery \%} &= -76.1252 + B * A^2 * 0.000764728 - B^2 * A * 0.000422058 + A^4 * 9.90851 - A^2 * 0.0645144 \\ A &= -26.7678 + \text{WHSV} * B * 0.159235 - \text{WHSV}^2 * 1.68632 + B * 1.94443 - B^2 * 0.011157 \\ B &= -843.718 + \text{WHSV} * 35.3068 - \text{WHSV} * T^2 * 0.000166972 + T * 4.47515 - T^2 * 0.00561868 \end{aligned}$$

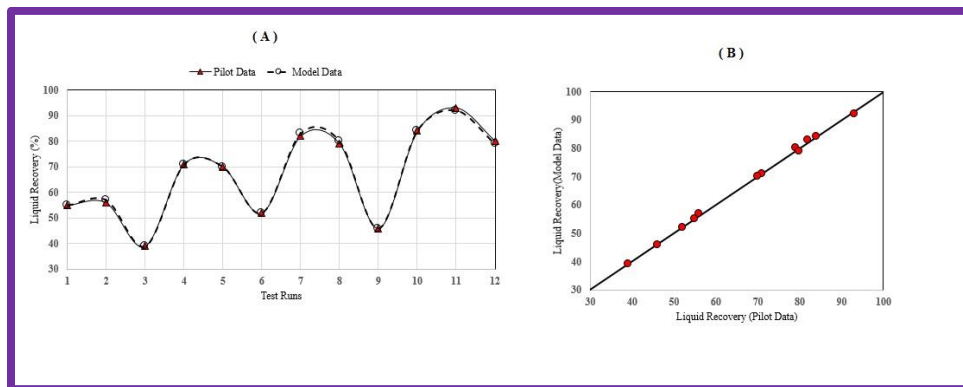


Figure 6. Comparison plots: A) Pilot liquid recovery vs. model data and B) Pilot liquid recovery vs. modeled

Table 7. Nodal expressions for GMDH neural network of removal sulfur conversion %

$$S \text{ Conversion} = -414.602 - B * A * 0.375169 + B * A^2 * 0.00137611 + A * 26.6726$$

$$A = 17.1374 + B^2 * 0.0104304$$

$$B = 328.735 - T * 0.679671 - T * P^2 * 0.000254402$$

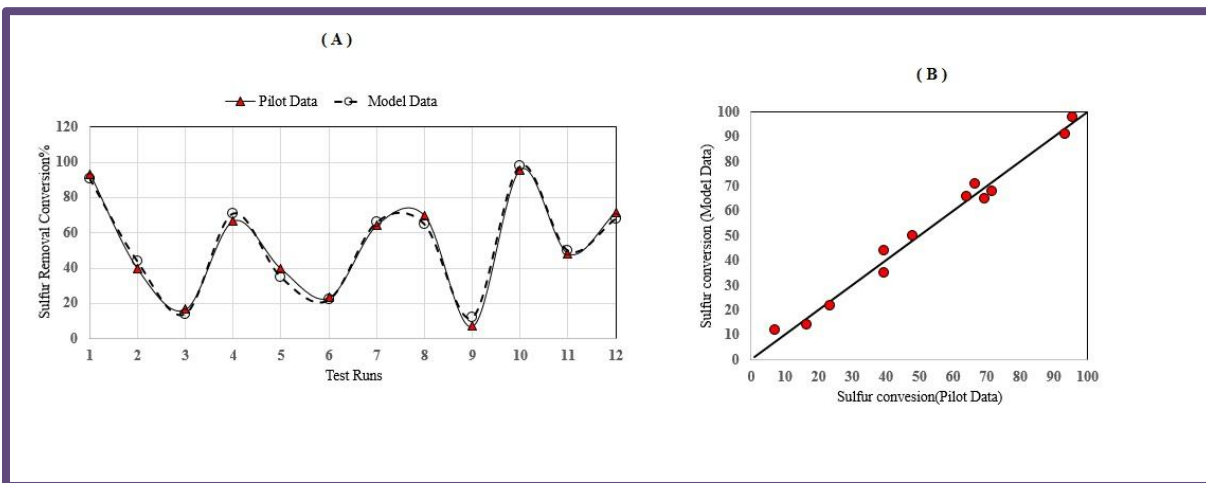


Figure 7. Comparison plots: A) Pilot vs. model data and B) sulfur conversion Pilot vs. modeled

The results show that this model can predict well the RON, benzene content in product, coke deposition, liquid recovery, sulfur conversion with the AAD % of 0.29%, 0.33%, 0.28%, 0.41 and 3.2 %, respectively. Moreover, the RMSE % of the mentioned variables are 0.34%, 0.41%, 0.41%, 0.64% and 3.4%, respectively.

It is supposed that the main deviation can be related to some factors including power fluctuation of instruments, calibration of analysis devices, human errors, and signal transmission that cannot be excluded from the collected data. However, from the presented results, it can be concluded that the proposed approach is reliable enough to be utilized for predicting the behavior of the heavy naphtha catalytic reforming unit.

5. Conclusion

In this work, a group method of data handling (GMDH) modeling approach was applied to predict and model significant output variables of a zeoforming unit on bench scale experiments. These process output variables were RON, benzene content in product, coke deposition, liquid recovery and sulfur conversion. Then, by using the proposed model, the influence of operating conditions variables were studied.

Twelve test runs were used to construct and train the GMDH network for the target zeoforming plant. It was concluded that a GMDH network with three neurons in the intermediate layer was satisfying to simulate output variables of zeoforming i.e. RON, benzene content in product, coke deposition, liquid recovery and sulfur conversion with small value of the AAD% and RSME%. Consequently, the GMDH can be a reliable and accurate tool to model zeoforming plant for sensitivity analysis, optimization and troubleshooting purposes without tackling the complexity of fundamental methods.

References

- [1] Stepanov VG, lone KG, and Snytnikova GP. Zeolite catalysts in the upgrading of low-octane hydrocarbon feedstocks to unleaded gasolines. *Catalysts in Petroleum Refining and Petrochemical Industries*, 1995; 477-482.
- [2] Kornblit L, Marchut EA, Jęczmionek L, Bozek S, Lenartowicz L, Mikrut G. *Petroleum & coal*, 2004; 46(3): 63-68.
- [3] Anunziata OA, and Pierella LB. Selective conversion of light gasoline into aromatic hydrocarbons over shape selective zeolites, I. Catalytic activity of various zeolites for aromatization of light gasoline, heavy gasoline and coker naphtha. *React. Kinet. Catal. Lett.*, 1993; 49(2): 311-317.

- [4] Samborskaya MA, Mashina VV, Cherednichenko OA, Makarovskikh AV. Modeling of reactor of straight-run gasoline fractions refining on zeolite catalysts. *Procedia Chemistry*, 2015; 15: 237-244.
- [5] Hodala JL, Halgeri AB, Shanbhag GV, Reddy RS. Aromatization of C5-rich Light Naphtha Feedstock over Tailored Zeolite Catalysts: Comparison with Model Compounds (n-C5-n-C7). *Chemistry Select*, 2016; 1: 2515-2521.
- [6] Ostrovskii NM, Rovenskaja SA, and Echevski GV. Aromatization of Light Naphtha Fractions on Zeolites. 2. Model of Catalyst Deactivation. *Chem Ind.*, 2004; 58(3): 104-108.
- [7] Rovenskaja SA, Ostrovskii NM. Aromatization of Light Naphtha Fractions on Zeolites. 1. Kinetic Model. *Chem Ind.*, 2003; 57(9): 399-403.
- [8] Stepanov VG, and Ione KG. Petrol Production from Virgin Fraction of oil and Gas Condensates with the use of Zeoforming Process. *Chemistry for Sustainable Development*, 2005; 13: 805-818.
- [9] Golmohammdi H, Rashidi A, Safdari SJ. Prediction of ferric iron precipitation in bioleaching process using partial least squares and artificial neural network. *Chem. Ind. Chem. Eng. Q.*, 2013; 19: 321-331.
- [10] Elkamel A, Al-Ajmi A, Fahim M. Modeling the Hydrocracking Process Using Artificial Neural Networks. *Pet. Sci. Technol.*, 1999; 17: 931-954.
- [11] Eslamloueyan R, Setoodeh P. Optimization of Fed-Batch Recombinant Yeast Fermentation for Ethanol Production Using A Reduced Dynamic Flux Balance Model Based on Artificial Neural Networks. *Chem. Eng. Commun.*, 2011; 198(11): 1309-1338.
- [12] Zahedi G, Fgaier H, Jahanmiri A, Al-Enezi G. Artificial Neural Network Identification and Evaluation of Hydrotreater Plant. *Pet. Sci. Technol.* 2006; 24(12): 1447-1456.
- [13] Joseph B, Wang FH, Shieh PS. Exploratory data analysis: A comparison of statistical methods with artificial neural networks. *Comput. Chem. Eng.*, 1992; 16(4), 413-423.
- [14] Milic P, Rajkovic KM, Milicevic PM, Milic SM, Brdaric TP, Pavelkic VM. Comparison, Artificial Neural Network Modeling and Genetic Algorithm Optimization of The Resinoid and Potassium Yields from White Lady's Bedstraw (*Galium mollugo* L.) By Conventional, Reflux and Ultrasound-Assisted Aqueous-Ethanol Extraction. *Chem. Ind. Chem. Eng. Q.* 2013; 19(1), 141-152.
- [15] Atashrouz S, Amini E, Pazuki G. Ionics, Modeling of surface tension for ionic liquids using group method of data handling. 2015; 21(6): 1595-1609.
- [16] Manamalli D, Kanagasabapathy P, Dhivya K. Expert Optimal Control of Catalytic Reformer Using ANN. *Chem. Eng. Commun.*, 2006; 193:729-742.
- [17] Sadighi S, Mohaddecy SR. *Int. J. Technol.*, Predictive modeling for an industrial naphtha reforming plant using artificial neural network with recurrent layers. 2013; 2: 1-11.
- [18] Ivakhnenko AG. *Polynomial Theory of Complex Systems*. IEEE Transactions on Systems, Man, and Cybernetics, 1971; 364-378.
- [19] Fujii K, Yamamoto T. Development of a Nonlinear Soft Sensor Using a GMDH Network for a Refinery. *Crude Distillation Tower Electr. Eng. Jpn.*, 2014; 188(6): 31-38.

To whom correspondence should be addressed: Reza Seif Mohaddecy, Catalysis Technologies Development Division, Research Institute of Petroleum Industry (RIPI), P.O. Box 14665-137, Tehran, Iran,
E-mail: seifsr@ripi.ir

Seismic Interpretation and Petrophysical Analysis of a Cretaceous Reservoir in Lower Indus Basin, Pakistan

Mohib Ullah¹, Shazia Asim¹, Yasir Bashir²

¹ Department of Earth Sciences, Quaid-e-Azam University, Islamabad, Pakistan

² School of Physics, Geophysics Section, Universiti Sains Malaysia, 11800 USM, Penang, Malaysia

Received June 26, 2020; Accepted October 15, 2020

Abstract

Seismic interpretation delineates the subsurface features (structural and stratigraphic) that are favorable for hydrocarbons' accumulation and Petrophysical analysis evaluates the reservoir characterization in detail. In this paper, 2D seismic data of the Hala area is used to study the structural traps that may be favorable for hydrocarbons. AdamX-01 well in the study area is producing. Petrophysical and facies analysis give information about the reservoir parameters. Interpretation incorporates well data. Sands of Lower Goru Formation (Cretaceous) act as a reservoir. Horst and Graben subsurface geological structures are delineated at reservoir levels by using TWT and depth structures maps. Chiltan Limestone Formation (Jurassic) is also marked and contoured in time and depth domains. The petrophysical analysis gives two potential zones with high hydrocarbon saturations. Facies modeling confirms reservoir sands. Integrating the geophysical techniques, possible hydrocarbons, and new potential zones are identified.

Keywords: Seismic interpretation; Petrophysics; Seismic attribute; Reservoir; Unconventional; Indus Basin.

1. Introduction

Seismic interpretation is the art and science of finding, identifying, correlating, and understanding the geological structure of the subsurface and its layering through geologic time using seismic data. Human seismic interpretation is not a linear process where a discrete search, identification, correlation, and understanding are sequentially performed, but rather, it is a global iterative process that combines these steps in a non-deterministic manner using information concealed in the seismic data [1]. For this purpose, well data is also incorporated, where the real geology is known. Therefore it is vitally essential to be in affinity with other information about the area, consisting of gravity, magnetic data, well data, and surface geology [2]. The seismic data uses bright spot amplitude anomaly as a hydrocarbons indicator. The reflection coefficient is a characteristic of acoustic impedance that exists due to strong lithological change [3]. Petro-physical interpretation is the well log evaluation of the estimation at the ratio of gas, oil, and water in the reservoir. Density can be an important parameter to differentiate lithologies and estimate other petrophysical properties, such as porosity or fluid content [4]. It is used to check the presence of hydrocarbons and other fluids. The hydrocarbon amount in the reservoir is the function of porosity and hydrocarbon Saturation of the reservoir. The efficiency of a reservoir depends upon permeability. On the groundwork concerning these strategies, hydrocarbon leads can be identified.

1.1. Geology of the study area

The southern Indus Basin is characterized as an extensional basin by the tectonic uplifting of the western margin concerning the Indo-Pak plate. Structural fashion reflects gradual development over the sedimentary basin regarding Pakistan. Pakistan encompasses a couple of sedimentary-basins, (1) Indus-basin and (2) Baluchistan-Basin, which flourished within different geological periods through the Cretaceous /Paleocene along the strike-slip fault named

as Ornach-Nal/Chaman fault. Indus-Basin is further divided among (a) Upper Indus Basin (b) Lower Indus Basin which is further divided into Central Indus Basin and Southern Indus Basin, based on the structural administration and petroleum potentialities [5].



Figure 1. Boundaries of the Southern Indus Basin

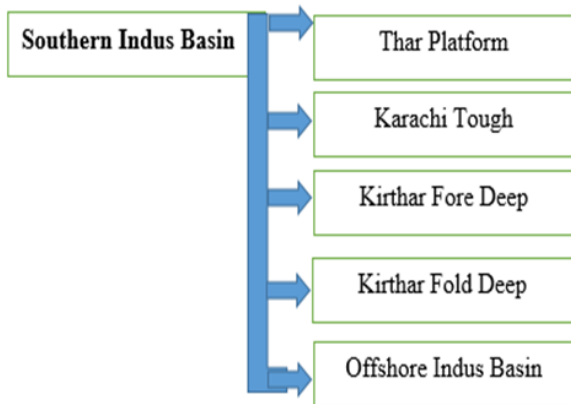


Figure 2. Classification of Southern Indus Basin

Lower-Indus basin includes the greatest gas producing fields of Indus Basin and covers the southern section of Pakistan. The study area is located in DADHAR District Sindh and is called HALA Block with the location of Latitude-25°48'43"N and Longitude-68°25'45" E and elevation of 27.84 m above mean sea level.

Southern Indus Basin is limited in North by the Middle Indus Basin, in East with the Indian shield, the Axial Belt in the west and Offshore Area in the south [5] (Figures 1 and 2). Sukkur Rift divides Lower Indus basin into Central Indus basins and Southern Indus basin. By Zaigham and Mallick [6] Southern basin lies in extensional regimes, horst and graben structures are formed throughout the basin which affects the hydrocarbons generation, migration, and trapping mechanism. The sands of Lower Goru Formation of Cretaceous age act as a reservoir in Lower Indus Basin (Figure 3). Southern Indus basin has been divided into five units (Figure 3).

SYSTEM	SERIES	FORMATION	LITHOLOGY	HYDROCARBON SIGNIFICANCE				
				NOMENCLATURE	RESERVOIR	SOURCE	SEAL	No. of DISCOVERIES
TERTIARY	HOLOCENE	ALLUVIUM	ALLUVIUM	ALLUVIUM				
		GAJINARI	NARIGAJ UNDIFF SAND/SHALE					
	EOCENE	KIRTHAR	KIRTHAR LIMESTONE					
		LAKI	LAKI SHALE					
	PALEOGENE	RANIKOT	RANIKOT SAND					
KHADRO		VOLCANIC/BASALT KHADRO SAND						
CRETACEOUS	UPPER	UPPER GORU	UPPER GORU SHALE					
		LOWER	UPPER SANDS				45	
	UPPER SHALE							
	MIDDLE SANDS					6		
	LOWER SHALE					1		
	BASAL SANDS				7			
SEMPAR	SEMPAR SANDS & SHALES							
JURASSIC	UPPER							
	MIDDLE	CHILTAN	CHILTAN LIMESTONE					
	LOWER	SHINAWARI/DATTA	LIASSIC SAND					

Figure 3. Generalized stratigraphy of Lower Indus basin [7]

2. Database and methodology

2.1. Data used in research work

2D Seismic and well data of the HALA area is obtained from LMKR on the special approval from DGPC and Dept. of Earth Sciences, QAU. The 2D seismic lines and well data concerning the HALA area are shown in Tables 1, 2, and 3.

Table 1. Total number of dip & strike lines and wells data in 2D survey

Line Name	Line Type	Line Name	Line Type
GPPL04-HAL_04	Dip Line	GPPL04-HAL_16	Dip Line
GPPL04-HAL_06	Dip Line	GPPL04-HAL_01	Strike Line
GPPL04-HAL_08	Dip Line	GPPL04-HAL_05	Strike Line
GPPL04-HAL_10	Dip Line	GPPL04-HAL_07	Strike Line
GPPL04-HAL_12	Dip Line	GPPL04-HAL_09	Strike Line

Table 2. Well in the study area

Well Names	Latitude (Degree)	Longitude (Degree)	Start depth (m)(KB)	End depth (m)	Status
AdamX-01	25 0 49' 1"	68036'37"	31	3566	GAS/CON

Table 3. Well Logs Detail of Adamx-01

Logs	AdamX-01	Logs	AdamX-01
GR	Present	DT	Present
SP	Present	MSFL	Present
CALI	Present	LLS	Present
NPHI	Present	LLD	Present
RHOB	Present		

2.2. Base map

The base map shows seismic lines with shot points' annotations, well location AdamX-01, and grid information. Geophysicist generally utilizes maps which exhibit the orientation regarding seismic lines or specific points at which seismic records (data) had been acquired (Figure 4).

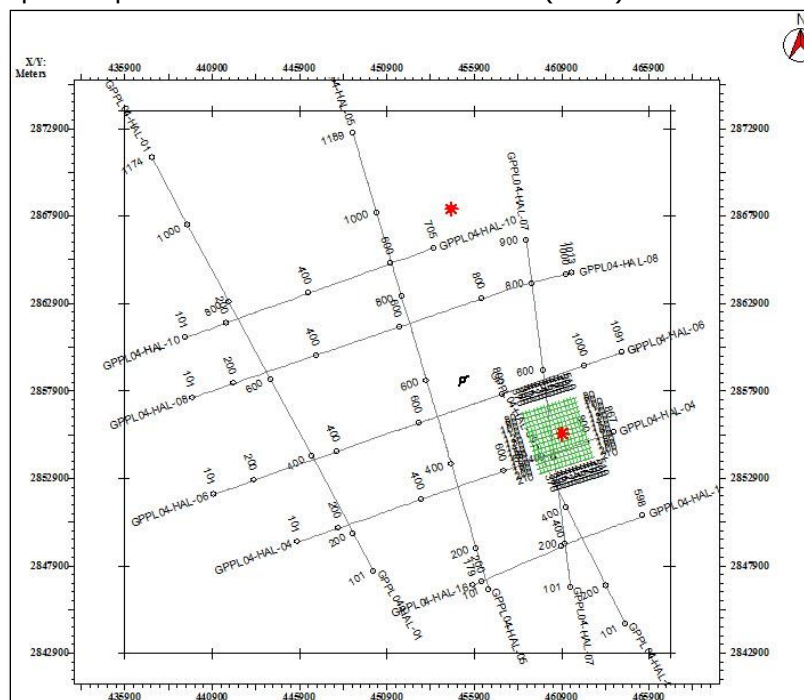


Figure 4. Base map of the area showing location and orientation of seismic lines

2.3. Methodology

The synthetic seismogram is a 1D forward model regarding the acoustic model of the earth. It is estimated by convolution over the reflection coefficient computed from sonic and density logs along the wavelet extracted out of seismic data [7-9]. The Synthetic seismogram over AdamX-01 well, generated and the correlated to different horizons on seismic. Different faults have been marked with the aid of viewing lateral discontinuity of the horizons. The time contour map at Lower Goru Formation (Middle sand, Upper Basal sand, Lower Basal sand) and Chiltan Limestone are constructed by selecting the time of seismic horizons against every shot point. The velocity from TD chart is calculated and the depth contour maps are generated.

For petrophysical analysis, different logs are used such as 1st lithologic track (GR, SP, and HCALI log), 2nd Resistivity track (RLA5 (LLD), RLA3 (LLS), RXO (MSFL) logs) and 3rd porosity track (DT, RhoB, TNHI logs). The petrophysical analysis is done in order to find different reservoir properties. First of all volume of shale is calculated from GR log after that Sonic porosity, average porosity, and effective porosity is calculated and then the water saturation and hydrocarbons saturation is computed in the reservoir zones. The logs are further analyzed for the identification of different possible resources plays and mature source rock formation using Δ log R technique then the modified Δ log R technique [10].

3. Results and discussions (seismic lines)

Lower Indus Basin holds its significance for gas-bearing reservoirs at various levels. Various studies have been carried out at these reservoirs [11-16]. Hala area is relatively less explored and production from AdamX-01 shows potential for further exploration. Subsurface structures favor promising leads for prospect generation and well developments.

3.1. Interpretation of GPPL 04-HAL-04, GPPL04-HAL-06

Horst and graben structures are marked on seismic lines. Four major faults and some minor step faults are present. Three horizons of Lower Goru Formation; Middle Sand, Upper Basal Sand, Lower Basal Sand, and one horizon of Chiltan limestone Formation, are marked on the seismic line GPPL 04-HAL-04 at TWT 1.835Sec, 2.072Sec, 2.135Sec and 3.26Sec respectively. The time over the Horizons increases west to east which indicates that the direction of sedimentation is east to west. The two horst and two graben structures are formed and well was drilled on the horst structure. While on the line GPPL04-HAL-06 three horst and two graben structures are formed. The horizons are marked at the time at 1.89Sec, 2.16Sec, 2.25Sec, and 3.25Sec respectively. The seismic lines GPPL04-HAL-04 and GPPL04-HAL-06 are dip lines and all horizons and faults marked are shown in Figure 5 and 6.

3.2. Interpretation of GPPL04-HAL-08, GPPL04-HAL-10

The same horizons are marked on GPPL04-HAL-08 and GPPL04-HAL-10. These are east-west oriented dip lines in the Northern part of the study area. The seismic two way travel time for the horizons on GPPL04-HAL-08 is 1.76Sec, 2.009Sec, 2.10Sec, and 3.13Sec respectively. The horizons on the line GPPL04-HAL-10 are at the TWT of 1.84Sec, 2.139Sec, 2.25Sec, and 3.38Sec respectively. Similar series of Normal faults are marked as in previous seismic lines. The interpreted seismic lines are shown in Figures 7 and 8.

3.3. Interpretation of GPPL04-HAL-16

GPPL04-HAL-16 is an east-west oriented dip line in the Southern part of the Hala area. Horizons marked on the line have TWT of 2.11Sec, 2.31Sec, 2.42Sec, and 3.31Sec respectively. Similar series of faults are marked as in previous lines forming horst and graben structures. The interpreted seismic line is shown in Figure 9.

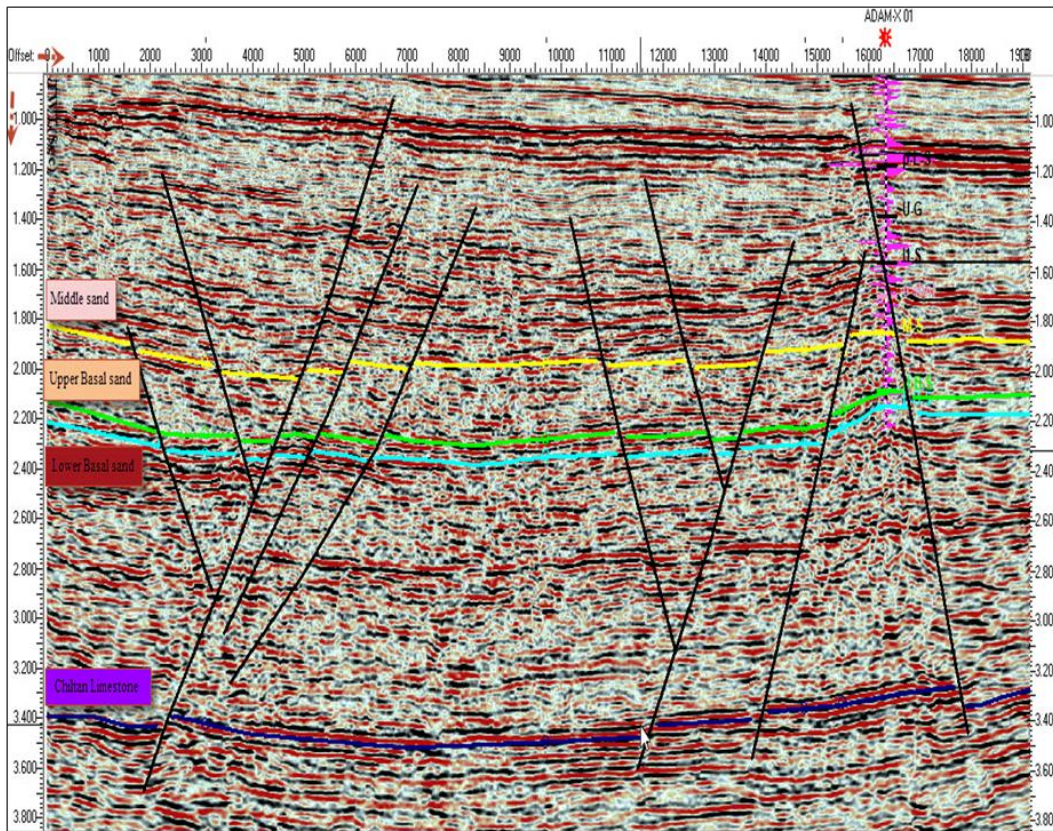


Figure 5. Marked seismic line GPL04-HAL-04

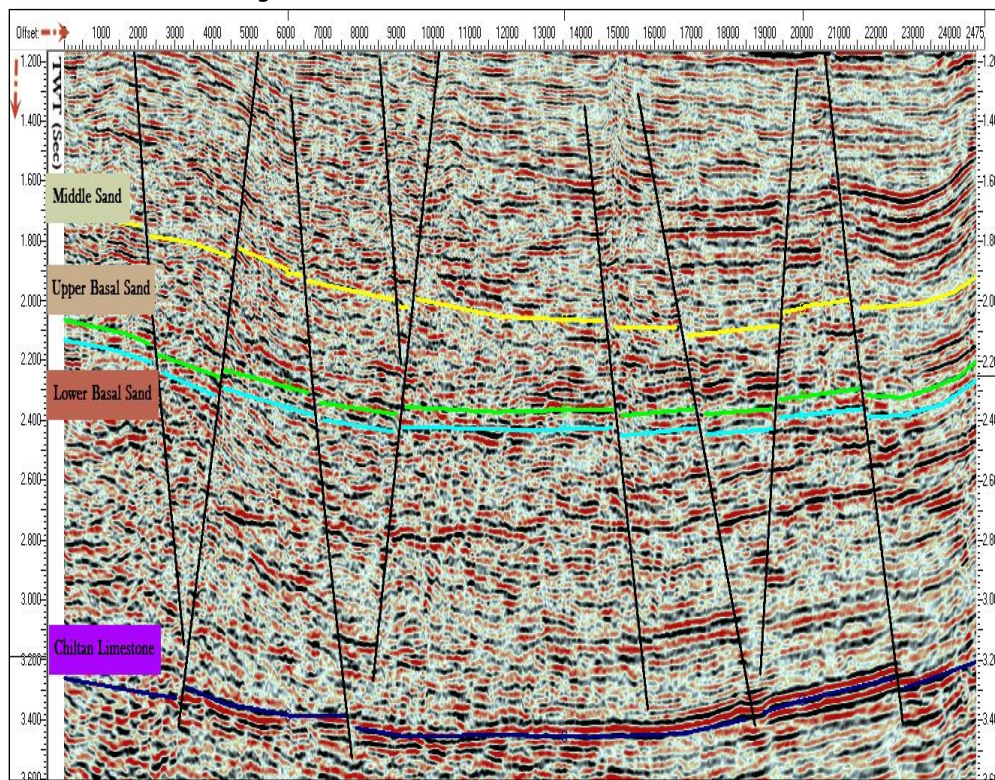


Figure 6. Interpreted seismic line GPL04-HAL-06

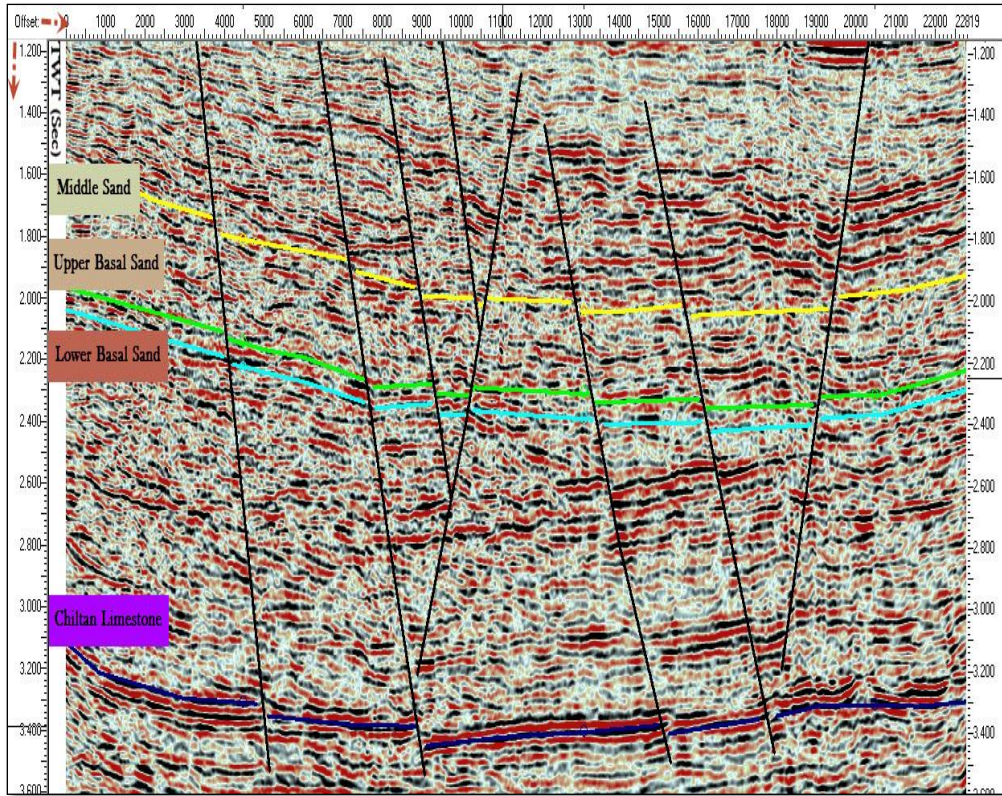


Figure 7. Interpreted seismic line GPPL04-HAL-08

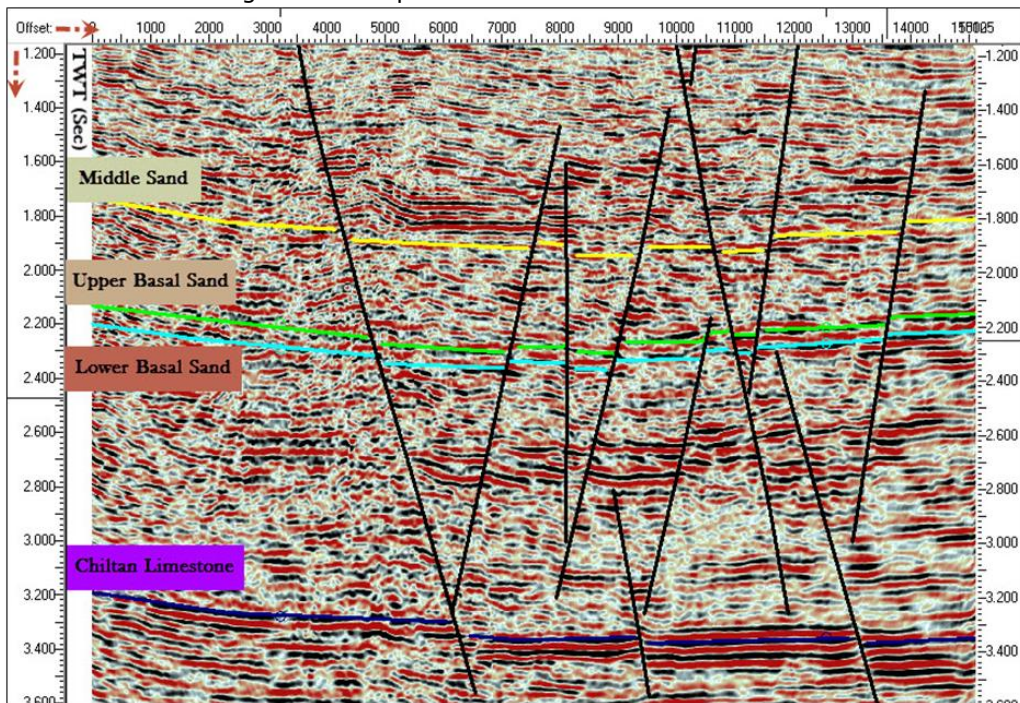


Figure 8. Interpreted seismic line GPPL04-HAL-10

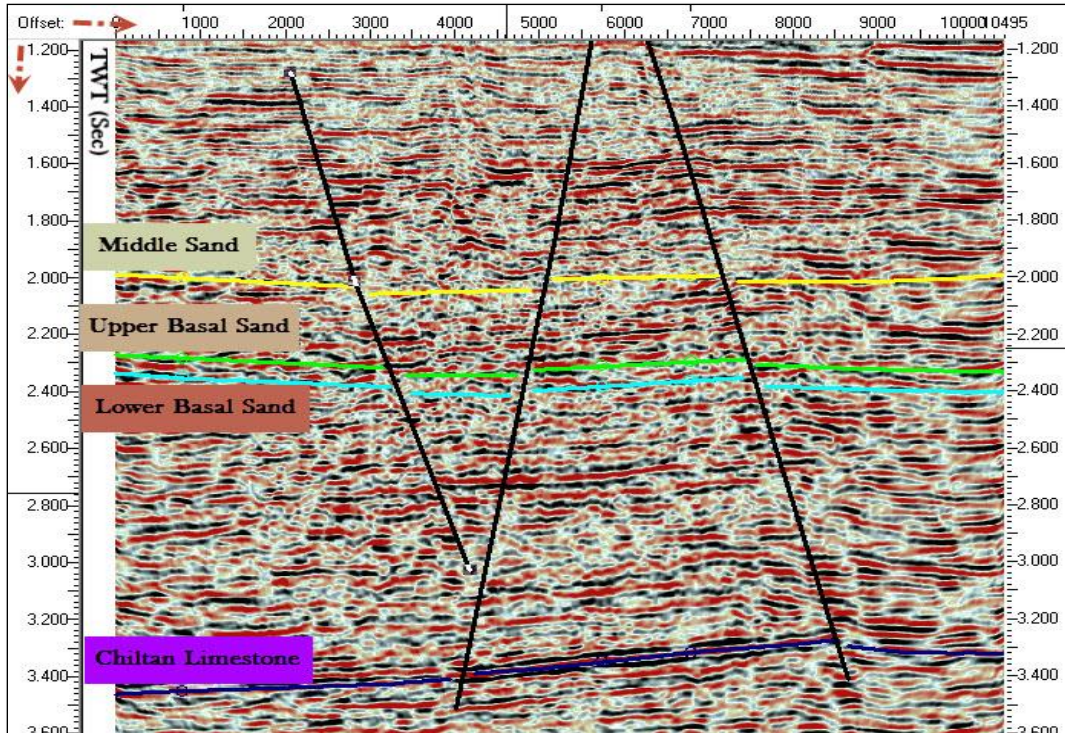


Figure 9. Marked seismic section of line GPPL04-HAL-16

3.4. Fault correlation

In this study, seven major faults are correlated on the base map for horizons of Upper Basal Sand and Lower Basal Sand of Lower Goru Formation. These faults are forming horst and graben structures and a well is drilled at horst structure. The faults polygon maps are constructed for F1, F2, F3, F4, F5, F6, and F7 at different horizons (Figures 10 and 11).

3.5. Time contours maps

The contour maps summarize the interpretation work. These maps are called contour maps as like the imaginary lines which join points of equal time or depth or any other variables [16]. Contours are the 3D representation of the 2D surface. The close contour values indicate steep gradients, increased values show depression, and vice versa. Hence these contours essentially show the slope/dip or structural relief of that formation. Time contour maps are generated for four horizons (Figures 12 to 15).

3.6. Time map of middle sand

The time contour map of middle sand is shown in Figure 12. The contour shows the deepest section on the Horizon within the time 1.977-2.116 seconds is at graben and the shallowest section is toward the western side of the formation up in accordance with 1.596-1.699 seconds. A three-way closure is formed between purple (F4) and green (F5) fault and that can be a potential structural trap for hydrocarbon.

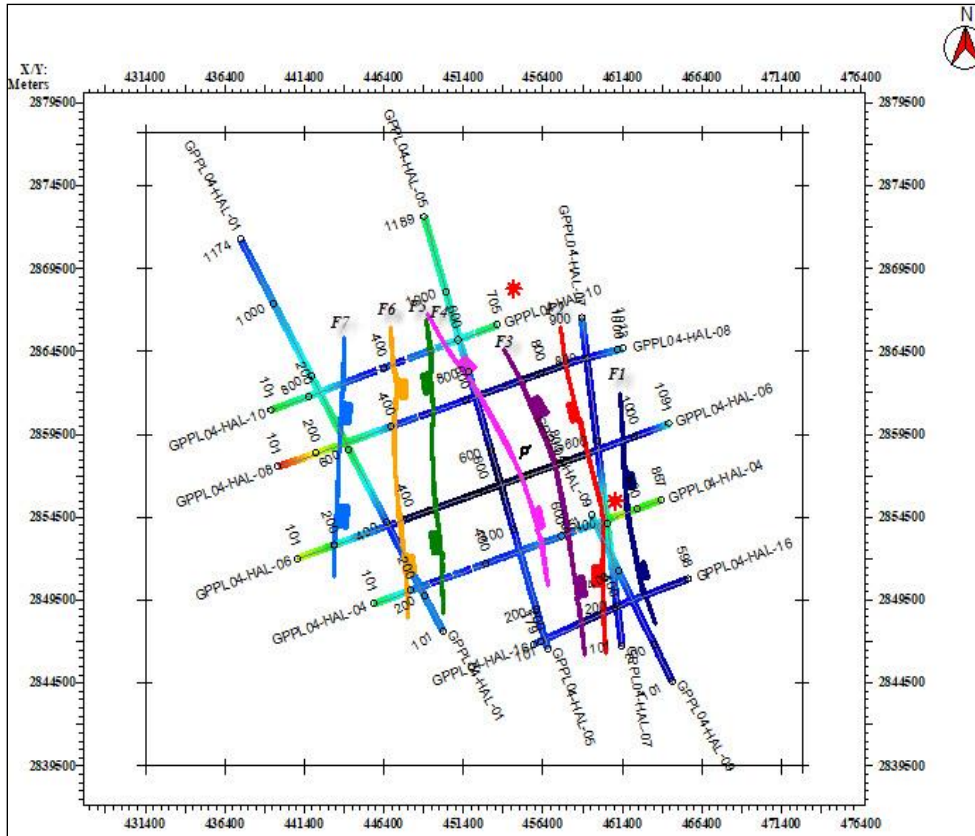


Figure 10. Faults polygon on base map F1, F2, F3, F4, F5, F6, F7 of Upper Basal Sand

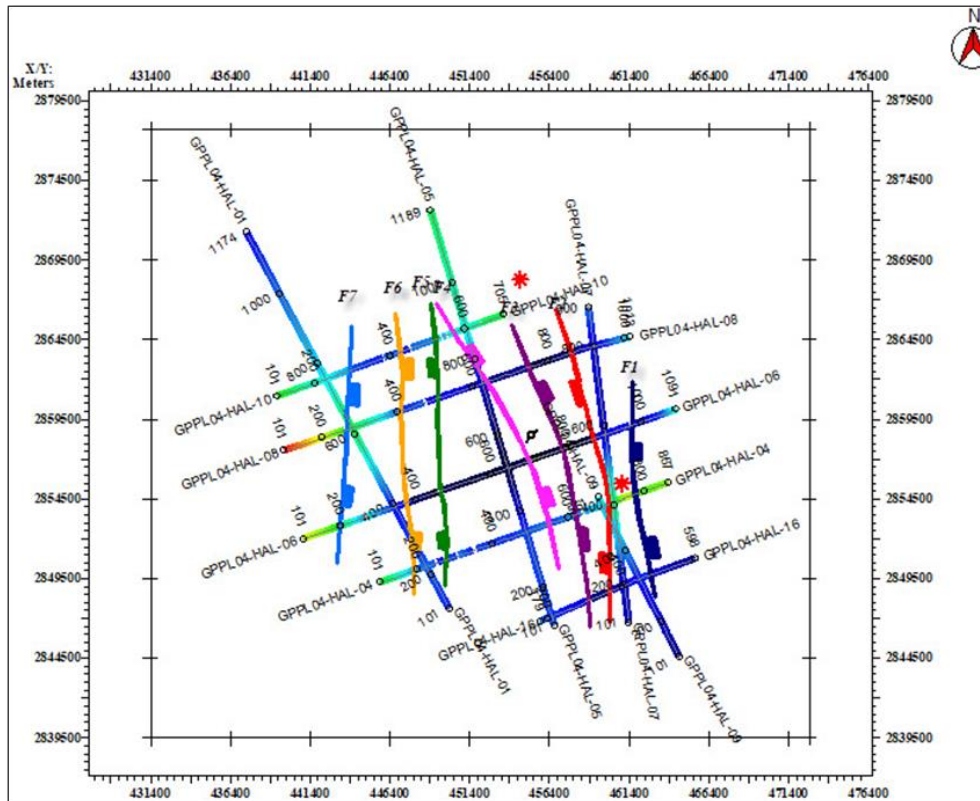


Figure 11. Faults polygons F1, F2, F3, F4, F5, F6, and F7 (right to left) of Lower Basal Sand

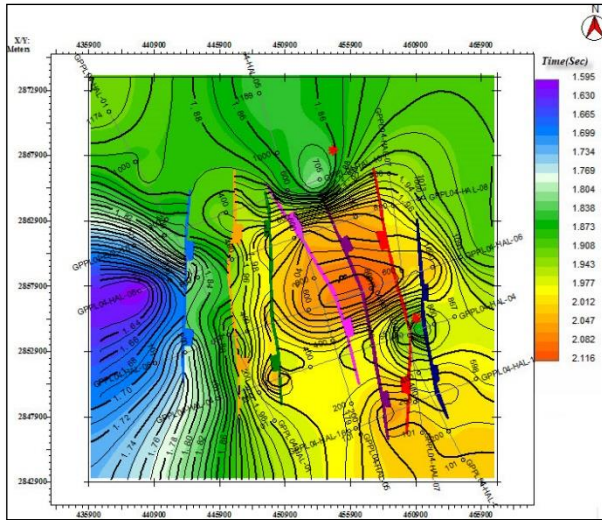


Figure 12. Time contour map of middle sand

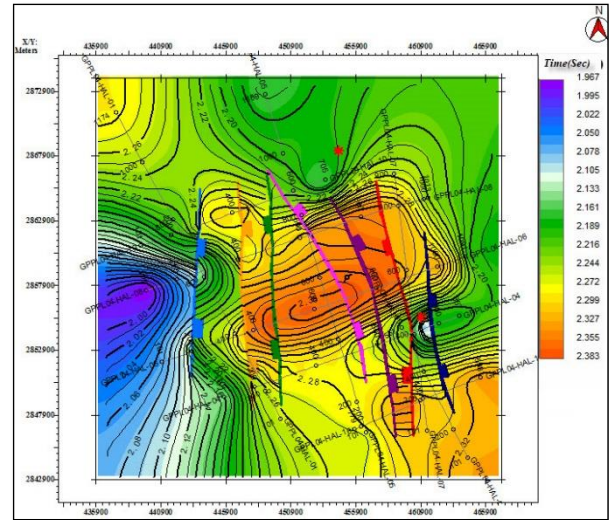


Figure 13. Time Contour Map of Upper Basal Sand

3.7. Time map of Upper Basal Sand

The time contour map of upper basal sand is prepared at 0.010 seconds (10 milliseconds) contour intervals. The time contour shows the highest time 2.272-2.283 seconds at graben on the east side the shallow part is toward the west at time 1.967-2.078 second. Seven faults have been correlated. A well is drilled at three-way closure beside F1 and a lead can be marked close to F4 at a similar closure (Figure 13).

3.8. Time map of Lower Basal Sand

The time contour chart on the main reservoir lower basal sand is organized by means of SMT Kingdom software. The time contour shows the deep part of the horizon with time above in accordance with 2.341-2.451 seconds is at widespread graben between the east side aspects while the shallow part is toward the west with time 2.038-2.148 second. Similar faults are correlated at the top of Lower Basal Sand (Figure 14). A well is present at the horst structure bounded by F1 and F2. A potential horst structure is bounded by F4 and F5.

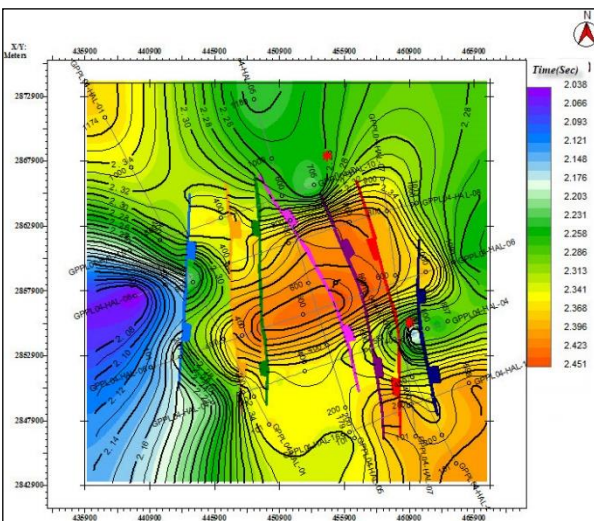


Figure 14. Time Contour Map of Lower Basal Sand

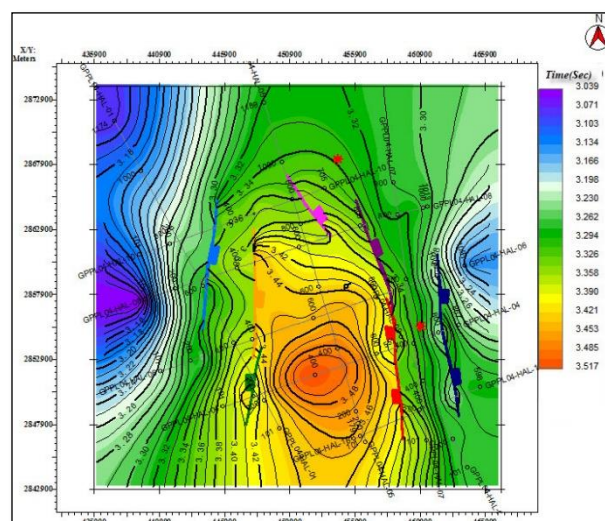


Figure 15. Time Contour Map of Chiltan Limestone Sand

3.9. Time Contour Map of Chiltan Limestone

The contour map generated for Chiltan limestone shows a graben structure in the center of the area (Figures 15). Chiltan is an outstanding reflector that acts as good reservoir at several locations with shales providing a seal at the top and a presence of source at a deeper level where it attains good maturity [12-14].

3.10. Depth Contour Maps

Figures 16 to 19 show the depth contour maps of middle sand, upper basal sand, and lower basal sand and Chiltan Formation. Depths are calculated using the time values and velocities calculated from DT-log at four horizons by simple relation $S=V*TWT/2$. The main reservoir in the Hala area is Lower basal sand and Talhar shale act as a seal.

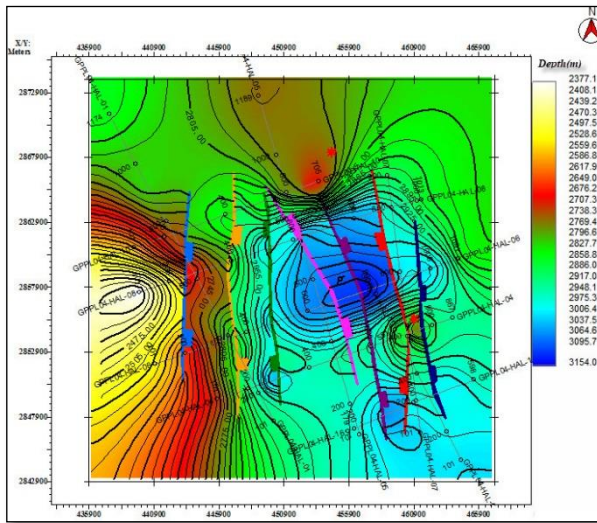


Figure 16. Depth Contour Map of Middle Sand

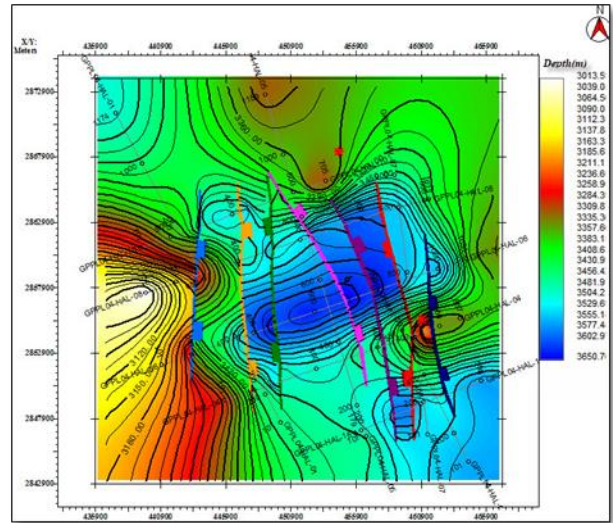


Figure 17. Depth Contour Map of Upper Basal sand

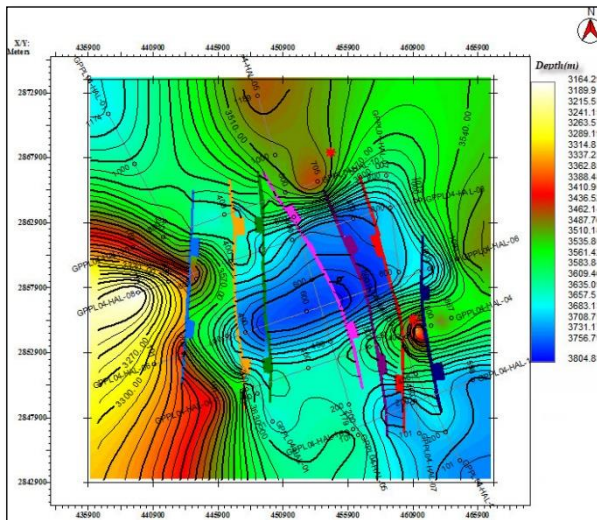


Figure 18. Depth Contour Map of Lower Basal Sand

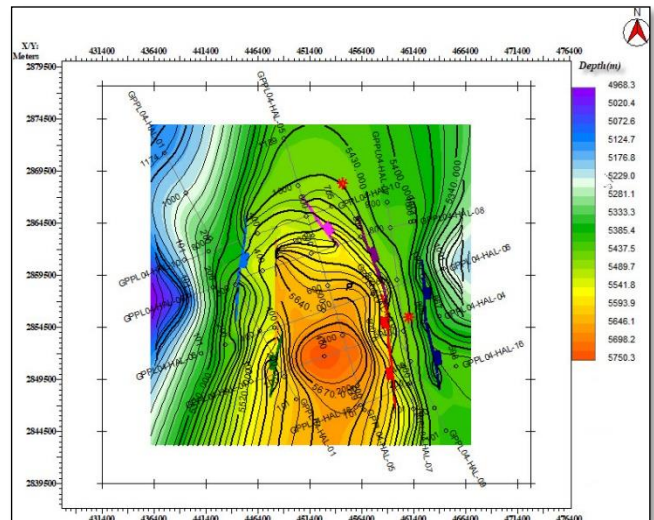


Figure 19. Depth contour map of Chiltan Limestone

Chiltan Formation is the most outstanding and prominent formation in the Lower Indus Basin. The depth structural map with seven faults has been plotted. The depth contour maps concerning middle sand, upper basal sand, and lower basal sand ranges from 2377-3154m, 3014-3651m, and 3165-3804m respectively and over Chiltan Formation the depths range

4100-4800m. The 2D & 3D Depth contour maps of the above-mentioned horizons are shown in Figures 16, 17, 18, and 19 respectively.

4. Petrophysical analysis

The petrophysical studies are related to the physical characteristics of rocks along with the fluid behavior relationship in the rock body, such as permeability, porosity, and density. These properties directly affect the fluid movement within the rock body. These properties are also directly linked with the zone of interest called reservoir rock, which is the basic objective of this chapter for detailed analysis. These analyses are done through well log data. The results of this limited area are implemented in the whole reservoir.

These petrophysical properties are used to detect and quantify the volume of hydrocarbons in the wells and implemented in the whole area of interest. The quantity of hydrocarbons in a reservoir, the amount required, is no longer through log directly, as instead are the best guess by relation.

4.1. Data Set

The dataset includes different log curves that are mostly presented in different tracks for analysis. In the First track, Gama Ray log, SP log, and caliper log, whereas Resistivity logs (LLD, LLS, and MSFL) are used in the second track. Sonic log (DT), Density log, and Neutron log are placed in the third track. The first track is called lithology track, the second track is called resistivity track and the third track is called porosity track.

Parameters determined are as follows;

- The volume of shale.
- Porosity.
- The resistivity of water in the reservoir.
- Water saturation.
- Hydrocarbons saturation.
- The probable hydrocarbon zone from where these Hydrocarbons can be extracted.

4.2. Results and discussion (Adamx-01 Well)

All the available log data is used to interpret the well (Adamx-01). Different petrophysical properties as the volume of shale, porosities (density derived porosity, sonic derived porosity, average porosities, and effective porosity), water saturation, a bulk volume of water, and finally the hydrocarbon saturation are computed. These parameters are explained in Figure 20. Three zones are selected after the detailed analysis of all logs in Lower Basal Sands of Lower Goru Formation and their derived results are given in Table 4.

Table 4. Petrophysical properties of Zones in Study area

Petrophysical properties of Zone 1		Petrophysical Properties of Zone 2	
Depth Range	3389m-3402m	Depth Range	3440m-3452m
Thickness	13m	Thickness	12m
Sonic Porosity	14%	Sonic Porosity	14%
Average porosity	21%	Average Porosity	21%,
Effective Porosity	13%	Effective Porosity	14%
Water Saturation	47%	Water Saturation	15%,
Hydrocarbon Saturation	53%	Hydrocarbon Saturation	85%,
Petrophysical Properties of Zone 3			
Depth Range	3510m-3522m		
Thickness	12m		
Sonic Porosity	13%,		
Average Porosity	16%,		
Effective Porosity	9%		
Water Saturation	13%,		
Hydrocarbon Saturation	87%,		

Similarly, the zone-2 has more clean sands as shown by GR and volume of shale curves. The porosity logs show greater porosity values in this zone of interest. The possibility of fluid presence is given by the crossover values between density and neutron density logs.

In 3rd zone of interest, GR and volume of shale show a high percentage of sand. The water saturation and hydrocarbon saturation are 13% and 87% respectively. The porosities are good. The crossover of values between the density log and neutron density log show light hydrocarbon is present in the zone of interest. The zone-2 and zone-3 are more suitable as compared to zone-01.

4.3. Facies modeling

Facies are mostly considered as bodies of rocks that show some specific characters but ideally, these are rock units that form under a certain condition of sedimentation, displaying a particular process or environment of deposition. Various kinds of facies are identified based on structure, composition, and sedimentary texture. Different types of sedimentary environments are known such as, a continental includes glacial, alluvial fan, river channel, floodplain, aeolian, and lacustrine environments. Transitional (shoreline) environment includes delta, beach, Barrier Island, lagoon, and tidal flats. The marine environment includes coral reefs and submarine facies. Each unit (facies) possesses a distinctive set of characteristics reflecting the condition in a particular environment. The facies reflect a high energetic and low energetic hydrodynamic condition that is either related to gradually increasing water depths or are produced by superimposed high energy events, for instance, during storms.

Facies model provides additional aid to the understanding of the sedimentary environment. Different models can be made to explain a given set of data, depending on which aspect of the facies should be highlighted most to get much information about it.

4.4. Facies Analysis of Adamx-01 well

The facies modeling of Lower Goru formation in Adamx-01 well shows interbedded shale and sandstone. A depth range of Lower Basal Sand from 3400 to 3460m is selected for facies analysis that acts as a reservoir in the project area. Three log curves are used for the facies modeling that is RHOB (unit: gram per centimeter cube and value range from 2.3-3) on x-axis, LLD (unit: ohm-m and value range from 0-200) on y-axis and GR (measured as count per second and its range is 30 to 250 in API) is coded on z-axis (Figure 21). The interbedded sands are clearly defined with low values of GR, high values of LLD matching with the Zone-2 of petrophysical analysis.

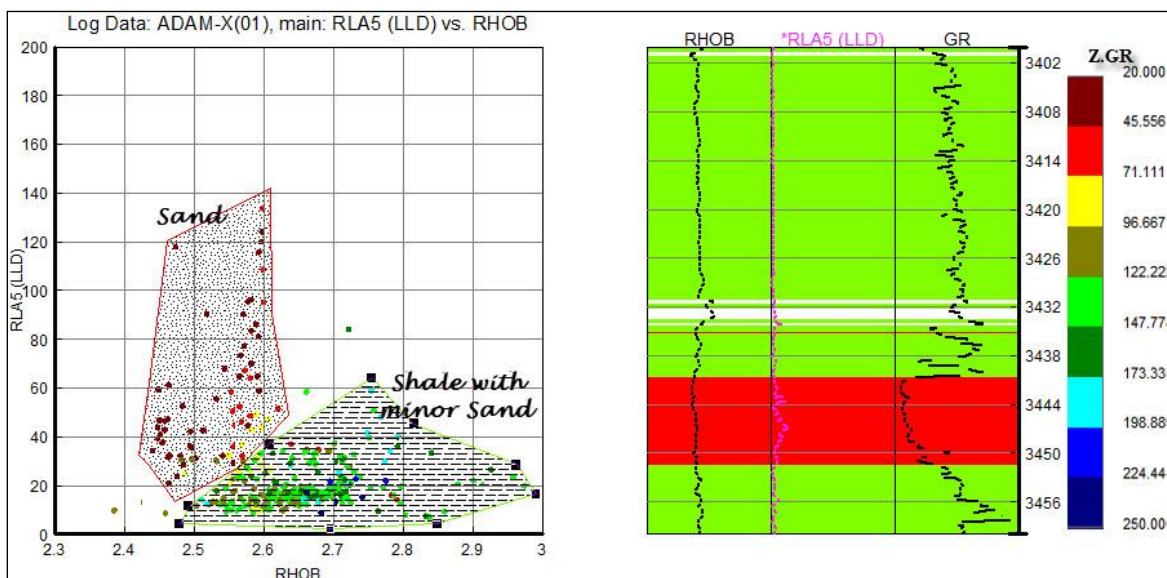


Figure 21. Cross Plots of RHOB, GR, LLD Logs at Reservoir Level (Adamx-01 Well)

4.5. Cross-Plot of Neutron and Density log

In the petrophysical interpretation, neutron and density plots are widely used for lithology discrimination. The cross plots are generated for the reservoir zone i.e. Lower Basal Sand (3400 m to 3460 m) in Adamx-01. Cross plot for the productive zones of the well is displayed in Figures 22. The values for the sands and shale are clearly separated from each other.

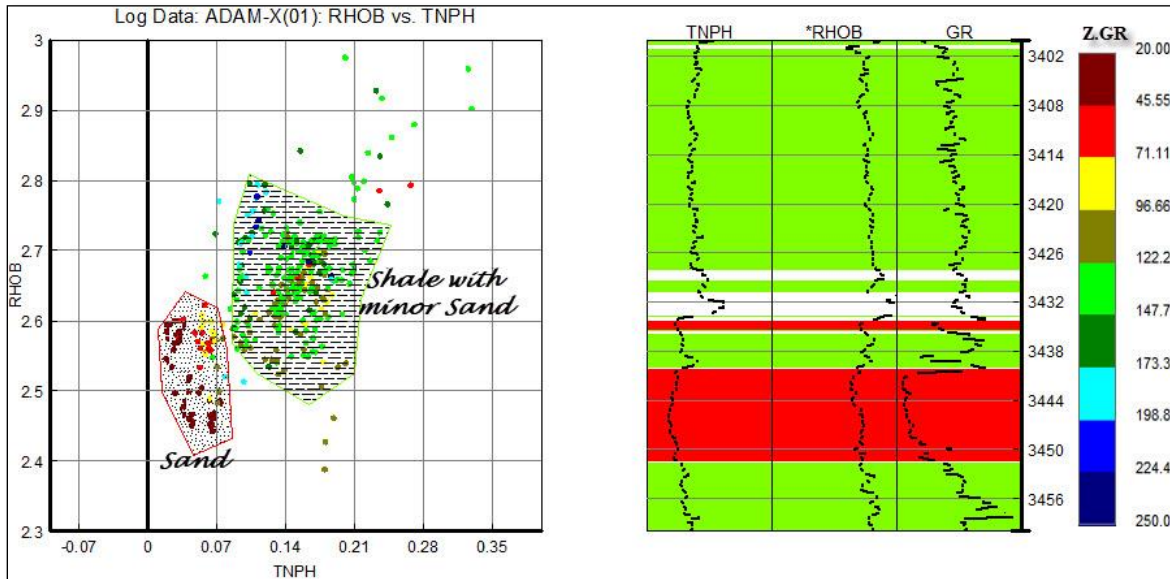


Figure 22. Cross Plot of TNPHI, GR, RHOB at Reservoir Level (Adamx-01 Well)

5. Conclusions

The principal purpose of this research was to interpret structures, identify lithology, and delineate recent prospect zones within the study area for optimum field development. Structural interpretation indicates normal faulting in the Hala area. It is confirmed that North-South trending horst and graben structures are present, indicating extensional regime due to rifting of Indian plate from African plate during Jurassic and early Cretaceous.

Contour maps of Lower Goru formation exhibit closures at the center portion. Petro-physical analysis of AdamX-01 confirms the significant porosity and amount of hydrocarbons that is economically favorable for exploration in Basal Sands of Lower Goru Formation.

Acknowledgment

The authors would like to acknowledge, Department of Earth Sciences, QAU, Islamabad for providing research facilities; Directorate General of Petroleum Concessions (DGPC, Pakistan), and LMKR for providing data set to perform this research. We also want to thank for collaborative research with the School of Physics, Geophysics section at Universiti Sains Malaysia (USM).

References

- [1] Imhof M, and Xu P. Method for seismic interpretation using seismic texture attributes. WO2011005353A1.
- [2] Kearey P, Brooks M, and Hill I. An introduction to geophysical exploration. John Wiley & Sons, 2013, ISBN: 978-0-632-04929-5.
- [3] Telford WM, Geldart LP, and Sheriff RE. Applied geophysics. Cambridge University Press, 1990.
- [4] Quijada MF and Stewart RR. Density estimations using density-velocity relations and seismic inversion. CREWES Res Rep, 2007; 19: 1-20.
- [5] Khan MA, Ahmed R, Raza HA, and Kemal A. Geology of petroleum in Kohat-Potwar depression, Pakistan. Am. Assoc. Pet. Geol. Bull., 1986; 70(4): 396-414.

- [6] Zaigham NA, and Mallick KA. Prospect of hydrocarbon associated with fossil-rift structures of the southern Indus basin, Pakistan. *Am. Assoc. Pet. Geol. Bull.*,2000; 84(11): 1833–1848.
- [7] Bashir Y, Ghosh DP, Weng Sum C, and Janjuhah HT. Diffraction Enhancement Through Pre-Image Processing: Applications to Field Data, Sarawak Basin, East Malaysia. *Geosciences*, 2018; 8(2): 74, 2018.
- [8] Bashir Y, Ghosh DP, Weng Sum C. Influence of seismic diffraction for high-resolution imaging: applications in offshore Malaysia. *Acta Geophys.*, 2018; 66: 305–316.
- [9] Bashir Y, Ghosh DP, Weng Sum C, and Mahgoub M. Depth imaging using innovative algorithm for high-resolution seismic. in *RDPETRO 2018: Research and Development Petroleum Conference and Exhibition*, Abu Dhabi, UAE, 9-10 May 2018, 2018, pp. 20–23.
- [10] Alam MSM, Wasimuddin M, and Ahmad SSM. Zaur Structure, A Complex Trap in a Poor Seismic Data Area. in *BP Pakistan Exploration & Production Inc. Annu. Tech. Conf.(ATC)*, Islamabad, Pakistan, November, 2002, pp. 2–4.
- [11] Asim S, Qureshi SN, Mirza Q, Saleem U, Ali S, Haroon M, Tahir M. Structural and stratigraphical interpretation of seismic profiles along Safed Koh trend (Eastern part of Sulaiman fold belt), Pakistan. *Univers J Eng Sci*, 2014; 2(4): 77–95.
- [12] Munir A, Asim S, Bablani SA, and Asif AA. Seismic data interpretation and fault mapping in Badin Area, Sindh, Pakistan. *Sindh Univ. Res. Journal-SURJ (Science Ser.)*, 2014; 46(2): 133-142.
- [13] Asim S, Khan N, Qureshi SN, Hussain F, and Bablan SA. Study of a Stratigraphic Trap of Paleocene/Late Cretaceous Age with the Help of Seismic Data in Sulaiman Foredeep and Kirthar Foredeep Area (Central & Southern Indus Basin, Pakistan). *Int. J. Geosci.*, 2014; 5(10): 1049.
- [14] Asim S, Bablani SA, Hussain M, Abbasi SA, Qureshi SN, and Asif SK. Petrophysical and Well Log Evaluation of Dry Holes in Fort Abbas area, Punjab Platform, Pakistan. *Sindh Univ. Res. Journal-SURJ (Science Ser.)*, 2016; 47(1): 5-8.
- [15] Asim S. Study of crustal variations in the part of Central Indus Basin with the help of integrated geophysical data. PhD Thesis Quaid-i-Azam University Islamabad, 2009.
- [16] Coffeen JA. *Seismic exploration fundamentals*. Pennwell Books (January 1, 1895), ISBN 10: 0878142959.

To whom correspondence should be addressed: Dr. Yasir Bashir, School of Physics, Geophysics Section, Universiti Sains Malaysia, 11800 USM, Penang, Malaysia, E-mail: yasir.bashir@usm.my